

Chronologies and palaeoenvironments of humid phases in the western Nefud Desert, Saudi Arabia over the past 500 ka

Richard Clark-Wilson

**Thesis submitted for the degree of Doctor of Philosophy,
Royal Holloway University of London**

September 2020

**Institution of study:
Centre for Quaternary
Research
Department of Geography
Royal Holloway
University of London**

Declaration of Authorship

I, Richard Clark-Wilson, hereby declare that this thesis and the work presented in it is entirely my own. Where I have consulted the work of others, this is always clearly stated.

Signed: R.L.Clark-Wilson

For Mum

Acknowledgements

First and foremost, I would like to thank my supervisors Professor Simon Armitage and Professor Ian Candy for the great deal of support and encouragement over the past four years. I would also like to thank Dr Alice Milner for her support as my advisor and to the CQR research group and fellow PhD candidates for making the department a great place to do research. I would also like to thank the Palaeodeserts team led by Professor Mike Petraglia and Dr Huw Groucutt along with our Saudi collaborators. The two field seasons in which I participated provided a wealth of experience and numerous insightful discussions. I would like to thank Dr Paul Breeze (KCL) for help with GIS, and Dr David Ryves (Loughborough) and Dr Wing Wai Sung (NHM) for their work in diatom analysis. Thanks also go to Dr Adrian Palmer for assistance in making thin-sections, Dr Anne-Lise Jourdan at the Bloomsbury Environmental Isotope Facility for running isotope samples, and to James Brakeley and Jerry Morris for running X-ray diffraction samples. Thanks also go to all the Geography laboratory and support staff who have helped endlessly over the past four years. Thanks go especially to Iñaki for his help in Munro Fox, the Luminescence Laboratory and his love of loud music in the laboratory, and to Dr Marta Perez Fernandez for her help with diatom preparation. Thank you to my fellow members of the Luminescence lab group – Eric and Nathalie – for sharing their knowledge and experience. Thank you to my family – Dad, Mum, Helen, Fi, Beth and David – who provided support and encouragement at all stages of my PhD and enthusiastically explain to others what ‘Quaternary Science’ is! Finally, thank you to Laura who has provided endless amount of support while simultaneously putting up with me (especially over the final weeks of this thesis!).

Abstract

Orbitally-driven humid phases in arid regions such as the Arabian and Saharan Deserts have played an important biogeographic role in ancient human dispersals, range expansions/contractions and population structure. The timing and regional climatic pattern of humid phases has been shown by multiple long-term continuous palaeoenvironmental records from both marine and terrestrial (speleothems and long palaeolake cores) archives. However, these records lack detailed information at the scale at which humans interact with the environment, meaning these interactions are poorly understood. To address this, this thesis applies luminescence dating alongside multi-proxy palaeoenvironmental analysis to carbonate/siliceous sediment beds preserved in interdunal depressions in the western Nefud Desert, Saudi Arabia. While these deposits are short relative to many marine, speleothem and palaeolake records, they provide “snapshots” of the palaeoenvironmental conditions experienced by ancient humans. Importantly, these deposits are often directly associated with Lower and Middle Palaeolithic archaeology, fossils or footprints demonstrating they were an important locus for ancient human activity during humid phases.

The luminescence dating demonstrates that carbonate/siliceous sediment beds most likely formed during humid intervals that occurred during warm marine isotope stages or sub-stages over the past c. 500,000 years, with the exception of the Holocene. Multi-proxy analysis reveals that the carbonate/siliceous sediment beds consistently represent perennial but shallow freshwater interdunal lakes, irrespective of the time-interval they formed in. This thesis therefore argues that the western Nefud Desert, within the continental interior of the Arabian Peninsula, has repeatedly provided perennial freshwater resources for ancient humans and other fauna over the past c. 500,000 years. This may have enabled multiple pulses of hominin dispersals into the Arabian Peninsula over the past c.500,000 years.

Table of Contents

Chapter 1 - Introduction	1
1.1 Scientific rationale	1
1.2 Site introduction and brief overview of previous work	4
1.3 Aims and objectives	7
1.3.1 Aims	7
1.3.2 Objectives	7
1.4 Thesis structure	9
Chapter 2 – Quaternary climate drivers in the Saharo-Arabian desert belt and Levant	10
2.1 Introduction	10
2.2 Hydroclimate of the Saharo-Arabian desert belt and Levant	10
2.2.1 Modern Hydroclimate	10
2.2.2 Quaternary hydroclimatic change	13
2.3 Palaeoenvironmental archives across the Saharo-Arabian desert belt and Levant over the past ~500 ka	19
2.3.1 Marine records	19
2.3.2 Terrestrial records	25
2.4 Palaeoenvironment of the Nefud Desert over the past 0.5 Ma	30
2.4.1 Early palaeoenvironmental research	30
2.4.2 Recent palaeoenvironmental research.....	31
2.4.3 Palaeontology/Zooarchaeology of the Nefud Desert	37
2.5 Hominin dispersals into Arabia over the past 0.5 Ma	40
2.6 Chapter summary	44
Chapter 3 – Palaeoenvironmental analysis of interdunal lacustrine and palustrine sediments in low-latitudes	45
3.1 Introduction	45
3.2 Model for interdunal lake development in the western Nefud Desert	46
3.3 Lacustrine, palustrine and calcrete sediments	51
3.3.1 Lacustrine environments	53
3.3.2 Palustrine environments.....	55
3.3.3 Calcretes and rhizoliths.....	57
3.3.4 Summary.....	57
3.4 Carbonate sedimentation	58
3.5 Clastic sedimentation	62
3.6 Stable isotope analysis of inorganic authigenic carbonates	63
3.6.1 Basic principles	63
3.6.2 Fractionation	64
3.6.3 Isotope measurement and reporting	66
3.6.4 Factors that control the $\delta^{18}\text{O}$ of freshwater carbonates	66
3.6.6 Practical considerations when interpreting the stable isotope record	79
3.6.7 Authigenic carbonate isotopic sequences from lacustrine records in the Nefud Desert	80
3.7 Palaeoecological proxies	81

3.8 Chapter summary.....	82
Chapter 4 – Luminescence dating.....	84
4.1 Introduction.....	84
4.2 Overview of Luminescence Dating.....	84
4.3 Physical basis of luminescence production	86
4.3.1 Quartz optically stimulated luminescence (OSL)	90
4.3.2 Feldspar infrared stimulated luminescence (IRSL) signal	92
4.3.3 Measuring the Equivalent Dose (D_e): the single-aliquot regenerative (SAR) dose technique	94
4.4 The Environmental Dose Rate	97
4.4.1 Basic Principle	97
4.4.2 Conversion factors.....	98
4.4.3 Modifications to the dose rate	99
4.4.4 Moisture content.....	101
4.4.5 Cosmic dose.....	102
4.5 Common problems in luminescence dating	103
4.5.1 Disequilibrium.....	103
4.5.2 Beta-dose heterogeneity	104
4.5.3 Partial bleaching	105
4.5.4 Post depositional mixing.....	105
4.6 Summary	106
Chapter 5 – Methodology	107
5.1. Introduction.....	107
5.2 Fieldwork, site selection and site justification	107
5.2.1 Fieldwork and site selection	107
5.3 Palaeoenvironmental methods	113
5.3.1 Bulk sedimentology	114
5.3.2 Thin-section preparation and analysis.....	114
5.3.3 Stable isotope preparation	115
5.3.5 Diatom palaeoecology	118
5.4 Summary	120
Chapter 6 – Geochronology: timing of humid phases in the western Nefud Desert, Saudi Arabia	121
6.1 Introduction.....	121
6.2 Sample collection and analysis.....	121
6.3 OSL measurements	123
6.3.1 Equipment	123
6.3.2 Equivalent dose (D_e) measurement and determination	124
6.3.3 Environmental dose rate calculations	136
6.4 Age estimation and interpretation	138
6.4.1 Al Wusta Playa	139
6.4.2 Site 16.3	141
6.4.3 Al Wusta	142
6.4.4 Alathar	144
6.4.5 WNEF16_28	145
6.4.6 KAM4	145
6.4.7 Ti’s al Ghadah	151

6.5 Division of sites into a chronological framework	153
6.6 Northern Hemisphere (NH) insolation as a key control on amount of rainfall to the Nefud	155
6.7 Summary	156
Chapter 7 – Al Wusta Playa palaeoenvironmental results	158
7.1 Introduction	158
7.2 Sedimentology	158
7.2.1 Bulk-sedimentology	158
7.2.2 Microfacies analysis	161
7.3 Depositional model	162
7.4 Summary	163
Chapter 8 – Al Wusta palaeoenvironmental results	165
8.1 Introduction	165
8.2 Sedimentology of PD40	167
8.2.1 Bulk-sedimentology	167
8.2.2 Microfacies analysis	169
8.3 $\delta^{18}\text{O}$ and $\delta^{13}\text{C}$ analysis of PD40	170
8.4 Depositional model for PD40	173
8.5 Comparison of PD40 with previous research at Al Wusta	176
8.6 Summary	181
Chapter 9 – Alathar palaeoenvironmental results	183
9.1 Introduction	183
9.2 Sedimentology	185
9.2.1 Bulk sedimentology	185
9.2.2 Microfacies analysis	188
9.3 Diatom palaeoecology	190
9.4 Depositional model	190
9.5 Summary	194
Chapter 10 – WNEF16_28 palaeoenvironmental results	195
10.1 Introduction	195
10.2 Sedimentology	196
10.2.1 Bulk-sedimentology	196
10.2.2 Microfacies analysis	199
10.3 $\delta^{18}\text{O}$ and $\delta^{13}\text{C}$	200
10.4 Diatom palaeoecology	202
10.5 Depositional model	203
10.6 Summary	207
Chapter 11 – Ti's al Ghadah palaeoenvironmental results	209
11.1 Introduction	209

11.2 Ti's al Ghadah 1	212
11.2.1 Sedimentology	212
11.2.3 $\delta^{18}\text{O}$ and $\delta^{13}\text{C}$	216
11.2.4 Diatom palaeoecology	217
11.3 Ti's al Ghadah 2	217
11.3.1 Sedimentology	217
11.3.2 $\delta^{18}\text{O}$ and $\delta^{13}\text{C}$	219
11.4 Depositional model	221
11.5 Summary	225
Chapter 12 – Khall Amayshan 4 (KAM4) palaeoenvironmental results	226
12.1 Introduction	226
12.2 KAM4 lake 1	226
12.2.1 Sedimentology	228
12.2.1.1 Bulk sedimentology	228
12.2.1.2 Microfacies descriptions	229
12.2.2 $\delta^{18}\text{O}$ and $\delta^{13}\text{C}$	230
12.2.3 Diatom palaeoecology	232
12.2.4 Depositional model	233
12.3 KAM4 lake 2	237
12.3.1 Sedimentology	237
12.3.2 $\delta^{18}\text{O}$ and $\delta^{13}\text{C}$	241
12.3.3 Diatom palaeoecology	242
12.3.4 Depositional Model	242
12.4 KAM4 lake 3	246
12.4.1 Sedimentology	246
12.4.2 $\delta^{18}\text{O}$ and $\delta^{13}\text{C}$	249
12.4.3 Diatom palaeoecology	250
12.4.4 Depositional model	251
12.5 KAM4 lake 3a	253
12.5.1 Sedimentology	253
12.5.2 $\delta^{18}\text{O}$ and $\delta^{13}\text{C}$	256
12.5.3 Depositional model	258
12.6 KAM4 lake 3b	259
12.6.1 Sedimentology	259
12.6.2 $\delta^{18}\text{O}$ and $\delta^{13}\text{C}$	262
12.6.3 Depositional model	263
12.7 KAM4 lake 4	264
12.7.1 Sedimentology	265
12.7.2 $\delta^{18}\text{O}$ and $\delta^{13}\text{C}$	270
12.7.3 Diatom palaeoecology	271
12.7.4 Invertebrate palaeoecology	272
12.7.5 Depositional model	273
12.8 Summary of KAM4 interdunal basin	276
Chapter 13 – Comparison on the humid phases in the western Nefud Desert with the regional record over the last ~500,000 years	278
13.1 Introduction	278
13.2 Humid phases in the western Nefud sand sea over the last ~500 ka	279

13.2.1 Multiple humid phases in the western Nefud sand sea during Marine Isotope Stage 5.....	279
13.2.2 Middle Pleistocene humid phases	291
13.2.4 Late Glacial/Holocene.....	299
13.2.5 Comparison of humid intervals in the western Nefud Desert over the past 500,000 years.	301
13.3 Comparison of humid intervals in the western Nefud Desert with palaeoenvironmental records from the Arabian Peninsula and Levant.....	305
13.3.1 Northern Arabia, the Negev and northeast Africa	305
13.3.2 Levant and the Eastern Mediterranean Basin	315
13.3.3 Southern and Central Arabia	317
13.4 Summary.....	329
<i>Chapter 14 – Human demography and dispersals in the western Nefud Desert and Arabian Peninsula over the past ~500 ka</i>	<i>331</i>
14.1 Introduction	331
14.2 Human history in the western Nefud Desert.....	331
14.2.1 Drinkable, perennial water resources during the Middle and Upper Pleistocene	332
14.2.2 Human activity during the Holocene humid phase	338
14.2.3 Summary.....	340
14.3 The western Nefud Desert as part of a wider dispersal route out of Africa	340
14.3.1 A continental dispersal route using palaeohydrological corridors – the western Nefud Desert as part of a wider habitable landscape.	341
14.3.2 Middle Pleistocene hominin population dynamics.....	344
14.4 Summary.....	349
<i>Chapter 15 - Conclusion</i>	<i>350</i>
15.1 Conclusions and key findings.....	350
15.2 Future work	352
<i>Bibliography</i>	<i>355</i>
<i>Appendices</i>	<i>379</i>
Appendices 1: Stable oxygen and carbon isotope data.....	379
Appendices 2: Micromorphology images	390

List of Figures

Chapter 1 – Introduction

Figure 1.1 – Overview of the Nefud Desert from Breeze et al. (2017) 6

Figure 1.2 – Left: The distribution of undated ‘palaeolake’ deposits identified via multi-spectral classifications and GIS analysis from Breeze et al. (2015). Right: Basin depths of interdune depressions across the Nefud Desert from Breeze et al. (2017). 6

Chapter 2 – Quaternary climate drivers in the Saharo-Arabian desert belt and Levant

Figure 2.1 – Modern annual precipitation over the Arabian Peninsula derived from WorldClim data from Jennings et al. (2015) 12

Figure 2.2 – Components of summer monsoons from Mohtadi et al. (2016) 14

Figure 2.3 – Simulations of precipitation anomaly (relevant timeslice minus preindustrial (PI)) at 130, 125 and 120 ka time-slices using the fully coupled Earth system model ECHAM5/MPIOM (Jungclaus et al., 2006) with a stable isotope diagnostic (Werner et al., 2011). Figure from Gierz et al. (2017). 16

Figure 2.4 – Examples of modern-day moisture bearing tropical plumes extending from western Africa across the Saharo-Arabian desert belt from Tubi and Dayan (2014). 17

Figure 2.5 – Modelled winter (DJF) precipitation (mm/day) (Picture B) and precipitation minus evaporation (Picture D) for 125 ka using CCSM3 climate model after Kutzbach et al. (2014). 18

Figure 2.6 – Schematic diagram of sapropel formation in the eastern Mediterranean Sea, from Rohling et al. (2015) 20

Figure 2.7 – Humidity/aridity index over the past 3 million years modified after Grant et al. (2017) 23

Figure 2.8 – Stable hydrogen isotopic composition of leaf waxes corrected for ice-volume from Gulf of Aden (core RC09-166) over the past 200 ka from Tierney et al. (2017). 24

Figure 2.9 – Record of South Arabian Humid Phases (SAHPs) constructed from speleothem Y99 from Mukalla Cave, Yemen from Nicholson et al. (2020). 27

Figure 2.10 – Interdunal palaeolake deposits studied by Rosenberg et al. (2013) with red labels representing Middle Pleistocene deposits and black labels representing MIS 5 sites. Image taken from Rosenberg et al. (2013).	32
Figure 2.11 – OSL ages of palaeolakes in the Nefud Desert from Rosenberg et al. (2013).	34
Figure 2.12 – Key environmental records published up to 2018 from across the Arabian Peninsula taken from Parton et al. (2018) and references therein.	36
Figure 2.13 – Hippopotamid remains found within the western Nefud Desert from Stewart et al. (2020b).	39
Figure 2.14 – Potential dispersal routes across the Arabian Peninsula over the Pleistocene, from Petraglia et al. (2018)	41
 Chapter 3 – Palaeoenvironmental analysis of interdunal lacustrine and palustrine sediments in low-latitudes	
Figure 3.1 – Landscapes of present-day western Nefud Desert	45
Figure 3.2 – Schematic figure showing the idealised model for the development of perennial interdunal lakes in the western Nefud Desert during humid phases.	49
Figure 3.3 – Continued from figure 3.2...Schematic figure showing the idealised model for the development of perennial interdunal lakes in the western Nefud Desert.	50
Figure 3.4 – Continuum of depositional environments for calcretes, palustrine and lacustrine sediments along with associated microfacies from Alonso-Zarza (2003).	52
Figure 3.5 – General model for interdunal hardwater lake environments redrawn after Wright (1990).	54
Figure 3.6 – Example microfacies from (A) Al Wusta and (B) Site 16.3 of homogenous primary lake mud (microsparite) deposited on the floor of perennial interdunal lake bed in the sub-littoral to profundal zone (Clark-Wilson, 2016; Groucutt et al., 2018).	54
Figure 3.7 – Microfacies from the top of Site 16.3 that represent a shallow lacustrine (littoral), or potentially a weakly developed palustrine, environment (Clark-Wilson, 2016).	56

Figure 3.8 – The chemical reactions that lead to the precipitation of carbonate in hardwater lakes.	59
Figure 3.9 – The relationship between pH and proportions of inorganic carbon species in solution in hard water lakes from Wetzel (1975)	60
Figure 3.10 – Evaporite precipitation sequence redrawn from Verrecchia (2007)	61
Figure 3.11 – Basic information regarding oxygen and carbon isotopes, redrawn after Mook (2000).	64
Figure 3.12 – A diagram outlining the three different processes of isotopic fractionation from Mook (2006).	65
Figure 3.13 – Controls on the oxygen isotope composition of lacustrine carbonates, modified after Leng and Marshall (2004) to show the tropical/sub-tropical effects on $\delta^{18}\text{O}$ of precipitation.	67
Figure 3.14 – Scatter plots demonstrating the amount effect as the dominant control on the $\delta^{18}\text{O}$ value of precipitation in tropical and sub-tropical locations from Rozanski et al. (1993).	69
Figure 3.15 – Schematic representation of the rain-out (continental) effect as Rayleigh distillation progressively depletes the heavier isotope, leading to an enrichment in the lighter isotope as the air mass moves further from its source. This results in negative $\delta^{18}\text{O}$ values. Redrawn and modified from Hoefs (1997).	70
Figure 3.16 - $\delta^{13}\text{C}$ vs $\delta^{18}\text{O}$ redrawn from Leng and Marshall (2004).	74
Figure 3.17 – Major sources of carbon into lakes and their carbon isotope values redrawn after Leng and Marshall (2004).	77
 Chapter 4 – Luminescence dating	
Figure 4.1 – Rechargeable battery analogue to describe the process of luminescence dating, from Smedley (2018)	85
Figure 4.2 – Energy level diagram redrawn after Bailey (2001).	86
Figure 4.3 – Example dose-response curves (DRCs) using an exponential + linear fit from two samples analysed as part of this thesis.	89
Figure 4.4 – Examples of (A) continuous-wave OSL curve, (B) a linear-modulated OSL curve and (C) the separate components of the	91

luminescence signal (fast, medium and 3 x slow), from Wintle and Adamiec (2017).

Figure 4.5 – An overview of the calculation of the environmental dose rate (D) in luminescence dating from Durcan et al. (2015). 98

Figure 4.6 – Grain size attenuation factors for the β dose from Durcan et al. (2015), using data from Mejdahl (1979), Brennan (2003), Guerin et al. (2012) and Readhead (2002). 100

Figure 4.7 – Cosmic ray penetration depth from Durcan et al. (2015) with data from Barbouti and Rastin (1983) (yellow and red dots) and from Prescott and Hutton (1988) black squares. 103

Chapter 5 – Methods

Figure 5.1 – Flowchart showing the progression of research. 108

Figure 5.2 – The location of each of the interdunal sites in the western Nefud Desert presented in this thesis, along with Site 16.3 which was analysed as part of my MSc thesis (Clark-Wilson, 2016). 109

Figure 5.3 – Comparison chart from the image analysis laboratory used to estimate the percentage coverage of allogenic sand/silt grains at the lowest magnification (x20). 115

Chapter 6 – Geochronology: timing of humid phases in the western Nefud Desert, Saudi Arabia

Figure 6.1 – Schematic diagram showing the steps from sample collection in the field through to purified quartz/feldspar for D_e measurement (left branch) and dose rate calculation (right branch). 122

Figure 6.2 - Preheat plateau dose recovery tests from all new data presented in this thesis. 126

Figure 6.3 – Abanico plots for a) PD61 Alathar, b) PD62 Alathar and c) PD12 KAM4 lake 3. 127

Figure 6.4 – Example abanico plots of the equivalent dose distributions from Alathar (top row), WNEF16_28 (middle row) and KAM4 (bottom row). 135

Figure 6.5 - Ages from Al Wusta Playa shown alongside the NH summer insolation at 30°N (Berger and Loutre, 1991) and the marine oxygen isotope record from the LR04 stack (Liessecki and Raymo, 2005). 140

Figure 6.6 – Ages from site 16.3 (Clark-Wilson, 2016) shown alongside NH summer insolation at 30°N (Berger and Loutre, 1991) and the marine oxygen isotope record from the LR04 stack (Liesecki and Raymo, 2005).	142
Figure 6.7 - Ages from Al Wusta (Groucutt et al., 2018) shown alongside NH summer insolation at 30°N (Berger and Loutre, 1991) and the marine oxygen isotope record from the LR04 stack (Liesecki and Raymo, 2005).	143
Figure 6.8 - Ages from Alathar shown alongside NH summer insolation at 30°N (Berger and Loutre, 1991) and the marine oxygen isotope record from the LR04 stack (Liesecki and Raymo, 2005).	144
Figure 6.9 - Ages from WNEF16_28 shown alongside NH summer insolation at 30°N (Berger and Loutre, 1991) and the marine oxygen isotope record from the LR04 stack (Liesecki and Raymo, 2005).	145
Figure 6.10 - Ages from KAM4 shown alongside NH summer insolation at 30°N (Berger and Loutre, 1991) and the marine oxygen isotope record from the LR04 stack (Liesecki and Raymo, 2005).	147
Figure 6.11 - Ages from Ti's al Ghadah (Rosenberg et al., 2013; Stimpson et al., 2016) shown alongside NH summer insolation at 30°N (Berger and Loutre, 1991) and the marine oxygen isotope record from the LR04 stack (Liesecki and Raymo, 2005).	152
Figure 6.12 – Summary of all ages relevant to sedimentary sequences studied in this thesis shown alongside NH summer insolation at 30°N (Berger and Loutre, 1991) and the marine oxygen isotope record from the LR04 stack (Liesecki and Raymo, 2005).	154
 Chapter 7 – Al Wusta Playa palaeoenvironmental results	
Figure 7.1 – Overview of the recharge playa within the Al Wusta interdunal basin.	159
Figure 7.2 – Sedimentary sequence from the trench dug into the Al Wusta Playa.	160
Figure 7.3 – Close up image of unit 3. Bulk sedimentology shows this unit consists of silty sands with gravels and contains a small component of calcite, gypsum and birnessite.	160
Figure 7.4 – Photomicrographs in plane-polarised light from the Al Wusta recharge playa.	161
 Chapter 8 – Al Wusta palaeoenvironmental results	

Figure 8.1 – Overview of the Al Wusta site.	166
Figure 8.2 – Sedimentary sequence from trench PD40.	168
Figure 8.3 – Sedimentary log of PD40 along with CaCO ₃ (blue), δ ¹⁸ O (red) and δ ¹³ C (green).	169
Figure 8.4 – Photomicrographs in cross-polar (XPL) light of thin-sections from trench PD40.	171
Figure 8.5 – Covariation between δ ¹⁸ O and δ ¹³ C at PD40.	173
Figure 8.6 - Summary diagram of diatom assemblage from trench PD15, produced by Wing-Wai Sung.	179
Figure 8.7 - Summary diagram of diatom assemblage from trench PD16, produced by Wing-Wai Sung.	180
Figure 8.8 – Altitudinal relationship between each sedimentary sequence	181
Chapter 9 – Alathar palaeoenvironmental results	
Figure 9.1 – Location of the Alathar interdunal basin within the western Nefud Desert (red star).	183
Figure 9.2 – Overview of the Alathar interdunal basin.	184
Figure 9.3 – Site pictures from Alathar.	185
Figure 9.4 - Stratigraphic log of the first section (units 1 – 4) and the second section (units 5 – 7).	186
Figure 9.5 – Photomicrographs of thin-sections taken from the Alathar palaeolake bed.	189
Figure 9.6 – The surface of unit 4b. This shows a human footprint (located to the right of the camera lens cap). A desiccation crack runs directly through the footprint, while another is located in the top left portion of the picture.	193
Chapter 10 – WNEF16_28 palaeoenvironmental results	
Figure 10.1 - Location of the WNEF16_28 interdunal basin within the western Nefud Desert (red star).	195
Figure 10.2 – Sedimentary sequence from WNEF16_28.	197

Figure 10.3 – Sedimentary logs along with CaCO ₃ (blue), δ ¹⁸ O (red) and δ ¹³ C (green) stratigraphies for the sedimentary sequence at WNEF16_28.	198
Figure 10.4 – Photomicrographs of thin-sections through the sedimentary sequence.	200
Figure 10.5 – Covariance between δ ¹⁸ O and δ ¹³ C at WNEF16_28 excluding the calcitic rhizolith.	202
 Chapter 11 – Ti’s al Ghadah palaeoenvironmental results	
Figure 11.1 – (A) Location of the Ti’s al Ghadah interdunal basin within the western Nefud Desert (red star). Other black dots represent other interdunal sites studied in this thesis. Inset map shows the location of the Nefud Desert on the Arabian Peninsula. (B) Digital elevation model of the interdunal basin at TAG with OSL sample locations, trenches and key features highlighted (Breeze, unpub).	210
Figure 11.2 – The complete stratigraphic sequence recorded at Ti’s al Ghadah as described by Stimpson et al. (2016) and later revised by Stewart et al. (2019).	211
Figure 11.3 – Sedimentary sequence at Ti’s al Ghadah 1, with thin-section sample locations highlighted.	213
Figure 11.4 - Sedimentary log along with CaCO ₃ (blue), δ ¹⁸ O (red) and δ ¹³ C (green) for Ti’s al Ghadah 1.	214
Figure 11.5 – Photomicrographs of thin-sections through the sedimentary sequence at Ti’s al Ghadah 1.	215
Figure 11.6 - Covariation between δ ¹⁸ O and δ ¹³ C at Ti’s al Ghadah 1.	216
Figure 11.7 - Sedimentary sequence at Ti’s al Ghadah 2, with thin-section sample locations highlighted.	218
Figure 11.8 - Sedimentary log along with CaCO ₃ (blue), δ ¹⁸ O (red) and δ ¹³ C (green) for Ti’s al Ghadah 2.	219
Figure 11.9 – Photomicrographs of microfacies from Ti’s al Ghadah 2.	220
Figure 11.10 - Covariation between δ ¹⁸ O and δ ¹³ C at Ti’s al Ghadah 2.	221
Figure 11.11 - δ ¹⁸ O and δ ¹³ C from Ti’s al Ghadah 1 (diamonds) plotted against Ti’s al Ghadah 2 (crosses).	224

Chapter 12 – Khall Amayshan 4 (KAM4) palaeoenvironmental results

Figure 12.1 – (A) Location of the KAM4 interdunal basin within the western Nefud Desert (red star).	227
Figure 12.2 – Sedimentary sequence from KAM4 lake 1. Unit boundaries are represented by a solid black line.	228
Figure 12.3 - Sedimentary log along with CaCO ₃ (blue), δ ¹⁸ O (red) and δ ¹³ C (green) stratigraphy for KAM4 lake 1.	229
Figure 12.4 – Photomicrographs of thin-sections from KAM4 lake 1.	231
Figure 12.5 - Covariation between δ ¹⁸ O and δ ¹³ C for KAM4 lake 1.	232
Figure 12.6 – Summary diagram of KAM4 lake 1 diatom assemblage analysed by Wing Wai Sung.	233
Figure 12.7 – The sedimentary section of KAM4 lake 1.	234
Figure 12.8 - Sedimentary sequence from KAM4 lake 2.	238
Figure 12.9 – Sedimentary log with CaCO ₃ (blue), δ ¹⁸ O (red) and δ ¹³ C (green) curves for KAM4 Lake 2.	238
Figure 12.10 - Photomicrographs of thin-sections from KAM4 lake 2.	240
Figure 12.11 - Covariance between δ ¹⁸ O and δ ¹³ C at KAM4 Lake 2.	241
Figure 12.12 - Summary diagram of KAM4 lake 1 diatom assemblage analysed by Wing Wai Sung.	242
Figure 12.13 – Sedimentary sequence from KAM4 lake 3.	247
Figure 12.14 – Sedimentary log with CaCO ₃ (blue), δ ¹⁸ O (red) and δ ¹³ C (green) curves for KAM4 lake 3.	247
Figure 12.15 – Photomicrographs of thin-sections from KAM4 lake 3.	249
Figure 12.16 - Covariation between δ ¹⁸ O and δ ¹³ C at KAM4 Lake 3.	250
Figure 12.17 - Summary diagram of diatom assemblage from KAM4 lake 3.	251
Figure 12.18 - Sedimentary sequence from KAM L3a. Unit boundaries are represented by a solid black line and sub-unit boundaries by a dashed line.	254

Figure 12.19 - Sedimentary log with CaCO ₃ (blue), δ ¹⁸ O (red) and δ ¹³ C (green) curves for KAM4 Lake 3a.	255
Figure 12.20 - Photomicrographs of thin-sections from KAM4 lake 3a.	256
Figure 12.21 – Covariance between δ ¹⁸ O and δ ¹³ C for KAM4 lake 3a.	257
Figure 12.22 - Sedimentary sequence from KAM L3b.	260
Figure 12.23 - Sedimentary log with CaCO ₃ (blue), δ ¹⁸ O (red) and δ ¹³ C (green) curves for KAM4 Lake 3b.	261
Figure 12.24 - Photomicrographs of thin-sections from KAM4 lake 3b.	262
Figure 12.25 – Covariance between δ ¹⁸ O and δ ¹³ C at KAM4 lake 3b.	263
Figure 12.26 - Sedimentary sequence from KAM lake 4.	266
Figure 12.27 - Sedimentary log with CaCO ₃ (blue), δ ¹⁸ O (red) and δ ¹³ C (green) curves for KAM4 lake 4.	267
Figure 12.28 - Photomicrographs of thin-sections from KAM4 lake 4.	269
Figure 12.29 - Covariance between δ ¹⁸ O and δ ¹³ C at KAM4 lake 4.	271
Figure 12.30 – Diatom palaeoecology of the KAM4 lake 4 sequence carried out by Wing-Wai Sung.	272
Chapter 13 – Comparison on the humid phases in the western Nefud Desert with the regional record over the last ~500,000 years	
Figure 13.1 – The distribution of directly dated or bracketed MIS 5 palaeolake deposits across the western Nefud Desert.	279
Figure 13.2 – Chronology of directly dated or bracketed MIS 5 palaeolake deposits dated to MIS 5 from the western Nefud Desert, including data from Rosenberg et al. (2013), Clark-Wilson (2016) and Groucutt et al. (2018).	282
Figure 13.3 - Example photomicrographs of fine-grained carbonate rich marls across four of the MIS 5 sites presented here.	284
Figure 13.4 – Isotopic data for MIS 5 palaeolake sequences.	288
Figure 13.5 – Photomicrographs of (A) Al Wusta 19 – 22 cm above base and (B) Alathar. 139 – 141 cm above base.	290

Figure 13.6 - The distribution of directly dated or bracketed Middle Pleistocene palaeolake deposits across the western Nefud Desert.	291
Figure 13.7 - Chronology of directly dated Middle Pleistocene palaeolake deposits dated to MIS 7, 9 and 11/13 from the western Nefud Desert.	293
Figure 13.8 – Example photomicrographs of microfacies from Middle Pleistocene deposits.	295
Figure 13.9 - Isotopic data for Middle Pleistocene palaeolake sequences.	296
Figure 13.10 – KAM4 lake 4 sedimentary sequence (118 cm from base of non-aeolian sediment (Unit 2a) to the top of Unit 4b) with sedimentary sequence, facies, depositional environment and position of water table noted.	298
Figure 13.11 – The height above sea level (m) of Al Wusta Playa (Holocene) vs MIS 5a marl beds.	300
Figure 13.12 – Distribution of key terrestrial palaeoenvironmental archives that record periods of increased humidity across Northern Arabia, the Negev, the Levant and Northeast Africa that are cited in text.	305
Figure 13.13 - Distribution of studied palaeolake deposits across the western Nefud Desert from this thesis, Petraglia et al. (2011, 2012), Rosenberg et al. (2013), Jennings et al. (2016), Groucutt et al. (2018) and Stewart et al. (2020).	306
Figure 13.14 – Distribution of ages for all palaeoenvironmental records from the Nefud Desert over the past ~500 ka.	308
Figure 13.15 – Location of the Negev Desert (panels A and B) along with the location of speleothem records from Vaks et al. (2010).	311
Figure 13.16 – Distribution of ages for key palaeoenvironmental records that record increased humidity across Northern Arabia, the Negev Desert, Northeast Africa and the Levant over the past ~500 ka.	313
Figure 13.17 - Distribution of key terrestrial (black dots) and marine (red dots) palaeoenvironmental archives cited in text that record periods of increased humidity across the central and southern portion of the Arabian Peninsula.	318
Figure 13.18 – The timing and palaeoenvironmental record of the Y99 speleothem, Mukalla Cave, Oman from Nicholson et al. (2020).	319

Figure 13.19 – Compilation of climate models that precipitation pattern and amount over the Arabian Peninsula during the last interglacial.	321
Figure 13.20 – Comparison of the microfacies of the ‘limestone facies’ of MIS 5 Rub’ al Khali interdunal lakes (a – e) from Matter et al. (2015) with microfacies from MIS 5 interdunal lakes from the western Nefud Desert (1 and 2).	324
Figure 13.21 – Distribution of ages for key palaeoenvironmental records that record increased humidity across southern Arabia over the past ~500 ka, compared with the record from the Nefud Desert (A).	326
 Chapter 14 – Human demography and dispersals in the western Nefud Desert and Arabian Peninsula over the past ~500 ka	
Figure 14.1 – Distribution of archaeological sites across the western Nefud Desert modified from Breeze et al. (2017).	333
Figure 14.2 – Map of harrats of Arabia, taken from Groucutt et al. (2020).	335
Figure 14.3 – The distribution of palaeolake deposits across the western Nefud Desert from Breeze et al. (2017) as mapped by multi-spectral classifications and GIS analysis (Breeze et al., 2015).	336
Figure 14.4 – Key dated Holocene archaeological sites and cultural transformations across the Arabian Peninsula from Petraglia et al. (2020) and references therein.	339
Figure 14.5 - The archaeological and palaeohydrological context of the Nefud Desert focused on MIS 5, though such a route is plausible for other humid phases.	342
Figure 14.6 – Key points in Homo sapiens origin and out-of-Africa dispersals relative to directly dated wetland sediments from the western Nefud Desert.	348

List of Tables

Chapter 2 – Quaternary climate drivers in the Saharo-Arabian desert belt and Levant

Table 2.1 – Age control points for sapropels S1 – S10 from ODP site 968, from Ziegler et al. (2010). Orbital tuning is used to date sapropel layers, and the method is discussed further in the text below.	21
---	----

Chapter 3 – Palaeoenvironmental analysis of interdunal lacustrine and palustrine sediments in low-latitudes

Table 3.1 – Summary of hydrological/palaeoclimatic records that the $\delta^{18}\text{O}$ ratios of authigenic carbonates are likely to record in lakes of different volumes (very small to large), from Leng and Marshall (2004) and references therein.	73
---	----

Chapter 4 – Luminescence dating

Table 4.1 – The modified SAR protocol used for D_e measurement of quartz in this thesis.	95
--	----

Table 4.2 – Modified SAR protocol used for D_e measurement of feldspar.	96
---	----

Chapter 5 – Methods

Table 5.1 - Assessment criteria used by Breeze et al. (2017) for each study site.	109
---	-----

Table 5.2 – Significance of each site studied within this thesis, based on the criteria from Breeze et al. (2017) outlined in Table 5.1.	110
--	-----

Table 5.3 – Isotopic values for paired bulk and sieved fractions from Al Wusta, WNEF16_28 and Site 16.3.	116
--	-----

Chapter 6 – Geochronology: timing of humid phases in the western Nefud Desert, Saudi Arabia

Table 6.1 – The optimal preheating regimes from preheat plateau dose recovery tests (PP) and dose recovery tests (DR) from the samples selected for this analysis at each site.	125
---	-----

Table 6.2 - The number of coarse-grain aliquots (180 – 210 μm), with exception of PD14 KAM4 lake 4 which had a grain size of 60 – 90 μm) which were measured, rejected after application of the criteria outlined in the text and accepted for inclusion in the calculation of D_b .	128
--	-----

Table 6.3 – As per Table 6.2 but for fine-grained aliquots (4 – 11 μm).	129
Table 6.4 - Age variations for each sample depending on oversaturation rejection criteria (see Text for full discussion).	130
Table 6.5 - As per Tables 6.2 and 6.3 but for coarse-grained feldspar aliquots (4 – 11 μm).	133
Table 6.6 – Summary of environmental dose rate data for all samples analysed within this thesis.	137
Table 6.7 – Summary data for all luminescence data discussed in following sections.	138
 Chapter 8 – Al Wusta palaeoenvironmental results	
Table 8.1 – X-ray diffraction results from trenches PD40.	168
Table 8.2 - Descriptive statistics for $\delta^{18}\text{O}$ values of lake carbonates at Al Wusta, including trenches PD15, PD16 and PD17 from Clark-Wilson (2016).	172
Table 8.3 - Descriptive statistics for $\delta^{13}\text{C}$ values of lake carbonates including trenches PD15, PD16 and PD17 from Clark-Wilson (2016).	172
Table 8.4 – X-ray diffraction results from all trenches across Al Wusta (Clark-Wilson, 2016).	177
 Chapter 9 – Alathar palaeoenvironmental results	
Table 9.1 - X-ray diffraction results for Alathar.	188
 Chapter 10 – WNEF16_28 palaeoenvironmental results	
Table 10.1 – X-ray diffraction results from WNEF16_28.	198
Table 10.2 – Descriptive statistics for $\delta^{18}\text{O}$ values of lake carbonates at WNEF16_28.	201
Table 10.3 – Descriptive statistics for $\delta^{13}\text{C}$ values of lake carbonates at WNEF16_28.	201
 Chapter 11 – Ti’s al Ghadah palaeoenvironmental results	
Table 11.1 – Correlation of units identified in this thesis compared with units ascribed during previous work (see Fig 11.2).	212

Table 11.2 – X-ray diffraction results from Ti’s al Ghadah 1.	213
Table 11.3 - Descriptive statistics for $\delta^{18}\text{O}$ values of lake carbonates at Ti’s al Ghadah 1.	216
Table 11.4 - Descriptive statistics for $\delta^{13}\text{C}$ values of lake carbonates at Ti’s al Ghadah (TAG) 1.	216
Table 11.5 – X-ray diffraction results from Ti’s al Ghadah 2.	218
Table 11.6 - Descriptive statistics for $\delta^{18}\text{O}$ values of lake carbonates at Ti’s al Ghadah (TAG) 2.	219
Table 11.7 - Descriptive statistics for $\delta^{13}\text{C}$ values of lake carbonates at Ti’s al Ghadah (TAG) 2.	219
Chapter 12 – Khall Amayshan 4 (KAM4) palaeoenvironmental results	
Table 12.1 – X-ray diffraction results from KAM4 lake 1.	229
Table 12.2 - Descriptive statistics for $\delta^{18}\text{O}$ values of lake carbonates at KAM4 lake 1.	230
Table 12.3 - Descriptive statistics for $\delta^{13}\text{C}$ values of lake carbonates at KAM4 lake 1.	230
Table 12.4 - X-ray diffraction data from KAM4 lake 2.	239
Table 12.5 - Descriptive statistics for $\delta^{18}\text{O}$ values of lake carbonates at KAM4 lake 2.	241
Table 12.6 - Descriptive statistics for $\delta^{13}\text{C}$ values of lake carbonates at KAM4 lake 2.	241
Table 12.7 – X-ray diffraction data from KAM4 lake 3.	248
Table 12.8 - Descriptive statistics for $\delta^{18}\text{O}$ values of lake carbonates at KAM4 lake 3.	250
Table 12.9 - Descriptive statistics for $\delta^{13}\text{C}$ values of lake carbonates at KAM4 lake 3.	250
Table 12.10 – X-ray diffraction data from KAM4 lake 3a.	254
Table 12.11 - Descriptive statistics for $\delta^{18}\text{O}$ values of lake carbonates at KAM4 lake 3a.	257

Table 12.12 - Descriptive statistics for $\delta^{13}\text{C}$ values of lake carbonates at KAM4 lake 3a.	257
Table 12.13 – X-ray diffraction data from KAM4 lake 3b.	260
Table 12.14 - Descriptive statistics for $\delta^{18}\text{O}$ values of lake carbonates at KAM4 lake 3b.	262
Table 12.15 - Descriptive statistics for $\delta^{13}\text{C}$ values of lake carbonates at KAM4 lake 3b.	263
Table 12.16 – X-ray diffraction data from KAM4 lake 4.	267
Table 12.17 - Descriptive statistics for $\delta^{18}\text{O}$ values of lake carbonates at KAM4 lake 3b.	270
Table 12.18 - Descriptive statistics for $\delta^{13}\text{C}$ values of lake carbonates at KAM4 lake 3b.	270
Chapter 13 – Comparison on the humid phases in the western Nefud Desert with the regional record over the last ~500,000 years	
Table 13.1 – Summary palaeoenvironmental data of each MIS 5 sequence studied here.	285
Table 13.2 – Summary palaeoenvironmental data of each Middle Pleistocene sequence studied here.	294

List of Equations

Chapter 4 – Luminescence dating

Eq. 4.1 – Equation for determining the age of a luminescence sample.	85
Eq. 4.2 – Equation for determining the mean time an electron is expected to reside in an electron trap.	88
Eq. 4.3 – Calculation for the environmental dose rate.	97
Eq. 4.4 – Accounting for isotope specific attenuation factors for β dose rate.	99
Eq. 4.5 – Accounting for isotope specific attenuation factors for α dose rate.	99
Eq. 4.6 – Correction for moisture content when calculating the α dose rate.	101
Eq. 4.7 – Correction for moisture content when calculating the β dose rate.	101
Eq. 4.8 – Correction for moisture content when calculating the γ dose rate.	101

Chapter 1 - Introduction

1.1 Scientific rationale

The Saharo-Arabian desert belt has experienced pronounced and repeated hydroclimatic change over the Quaternary (Grant et al., 2017; Larrasoña et al., 2003; Nicholson et al., 2020). For much of the Middle and Upper Pleistocene the region has been arid to hyper-arid with limited freshwater or edible flora or fauna, making it a major barrier to prehistoric human movement (Groucutt et al., 2015a). However, several studies have shown that the region experienced repeated humid periods associated with the northwards extension of tropical moisture sources caused by strong northern hemisphere (NH) summer insolation (Herold and Lohmann, 2009; Jennings et al., 2015; Nicholson et al., 2020; Parton et al., 2018; Rosenberg et al., 2013, 2011). This transformed the region into a resource-rich landscape with large freshwater resources (palaeorivers and palaeolakes), vegetation and prey capable of supporting human and faunal dispersals (Breeze et al., 2016; Drake et al., 2011). This transformation played a critical role in ancient human demography and dispersals, including hominin expansions beyond Africa (Blome et al., 2012; Breeze et al., 2016; Drake et al., 2011; Groucutt et al., 2015a; Timmermann and Friedrich, 2016).

Despite this, the terrestrial record of Quaternary hydroclimatic change in the Saharo-Arabian desert belt is limited beyond the Holocene. This means the understanding of resource availability and its distribution across the landscape is poor, and this limits the understanding of hominin interactions over the Quaternary. The lack of terrestrial archives is in part due to preservation bias as records of previous humid phases are eroded from the landscape in a highly dynamic dryland environment. Consequently, marine and speleothem sediments have predominantly been used as an archive for long-term terrestrial landscape response to Quaternary hydroclimatic change (Grant et al., 2017; Larrasoña et al., 2003; Lourens, 2004). Marine sediments mostly use terrigenous dust (e.g. Larrasoña et al., 2003) or organic-rich layers known as sapropels (Emeis et al., 2000; Lourens, 2004; Lourens et al., 1996) to record continental hydroclimatic change across the Saharo-Arabian desert belt. They provide long and

continuous records of hydrological change that extend over the entire Quaternary period (Grant et al., 2017; Larrasoña et al., 2003). Speleothems – secondary mineral deposits formed in caves – provide a more fragmentary record of hydrological change but now extend back over 1 Ma (Nicholson et al., 2020). Speleothems only form when annual rainfall exceeds 300 mm yr⁻¹ (Vaks et al., 2010, 2013). Consequently, where they are found across the Saharo-Arabian desert belt they represent periods where humidity was substantially higher than the present day. Speleothem growth is recorded in southern Arabia (Mukalla Cave, Yemen and Hoti Cave, Fleitmann et al., 2003; Nicholson et al., 2020), northern Arabia in the Negev Desert (Vaks et al., 2010, 2007, 2006) and in northeast Africa at Wadi Sannar Cave (El-Shenawy et al., 2018).

Studies on both marine and speleothem sediments show evidence for increased humidity during warm marine isotope stages or sub-stages such as MIS 5a, 5e, 7a, 7e (Grant et al., 2017; Nicholson et al., 2020). However, while these sediments provide long records of hydrological change, they are limited in that their combined spatial distribution leaves a large geographical gap in the Saharo-Arabian interior. For example, the spatial distribution of speleothems archives is largely restricted to the fringes of the Arabian Peninsula. Consequently, these archives do not provide a direct record of the local terrestrial palaeoenvironment during humid phases, meaning resource distribution and availability at a human-scale is poorly understood. This is problematic for studies of human demography and dispersal as humid phases recorded in both marine and speleothem records are often used to infer ‘windows of opportunity’ during which hominins may have occupied and dispersed across the continental interiors of the Sahara and the Arabian Peninsula (Larrasoña et al., 2013; Nicholson et al., 2020). This assumption cannot be justified without detailed analysis of terrestrial archives that occur along potential dispersal pathways, since a humid period can only facilitate hominin occupation when it yields accessible drinkable water.

To understand the broad patterns and timings of hominin dispersal across the Saharo-Arabian desert belt along with the nature of human-environment interactions, it is therefore critical to investigate sedimentary archives that record resource availability on the landscape. Such archives include lacustrine, palustrine, calcrete, palaeosol, tufa

and fluvial sediments (e.g. Groucutt et al., 2018; Petraglia et al., 2012; Rosenberg et al., 2013). As noted above, such records are rarely preserved in the landscape due to deflation in subsequent dry phases. A full review of these records over the timeframe of this study is presented in Chapter 2. This thesis focuses on interdunal carbonate/siliceous sediments preserved in interdunal basins the western Nefud Desert in the Arabian Peninsula (see section 1.2). Such sediments are commonly referred to as 'limestone', 'marl', 'diatomite' or 'palaeolake' sediments in the literature (Breeze et al., 2017; Groucutt et al., 2018; Matter et al., 2015a; Rosenberg et al., 2013, 2011). This thesis refers to them as carbonate/siliceous sediments until the evidence for their depositional environment has been presented in Chapters 8 – 12.

In order to address the question of resource availability during time intervals of importance to early human dispersals, this study investigates a number of key sedimentary sequences from archaeological sites in interdune depressions from the western Nefud Desert, Saudi Arabia. These sites contain evidence for both humid phases and human occupation in the form of interdunal carbonate or siliceous deposits in association with stone tools, fossils or footprints (Breeze et al., 2017; Groucutt et al., 2018; Stewart et al., 2020a). This study provides high-resolution sedimentological, geochemical and palaeoecological analysis of these carbonate and siliceous sediments as well as robust dating of the humid phases which formed them. These new analyses allow us to address questions such as whether the Nefud waterbodies contained freshwater and whether they were perennial (i.e. existed year-round). The answers to these questions have important implications for the way in which humans could have utilised these resources. Moreover, the timing of these deposits provides insights as to whether multiple insolation-driven humid intervals allowed discrete dispersals into northwestern Arabia over the past ~500 ka.

The data produced here in combination with previously published dated sites elsewhere in the region (Clark-Wilson, 2016; Groucutt et al., 2018; Rosenberg et al., 2013), will allow the temporal and spatial distribution of freshwater resources in the western Nefud Desert over the past ~500 ka to be assessed. This knowledge is critical for testing hypotheses regarding hominin population dynamics in northwestern Arabia over the

past ~500 ka; a period which includes a number of important events in hominin prehistory, such as *Homo sapiens* expansion beyond Africa (Groucutt et al., 2018, 2015a).

1.2 Site introduction and brief overview of previous work

The Nefud Desert is the northern most sand sea in Arabia, covers an area of approximately 58,500 km², and is located between latitudes 27°8' and 29°45' at an average altitude of 900 m (Fig 1.1, Breeze et al., 2017). Importantly, it is situated ~500 km southeast of the Sinai Peninsula, the only terrestrial connection between Africa and Arabia during the Quaternary. As such, the Nefud Desert was accessible for populations expanding beyond Africa and into the Arabian Peninsula via a 'northern' dispersal route (Breeze et al., 2016). The Nefud may have also have been accessible from the south if humans entered Arabia via a 'southern route' across the southern Red Sea (Armitage et al., 2011; Lambeck et al., 2011). The Nefud Desert is currently in receipt of between 60 – 90 mm of annual rainfall and is classified as hyper-arid (Edgell, 2006). The vegetation cover is sparse, and is dominated by shrubs (*Artemisia*, *Calligonum* and *Ephedra*), tufted grasses (*Stipagrostis*) and *Cyperus* (Schulz and Whitney, 1985). The underlying geology consists of Cambro-Ordovician sandstones from the interior shelf of Arabia that dip gently towards the east-northeast (Wagner, 2011). Eocene to late Oligocene aged ferricrete and iron-rich silcretes have also been observed (Whitney et al., 1983), while cemented 'white sands' of probable Quaternary age that represent 'palaeodunes' are often exposed in interdunal basins and frequently underlie younger palaeolake lake sediments (Breeze et al., 2017). Groundwater in the region comes from the Saq aquifer (Alsharhan et al., 2001; Lloyd and Pim, 1990).

The western and central Nefud Desert are dominated by large, densely packed compound barchanoid dunes that reach up to 80 m in height (Fig 1.1) (Breeze et al., 2017; Parton et al., 2018). Between these dunes are interdunal basins that are deepest in the western portion of the desert (see Fig 1.2, Breeze et al., 2015). The frequency and depth of interdunal basins provides areas for water to accumulate via runoff or by a regional rise in the water table, and for interdunal wetlands to develop during humid

phases, as shown by palaeohydrological modelling (Fig 1.2) (Breeze et al., 2015, 2017). The sediments formed within these interdunal wetlands (lakes or palustrine environments) are mechanically stronger than surrounding dune sands and are frequently preserved in the landscape as inverted relief features. Spectral analysis using GIS software shows a concentration of carbonate or siliceous sediments in the Nefud Desert (Fig 1.2) (Breeze et al., 2015). The presence of these deposits attest to episodic hydrological shifts towards wetter conditions in the past, where increased annual rainfall recharged aquifers and raised the groundwater table to intersect with interdunal basins (Schulz & Whitney 1986; Rosenberg et al. 2013; Breeze et al. 2017). Palaeohydrological mapping also demonstrates the probable existence of numerous lake basins on the southern and northern edges of the Nefud sand sea, along with structural basins within the sand sea (e.g. the Jubbah Basin; Parton et al., 2018) ranging in size from <1 km² to ~400 km² (Breeze et al., 2015).

Palaeoenvironmental work on interdunal palaeolake deposits began in the 1980's (Schulz and Whitney, 1986) but was followed by a long hiatus in research. Subsequent investigations restarted over the past decade (Groucutt et al., 2018; Petraglia, 2011; Rosenberg et al., 2013) (a detailed overview of this research is provided in Chapter 2). This research has focused primarily on archaeological (Groucutt et al., 2018; Scerri et al., 2015), palaeoenvironmental (Groucutt et al., 2018; Parton et al., 2018; Rosenberg et al., 2013) and palaeontological (Stimpson et al., 2016; Stewart et al., 2019, 2020b). This second phase of research activity has shown the Nefud Desert was a locus of hominin and faunal activity during Quaternary humid phases, with fossil and footprint evidence for *Homo sapiens* occupation during MIS 5 (Groucutt et al., 2018; Stewart et al., 2020a).

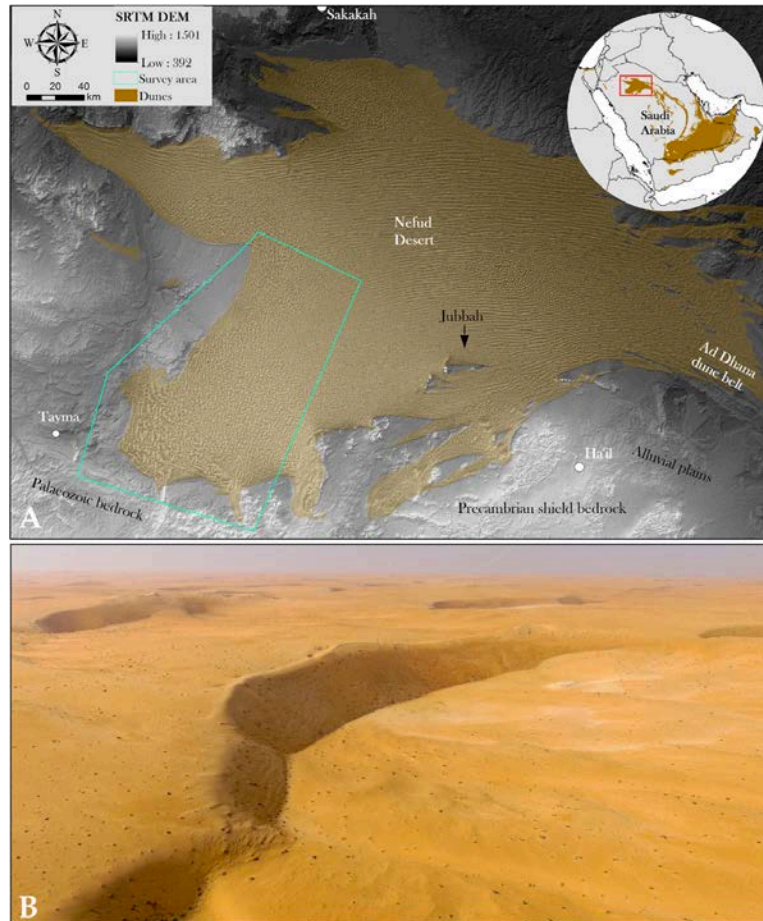


Figure 1.1 – Overview of the Nefud Desert from Breeze et al. (2017). (A) The outline of the Nefud desert with the present dune cover shown (in brown), key sites such as Jubbah and Tayma marked, and the study area of the western Nefud desert outlined by the green box. Inset image shows the location of the western Nefud sand sea within the Arabian Peninsula. (B) Aerial photograph showing the current landscape of the western Nefud Desert, which is characterised by large compound barchanoid dunes that reach up to 80 m in height.

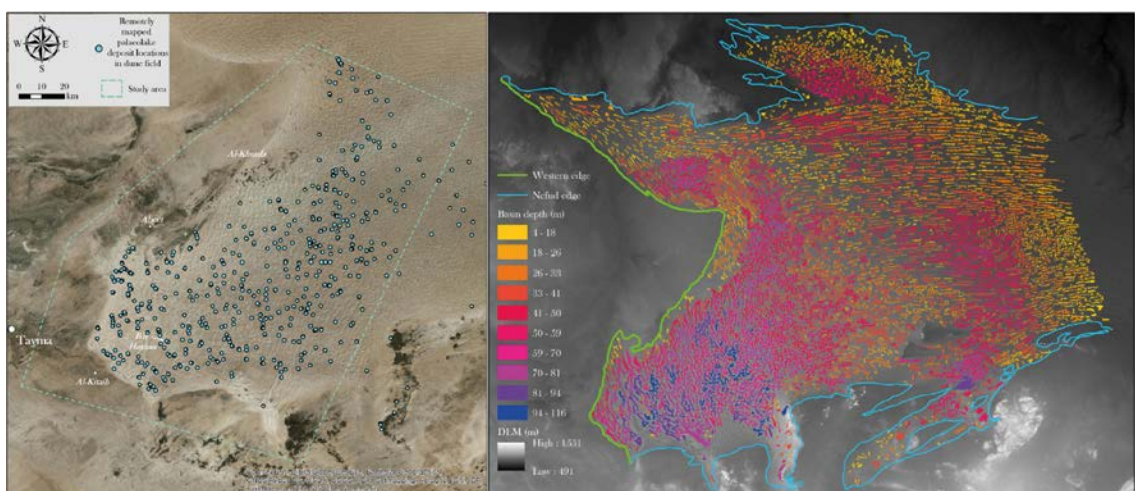


Figure 1.2 – Left: The distribution of undated 'palaeolake' deposits identified via multi-spectral classifications and GIS analysis from Breeze et al. (2015). Right: Basin depths of interdune depressions across the Nefud Desert from Breeze et al. (2017). The image on the left demonstrates numerous interdune palaeolake deposits are spread across the Nefud Desert, while the image on the right shows that interdune basin depths are deepest in the western portion of the Nefud Desert.

1.3 Aims and objectives

1.3.1 Aims

This thesis will determine the timing of humid phases and their palaeohydrological expression in the western Nefud Desert, Saudi Arabia over the past ~500 ka. To achieve this, the following subsidiary aims have been set:

1. To establish the timing of humid intervals in the western Nefud Desert by using luminescence dating and the published literature.
2. To determine the palaeoenvironment(s) of the western Nefud Desert during humid intervals by applying multi-proxy palaeoenvironmental analysis to interdunal carbonate or siliceous sediments.
3. To use the chronological framework constructed from aim 1 to better understand the timing of human occupations and dispersals through the western Nefud Desert during humid phases.
4. To use the palaeoenvironmental framework constructed from aim 2 to better understand the nature of human-environment interactions in the western Nefud Desert during humid phases.

1.3.2 Objectives

To achieve the aims stated above, the following objectives need to be achieved:

1. Visit a selection of the sites identified by Breeze et al. (2015, 2017) identified as having significant palaeoenvironmental potential along with significant archaeological and fossil assemblages (see Chapter 5 for explanation of this criteria).
2. Log and describe the sedimentology of interdunal carbonate or siliceous sediments from across the western Nefud Desert, and recover sample blocks for further laboratory analysis.

3. Take luminescence samples from key sequences to establish the age of each carbonate or siliceous deposit.
4. Apply bulk sedimentological techniques such as X-ray diffraction and calcimetry to compliment sedimentary descriptions from the field and determine the mineralogy and % carbonate of the sedimentary sequences.
5. Undertake micromorphological analysis on the carbonate and siliceous sediments, which will be combined with bulk-sedimentological analysis. From this the depositional environment in which the sediments were deposited will be inferred, such as whether they were deposited on the beds of perennial lakes or ephemeral palustrine systems.
6. Apply stable oxygen and carbon isotope analysis through each carbonate sequence to generate stable isotope stratigraphies for each sequence. Combine this analysis with X-ray diffraction to reconstruct palaeohydrology of the systems in which the sediments were deposited. The $\delta^{18}\text{O}$ stratigraphies will also allow the hydrological stability of these systems to be investigated.
7. Collaborate with other researchers who have undertaken palaeoecological analysis, predominantly consisting of diatom palaeoecology, and use this data where it is available to compliment the isotopic and X-ray diffraction analysis in reconstructing the palaeohydrology of the carbonate/siliceous sediments.
8. Combine the sedimentological, stable oxygen and carbon isotope analysis and palaeoecological analysis to construct a detailed depositional model for each sedimentary sequence.
9. Combine the depositional model and chronology from each sequence to investigate the nature of humid intervals through time, and then compare the palaeohydrology of each interdunal carbonate/siliceous sedimentary sequence deposited over the past ~500 ka.
10. Synthesise the palaeoenvironmental and palaeoclimatic record of the Arabian Peninsula, northeast Africa and the Levant of the past ~500 ka to place the palaeoenvironmental history of the western Nefud Desert into a regional context.
11. Use the palaeoenvironmental/palaeohydrological analysis from the western Nefud Desert to better understand human-environment interactions in the

Nefud, and use the wider regional synthesis to understand how the Nefud fits into broader patterns of human movements over the past ~500 ka.

1.4 Thesis structure

This thesis is divided into 15 chapters. Chapter 2 provides a review of the Quaternary climate drivers in the Saharo-Arabian desert belt and the Levant, the palaeoenvironmental archives and proxies across the same region, the palaeoenvironmental history of the Nefud Desert, and the history of Hominin dispersals into the Arabian Peninsula over the past 500 ka. Chapter 3 provides a review of interdunal lacustrine and palustrine carbonates in the low-latitudes. This discusses a model for the formation of interdunal lakes in the western Nefud Desert as well as a discussion regarding the palaeoenvironmental proxies found within them. Chapter 4 provides a review of the luminescence dating techniques used in this thesis. Chapter 5 outlines the palaeoenvironmental methods (i.e. sedimentological and isotopic) used in this study, as well as an outline of the diatom methods used by collaborators. Chapter 6 focuses on analysis of the luminescence data, and provides a chronology for the sites presented within this study. Chapters 7 – 12 present the palaeoenvironmental results from each site. Each palaeoenvironmental results chapter ends with a depositional model for the sedimentary sequence(s) studied. The sites are presented in age order, from youngest to oldest, based on the luminescence chronology from Chapter 6. The only exception to this is KAM4, which is presented last (chapter 12) as it contains several lake sequences of differing ages. Chapter 13 combines the chronology and palaeoenvironmental analysis from all sites and interprets the record of humid phases in the western Nefud Desert over the past ~500 ka. The record from the western Nefud Desert is subsequently compared with palaeohydrological records from the Arabian Peninsula, Levant and northeast Africa. Chapter 14 places the palaeohydrological record of the western Nefud Desert into the context of human demography and dispersals into the Arabian Peninsula. Chapter 15 presents the main conclusions of this study.

Chapter 2 – Quaternary climate drivers in the Saharo-Arabian desert belt and Levant

2.1 Introduction

Over the Quaternary (past 2.58 Ma, Head and Gibbard, 2015), the major climatic shifts in the Saharo-Arabian desert belt are characterised by changes in effective moisture balance, leading to alternating humid and arid phases (Grant et al., 2017; Larrasoana et al., 2003; Nicholson et al., 2020). These changes are driven by orbital parameters which control the latitudinal distribution of solar energy – insolation – that reaches the Earth’s surface (Berger and Loutre, 1991). Humid phases produce pronounced changes in the surface hydrology of the Saharo-Arabian desert belt, and this is recorded in a range of marine and terrestrial palaeoclimatic archives (see section 2.3). It is becoming increasingly apparent that these humid intervals have played an important role in ancient human dispersals, range expansions/contractions and population structure over the Pleistocene (Drake et al., 2011; Groucutt et al., 2015a). The aim of this thesis (see Chapter 1.3) is to reconstruct the timing and character of humid phases in the western Nefud Desert, and use this to better understand how humid phases have influenced ancient human demographic processes (i.e. population dispersals) in the region. Consequently, this chapter will review: (1) Hydroclimate of the Saharo-Arabian desert belt and Levant and northeast Africa over the past ~500 ka; (2) Palaeoclimatic archives across the same regions over the past ~500 ka; (3) Palaeoenvironment of the Nefud Desert over the past ~500 ka; (4) Hominin dispersals into Arabia over the last ~500 ka.

2.2 Hydroclimate of the Saharo-Arabian desert belt and Levant

2.2.1 Modern Hydroclimate

An understanding of the modern hydroclimatic setting of the Arabian Peninsula is an important first step in placing Quaternary climatic change into context. The modern

distribution of rainfall over the Arabian Peninsula (see Fig 2.1) is controlled by complex interactions between multiple climate systems (Parton et al., 2015). These are the Indian and African monsoon systems in southern Arabia, the Active Red Sea Trough and Tropical Plumes in central/northern Arabia, and the mid-latitude Westerlies/Mediterranean Cyclones in northern Arabia. Presently, African – Indian monsoonal rains are restricted to the southern reaches of the Arabian Peninsula, reaching the Yemen Highlands and the Asir Mountains of Saudi Arabia in the summer months (May – September) (Jennings et al., 2015; Parker, 2009). Monsoon systems are strongly seasonal and driven by land-sea thermal contrasts where greater insolation in the summer months warms land masses quickly relative to surrounding oceans due to differences in their specific heat capacity (see Fig 2.2). This creates areas of low-pressure over land that drags moisture-rich air from surrounding higher-pressure zones over the ocean. Latent heat release during cloud formation over land leads to more buoyant air masses and enhanced moisture convection (Fig 2.2). The increase in insolation during the summer pushes the intertropical convergence zone (ITCZ) and its associated monsoonal belt to a more northerly position, up to 12°N of the equator (Parton et al., 2015). However, this is not close to the location of the western Nefud Desert which is ~28°N of the equator.

The mid-latitude Westerlies (MLW) provide between 40 – 50% of the total precipitation in northern Arabia, delivering water during winter months (October – April) (Parton et al., 2015). Over the winter months the ITCZ is driven southwards by the East Atlantic/West Russian (EAWR) pressure system and the Azores high pressure of the North Atlantic Oscillation (Jennings et al., 2015). This leads to cold air overlying warm oceans, which generates moisture bearing westerly winds that originate in the eastern Mediterranean and move down across the Arabian Gulf (Jennings et al., 2015). The impact of winter Mediterranean Cyclones diminishes southwards from the Levant towards the northern Red Sea (Armon et al., 2019) as is also shown by the modern distribution of speleothem growth in the Levant/Negev Desert (Vaks et al., 2010), and it does not currently influence the Nefud Desert.

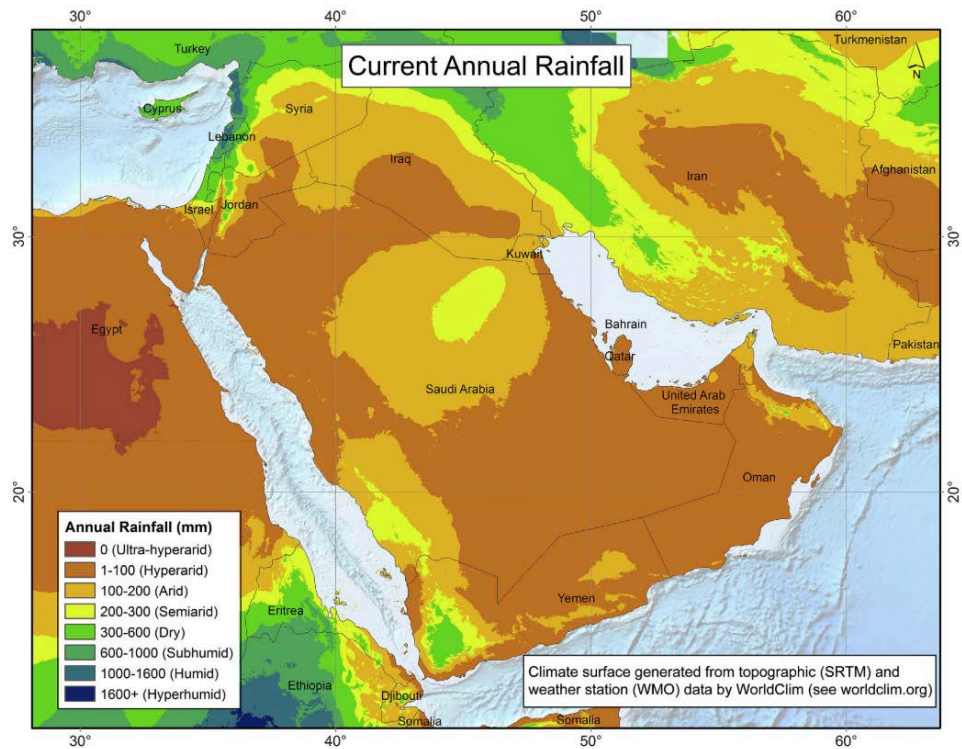


Figure 2.1 – Modern annual precipitation over the Arabian Peninsula derived from WorldClim data from Jennings et al. (2015). Currently rainfall is between 1 – 100 mm over much of the Arabian Peninsula including the western Nefud Desert, making the area hyper-arid.

Tropical-extratropical atmospheric interactions also bring rainfall to northern Arabia via the Active Red Sea Trough and Tropical Plumes. The Active Red Sea Trough (ARST) is an infrequent weather system that is associated with extreme precipitation and flash flooding across the Middle East (De Vries et al., 2013). This system brings rare rainfall during the autumn, and to a lesser extent during the winter and spring (De Vries et al., 2013). The Red Sea Trough (RST) is a synoptic – i.e. large scale – system that refers to a low-level pressure trough which runs from the current African monsoon region northwards towards the eastern Mediterranean (De Vries et al., 2013). When this synoptic system is accompanied by a midlatitude upper trough it leads to unstable conditions which trigger convective storms (ARSTs) (De Vries et al., 2013). ARSTs are spatiotemporally localised and intensive storms (Armon et al., 2018). Tropical plumes are elongated cloud bands that transfer tropical moisture from equatorial to extra-tropical zones during the winter and spring (see Fig 2.4) (Tubi and Dayan, 2014; Ziv, 2001). Rainstorms can develop in the exit regions of tropical plumes, and occur over longer periods (up to tens of hours) over a greater geographical range than ARSTs (Ziv, 2001).

Both ARSTs and tropical plumes can deliver or exceed the annual average rainfall amount to the northern Sahara or Red Sea regions (Hartman et al., 2020; Ziv, 2001)

Other minor climate systems that affect the Arabian Peninsula are (1) independent low pressure cells in northern and eastern Arabia caused by winter air masses from the Mediterranean meeting the Zagros Mountains (Jennings et al., 2015); and (2) tropical cyclones formed within the Arabian Sea (Kwarteng et al., 2009).

2.2.2 Quaternary hydroclimatic change

Long-term orbital cycles have driven large-scale changes in the Earth's climate system over the Quaternary (Hays et al., 1976). Orbital cycles occur on three temporal cycles: (1) eccentricity (95 – 136 ka cycle), the change of the planet's orbit from circular to elliptical and back; (2) obliquity of the ecliptic (~41 ka cycle), the change in the tilt of the earth's axis between 21°39' to 24°36'; and (3) precession of the equinoxes (19 – 23 ka cycle), the wobble of the Earth (Hays et al., 1976). Together these orbital cycles change the seasonal and latitudinal distribution of insolation the Earth receives over millennial timescales (Hays et al., 1976). In the low-latitudes, variations in eccentricity-modulated-precession are the most influential driver of climatic change where millennial-scale variations in insolation govern large-scale hydroclimatic change (Prell and Kutzbach, 1987).

2.2.2.1 African monsoon

Variations in the spatial extent of the African monsoon are the dominant driver of hydroclimatic change in the Saharo-Arabian desert belt (Rossignol-Strick, 1983), though the Indian Summer Monsoon may impact the southerly reaches of the Arabian Peninsula (Jennings et al., 2015). Arid phases in the Saharo-Arabian desert belt are the norm and occur during periods of moderate to low northern hemisphere (NH) summer insolation such as the present day. However, episodic humid phases do occur in response to high NH summer insolation. The physical mechanism for this is as follows. Summer insolation

in the Northern Hemisphere (NH) closely follows eccentricity-modulated-precession, and is at its peak during precession minima when the NH summer solstice occurs at perihelion (Mohtadi et al., 2016; Prell and Kutzbach, 1987). When this occurs, the increase in NH insolation causes early summer surface temperatures over the North African land mass to rise more quickly relative to the surrounding oceans, and results in a strong land-sea thermal gradient (Mohtadi et al., 2016). This increases atmospheric humidity and wind-circulation intensity, and ultimately increases the northerly extent of the African monsoon system through intensified zonal transport of moisture from the Atlantic Ocean (see Fig 2.2) (Gierz et al., 2017; Herold and Lohmann, 2009; Merlis, 2010; Mohtadi et al., 2016).

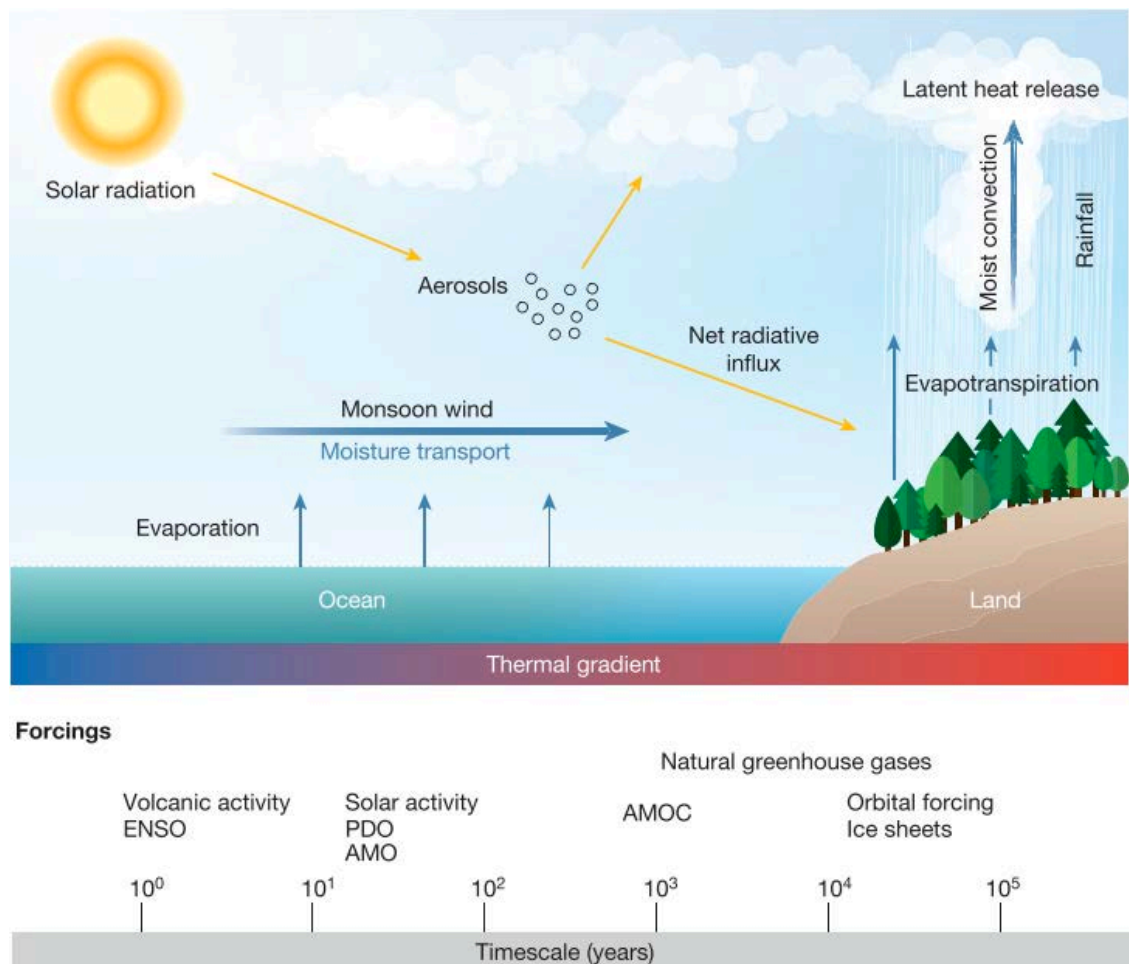


Figure 2.2 – Components of summer monsoons (from Mohtadi et al., 2016). The upper picture shows the mechanism for the summer monsoon. Here increased warming of the landmass relative to the ocean generates a thermal gradient and a ‘monsoon wind’ that transports moisture rich air from high-pressure zones over the ocean to low-pressure zones on land. Evapotranspiration on land then leads to latent heat release, moisture convection, and monsoonal rainfall. The lower picture shows the forcing timescales, with the focus of this study being on orbital forcing which occurs on 10^4 to 10^5 cycles.

It is important to note that hydroclimatic change caused by precession forcing is not just a simple change in the summer position of the ITCZ, but instead a shift in precipitation from the ocean to land (Mohtadi et al., 2016). Further feedback mechanisms can intensify monsoonal rainfall over land, such as enhanced convection and water recycling due to greater vegetation and increased evapotranspiration (Fig 2.2) (Mohtadi et al., 2016). Conversely, variations in aerosols such as dust, and cloud formation and properties, can increase/decrease the amount of solar radiation received by the Earth (Fig 2.2) (Mohtadi et al., 2016; Pausata et al., 2016). Both feedback systems exert strong controls over the monsoon system (Tierney et al., 2017b). These sub-Milankovich factors operate at timescales which are too short to resolve with the chronology used here, where uncertainties are on the scale of thousands of years.

As changes in the spatial extent of the monsoon system across the Saharo-Arabian desert belt are predominantly driven by eccentricity-modulated-precession, humid phases in the region are expected to occur periodically during periods of high NH summer insolation. These occur during interglacial (e.g. MIS 11 or MIS 5e) or interstadial (e.g. MIS 5a) periods (Nicholson et al., 2020; Rossignol-Strick, 1983). The absolute northerly extent of monsoon rains during humid intervals is difficult to establish. Climate models focused on Marine Isotope Stage (MIS) 5e shows differing northern limits based on model boundaries, though typically show that the northerly extent of monsoonal rainfall reaches the western Nefud Desert (e.g. Fig 2.3; Fig 13.18) (Gierz et al., 2017; Herold and Lohmann, 2009; Jennings et al., 2015). A recent isotope-enabled climate model along with new proxy evidence now implies that monsoonal rains may have extended as far north as the Levant during MIS 5e (Orland et al., 2019). Furthermore, the spatial extent and intensity of monsoon rains may vary between humid phases depending on NH summer insolation patterns (Nicholson et al., 2020; Rossignol-Strick, 1983).

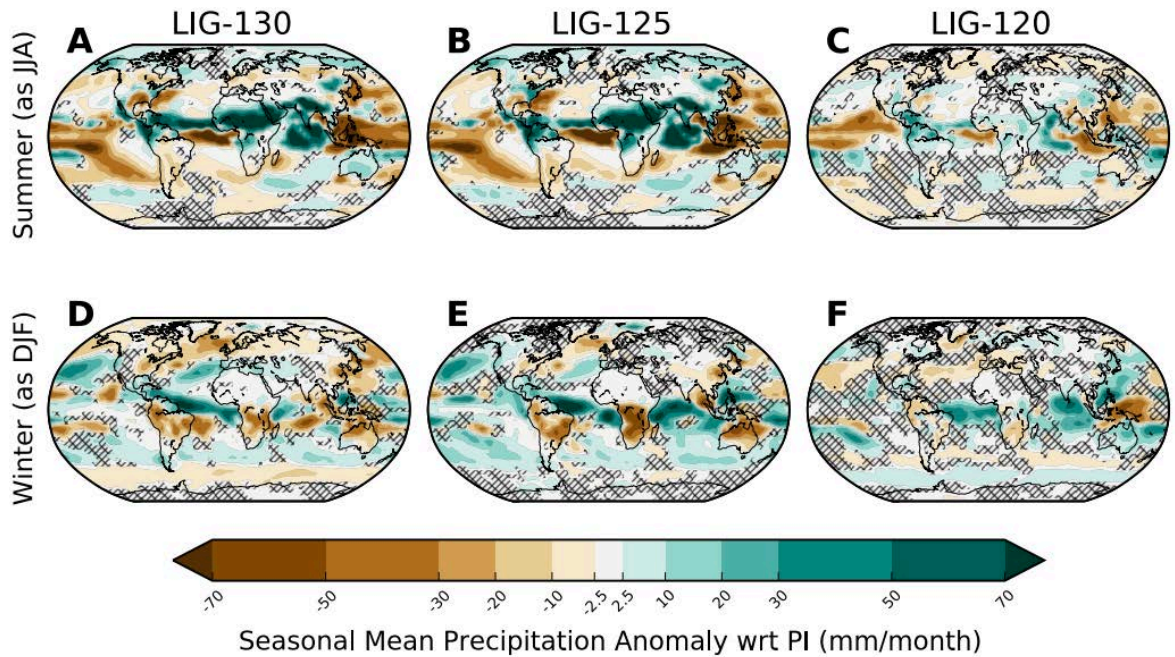


Figure 2.3 – Simulations of precipitation anomaly (relevant timeslice minus preindustrial (PI)) at 130, 125 and 120 ka time-slices using the fully coupled Earth system model ECHAM5/MPIOM (Jungclaus et al., 2006) with a stable isotope diagnostic (Werner et al., 2011). Figure from Gierz et al. (2017). Summer rainfall at 130 and 125 ka increases over the Saharo-Arabian desert belt while not clear increase in rainfall is present at 120 ka. There is a slight increase in winter rainfall over the eastern Mediterranean at 130 ka (D) but this does not appear to extend into northern Arabia. This climate model suggests a strongly seasonal climate to northern Arabia during humid phases.

2.2.2.2 Red Sea Synoptic Trough/Low Latitude (Tropical) Plumes

While there is now proxy evidence that monsoonal rains reached as far north as the Levant, it is not clear as to the amount of rainfall that reached northern Arabia and the Levant via this source. It has been suggested that the increase in monsoonal rainfall to northern Arabia and the Levant would constitute an increase in rainfall between less than 1 mm to a few mm per day during summer months (Hartman et al., 2020; Herold and Lohmann, 2009; Kutzbach et al., 2020; Orland et al., 2019). It has been questioned if this would be enough rainfall to lead to widespread change of the surface hydrology in this region, such as the development of interdunal lakes (Hartman et al., 2020). As such, authors have invoked enhanced activity of other tropical moisture sources such as the Active Red Sea Trough or Tropical Plumes to explain increased humidity (Enzel et al., 2015; Hartman et al., 2020; Waldmann et al., 2010). It is not clear how these climate mechanisms have varied over Quaternary timescales. It is plausible that both an

increased northerly range in summer monsoonal rainfall combined with enhanced activity of other autumnal/winter/spring tropical moisture sources contributed to increased humidity in the western Nefud Desert and northern Arabia.

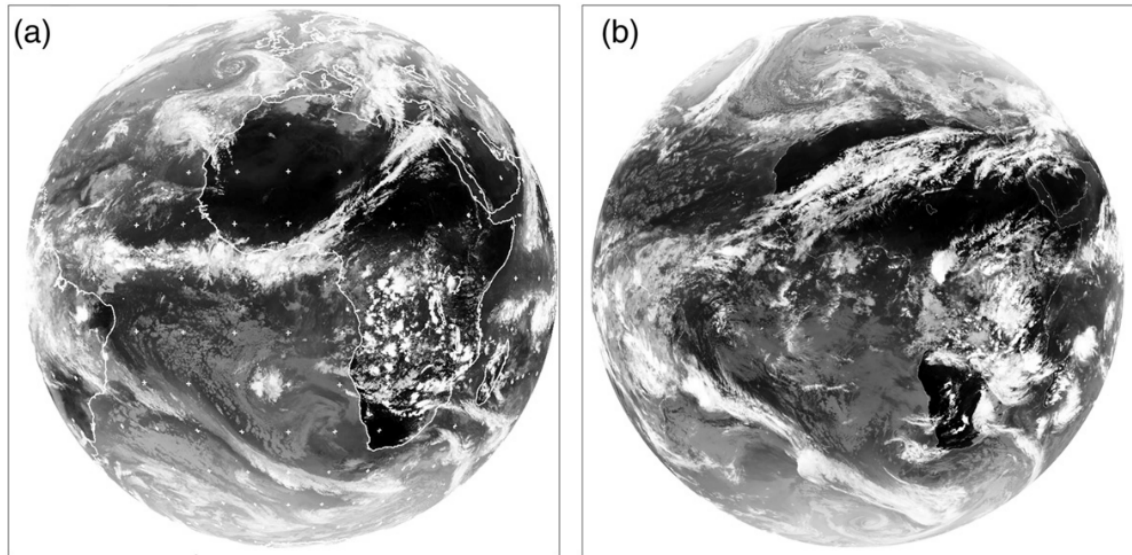


Figure 2.4 – Examples of modern-day moisture bearing tropical plumes extending from western Africa across the Sahara-Arabian desert belt from Tubi and Dayan (2014). Enzel et al. (2015) suggest that an increase in winter and spring tropical plumes could account for humid phases over the Quaternary.

2.2.2.3 Mid-Latitude Westerlies (MLW)/East Mediterranean cyclonic systems

The northern latitudes of the Saharo-Arabian belt (i.e. northern Arabia) could also be influenced by variations in the mid-latitude westerlies (MLW). The spatiotemporal variations of the MLW are poorly understood and multiple mechanisms have been proposed to explain them. Firstly, it has been argued that they vary with global temperatures and ice sheet expansion/contraction, where they contract towards the poles during interglacials but extend further south during cooler phases (Blome et al., 2012; Toggweiler and Russell, 2008). Conversely, it has been argued that they vary with summer season insolation as monsoonal rainfall does (Fig 2.5) (Kutzbach et al., 2014). During periods of maximum northern hemisphere seasonality, where precession minima coincide with winter aphelion and a minimum in NH winter insolation, climate models suggest an increase of MLW rainfall to the Eastern Mediterranean and western Asia (see Fig 2.5) (Kutzbach et al., 2014; Mehterian et al., 2017). This is due to the

southerly displacement of the Hadley and Ferrell cells, resulting in a southerly displacement of storm tracks (Kutzbach et al., 2014; Mehterian et al., 2017).

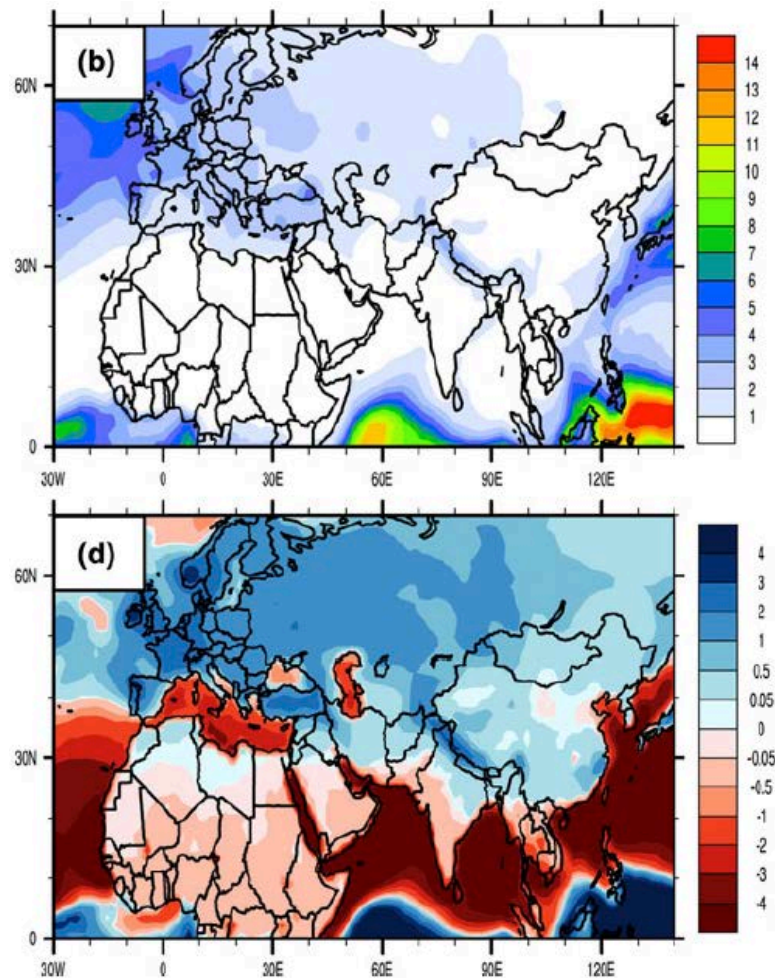


Figure 2.5 – Modelled winter (DJF) precipitation (mm/day) (Picture B) and precipitation minus evaporation (Picture D) for 125 ka using CCSM3 climate model after Kutzbach et al. (2014). This shows there is an increase in winter rainfall over the eastern Mediterranean, Levant and western Asia during MIS 5 but this does not appear to extend to the latitude of the Nefud Desert in northern Arabia.

Importantly, climate models do not show increased winter (DJF) precipitation as far south as the Nefud, with a sharp boundary at the Negev Desert/Sinai Peninsula (Fig 2.5) (Kutzbach et al., 2014). Nevertheless, the MLW cannot be considered insignificant to the Nefud Desert’s hydrology over the Pleistocene. Recently, a lagged onset of humidity in northern Arabia (Tayma) compared to the SE Mediterranean and Levant during the Holocene Humid Phase has been observed based on the presence of the S1 tephra isochron (Neugebauer et al., 2017). This has been used to support the argument that a southerly displacement of winter Mediterranean Cyclones were the main source of moisture during this time period (Neugebauer et al., 2017). Tayma lies just ~35 km from

the western edge of the Nefud Desert and ~85 km from study sites presented in this thesis. At present it is not clear to what extent MLW/Mediterranean rainfall impacted the Nefud's hydrology in the past.

2.3 Palaeoenvironmental archives across the Saharo-Arabian desert belt and Levant over the past ~500 ka

Numerous palaeoenvironmental archives from around the Arabian Peninsula, Levant and northeast Africa document pronounced hydroclimatic change in the region over the past ~500 ka in response to spatial variations in atmospheric circulation systems. This section aims to introduce the key palaeoenvironmental archives from across the region. Marine and terrestrial archives are considered in turn.

2.3.1 Marine records

Marine archives from locations surrounding the Arabian Peninsula and North Africa provide continuous but low-resolution environmental records. Consequently, they are ideal for recording millennial-scale monsoon dynamics and hydroclimatic change over the Quaternary and have been used to construct aridity/humidity indexes for North Africa (Grant et al., 2017). This section focuses on three key proxies found in marine archives: sapropel layers, terrigenous dust flux and the δD of leaf wax.

2.3.1.1 Sapropel layers

Sapropel events recorded in eastern Mediterranean ocean cores provide an extensive record of changes in monsoon intensity over the Quaternary (Rohling et al., 2015; Rossignol-Strick, 1983). Sapropel layers are organic-rich sediments with C_{org} (organic carbon) levels reaching 15% (Rohling et al., 2015). They are formed during periods of high freshwater input into the eastern Mediterranean basin due to enhanced precipitation in the Ethiopian Highlands and subsequent increased Nile Discharge during precession-driven monsoon peaks (Rohling et al., 2015; Rossignol-Strick, 1983). This

results in density stratification and the interruption of deep-water formation in the eastern Mediterranean, leading to anoxic bottom water conditions and the preservation of organic matter (see Fig 2.6) (Rohling et al., 2015). Increased freshwater input is supported by negative $\delta^{18}\text{O}$ excursions as measured in planktonic foraminifera and high dissolved Ba (Grant et al., 2012; Rohling et al., 2015).

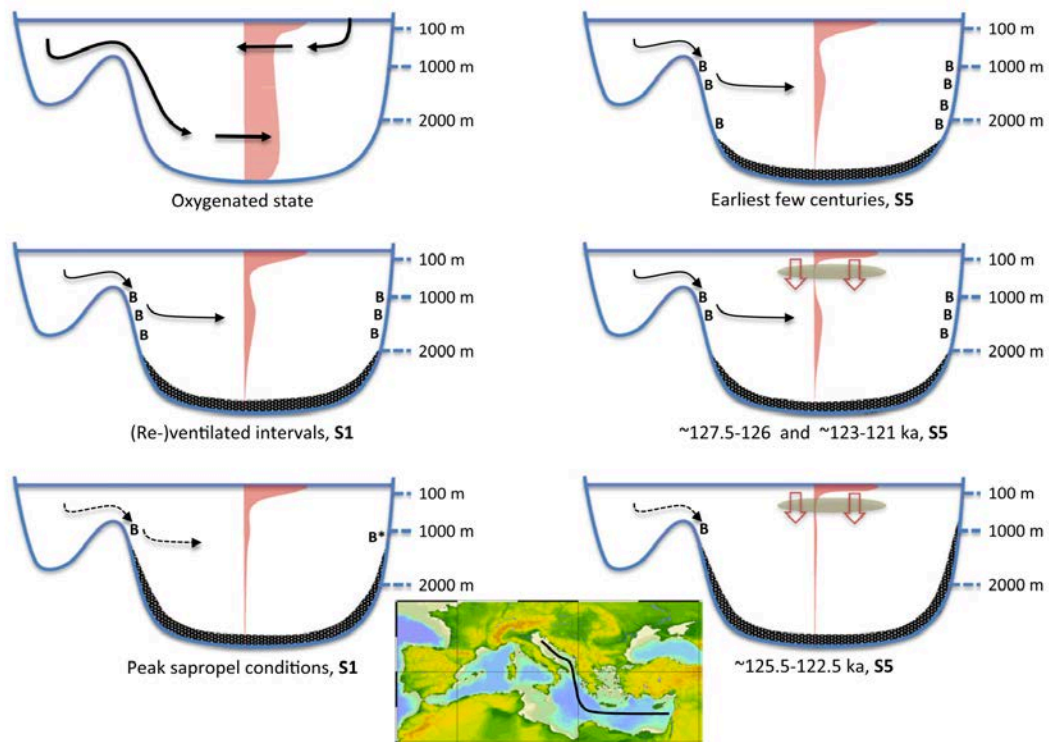


Figure 2.6 – Schematic diagram of sapropel formation in the eastern Mediterranean Sea, from Rohling et al. (2015). The three diagrams on the left show the current oxygenated state (top left) and then two ‘ventilation stages’ during the deposition of the S1 sapropel (Holocene). The three diagrams on the right show different stages of the S5 sapropel formation (MIS 5e). The pink shadow represents oxygen levels through the water column which fall to a minimum in the hypolimnion during peak sapropel formation. The black hatching represents anoxic sea floor conditions. The brown shading represents ‘photic layer’ euxinia – i.e. where waters are anoxic.

Sapropel events are dated by astronomical tuning, where maxima in the June insolation curve at 65°N are used as age calibration points for sapropel mid points (Lourens, 2004; Lourens et al., 1996; Ziegler et al., 2010). It is argued there is a time lag of 3000 years between the insolation maximum and the sapropel midpoint, based on radiocarbon dating of sapropel 1 which occurs at ~ 8.5 ka (Lourens et al., 1996). Subsequent chronological work has been undertaken, correlating the planktonic $\delta^{18}\text{O}$ record from ODP site 968 to the Chinese speleothem records (Ziegler et al., 2010) and the Aegean core LC21 to the Soreq Cave record (Grant et al., 2012). However, these studies only

change the original age-model of the sapropel records in a minor way. On this basis, sapropel events occur during summer insolation peaks in the northern hemisphere and therefore occur during northern hemisphere interglacial periods (e.g. MIS 5e) and interstadial periods (e.g. MIS 5a and 3) (see Table 2.1). They are numbered in age order, with “S1” being the youngest (~8.5 ka), through to the Miocene (Rohling et al., 2015). Nevertheless, their chronology is poorly defined as there are numerous age estimates for S1 (see section 7.3, Williams et al., 2015), with no direct radiometric ages from older sapropel events and no age ranges given. Therefore, using sapropel ages to infer the timing of humidity across the Saharo-Arabian desert belt must be done with caution. Recently, independently dated extreme flood episodes in the valleys of the Blue, White and main Nile have been linked to sapropel events over the last 125,000 years (Williams et al., 2015).

Table 2.1 – Age control points for sapropels S1 – S10 from ODP site 968, from Ziegler et al. (2010). Orbital tuning is used to date sapropel layers, and the method is discussed further in the text below.

Event	Composite depth (cm)	Age (ka)
Coretop	0.00	0
S1 (top)	0.58	6.5
S1 (bottom)	0.84	10.2
S3 (top)	5.40	77.3
S3 (bottom)	5.58	83.9
Precursory S3 (top)	5.64	86.6
Precursory S3 (bottom)	5.86	91
S4 (top)	6.47	99.6
S4 (bottom)	6.57	104
Precursory S4 (top)	6.73	105.9
Precursory S4 (bottom)	6.81	109.7
S5 (top)	7.63	121.4
S5 (bottom)	7.96	129.5
S6 (top)	10.36	165.5
S6 (interruption)	10.69	169.8
S6 (bottom)	10.95	178.5
S7 (top)	11.77	191.9
S7 (bottom)	12.19	198.5
S8 (top)	12.67	209.5
S8 (interruption)	12.90	213
S8 (bottom)	13.22	224.1
S9 (midpoint)	13.82	239
S' (midpoint)	16.18	288
S10 (midpoint)	17.50	331

2.3.1.2 Terrigenous dust record

Terrigenous dust in marine archives record aeolian dust supply, composition, grain size and reflectance, and have been used as a proxy that records continental hydroclimatic change (e.g. deMenocal et al., 2000). Terrigenous records from the central Red Sea (core KL 11) and Gulf of Aden (core KL 15) show lower median grain sizes during peak interglacial periods (Fleitmann, 1997 referenced in Nicholson et al., 2020) while ODP site 721/722 in the Arabian Sea shows a lower percentage of aeolian dust during interglacial periods (deMenocal, 1995). Furthermore, dust flux minima are correlated with insolation maxima from ODP site 967 in the Eastern Mediterranean over the past ~3 Ma (Larrasoña et al., 2003). In such records, lower dust influx is interpreted to be due to greater landscape stability due to increased vegetation cover in response to increased humidity. This leads to lower erosion and thus lower input of coarse grain material into marine sediments. Conversely, during arid phases landscape stability is decreased since vegetation cover is low. Lake beds also become exposed during arid phases and can generate large amounts of dust (e.g. the Bodélé Depression, Chad; Washington et al., 2009). While terrigenous dust records provide long and continuous records of hydroclimatic change, the controls on the mobilisation, transport and deposition of dust are influenced by multiple non-linear variables. This includes wind strength and direction in addition to vegetation density, erosion and production of dust as described above (Nicholson et al., 2020). Consequently, it is difficult to relate them to hydroclimatic change on the terrestrial landscape at a local scale.

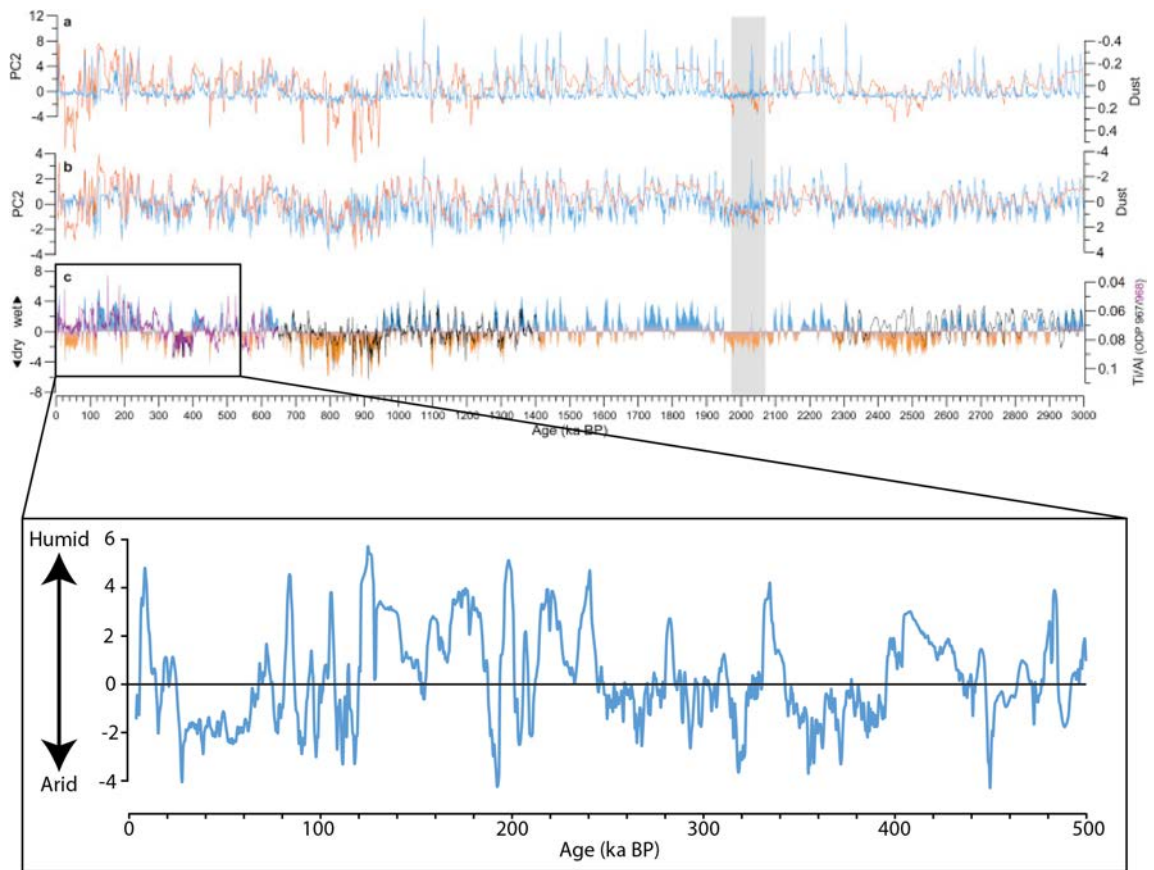


Figure 2.7 – Humidity/aridity index over the past 3 million years modified after Grant et al. (2017). Top: (A) This shows the PC2 (sapropel record) in blue from Grant et al. (2017) and the ODP967 dust record from Larrasoña et al. (2003). (B) Shows the same as above but with the time-series transformed to a standard normal distribution. (C) This shows the humid/aridity index as constructed based on the integration of the PC2 ‘sapropel’ signal and the ODP967 dust record (Grant et al., 2017). Blue shading = increased moisture. Orange shading represents aridity. The bottom figure focuses on the past 500 ka, which is the focus of this study. Positive values equate to humid intervals and negative values equate to arid intervals. Multiple humid intervals are observed over the past 500 ka based on this index, with peak humidity occurring during the Holocene, MIS 5a, 5c, 5e, 7 and beyond. Surprisingly this record also shows increased humidity for much of MIS 6, which is inconsistent with other terrestrial archives.

Most recently, Grant et al. (2017) constructed a North African humidity/aridity index based on XRF scanning the marine core ODP 967 and the aeolian dust record from the same core (Larrasoña et al., 2003) (Fig 2.7). Grant et al. (2017) identify two principal components from XRF scanning related to detrital inputs (PC1) and a sapropel signal (PC2). The latter signal, which is a ‘wet-sensitive’ proxy that tracks increased run off into the eastern Mediterranean, is combined with the ‘dry-sensitive’ proxy of aeolian dust of Larrasoña et al. (2003), which tracks Saharan desertification, to compose a humidity/aridity index for the past 3 million years (Grant et al., 2017). This shows multiple humid phases occurred over the North African continent over the past ~500 ka, with the humid signals related to interglacial periods such as the Holocene, MIS 5e, 7 and 9 (Fig 2.7). Humid periods also occur during MIS substages such as 5c and 5a.

2.3.1.3 δD_{wax} from marine records

δD_{wax} records off the coast of West Africa and the Gulf of Aden (Arabian Peninsula) from core RC09-166 provide detailed reconstructions of hydroclimatic change in the Sahara and Arabian Peninsula over the Holocene (Tierney et al., 2017b) and the past 200 ka (Tierney et al., 2017a). Variations in δD_{wax} through marine sediments reflect variations in rainfall amount as δD_p has a strong relationship with the amount of rainfall in the low-latitudes: more positive δD_p reflects lower rainfall and more negative δD_p reflects higher rainfall (Tierney and deMenocal, 2013). The Holocene record is derived from four marine sediment cores that form a transect from 19°N to 31°N along the west coast of Africa (GC68, GC49, GC37 and GC27), and demonstrate increased monsoonal rainfall to 31°N during the Holocene Humid Period (11 – 5 ka). Core RC09-166 from the Gulf of Aden records palaeohydrological conditions from the Horn of Africa and Afar regions, and shows there was increased rainfall during the early Holocene, MIS 5a, 5c, 5e and 7a in the Gulf of Aden (Fig 2.8) (Tierney et al., 2017b, 2017a).

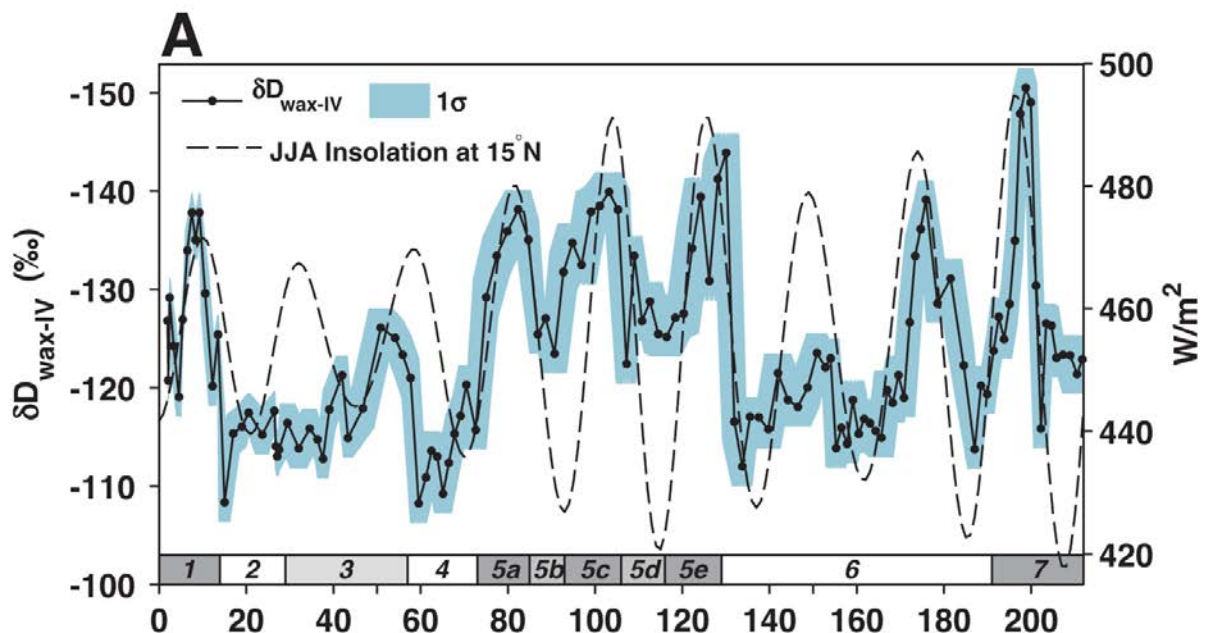


Figure 2.8 – Stable hydrogen isotopic composition of leaf waxes corrected for ice-volume from Gulf of Aden (core RC09-166) over the past 200 ka from Tierney et al. (2017). The black line shows median values while the blue shading shows analytical and chronological 1σ uncertainty (Tierney et al., 2017). The dashed line represents June-July-August insolation at 15°N. More negative δD_{wax-IV} values relate to greater rainfall amount, with multiple periods of increased rainfall related to the Holocene, MIS 5a, 5c, 5e, 6 and 7.

2.3.2 Terrestrial records

For the purposes of this thesis, terrestrial records have a distinct advantage over marine records because they directly record hydroclimatic change in the landscapes that ancient humans and fauna occupied. However, they are often temporally discontinuous, and few records extend beyond the Last Interglacial. Terrestrial records relevant to this thesis can be split into the following categories: (1) speleothems, (2) lacustrine/palustrine records, (3) travertines/tufas, (4) palaeosols and (5) fluvial records. A greater focus will be put on the speleothem records and the lacustrine/palustrine records. Speleothems provide a large amount of palaeoclimatic information that are important for understanding regional atmospheric circulation over the Levant and Saharo-Arabian desert belt, while lacustrine/palustrine records directly record surface hydrology and are the focus of this thesis.

2.3.2.1 *Speleothem records*

Speleothems, which are secondary mineral deposits in caves such as stalagmites and flowstones, are the most widely studied terrestrial palaeoenvironmental archive across the Levant and Saharo-Arabian desert belt. They occur in Egypt (El-Shenawy et al., 2018; Osmond and Dabous, 2004), the Levant (Bar-Matthews et al., 2003, 2000; Frumkin et al., 1999; Nehme et al., 2018, 2015), the Negev Desert (Vaks et al., 2007, 2006), Oman (Burns et al., 2001; Fleitmann et al., 2003) and Yemen (Fleitmann et al., 2011; Nicholson et al., 2020). Speleothem records in the Saharo-Arabian desert belt (excluding records from the Levant) typically only record growth during periods of strong NH summer insolation such as the mid-Holocene, MIS 5a, 5c, 5e, 7a, 7e, 9c, 9e and beyond into the Early-Middle Pleistocene (see Fig 2.9) (Nicholson et al., 2020). Conversely, no growth occurs in intervening low NH summer insolation periods when annual precipitation is below 300 mm yr⁻¹ (Vaks et al., 2013, 2010). Consequently, at the first order speleothem growth provides a presence/absence record of increased continental humidity across the Saharo-Arabian desert belt.

High-resolution $\delta^{18}\text{O}$ records in combination with precise U-series chronologies from speleothems are a powerful tool for palaeoclimatic reconstruction. The typical pattern across all speleothem records in the Saharo-Arabian desert belt, including continuous records from the Levant, is that $\delta^{18}\text{O}$ values are more negative during peak humid intervals (e.g. Bar-Matthews et al., 2003; Vaks et al., 2007; Fleitmann et al., 2011; El-Shenawy et al., 2018; Nicholson et al., 2020). The exact mechanism responsible for these more negative $\delta^{18}\text{O}$ values varies between regions, though almost always directly or indirectly relates to increased monsoonal rainfall over the Saharo-Arabian desert belt.

In Oman and Yemen, more negative $\delta^{18}\text{O}$ during humid phases is linked to an increased influence of low- $\delta^{18}\text{O}$ monsoonal rainfall relative to higher- $\delta^{18}\text{O}$ Mediterranean rainfall, along with an increase in the total amount of rainfall (Fig 2.6) (Fleitmann et al., 2011, 2003; Nicholson et al., 2020). Low rainfall results in more effective evaporitic enrichment of precipitation at the cloud base leading to more positive $\delta^{18}\text{O}$ values, while the effect of evaporitic enrichment is less during phases of greater monsoonal rainfall leading to more negative $\delta^{18}\text{O}$ values (Rozanski et al., 1993). Recent analysis of stalagmite Y99 at Mukalla Cave, Yemen, records a total number of 21 humid periods over the past 1.1 Ma and has used $\delta^{18}\text{O}$ as a proxy for rainfall amount (Fig 2.9) (Nicholson et al., 2020). This allows the comparison of humid intervals in southern Arabia and suggests that every previous southern Arabian humid phase was wetter than the Holocene, while MIS 5e and 7a were the wettest interglacials over the past ~500 ka (Nicholson et al., 2020). Furthermore, seasonally resolved isotopic analysis from Mukalla Cave suggests strongly seasonal rainfall during humid phases, with a wet summer and dry winter (Nicholson et al., 2020).

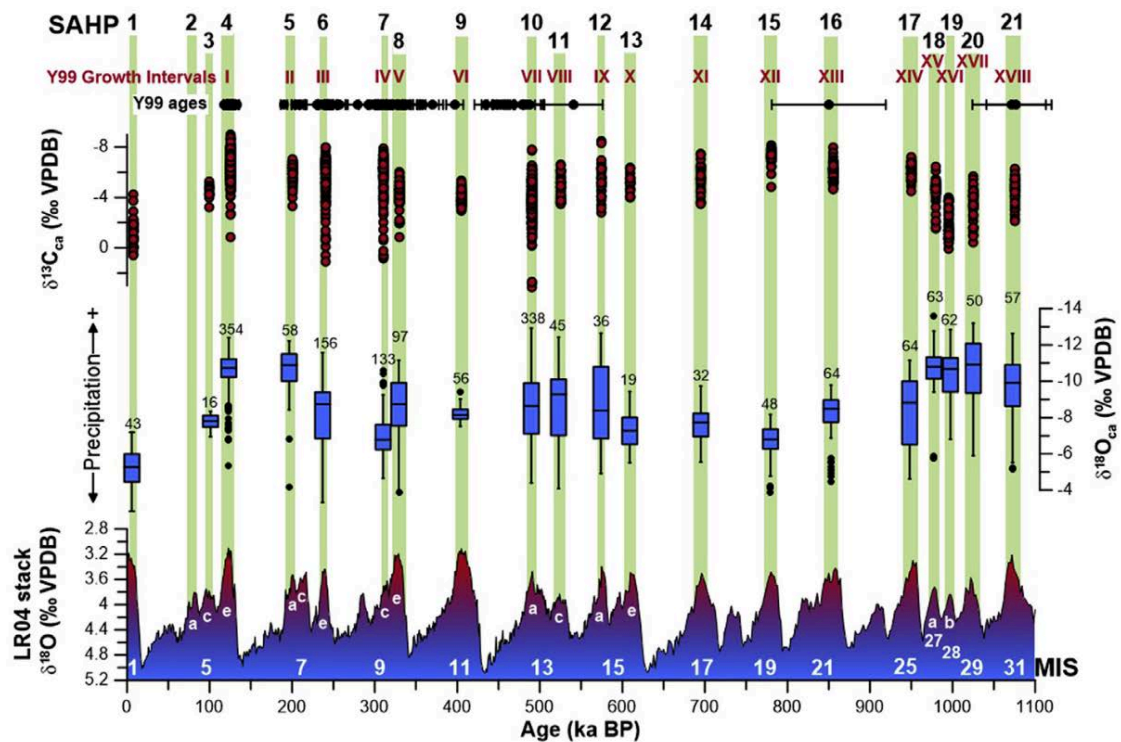


Figure 2.9 – Record of South Arabian Humid Phases (SAHPs) constructed from speleothem Y99 from Mukalla Cave, Yemen from Nicholson et al. (2020). SAHPs are shown by horizontal green bars and are labelled from 1 – 21 in age order. SAHPs 1 – 8 are derived from direct U/Th ages while SAHPs 9 – 21 are assigned ages based on a combination of U/Pb dating and orbital tuning (Nicholson et al., 2020). Growth intervals and ages are shown along the top of the figure. $\delta^{13}\text{C}$ values for each growth interval are shown by red dots and $\delta^{18}\text{O}$ values shown in blue boxplots. The latter are a proxy for amount of precipitation with more negative values associated with greater rainfall. The LR04 benthic $\delta^{18}\text{O}$ stack is shown at the bottom (Liesiki and Raymo, 2005).

In NE Africa, the Levant and the Negev, the more depleted $\delta^{18}\text{O}$ values recorded during high-insolation periods are linked to several processes. Firstly, it is suggested that increased freshwater flooding from the Nile into the eastern Mediterranean (EM) basin lowered the $\delta^{18}\text{O}$ of surface waters in the region, which is the source of winter rainfall to the Levant/Negev speleothems (Bar-Matthews et al., 2003). Secondly, it has been suggested that an incursion of low- $\delta^{18}\text{O}$ summer monsoon rainfall extended north eastwards into the region during NH summer insolation peaks (El-Shenawy et al., 2018; Orland et al., 2019). The $\delta^{18}\text{O}$ becomes depleted through Rayleigh distillation, as moisture is transported from the Atlantic and across the North African continent to NE Africa and the Levant (El-Shenawy et al., 2018). This interpretation runs contrary to climate models that suggest monsoonal rains did not extend as far north as the Levant (Herold and Lohmann, 2009; Jennings et al., 2015; Prell and Kutzbach, 1987). However, seasonally resolved $\delta^{18}\text{O}$ signals from Soreq Cave, combined with an isotope-enabled

climate model from the same study, suggest that summer monsoonal rains did extend into the Levant and contribute to the depleted $\delta^{18}\text{O}$ signal in speleothems in the region (Orland et al., 2019). The increase in both winter and summer rainfall in the Levant, NE Africa and potentially northern Arabia is in contrast to the highly seasonal distribution of rainfall in southern Arabia (Nicholson et al., 2020).

While multiple mechanisms are invoked to explain the same negative shift in isotopic values from speleothems across southern Arabian, NE Africa, the Negev and the Levant, all mechanisms are associated with variations in orbitally-driven spatial variations in monsoon rainfall. Interestingly, the Holocene $\delta^{18}\text{O}$ values from Mukalla, Yemen (Fig 2.9) are the most positive and this suggests greater environmental aridity relative to other humid phases.

2.3.2.2 Lacustrine records

Lacustrine records are widespread across the Saharo-Arabian desert belt, and at the most basic level provide a first-order proxy that demonstrate past humid conditions on the terrestrial landscape. However, the majority of records are restricted to the Holocene due to the erosive nature of desiccated dryland environments and the consequent low preservation potential of older deposits.

In the Arabian Peninsula, evidence for lacustrine deposits related to increased rainfall during the Holocene comes from records in northern Arabia (Jubbah - Parton et al., 2018; Tayma - Engel et al., 2011; Dinies et al., 2015), southern Arabia (Al-Hawa - Lézine et al., 2010; Mundafan - Rosenberg et al., 2011) and southeastern Arabia (Wahalah, Awafi - Parker et al., 2006; Parker et al., 2016; Wahiba Sands - Radies et al., 2004). Sedimentary and palaeoecological data are usually interpreted as representing perennial and occasionally freshwater lake systems that develop in response to increased precipitation, more abundant groundwater and increased spring outflow in terminal basins (Engel et al., 2016). However, this interpretation is not universally accepted (Enzel et al., 2015). In the Sahara, the Oxford Lake Level Database (OLLD)

records variations in lake volume across the African continent over the Holocene, and demonstrates lake high stands in North Africa at c. 9 ka in response to the northward extension of monsoon rains caused by increased NH summer insolation (Street-Perrott et al., 1989 referenced in Tierney et al., 2011). More recent evidence for increased Holocene/Terminal Pleistocene humidity within North Africa comes from lake-level fluctuations in Megalake Chad, where increased humidity is first recorded at 15 ka and reached a high stand at 11.5 ka which abruptly ended at 5 ka (Armitage et al., 2015).

Evidence for phases of lake formation or highstands in the Saharo-Arabian desert belt prior to the Holocene is more limited, while uncertainties on ages become so large as to make it difficult to assign records to marine isotope stages or sub-stages. Nonetheless, lacustrine sediments have been dated to MIS 3 in southeastern Arabia (Parton et al., 2013), the Nefud Desert (Jennings et al., 2016) and central Jordan (Moumani et al., 2003). During MIS 5 lacustrine sediments were deposited in southeastern Arabia (Rosenberg et al., 2012), southern Arabia (Groucutt et al., 2015d; Matter et al., 2015a; Rosenberg et al., 2011), the Nefud Desert (Groucutt et al., 2018; Parton et al., 2018; Rosenberg et al., 2013), Jordan (Cordova et al., 2013; Macumber, 2008; Moumani et al., 2003; Petit-Maire et al., 2010) and North Africa/Sahara (Armitage et al., 2007; Causse et al., 2003; Lezine and Casanova, 1991). Middle Pleistocene lacustrine records prior to MIS 5 have been recovered from the Nefud Desert (Parton et al., 2018; Rosenberg et al., 2013), Jordan (Cordova et al., 2013; Petit-Maire et al., 2010) and North Africa (Causse et al., 2003). It is important to interpret these deposits with caution as the chronologies are often poorly constrained. For example, the Azraq lacustrine beds from Jordan yield U-Th dates with a 2σ age range between 206 – 86 ka (Macumber, 2008), while other less extreme examples contain age ranges greater than the length of precession cycles (e.g. Moumani et al., 2003). These archives are discussed further in Chapter 13.

2.3.2.3 Other terrestrial archives

Various other terrestrial archives record hydroclimate change and increased humidity across the Saharo-Arabian over the past 500 ka. These include travertines/tufas from

the Negev (Waldmann et al., 2010) and Egypt (e.g. Smith et al., 2004; Hamdan and Brook, 2015), the Nefud (Petraglia et al., 2011) and Sinai Peninsula (Roskin et al., 2013, 2011), and the activation of fluvial networks or alluvial aggradation from central Arabia (Matter et al., 2016; McLaren et al., 2009) and the Sinai Peninsula (Faershtein et al., 2016). These records are discussed further in Chapter 13.

2.4 Palaeoenvironment of the Nefud Desert over the past 0.5 Ma

The research presented in this thesis is focused on reconstructing the nature and timing of humid phases in the western Nefud Desert, based on multi-proxy analysis and dating of interdunal carbonate/siliceous sediments. This section will therefore review the existing literature on Quaternary hydroclimatic change in the region.

2.4.1 Early palaeoenvironmental research

Early palaeoenvironmental investigations of interdunal carbonate or siliceous sediments and/or their associated archaeology in the Nefud Desert were carried out in the 1980s (Garrard et al., 1981; Schulz and Whitney, 1986; Whitney et al., 1983; Whitney and Gettings, 1982). Palaeoenvironmental work was first undertaken on the Bi'r Hayzan diatomite deposit, located in the southwestern arm of the Nefud at 27°35'40"N, 39°10'23"E (Whitney and Gettings, 1982). Based on the presence of freshwater diatoms and pure laminated diatomite, the authors conclude that the deposit represents a freshwater lake with an area of at least several km² and a depth of up to 10 m, that lay within a stabilised landscape (Whitney and Gettings, 1982).

Schulz and Whitney (1986) added to this with studies of seven 'marl' beds in the southern and central Nefud. These deposits were split into Upper Pleistocene and Holocene lakes based on radiocarbon dating, extent and geomorphic setting. The Upper Pleistocene lakes are described as extended marls, calcareous crusts and, rarely, diatomite and were interpreted as representing lakes that were several km² in area (Schulz and Whitney, 1986). In contrast, Holocene lakes consisted of thin-layers of marls, cemented sands and rare diatomites, and were interpreted as small, fluctuating, swamp

like water bodies (consistent with palustrine environments) (Schulz and Whitney, 1986). Palynology data from both 'Upper Pleistocene' and 'Holocene' lakes are comparable to modern-day semi-desert flora, with grasses such as *Gramineae* and *Cyperaceae*, shrubs including *Calligonum*, *Artemisia* and *Fagonia*, and herbs like *Compositae* present (Schulz and Whitney, 1986). In addition, the presence of *Phragmites* and *Typha* imply swamp environments surrounding palaeolakes, as well as a dense herb cover (Schulz and Whitney, 1986).

The overarching palaeoclimatic interpretations given by these early researchers relied on radiocarbon dates are not consistent with the more recent luminescence-based chronology, and were likely contaminated by younger meteoric water (Rosenberg et al., 2013). For example, Bi'r Hayzan was originally deemed an 'Upper Pleistocene' lake by Schulz and Whitney (1986), but recent OSL and TT-OSL dating of the deposit by Rosenberg et al. (2013) places the lake between 366 ± 57 ka (sands underlying the diatomite sediments) and 104 ± 9 ka (sands overlying lake sediments). Nonetheless, the palaeoenvironmental analysis including palynology, sedimentology, diatom analysis and elemental chemistry remain valid, and are integral to informing interpretations regarding humid phases in the western Nefud Desert today.

2.4.2 Recent palaeoenvironmental research

Petraglia et al. (2011) led a revival in palaeoenvironmental work in the Nefud following an extended hiatus. This study focused on the site Jebel Quattar 1 (JQ1) which is located within the Jubbah Basin (see Fig 1.1 for location of Jubbah). The site features a ~3 metre stratigraphic sequence composed of interdigitated palaeosol, sand and calcrete units, capped by dune sands (Petraglia et al., 2011). Two OSL samples were taken from palaeosol units below and above the main calcrete unit whilst a third sample was taken from the uppermost calcrete unit immediately below the capping dune sands. The lowermost palaeosol was dated to 211 ± 16 ka (MIS 7), the intermediate palaeosol to 95 ± 7 ka (MIS 5c) and the uppermost calcrete unit as 75 ± 5 ka (MIS 5a). Petraglia et al. (2011) infer that the main calcrete unit formed during MIS 5e (Petraglia et al., 2011). In

terms of chronology, this was the first sign that the radiocarbon dates from the earlier research underestimated the age of the lake deposits and humid phases.

Phytolith and carbon isotope analysis on the inferred MIS 5e calcrete and the MIS 5c palaeosol at JQ1 indicate a vegetation consisting C₃ Pooid-dominated grassland with more minor C₄ Panicoid and Chloridoid components being present (Petraglia et al., 2011). The MIS 5a calcrete differs from this in that it shows an increase in C₄ Chloridoid grasses and a 2% shift towards more positive $\delta^{13}\text{C}$ values which indicates a drier environment; though C₃ Pooids are still dominant in the section (Petraglia et al., 2011). This demonstrates potential variability in the landscape between separate humid phases during MIS 5. The dominance of grasses also supports earlier palaeoenvironmental work by Schulz and Whitney (1986).

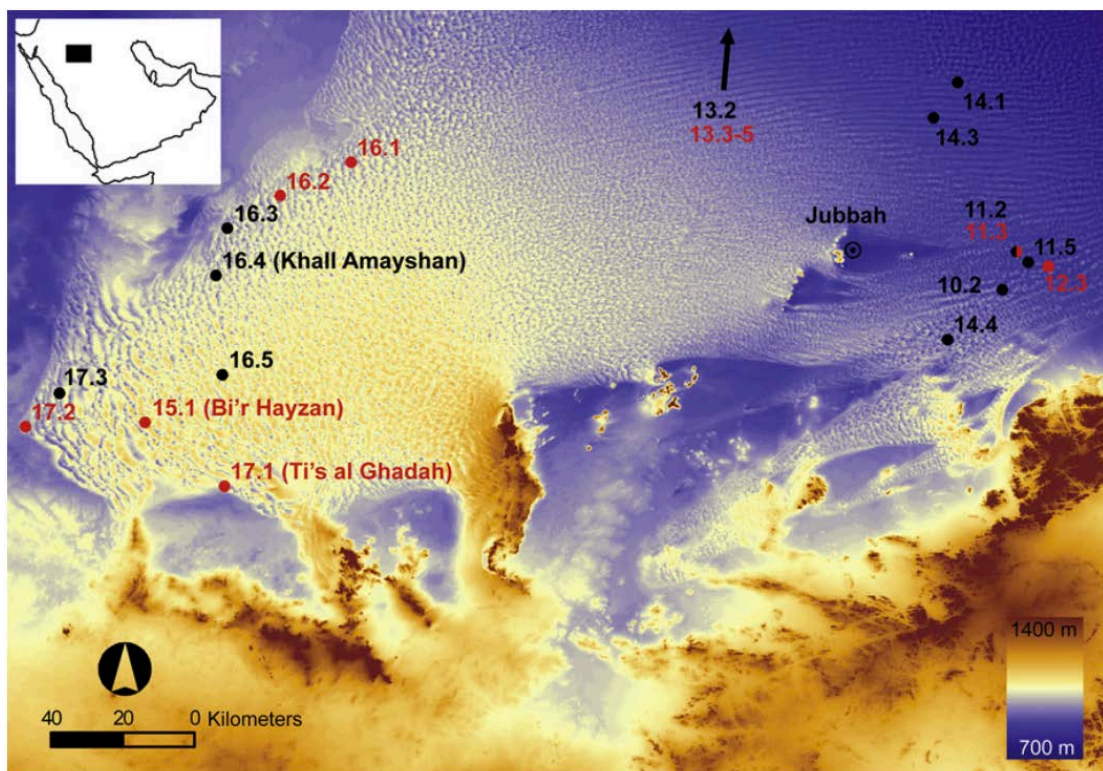


Figure 2.10 – Interdunal palaeolake deposits studied by Rosenberg et al. (2013) with red labels representing Middle Pleistocene deposits and black labels representing MIS 5 sites. Image taken from Rosenberg et al. (2013).

Rosenberg et al. (2013) focused on carbonate/siliceous sediments from interdunal depressions within the Nefud sand sea. They used a combination of diatom palaeoecology, macroscale sedimentology and luminescence dating in order to decipher

the nature of the water bodies (e.g. size and water depth) along with the timing of their formation. Nine palaeolake sequences were reported from the western Nefud Desert with luminescence dating (OSL and TT-OSL) showing phases of lake development and humidity closely aligned with interglacial periods over the Middle and Upper Pleistocene (Fig 2.10, 2.11) (Rosenberg et al., 2013). Eight of the nine lacustrine sequences studied are described as diatomite with only one described as calcareous marl (Site 16.1) (Rosenberg et al., 2013). Rosenberg et al. (2013, pp. 114) suggest the diatomaceous composition of the sediment is linked to a pure sand and quartzose environment favourable for clear, acidic and siliceous waters. This contrasts with other interdunal sediments in the western Nefud that are carbonate-rich (e.g. Al Wusta; Groucutt et al., 2018). Subsequent analysis of Site 16.3 which is described as 'laminated white diatomite' based on field observations by Rosenberg et al. (2013) shows this sedimentary sequence is dominated by homogenous carbonate (Clark-Wilson, 2016). As such, it is not clear whether sections described as diatomite by Rosenberg et al. were all truly diatomite.

Despite this it is true that some palaeolake sequences contain no carbonate while others are dominated by it. This reflects variations in the hydrology of interdunal lakes across the Nefud Desert. The exact model for the difference between lakes has not been described, but reflects the fact that some lakes will contain more acidic waters that either lacked the physical conditions (i.e. lack of carbonate and calcium ions) required to form carbonate, or lacked the biological or physical mechanisms to increase pH and precipitate carbonate (see Chapter 3.4 for discussion on carbonate precipitation).

Rosenberg et al. (2013) argue that Middle Pleistocene lakes were extensive while Upper Pleistocene lakes were smaller with fluctuating waterbodies. This is an interpretation that parallels the distinction between Upper Pleistocene and Holocene lakes made by Schulz and Whitney (1986). The interpretation of extensive Middle Pleistocene lakes is based on diatom assemblages and macrofacies of three sites (Bi'r Hayzan, 16.2 and 17.2), along with faunal evidence from a fourth (Locality 2/Ti's al Ghadah; Thomas et al., 1998; Stimpson et al., 2015, 2016; discussed in section 2.4.2). All three sites contain laminated facies, whilst diatom data from Bi'r Hayzan (previously studied by Whitney

and Gettings, 1982) shows a dominance of freshwater planktonic diatom species such as *Aulacoseira granulata* and *Stephanodiscus cf rotula*. The latter species suggests deep, stable conditions (Rosenberg et al., 2013). Together these features are indicative of the distal facies of an extensive freshwater lake (Rosenberg et al., 2013). Exactly how extensive the freshwater lake was is not known but, Le Nindre (1986) referenced in Rosenberg et al. (2013) suggests that the horizontal bedding of these deposits could mean that diatomite underlies a large portion of the south-western Nefud. Breeze et al. (2017) are sceptical of this suggestion since they observe MIS 11 deposits occurring at different altitudes with ‘near shore’ sediments lying 40 m beneath ‘basin centre’ sediments. SRTM data also shows the regional topography is not consistent with a single-large lake body (Breeze et al., 2017). In contrast, Rosenberg et al. (2013) suggest that Upper Pleistocene lakes were shallower, with fluctuating water tables, based on the frequency of burrows, plant remains, inclined bedding and diatom assemblages.

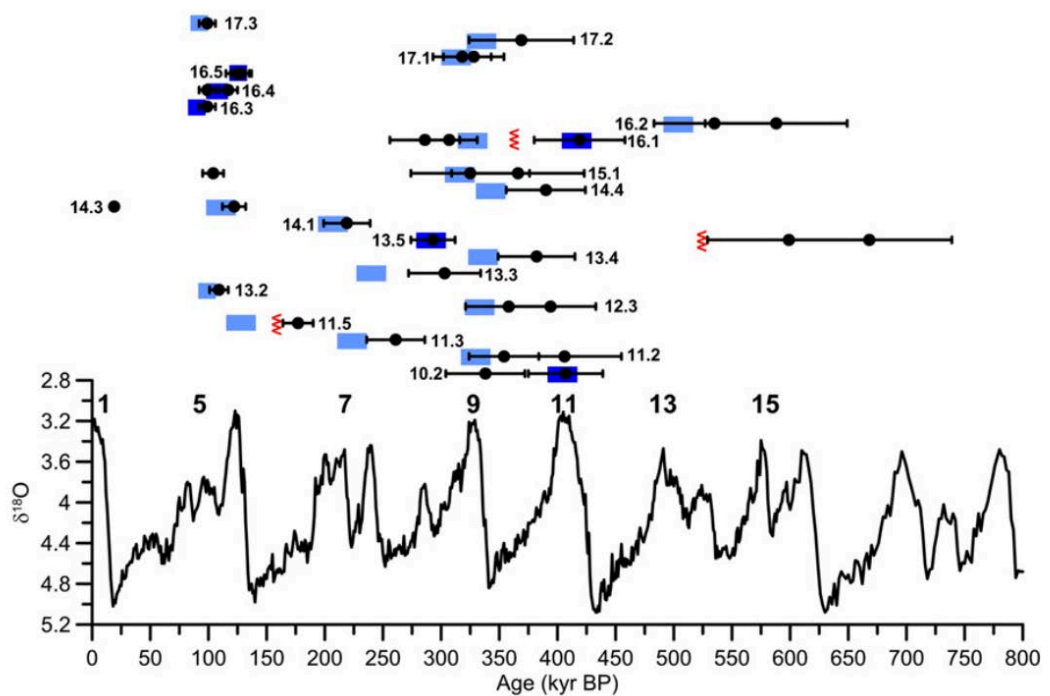


Figure 2.11 – OSL ages of palaeolakes in the Nefud Desert from Rosenberg et al. (2013). Note that light blue represents indirectly dated samples (underlying sands) and dark blue represents directly dated samples).

Rosenberg et al. (2013) suggest that the origin of moisture in the western Nefud Desert during humid intervals was the east African Monsoon, where increased rainfall in the Hijaz Mountains (Sarawat) could have captured rainfall and directed it inland towards

the Nefud via surface water channels and groundwater (Rosenberg et al., 2013). Such an interpretation is consistent with the modelled and observed northerly extent of monsoonal rainfall during a humid interval during MIS 5e (Herold and Lohmann, 2009; Orland et al., 2019).

Jennings et al. (2016) also report lake development at Al Marrat on the southern edge of Nefud Desert that dates to MIS 3 (53.9 ± 4.1 and 56.2 ± 6.5). This site lies ~125 km to the east of the western Nefud Desert, and is hydrologically different from interdunal palaeolake sequences in that it lies within a structural basin. Consequently, the existence of an MIS 3 age lake at Al Marrat does not necessarily imply that contemporaneous lakes existed in the Nefud. The stratigraphic profile is comprised of interstratified marls and calcrete. Unit 3, which contains marly silts with evidence for root activity, represents a shallow but stable waterbody and was deposited during the most humid period represented within the sequence (Jennings et al., 2016). Unit 4 contains nodular calcareous platykurtic silts with root voids and gypsiferous nodules, thus reflecting a more arid palustrine environment. Importantly, it is from this unit that lithics were found eroding from the sequence (Jennings et al., 2016). Phytolith analysis from this unit suggests that a C₃ grassland dominated, with some C₄ influences. This is similar to the results from Petraglia et al. (2011) from the MIS 5 site JQ-1 in the Jubbah region, that lies ~50 km from Al Marrat.

Parton et al. (2018) undertook detailed palaeoenvironmental analysis from in the Jubbah basin. Jubbah is a large endoheic depression, covering a total area of ~177 km², that lies in the south-central Nefud approximately 160 km to the east of the study sites presented in this thesis (see Fig 1.1). Four sedimentary sequences were excavated at Jubbah and multi-proxy palaeoenvironmental analysis and luminescence dating applied to each sequence. Direct dating of the wetland deposits demonstrates that lake development and humid intervals occurred at Jubbah during MIS 11/9, 7, 5e, 5a, 3 and the Holocene (Fig 2.12) (Parton et al., 2018). Multi-proxy palaeoenvironmental analysis including diatom palaeoecology, $\delta^{18}\text{O}$ and $\delta^{13}\text{C}$ analysis and bulk sedimentology shows that lake levels varied between and within humid intervals, with a large freshwater lake present during MIS 5e, while brackish lacustrine/palustrine environments with

fluctuating water-levels occurred during MIS 5a and 3 (Parton et al., 2018). The Holocene lake is characterised by astatic, evaporitic and more saline waters between ~12 – 9 ka, and then shallow, fluctuating but freshwater conditions from ~9 – 6.5 ka (Parton et al., 2018). Human occupation during the Middle Palaeolithic, Epipalaeolithic and Neolithic periods is also evident at Jubbah (Parton et al., 2018).

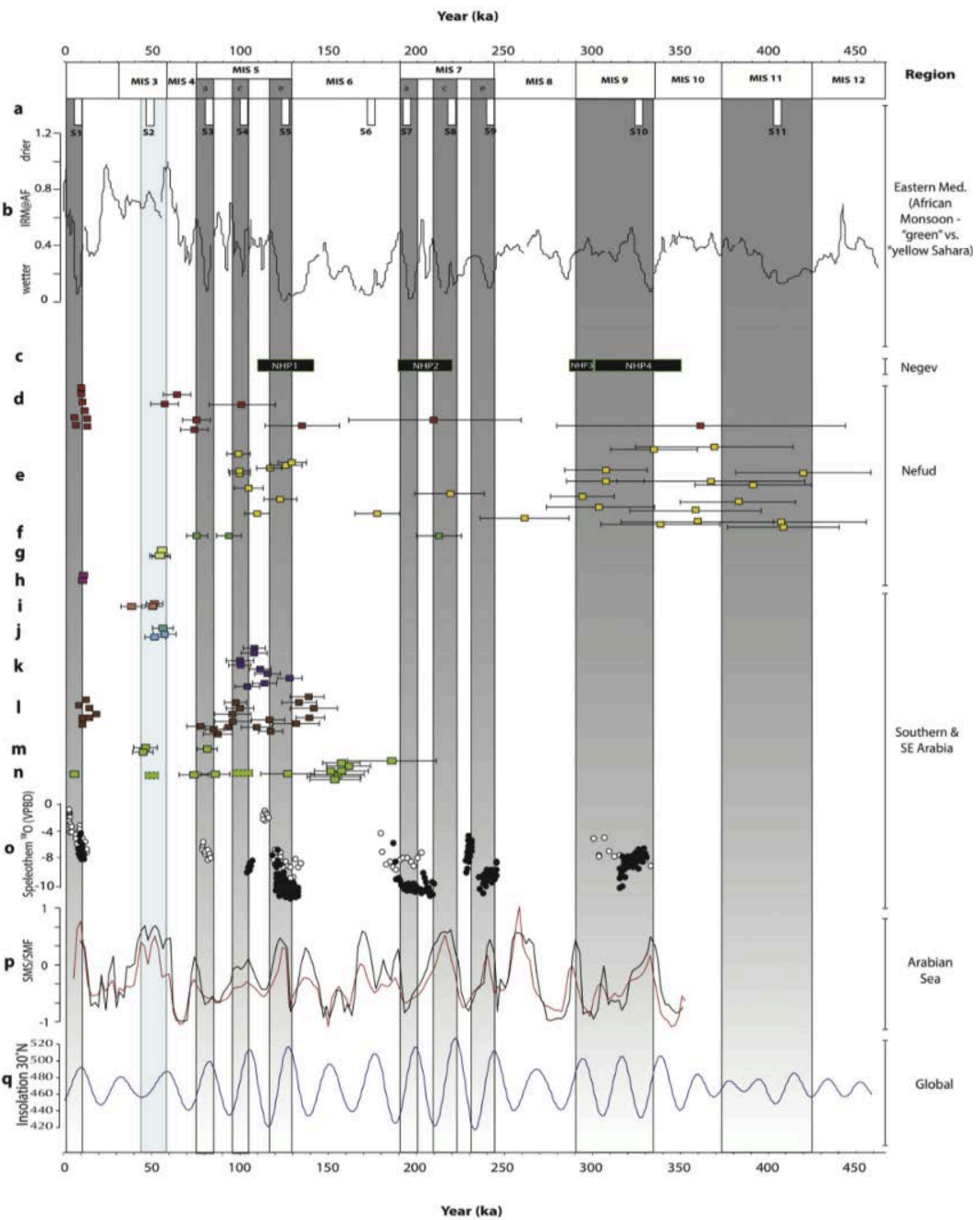


Figure 2.12 – Key palaeoenvironmental records published up to 2018 from across the Arabian Peninsula taken from Parton et al. (2018). It is evident that humid records correlate with warm marine isotope stages and sub-stages, though uncertainties beyond MIS 5 make it impossible to directly correlate records from the western Nefud Desert (D, Parton et al., 2018; E, Rosenberg et al. 2013) with other regional records (A – C, F – P). (a) Eastern Mediterranean sapropels (Zhao et al., 2011); (b) dust flux from ODP967 (Larrasoana et al., 2003); (c) Negev humid periods (NHPs)

(Vaks et al., 2010); (d) Lake/wetland ages from Jubbah (Parton et al., 2018); (e) Nefud palaeolake ages from Rosenberg et al., 2013); (f) inferred lake age formation from JQ1 at Jubbah (Petraglia et al., 2012); (g) Al Marrat – Nefud Desert (Jennings et al., 2016); fluvio-lacustrine sequence in eastern UAE (Parton et al., 2013); lake formation from Saiwan, Oman (Rosenberg et al., 2012); lake ages from Mundafan and Khujaymah, Rub al Khali (Rosenberg et al., 2011); (m & n) activation of the Al Ain alluvial fan system eastern UAE at Remah (m) (Farrant et al., 2012) and Al Sibetah (n) (Parton et al., 2015); Speleothem $\delta^{18}\text{O}$ records from Mukalla and Hoti Caves (Fleitmann et al., 2011); (p) summer monsoon stack (SMS) and summer monsoon factor (SMF) of monsoon intensity proxies from the Arabian Sea (Clemens and Prell, 2003); (q) June insolation at 30°N (Berger and Loutre, 1991).

Most recently, published work from Al Wusta (Groucutt et al., 2018), and unpublished MSc work from Site 16.3 (Clark-Wilson, 2016), use multi-proxy palaeoenvironmental analysis on interdunal lake sediments to demonstrate the presence of perennial freshwater lakes within the western Nefud Desert during MIS 5a. Microfacies analysis demonstrates that both lake bodies contained homogenous microsparite with no evidence for pedogenic processes or sub-aerial exposure. X-ray diffraction (XRD) shows a dominance of calcite and lack of evaporites, stable isotope analysis shows no covariance between $\delta^{13}\text{C}$ and $\delta^{18}\text{O}$ and small $\delta^{18}\text{O}$ ranges, indicative of non-evaporitic waterbodies (Talbot, 1990). Diatom analysis shows a dominance of freshwater species. Taken together these lines of evidence show that the western Nefud Desert contained non-evaporitic interdunal lake bodies that contained fresh drinkable waters during MIS 5a. Furthermore, Al Wusta yielded a *Homo sapiens* fossil, demonstrating the importance of interdunal sites within the western Nefud Desert to ancient human occupations and dispersals (Groucutt et al., 2018). Additional analysis from Al Wusta is presented within this thesis.

2.4.3 Palaeontology/Zooarchaeology of the Nefud Desert

Multiple studies have assessed fossil assemblages within the western Nefud Desert, which are predominantly found on the landscape surface in association with palaeolake deposits or eroding out from these deposits (Groucutt et al., 2018; Stewart et al., 2020b, 2019, 2017; Stimpson et al., 2016, 2015; Thomas et al., 1998). A widespread taxonomic and taphonomic review of Pleistocene fossil assemblages shows fauna include genus/species such as Elephantidae and *Hippopotamus* which are consistent with a well-watered semi-arid grassland environment (Stewart et al., 2020b). However, it is important to note that fossils often display attrition due to wind abrasion, insolation,

and salt weathering due to their exhumation from palaeolake deposits and subsequent position on the landscape surface of a desert environment (Stewart et al., 2020b).

The most complete fossil assemblage comes from Unit 5 at Ti's al Ghadah (TAG) in the western Nefud Desert, dated to between 300 – 500 ka (Rosenberg et al., 2013; Stimpson et al., 2016; Stewart et al., 2019). The dominance of even-toed ungulates (e.g. Oryx) combined with high $\delta^{13}\text{C}$ values (-0.8 to 3.3‰) from mammalian teeth (e.g. Elephants, Oryx, Hartebeest, Equids) are consistent with a semi-arid C4 dominated grassland environment (Roberts et al., 2018; Stewart et al., 2019). The presence of large-bodied fish (*Pisces osteoglossiformes*) (Thomas et al., 1998), Aves with aquatic affinities (grebe and duck) and large mammals such as Elephantidae (who live in in large family groups and require up to 360 l of water a day) further indicate the presence, at least seasonally, of a large standing water body at Ti's al Ghadah (Stewart et al., 2019; Stimpson et al., 2016). Carnivores such as *P. cf. gombaszogensis* (Eurasian jaguar), *Canis anthus* (African golden wolf) and *Crocuta crocuta* (spotted hyaena) were also present in the fossil record at Ti's al Ghadah (Stimpson et al., 2016). The presence of such carnivores implies a substantial biomass, as large carnivores require a productive landscape to attract populations of prey animals (Stimpson et al., 2016). Stewart et al. (2019) notes that the presence of vultures at the site implies no tree/bush cover, while mortality profiles suggests ambush predation was prevalent, which is indicative of the presence of long grasses.

Further palaeoenvironmental data at Ti's al Ghadah has been gained from the analysis of $\delta^{18}\text{O}$ of fossil teeth (Roberts et al., 2018). Roberts et al. (2018) compare the $\delta^{18}\text{O}$ of teeth from obligate vs non-obligate (obtain most water from plant-based sources) drinkers from the Unit 5 fossil assemblage at Ti's al Ghadah with modern-day samples from Arabia and East Africa. As environmental humidity is the key source of fractionation in leaf water $\delta^{18}\text{O}$, the assumption is that there would be a smaller difference in median $\delta^{18}\text{O}$ values between obligate and non-obligate drinkers during more humid intervals where environmental humidity would be lower (Roberts et al., 2018). Conversely, there would be a greater difference during arid phases. The results

show little difference in $\delta^{18}\text{O}$ between obligate and non-obligate drinkers, which is consistent with East African sites such as Laikipia (Kenya) and Tsavo (Kenya). However, they differ from modern-day Arabia, where the difference is greater reflecting the greater aridity in present day Arabia (Roberts et al., 2018).

A fossil assemblage has also been recovered from MIS 5a site Al Wusta (Groucutt et al., 2018). Specimens present include those from classes Mammalia, Aves and Reptilia, while notable species include *Hippopotamus*, *Pelorovis*, and *Kobus* (Groucutt et al., 2018). The presence of *Hippopotamus* and *Kobus* indicates the presence of permanent waterbodies at the site while the overall faunal assemblage is dominated by grazers, consistent with an open grassland environment (Groucutt et al., 2018). Further evidence of *Hippopotamus* in the western Nefud Desert has been recorded at Site 16.3, dated to MIS 5a, and KAM4 lake 4 which is dated as part of this thesis (Stewart et al., 2020b).

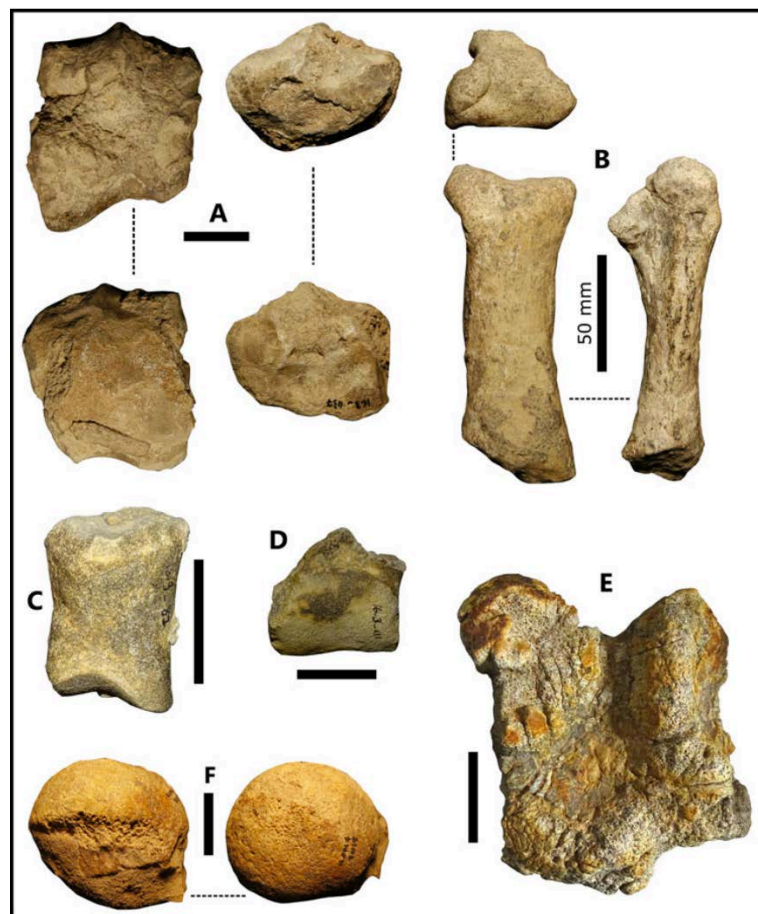


Figure 2.13 – Hippopotamid remains found within the western Nefud Desert from Stewart et al. (2020b). Hippopotamus remains along with elephant, show the western Nefud was humid enough for the dispersal of large water dependent taxa into the region (Stewart et al., 2020b).

In summary, fossil assemblages from the western Nefud Desert are consistent with increases in absolute humidity compared to the present day, with an environment dominated by a savanna like grassland within which permanent waterbodies existed (Thomas et al., 1998; Stimpson et al., 2015, 2016; Stewart et al., 2017, 2019, 2020b; Groucutt et al., 2018; Roberts et al., 2018).

2.5 Hominin dispersals into Arabia over the past 0.5 Ma

The Arabian Peninsula lies between Africa and Eurasia and thus holds a critical geographic position at the interface of hominin dispersals between the two continents over the past ~500 ka. While the peninsula has been arid for much of the past ~500 ka, the episodic humid phases discussed above potentially provide freshwater resources and brief windows for human occupation and dispersal across the Peninsula (Breeze et al., 2016). A substantial archaeological literature attests to human occupation in, and dispersal through, the Arabian Peninsula from the Lower Palaeolithic (Acheulean) through to the Neolithic/Holocene (Armitage et al., 2011; Groucutt et al., 2018, 2016, 2015b, 2015d, 2015c; Hilbert et al., 2014; Petraglia and Alsharekh, 2003; Scerri et al., 2018b; Shipton et al., 2018).

The earliest dated evidence of hominin activity in the Arabian Peninsula comes from Ti's al Ghadah in the western Nefud Desert (Roberts et al., 2018). Here V-shaped cut marks on ungulate rib fragments along with stone tools (chert flakes and retouched flakes) were found within Unit 5 (Roberts et al., 2018), which dates to between 300 – 500 ka (Rosenberg et al., 2013; Stimpson et al., 2016).

The Acheulean (Lower Palaeolithic) represents the longest-lasting stone-tool tradition in human prehistory, spanning ~1.5 Ma (Scerri et al., 2018). Acheulean technology (Lower Palaeolithic) has been documented across Arabia with numerous finds at Dawadmi in central Arabia (Scerri et al., 2018b; Shipton et al., 2018), the Nefud Desert in Northern Arabia (Scerri et al., 2015), Wadi Fatimah in western Arabia (Groucutt and Petraglia, 2012) and various other locations (see Fig 4 in Groucutt and Petraglia, 2012).

Acheulean finds predominantly occur as surface finds exposed via deflation, and lack stratigraphy or chronological control (Scerri et al., 2018). Nevertheless, Acheulean artefacts were found in section at Saffaqah in central Arabia where they have been dated to MIS 7 (Scerri et al., 2018b). The Acheulean complex at Saffaqah does not resemble that found in the southwestern Nefud (Scerri et al., 2015), but does resemble late Acheulean sites in eastern Africa. Conversely, the southwestern Nefud Acheulean is more similar to the late Acheulean in the Levant (Scerri et al., 2018). The spatial variability in the Acheulean techno-complex across the Arabian Peninsula may indicate several waves of hominin dispersals into the Arabian Peninsula in response to hydroclimatic change on the Peninsula (Scerri et al., 2018), or different raw material resource availability between locations influencing technological behaviours. However, the limited chronological control means it is difficult to assess spatio-temporal variations between Acheulean populations in the Peninsula.

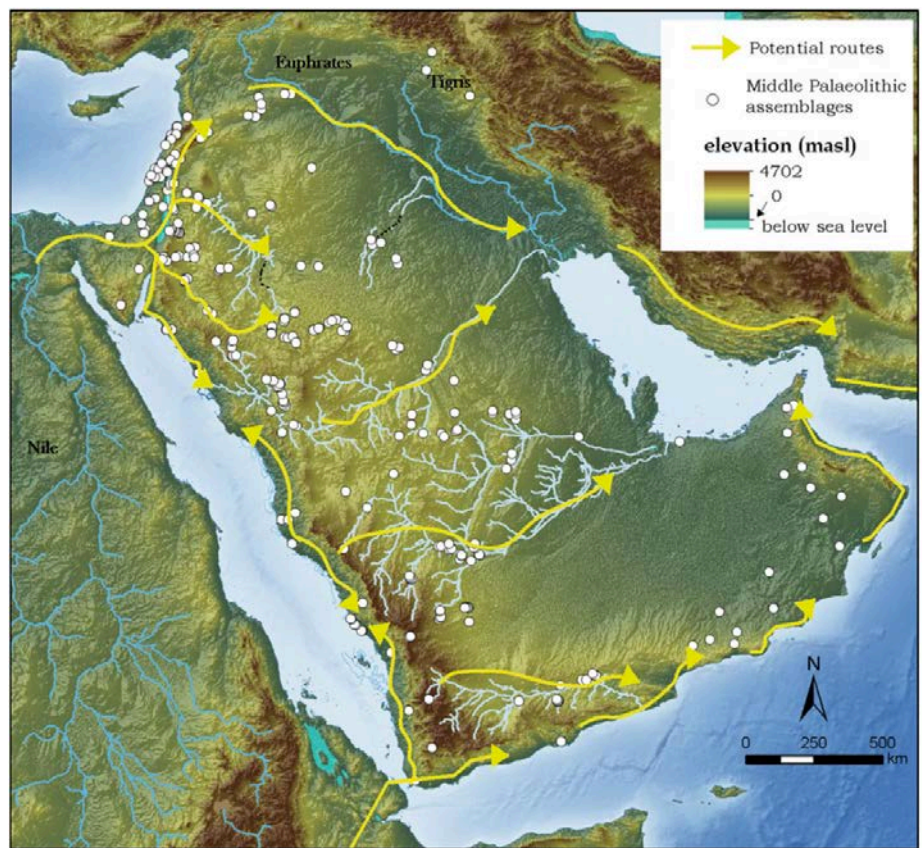


Figure 2.14 – Potential dispersal routes across the Arabian Peninsula over the Pleistocene, from Petraglia et al. (2018). A northern exit from Africa crosses the Sinai Peninsula before expanding southwards into the Arabian Peninsula or northwards to the Levant. A southern exit from Africa requires sea faring across the southern Red Sea. Once into Arabia from either the north or south, humans may have tracked the coastline or followed freshwater resources (rivers and lakes) in the Arabian interior. They could track such resources across trans-continental drainage systems to the Gulf.

The Middle Palaeolithic (MP) covers the period from 300,000 to 30,000 years ago and is a stone-tool technology complex associated with both modern humans and Neanderthals (Groucutt and Blinkhorn, 2013). The onset of the MP in the Levant and Arabian Peninsula is observed at Tabun Cave, where Levallois technology is dated to between ~190 – 260 ka (Mercier and Valladas, 2003). The first MP in direct association with *Homo sapiens* occurs at Mislaya Cave in the Levant (Hershkovitz et al., 2018). Here, Early Middle Palaeolithic (EMP) stone tool assemblages were found alongside *Homo sapiens* fossils, dated to between 177 – 194 ka (Hershkovitz et al., 2018), though these ages are debated (Sharp and Paces, 2018). Such ages suggest an overlap with the late Acheulean technology in central Arabia. Consequently, it is suggested that the late Acheulean at Saffaqah, Central Arabia formed part of the terminal archaic landscape encountered by modern humans as they expanded beyond Africa and into Arabia (Scerri et al., 2018b).

Numerous MP sites dating from MIS 5 to MIS 3, as well as undated sites, are found in the Arabia Peninsula, demonstrating repeated hominin occupations (see Fig 2.14). In southeastern Arabia, the site of Jebel Faya contains three assemblages of Middle Palaeolithic stone tools (Assemblage A, B and C) (Armitage et al., 2011). Assemblage C dates to between ~82 - 143 ka based on OSL ages and is comparable to the African Middle Stone age, leading to the authors to suggest a southern dispersal route across the southern Red Sea into Arabia (Armitage et al., 2011). Assemblages A and B are indicative of later autochthonous developments as late as ~40 ka (Armitage et al., 2011). Further Middle Palaeolithic assemblages across the southern portion of the Arabian Peninsula occur in Dhofar, Oman (Rose et al., 2011), Huqf, Oman (Jagher et al., 2009 referenced in Groucutt and Petraglia, 2012) and Yemen (Delagnes et al., 2012). As with Assemblages A and B at Jebel Faya, these assemblages are suggested to reflect local autochthonous developments (Groucutt et al., 2016).

Middle Palaeolithic assemblages have been described in the Rub' al Khali (Empty Quarter) at Mundafan (Crassard et al., 2013; Groucutt et al., 2015d), the Nejd plateau (Groucutt et al., 2016), Jubbah (Groucutt et al., 2015c; Petraglia et al., 2011), Al Marrat

(Jennings et al., 2016) and the western Nefud Desert (Groucutt et al., 2018; Scerri et al., 2015). There is a notable diversity in Middle Palaeolithic assemblages recorded in Saudi Arabia, and this suggests that demographic processes within the Arabian landscape between MIS 5 – MIS 3 were complex (Scerri et al., 2014b). In addition to archaeological evidence, a fossil attributed to *Homo sapiens* was found in association with a Middle Palaeolithic stone tool assemblage at Al Wusta in the western Nefud Desert (Groucutt et al., 2018). It is likely humans followed freshwater resources into the region. Breeze et al. (2016) demonstrate the existence of at least one palaeohydrological corridor during MIS 5e and MIS 5a named the 'Tabuk corridor' (see Fig 14.5) that runs from northeast Africa to the Arabian Peninsula. This corridor emphasises freshwater connectivity, where freshwater resources (i.e. rivers and lakes) lay close enough together to allow human populations to travel between them (Breeze et al., 2016). The maximum gap between resources is estimated as ~35 km (Breeze et al., 2016).

There is no evidence for Upper Palaeolithic archaeology in the Arabian Peninsula while Epi-Palaeolithic archaeology is sparse, though a recent Epi-Palaeolithic assemblage was described from an area close to Jubbah (Hilbert et al., 2014). In contrast, the archaeological record attributed to the Holocene and Neolithic is rich (Groucutt and Petraglia, 2012). For example, within the western Nefud Desert, recent analysis from Alshabah has dated Neolithic pastoralist activity to between 6.5 ± 0.7 ka and 7.3 ± 0.9 ka based on luminescence dating of hearths and ^{14}C dating of charcoal (Scerri et al., 2018a). This directly highlights the use of interdunal basins for pastoralist mobility strategies during the Holocene humid phase. Additionally, there are undated sites in the same area that host hearths, ostrich eggshell fragments, grindstone fragments, arrowheads and pottery (Breeze et al., 2017). Similar sites are observed at Jubbah (Guagnin et al., 2017) and from the Empty Quarter (Crassard et al., 2013). Numerous structures that are thought to be of late-Holocene age were also observed on the edges of the western Nefud Desert (Breeze et al., 2017).

2.6 Chapter summary

This chapter has reviewed the hydroclimatic change across the Saharo-Arabian desert belt over the Quaternary, the palaeoclimatic archives that record these changes, the history of research in the western Nefud Desert, and hominin dispersals across the Arabian Peninsula and the Nefud Desert over the past 500 ka. Key points are:

- Orbital-scale variability in multiple atmospheric circulation systems has driven large-scale hydroclimatic change in the Saharo-Arabian desert belt over the Quaternary.
- Prolonged arid phases are punctuated by brief humid intervals where high summer northern hemisphere insolation increases the northerly extent of the African monsoon, and potentially enhances the activity of autumnal/winter/spring tropical and extra-tropical systems such as the Active Red Sea Trough and Tropical Plumes. Additionally, westerly-derived winter rainfall could be pushed south. Synchronous activation of these systems could lead to a combination of wetter summers (monsoon) and autumn/winter/spring (Active Red Sea Trough/Tropical Plumes/MLW) in northern Arabia.
- Hydroclimatic change is most clearly observed in long marine (e.g. Rohling et al., 2015; Larrasoana et al., 2003) and speleothem records (e.g. Nicholson et al., 2020). Alongside these records, terrestrial archives such as lacustrine/palustrine sediments, tufas/travertines and palaeosols developed in response to increased humidity.
- Within the western Nefud Desert, the focus of this thesis, evidence of past humidity is reflected by numerous interdunal carbonate or siliceous sediments that have been interpreted as lacustrine sediments (Groucutt et al., 2018; Rosenberg et al., 2013) dated to warm marine isotope stages (e.g. MIS 5e) and substages (e.g. MIS 5a).
- Humid intervals in the region have played a key role in facilitating hominin dispersals over the past 0.5 Ma, as shown by the archaeological record in the western Nefud Desert that spans from the Lower Palaeolithic through to the Neolithic/Holocene.

Chapter 3 – Palaeoenvironmental analysis of interdunal lacustrine and palustrine sediments in low-latitudes

3.1 Introduction

As summarised in Chapter 2, the main indicators of past humid phases in the western Nefud Desert are interdunal carbonate/siliceous deposits (Fig 3.1). Consequently, to understand the significance of humid phases we need to understand the hydrology of the waterbodies in which these sediments were deposited. The literature on general lacustrine processes is extensive but is more limited regarding interdunal lakes in semi-arid regions. This chapter will begin by describing the existing views on the nature of interdunal lakes within the Nefud Desert, before discussing the literature on lake processes that are relevant to such systems. It will end with a discussion on the palaeoenvironmental proxies found within the deposits.

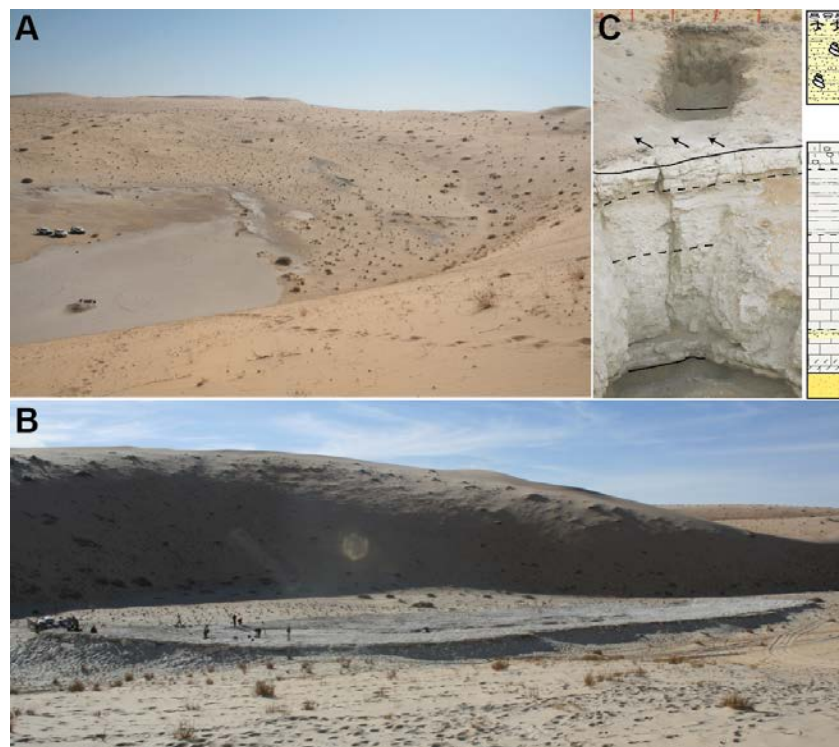


Figure 3.1 – Landscapes of present-day western Nefud Desert. (A) Overview of the Al Wusta interdunal basin from the top of the adjacent barchanoid dune. Lake sediments are present as inverted relief features composed of two ridges. These are present in the centre and right side of the panel, with the modern-day recharge playa on the left side of the panel. (B) An example of a well-preserved interdunal siliceous bed, which shows the elongated form of a former interdunal lake. (C) Example of a sedimentary sequence from Al Wusta (Groucutt et al., 2018). This sequence broadly fits into the sequence described in figures 3.2 and 3.3.

3.2 Model for interdunal lake development in the western Nefud Desert

A number of studies have reported that interdunal carbonate/siliceous deposits from the western Nefud Desert represent interdunal lakes (Groucutt et al., 2018; Schulz and Whitney, 1986; Stimpson et al., 2016; Whitney and Gettings, 1982), and similar work has been undertaken in the Rub' al Kahli desert (McClure, 1976, 1984; Rosenberg et al., 2011; Matter et al., 2015) and the Ramlat as-Sab'atayn desert (Lézine et al., 2010, 1998). The models put forward for interdunal lake development vary subtly depending on time interval (e.g. Middle vs Upper Pleistocene; Rosenberg et al., 2013) and location (e.g. western Nefud Desert vs Rub' al Khali). However, all models require broadly the same changes in environmental conditions to form: an increase in effective precipitation and a rise in the regional water table.

The general model for interdunal lake development follows six stages (Fig 3.2 and 3.3). Phase 1 represents arid conditions, such as those in the western Nefud Desert during the present day. Annual rainfall is between 60 – 90 mm (Edgell, 2006) and there are currently no interdunal lakes in the sand sea, though rare heavy rainfall events can produce standing waterbodies on interdunal playas that persist for months (Breeze et al., 2017). Consequently, the development of seasonal or perennial interdunal lakes requires an increase in effective precipitation – i.e. the total difference between precipitation and evapotranspiration.

Phase 2 represents the onset of lacustrine/palustrine conditions (Fig 3.2). As there are no interdunal lakes or wetlands today, it is evident that an increase in precipitation is initially required in order to produce lakes (as opposed to a reduction in evapotranspiration). An increase in precipitation would either (1) recharge aquifers and raise the regional water table so it intersects with the lower parts of interdunal basins leading to lake development, and/or (2) directly increase precipitation over the western Nefud Desert so that the infiltration capacity of dunes is exceeded leading to overland flow (slope/excess infiltration runoff) in addition to through-flow (subsurface storm flow) into interdunal basins. It is probable that both processes lead to interdunal lake

development. Groucutt et al. (2018) suggest an increase in the regional water table led to interdunal lake development at Al Wusta, as the lake waters must have interacted with groundwaters in order to gain the ions required for the precipitation of calcite, gypsum and halite. Matter et al. (2015) makes the same point for MIS 5 interdunal lake sediments from the Rub' al Khali. However, Rosenberg et al. (2013) notes that eleven out of twenty-one sites have a diatomaceous composition indicative of acidic, siliceous waters. This instead implies that some interdunal lakes have limited interaction with groundwaters and are predominantly rainfall-fed lake systems. Alternatively, they may lack the physical or biological mechanisms to produce carbonate. The total amount of precipitation required for the inception of interdunal lake development must be greater than $150 \pm 50 \text{ mm a}^{-1}$. This amount of rainfall was enough to produce a lake at nearby Tayma during the Holocene humid interval (Engel et al., 2011), but not enough to lead to lake development in the western Nefud sand sea at the same time (Rosenberg et al., 2013). It is also plausible that lake formation was supported via a reduction in evapotranspiration during humid intervals owing to greater cloud coverage and lower summer temperatures (Herold and Lohmann, 2009).

The sediments accumulated during phase 2 are typically carbonate-rich sandy marls (Fig 3.2). Fine-grained carbonate likely precipitates in response to increased productivity during the summer months (see section 3.4) while allogenic sands are washed into the basin from a landscape which is yet to fully respond to pluvial conditions (i.e. it is poorly vegetated). The lake may also be shallower during this phase relative to the following phase, meaning the site of sedimentation would be closer to lake edge and readily accumulate any allogenic material as it is washed into the lake basin via fluvial or aeolian processes.

Phase 3 represents peak humidity where stable perennial freshwater lakes exist (Groucutt et al., 2018). Here recharge balances evaporation and outflows, while homogenous or laminated fine-grained carbonate rich marl (micrite or microspartie) is precipitated where waters are alkaline and is not where waters are acidic. In the latter instance siliceous sediments form. Vegetation development stabilises surrounding dunes and limits the transport of allogenic material into the lake basin, while rooted

macrophytes (e.g. *Phragmites* and *Typha*; Schulz and Whitney, 1986) in the littoral zone of the lake also buffer allogenic input to the more profundal zone of the lake and the site of sedimentation. The exact nature of lakes at this stage vary, with Rosenberg et al. (2013) suggesting that interdunal lakes deposited during the Middle Pleistocene were larger and deeper, compared to Upper Pleistocene lakes which were small and isolated. Groucutt et al. (2018) demonstrate that the Al Wusta lake, dated to MIS 5a, was shallow but also stable, perennial and contained freshwater based on isotopic, micromorphological and diatom analysis. The analysis of further interdunal carbonate sediments using the multi-proxy method of Groucutt et al. (2018) will enable the testing of whether MIS 5 lake deposits were truly isolated systems, and whether Middle Pleistocene lake bodies actually represented deeper, larger waterbodies compared to MIS 5 lake deposits.

Phase 4 represents the transition from lacustrine sedimentation to sedimentation in a shallower, perhaps palustrine waterbody. Palustrine waterbodies are defined here as being <1 m in depth with the sediment bed being periodically exposed and experiencing pedogenic alteration or desiccation (Alonso-Zarza, 2003). Shallow lacustrine or palustrine systems are represented by multiple sedimentary facies. At Al Wusta, sediments at the top of the marl sequence consist of a hardpan carbonate (Groucutt et al., 2018), where calcite precipitation is concentrated and cemented around macrophyte roots at the lakes edge. This is likely due to the fact that macrophytes provide nucleation sites for carbonate precipitation (Leng and Marshall, 2004). Alternatively, at Ti's al Ghadah the sedimentary facies in the upper section of the sequence fluctuate between marl and sand-rich beds (alluvial intercalculations) suggesting that the site of sedimentation was more prone to fluctuations in the water level (Stewart et al., 2019; Stimpson et al., 2016). Here marls would be deposited during periods of higher water levels, while clastic sedimentation would occur during periods of low water levels. The presence of hardpan carbonate and interdigitated marl/sandy facies reflect a reduction in lake volume and contraction of the waterbody, with sedimentation transitioning from a profundal zone to littoral zone. It is not clear whether the change in lake volume is caused by internal lake processes where progressive sediment accumulation reduces accommodation space or is caused by a

transition to greater environmental aridity where the water table falls below the interdune surface.

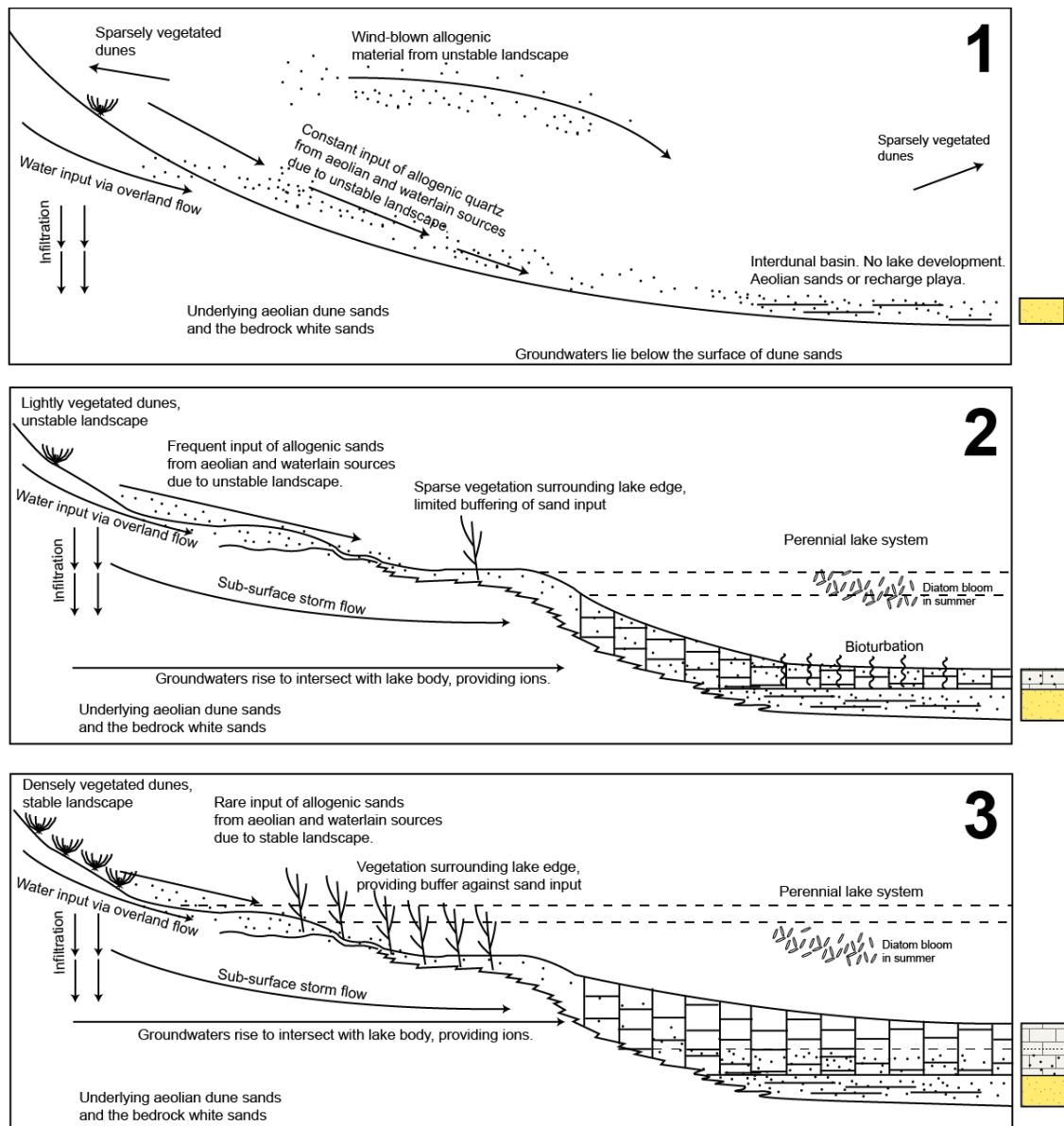


Figure 3.2 – Schematic figure showing the idealised model for the development of perennial interdunal lakes in the western Nefud Desert during humid phases. Three stages are shown representing the time period from aridity to peak humidity. (1) The modern-day environment, with annual rainfall between 60–90 mm and no interdunal lakes present. Rare rainfall events may lead to sheetwash of silts and sands into the interdunal basin forming a recharge playa, or the interdune dune surface may be dominated by aeolian sands. (2) The onset of the humidity. Lake development occurs quickly in response to increased precipitation and raised regional water table. The lake is shallow but precipitates carbonate. The bottom waters are well oxygenated, and it is likely bioturbation and wind-induced mixing homogenise the lake bottom sediments. The landscape is also yet to respond fully to increased effective precipitation, meaning surrounding dunes remain sparsely vegetated as does the lake edge. Consequently, sands and silts are readily transported into the lake basin, and this is recorded in the sedimentology where carbonates are sand rich at the onset of the sequence. (3) Peak humidity and perennial lake conditions. Water levels are probably still shallow, with the lake bottom effected by bioturbation and wind-induced mixing. However, laminations may be preserved where lake depth is greater. Dense vegetation stabilises surrounding dune sands while the lake edge likely contains reeds, sedges and other vegetation, buffering any sand input. Consequently, lake carbonates deposited during this stage of the lakes existence contain little allogenic material.

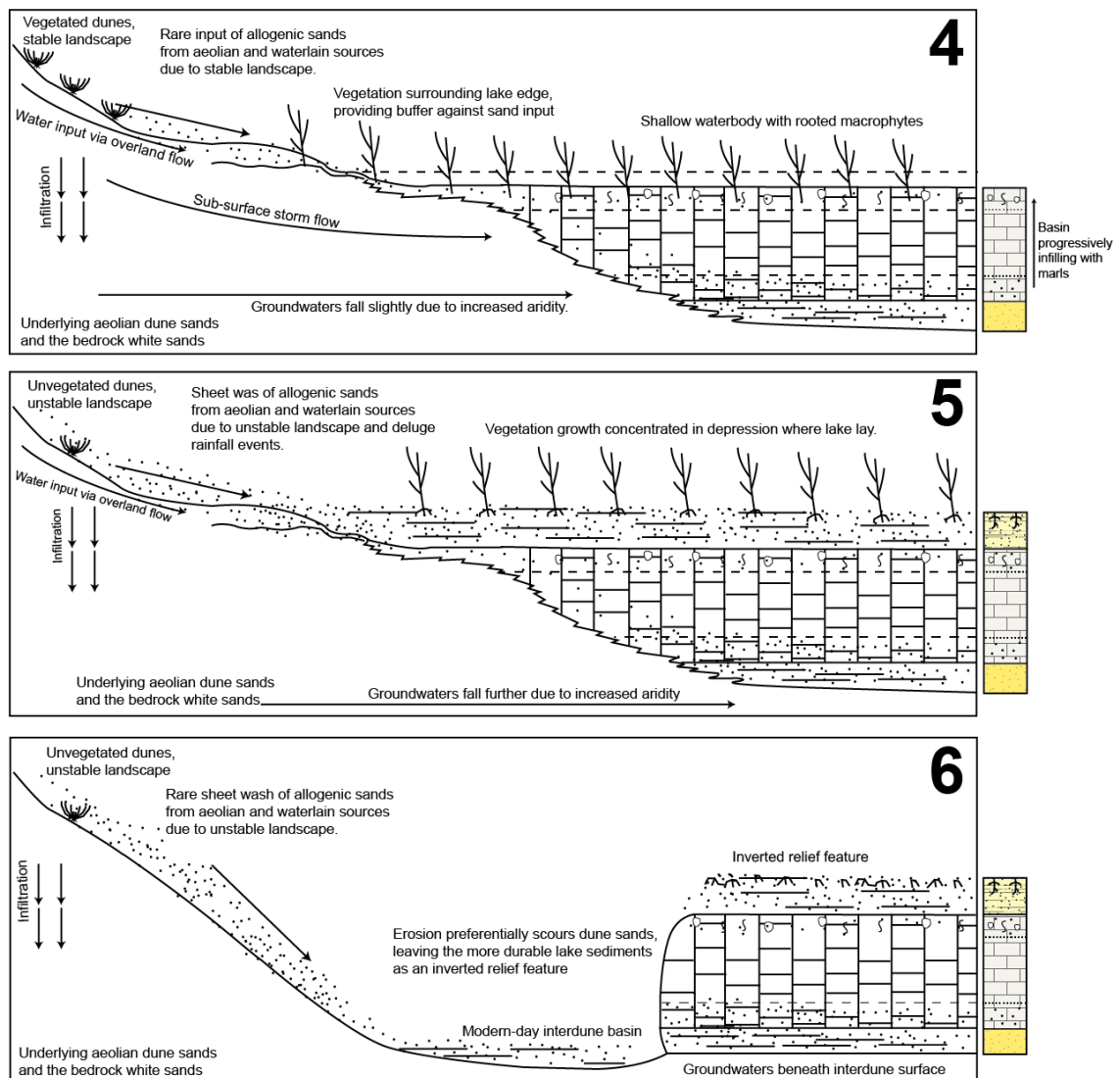


Figure 3.3 – Continued from figure 3.2...Schematic figure showing the idealised model for the development of perennial interdunal lakes in the western Nefud Desert. Three stages are shown representing the time period following peak humidity back to aridity. (5) During and following peak humidity the accumulation of marls results in basin infilling and a reduction in lake volume. It is also possible that the water table lowered slightly in response to increasing aridity. As the lake depth decreases, the lacustrine environment turns into a palustrine environment. Here shallow water levels and rooted macrophytes concentrate calcite precipitation around roots, leading to well-cemented marls or 'stem marls'. These frequently cap marl sequences. (6) Following the complete desiccation of the lake body, crudely laminated sands with some gravel clasts are deposited via sheet wash processes. Here increasing aridity reduces any sediment buffers around the interdunal depression while dunes become more unvegetated and unstable. This results in increased sand availability and the in wash of sands into the basin during deluge rainfall events. Calcitic rhizoliths are found within these sequences, and relate to vegetation growth in the basin as this is where the greatest water availability would occur. (6) Return to aridity, with lake marls present as an inverted relief feature in the interdunal basin after the preferential erosion of aeolian sands.

Phase 5 represents the final phase of humidity before a return to aridity. Following the desiccation of the lake body, crudely laminated sands with gravel inclusions are recorded at Al Wusta and at Ti's al Ghadah (Groucutt et al., 2018; Stewart et al., 2019; Stimpson et al., 2016). Shells of *Melanoides tuberculata*, which are a freshwater mollusc

though have a high tolerance for changing hydrological conditions, are also recorded within this unit at Al Wusta. These sediments most likely represent sheet wash of sands into the interdunal basin caused by heavy rainfall events. These sediments are capped by sand-rich calcitic rhizoliths which are organosedimentary features that preserve root structures (Klappa, 1980) and reflect fully terrestrial sedimentation. Phase 6 represents the return to aridity. Here the preferential erosion of aeolian sands compared to the mechanically stronger marls results in the lake beds being preserved as inverted relief features in the landscape.

The model described above suggests that interdunal sediments represent small, shallow and isolated lacustrine/palustrine systems that follow a simple transgressive-regressive cycle in response to hydroclimatic change (Wright, 1990). To summarise, following the onset of humidity, the water table rises in response to increased precipitation leading to perennial lake development while increased vegetation stabilises surrounding dunes (Fig 3.2). Sedimentation within the lake basin leads to basin infilling, while at the same time the water level may drop in response to increasing environmental aridity following peak humidity (Fig 3.3). Once the water table drops below the lake bed, sands are deposited on the marls via sheet wash following deluge rain events, and vegetation colonises the surface of these deposits leading to the formation of calcitic rhizoliths (Fig 3.3). In the present day, paleolake sediments are then preserved as inverted relief features because they are more durable than the surrounding aeolian sands.

3.3 Lacustrine, palustrine and calcrete sediments

The model for interdunal lake development in the western Nefud Desert fits broadly into a continuum that ranges from perennial subaqueous environments, to intermittently subaqueous environments that are periodically subaerially exposed and subject to pedogenic and desiccation processes (palustrine), to fully terrestrial environments (soils/calcretes) (Fig 3.4) (Alonso-Zarza, 2003). This continuum is defined by the duration of sub-aerial exposure experienced by the sediment bed, and this is driven by variations in the elevation of the water table (Alonso-Zarza, 2003). For example, the sediment bed of a perennial lake body will never be subaerially exposed

while the sediment bed of a palustrine environment will be. Sedimentary features at the macroscale and microscale such as sorting, grain size, texture and microstructure are often diagnostic of specific depositional settings along this continuum (Fig 3.4). Lacustrine, palustrine and calcrete environments and their associated sedimentary and microfacies are summarised below.

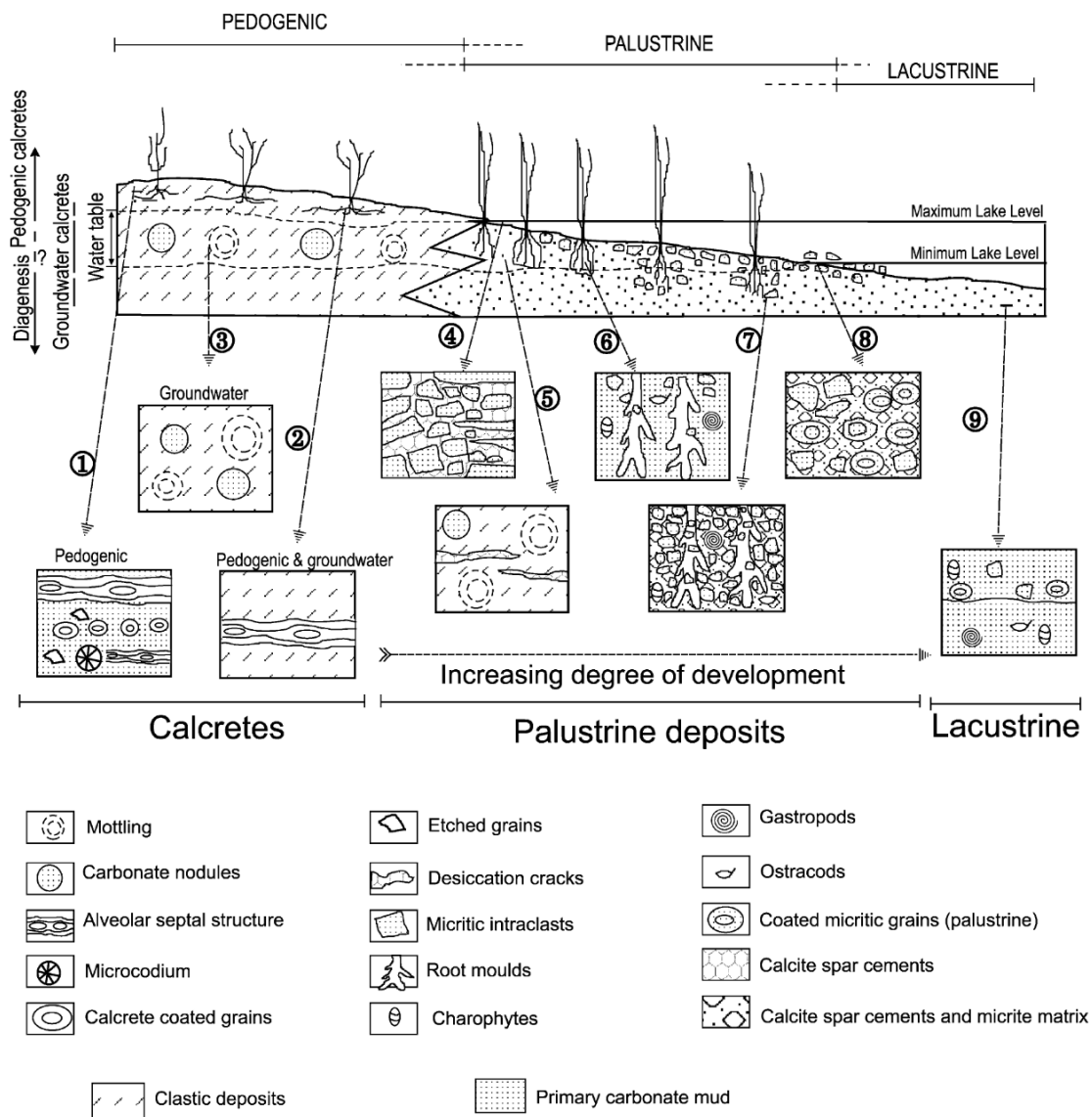


Figure 3.4 – Continuum of depositional environments for calcretes, palustrine and lacustrine sediments along with associated microfacies (from Alonso-Zarza, 2003). The continuum runs from a fully terrestrial depositional environments (calcretes, left side of figure) to fully subaqueous deposition (perennial lacustrine – right side of figure). Palustrine and lacustrine sedimentation are most relevant for understanding interdunal lakes in the western Nefud Desert based on the current depositional model for interdunal lakes (see figures 3.2 and 3.3).

3.3.1 Lacustrine environments

In perennial lacustrine systems the lakebed is never sub-aerially exposed and primary lake mud is deposited. In areas with groundwaters rich in Ca^{2+} (calcium) and CO_3^{2-} (carbonate) ions the primary lake mud will be composed of calcite (see section 3.4). The lake itself can be split into four broad zones; littoral, sub-littoral, profundal and pelagic (see Fig. 3.5) (Wright, 1990). The latter is not relevant to interdunal lakes given their limited accommodation space. The littoral and sub-littoral zones are characterised by a bench platform and bench slope. Sedimentation is usually greatest in these zones relative to profundal locations as carbonate production is high around plants (macrophytes and charophytes) (Wright, 1990). The shallow nature of these zones means they are typically polymictic (well-mixed) as they are exposed to physical/biological lake processes such as wind and bioturbation. This leads to sedimentary facies with homogenised and unaltered primary lake mud (see Fig 3.6) (Alonso-Zarza, 2003; Groucutt et al., 2018; Pettigrew et al., 2019; Wright, 1990). Bivalve and ostracod remains are also common within these zones, while siliclastic material will vary depending on the amount of baffling by nearshore reeds and sedges along with the density of vegetation that stabilises surrounding dunes (Wright, 1990). In lower gradient interdunal lakes alluvial intercalculations may be present, where allogenic sands are washed into the littoral/sub-littoral areas during storm events or periods of low-lake level (Wright, 1990).

The profundal zone lies further from the lake shore and, where stratification is present, beneath the thermocline (Fig 3.5, diagram '2'). It typically experiences lower sedimentation rates due to lower rates of calcite precipitation, though biologically mediated calcite precipitation still occurs in response to diatom blooms (Wright, 1990). If the lake depth is great enough then facies from this zone may preserve laminations, because the sediment is less disturbed due to stratification and anoxic bottom water conditions which prevent surface-wind induced turbulence or bioturbation (see Fig 3.5) (Wright, 1990). However, polymictic conditions occur where lake depth is not great enough to induce stratification. This means that lake bottom sediments in the profundal

zone can become homogenised via bioturbation and wind-induced mixing (Fig 3.5; panel 1).

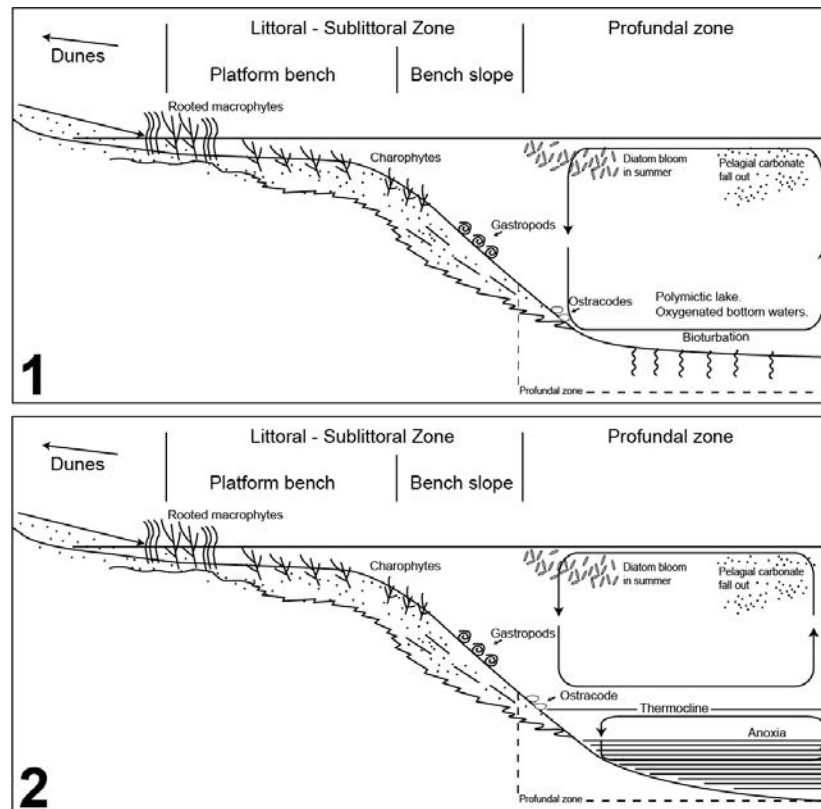


Figure 3.5 – General model for interdunal hardwater lake environments redrawn after Wright (1990). The littoral zone is shallow and contains rooted macrophytes and chara. Carbonate production initiated by plants is high compared to the profundal zone, and this results in the development of a platform bench. This transitions to a bench slope in the sublittoral zone where carbonate precipitation is not as high due to lower vegetation. The profundal zone has a much lower sedimentation rate with pelagic carbonate fallout and diatom blooms from the photic zone generating the sediment present. Picture 1 (top) shows a polymictic shallow lake where there is never/rarely stratification and bottom waters are well-oxygenated with homogenised sediments due to bioturbation and wind-mixing. Picture 2 (bottom) shows a deeper, stratified lake with a thermocline and anoxic bottom waters, where laminations are likely to be preserved.

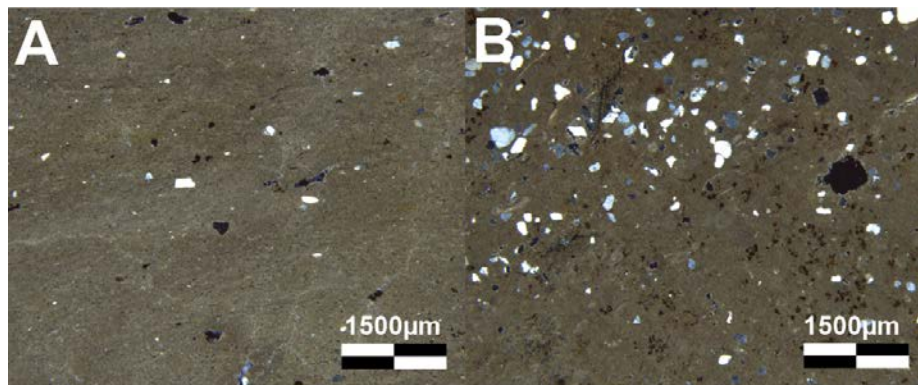


Figure 3.6 – Example microfacies from (A) Al Wusta and (B) Site 16.3 of homogenous primary lake mud (microsparite) deposited on the floor of perennial interdunal lake bed in the sub-littoral to profundal zone (Clark-Wilson, 2016; Groucutt et al., 2018). The sediment is composed of a homogenous microstructure with a groundmass of microsparite. No pedogenic or desiccation features such as distinct planar voids, brecciation or micritic intraclasts are present. The only difference between the two thin-sections is the number of siliclastic grains present. Siliclastic grains rare in picture A and more frequent in picture B.

At the micro-scale, littoral carbonate sediments are characterised by homogenous primary lake mud with ostracod and bivalve remains, siliclastic allogenic grains, coated micritic grains and micritic intraclasts (see microfacies 7, 8 from Fig 3.4, Fig 3.6) (Alonso-Zarza, 2003; Freytet and Verrecchia, 2002). Microfacies from more profundal zones will show unaltered homogenous primary lake mud with rare siliclastic grains, rare ostracod and bivalve remains and rare micritic intraclasts (see microfacies 9 from Fig 3.4). If the lake is stratified with anoxic bottom waters, it is also likely that fine mm-scale laminations will be preserved. These laminations may relate to seasonal variations in productivity where high productivity produces small micritic crystals and lower productivity produces larger microsparite/sparite crystals, forming laminated microsparite and micrite layers (Wright, 1990). Non-productive seasons may produce a detrital layer. Examples of such fine-scaled laminations have not yet been described in detail in the western Nefud Desert, though field observations suggests that they are present at Bi'r al Hayzan in the central portion of the desert (Rosenberg et al., 2013; Schulz and Whitney, 1986).

3.3.2 Palustrine environments

Palustrine environments are defined as waterbodies that have a mean water depth of <1 m and have sediment beds that are intermittently sub-aerially exposed during periods of lower water levels (Fig 3.4) (Alonso-Zarza, 2003; Freytet and Verrecchia, 2002). They typically occur in low energy and low gradient environments that are susceptible to small fluctuations in water level. This includes shallow waterbodies that lie between siliclastic sediments in semi-arid to sub-humid climates with marked seasonality (Alonso-Zarza, 2003). Consequently, palustrine systems may be expected in interdunal basins in the western Nefud Desert during humid phases though their presence may depend on basin morphology.

To form palustrine sediments, sub-aerial exposure must occur for enough time for desiccation or soil forming processes (pedogenic alteration) to take place within the primary lake mud (Freytet, 1965, 1971 referenced in Alonso-Zarza, 2003). Desiccation

or emersion features can develop within a single season, though pedogenesis requires long-term paleoenvironmental stability (Alonso-Zarza, 2003). Pedogenic alterations relate to desiccation, physical and chemical processes, and root and soil organism activity (Alonso-Zarza, 2003). The microfacies of the sediment can indicate the degree of sub-aerial exposure, with mottled limestones and nodular/brecciated limestones representing less developed palustrine limestones produced via physiochemical processes, while more developed palustrine limestones may be granular with a pseudomicrokarst (Alonso-Zarza, 2010). The former are the most often observed in this thesis.

At the microscale, palustrine sediments show features such as brecciation and nodule development, intraclasts, coated grains, cementation, organic root traces, marmorisation and planar voids (see microfacies 4, 5 and 6 in Fig 3.4) (Alonso-Zarza, 2003; Durand et al., 2010; Freydet and Verrecchia, 2002). It is important to note that some features above, such as marmorisation, can also occur via post-depositional groundwater movements and be unrelated to palustrine processes. Multi-proxy analysis including stable oxygen and carbon isotope analysis can help identify where this is the case.

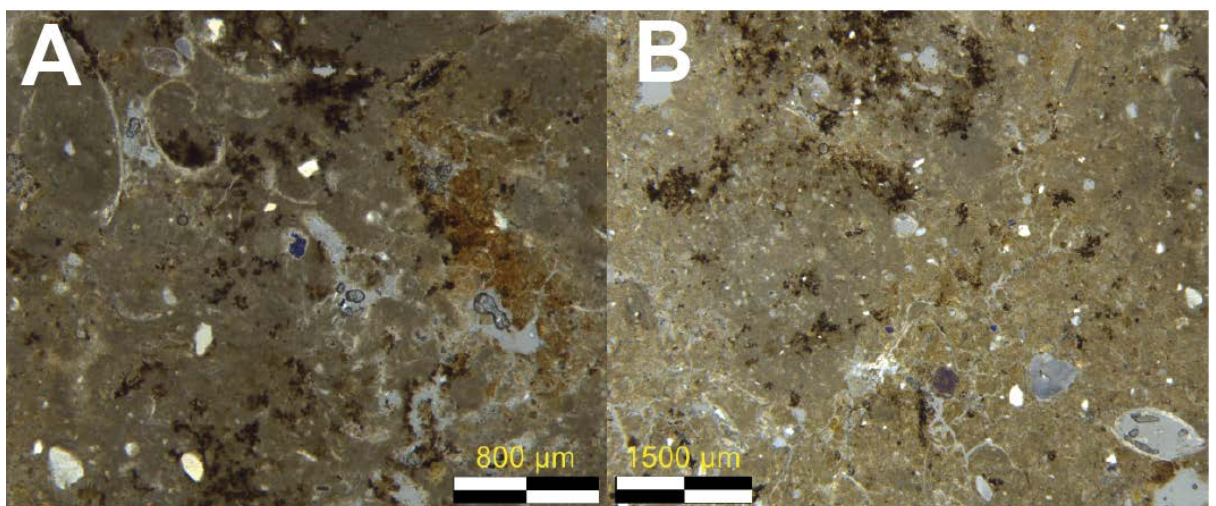


Figure 3.7 – Microfacies from the top of Site 16.3 that represent a shallow lacustrine (littoral), or potentially a weakly developed palustrine, environment (Clark-Wilson, 2016). Relative to Fig 3.6, the microfacies here shows a more prismatic structure with planar voids along with a greater proportion of micrite and frequent ostracod shells. There is also greater evidence for marmorisation with light iron staining present in picture A, while the black clusters are interpreted as being amorphous organic remains. Such microfacies are rare, with this being the one of its kind in Clark-Wilson (2016).

3.3.3 Calcretes and rhizoliths

Calcretes and rhizoliths form in fully terrestrial environments in either the vadose (unsaturated) or phreatic (saturated) zones (see Fig 3.4), and form through carbonate displacing or replacing material in soil, rock or sediment within a soil profile (Alonso-Zarza, 2003; Watts, 1980). Pedogenic calcretes form via the accumulation of carbonate through illuviation in the Bk or K horizons of soil in the vadose zone (Tanner, 2010). In contrast, groundwater calcretes form in the phreatic zone by the action of groundwater flow and capillary draw (Tanner, 2010). Pedogenic calcrete formation requires stable conditions for tens to thousands of years, though groundwater calcretes can form in a shorter period of time (Alonso-Zarza, 2003). Pedogenic calcretes and rhizoliths are sometimes found capping interdunal lake sequences (e.g. Al Wusta; Groucutt et al., 2018) and demonstrate the presence of terrestrial sedimentation following the desiccation of the waterbody (stage 5; Fig 3.3).

3.3.4 Summary

Marked environmental gradients within lacustrine and palustrine systems along with their sensitivity to environmental change means that they can move along the continuum outlined above in either direction. These changes can occur abruptly (Talbot and Allen, 1990; Wright, 1990). This results in sedimentary sequences that represent transgressive-regressive cycles in response to hydroclimatic changes (Wright, 1990), as is outlined in the model for interdunal lake development shown in Figs 3.2 and 3.3. Interdunal sedimentary sequences studied within this thesis predominantly display sedimentary and proxy characteristics typical of the accumulation of carbonate-rich sediments on the beds of lacustrine waterbodies. As such, attention will turn to carbonate and clastic sedimentation in interdunal lacustrine environments and the isotopic analysis of these sediments.

3.4 Carbonate sedimentation

The majority of sediments presented within this thesis are composed of authigenic calcium carbonate (CaCO_3). A prerequisite for calcium carbonate deposition is a sufficiency of Ca^{2+} (calcium) and CO_3^{2-} (carbonate) ions within lake waters. These are primarily sourced from the chemical weathering and dissolution of salts and carbonates from lithologies within the catchment area such as limestone, volcanoclastic and mafic silicate rocks (Decampo, 2010). Here carbon dioxide combines with water in the atmosphere to create carbonic acid, which then chemically weathers the carbonate material in the catchment releasing Ca^{2+} (calcium) and 2HCO_3^- (bicarbonate) ions into surface runoff, groundwaters and eventually lake waters. Limestones are present in the immediate catchment area in the form of relic interdunal marls, while limestones are also present to the northeast of the Nefud Desert. Volcanoclastic lithologies are located to the south/southwest of the Nefud at Harrat Khaybar and Harrat al Ithnayn (Groucutt, 2020).

Solid inorganic authigenic calcium carbonate is precipitated from water within the lake basin via biological (photosynthesis) or physical (temperature, CO_2 degassing, evaporation) processes that elevate Ca^{2+} and CO_3^{2-} concentrations to supersaturation (Fig 3.9) (Talbot and Allen, 1996; Wright, 1990). Supersaturation occurs where the solution (lake water) contains more dissolved material (Ca^{2+} and CO_3^{2-} ions) than the solvent (H_2O) can dissolve.

The processes leading to supersaturation are well documented in temperate hardwater lakes such as those in the UK (e.g. Marshall et al., 2002). Carbonate precipitation occurs during the spring/summer months via a combination of increased temperatures and productivity. The solubility of dissolved carbon dioxide is temperature dependent and reduces in response to increased lake water temperatures. Simultaneously, increased productivity leads to increased photosynthesis, where CO_2 pressure is reduced as plants take up CO_2 . The removal of CO_2 via both of these processes reduces the amount of carbonic acid in the lake water, which lowers the number of hydrogen ions and increases pH. At pH 6 – 8 carbonic acid dissociates its first hydrogen ion, and then at pH 8 and

above dissociates its second hydrogen ion (Fig 3.8) (Decampo, 2010). This process concentrates carbonate and calcium ions to supersaturation, where they combine and precipitate out of solution (Decampo, 2010). It is not clear how carbonate would be precipitated in interdunal lakes in semi-arid/sub-humid conditions in the Nefud Desert. It is possible that carbonate precipitation would follow a similar trend to temperate lakes, where high productivity and lake temperatures occur during the summer in response to a summer monsoon season. However, it is also conceivable that carbonate precipitation could occur in response to evaporitic concentration of ions during arid winter seasons.

The crystal size of carbonate precipitate relates to the degree of supersaturation. Smaller crystals (micrite) are formed during periods of high supersaturation (i.e. peak productivity/evaporitic concentration) while larger crystals (sparite) are related to lower supersaturation (Wright, 1990). Variations in crystal size can form fine-scaled laminations that may represent seasonal changes in productivity. In this case biogenic varves could be present, if lake waters were of sufficient depth and stratified so that no bioturbation or wind-induced mixing occurs.

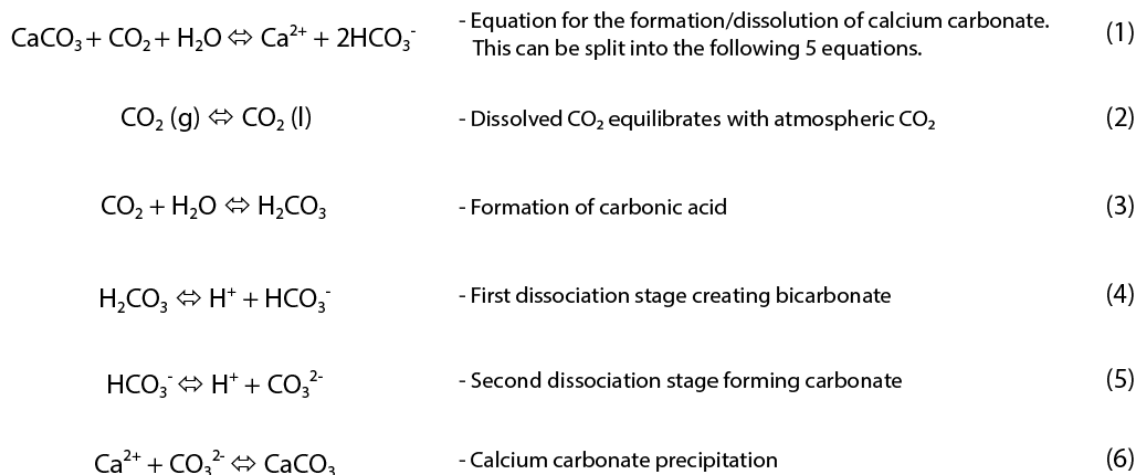


Figure 3.8 – The chemical reactions that lead to the precipitation of carbonate in hardwater lakes. Equation 1 shows the formation/dissolution of carbonate which is broken down into five subsequent reactions (equations 2 – 5).

Calcium carbonate or low-Mg calcite typically precipitates in non-evaporitic freshwater basins where recharge balances or exceeds evaporation (Wright, 1990). In basins where evaporation exceeds recharge, as may have been the case in shallow interdunal basins

in semi-arid environments, the ion concentration gradually increases and evolves. As Ca^{2+} (calcium) and CO_3^{2-} (carbonate) ions are depleted, evaporites such as gypsum and halite will precipitate as the chemistry of the lake waters become more evolved (Fig 3.10). The exact precipitate depends on the initial lake water chemistry (Fig 3.10) (Decampo, 2010). The mineralogy of the sediments in the geological record is therefore a key indicator of the hydrology of the lake system in which they were deposited. This has further significance for the Nefud Desert, where a critical question revolves around whether lakes contained 'drinkable' fresh water. If they contain evaporites then it is likely that the lakes did not always provide useful resources for humans, being too saline or brackish.

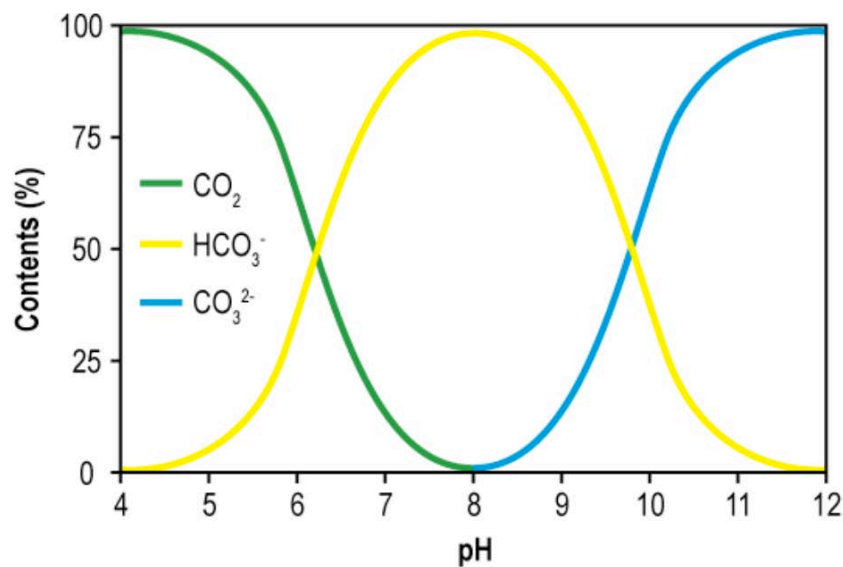


Figure 3.9 – The relationship between pH and proportions of inorganic carbon species in solution in hard water lakes from Wetzel (1975). Carbonate precipitation will occur above pH 8 as CO_3^{2-} becomes supersaturated.

It is important to consider the role of carbonate formation when interpreting oxygen and carbon stable isotope records, which are discussed in section 3.6. The carbon isotope signal from carbonate records the $\delta^{13}\text{C}$ of total dissolved inorganic carbon, which derives from the dissolution of CO_2 in water. Conversely, the oxygen isotopic composition records the $\delta^{18}\text{O}$ of lake waters (Candy et al., 2011). Oxygen can also be derived from CO_2 , though the variability in $\delta^{18}\text{O}$ from CO_2 is far smaller than that derived from lake waters. Consequently, any variability in the oxygen isotope record is likely to be driven by changes in the $\delta^{18}\text{O}$ of lake water as opposed to CO_2 .

Siliceous sediments, which lack any carbonate, are deposited where there is not sufficient Ca^{2+} (calcium) and CO_3^{2-} (carbonate) ions, or where the biological/physical processes that lead to calcium carbonate precipitation do not occur. Siliceous wetland sediments are composed of the remains of diatom frustules deposited within the lake body, allogenic siliclastic grains and siliceous (quartz gel) precipitate (Decampo, 2010). This typically occurs in waterbodies fed predominantly by rainfall and surface runoff, where waters have little interaction with the local geology, or where the bedrock geology is low in Ca^{2+} (e.g. felsic igneous).

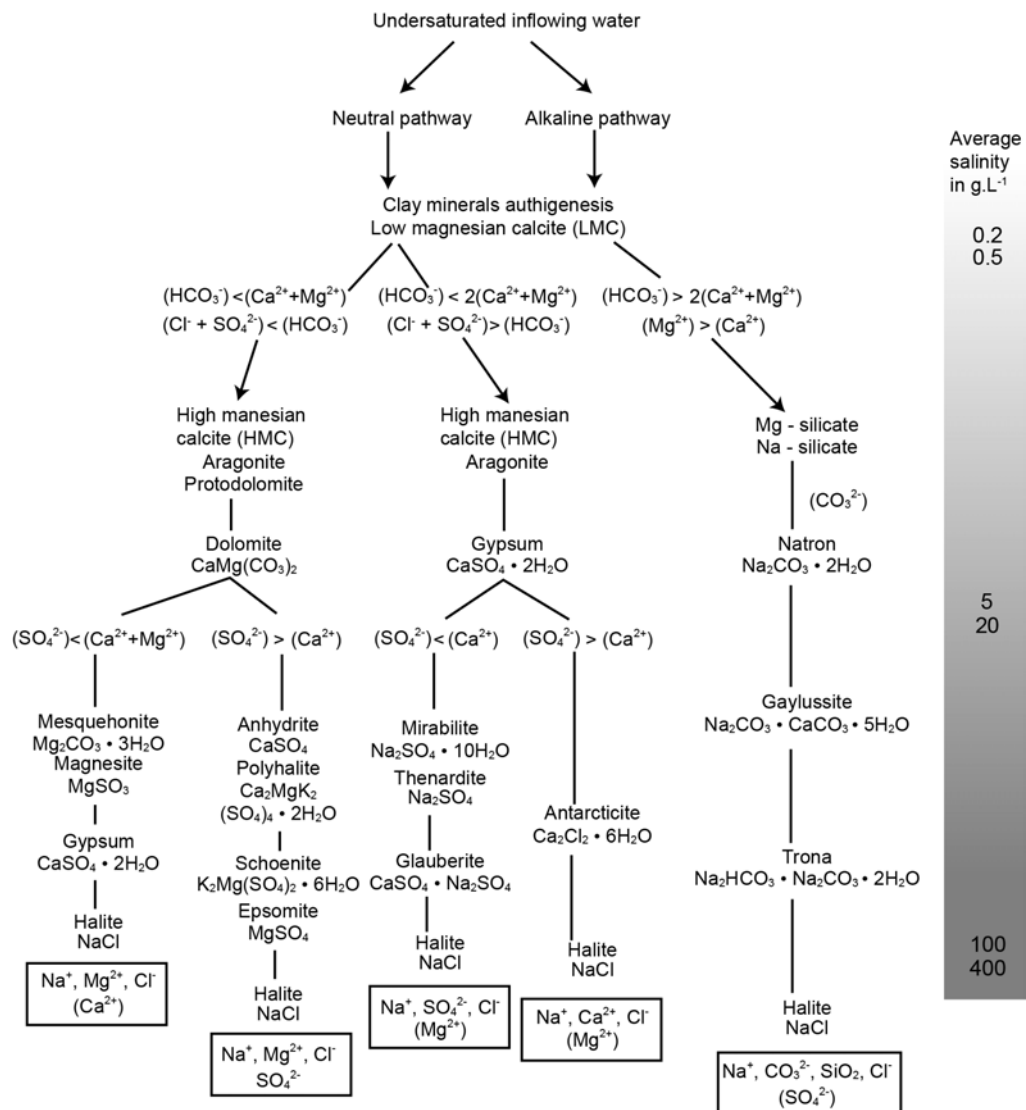


Figure 3.10 – Evaporite precipitation sequence redrawn from Verrecchia (2007). Most hardwater lakes follow a neutral pathway, with low-magnesian calcite precipitating at low salinities, after which evaporites such as gypsum and halite are formed as the waters become more evolved.

3.5 Clastic sedimentation

Clastic material also forms a prominent contribution to the sediment load in interdunal lake systems. These materials include silts, sands and gravels (siliclastic) and detrital carbonate sourced from the surrounding environment (allogenic). They are transported into the lake body via aeolian processes (e.g. dust storms) or via fluvial processes (e.g. sheet wash from surrounding dunes or in suspension/bedload in small rivulets formed during deluge rainfall events) (Talbot and Allen, 1996).

The local drainage basin influences the nature of clastic sedimentation greatly and in sand seas such as the western Nefud where there is high sediment availability, there is the potential for a large contribution of allogenic sands into lake basins. Seasonal variations in climate during humid phases may also be important in regions such as the Nefud, where sediment transport via sheetwash and rivulets may be important during wet monsoon seasons whereas aeolian transport may be more prominent during dry seasons. The transport of allogenic sediment into the lake basin during humid phases will also be influenced by the density of local vegetation in the surrounding landscape, which act to stabilise surficial sediments and reduce available sediment load. Nearshore macrophytes such as reeds and sedges form swamps in the littoral area of lake basins and form effective sediment traps for fine-grained sediment (see Fig 3.2) (Talbot and Allen, 1996). Consequently, the littoral zone accumulates a greater proportion of clastic sediments than offshore profundal zones. Clastic sediments are transported into profundal zones via numerous mechanisms such as interflows, underflows and gravity flows which are influenced by lake circulation/stratification patterns and rates of sediment supply (Talbot and Allen, 1996). Based on the most recent analysis it appears that clastic material does not form a large part of the sediment load during peak humidity (e.g. Fig 3.6), but do make a more substantial contribution at the beginning and end of the sequences (see stage 2 and 5, Fig 3.2 and Fig 3.3) (Clark-Wilson, 2016; Groucutt et al., 2018).

3.6 Stable isotope analysis of inorganic authigenic carbonates

The analysis of oxygen and carbon stable isotopes within lacustrine carbonate sequences in the low-latitudes are an important tool for (1) reconstructing lake basin hydrology (Talbot, 1990) and (2) investigating wider climatic circulation patterns (Rozanski et al., 1993). There are very few isotopic records from the Arabian deserts belt, with records restricted to speleothems in southern Arabia (Nicholson et al., 2020), the Negev (Vaks et al., 2006), northeast Africa (El-Shenawy et al., 2018) and the Levant (Bar-Matthews et al., 2003; Frumkin et al., 1999), the Jubbah palaeolake sequence in the Nefud (Parton et al., 2018) and a single sequence from the al-Hawa depression in the Ramlat as-Sabtayn desert (Lézine et al., 1998). There is an absence of records from the Arabian interior, with the exception of Jubbah palaeolake, so the interdunal lacustrine carbonates presented here provide an opportunity to bridge this gap. This sub-section will cover the following topics: (1) basic principles of oxygen and carbon isotopes; (2) controls on the $\delta^{18}\text{O}$ of lacustrine carbonates; (3) controls on the $\delta^{13}\text{C}$ of lacustrine carbonates.

3.6.1 Basic principles

The analysis of stable oxygen (^{16}O and ^{18}O) and carbon (^{12}C and ^{13}C) isotopes for palaeohydrological studies is based on the principle that isotopes of the same element are chemically identical (same number of protons) but have different masses (different number of neutrons) (Fig 3.11) (Mook, 2000). Consequently, the relative proportions of heavy to light isotopes vary between reservoirs (e.g. calcite or lake water) in response to physical or biological processes (Mook, 2000). The basis for this is that heavier isotopes (1) react more slowly than lighter isotopes as they have a lower diffusion velocity, and (2) have a greater binding energy than lighter isotopes, meaning heavier isotopes require greater energy to undergo phase changes (Mook, 2000). Both of these factors mean that heavier isotopes are less mobile and react less readily than lighter isotopes (Mook, 2000). This process is termed “mass-dependent fractionation” and will occur during phase changes such as liquid to gas (evaporation).

		Stable isotopes of Oxygen			Stable isotopes of Carbon		A
$\begin{matrix} A \\ Z \\ X \end{matrix}$	A = Atomic mass	$^{16}_8\text{O}$	$^{17}_8\text{O}$	$^{18}_8\text{O}$	$^{12}_6\text{C}$	$^{13}_6\text{C}$	
	Z = Atomic number	(99.76%)	(0.035%)	(0.2%)	(98.9%)	(1.1%)	
	X = Chemical symbol of element						

		B
$R = \frac{\text{Abundance of rare isotope}}{\text{Abundance of abundant isotope}}$		
$\delta^{18}\text{O} = 1000 \times \left[\frac{\left(\frac{^{18}\text{O}}{^{16}\text{O}} \right)_{\text{sample}} - \left(\frac{^{18}\text{O}}{^{16}\text{O}} \right)_{\text{standard}}}{\left(\frac{^{18}\text{O}}{^{16}\text{O}} \right)_{\text{standard}}} \right]$	$\delta^{13}\text{C} = 1000 \times \left[\frac{\left(\frac{^{13}\text{C}}{^{12}\text{C}} \right)_{\text{sample}} - \left(\frac{^{13}\text{C}}{^{12}\text{C}} \right)_{\text{standard}}}{\left(\frac{^{13}\text{C}}{^{12}\text{C}} \right)_{\text{standard}}} \right]$	

Figure 3.11 – Basic information regarding oxygen and carbon isotopes, redrawn after Mook (2000). (A) The nuclear notation of an element with the stable isotopes of oxygen and carbon shown. The number underneath each stable isotope signifies its abundance, and the lighter isotopes are most abundant (Mook, 2006). (B) The standard notation used to represent isotopic ratios. δ values are represented in parts per mil (‰) as the fractionation of isotopes is so small (Mook, 2000).

3.6.2 Fractionation

Processes of isotopic fractionation can be split into three (Fig 3.11): (1) equilibrium fractionation, (2) kinetic fractionation and (3) non-equilibrium fractionation (Mook, 2000).

Equilibrium isotopic fractionation occurs between a reactant and a product, and equilibrium is defined as occurring when the ratio of light to heavy isotopes in both end members is equal (Mook, 2000). In order for isotopic equilibrium to occur there must be an isotope exchange mechanism whereby there is (1) forward and backward reactions between a reactant and product where the flux of isotopes is equal, (2) isotopes are well-mixed between the two reservoirs, and (3) the reservoirs themselves are well-mixed (Clark and Fritz, 1997; Mook, 2000). While the ratio of light to heavy isotopes must be equal, the absolute number of isotopic compositions (molecules) may not be (Mook, 2000).

Kinetic fractionation is an irreversible unidirectional process where the reaction product becomes enriched in the lighter isotope (Mook, 2000). An example of kinetic

fractionation can be given using an idealised process of evaporation/condensation. Here, evaporation of water with the immediate withdrawal of vapour from any further contact with the lake water (which is unrealistic in nature) would represent kinetic fractionation as the vapour would become enriched in the lighter ^{16}O . Further examples include biological processes, such during the fixation of CO_2 during photosynthesis where ^{12}C is preferentially incorporated into plant material leading to enriched $\delta^{13}\text{C}$ values in the water reservoir (Clark and Fritz, 1997).

Non-equilibrium fractionation occurs where kinetic conditions are not met (i.e. the reaction is not purely irreversible) yet equilibrium conditions cannot be demonstrated (Mook, 2000). This is common in nature (Mook, 2000). Again, the example of evaporation/condensation provides a good example of this process. In nature, the water vapour from the evaporation of surface lake waters is not completely separated from the lake body due to condensation of vapour, but there is not an identical reverse reaction due to net evaporation and the fact that the degree of irreversibility cannot be quantified (Mook, 2000). The net effect of this process in a lake body affected by high rates of evaporation would be an increase in the proportion of heavy isotopes in the lake water, due to the preferential removal of the lighter isotope.

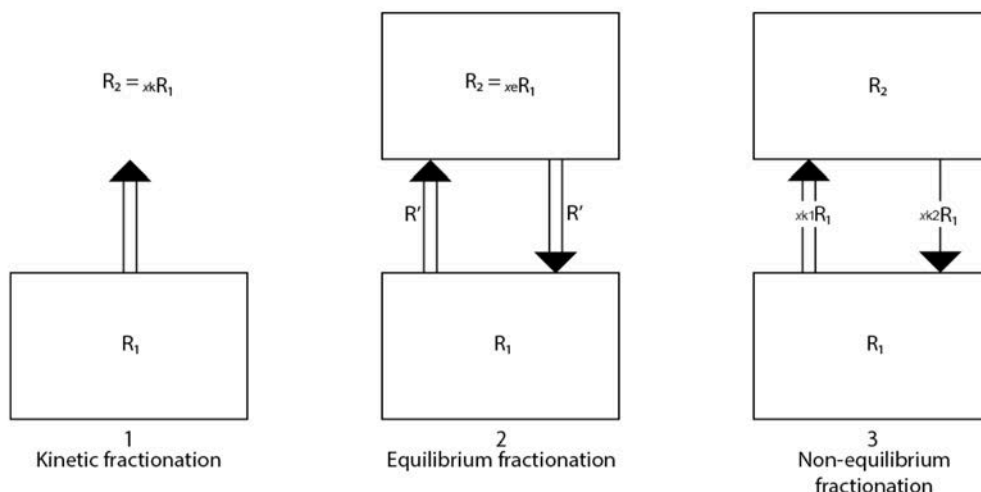


Figure 3.12 – A diagram outlining the three different processes of isotopic fractionation from Mook (2006). Left: Kinetic fractionation is an irreversible unidirectional process where the reaction product becomes enriched in the lighter isotope. Centre: Equilibrium fractionation occurs between a reactant and a product, and equilibrium is defined as being when the ratio of light to heavy isotopes in both end members is equal. Right: Non-equilibrium fractionation is where kinetic conditions are not met (i.e. the reaction is not purely irreversible) yet equilibrium conditions cannot be demonstrated.

3.6.3 Isotope measurement and reporting

Oxygen and carbon isotope ratios from calcite are measured using a mass spectrometer, where calcite is dissolved using phosphoric acid and converted to CO₂. The isotopic ratios are then reported against the international standard of the Vienna Pee Dee Peleminite (VPDB) (Friedman et al., 1982) to enable the comparison of results between different laboratories. This point is especially important given that isotopic measurements within this study were carried out at two different facilities. Where the isotopic ratio is depleted in the heavier isotope relative to the standard, then the δ value will be negative and vice versa. The way in which the δ value is calculated is shown in Fig 3.11, B.

3.6.4 Factors that control the $\delta^{18}\text{O}$ of freshwater carbonates

The $\delta^{18}\text{O}$ of freshwater lake carbonates, assuming equilibrium mineral fractionation, are controlled by the temperature and $\delta^{18}\text{O}$ value of the lake water in which it precipitates (see Fig 3.13) (Leng and Marshall, 2004). The $\delta^{18}\text{O}$ of the lake water is controlled by the $\delta^{18}\text{O}$ of recharge water that in turn is controlled by the $\delta^{18}\text{O}$ of precipitation. Multiple variables influence the $\delta^{18}\text{O}$ at each stage of the hydrological cycle from source (i.e. ocean) to endpoint (calcite). To make palaeohydrological or palaeoclimatic inferences from the $\delta^{18}\text{O}$ record from carbonates these variables must be understood. As such, the following section of this chapter will outline these processes beginning with variables that control the $\delta^{18}\text{O}$ of rainfall.

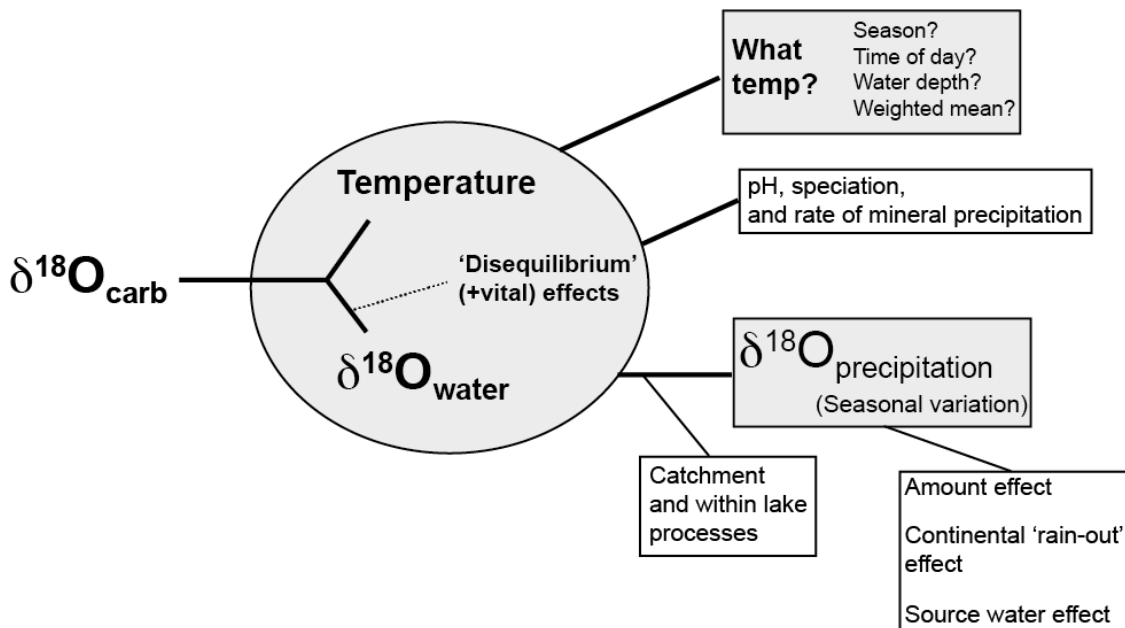


Figure 3.13 – Controls on the oxygen isotope composition of lacustrine carbonates, modified after Leng and Marshall (2004) to show the tropical/sub-tropical effects on $\delta^{18}\text{O}$ of precipitation. This includes the amount effect, continental 'rain-out' effect (Rayleigh distillation) and the source water effect.

3.6.4.1 Variables controlling the $\delta^{18}\text{O}$ of rainfall

The $\delta^{18}\text{O}$ of rainfall is influenced by several processes such as changes in the $\delta^{18}\text{O}$ at the moisture source, changes in atmospheric circulation patterns and air mass trajectory, the amount effect, continentality, latitude and temperature. These are outlined below.

Changes in $\delta^{18}\text{O}$ of source water. The $\delta^{18}\text{O}$ of source water dictates the initial $\delta^{18}\text{O}$ of precipitation. Changes in its composition can therefore influence the $\delta^{18}\text{O}$ content of lake waters and lacustrine carbonates. It has been demonstrated that over interglacial to glacial time cycles the $\delta^{18}\text{O}$ of ocean water evolves in response to changes in ice-volume, where ^{16}O becomes trapped in global ice and ocean water becomes enriched in ^{18}O (Lisiecki and Raymo, 2005). It has also been suggested that freshwater flooding into the eastern Mediterranean sea from the Nile during peak monsoonal rainfall led to more negative $\delta^{18}\text{O}$ values in the eastern Mediterranean sea during past interglacials (Bar-Matthews et al., 2003; Grant et al., 2012). The impact of such changes has been observed in isotopic records from speleothems in the Levant (Bar-Matthews et al., 2003) and lacustrine records across the eastern Mediterranean (Roberts et al., 2008). Given that the Nefud Desert potentially received moisture derived from the eastern

Mediterranean it is important to consider these impacts. A depleting trend in $\delta^{18}\text{O}$ through an interdunal carbonate sequence could in theory relate to the progressive depletion in $\delta^{18}\text{O}$ of eastern Mediterranean seawater in response to freshwater flooding. Likewise, monsoonal rainfall is also suggested to reach northern Arabia from moisture originating from the Atlantic Ocean via zonal transport (Gierz et al., 2017; Herold and Lohmann, 2009). Because humid phases occur during both interglacial (e.g. MIS 5e) and interstadial (e.g. MIS 5a) periods, where ocean water would have differing $\delta^{18}\text{O}$ compositions, it is plausible that variations in $\delta^{18}\text{O}$ records from carbonates between these two periods could reflect this.

Latitude, temperature & the amount effect. The controls on $\delta^{18}\text{O}$ of precipitation in rainfall is correlated with latitude. In the temperate mid to high latitudes the dominant control is temperature. This relationship is demonstrated by the global meteoric water line, where $\delta^{18}\text{O}$ and $\delta^2\text{H}$ co-vary along latitudinal gradients (Craig, 1961). This relationship breaks down in the low latitudes, such as the Saharo-Arabian desert belt, where the dominant control on the $\delta^{18}\text{O}$ of precipitation is the amount of rainfall (Rozanski et al., 1993). This, termed the “amount effect”, is the process whereby greater amounts of rainfall are correlated with more negative $\delta^{18}\text{O}$ values and vice versa (see Fig 3.14) (Rozanski et al., 1993). This relationship is caused by less effective evaporitic enrichment of the $\delta^{18}\text{O}$ of precipitation at the cloud base during periods of high rainfall relative to periods of low rainfall (Rozanski et al., 1993). This means more ^{16}O remains in the cloud base and $\delta^{18}\text{O}$ values are therefore more negative (Rozanski et al., 1993). Consequently, $\delta^{18}\text{O}$ records of carbonates (lake, tufa or speleothem) across the Arabian Peninsula and North Africa may reflect temporal and spatial patterns in the amount of rainfall over the Quaternary (e.g. Fleitmann et al., 2011; Nicholson et al., 2020).

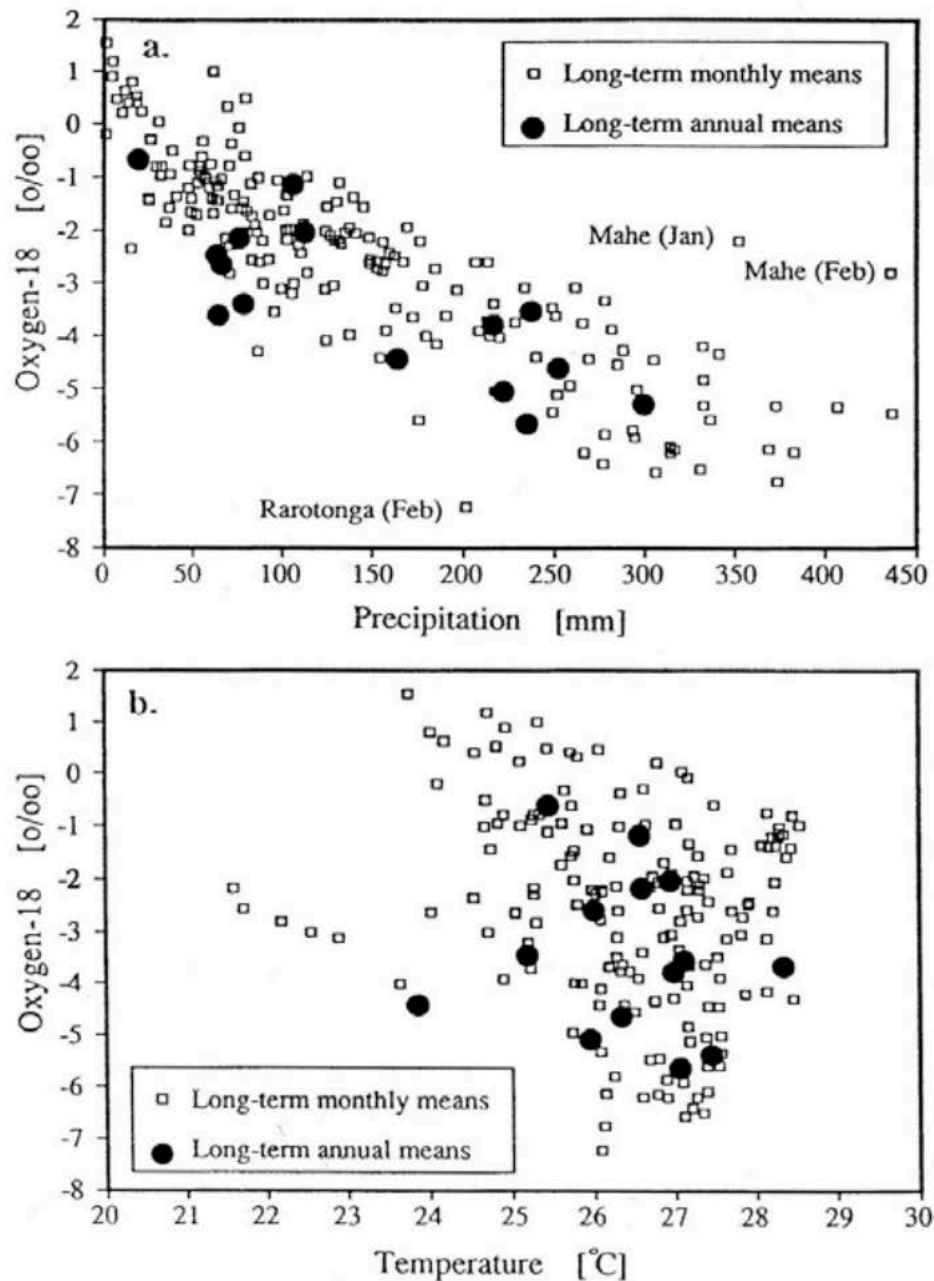


Figure 3.14 – Scatter plots demonstrating the amount effect as the dominant control on the $\delta^{18}\text{O}$ value of precipitation in tropical and sub-tropical locations from Rozanski et al. (1993). The graphs show average monthly and annual $\delta^{18}\text{O}$ means in response to precipitation (top) and temperature (bottom). The top graph shows there is a clear correlation between the amount of rainfall and the $\delta^{18}\text{O}$ of precipitation (high rainfall = negative $\delta^{18}\text{O}$ values). The bottom graph shows there is no correlation between $\delta^{18}\text{O}$ of precipitation and temperature.

Atmospheric circulation, air mass trajectory, continentality and altitude. The Nefud Desert lies in a continental setting at the interface of multiple climatic systems that have shifting spatial scales in response to orbital forcing over the Quaternary (Parton et al., 2015). Consequently, an understanding of the impact that changes in atmospheric circulation and air mass trajectory has on the $\delta^{18}\text{O}$ of precipitation is necessary.

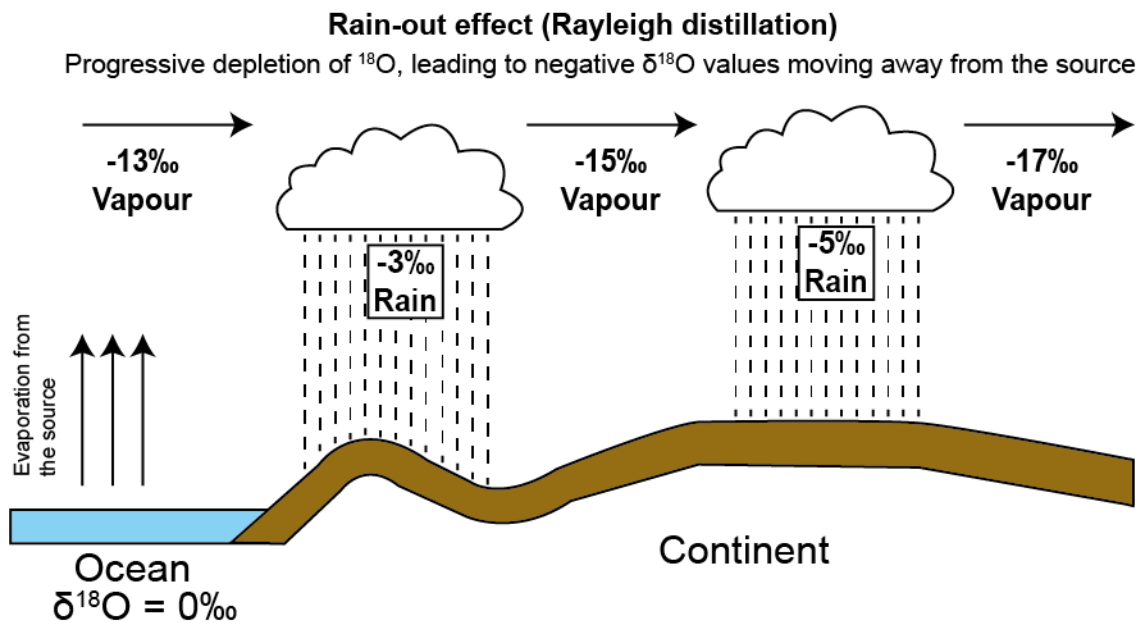


Figure 3.15 – Schematic representation of the rain-out (continental) effect as Rayleigh distillation progressively depletes the heavier isotope, leading to an enrichment in the lighter isotope as the air mass moves further from its source. This results in negative $\delta^{18}\text{O}$ values. Redrawn and modified from Hoefs (1997).

In continental settings that lie in a distal location relative to the origin of the source water, the $\delta^{18}\text{O}$ will be depleted via the rain-out (continental) effect. This is because the $\delta^{18}\text{O}$ signal will gradually deplete as an airmass moves further from its moisture source due to Rayleigh distillation. This is the process where the ^{18}O is preferentially rained out as the heavier isotope condenses more readily and is preferentially removed in precipitation (Fig 3.15) (Clark and Fritz, 1997). An instructive example comes from the comparison of MIS 5e speleothem records in Egypt and the Negev with Holocene speleothems from the Levant (El-Shenawy et al., 2018). The former are interpreted as having a monsoonal moisture source whereas the latter source their rainfall from the mid-latitude westerlies (MLW) (El-Shenawy et al., 2018). The speleothems derived from monsoonal rainfall have more negative $\delta^{18}\text{O}$ values compared with those derived from MLW rainfall. This is a consequence of the rain-out effect, where moisture transported from the Atlantic via the African Monsoon is preferentially depleted of ^{18}O as the air mass moves eastwards across the continent (El-Shenawy et al., 2018; Gierz et al., 2017; Herold and Lohmann, 2009). As the same monsoonal rainfall is thought to be a potential source of moisture to the Nefud (Jennings et al., 2015; Rosenberg et al., 2013) then

similar depleted isotopic values may be observed. Conversely, if the Nefud receives additional moisture from the MLW then $\delta^{18}\text{O}$ values may be more positive.

It is also important to consider the impact altitude has on the isotopic signal as the Nefud lies at ~ 900 m asl. Like the process of “rain-out” described previously, increasing altitude results in more depleted $\delta^{18}\text{O}$ of precipitation due to adiabatic cooling, with a global relationship of -2.8‰ per 100 m (Clark and Fritz, 1997; Poage and Chamberlain, 2001).

3.6.4.2 Variables controlling the $\delta^{18}\text{O}$ of recharge waters

The $\delta^{18}\text{O}$ of recharge waters (i.e. groundwaters or surface run-off sourced from rainfall and transported to the lake basin) can also be modified, thus influencing the $\delta^{18}\text{O}$ of lake waters and freshwater carbonates. Recharge occurs from direct precipitation, surface run-off or from groundwater recharge (Darling, 2004). Where lakes contain high authigenic mineral input, as is the case in the Nefud palaeolakes, it is likely the systems derive the majority of their moisture from groundwaters (Darling, 2004). This can either be via direct recharge into the basin via phreatic water, or by inflow from rivers and streams whose water is derived from groundwater (Darling, 2004). As such, it is important to consider the ways in which the $\delta^{18}\text{O}$ of rainfall can be modified during groundwater recharge.

The western Nefud Desert is currently hyper-arid with no permanent standing water bodies in interdunal basins. The geomorphology is dominated by large dunes and the underlying geology is sandstone (Breeze et al., 2017). Consequently, a regional rise in the groundwater table is required to form interdunal lakes where the water table intersects the dune surface (see Figure 3.2). A rise in the water table would result from increased precipitation percolating through the dunes and from rivers and streams that feed into the dune field and/or via direct rainfall over the region (Breeze et al., 2015; Rosenberg et al., 2013). Given the current aridity of the region and lack of comparable hydrological systems it is not clear how precipitation $\delta^{18}\text{O}$ would be modified during recharge. Moreover, little is known about the aquifer which supplies water to the

western Nefud. Hypothetically, the $\delta^{18}\text{O}$ of this water would probably reflect the annual average of $\delta^{18}\text{O}$ precipitation, which in the Nefud could be composed of summer monsoon rainfall (Jennings et al., 2015), and autumnal/winter/spring rainfall from the Active Red Sea Trough, Tropical Plumes and MLW rainfall (Enzel et al., 2015; Neugebauer et al., 2017). Evaporitic enrichment of the $\delta^{18}\text{O}$ signal either before or after the water has passed through the aquifer could modify the $\delta^{18}\text{O}$ of precipitation, especially given that the Nefud likely experienced high summer temperatures given its sub-tropical location and semi-arid to sub-humid climate. However, any evaporitic effect was probably limited as groundwaters flowed beneath the surface of dune sands which would have protected waters from evaporation.

3.6.4.3 Variables controlling the $\delta^{18}\text{O}$ of lacustrine waters

Lake basin hydrology exerts an important control over the $\delta^{18}\text{O}$ of lacustrine waters. At the broadest scale, lake systems can be divided into an endoheic (closed) basin or an exorheic (open) basin. In reality these form two end points to a continuum along which a waterbody may shift over time in response to environmental change. Closed basin lakes only lose water through evaporation and seepage, and typically have a negative water balance with high evaporation to precipitation (E/P) ratios (Leng and Marshall, 2004; Talbot, 1990). As a consequence, the $\delta^{18}\text{O}$ signal in closed-basins is more positive (Fig 3.16), as the ^{16}O is preferentially lost to evaporation (kinetic fractionation), and more variable, leading to large ranges in $\delta^{18}\text{O}$ (Table 3.1). The same evaporitic process also result in a reduction in lake volume, degassing of CO_2 and more positive $\delta^{13}\text{C}_{\text{TDIC}}$ values (Talbot, 1990; Leng and Marshall, 2004). This process can lead to covariance between $\delta^{18}\text{O}$ and $\delta^{13}\text{C}_{\text{TDIC}}$, and the presence of covariance is used an indicator of hydrological closure in the geological record (Talbot, 1990; Li and Ku, 1997).

Table 3.1 – Summary of hydrological/palaeoclimatic records that the $\delta^{18}\text{O}$ ratios of authigenic carbonates are likely to record in lakes of different volumes (very small to large), from Leng and Marshall (2004) and references therein.

Features of lakes likely to produce temperature, δp or precipitation/evaporation reconstructions from isotopic composition of primary precipitates within a lake sediment				
Lake-water volume	Very small	Small-medium open lakes	Small-medium closed lakes	Large
Residence time	< 1 year ('open' lake)	≥ 1 year	10's years	100's years ('closed' lake)
Predominant forcing	$S, T, \delta p$	$T, \delta p$	P/E	P/E
$\delta^{18}\text{O}$ ranges through the Holocene	Often -ve values, small range of 1–2‰, possibly large range in ‰ for materials precipitated in different seasons e.g., Lake Chuma (Kola Peninsula) ^a , Lake Abisko (Sweden) ^b	Often -ve values, small range of 1–2‰ e.g., Hawes Water (UK) ^c , Lake Ammersee (Germany) ^d	-ve to +ve values, large swings (5 to > 10‰) e.g., Greenland lakes ^e , Lake Tilo (Ethiopia) ^f , Lake Golhisar (Turkey) ^g	+ve values, subdued signal homogenised by buffering of large lake volume e.g., Lake Malawi ^h , Lake Turkana (Kenya) ⁱ

S = seasonality, T = temperature, δp = isotope composition of precipitation, P/E = amount of precipitation relative to evaporation.

In exorheic (open) basins there is less opportunity for the isotopic modification of lake waters by evaporation, as there are inflows, outflows and shorter residence times (Talbot, 1990). The result of this is that the $\delta^{18}\text{O}$ of lake water more accurately reflects the $\delta^{18}\text{O}$ of the recharge waters, which in turn reflect the $\delta^{18}\text{O}$ of precipitation. As such, the $\delta^{18}\text{O}$ of lake carbonates in such systems reflect the controls on $\delta^{18}\text{O}$ of precipitation as opposed to internal lake basin hydrology. Nevertheless, caution is still required when interpreting the $\delta^{18}\text{O}$ record in such lakes as it has been shown evaporitic enrichment of the $\delta^{18}\text{O}$ signal can still occur even in exorheic (open) basins (Horton et al., 2016). Likewise, isotopic covariance can occur under certain climatic conditions in exorheic basins. For example, a seasonal shift to isotopically positive summer rainfall combined with more positive $\delta^{13}\text{C}$ due to increased lake productivity is proposed as the cause of isotopic covariance in a Holocene lake record from Michigan (Drummond et al., 1995).

Further complications to interpreting the isotopic record from exorheic basins relate to lake basin volume (Table 3.1), which is impossible to estimate accurately for interdunal palaeolakes in the Nefud. The ratio of lake basin volume to annual water flow dictates the seasonal variation in a lake waters $\delta^{18}\text{O}$ (Pearson and Coplen, 1978). If the volume of a basin is small compared to annual water flow, then the basin is likely to pick up seasonal variations in $\delta^{18}\text{O}$ (Pearson and Coplen, 1978). Conversely, if a basin is large

relative to annual water flow it is likely seasonal variation in recharge waters will be averaged out (Pearson and Coplen, 1978).

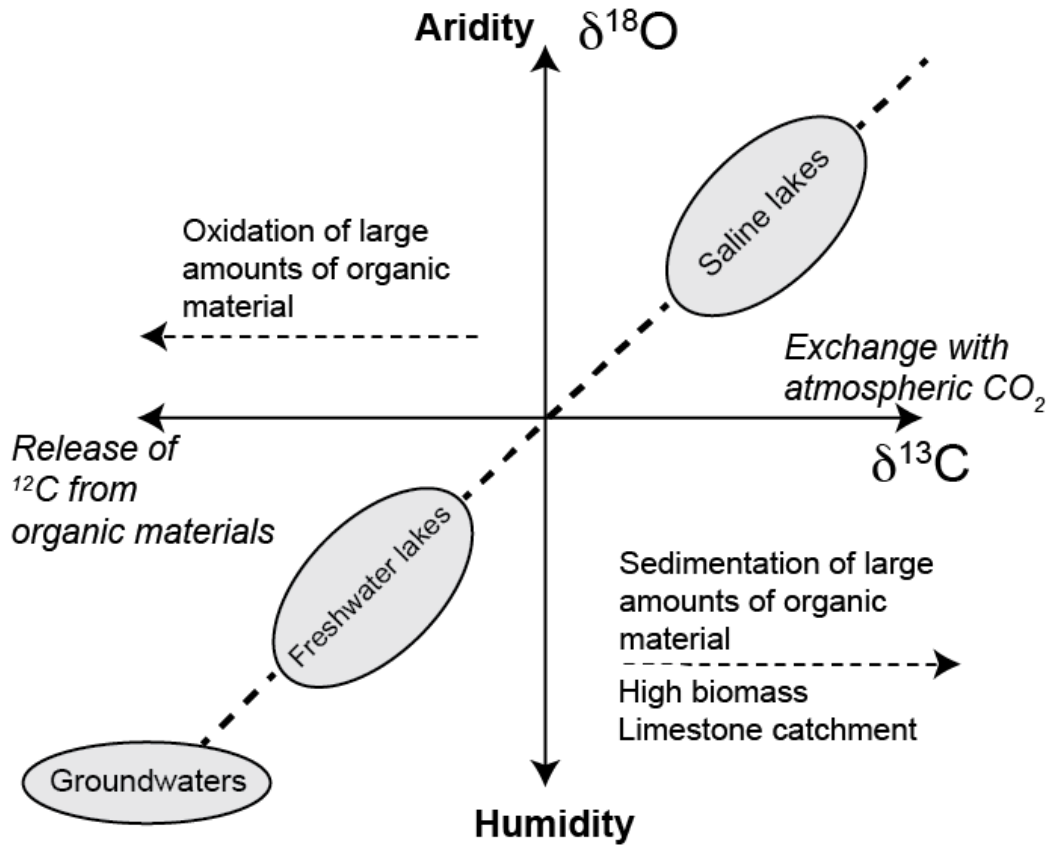


Figure 3.16 - $\delta^{13}\text{C}$ vs $\delta^{18}\text{O}$ redrawn from Leng and Marshall (2004). Hydrologically closed lakes show often show covariance between $\delta^{13}\text{C}$ and $\delta^{18}\text{O}$. The $\delta^{18}\text{O}$ signal becomes more positive due to increased evaporation while $\delta^{13}\text{C}$ becomes more positive in response to equilibration with atmospheric CO_2 Leng and Marshall (2004). Such lakes would position in the top right quadrant of the graph. Hydrologically open lakes often show limited or no covariance as there is minimal evaporitic enrichment of the $\delta^{18}\text{O}$ signal. In addition, limited equilibration with atmospheric CO_2 means $\delta^{13}\text{C}$ remains low due to the low $\delta^{13}\text{C}$ of recharge waters caused by plant respiration and CO_2 production in soils (Leng and Marshall, 2004). $\delta^{13}\text{C}$ values maybe high despite limited time to move into equilibrium with atmospheric CO_2 where the lake is in a marine limestone catchment, there is high productivity (biomass) within the lake taking up ^{12}C , there is sedimentation of large amounts of organic material, or where the surrounding landscape is dominated by C4 vegetation (Leng and Marshall, 2004).

Seasonal variations in lake water $\delta^{18}\text{O}$ are important to consider in terms of timing of calcite precipitation. For example, interdunal lakes within the Nefud may have had multiple moisture sources along with a small lake volume. As such they could have been susceptible to seasonal variations in the $\delta^{18}\text{O}$ of rainfall and therefore lake water $\delta^{18}\text{O}$. Consequently, changes in timing of peak calcite precipitation may have influenced the $\delta^{18}\text{O}$ value of calcite. Nevertheless, given the bulk sampling approach employed here, interannual variability is unlikely to affect the bulk $\delta^{18}\text{O}$ values of the carbonate.

Additionally, little is known about the groundwater reservoir supplying water to the Nefud and this may have been large and well-mixed.

Lake monitoring has shown that $\delta^{18}\text{O}$ and $\delta^{13}\text{C}$ can change through the vertical profile of a water column (e.g. Lehmann et al., 2004), meaning that the depth at which calcite is precipitated can influence the isotopic values that are recorded. The Nefud Desert lakes must have been relatively small in volume, due to limited accommodation space, and that previous research suggests they were shallow and well-mixed (Groucutt et al., 2018). Consequently, it is unlikely that the depth of precipitation has a serious influence on the isotopic values of calcite measured in this study.

3.6.4.4 Controls over the $\delta^{18}\text{O}$ of calcite during mineral precipitation

Calcite precipitation from solution imparts a temperature dependent fractionation effect on $\delta^{18}\text{O}$ (Craig, 1965; Leng and Marshall, 2004). This is caused by the thermodynamic behaviour of isotopes, where lower water temperatures cause a larger fractionation effect between ^{16}O and ^{18}O (Leng and Marshall, 2004). As such, carbonates precipitated in lower water temperatures have higher $\delta^{18}\text{O}$ values than those precipitated in higher water temperatures. This relationship has been quantified with an $\delta^{18}\text{O}$ depletion of approximately 0.24‰ per 1°C increase in temperature, assuming fractionation under equilibrium conditions (Craig, 1965). The temperature at which calcite precipitates is therefore a fundamental control on the $\delta^{18}\text{O}$ of freshwater carbonates, and it is probable that changes in the $\delta^{18}\text{O}$ of calcite through a stratigraphic sequence reflect changes in the temperature of water in which it was precipitated.

3.6.4.5 Summary: Key controls on the $\delta^{18}\text{O}$ of freshwater carbonates

The previous sections have outlined the controls on the $\delta^{18}\text{O}$ through the hydrological cycle, from the initial evaporation from the ocean through to sedimentation in lake carbonates. It is evident that the transport history of lake water influences the final composition of the $\delta^{18}\text{O}$ values of calcite. Within this thesis, isotope analysis will

primarily be used to infer information regarding lake basin hydrology, such as the degree of hydrological closure and evaporitic enrichment (Talbot, 1990). Where it is demonstrated that lakes are freshwater, non-evaporitic and have not undergone diagenesis, it may be possible to use the $\delta^{18}\text{O}$ value of calcite to infer further palaeoclimatic information such as source of moisture and atmospheric circulation patterns. However, in order to do so assumptions, must be made regarding the temperature of calcite precipitation.

3.6.5 Factors that control the $\delta^{13}\text{C}$ of freshwater carbonates

The $\delta^{13}\text{C}$ of authigenic lacustrine carbonates are predominantly controlled by the $\delta^{13}\text{C}$ of dissolved inorganic carbon content ($\delta^{13}\text{C}_{\text{TDIC}}$) derived from HCO_3^- (bicarbonate) within the lake water (Leng and Marshall, 2004). There is a negligible temperature effect during carbonate precipitation between lake water $\delta^{13}\text{C}_{\text{TDIC}}$ and carbonate (Romanek et al., 1992). Consequently, the $\delta^{13}\text{C}$ of carbonate reflects the $\delta^{13}\text{C}$ of TDIC of lake waters (Leng and Marshall, 2004). This is controlled by a variety of processes at the catchment scale and within the lake basin itself (Leng and Marshall, 2004), meaning that the $\delta^{13}\text{C}$ of carbonate can provide information regarding the lacustrine carbon cycle.

3.6.5.1 Lake catchment processes

The $\delta^{13}\text{C}_{\text{TDIC}}$ of recharge waters into a lake derive from carbon sourced from plant respiration and CO_2 from soils (Leng and Marshall, 2004), along with carbon sourced from any marine limestones found in the catchment (Hammarlund et al., 1997). The relative proportion of these inputs will control the $\delta^{13}\text{C}_{\text{TDIC}}$ of lake waters. It is not clear whether there are any marine limestones the Nefud catchment, with the immediate underlying geology described as Cambro-Ordovician sandstones and Eocene to late Oligocene ferricrete and iron-rich silcretes (Wagner, 2011; Whitney et al., 1983).

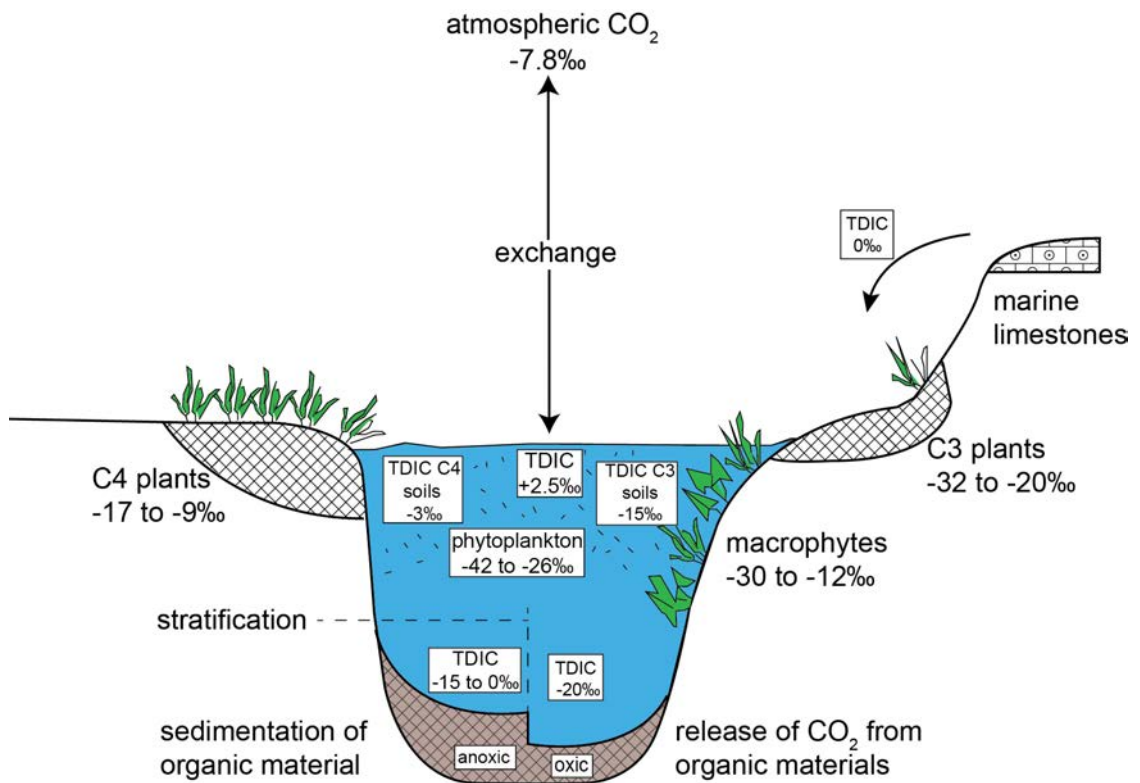


Figure 3.17 – Major sources of carbon into lakes and their carbon isotope values redrawn after Leng and Marshall (2004). Note the key difference in isotopic values between C3 and C4 plants and TDIC C3 and TDIC C4 soils, with C4 yielding more positive carbon isotope values. Exchange with atmospheric CO₂ will also lead to more positive values, as will any input of marine carbonates.

The $\delta^{13}\text{C}_{\text{TDIC}}$ of recharge waters vary depending on the productivity of the landscape. In regions with low landscape productivity (i.e. limited vegetation and soil development) it is expected that groundwaters will be dominated by $\delta^{13}\text{C}$ derived from marine limestones, with values typically between -3 and +3 (Andrews et al., 1997). Conversely, in productive landscapes with greater soil development and more abundant vegetation, $\delta^{13}\text{C}_{\text{TDIC}}$ is likely to be more negative due to the increased contribution of isotopically light ¹²C liberated from the decay of organic matter in the soil (Leng and Marshall, 2004). The photosynthetic pathway of vegetation (i.e. C3, C4, CAM) controls the value of the $\delta^{13}\text{C}$ from soil zone respiration and organic matter decay. In semi-arid regions such as the western Nefud Desert, even during humid phases, it is likely that C4 plants were the dominant vegetation type on the landscape (Roberts et al., 2018; Thomas et al., 1998). However, palaeoenvironmental analysis from the western Nefud Desert basins of Jubbah (Petraglia et al., 2011) and Al Marrat (Jennings et al., 2016) suggests C3 vegetation were dominant at these locations during humid intervals. This is due to the

fact that both these basins are structural, with groundwaters having been close to the land surface as recently as the 19th century (Parton et al., 2018). It is also likely that arid-adapted vegetation that follow the crassulacean acid metabolism (CAM) photosynthesis pathway may also have been present.

C4 taxa typically have $\delta^{13}\text{C}$ values between -17‰ and -9‰, C3 taxa have $\delta^{13}\text{C}$ values ranging between -35‰ to -20‰, while CAM taxa have ranges between -35‰ and -9‰ (Leng and Marshall, 2004; Ting, 1985). HCO_3^- in equilibrium with CO_2 gas is +10‰ greater than soil CO_2 (Romanek et al., 1992; Leng and Marshall, 2004), meaning HCO_3^- derived from a landscape dominated by C4 plants would be expected to have $\delta^{13}\text{C}_{\text{TDIC}}$ between -7‰ and +1‰ (Leng and Marshall, 2004). If C3 plants were present on the landscape, then $\delta^{13}\text{C}_{\text{TDIC}}$ would be expected to be isotopically more negative (Leng and Marshall, 2004). It is more difficult to distinguish C3 and C4 taxa from CAM taxa given the wide range of $\delta^{13}\text{C}$ values.

3.6.5.2 Within-lake processes

Several processes within the lake system control the $\delta^{13}\text{C}_{\text{TDIC}}$ value of the waters. Lake waters equilibrate with atmospheric CO_2 through time (Usdowski and Hoefs, 1990; Leng and Marshall, 2004), and extent to which this occurs is dependent upon residence time. Closed lake systems with long residence times and slow throughflow allow equilibrium to be reached, and this results in $\delta^{13}\text{C}_{\text{TDIC}}$ values of between ~0‰ to +2‰ (Leng and Marshall, 2004). It must be noted that these values are similar for lakes where $\delta^{13}\text{C}$ of groundwaters are predominantly influenced by marine carbonates or by C4 vegetation. This highlights the difficulty in picking apart drivers of the $\delta^{13}\text{C}$ record. Open systems with shorter residence times and higher rates of throughflow will not move into equilibrium with atmospheric CO_2 and have more negative $\delta^{13}\text{C}_{\text{TDIC}}$ values. Other within lake processes that impact the $\delta^{13}\text{C}$ values include the preferential removal of ^{12}C , and subsequent enrichment of $\delta^{13}\text{C}$, during photosynthesis by aquatic plants (Leng and Marshall, 2004). Vertical stratification of the water column and its impact on the

oxidation/reduction of organic matter (Teranes and McKenzie, 2001) and methogenesis (Herczeg, 1988) also influence water column $\delta^{13}\text{C}$.

3.6.6 Practical considerations when interpreting the stable isotope record

3.6.6.1 Diagenetic alteration of the isotopic signal from freshwater carbonates

Over the timeframe of this study – the last 500 ka – it is important to consider the potential impact that diagenesis may have had on the isotopic values of ancient carbonate. Diagenesis of lacustrine carbonates in the western Nefud Desert would probably be caused by the intrusion of younger meteoric waters or groundwaters during subsequent humid phases following deposition. This may lead to recrystallisation, micritization or cementation in pore spaces (Gierlowski-Kordesch, 2010). These processes can overprint and reset the isotopic signal of primary (i.e. the original) carbonate and lead to more or less enriched values depending on the isotopic composition of later meteoric or ground waters (Gierlowski-Kordesch, 2010). For example, diagenetic calcite from Miocene carbonates in the Ebro basin are more depleted in $\delta^{18}\text{O}$ relative to primary carbonate due to the interaction of meteoric waters associated with higher lake levels following karstification processes (Arenas et al., 1999). Diagenesis that may have influenced the primary isotopic signal can be identified in thin-section, as large sparitic crystals formed through aggrading neomorphism can be readily differentiated from primary microsparite/micrite (Gierlowski-Kordesch, 2010).

3.6.6.2 Lacustrine carbonate fractions

Inorganic authigenic carbonates precipitated from the water column during periods of supersaturation form only one component of the material preserved within lacustrine carbonates. Other carbonates include biogenic shell material (i.e. ostracod and mollusc shells) (Holmes, 2001; Leng et al., 2010), detrital carbonates from older deposits within the basin, and algal carbonates (Andrews et al., 2004). The mixture of different carbonate species is problematic because either they record different isotopic values in response to the same environmental conditions, or they form during different seasons

(Leng and Marshall, 2004). Consequently, changes in isotopic values through a sequence could reflect variations in the proportions of each carbonate species analysed as opposed to environmental variables. These effects can be diagnosed through the use of micromorphology, which can identify the amount or variability of carbonate species present (i.e. the number of biogenic shells present or whether the carbonate is authigenic or washed into the basin). Previous microfacies work (see section 3.3.1; Fig 3.6) demonstrates that the Nefud marls are dominated by authigenic carbonate, with shell and detrital components being rare (Groucutt et al., 2018).

3.6.6.3 (Dis)Equilibrium conditions in authigenic carbonates

The use of $\delta^{18}\text{O}$ of calcite as a proxy requires the assumption that calcite was precipitated in equilibrium with the $\delta^{18}\text{O}$ of lake water. If this is the case, then only temperature and the isotopic composition of lake water influence the isotopic composition of the mineral, and this process can be predicted by thermodynamics (Leng and Marshall, 2004). In reality it is not possible to tell whether equilibrium mineral fractionation occurred in the geological record where no direct present-day analogues can be studied (as is the case in the western Nefud Desert). Various studies have assessed whether equilibrium mineral fractional occurs. Some studies show mineral offsets in $\delta^{18}\text{O}$ of $<1\text{‰}$ (Jones and Marshall, 2002), but other studies have demonstrated larger offsets in the region of 2 to 3‰ (Fronval et al., 1995). A laboratory study by McCrea (1950) suggests the rate of crystal precipitation can enrich the mineral phase of ^{16}O , while other studies suggest that it has little effect on the isotopic composition of calcite (Tautani et al., 1969). More recent studies, which used direct measurements of water temperature and lake water $\delta^{18}\text{O}$, along with calcite $\delta^{18}\text{O}$, suggest that calcite precipitation occurs in equilibrium within uncertainties (Marshall et al., 2002).

3.6.7 Authigenic carbonate isotopic sequences from lacustrine records in the Nefud Desert

One single isotopic sequence has been published from the western Nefud Desert at Al Wusta (Groucutt et al., 2018), and an additional sequence for Site 16.3 was presented

in the author's MSc thesis (Clark-Wilson, 2016). At both sites $\delta^{13}\text{C}$ values predominantly lie within a narrow range between -1 to +3‰, with the exception of the very onset of the sequence at Al Wusta where $\delta^{13}\text{C}$ values are more negative (Clark-Wilson, 2016; Groucutt et al., 2018). $\delta^{18}\text{O}$ values range between -3.56‰ to -0.09‰ at Al Wusta and between -0.85‰ and 4.33‰ at Site 16.3, showing a distinct difference. In both sequences there is limited evidence for covariance between $\delta^{13}\text{C}$ and $\delta^{18}\text{O}$, indicating that carbonate was precipitated in open, non-evaporitic lake systems (Talbot, 1990). More isotopic analysis at a higher resolution has been undertaken at Al Wusta as part of this thesis.

A further isotope stratigraphy exists for a marl sequence at site JB1 in the Jubbah Basin of the southern Nefud (Parton et al., 2018). The trends in isotopic values vary between units within the sequence, but they are generally interpreted as reflecting changes in the precipitation/evaporation balance. For example, the upper ~2 m of the sequence (the Holocene sequence) yields $\delta^{18}\text{O}$ values ranging between -9.3‰ and +8.2‰, and $\delta^{13}\text{C}$ values ranging between -13.5‰ and -1.4‰. Such large ranges are interpreted as indicating the presence of a shallow, evaporitic water body with seasonally fluctuating levels (Parton et al., 2018). Conversely zone IV, which was deposited during MIS 5a, contains progressively enriching isotope values ($\delta^{18}\text{O} = -5.5‰$ to +2.8‰. $\delta^{13}\text{C} = -11.1‰$ to -4.3‰). This is interpreted as reflecting the transition from lacustrine to palustrine conditions (Parton et al., 2018). It is notable that the ranges in $\delta^{18}\text{O}$ at Jubbah are greater than those observed at Al Wusta or Site 16.3 (Clark-Wilson, 2016; Groucutt et al., 2018).

3.7 Palaeoecological proxies

Palaeoecological proxies such as diatoms, ostracods, molluscs and pollen provide powerful tools to reconstruct the past environment from lake archives. They give diagnostic hydrological information such as pH, lake depth, nutrient content and salinity. However, in arid and hyper-arid environments their preservation is often poor, and this limits their use in research. Despite the poor preservation, these proxies are still useful environmental indicators where they are present. Several studies from the Arabian Peninsula (e.g. Rosenberg et al., 2013, 2011) have employed diatom palaeoecology. At

a minimum, diatom palaeoecology gives a qualitative reconstruction of lake hydrology based on ratio of freshwater, oligo-, meso- and poly-saline species present within an assemblage (e.g. Rosenberg et al., 2013). Quantitative analyses can also be employed to pick out environmental drivers of changes in diatom species compositions such as changes in pH, lake depth, phosphorus levels and salinity (Groucutt et al., 2018), though such analysis may be hampered by low preserved diatom abundances. Due to the typically poor preservation of palaeoecological proxies, this thesis focuses on the sedimentological and geochemical proxies discussed above as the main tool in reconstructing palaeoenvironments within this thesis. However, palaeoecological work has been undertaken by colleagues on many of the sedimentary sequences presented here, and these will be discussed alongside the isotopic and sedimentary results where appropriate.

3.8 Chapter summary

The review above highlights a number of key points regarding interdunal lacustrine and palustrine sediment deposits, the environments in which they were formed and the palaeoenvironmental proxies found within them. The key points are:

- Interdunal carbonate/siliceous deposits are widespread across the western Nefud Desert. These have previously been interpreted as palaeolake deposits (Clark-Wilson, 2016; Groucutt et al., 2018; Rosenberg et al., 2013) and were deposited during humid phases. They provide a key tool for reconstructing the nature and timing of humid intervals in the region.
- A model for interdunal lake development is proposed based on current research (Groucutt et al., 2018) and follows six phases. These are as follows: (1) aridity prior to lake development where the interdunal basin contains aeolian sands or a recharge playa, (2) transition to increased humidity, a rise in the regional water table and onset of lake development; (3) perennial and stable lake system during peak humidity; (4) transition towards shallower lacustrine or palustrine conditions in response to basin infilling or increased environmental aridity; (5) desiccation of the lake and deposition of laminated sands with gravels and calcitic rhizoliths in response to sheet wash processes and terrestrial vegetation

growth; (6) a return to aridity with deflation leaving palaeolake sediments exposed as inverted relief features in the modern environment.

- Lacustrine and palustrine systems exist along a continuum defined by the amount of sub-aerial exposure of the sediment. Lacustrine systems are characterised by perennial sub-aqueous conditions while palustrine systems are periodically sub-aerially exposed and effected by pedogenic processes.
- Lacustrine and palustrine systems can be identified in the sedimentary record through a combination of bulk- and micro-sedimentology, stable oxygen and carbon isotope analysis, and palaeoecological (e.g. diatom) analysis.
- In the geological record, lacustrine systems are characterised by unaltered primary lake mud which at the microscale consists of homogenous or laminated microsparite/micrite. Palustrine systems are characterised by primary lake mud which has undergone alteration via desiccation/emersion or pedogenic processes.
- Stable $\delta^{18}\text{O}$ and $\delta^{13}\text{C}$ isotope analysis of carbonate provides palaeohydrological information such as the degree of hydrological closure of the lake body.
- $\delta^{18}\text{O}$ analysis also provides the opportunity to assess wider palaeoclimatic questions assuming that the $\delta^{18}\text{O}$ signal is not driven by variations in precipitation/evaporation balance.
- Palaeoecological proxies such as diatoms are typically poorly preserved within palaeolake sediments, though they still provide useful information when used in conjunction with the proxies outlined above.

Chapter 4 – Luminescence dating

4.1 Introduction

An aim of this thesis is to determine the timing of humid intervals in the western Nefud Desert, Saudi Arabia over the past ~500 ka. To achieve this aim, luminescence dating of sands associated with wetland sediments has been undertaken at all sites studied. In some cases, it was possible to extract dateable material from the wetland sediments themselves, allowing direct dating of the humid phases that they represent. Elsewhere dates have been obtained from aeolian sands underlying wetland sediments, and from waterlain sands overlying them, yielding “bracketing” ages for the humid phase. The applicable time range of luminescence dating, along with the depositional setting of the sediments analysed, makes luminescence the ideal dating technique for sediments in the Nefud Desert. Luminescence ages have been produced using quartz at all sites, and feldspar where necessary. At some sites additional dating work using uranium-series (U-series) and U-series combined with electron spin resonance (U-ESR) has been undertaken on fossil material (Groucutt et al., 2018; Stimpson et al., 2016). This work was carried out by an external laboratory, and it is beyond the scope of this thesis to discuss the methodological and technical aspects of their analyses. This chapter aims to introduce the principles, physics and uncertainties associated with luminescence dating that are relevant to this thesis.

4.2 Overview of Luminescence Dating

Luminescence dating determines the time elapsed since mineral grains were last exposed to sunlight or heat. It has been applied widely in palaeoenvironmental and archaeological studies to place study sites into a chronometric framework (Roberts et al., 2015). Once mineral grains are protected from sunlight or heat, electrons are progressively displaced from their original place in the crystal lattice and accumulate in “traps” (see section 4.3). The displacement of electrons occurs due to ionising radiation produced during the decay of naturally occurring radioisotopes (see section 4.4). When mineral grains are exposed to photons of a sufficient energy (sunlight or laboratory

induced), trapped electrons held within electron traps are excited and move from the electron trap to a recombination centre (Wintle and Adamiec, 2017). When the recombination centre is a luminescent centre, this process leads to the emission of light (photon). The amount of light emitted is proportional to the number of trapped electrons, which are in turn proportional to the radiation dose (measured in grays, (Gy)) which the mineral grain has absorbed. Because the parent isotopes of naturally occurring radioactive decay series are long-lived relative to the timescale over which luminescence dating is applicable, the environmental dose rate is constant over time, and hence the radiation dose absorbed by the mineral grain is directly proportional to the amount of time since the mineral grain was last exposed to sunlight. The radiation dose absorbed by a mineral grain during burial is termed the palaeodose, and luminescence measurements yield a laboratory estimate of this quantity, termed the equivalent dose (D_e). The time elapsed since the mineral grain was last exposed to sunlight is then determined by dividing the laboratory measured equivalent dose by the environmental dose rate:

$$\text{Age (ka)} = \frac{\text{Equivalent dose (De)}}{\text{Environmental dose rate (Gy/ka)}} \quad (\text{Eq. 4.1})$$

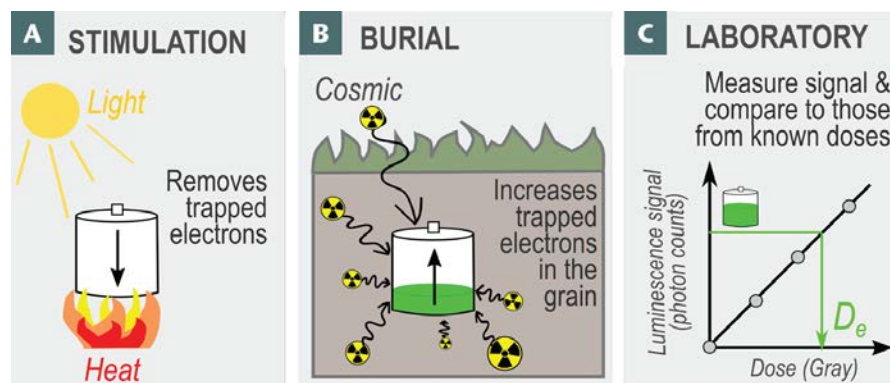


Figure 4.1 – Rechargeable battery analogue to describe the process of luminescence dating, from Smedley (2018). (A) Sand grains are stimulated by naturally occurring sunlight (optically stimulated) or heat (thermally stimulated) which removes trapped electrons from the crystal lattice of sand grains (empties battery). (B) Once sand grains are buried (lies beneath the land surface) they are protected from optical stimulation and gradually accrue energy from the external and internal decay of naturally occurring radioisotopes and from cosmic sources. This gradually increases the trapped electrons in the sand grains (i.e. the battery is charging). The number of trapped electrons is directly proportional to the amount of time since the sand grain was last exposed to sunlight or heated. (C) The energy stored within the sand grains are measured in the laboratory, which is converted into an ‘equivalent dose’ by comparing the natural luminescence intensity with a number of known doses, which produce a ‘dose response curve’.

4.3 Physical basis of luminescence production

The phenomenon of luminescence within quartz and feldspar is best described via an energy-level depiction of insulating solids (Fig. 4.2) (Preusser et al., 2008; Wintle and Adamiec, 2017). The atomic structure of quartz and feldspar crystal lattices are constructed of positively and negatively charged ions. In the real world, the atomic structure of the crystal lattice within mineral grains contains point defects which can be intrinsic structural faults (e.g. Si- or O-vacancy in quartz) or related to impurities formed during crystal growth that can be further altered in the presence of subsequent ionising radiation (Preusser et al., 2009). Consequently, point defects are areas with localized energy states with an excess or absence of positive or negative ions (Preusser et al., 2009). Areas of weak positive charge (i.e. a negative ion vacancy), are capable of capturing and retaining electrons diffusing through the crystal lattice as a result of ionising radiation, and hence are referred to as electron traps.

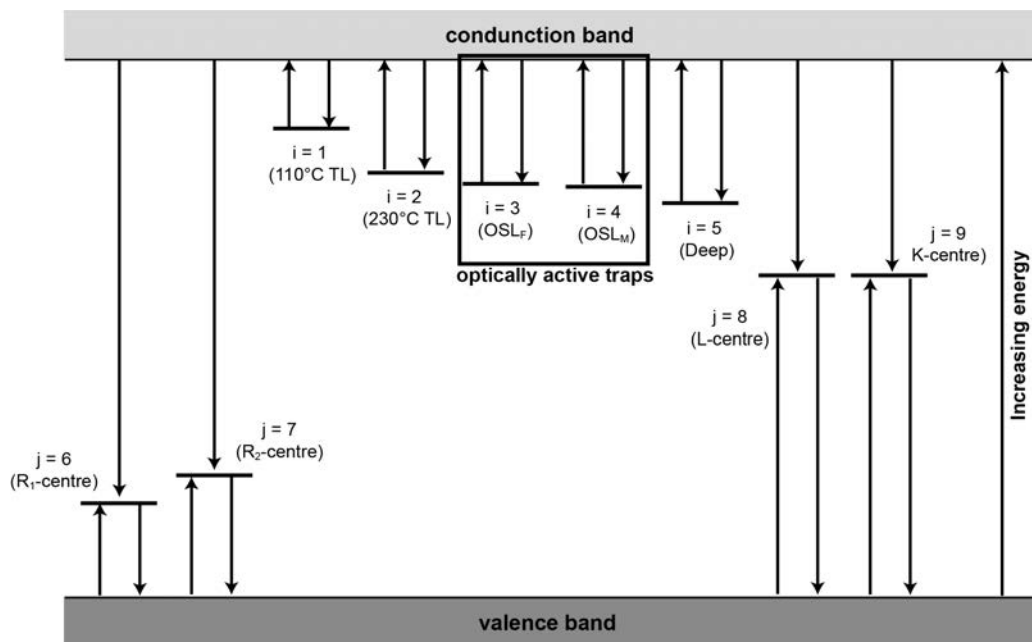


Figure 4.2 – Energy level diagram redrawn after Bailey (2001). Electrons in an unexcited state are in the ‘valence band’ while those in ‘excited’ states lie above the valence band. As electrons become excited, due to ionising radiation from external and internal sources, they diffuse through the crystal structure of the mineral grain and will either (a) become trapped at a higher energy state in an electron trapping centre (denoted by ‘i’) or (b) immediately return to the valence band via a recombination centre (denoted by ‘j’), emitting heat or light as they do so. Electron trapping centres occur at different energy depths beneath the conduction band. Only electrons captured in traps with trap depths greater than ~1.6 eV or more are useful for dating late Quaternary sediments. Electron traps ‘i = 3 (OSL_F)’ and ‘i = 4 (OSL_M)’ occur at a greater depth than ~1.6 eV and give rise to photo-stimulated luminescence signals that reflect the fast and medium OSL components (Bailey, 2001). These traps are highlighted by the black rectangle and are labelled ‘optically active traps’.

Electrons in an unexcited state are “attached” to their parent atoms and are said to be in the “valence band”. Ionising radiation from sources external and internal to the mineral grain (see section 4.4) provide electrons in the valence band with sufficient energy to escape their parent atom and diffuse through the crystal structure of the mineral grain. These electrons are said to be in the “conduction band”. The loss of an electron from the parent atom leaves an electron vacancy or “hole”. This hole, which is also referred to as a “recombination centre” is an area of positive charge, which is therefore capable of attracting a diffusing electron. When electrons are activated to a higher energy state by the ionising radiation, they can diffuse through the crystal until they are captured by an area of positive charge (Aitken, 1998; Preusser et al., 2008). In practice, the majority of activated electrons immediately return to a ground-state in the valence band of their parent atom, dissipating the energy absorbed from ionising radiation as heat or light. This latter phenomenon is referred to as “radioluminescence” and is the reason that in popular culture radioactive substances are depicted as glowing. However, a small proportion of activated electrons are trapped and stored at a higher energy state by electron traps, with an energy lower than that of the conduction band, but higher than electrons in the valence band. (Aitken, 1998; Preusser et al., 2008). The geological stability of an electron in an electron trap, and therefore its use for dating Quaternary materials, is determined by its “depth” beneath the conduction band (Aitken, 1998) – i.e. the difference in energy between the electron in the trap and that of the conduction band (Fig 4.2). This represents the additional energy that an electron must acquire to escape the trap and diffuse freely through the conduction band. Only electrons captured in traps with trap depths greater than ~1.6 eV or more are useful for dating late Quaternary sediments (Aitken, 1998; Li et al., 2014; Preusser et al., 2008). Shallower (lower trap depth) traps will lose a proportion of their trapped electrons during ambient temperature burial, meaning that luminescence signals from these traps will underestimate the true burial age of the sample. The mean time that an electron is expected to reside in a trap is given by the Equation 4.2:

$$\tau(s) = s^{-1} \exp \frac{E_t}{k_B T} \quad (\text{Eq. 4.2})$$

where s is the frequency factor (the rate of detrapping if activation energy was zero), E_t the thermal activation energy, k_B is Boltzmann's constant and T is absolute temperature (Bailey et al., 1997). Electrons accumulate in geologically stable traps over time, and the number of trapped electrons provides a proxy for the total amount of radiation dose absorbed by the mineral since the trap was last emptied.

Electrons are evicted from an electron trap when they absorb sufficient energy to reach the conduction band (Preusser et al., 2009). In all cases, electrons can be evicted by heating the mineral grain, but some traps are also capable of being emptied by exposure to sunlight (in nature) or artificial light (in the laboratory). These latter traps are emptied in nature by sunlight exposure during subaerial transportation, and therefore the trapped charge population that they contain after a period of burial can be used to determine the age of a sediment body. Once in the conduction band an electron may either be retrapped or captured by an 'electron hole' within a recombination centre (Preusser et al., 2008). "Recombination" of an electron with a hole results in the dissipation of energy as heat or light. During laboratory stimulation of a sample, when optically sensitive traps are being completely emptied by optical stimulation, the number of photons emitted by recombining electrons is directly proportional to the number of electrons evicted from the trap, which is in turn proportional to the radiation dose absorbed by the mineral grain during burial (Aitken, 1998). However, since the number of electron traps in any given mineral grain is finite, the rate of trap filling changes with dose, eventually reaching a saturation level where all traps contain an electron (Preusser et al., 2008). Consequently, the relationship between absorbed dose and luminescence signal is non-linear, and is usually best approximated by a saturating exponential, or saturating exponential plus linear form (Fig 4.3).

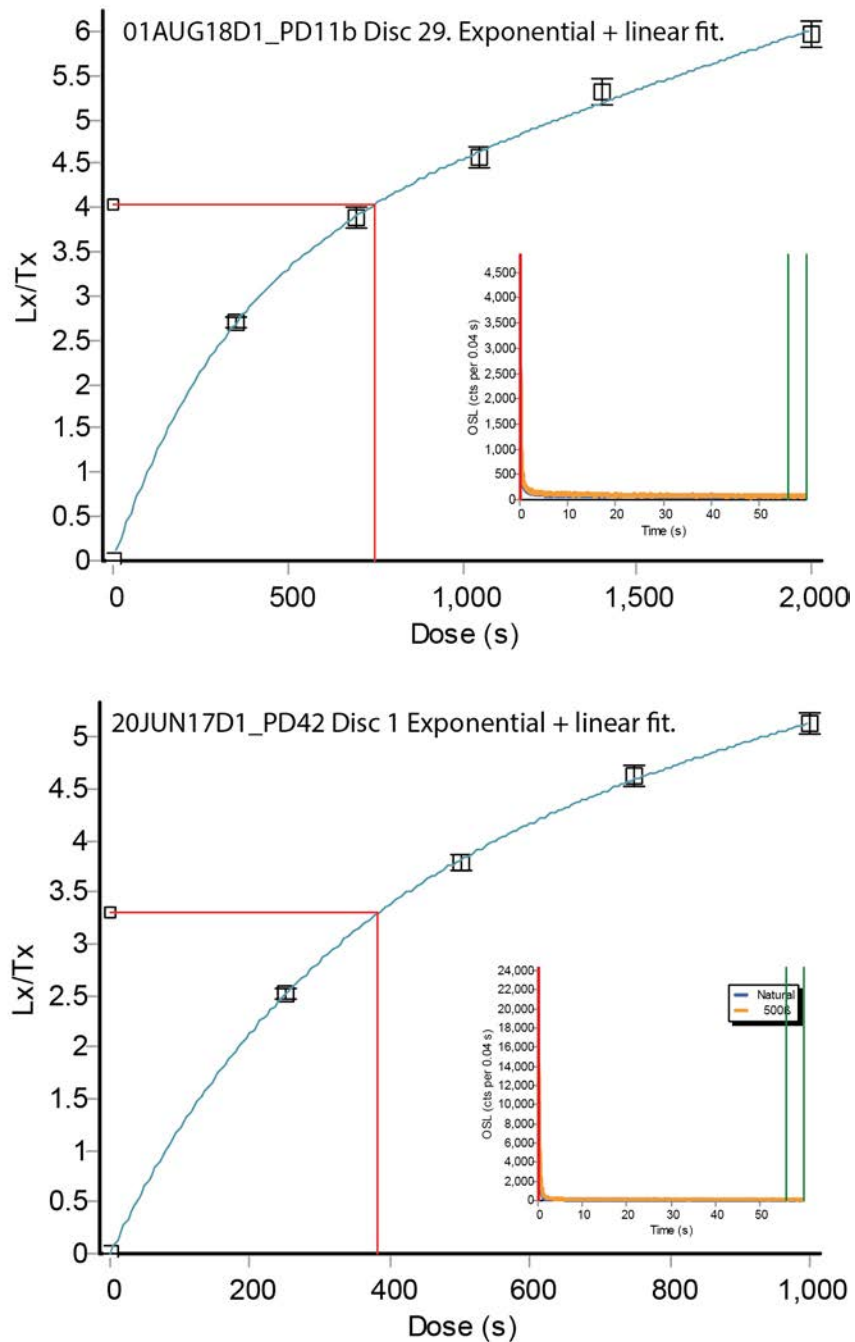


Figure 4.3 – Example dose-response curves (DRCs) using an exponential + linear fit from two samples analysed as part of this thesis. Note that in this example the dose is measured in seconds (s) rather than grays (Gy). The inset images show the OSL counts per 0.04 s during stimulation. DRCs are generated by measuring the charge stored within the grain (natural dose), before measuring a number of known regenerative doses that fall both above and below the charge stored within the grain. This produces an estimate of the total amount of dose absorbed by the grain over its burial history, termed the ‘equivalent dose’. As discussed in text, the relationship between the absorbed dose and luminescence signal is non-linear as the number of electron traps within a grain is finite and gradually fills over time until a saturation level is reached. Consequently, the DRC must be fitted using an exponential or exponential + linear fit. As the dose increases (moving to the right side of the graph) the number of available electron traps reduces and the curve ‘flattens’. Equivalent doses that lie towards this end of the growth curve, and are close to saturation, can therefore contain large, asymmetric uncertainties (Wintle and Murray, 2006). Criteria to overcome this issue where it occurs are discussed in Chapter 6.

4.3.1 Quartz optically stimulated luminescence (OSL)

Quartz is the second most abundant mineral on the planet, is present in most depositional environments and is resistant to weathering under most circumstances. The quartz luminescence signal is very rapidly reset by sunlight exposure, and most quartzes are capable of recording absorbed doses up to ~200 Gy. This equates to a maximum attainable quartz OSL age of ~200 ka assuming an environmental dose rate of 1 Gy/ka. In reality, the Nefud Desert is a low dose environment with many reported dose rates to quartz lying below 1 Gy/ka (e.g. Groucutt et al., 2018; Rosenberg et al., 2013). Consequently, the age range of quartz may be slightly greater than 200 ka and covers a large portion of the time range investigating within this thesis. Quartz OSL is widely used for dating archaeological contexts, because its luminescence properties are simple, well understood and relatively uniform (Roberts et al., 2015; Wintle and Adamiec, 2017). For these reasons, most luminescence ages presented in this thesis were measured on quartz.

OSL dating of quartz is based on the optical stimulation of light-sensitive electron traps by visible light in the green-blue part of the spectrum (Huntley et al., 1985). Light emission from optical stimulation of quartz is typically detected in the ultraviolet range (Huntley et al., 1985). The quartz OSL signal is usually measured using continuous-wave OSL (CW-OSL), whereby the stimulation power (mW/cm^2) is constant throughout optical stimulation. It has been observed that this signal cannot be characterised by a single exponential decay function, implying that the signal is a composite derived from several optically sensitive traps (Bailey, 1997; Smith et al., 1986). Instead, mathematical deconvolution of the CW-OSL signal demonstrates that the signal comprises multiple components (see Fig 4.4). Initially, the signal was divided into a fast and medium component (Smith and Rhodes, 1994) before an additional slow component was added (Bailey et al., 1997). These names reflect the rate at which the luminescence signal is depleted under optical stimulation, with the fast component decaying to a negligible level quickly. Further studies have identified that the slow component can itself be subdivided into least three (Singarayer and Bailey, 2004) and possibly four (Jain et al.,

2003; Singarayer and Bailey, 2003) discrete components. A rare thermally unstable ultrafast component has also been identified in certain samples (Choi et al., 2003; Jain et al., 2008, 2003). Each component has its own thermal and optical properties, and they have been used to inform and construct the ‘band-gap diagram’ shown in Fig. 4.2. Fortuitously, the fast component has the ideal optical properties for reliable quartz OSL dating as it is readily bleached in nature (Li and Li, 2006) and is sufficiently thermally stable for dating over the Quaternary time range (Wintle and Adamiec, 2017; Wintle and Murray, 2006).

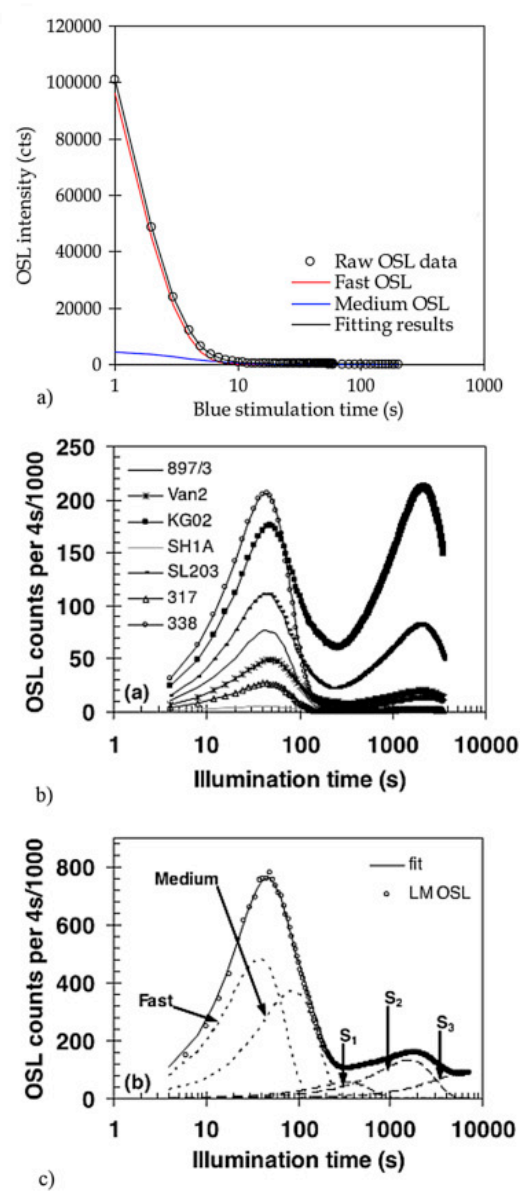


Figure 4.4 – Examples of (A) continuous-wave OSL curve, (B) a linear-modulated OSL curve and (C) the separate components of the luminescence signal (fast, medium and 3 x slow), from Wintle and Adamiec (2017). It is the fast signal that is used for reliable OSL dating as it derives from a geologically stable trap and is readily bleached in nature.

However, not all quartz CW-OSL signals are dominated by a fast component and when this is the case it can lead to uncertainties in D_e estimation. Firstly, the widely adopted single-aliquot regenerative (SAR) dose method (discussed in section 4.3.3) was developed using fast component dominated samples (Murray and Wintle, 2000), meaning that the application of this method on non-fast dominated samples may lead to errors. For example, it has been suggested that the SAR protocol is unsuitable for dating materials dominated by the medium and slow components (Jain et al., 2003). Additionally, it has been suggested that the medium component traps are not sufficiently stable to allow reliable dating of pre-Holocene materials (Steffen et al., 2009), whilst thermal transfer of charge into the medium and slow components during measurement procedures can lead to age overestimates (Jain et al., 2003). Consequently, it is important to identify whether the signal is fast-dominated or not. In order to isolate the fast component, luminescence signals are determined by integrating the signal produced during the initial period of optical stimulation (typically less than the first second of stimulation) with a background signal derived from the last ~10 % of the stimulation period subtracted (Banerjee et al., 2000). Subtraction of a background signal largely removes contributions from the slow component, which decays so slowly under laboratory illumination as to yield a near-constant luminescence intensity. Conversely, the fast component signal depletes so fast under laboratory illumination that it dominates the first ~1 s of stimulation, after which it is depleted to a negligible level and the medium component becomes dominant.

4.3.2 Feldspar infrared stimulated luminescence (IRSL) signal

Although dating materials using quartz OSL signals offer a number of advantages over measuring feldspars, notably: 1) more rapid zeroing of the signal by sunlight; 2) the greater abundance of quartz in most samples and 3) high geological stability of the quartz OSL signal, a single feldspar age was produced. Although more prone to weathering and therefore less common than quartz in most sediments, feldspar is present in sufficient quantities for dating purposes at some sites in the Nefud Desert. Feldspar minerals themselves are geochemically complex with a more intricate crystallographic structure than quartz (Smedley, 2018). Multiple chemical compositions

of feldspar exist, but K-rich feldspars (alkali feldspars) are typically targeted for luminescence dating. The luminescence signal from K-feldspars are stimulated using infrared photons (870 nm), whilst the blue (~400 nm) luminescence emissions (termed infra-red stimulated luminescence, IRSL) are used for age determination (Hütt et al., 1988). Whilst the luminescence signal from feldspar is usually brighter than that of quartz, the principal advantage of dating samples using IRSL is that the signal saturates at much higher absorbed doses than OSL, extending the time range of the technique to cover Middle Pleistocene sediments (Li et al., 2014). Further benefits include the high internal dose rate within K-feldspars originating from the presence of ^{40}K and ^{87}Rb within the crystal lattice. This increases the precision of samples with low external environmental dose rates where there may be uncertainties associated with moisture content, heterogenous beta microdosimetry or unquantifiable changes in overburden and cosmic dose rate over the burial history (Huntley and Lamothe, 2001). For these reasons, measurement of K-feldspars may be a better choice than quartz for luminescence dating samples >200 ka.

However, the IRSL signal obtained by stimulating feldspars at ~50°C has been limited by a phenomenon known as anomalous fading (Wintle, 1973). Anomalous fading is the process of leakage of electrons from the geologically stable traps that give rise to the IRSL signal at a rate much faster than would be expected based on their trap depth (Li et al., 2014; Wintle, 1973). Fading is a time-dependant phenomenon, so it primarily affects the natural signal, which accumulates during burial, rather than laboratory signals resulting from rapid irradiation in a luminescence instrument. Consequently, the natural luminescence signal is lower than the signal induced by a similar radiation dose administered in the laboratory, meaning that without correction fading leads to age underestimates. One solution to this problem is to quantify the rate of fading, termed a “g-value” (Huntley and Lamothe, 2001; Lamothe et al., 2003), and correct the natural luminescence signal accordingly. However, beyond ~200 ka this approach often results in a correction that is the same order of magnitude as the signal being corrected, which makes the accuracy of the resulting age unacceptably dependant on the accuracy of the measured g-value. Consequently, numerous attempts have been made to identify a non-fading IRSL signal (Huntley and Lamothe, 2001; Lamothe et al., 2003; Lamothe and

Auclair, 1999; Li et al., 2008; Sanderson and Clark, 1994; Tsukamoto et al., 2006). The most successful method for isolating a non-fading feldspar signal is the post-IR IRSL method (pIR-IRSL) (Thomsen et al., 2008). The pIR-IRSL signal is measured at an elevated stimulation temperature (e.g. 225°C) after an initial low temperature stimulation at 50°C (see Table 4.2). The low temperature stimulation depletes the “easy-to-fade” IRSL signal, before measuring the more stable pIR-IRSL signal (Li et al., 2014; Thomsen et al., 2008). It has been demonstrated that the pIR-IRSL signals measured at both 225 °C and 290 °C have average g-values, based on 13 previous studies, of 1.5 ± 0.1 and $1.1 \pm 0.1\%$ per decade of time (Li et al., 2014). These values are sufficiently low that no fading correction is required.

Despite the advantages of the pIR-IRSL signal, there are important factors that need to be taken into account. The traps from which the pIR-IRSL_{225/290} signal originates are slower to bleach than those for the 50°C IRSL signal, which is in turn slower to bleach than the fast quartz OSL signal (Li and Li, 2011; Thomsen et al., 2008). Solar bleaching experiments demonstrate that it requires several hours of exposure to simulated sunlight to fully bleach the pIRIR₂₂₅ signal (Buylaert et al., 2012). However, the aeolian setting of the sands dated in this study mean that insufficient sunlight exposure prior to burial should not lead to age overestimates. A non-bleachable component (residual) has also been observed from pIR-IRSL signals (Li et al., 2014), though this does not usually exceed ~5 Gy, which is negligible when dating Middle Pleistocene samples. In the present study, practical considerations also limit the opportunities for using pIR-IRSL dating methods, since the Nefud Desert sands contain very little potassium feldspar. For these reasons, pIR-IRSL dating was only used on one of the samples analysed in this thesis.

4.3.3 Measuring the Equivalent Dose (D_e): the single-aliquot regenerative (SAR) dose technique

The key breakthrough for luminescence dating was the development of the single-aliquot regenerative (SAR) dose technique (Tables 4.1 and 4.2) (Murray and Wintle, 2003, 2000). This method enables multiple regenerative doses to be applied to the same

aliquot or grain, by tracking and correcting for the effects of sensitivity changes induced by the thermal treatment during the measurement procedure (Murray and Wintle, 2000). Sensitivity changes are changes in the luminescence produced per unit dose. Without correction, these changes result in a distorted growth curve and the calculation of an incorrect equivalent dose. Sensitivity correction is performed by applying a consistent test-dose (T_n/T_x) after measuring each regenerative dose (including the natural dose) (Murray and Wintle, 2000). The natural (L_n) or regenerated signal (L_x) is then normalised to the subsequent test dose (T_n/T_x). To test that the sensitivity correction has worked, a recycling test is undertaken at the end of the measurement sequence. This compares the luminescence response (L_1/T_1) of the first regenerative dose to an identical dose at the very end of the measurement sequence (Murray and Wintle, 2000). If the sensitivity correction has been successful, the ratio of the two measurements should be identical. Sensitivity correction is generally considered to be adequate when this “recycling ratio” is consistent with unity at two standard errors. The SAR method is used throughout this thesis, for both single-aliquot and single-grain analysis of quartz (Table 4.1) and single-aliquot analysis of feldspar (Table 4.2).

*Table 4.1 – The modified SAR protocol used for D_e measurement of quartz in this thesis. L_n – natural luminescence signal. L_x – laboratory induced luminescence signal, where L_1 is the luminescence response to the first regeneration dose etc. T_x – laboratory induced test dose luminescence signal. *Step 3 was only used when calculating the IR depletion point.*

Step	Treatment	Measured
1	Beta irradiation (known dose) (zero for natural and recuperation point)	
2	Preheat 1 (PH1) (180 – 260°C) held for 10 s	
3*	IRSL at room temperature for 40 s	
4	Optical stimulation at 125°C for 60 s with blue LEDs	L_n or L_x
5	Beta irradiation (test dose)	
6	Preheat 2 (PH2) (160°C, 220°C) held for 5 s	
7	Optical stimulation at 125°C for 60 s with blue LEDs	T_n or T_x
8	Optical bleach at 280°C for 100 s	
9	Return to stage 1	

Table 4.2 – Modified SAR protocol used for D_e measurement of feldspar. L_n – natural luminescence signal. L_x – laboratory induced luminescence signal. T_x – laboratory induced test dose.

Step	Treatment	Measured
1	Beta irradiation (zero for natural and recuperation point)	
2	Preheat 1 (250°C) held for 5 s	
3	IRSL at 50°C for 200 s	
4	IRSL at 225°C for 200 s	L_n or L_x
5	Beta irradiation (test dose)	
6	Preheat 2 (250°C) held for 5 s	
7	IRSL at 50°C for 200 s	T_n or T_x
8	IRSL at 225°C for 200 s	
9	IRSL at 290°C for 200 s	
10	Return to step 1	

Additional quality control tests incorporated into the SAR protocol include the infrared depletion test (IR depletion) (Duller, 2003) and the recuperation test (Murray and Wintle, 2000). The IR depletion test is undertaken to ensure there is no feldspar signal contamination in the OSL signal from quartz. This is achieved by comparing the sensitivity corrected luminescence intensities (L_x/T_x) of a dose with IR illumination prior to measurement with that for the same dose without IR illumination (Duller, 2003). Because the quartz luminescence signal is not sensitive to IR wavelengths, but feldspar is, the ratios of these two measurements should be consistent with unity where feldspar contamination is negligible. If the ratio of the two measurements, termed the “IR depletion ratio”, is consistent the grain/aliquot is accepted. Recuperation of the OSL signal is the process whereby there is a transfer of charge from deeper electron traps to the luminescence emitting trap due to the previous cycle of irradiation, preheating and stimulation. This phenomenon can lead to age overestimation (Wintle and Murray, 2006). To diagnose recuperation, a zero-dose regeneration cycle is added to the SAR measurement sequence (Murray and Wintle, 2000) (Murray and Wintle, 2000). If the signal (L_x/T_x) observed during this step is >5% of the natural luminescence signal (L_n/T_n), then recuperation is deemed to be negligible and the grain/aliquot is accepted for age calculation (Murray and Wintle, 2000). It is also important to remove saturated aliquots – i.e. those aliquots where the electron-traps are full, cannot absorb more dose, and are therefore not reliable indicators of age. Although a considerable body of literature exists concerning the diagnosis and treatment of saturated aliquots, there is little consensus on the most appropriate method for dealing with this phenomenon.

Consequently, the treatment of saturated aliquots is discussed for each site where it is relevant in Chapter 6.

4.4 The Environmental Dose Rate

The environmental dose is the denominator of the age equation (Eq. 4.1) and is therefore equally as important as the equivalent dose. It is calculated as follows:

$$D_R = D_\alpha + D_\beta + D_\gamma + D_{cosmic} \quad \text{Eq. 4.3}$$

Where D_R is the total environmental dose rate, D_α is the total α dose rate, D_β is the total β dose rate, D_γ is the total γ dose rate and D_{cosmic} is the total cosmic dose rate. The α dose rate is assumed to be negligible in 180 – 210 μm quartz where the HF etch is assumed to have removed α dosed material.

This section will discuss the separate components of the environmental dose rate, along with physical (e.g. grain size) and environmental factors (e.g. moisture content) that affect them (Fig 4.5).

4.4.1 Basic Principle

Four types of radiation contribute to the environmental dose: alpha (α), beta (β) and gamma (γ) radiation along with cosmic radiation (Eq. 4.3). The first three types of radiation derive from the local sediment matrix which contains naturally occurring radionuclides. The most important are Uranium (U), Thorium (Th) and Potassium (K). Uranium (^{238}U and ^{235}U) and Thorium (^{232}Th) are the parent isotopes for complex decay chains which yield α , β and γ radiation. Conversely, potassium (^{40}K) decays to stable isotopes calcium (^{40}Ca) or argon (^{40}Ar), via the emission of a single β particle and γ ray respectively. Importantly, potassium feldspars contain internal K (Smedley et al., 2012), whereas quartz has a negligible internal dose rate (Jacobs et al., 2006). The potassium within feldspars results in an internal dose that must be accounted for when calculating

the total environmental dose rate. Although grain-to-grain variations in K content are known to occur in potassium feldspar (Smedley et al., 2012), and this may add uncertainty to the dose rates for individual grains, it is reasonable to assume an internal K content of $12.5 \pm 0.5\%$ for multi-grain aliquots (Huntley and Baril, 1997).

4.4.2 Conversion factors

Conversion factors are used to derive the α , β and γ dose rates from radionuclide concentrations of U, Th and K (see Fig 4.5). Conversion factors themselves are derived from nuclear tables that undergo constant revision (Adamiec and Aitken, 1998; Liritzis et al., 2013). There was no need to use conversion factors for β and γ dose rates as they were directly counted. However, for the samples that included an α dose component, the conversion factors of Adamiec and Aitken were used (Adamiec and Aitken, 1998).

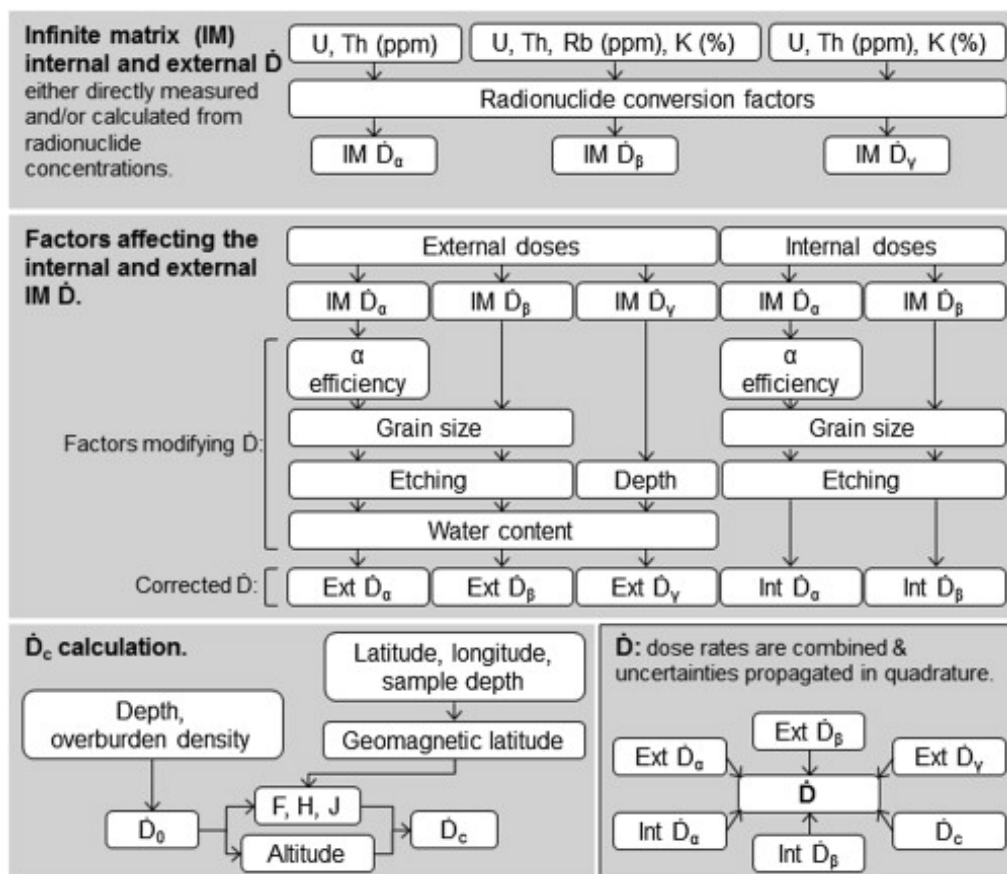


Figure 4.5 – An overview of the calculation of the environmental dose rate (D) in luminescence dating from Durcan et al. (2015). The upper box shows the internal and external dose inputs to sands, which in the case of this thesis have been directly measured. The middle box shows the factors which affect the internal and external infinite matrix dose. These are discussed in sections 4.4.2 and 4.4.3. The bottom left box shows the inputs to the cosmic dose rate, discussed in section 4.4.5. The bottom right box shows the total calculation of the environmental dose rate. Int = internal. Ext = external.

4.4.3 Modifications to the dose rate

Ionising radiation loses energy as it interacts with the material through which it passes. This “attenuation” of the dose rate with distance must be accounted for when calculating the environmental dose. In a typical mineral grain, α and β particles travel 20 – 30 μm and $\sim 3\text{mm}$ respectively, before they have dissipated all their energy (Fig 4.6). Consequently, only the outer surface of a 200 μm diameter mineral grain will receive an α dose from external radiation, while a measurable decrease in β dose towards the middle of a grain is also observed. These effects are accounted for in the dose rate calculation by multiplying the α and β dose rates by isotope specific attenuation factors (Bell, 1980; Mejdahl, 1979):

$$D_{\beta} = (U \times A_U^{\beta}) + (Th \times A_{Th}^{\beta}) + (K \times A_K^{\beta}) \quad \text{Eq. 4.4}$$

Where D_{β} is the total β dose rate, U , Th and K are the concentrations of uranium, thorium and potassium in (Gy/ka) and A_U^{β} being the attenuation factor for β radiation due to uranium etc.

$$D_{\alpha} = (U \times A_U^{\alpha}) + (Th \times A_{Th}^{\alpha}) + (K \times A_K^{\alpha}) \quad \text{Eq. 4.5}$$

Where D_{α} is the total α dose rate, U , Th and K are the emission counted concentrations of uranium, thorium and potassium in (Gy/ka) and A_U^{α} being the attenuation factor for α radiation due to uranium etc. Note that the α dose rate is commonly assumed to be negligible in 180 – 210 μm diameter quartz grains due to chemical pretreatment (HF etch) which removes the outer α irradiated portion of the grain. Gamma rays travel up to 30 cm in sediment, and therefore there is no appreciable decrease in the γ dose rate from the edge to the centre of sand-sized grains, so no attenuation correction is necessary.

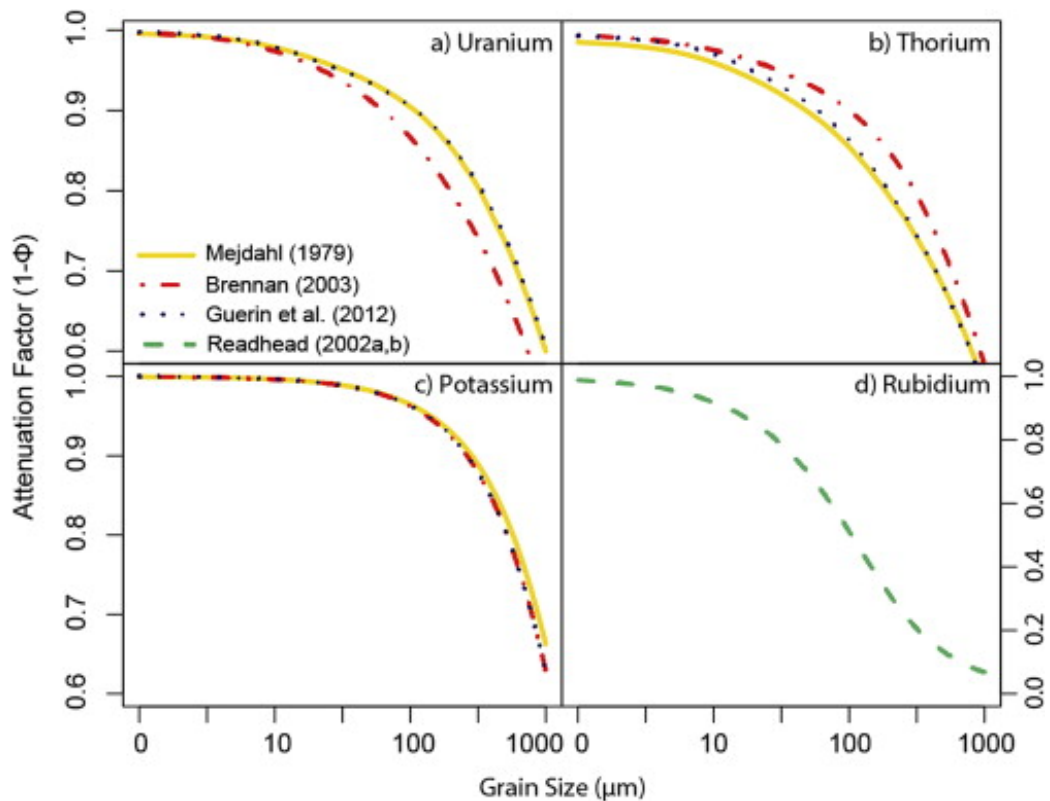


Figure 4.6 – Grain size attenuation factors for the β dose from Durcan et al. (2015), using data from Mejdahl (1979), Brennan (2003), Guerin et al. (2012) and Readhead (2002). There is little difference between the attenuation factors, and here we use the attenuation factor of Mejdahl (1979).

In addition to attenuation effects, alpha particles are so highly ionising that they saturate all the luminescence traps that lie along their decay tracks (Aitken, 1985; Durcan et al., 2015). Consequently, the dose absorbed by a mineral grain due to alpha irradiation is far lower than the amount of energy dissipated by the alpha particle. The discrepancy between these two values can be expressed as the alpha efficiency value (*α -value*) (Aitken and Bowman, 1975), which is the “ratio of luminescence per unit alpha track length to the luminescence per unit absorbed beta dose” (Durcan et al. 2015 p.56). The *α -value* varies both with mineral and grain-size, and in this thesis values of 0.038 ± 0.002 for fine-grained quartz (Rees-Jones, 1995) and 0.15 ± 0.05 for coarse-grained feldspar (Balescu and Lamothe, 1994) have been used. Coarse-grained quartz is routinely etched in hydrofluoric acid (HF) to remove the alpha irradiated outer portion of the grains (Fleming, 1970), and hence the alpha dose to this material is assumed to be zero. This is the case for all 180 – 210 μm quartz grains analysed in this thesis. Lastly, as noted above, chemical etching is used to remove that alpha irradiated portion of quartz grains. However, this also removes the most highly irradiated β portion of the grain, and this

must be corrected for. Etched attenuation values here were calculated for the β dose here using Bell (1979).

4.4.4 Moisture content

Water in the interstices between grains absorbs ionising radiation that, in a completely dry sediment body, would be absorbed by mineral grains. Consequently, moisture lowers the dose rate experienced by mineral grains within a sediment body relative the dose rate which would be expected based on the radioisotope content. Higher moisture contents equate to lower environmental dose rates. It is therefore critical to estimate the mean moisture content of the sediment over the burial period of the sample. This is calculated as follows:

$$D_{\alpha} = \frac{D_{\alpha,dry}}{1 + 1.49W} \quad \text{Eq. 4.6}$$

$$D_{\beta} = \frac{D_{\beta,dry}}{1 + 1.25W} \quad \text{Eq. 4.7}$$

$$D_{\gamma} = \frac{D_{\gamma,dry}}{1 + 1.14W} \quad \text{Eq. 4.8}$$

Where D_{α} , D_{β} and D_{γ} are the total α , β and γ dose rates, $D_{\alpha,dry}$ etc. are the 'dry' dose rates calculated in equations 4.4 and 4.5 and W is the water content. The attenuation factors for moisture content are 1.49, 1.25 and 1.14 for α , β and γ respectively (Aitken and Xie, 1990; Zimmerman, 1971).

The samples analysed in this study are aeolian sands deposited in dunes or sands deposited within palaeolakes. Whilst water has existed above the samples at points in time (during the existence of palaeolakes, when the underlying sediment will be saturated), the duration of these conditions is very short relative to the overall burial history of the sample, because aridity is the common environmental mode in the Nefud Desert over the Pleistocene (i.e. humidity only occurs during phases of high summer-insolation during interglacial phases) (Parton et al., 2015). It is reasonable to assume the moisture content for all samples in this study to be $5 \pm 2.5\%$. The 2σ range of this water

content covers completely dry sand (0 % moisture content) and saturated 25 % of the burial period (saturation water content of spherical, uniformly sized quartz grains is ~40 %, Duller, 1996). Consequently, this value covers the full range of potential depositional conditions which could have been experienced by the samples presented in this thesis.

4.4.5 Cosmic dose

The cosmic dose rate derives from galactic primary cosmic rays along with a solar output component (Durcan et al., 2015; Prescott and Hutton, 1994). These are split into two components: a 'hard' component consisting of muons that penetrates up to 6 m depth and 'soft' component consisting of electrons that penetrates up to 0.6 m (Fig 4.7) (Barbouti and Rastin, 1983; Prescott and Hutton, 1994). The input of cosmic rays also increases with altitude, due to reduced absorption by the atmosphere, and geomagnetic latitude, due to the Earth's magnetic field. Consequently, when calculating the cosmic dose to a sample, the historical overburden density (depth of overlying sediment x density of sediment through time), altitude, latitude and longitude of the sampling location must all be considered (Fig 4.5). The overall input of the cosmic dose towards the total environmental dose is typically small but not negligible (<10%) (Durcan et al., 2015). However, relative contribution of the cosmic dose increases where the dose rate due to radioisotopes in the sediment is low, as is the case in carbonate lake sediments and aeolian dune sands in the western Nefud Desert (Groucutt et al., 2018).

In addition, it is probable that cosmic rays fluctuate through time in response to changing solar output and galactic primary cosmic rays (Prescott and Hutton, 1994). To account for this a $\pm 10\%$ uncertainty is included within cosmic ray calculations (Durcan et al., 2015). More problematic is that in certain burial contexts it is impossible to know the mean burial depth of samples. This is especially the case in the western Nefud Desert where little is known about the history of dune migration, and where migrating barchan and longitudinal dunes can reach up to 80 m in height (Breeze et al., 2017). In the absence of better information, the present-day burial depth had been used to calculate cosmic ray dose rates for the purposes of age determination.

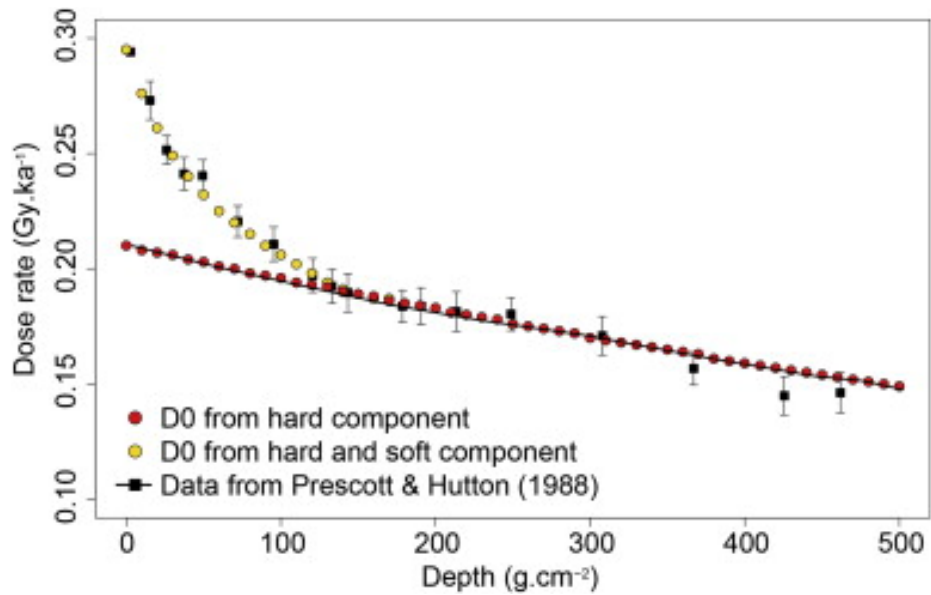


Figure 4.7 – Cosmic ray penetration depth from Durcan et al. (2015) with data from Barbouti and Rastin (1983) (yellow and red dots) and from Prescott and Hutton (1988) black squares. The soft component which consists of electrons only penetrates to ~0.6 m while the hard component which consists of muons penetrates up to 6 m depth (Barbouti and Rastin, 1983; Prescott and Hutton, 1994).

All dose calculations discussed in this section (Environmental Dose Rate) were performed in the Dose Rate and Age Calculator (DRAC) (Durcan et al., 2015).

4.5 Common problems in luminescence dating

A number of factors may cause estimates of the equivalent dose or environmental dose rate to be inaccurate. These are outlined below.

4.5.1 Disequilibrium

When calculating the environmental dose rate, the ^{238}U , ^{235}U and ^{232}Th decay series are typically assumed to be in secular equilibrium i.e. the activity of each member of the series is identical. This allows a single conversion factor (see Section 4.4.2) to be used in calculating the dose rate due to an entire decay series. Conversely, when a decay series is not in equilibrium (termed “disequilibrium”), dose rate due to a decay series will change over time, as it tends towards equilibrium, and will not be accurately represented by the conversion factor. Disequilibrium occurs in natural open systems where the different chemical behaviours of isotopes within the decay series leads to

atoms being added to or removed from a system via a number of processes (Olley et al., 1996). U-series disequilibrium is the most prevalent issue faced, since U is generally soluble in earth-surface conditions, yet the decay series contains insoluble, long-lived decay products (e.g. ^{230}Th and ^{226}Ra) meaning disequilibrium can last for many millennia and have a notable effect on dose rate (Olley et al., 1996). The shorter half-lives of daughter products in the Th-decay series means disequilibrium is not as much of an issue (Olley et al., 1996). U-series disequilibrium is particularly prevalent in depositional environments effected by periodic wetting and drying due to solubility of U, meaning it is often leached from the system (Krbetschek et al., 1994) and separated from its insoluble decay products. Nonetheless, evidence suggests that disequilibrium is rare in aeolian dune settings (Prescott and Hutton, 1995). Furthermore, in this thesis, dose rates have been calculated using emission counting techniques (beta counting and field gamma-spectrometry), which measures dose rate directly, and are therefore less vulnerable to error due to disequilibrium (Jacobs et al., 2008). Consequently, disequilibrium is unlikely to cause errors in the ages presented in this thesis.

4.5.2 Beta-dose heterogeneity

Beta-dose rate heterogeneity occurs where the β -emitters within a sediment body are concentrated in a small proportion of mineral grains (e.g. K-feldspar or zircon). In this case, grains close to the highly radioactive grain receive large beta doses whereas those further away do not due to the short range (2-3 mm) of beta particles. The opposite situation may also occur where relatively unradioactive materials such as precipitated carbonates shield grains nearby from beta radiation (Nathan and Mauz, 2008). In this latter case, dose rate models often have to be constructed to account for post-depositional carbonate cementation and its effect on the environmental dose rate through time (Nathan and Mauz, 2008). However, this is not necessary here as all luminescence samples were either taken from loose sands underlying or overlying sediments or from diatomite where X-ray diffraction shows no carbonate is present (Chapter 9 - Alathar). Where beta-dose heterogeneity occurs, individual grains within an undisturbed sediment body will receive different doses despite being buried for the same length of time within the same sediment body. Beta-dose heterogeneity is further

accentuated in environments with low environmental dose rates ($<1\text{Gy/ka}$) (Guérin et al., 2015), as is the case in the western Nefud Desert (Rosenberg et al., 2013; Groucutt et al., 2018b).

It is currently only feasible to measure the average environmental dose rate experienced by a sediment body, and beta-dose heterogeneity is therefore likely to be a major contributor to the “scatter” observed when multiple estimates of the equivalent dose are measured for a single sample (Guérin et al., 2015). This is particularly relevant when luminescence measurements are carried out at the single-grain level. However, the majority of ages presented in this thesis were calculated using data from multi-grain aliquots containing several hundred sand grains, and hence the equivalent doses are more likely to yield accurate ages due to averaging effects (Chauhan and Singhvi, 2011).

4.5.3 Partial bleaching

Partial bleaching occurs when mineral grains have not had their luminescence signal fully reset prior to burial, leading to age overestimation. Partial bleaching is rare in aeolian environments but can occur where mineral grains were transported, deposited and buried at night or during dust storms (Olley et al., 2004). Measurements of recently deposited sediments in a number of depositional environments suggests that residual dose left by incomplete bleaching is small ($<5\text{ Gy}$, Bailey et al., 2003), which is negligible in relation to the equivalent doses measured for the majority of samples presented in this thesis.

4.5.4 Post depositional mixing

Post-depositional mixing is the process whereby distinct sediment bodies, with different burial and/or bleaching histories, are mixed (Roberts et al., 2015). This can result in high overdispersion (the spread in equivalent doses after measurement uncertainties are excluded; Armitage et al., 2019) in measured equivalent doses, and calculated ages that do not reflect the true age of the sediment body of interest. Mixing occurs via biological processes where plant roots, animal burrowing and insect burrowing (bioturbation)

disturb sediment and via geomorphic processes such as slumping. Animal and insect burrowing probably occurs in loose aeolian dune sands the Nefud where populations of foxes and burrowing insects and reptiles are present. However, the impact of post-depositional mixing is mitigated through field sampling techniques where sections with clear evidence of disturbance (e.g. flakes of lacustrine carbonate mixed with aeolian sand) are avoided. Where palaeolake sediments were sampled, consolidated blocks were removed, and these are unlikely to have been subject to bioturbation due to their hardened nature. Post-depositional mixing can sometimes be identified by comparing overdispersion values between samples. Where post-depositional mixing is suspected, single-grain measurements can be performed, and the different populations of grains can be analysed by mathematical models (Galbraith et al., 1999).

4.6 Summary

This chapter has reviewed the key luminescence techniques used within this thesis. Key points are:

- Luminescence ages are calculated in this thesis using both optically stimulated luminescence (OSL) from quartz and infrared stimulated luminescence from feldspar (pIR-IRSL₂₉₀). Both techniques determine the time elapsed since the last bleaching event – i.e. the last time mineral grains were exposed to light or heat – and taken together are able to date samples over the timeframe this thesis seeks to investigate.
- The ubiquitous nature of quartz makes it the ideal mineral for dating most sites in the Nefud Desert, whilst the presence of K-feldspar in low quantities provides the opportunity to date samples which are too old for the application of OSL dating.

The methods followed for luminescence dating are described alongside the results in Chapter 6.

Chapter 5 – Methodology

5.1. Introduction

This chapter is split into two sections. The first outlines the justification for selecting the study sites presented in this thesis. The second outlines the methods used to achieve the aims and objectives set out in Chapter 1 (section 1.3). These include the methods used to reconstructing the palaeohydrology of the waterbodies that produced the carbonate and siliceous sediments studied. The luminescence dating methods are presented alongside the luminescence results in Chapter 6. It is important to note that the palaeoecological data presented here derives from work undertaken by Dr Wing-Wai Sung (Natural History Museum) and Dr David Ryves (Loughborough University). Diatom analysis was undertaken as part of the Palaeodeserts project either prior to the research programme presented here (Al Wusta, KAM4; work undertaken by Wing-Wai Sung) or during the research presented here (Alathar, WNEF16_28; work carried out by David Ryves). This analysis provides an additional proxy that supports microfacies and stable isotope analysis in interpreting the palaeohydrology of interdunal lake systems. The methods used for diatom preparation and analysis are therefore described here.

5.2 Fieldwork, site selection and site justification

5.2.1 Fieldwork and site selection

The distribution and density of palaeolake deposits across the western Nefud Desert was identified by Breeze et al. (2015) using GIS multi spectral analysis (see Fig 1.2). Fieldwork in subsequent field seasons focused on ground-truthing this initial GIS work and identifying potential sites for further analysis (Breeze et al., 2017, 2015). As a result of this exercise, sites were classified according to their archaeological, paleontological and palaeoenvironmental significance (see Table 5.1) (Breeze et al., 2017). From this, five interdunal sites consisting of 12 sedimentary sequences are analysed as part of this thesis (see Table 5.2 and Figure 5.1). The justification for this selection, and brief

descriptions of study sites are given below, and further descriptions of each site are given in the relevant results chapters.

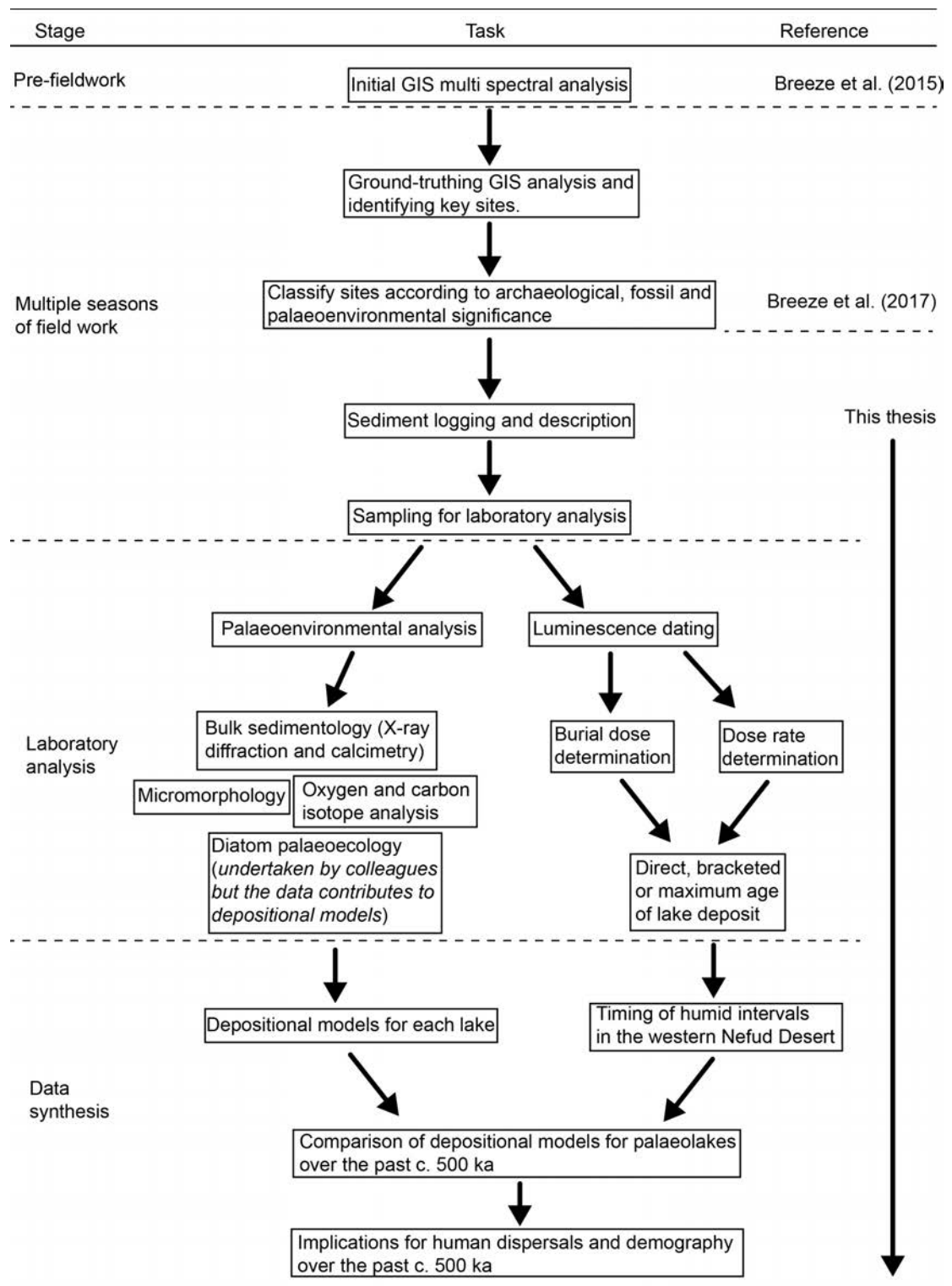


Figure 5.1 – Flowchart showing the progression of research. Note that initial GIS analysis, ground-truthing and classification of the significance of sites was done as part of previously published research by Breeze et al. (2015, 2017). All subsequent analysis was undertaken as part of this thesis or as part of earlier MSc work (Clark-Wilson, 2016).

Table 5.1 - Assessment criteria used by Breeze et al. (2017) for each study site. '+' = low significance. '++' = medium significance. '+++' = high significance. The significance of each study site was used to determine the study sites presented in this thesis (Table 5.2).

Record	Significance	Description of criteria
Archaeology	+	Small scale, low density scatters (<1 per m ²)
	++	Medium scale, mid density scatters (1 – 5 per m ²)
	+++	Large scale, high density scatters (>5 per m ²)
Fossils	+	Single isolated specimen
	++	Scattered remains likely representing several individuals
	+++	Diverse faunal assemblage representative of the local biocoenosis
Palaeoenvironmental archive	+	Small single palaeolake deposit with little vertical exposure
	++	Single palaeolake deposit with medium vertical exposure (<0.5 m)
	+++	Multiple discrete palaeolake deposits or a thickness of deposit >1 m with potential for geochronological and environmental archives

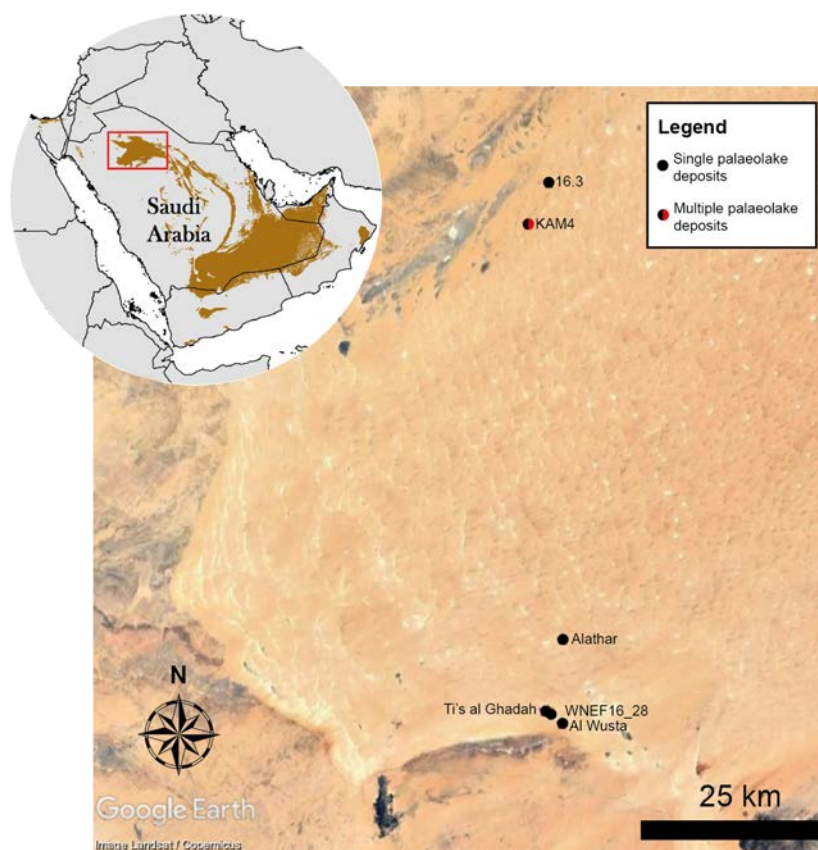


Figure 5.2 – The location of each of the interdunal sites in the western Nefud Desert presented in this thesis, along with Site 16.3 which was analysed as part of my MSc thesis (Clark-Wilson, 2016). Black dots = sites where only a single palaeolake sequence has been studied. Black/red dot = multiple palaeolake sequences studied within a single interdunal basin. Source of basemap; Google Earth. The inset map shows the location of the Nefud Desert within the Arabian Peninsula.

Table 5.2 – Significance of each site studied within this thesis, based on the criteria from Breeze et al. (2017) outlined in Table 5.1. Note that Al Wusta and Al Wusta Playa have the same significance as they are from the same interdunal basin. Alathar was found in the 2017 field season, and thus was not part of the assessment by Breeze et al. (2017). All contain ‘highly-significant’ palaeoenvironmental archives, and high to medium significance fossil and Middle Palaeolithic assemblages. Khall Amayshan 4 also contains an important Lower Palaeolithic assemblage, while some sites contain low-significance Neolithic/Holocene assemblages. LP – Lower Palaeolithic. MP – Middle Palaeolithic. N/H – Neolithic/Holocene.

Site	Archaeological significance			Fossil significance	Palaeo-environmental archive significance
	LP	MP	N/H		
Al Wusta	-	+++	+	+++	+++
Al Wusta Playa	-	+++	+	+++	+++
WNEF16_28		++		++	+++
Alathar*	N/A	N/A	N/A	N/A	N/A
Ti’s al Ghadah		++		+++	+++
Khall Amayshan 4	+++	+++	+	+++	+++

5.2.1.1 Al Wusta

Al Wusta (site code WNEF16_30) lies within an interdunal depression on the southwestern edge of the Nefud Desert (Fig 5.2) and was identified by Breeze et al. (2017) as having archaeological, fossil and palaeoenvironmental archives of high-significance (‘+++’) (Table 5.2). Directly to the west of the palaeolake deposit is the steep lee side slope of a large barchanoid dune and the rest of the site is surrounded by more gently sloping dunes. The palaeolake deposits consist of two ridges of exposed carbonate rich sediments, into which several trenches were dug for palaeoenvironmental analysis (see Chapter 8). The most extensive sequence, measured from the base of waterlain sediments upwards, is ~1.9 m in height (trench PD40). Previous palaeoenvironmental and geochronological work on these sediments carried out during the author’s MSc research (Clark-Wilson, 2016) and published in Groucutt et al. (2018) shows that the carbonate sediments represent a perennial, freshwater, open-system lake that dates to between ~86 - 95 ka (late MIS 5) and is most likely related to the summer insolation peak at 30°N at ~84 ka. A new sedimentary sequence from the site named PD40 is presented as part of this thesis.

5.2.1.2 Al Wusta Playa

In addition to the Marine Isotope Stage 5a palaeolake deposit at Al Wusta, there is also a recharge playa located at the lowest point in the current inter-dune depression (Chapter 7). While there is a large body of work on the Holocene humid phase in Arabia (see Petraglia et al. 2020 and references therein), there is limited evidence of Holocene humidity effecting the western Nefud Desert (Rosenberg et al., 2013). Therefore, sedimentological and geochronological work on the Al Wusta playa provides the opportunity to better understand the timing and nature of a Holocene humid phase within the western Nefud Desert. It also gives the unique chance to directly compare it to the humid phase represented by the MIS 5 palaeolake deposit that lies slightly higher in the landscape at the same site (Groucutt et al., 2018). The playa was excavated during the 2017 field season and contains 1.5 m of sediment with subtle stratigraphic changes. Thin-section analysis on these sediments will provide the first depositional model for Holocene sediments in the western Nefud Desert, whilst luminescence dates will be used to bracket or directly date key sedimentary units providing the first chronology for a Holocene humid phase within the Nefud.

5.2.1.3 WNEF16_28

WNEF16_28 is located towards the southwestern edge of the Nefud Desert, approximately a kilometre northwest of Al Wusta (Fig 5.2). No previous palaeoenvironmental or geochronological work has been undertaken at the site meaning the age and environmental characteristics of the palaeolake sediments preserved at the site were unknown. Nonetheless, Breeze et al. (2017) ranked the site with Middle Palaeolithic archaeological and palaeontological assemblages of mid-significance ('++') and a palaeoenvironmental archive of high significance ('+++'). The site itself is like Al Wusta, in that to the west is a steep lee side of a large barchanoid dune, though the dune is not as close to the deposits as at Al Wusta. Like Al Wusta, the rest of the site is surrounded by gently sloping dunes. The palaeolake deposit forms a single ridge which was originally excavated in 2016. This revealed a 1.42 m stratigraphic section measured from the base of wetland sediments upwards, containing carbonate

sediments, waterlain sands and calcitic rhizoliths. The palaeolake sediments are underlain by aeolian dune sands, which combined with the overlying waterlain sand layer, provides the opportunity to bracket the age of lake formation with luminescence dates. The age of the waterlain sands also directly dates the end of a humid phase, assuming these were deposited immediately following the cessation of carbonate sedimentation. The carbonate sediments provide an opportunity to undertake high-resolution sedimentary and stable oxygen and carbon isotope analysis to determine the depositional environment in which the sediments were deposited.

5.2.1.4 Alathar

Alathar (site code: WNEF17_1) is situated in the southwestern portion of the western Nefud Desert, approximately 13 km from the southern edge of the sand sea (Fig 5.1). The deposit sits as an inverted relief feature, rising above the modern basin floor, and comprises a ~1.8 m thick siliceous deposit overlying aeolian dune sands (Fig 9.1). The topography of the palaeolake is well preserved with a subtle concave shape dipping toward the centre of the remaining palaeolake deposit (Fig 9.1). The significance of the site is that it contains preserved hominin and faunal footprints within stratigraphic section (Stewart et al., 2020a).

5.2.1.5 Ti's al Ghadah

Ti's al Ghadah is located at the southwestern margin of the Nefud Desert in close proximity to Al Wusta and WNEF16_28 (Fig 5.2). Breeze et al. (2017) rank the Ti's al Ghadah palaeolake deposit as having a palaeontological assemblage and palaeoenvironmental archive of high-significance whilst having a Middle Palaeolithic archaeological assemblage of mid-significance. Previous work at the site has indicated that the palaeolake was of considerable size and perennial in nature (Thomas et al., 1998; Rosenberg et al., 2013). The palaeolake deposits themselves have been dated to 291 ± 34 ka (Stimpson et al., 2016) though the underlying fossil rich 'green' sand unit has conflicting ages of 318 ± 25 ka and 328 ± 26 ka (TT-OSL and pIRIR₂₉₀; Rosenberg et al., 2013) and ~500 ka (U-ESR dating on fossil material; Stimpson et al., 2016). The green

sands are interpreted as representing waterlain deposition via sheet/surface wash at the edge of a lake, prior to expansion of the waterbody in response to increased humidity (Stewart et al., 2019). Both the conflicting OSL and U-ESR dates are therefore deemed to originate for materials deposited at the beginning of the same humid interval. Given the discrepancies between the OSL and U/ESR data, the most conservative age estimate for the site is 300 – 500 ka.

There are no detailed sedimentological data from Ti's al Ghadah, though macroscale sedimentology and diatom analysis were performed by Rosenberg et al. (2013). The site was revisited during the 2017 field season during which two stratigraphic sections, located at either end of the NW - SE trending carbonate ridge that runs through the site, were logged and sampled for palaeoenvironmental analysis (Chapter 11). The site also contains an important fossil assemblage (see Chapter 2.4.2) (Stewart et al., 2019; Stimpson et al., 2016, 2015; Thomas et al., 1998).

5.2.1.6 Khall Amayshan 4 (KAM-4)

Khall Amayshan 4 (KAM4) is located towards the northern edge of the western Nefud Desert (Fig 5.2). Breeze et al. (2017) ranks KAM-4 as having Lower and Middle Palaeolithic archaeological assemblages, fossil and palaeoenvironmental archives of high-significance. KAM-4 itself contains six interdunal palaeolake deposits that may represent multiple humid phases over the past ~500 ka. This provides the unique opportunity to compare carbonate sediments deposited in the same interdunal basin between discrete humid phases.

5.3 Palaeoenvironmental methods

A combination of bulk sedimentology (including calcimetry and X-ray diffraction), micromorphology, and stable oxygen and carbon isotope analysis was undertaken as part of this thesis to reconstruct the depositional environment of the carbonate/siliceous sediment beds. These methods were chosen as they allow key questions regarding the hydrology of the waterbodies in which the sediments were

deposited to be answered, such as whether the waterbodies were perennial or ephemeral and whether or not they contained freshwater. Isotopic analysis also allows the identification of any abrupt changes in the hydrological environment. These sedimentological and geochemical proxies were preferred to diatom palaeoecology due to the poor preservation of diatoms within carbonate sediments (Groucutt et al., 2018). Nevertheless, diatom palaeoecology was carried out by colleagues within the Palaeodeserts team and is incorporated within depositional models here where it is available.

5.3.1 Bulk sedimentology

The carbonate/siliceous deposits at each site were initially surveyed in order to identify the best exposed stratigraphic sequences for further analysis. Once a suitable section was identified, it was logged and described to determine the sedimentary structure (bedding and units) and texture (sorting, grain size, colour). Each sedimentary sequence was measured from the base of non-aeolian sediments upwards (i.e. from the fine-grained carbonate rich marls, consolidated siliceous sediment, or waterlain sands). Aeolian sediments are almost always present at the base of each sequence, with the exception of Ti's al Ghadah. Where present, these sediments were designated as 'Unit 1'. Laboratory samples were collected by extracting coherent blocks from the section, recovering a continuous sedimentary sequence. In the laboratory, blocks were subsampled, powdered and analysed using Bascomb calcimetry (Gale and Hoare, 1991) and X-ray diffraction. These analyses yielded carbonate content and mineral composition respectively. X-ray diffraction work was carried out in the Department of Earth Sciences, Royal Holloway on a Philips PW1830/3020 spectrometer with copper $K\alpha$ X-rays. Mineral peaks were identified manually from the ICDD Powder Diffraction File database or using Match! software v3.9.0.

5.3.2 Thin-section preparation and analysis

Thin-section slides were prepared for microfacies analysis from fresh sediment blocks subsampled from larger block samples collected in the field. The size of each sediment

block extracted for thin-section preparation was variable owing to the friable and brittle nature of the sediments. It was ensured that thin-section samples were taken from each macroscale unit of each sedimentary sequence in order to represent the full sedimentary sequence. The sediments did not require acetone treatment as they were already dry and, due to their permeability, were directly impregnated with an Epoxy bonding resin. Thin-section preparation followed standard procedure of the Centre for Micromorphology at Royal Holloway University of London (Palmer et al., 2008).

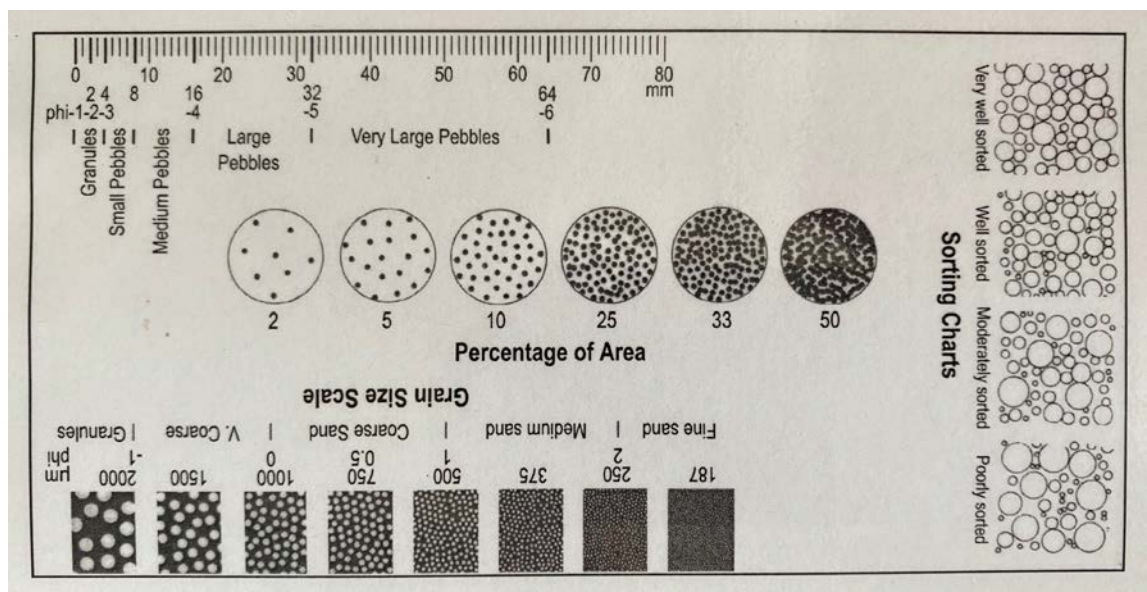


Figure 5.3 – Comparison chart from the image analysis laboratory used to estimate the percentage coverage of allogenic sand/silt grains at the lowest magnification (x20). This chart closely follows that of Folk (1951)

Thin-sections were analysed using an Olympus BX-50 microscope with magnifications from x20 to x200. Photomicrographs were captured with a Pixera Penguin 600es camera. Microfacies were qualitatively characterised describing the microstructure, texture (groundmass), void cover and type, estimated percentage coverage of allogenic grains, amount of organic material (e.g. shell fragments), and depletion and concentration features (e.g. void coatings/hypocoatings and carbonate or iron nodules).

5.3.3 Stable isotope preparation

All samples containing sufficient carbonate underwent isotopic analysis. It is standard practice to either (1) analyse the <63 μm size fraction to ensure the analysed fraction is pure authigenic carbonate as opposed to a mixture of biogenic and authigenic

carbonate, which contain different isotopic signatures; or (2) to use the microstructure of the sample, as identified under thin-section, to ensure that the analysed carbonate has not been affected by diagenesis. Many samples could not be sieved due to incipient cementation, but negligible evidence for diagenetic alteration of the primary calcite was observed under thin-section with the exception of KAM4 lake 1 and 2. Further discussion of the impact of diagenesis on these samples is provided in the relevant results chapter (Chapter 12). As such, bulk samples were analysed. This approach is limited as bulk samples contain variable quantities of biogenic (i.e. ostracod, mollusc shells etc.) and authigenic carbonates which have different isotopic signals from one another. Consequently, isotopic changes throughout the stratigraphy may be due to changes in relative abundance of authigenic vs biogenic carbonate components as opposed to environmental changes (Leng and Marshall, 2004). To demonstrate that bulk samples did not affect the derived isotopic data, samples that were friable enough to be sieved were disaggregated using sodium hexametaphosphate. A sub-sample of disaggregated material was homogenised and is referred to as the bulk sample hereafter. The <63 μm size fraction of the disaggregated material was isolated via sieving, and is referred to as the sieved sample hereafter. There was negligible difference between the isotopic values of the sieved and bulk samples (see Table 5.3), demonstrating that isotopic results generated using bulk samples from cemented material primarily reflect environmental changes rather than changes in the proportion of biogenic and authigenic carbonate. Moreover, the presence of biogenic material is rare in all microfacies, and therefore the authigenic carbonate component will dominate the stable isotope signature.

Table 5.3 – Isotopic values for paired bulk and sieved fractions from Al Wusta, WNEF16_28 and Site 16.3. The Site 16.3 and Al Wusta data originates from Clark-Wilson (2016). There is mostly a good agreement between pairs.

Site name	Sample Name	Depth	Bulk or Sieved	$\delta^{13}\text{C}$ corr (‰)	error (1s)	$\delta^{18}\text{O}$ corr (‰)	error (1s)	Lab
Al Wusta	I16-0021	40 cm	Bulk	1.13	0.04	-1.66	0.07	RHUL
	I16-0042	40 cm	Sieved	1.40	0.02	-1.95	0.02	RHUL
	I16-0032	20 cm	Bulk	1.94	0.02	-2.23	0.08	RHUL
	I16-0043	20 cm	Sieved	1.94	0.02	-2.49	0.06	RHUL
	I16-0033	30 cm	Bulk	1.70	0.05	-2.20	0.06	RHUL

	I16-0044	30 cm	Sieved	1.67	0.01	-2.20	0.06	RHUL
	I16-0034	40 cm	Bulk	0.17	0.01	-2.26	0.00	RHUL
	I16-0045	40 cm	Sieved	0.23	0.00	-2.99	0.01	RHUL
16.3	I16-0002	20 cm	Bulk	-2.18	0.03	2.97	0.06	RHUL
	I16-0035	20 cm	Sieved	-2.64	0.01	4.28	0.02	RHUL
	I16-0004	60 cm	Bulk	1.88	0.01	3.75	0.08	RHUL
	I16-0036	60 cm	Sieved	1.84	0.04	3.74	0.04	RHUL
	I16-0005	80 cm	Bulk	2.02	0.00	4.27	0.08	RHUL
	I16-0037	80 cm	Sieved	1.63	0.02	3.31	0.06	RHUL
	I16-0010	180 cm	Bulk	2.47	0.03	3.47	0.06	RHUL
	I16-0038	180 cm	Sieved	2.40	0.01	2.08	0.03	RHUL
	I16-0011	200 cm	Bulk	3.24	0.00	2.49	0.04	RHUL
	I16-0039	200 cm	Sieved	3.31	0.02	2.41	0.05	RHUL
	I16-0014	260 cm	Bulk	1.26	0.02	3.04	0.08	RHUL
	I16-0040	260 cm	Sieved	1.23	0.03	2.09	0.07	RHUL
WNEF16_28	I17-0202	50 cm	Bulk	0.79	0.03	-4.99	0.08	BEIF
	I17-0190	50 cm	Sieved	0.90	0.03	-5.08	0.08	BEIF
	I17-0203	60 cm	Bulk	1.61	0.03	-4.43	0.08	BEIF
	I17-0191	60 cm	Sieved	1.72	0.03	-4.63	0.08	BEIF
	I17-0204	70 cm	Bulk	0.79	0.03	-5.34	0.08	BEIF
	I17-0192	70 cm	Sieved	0.86	0.03	-5.42	0.08	BEIF
	I17-0205	90 cm	Bulk	0.94	0.03	-1.96	0.08	BEIF
	I17-0193	90 cm	Sieved	1.19	0.03	-1.15	0.08	BEIF

Bulk samples were analysed at both Royal Holloway University of London (RHUL) and the Bloomsbury Environmental Isotope Facility (BEIF). At RHUL, samples were weighed using a Cahn C-31 Microbalance. Measurements were then made using a VG PRISM series 2 mass spectrometer. Samples were run with internal (RHBNC-PRISM) and external (NBS-19, LSVEC) standards. 1σ uncertainties are 0.05‰ ($\delta^{18}\text{O}$) and 0.03‰ ($\delta^{13}\text{C}$). At the BEIF, samples were weighed using a Mettler Toledo XP6. Measurements were made on a ThermoFisher Delta Plus XP mass spectrometer with a Gasbench II preparation system. Samples were run with internal (BDH) and external (NBS-19) standards. 1σ uncertainties range from 0.03‰ to 0.08‰ for $\delta^{13}\text{C}$ and 0.05‰ to 0.08‰ to $\delta^{18}\text{O}$. All isotope data presented in this study are quoted against Vienna Pee Dee Peleminite (VPDB) standard (section 3.6.3).

5.3.5 Diatom palaeoecology

5.3.5.1 Preparation

Diatom preparation for sites Al Wusta, Site 16.3 and KAM4 was undertaken by Dr Wing Wai Sung. Briefly, preparation followed the standard water bath method of Renberg (1990). Samples were treated with 30% H₂O₂ and 5% HCl to digest organic material and remove calcium carbonate. Distilled water was added to dilute the samples after heating, which were then stored in the refrigerator for four days to minimise further chemical reactions. The samples were rinsed daily and allowed to settle overnight. A known volume of microspheres was added to the supernatant after the last rinse to enable calculation of the diatom concentration (Battarbee and Kneen, 1982). Diatom preparation for sites WNEF16_28 and Alathar was undertaken at Royal Holloway as part of this thesis (though analysis of these samples was undertaken by Dr. David Ryves). Here diatom preparation followed a slightly different method. Approximately 0.1 grams of dried sediment were placed into a centrifuge tube, immersed in 5 ml of 30% H₂O₂, and stored at room temperature until all organic material was removed. Samples were rinsed four times with deionised water and subsequently centrifuged for 4 minutes at 1200 rpm. Note that no microspheres were added to Alathar or WNEF16_28 samples. Diatom samples for all sites were pipetted onto round cover slips and air-dried at room temperature in a dust free environment before mounting with Naphrax diatom mountant. Diatom taxonomy for all samples followed previous studies (Krammer and Lange-Bertalot, 1991a, 1991b, 1988) and taxonomic revisions (Crawford et al., 2003; Navok et al., 2015).

5.3.5.2 Numerical analysis – Al Wusta and Site 16.3

Numerical analysis for Al Wusta and Site 16.3 was carried out by Wing-Wai Sung and presented in Groucutt et al. (2018), but is redescribed here. Prevalent trends in the diatom assemblage were explored using ordination analyses using CANOCO 4.5 of ter Braak and Šmilauer (2002). Detrended Correspondence Analysis (Hill and Gauch, 1980)

with detrending by segments and down-weighting of rare species was used to determine whether linear or unimodal models should be used for further analyses. If the gradient length of the first axis is <1.5 SD units, linear methods (Principal Components Analysis, PCA) should be used; however, if the gradient length is >1.5 SD units, unimodal methods (Correspondence Analysis) should be used (ter Braak and Prentice, 1988). As a result of this exploratory DCA, PCA was applied to site 16.3 and PD16, and CA to PD15. The dataset was square-root transformed (Hellinger transformation) to normalise the distribution prior to analyses (Legendre and Gallagher, 2001). Optimal sum-of-squares partitioning (Smol et al., 2005) with the program ZONE (Juggins, 1985) and comparison of the zones with the Broken-stick model using the program BSTICK (Bennett, 1996) were used to determine significant zones. Diatom preservation was assessed using the **F** index (Ryves et al., 2006, 2001) which is the ratio of visibly dissolved valves to all valves observed under light microscopy during counting. The **F** index varies from 0 and 1, with 1 implying all valves were pristine and 0, that all valves showed signs of dissolution. The planktonic: benthic ratio, habitat summary and concentration were also calculated for all the samples.

5.3.5.3 Numerical analysis – Alathar

Numerical analysis for Alathar was carried out by David Ryves and presented in Stewart et al. (2020a) but is redescribed here. At least 315 diatom valves were counted for each sample (mean 321 valves) under oil immersion with phase contrast illumination at $\times 1000$. Quantitative reconstructions were carried out using the programme C2 (v1.7.7; Juggins (2016) available at <https://www.staff.ncl.ac.uk/stephen.juggins/software/C2Home.htm>). Analog matching of fossil samples was performed within the combined African salinity dataset ($n=370$) from the European Diatom Database (EDDI) (Battarbee et al., 2001), which includes modern samples from northern and eastern Africa (Gasse et al., 1995). The closest analogues in all cases included both eastern and northern African samples (in agreement with the geographic location of the site), and hence the combined African dataset was used for our diatom-conductivity reconstructions. Inferred conductivity ($\mu\text{S cm}^{-1}$) was derived from fossil assemblages (% data) using a weighted-average transfer function

with inverse de-shrinking. The conductivity model performs well when internally validated by bootstrapping with 999 cycles ($r^2_{\text{boot}} = 0.755$, $\text{RMSEP}_{\text{boot}} = 0.466$ log units) and provides sample-specific errors on diatom-inferred conductivity which are significantly smaller (0.012–0.14 log conductivity units) than the overall predicted model errors (Fig. S3 in Stewart et al., 2020a).

5.4 Summary

This chapter has explained the rationale behind selecting sites for study in this thesis, and presented the methods used for palaeoenvironmental analysis. The key points are as follows:

- 12 sedimentary sequences in 5 interdunal basins in the western Nefud Desert have been studied as part of this thesis. Sites were chosen based on their archaeological, fossil and palaeoenvironmental potential based on previous research and field excavations.
- In order to reconstruct the depositional model of each sedimentary sequence a combination of bulk sedimentology, micromorphology and stable oxygen and carbon isotope analysis has been undertaken.
- Diatom palaeoecology was undertaken at some sites by colleagues from the Palaeodeserts team. These data contribute towards producing the depositional models for a number of sedimentary sequences studied here.

Chapter 6 – Geochronology: timing of humid phases in the western Nefud Desert, Saudi Arabia

6.1 Introduction

Optically stimulated luminescence (OSL) dating of quartz and post infrared, infrared analysis (pIRIR₂₂₅) dating of feldspars is used to produce a chronology for the timing of lake development and humidity in the western Nefud Desert. This chapter will provide a full overview of the luminescence dating work undertaken as part of this thesis, from sample collection to age estimation (Fig 6.1). For completeness, chronological datasets not produced as part of this thesis are reported in the age estimation and interpretation section for the key sites of Al Wusta, Site 16.3, Ti's al Ghadah and KAM4. Ages for Al Wusta and Site 16.3 were produced as part of a Masters thesis (Clark-Wilson, 2016), while data from Ti's al Ghadah was produced by Rosenberg et al. (2013) and Stimpson et al. (2016). In addition, preliminary unpublished data from KAM4 lakes 1, 2, 3 and 4 (samples KAM4-OSL 1-6) produced by Dr Laine Clark-Balzan (Clark-Balzan, per comms) is also presented alongside data produced within this thesis.

6.2 Sample collection and analysis

Samples for luminescence dating were collected from the sands beneath interdunal carbonate/siliceous sediments, sands within carbonate/siliceous sediments or from waterlain sands that occasionally overlie carbonate/siliceous sediments. At some locations, lake carbonate/siliceous deposits contained sufficient sand to allow the formation of the deposit to be directly dated. Elsewhere the age of the lake could be inferred from the ages for two samples, one within the underlying aeolian sands and one from the overlying waterlain sands. However, at some locations only the underlying sands were sampled, giving a maximum age for the lake since underlying sands should not be any younger than the overlying carbonate/siliceous sediments. Samples from underlying sands or overlying waterlain sands were collected by hammering an opaque tube into a cleaned section face. Samples taken from carbonate, diatomite or playa sediments were extracted as consolidated blocks and wrapped in multiple layers of

opaque plastic to protect them from sunlight before transportation back to Royal Holloway.

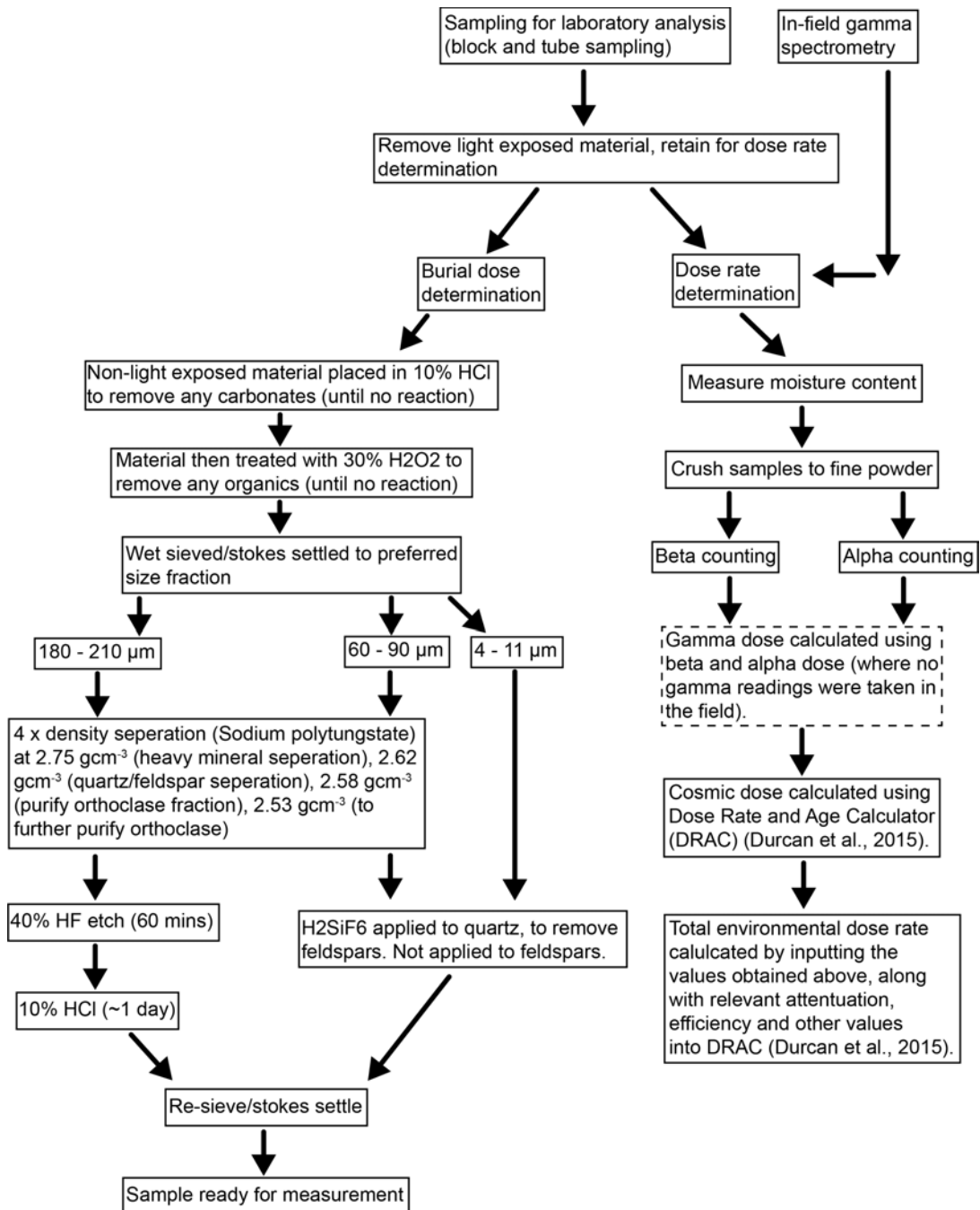


Figure 6.1 – Schematic diagram showing the steps from sample collection in the field through to purified quartz/feldspar for D_e measurement (left branch) and dose rate calculation (right branch).

Samples presented in this thesis were prepared as purified quartz in the 4 – 11 μm , 60 – 90 μm and 180 – 210 μm size fractions for standard quartz single-aliquot regenerative dose (SAR) measurements (Murray and Wintle, 2000, 2003) or as 60 – 90 μm potassium

feldspar fractions for post-infrared, infrared stimulated luminescence (IRIR₂₂₅) analysis (e.g. Thomsen et al., 2008). The 180 – 210 µm size fraction was preferred though other size fractions were used when the coarse-grain material available was limited. All samples were prepared under subdued red light in the Royal Holloway Luminescence Laboratory. First the sunlight exposed external portions of the sample were removed and retained for dose rate evaluation, leaving a sub-sample suitable for dating. The samples for dating were immersed in 10% HCl to remove any carbonate, and then, depending on organic content, were treated with H₂O₂ to remove organic matter. The remaining mineral fraction was wet-sieved to extract sand-sized fractions (60 – 90 µm or 180 – 210 µm) or Stokes settled to obtain the fine silt (4 – 11 µm) size fraction. Quartz was extracted from sand-sized material using density separations at 2.75 g/cm³ and 2.62 g/cm³. K-feldspars were extracted from the coarse fraction with further 2.58 g/cm³ and 2.53 g/cm³ density separations. Quartz in the 180 – 210 µm size fraction underwent an HF acid etch (23M HF for 60 min followed by a 24-hour immersion in 10M HCl). The 4 – 11 µm and 60 – 90 µm quartz were immersed for ~1 week in silica-saturated fluorosilicic (H₂SiF₆) to remove feldspars but retain the limited quartz sample. Etched quartz samples were re-sieved or Stokes settled to remove partially dissolved grains. All samples were stored in opaque containers prior to measurement. Before single-aliquot measurement, purified quartz/feldspar was placed as a 5 mm circular monolayer on a 9.7 mm diameter stainless steel discs using Silkospray oil applied via a 5 mm mask. The 4 – 11 µm size fraction was settled onto 10 mm diameter aluminium discs, placed in an oven at 50°C to dry and then stored in opaque containers prior to measurement.

6.3 OSL measurements

6.3.1 Equipment

All single-aliquot luminescence measurements presented here were carried out using the same Risø TL/OSL-DA-15 automated dating system (Bøtter-Jensen et al., 2003). Optical stimulation of single aliquots of quartz used blue light emitting diodes emitting at 470 nm with a stimulation power of 69.4 mW/cm². All infra-red (IR) stimulation was carried out using an IR laser diode array (870 nm, 206 mW/cm²). Quartz signals were

measured via a 7.5 mm thickness of Hoya U-340 filter, while feldspar signals were measured via a combination of 2 mm Schott BG-39 and 3 mm Schott BG-3 filters. All signals were detected using an Electron Tubes Ltd 9235QB15 photomultiplier tube. Irradiation was carried out using a 40 mCi $^{90}\text{Sr}/^{90}\text{Y}$ beta source giving with a dose rate of ~ 6 Gy/min to samples mounted on stainless steel. This source is calibrated relative to the National Physical Laboratory, Teddington ^{60}Co γ -source (Hotspot 800; Armitage and Bailey, 2005).

6.3.2 Equivalent dose (D_e) measurement and determination

6.3.2.1 Quartz D_e measurement

Equivalent doses (D_e) were measured for each sample using the single-aliquot regenerative-dose (SAR) method (Chapter 4.3.3) (Murray and Wintle, 2003, 2000). To ensure that the measurement conditions used were appropriate, preheat plateau dose recovery tests (Roberts et al., 1999) were performed on at least one sample from each site. Aliquots were first bleached using blue diodes (two 100 s bleaches at room temperature, separated by a 10,000 s pause to allow the 110 °C thermoluminescence trap to empty), after which a beta dose was administered. This dose, termed the “known dose”, was chosen to be similar to the equivalent dose of the natural sample. Groups of 8 aliquots were preheated (though aliquots routinely failed rejection criteria leaving between 3 – 8 aliquots for the calculation of the dose recovery ratio) at a range of commonly adopted preheating regimes, with preheat 1 (PH1) temperatures ranging between 180 – 260°C held for 10 seconds prior to measurement of the laboratory/test dose in combination with a preheat 2 (PH2) temperature of 160°C held for 5 seconds prior to the measurement of the test dose. A single combination of a PH1 of 260°C with a PH2 of 220°C was also tested. The preheating regime that yielded an equivalent dose/known dose value (dose recovery ratio) closest to unity was adopted for subsequent analyses on all samples from that site (Table 6.1).

Table 6.1 – The optimal preheating regimes from preheat plateau dose recovery tests (PP) and dose recovery tests (DR) from the samples selected for this analysis at each site. These preheating regimes were then adopted for subsequent analysis for all samples from each site. *Relaxed IR depletion criteria (PD49) - see text for discussion. PH1 – preheat 1 temperature. PH2 – preheat 2 temperature.

Site	Sample	PH1 (°C), 10 s	PH2 (°C), 5 s	Equivalent/kn own dose	N (number of aliquots)
Alathar	PD61 (DR)	200	160	1.02 ± 0.02	14
	PD62 (DR)	200	160	1.01 ± 0.04	16
WNEF16_28	PD18 (PP)	200	160	0.96 ± 0.03	6
KAM4	PD7 (PP)	240	160	0.98 ± 0.03	4
	PD12 (DR)	240	160	1.08 ± 0.03	14
Al Wusta Playa	PD49 (PP)*	180	160	1.02 ± 0.03	6*
	PD50 (PP)	260	160	1.02 ± 0.05	3

Preheating regimes used in the preheat plateau tests predominantly yielded dose recovery ratios between 0.9 and 1.1 with the exception of samples from Al Wusta Playa (Fig 6.2 and 6.3). No dose recovery experiments were undertaken for 4-11 µm samples (PD10, 14 and AWP1) due to limited quantities of these samples. Instead, these samples were measured using the optimal preheating regimes determined for coarse-grain quartz from the same site. For sample PD49, a large number of aliquots failed the IR depletion ratio test (Duller, 2003, see below) and sufficient data were only available when this rejection criterion was relaxed (from rejecting an aliquot where the IR depletion ratio was $>2\sigma$ below unity to rejecting it where the ratio was >0.2 below unity, i.e. 0.8 – 1). A further dose recovery test was applied to sample PD12 at KAM4 after the initial preheat plateau dose recovery test on sample PD7. This yielded a dose recovery ratio of 1.08 ± 0.03 , compared to the initial preheat plateau dose recovery test ratio of 0.98 ± 0.03 on sample PD7. This suggests that the preheating regime from the preheat plateau dose recovery tests on one sample may not apply to another sample from the same site. In this case, the higher dose recovery ratio from PD12 suggests that the recovered D_e for this sample may overestimate the true D_e and yield an older age than its true age. Contrary to other sites, only standard dose recovery tests were undertaken on samples PD61 and PD62 at Alathar using a preheat 1 of 200°C and a preheat 2 of

160°C. This yielded a dose recovery ratio in unity with 1 (PD61, 1.02 ± 0.02 ; PD62, 1.01 ± 0.04) and this preheating regime was employed for subsequent analysis.

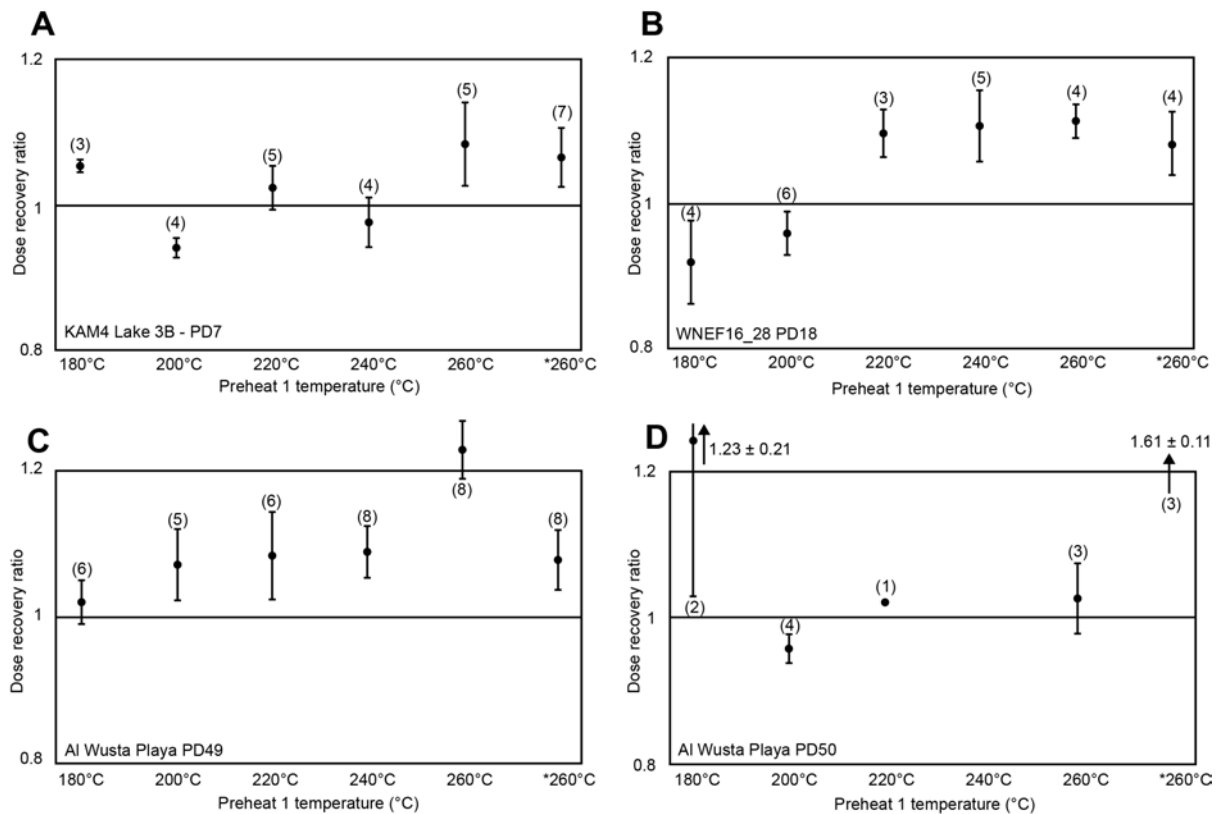


Figure 6.2 - Preheat plateau dose recovery tests from all new data presented in this thesis. Each scatter plot shows the dose recovery ratio (y-axis), defined as the equivalent dose/known dose, for each individual preheating regime (x-axis) from each site. Note that the preheat 2 temperatures are all 160°C, with the exception of the second 260°C preheat 1 temperature (the final point along the x-axis on every graph with an asterisk) which was combined with a preheat 2 temperature of 220°C. The dose recovery ratios include standard errors to 1σ , while the number in brackets above each ratio is the number of aliquots used to calculate the dose recovery ratio.

Optical stimulation was carried out at 125°C for 60 seconds using blue LEDs (470 nm). The OSL signal was calculated from the signal from the first 0.32 seconds of stimulation, with a background signal estimated from the last 4 seconds of the decay curve subtracted. Dose response curves (DRC) were fitted with a saturating-exponential-plus-linear function or an exponential function, and the standard error associated with each individual D_e determination was estimated by Monte Carlo simulation (1000 simulations). D_e determination, curve fitting and Monte Carlo simulation were performed using Luminescence Analyst software version 4.31.9 (Duller, 2007).

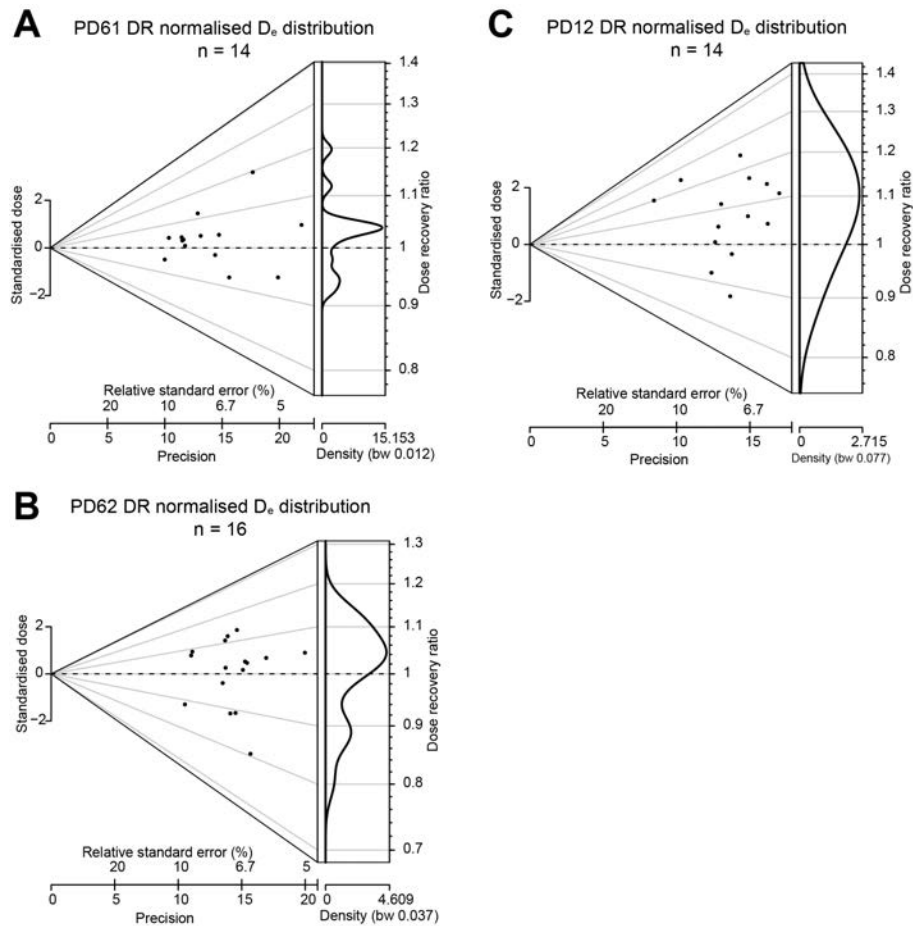


Figure 6.3 – Abanico plots for a) PD61 Alathar, b) PD62 Alathar and c) PD12 KAM4 lake 3. These display the normalised dose recovery data centred to unity (broken black line to 1 on y-axis) for accepted aliquots with a preheating regime of 200°C (Alathar) or 240°C (KAM4 lake 3) held for 10 seconds prior to the measurement of the regenerated dose (L_x) and 160°C held for 5 seconds prior to the measurement of the test dose (T_x). The dose recovery ratio is defined as measured equivalent dose (D_e)/known dose (D_r) and a value of 1 suggests that the recovered dose (equivalent dose) perfectly matches the known dose. The dose recovery ratio frequency distribution consistently lies above '1', suggesting that the equivalent dose slightly overestimates the known dose.

Data from individual aliquots were rejected where the aliquot yielded either an infrared (IR) depletion ratio $>2\sigma$ below unity (Duller, 2003) or a recycling ratio (RR) $>2\sigma$ different from unity (Murray and Wintle, 2000). These tests reject aliquots with feldspar contamination, or which have poor luminescence properties respectively. In addition, aliquots yielding natural luminescence intensities greater than the saturation level of the growth curve (i.e. “oversaturated” aliquots), those with $>5\%$ recuperation (the sensitivity corrected luminescence intensity at the 0 Gy dose point exceeded 5 % of the natural luminescence intensity) or those with uncertainties $> 30\%$ of the calculated D_e were rejected. A single sample from PD50 was rejected on the basis of being an outlier, where the D_e (s) was ~ 3 times greater than any other accepted aliquot (Disc 37; PD50_26JAN18D1). Rejection criteria were applied in the order described above with

only one rejection criteria being recorded per aliquot (see Table 6.2 and 6.3). An additional rejection criterion was added for samples PD50 and PD51 from Al Wusta Playa. These samples yielded relatively low burial doses (~ 1 to 9 Gy) and were prone to dose response curves (DRCs) that did not display monotonic growth. Aliquots were rejected where monotonic growth was not evident (i.e. the DRC did not pass through regeneration points). This rejection criterion was applied prior to the other criteria outlined above.

*Table 6.2 - The number of coarse-grain aliquots (180 – 210 μm), with exception of PD14 KAM4 lake 4 which had a grain size of 60 – 90 μm) which were measured, rejected after application of the criteria outlined in the text and accepted for inclusion in the calculation of D_b. Abbreviations are as follows: RR – recycling ratio; IR – infrared depletion ratio; recup – recuperation >5%; oversat – oversaturation; Err on Ln > 30% - uncertainties > 30% of the calculated D_e. *PD47 and 48 are oversaturated. **PD49 is based on oversaturation ‘approach 3’ whereas all other samples are based on oversaturation approach 2 (see text for discussion).*

Site	Sample	N	Failed RR	Failed IR	Failed recup	Failed oversat	Err on Ln > 30%	Poor Curve	Outlier	Rejected	Accepted
Alathar	PD60	48	1	29	0	3	0	0	0	34	15
	PD61	48	0	29	0	3	0	0	0	31	16
	PD62	48	1	11	0	4	0	0	0	16	32
WNEF 16_28	PD18	48	0	10	0	0	0	0	0	10	38
	PD42	48	0	3	0	0	0	0	0	3	45
KAM4 lake 3	PD11b	48	2	17	0	0	2	0	0	21	27
	PD12	48	1	12	0	0	1	0	0	14	34
KAM4 lake 3A	PD9	48	1	19	0	0	2	0	0	22	26
KAM4 lake 3B	PD7	48	2	21	0	0	1	0	0	24	24
	PD8	48	1	19	0	0	1	0	0	21	27
KAM4 lake 4	PD13	48	4	16	0	1	2	0	0	23	25
	PD14 (60 – 90)	24	4	0	0	0	0	0	0	4	20
Al	PD47*	48	0	32	0	9	1	0	0	42	6
Wusta Playa*	PD48*	48	0	23	0	21	0	0	0	44	4
	PD49**	48	1	34	0	0	0	6	0	41	7
	PD50	48	3	1	0	0	0	32	1	37	11
	PD51	48	0	0	0	0	0	39	0	39	9
	AWP1	12	0	0	0	0	0	0	0	0	12
Totals (n)		804	21	276	0	41	10	38	1	426	378
Totals (%)		N/A	2.61	34.33	0	5.1	1.24	4.73	0.12	52.99	47.01

Table 6.3 – As per Table 6.2 but for fine-grained aliquots (4 – 11 μm). Abbreviations are as follows: RR – recycling ratio; IR – infrared depletion ratio; recup – recuperation >5%; oversat – oversaturation; Err on Ln > 30% - uncertainties > 30% of the calculated D_e .

Site	Sample	N	Failed RR	Failed IR	Failed recup	Failed oversat	Err on Ln > 30%	Poor Curve	Rejected	Accepted
KAM4	PD10	11	1	0	0	0	0	0	1	10
L3a										
KAM4 L4	PD14	10	0	0	0	0	0	0	0	10
Al Wusta	AWP1	12	0	0	0	0	0	0	0	12
Playa										
Total (n)		33	1	0	0	0	0	0	1	32
Total (%)		N/A	3.03	0	0	0	0	0	3.03	96.97

At Alathar a novel approach to dealing with oversaturation was tested. Although a considerable body of literature concerning saturated/oversaturated aliquots exists, and various rejection criteria have been proposed, there is little consensus on the most appropriate method for dealing with this phenomenon. Consequently, while numerous studies recognise the need to reject saturated/oversaturated aliquots or grains, no standard criterion exists. To determine the sensitivity of the Alathar ages to different saturation/oversaturation rejection criteria, three separate analyses were performed (Table 6.4): (1) accept all aliquots for which Analyst yields a finite D_e ; (2) reject all aliquots yielding natural luminescence intensities (L_n/T_n) exceeding twice the curve fitting parameter D_0 when the DRC is fitted using a single saturating exponential function (Wintle and Murray, 2006); (3) reject aliquots where the natural luminescence intensity (L_n/T_n) exceeds the saturation level of a saturating exponential fit (using Analyst version 4.31.9) or, when fitted with a saturating-exponential-plus-linear function, where L_n/T_n exceeds 115% of L_x/T_x for the highest-dose regeneration point. The second criterion within Approach 3 is an attempt to codify the well-established practice of excluding data from aliquots which are clearly saturated/oversaturated, but for which the linear component of a saturating-exponential-plus-linear curve fit yields a finite D_e . It is only applicable where the largest regeneration dose is substantially higher than the sample's burial dose. In the present instance, the largest regeneration dose was 195 Gy and the largest sample burial dose (calculated using Approach 1) was 127 ± 10 Gy. Approach 1 includes very high D_e values and probably overestimated D_e due to the incorporation of saturated aliquots. This approach may be regarded as generating a maximum age.

Approach 2 excludes aliquots yielding high D_e s, some of which may provide accurate estimates of the absorbed dose. This approach may be regarded as generating a minimum age (Wintle and Adamiec, 2017 p. 24). Approach 3 is less stringent than Approach 2, and in the present study always yields D_e values lying between the other two options. The sample burial dose produced using Approach 3 is used, since Approach 1 probably yields overestimates while Approach 2 may yield underestimates. All burial doses from Alathar and other sites were estimated using this approach, with the exception of Al Wusta Playa (see discussion below).

Table 6.4 - Age variations for each sample depending on oversaturation rejection criteria (see Text for full discussion). Oversaturation rejection criteria: (1) accept all aliquots for which Analyst yields a finite D_e ; (2) reject all aliquots yielding natural luminescence intensities (L_n/T_n) exceeding twice the curve fitting parameter D_0 when the DRC is fitted using a single saturating exponential function (Wintle and Murray, 2006); (3) reject aliquots where the natural luminescence intensity (L_n/T_n) exceeds the saturation level of a saturating exponential fit (using Analyst version 4.31.9) or, when fitted with a saturating-exponential-plus-linear function, where L_n/T_n exceeds 115% of L_x/T_x for the highest-dose regeneration point. OD – stands for overdispersion, which is the amount of dispersion seen in dataset beyond that which is expected to occur naturally.

Site	Sample	Saturation/oversaturation rejection criteria	D_0 calculation method (n)	CAM D_0 (Gy)	OD (%)	Total dose rate, D_r (Gy/ka)	Age (ka)
Alathar	PD60	1	CAM (17)	125±14	41±8	0.44±0.02	286±34
		2	CAM (12)	96±7	20±5	0.44±0.02	221±19
		3	CAM (15)	111±10	34±7	0.44±0.02	255±27
	PD61	1	CAM (19)	124±10	32±6	0.95±0.04	130±12
		2	CAM (14)	109±9	26±5	0.95±0.04	115±10
		3	CAM (16)	115±9	28±5	0.95±0.04	121±11
	PD62	1	CAM (36)	127±10	41±5	1.08±0.05	118±11
		2	CAM (21)	104±9	38±6	1.08±0.05	97±10
		3	CAM (32)	121±9	39±5	1.08±0.05	112±10
Al Wusta Playa	PD47	1	CAM (15)	217±19	33 ± 7		
		2	CAM (6)	156±11	17 ± 5		
		3	CAM (14)	207±17	30 ± 6		
	PD48	1	CAM (25)	262±18	34 ± 5	N/A oversaturated	
		2	CAM (4)	170±11	21 ± 8		
		3	CAM (21)	246±17	32 ± 5		
	PD49	1	CAM (13)	124±24	68 ± 14	N/A - oversaturated	
		2	CAM (7)	72±10	37 ± 10	0.83±0.04	86±13
		3	CAM (12)	114±21	64 ± 13	N/A - oversaturated	

Six samples were taken at Al Wusta Playa, with the three stratigraphically lower samples (PD47 – 49) affected by oversaturation. When adopting oversaturation approaches 1 and 3 there is little difference in the estimated burial dose, with approach 3 yielding marginally lower burial doses as would be expected based on the rejection criteria (see Table 6.2). However, applying approach 2 considerably reduces the number of accepted aliquots and the burial dose (see Table 6.4). This is in contrast with Alathar where the burial dose does not alter meaningfully depending on the oversaturation criteria chosen

(i.e. the D_e does not move beyond the uncertainties of the D_e of the previous oversaturation criterion) (Table 6.4). Samples PD48 (unit 1 – cemented white sands) and PD47 (unit 2 – unconsolidated dune sands) are probably oversaturated as they predominantly yield high burial doses (e.g. >200 Gy) that lie close to the limit of quartz OSL dating. When approach 2 is applied only 4 – 7 aliquots pass the rejection criteria and the CAM D_e remains high (>150 Gy). Consequently, it is assumed both these samples are saturated, so finite ages are not calculated for these sample.

Sample PD49 originates from well-sorted sands that lie 8 cm below a unit associated with increased humidity (see Chapter 7). Approaches 1 and 3 yield extremely high OD (64 – 68%) making the CAM D_e an inappropriate model for determining the age of the sample. This also suggests there may be more than one grain population present in the sample. Approach 2 effectively removes all potentially saturated aliquots and yields a far lower burial dose based on a relatively small sample size ($n = 7$). This approach more accurately represents the true burial dose after rejecting saturated grains incorporated into the unit from the lower units related to PD47 and PD48. Ideally single-grain analysis could identify distinct populations in this sample but given that the sample does not directly relate to humidity it was not deemed necessary to undertake further analysis. In summary, presented in Table 6.7 displays rejection criteria using oversaturation approach 3 for all samples, with the exception of PD49 from Al Wusta Playa where approach 2 is used.

After application of the rejection criteria to the datasets, a number of patterns emerge. Notably, the majority of rejected aliquots failed the IR depletion test. Previous research in the western Nefud Desert attempted to overcome this issue by subjecting samples to a one-week H_2SiF_6 treatment followed by HCl rinse in addition to the HF etch (see S.I. Section 3.1 in Groucutt et al. (2018)), but their IR-depletion ratio failure rate for single-grains remained high. This implies that feldspar inclusions are common within quartz grains in the western Nefud Desert (Clark-Wilson, 2016; Groucutt et al., 2018; Jennings et al., 2016; Petraglia et al., 2012). A small proportion of samples failed the recycling ratio test, implying that changes in aliquot sensitivity through the measurement procedure were accurately corrected using the SAR technique (Murray and Wintle,

2000). A number of aliquots from PD50 and 51 were rejected on the basis that they did not produce monotonic dose response curves. Overall, the rejection rate of aliquots in this study is high (~53% of measured aliquots), and so more aliquots (n=48) were measured per sample than is normal. This approach yielded sufficient accepted aliquots for most samples to calculate the burial dose (see Table 6.2). In contrast to results from coarse grain (i.e. 210-180 and 90-60 μm) quartz samples, the 4-11 μm quartz samples had very low rejection rates (~3% from a sample of 33) (Table 6.3). Since the majority of aliquots from coarse grained samples were rejected for failing the IR depletion ratio test (except for samples PD50 and PD51), this difference supports our hypothesis that the coarse grains contain feldspar inclusions, since the very high surface area:volume ratio of 4-11 μm grains makes it unlikely that feldspar inclusions would survive an H_2SiF_6 etch. Conversely, the much lower surface area:volume ratio of coarser fractions, particularly the 210-180 μm grains, makes it more likely that inclusions could be in the interior of the grain and therefore shielded from etching. Lastly, although only one feldspar sample was measured, no aliquots were rejected. This result suggests that feldspar might be a useful dosimeter for future luminescence work in the Nefud Desert, though feldspar yields are very low meaning that this approach is only likely to be applicable to sand dominated samples i.e. the sands underlying lake deposits.

6.3.2.2 Feldspar pIRIR₂₂₅ De measurement

A single equivalent dose (D_e) using 60 – 90 μm feldspar (sample PD14, site KAM4 lake 4) was estimated using the single-aliquot regenerative-dose (SAR) pIR-IR stimulation at 225°C (pIRIR₂₂₅) protocol (see Table 4.2) (Thomsen et al., 2008). Net IR₅₀ and pIRIR₂₂₅ signals were calculated by subtracting a mean background signal from the final 13.3 s of simulation from the total signal emitted over the first 4.256 s. The same rejection criteria were applied as for quartz, with the exception of the IR depletion test which is inappropriate for feldspar measurements. All aliquots passed the rejection criteria (Table 6.5). Unlike quartz, the equivalent dose derived from the IRSL signal of feldspars are prone to anomalous fading (Wintle, 1973). It is therefore necessary to calculate fading rates (g-values) to prevent age underestimation (Huntley and Lamothe, 2001; Lamothe et al., 2003). Fading rates were calculated using Analyst 4.31.9 (Duller, 2007),

following Huntley and Lamothe (2001). This yielded g-values of $4.98 \pm 1\%$ (IR50) and $0.87 \pm 1.01\%$ (IR225). The latter value is similar to those derived from quartz and it is therefore assumed that no fading occurred and the net pIRIR₂₂₅ signal represents the true burial dose (Buylaert et al., 2012; Roberts, 2012; Lowick et al., 2012).

Table 6.5 - As per Tables 6.2 and 6.3 but for coarse-grained feldspar aliquots (4 – 11 μm). Abbreviations are as follows: RR – recycling ratio; recup – recuperation >5%; oversat – oversaturation; Err on Ln > 30% - uncertainties > 30% of the calculated D_e .

Site	Sample	N	Failed RR	Failed recup	Failed oversat	Err on Ln > 30%	Poor Curve	Rejected	Accepted
KAM4	L4 PD14 (60 – 90)	17	0	0	0	0	0	0	17

6.3.2.2 Equivalent dose (D_e) determination

To determine the age of a sample a single-burial dose (D_b) must be calculated from the accepted single-aliquots. As all samples represent well-bleached aeolian dune sands, or sands derived from such sands, D_b was calculated for all samples using the central age model (CAM) in the R luminescence package (Burow, 2017; Galbraith et al., 1999). Overdispersion (OD) values for the coarse-grain quartz ranged from $13 \pm 3\%$ (PD50) to $39 \pm 5\%$ (PD61) (see Table 7) and these are similar to reported values for single-aliquot data from site 16.3 (Clark-Wilson, 2016) and Ti's al Ghadah (Rosenberg et al., 2013). OD for fine-grain quartz ranged from $13 \pm 4\%$ (PD10) to $23 \pm 5\%$ (AWP1). The single coarse-grain feldspar sample had an OD of $6 \pm 2\%$. Examples of equivalent dose distributions from six selected samples are presented in Figure 6.4. While overdispersion is relatively high for coarse grain single-aliquot data from well-bleached dune sands, it is consistent with previous single-aliquot data from the Nefud Desert (Clark-Wilson, 2016; Groucutt et al., 2018; Jennings et al., 2016; Petraglia et al., 2012). Partial bleaching is not likely to be an issue as all sands have been introduced to their depositional environment via aeolian/fluvial mobilisation of well-bleached surficial sands. Post-depositional mixing is possible for loose aeolian dune samples as burrowing animals (e.g. foxes) occupy the western Nefud Desert. However, care was taken when sampling to avoid sediments that looked disturbed. Post-depositional mixing is less likely for consolidated carbonate/siliceous sediment, where consolidation via desiccation occurred shortly

after deposition, precluding the intrusion of younger grains (e.g. PD61,62 – Alathar). However, these samples display overdispersion values typical of loose sand samples, suggesting post-depositional mixing is not the primary cause of overdispersion.

Beta microdosimetry alone has recently been shown to be capable of causing single-grain overdispersion exceeding 25% (Armitage et al., 2019), and is likely to be the primary cause of the high values measured in the present study. This inference is supported by the low environmental dose rates for coarse-grain quartz samples from the Nefud (0.44 – 1.08 Gy/ka) combined with a low concentration of K-feldspar and heavy minerals identified by XRD analysis (see Chapters 7 - 12) or observed during laboratory density separations. Modelling by Mayya et al. (2006) has demonstrated that these factors (low total dose rate combined with the presence of K-feldspars) may yield high overdispersion values even for well-bleached, unmixed sediments, since the sparse K-feldspars/heavy minerals act as local “hotspots” of beta dose. We regard this scenario as the most plausible explanation of the high overdispersion observed in our datasets, in which case the CAM is the most appropriate age model to use (Guérin et al., 2013).

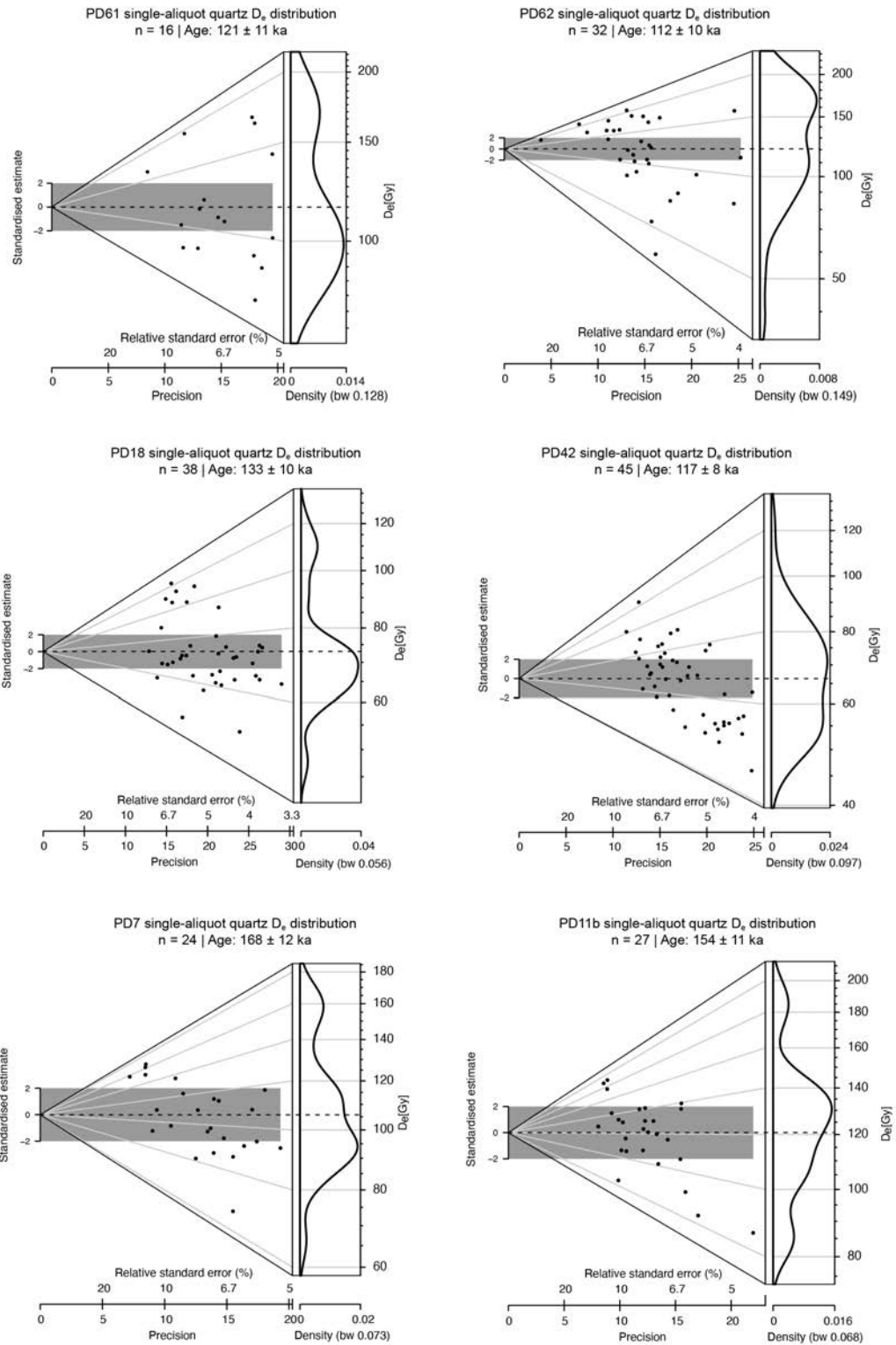


Figure 6.4 – Example abanico plots of the equivalent dose distributions from Alathar (top row), WNEF16_28 (middle row) and KAM4 (bottom row). The dark grey bar is centred at the CAM D_b (broken black line) and all the points that lie within the bar are consistent (at 2σ) with this dose. Overdispersion values are shown in Table 6.7. Abanico plots constructed using the `Plot_AbanicoPlot()` function in the R luminescence package (Dietze and Kreutzer, 2017; Dietze et al., 2016).

6.3.3 Environmental dose rate calculations

The environmental dose rate for HF etched quartz grains in the size fraction of 180 – 210 μm consists of external beta, gamma and cosmic ray components, whilst the environmental dose rate for 60 – 90 μm and 4 – 11 μm quartz also consists of an alpha component since this is not removed by H_2SiF_6 (hexafluorosilicic acid) etching. In addition to these components, dose rate for feldspars also consists of an internal beta dose component. Alpha dose rates were measured using a Daybreak 583 intelligent alpha counter. Here, background corrected total and “slow-pairs” (the rapid emission of two alpha particles by ^{220}Rn and ^{216}Po in the ^{232}Th decay series) count rates were used to calculate uranium and thorium concentrations assuming both to be in secular equilibrium. Alpha dose rates were calculated from these radioisotope concentrations using the conversion factors of Adamiec and Aitken (1998). External beta dose rates were measured using a Risø GM-25-5 low-level beta counting system (Bøtter-Jensen and Mejdahl, 1988), using MgO and Volkagem loess (De Corte et al., 2007) standards. Gamma dose rates were measured in the field using an EG&G Ortec digiDart-LF gamma-spectrometer. This instrument was calibrated using the “Oxford blocks” (Rhodes and Schwenninger, 2007), and dose rates were calculated using the “threshold” method (Mercier and Falguères, 2007). Where no field gamma spectrometry data was available, gamma doses were calculated using U, Th and K concentrations determined via alpha (Daybreak Model 583) and beta counting.

Dose rates were corrected for beta attenuation (Mejdahl, 1979), the etch depth (Bell, 1979), grain size and a water content of $5 \pm 2.5\%$. Alpha efficiency (a-value) values of 0.10 ± 0.02 (Olley et al., 1998) and 0.038 ± 0.002 (Rees-Jones, 1995) were used for the 60 – 90 μm and 4 – 11 μm quartz grains respectively. Internal dose rates for feldspars were calculated using an assumed %K content of $12.5 \pm 0.5\%$ (Huntley and Baril, 1997) and 400 ± 100 ppm ^{87}Rb (Huntley and Hancock, 2001). Internal absorption factors for potassium were calculated for 60 – 90 μm grains following Brennan (2003) while the absorbed dose rate from rubidium was taken from Readhead (2002). Both of these calculations were automatically done on the Dose Rate and Age Calculator (DRAC) (Durcan et al., 2015). Cosmic ray dose rates were calculated using site latitude,

longitude, elevation and present-day sediment burial depths (Prescott and Hutton, 1988). The total environmental dose rate and final age estimates were calculated using Dose Rate and Age Calculator (Table 6.6) (Durcan et al., 2015).

Table 6.6 – Summary of environmental dose rate data for all samples analysed within this thesis.

Site	Sample	Grain size (μm)	Depth (m)	Moisture (%)	Wet dose rate (Gy/ka)			Cosmic (Gy/ka)	Internal (Gy/ka)	Total dose rate (Gy/ka)
					α	β	γ			
Alathar	PD60	180 - 210	1.96 \pm 0.1	5 \pm 2.5	N/A	0.09 \pm 0.01	0.16 \pm 0.01	0.18 \pm 0.02	N/A	0.44 \pm 0.02
	PD61	180 - 210	1.02 \pm 0.1	5 \pm 2.5	N/A	0.39 \pm 0.03	0.36 \pm 0.02	0.20 \pm 0.02	N/A	0.95 \pm 0.04
	PD62	180 - 210	0.29 \pm 0.1	5 \pm 2.5	N/A	0.46 \pm 0.04	0.36 \pm 0.02	0.25 \pm 0.03	N/A	1.08 \pm 0.05
WNEF16_28	PD18	180 - 210	1.2 \pm 0.1	5 \pm 2.5	N/A	0.14 \pm 0.01	0.21 \pm 0.01	0.20 \pm 0.02	N/A	0.55 \pm 0.03
	PD42	180 - 210	0.3 \pm 0.1	5 \pm 2.5	N/A	0.12 \pm 0.01	0.19 \pm 0.01	0.25 \pm 0.03	N/A	0.57 \pm 0.03
KAM4 Lake 3	PD11b	180 - 210	0.40 \pm 0.1	5 \pm 2.5	N/A	0.30 \pm 0.02	0.24 \pm 0.01	0.24 \pm 0.02	0.78 \pm 0.04	0.78 \pm 0.04
	PD12	180 - 210	0.80 \pm 0.1	5 \pm 2.5	N/A	0.33 \pm 0.03	0.29 \pm 0.02	0.21 \pm 0.02	0.84 \pm 0.04	0.84 \pm 0.04
KAM4	PD9	180 - 210	0.75 \pm 0.1	5 \pm 2.5	N/A	0.20 \pm 0.02	0.22 \pm 0.01	0.21 \pm 0.02	N/A	0.63 \pm 0.03
Lake 3A	PD10 (FG)	4 - 11	0.40 \pm 0.1	5 \pm 2.5	0.08 \pm 0.01	0.63 \pm 0.05	0.26 \pm 0.01	0.24 \pm 0.02	N/A	1.21 \pm 0.06
KAM4	PD7	180 - 210	0.45 \pm 0.1	5 \pm 2.5	N/A	0.19 \pm 0.02	0.20 \pm 0.01	0.24 \pm 0.02	N/A	0.63 \pm 0.03
Lake 3B	PD8	180 - 210	0.40 \pm 0.1	5 \pm 2.5	N/A	0.20 \pm 0.02	0.21 \pm 0.01	0.24 \pm 0.02	N/A	0.65 \pm 0.03
KAM4	PD13	180 - 210	0.80 \pm 0.1	5 \pm 2.5	N/A	0.33 \pm 0.03	0.27 \pm 0.01	0.21 \pm 0.02	N/A	0.81 \pm 0.04
Lake 4 (quartz)	PD14	60 – 90	0.32 \pm 0.1	5 \pm 2.5	0.10 \pm 0.01	0.62 \pm 0.05	0.43 \pm 0.02	0.25 \pm 0.03	N/A	1.40 \pm 0.06
	PD14	4 – 11	0.32 \pm 0.1	5 \pm 2.5	0.11 \pm 0.02	0.65 \pm 0.05	0.43 \pm 0.02	0.25 \pm 0.03	N/A	1.44 \pm 0.06
KAM4 Lake 4 (Feldspar)	PD14	60 – 90	0.32 \pm 0.1	5 \pm 2.5	0.15 \pm 0.05	0.62 \pm 0.05	0.43 \pm 0.02	0.25 \pm 0.03	0.31 \pm 0.05	1.76 \pm 0.09
Al Wusta Playa	PD47	180 - 210	1.36 \pm 0.1	5 \pm 2.5	N/A	0.12 \pm 0.01	0.27 \pm 0.01	0.19 \pm 0.02	N/A	0.58 \pm 0.02
						0.01	0.01	0.02		0.63 \pm 0.03
	PD48	180 - 210	1.35 \pm 0.1	5 \pm 2.5	N/A	0.17 \pm 0.02	0.27 \pm 0.01	0.2 \pm 0.02	N/A	0.83 \pm 0.04
						0.02	0.01			0.63 \pm 0.03
	PD49	180 - 210	0.98 \pm 0.1	5 \pm 2.5	N/A	0.25 \pm 0.02	0.38 \pm 0.02	0.2 \pm 0.02	N/A	2.04 \pm 0.11
						0.02	0.02			1.67 \pm 0.07
	AWP1	4 - 11	0.76 \pm 0.1	5 \pm 2.5	0.25 \pm 0.02	1.05 \pm 0.08	0.53 \pm 0.07	0.21 \pm 0.02	N/A	1.51 \pm 0.06
0.08						0.07	0.02	1.67 \pm 0.07		
PD50	180 - 210	0.70 \pm 0.1	5 \pm 2.5	N/A	0.66 \pm 0.05	0.8 \pm 0.05	0.22 \pm 0.02	N/A	1.51 \pm 0.06	
					0.05		0.02		1.51 \pm 0.06	
PD51	180 - 210	0.27 \pm 0.1	5 \pm 2.5	N/A	0.56 \pm 0.04	0.69 \pm 0.04	0.26 \pm 0.03	N/A	1.51 \pm 0.06	
					0.04	0.04	0.03		0.63 \pm 0.03	

6.4 Age estimation and interpretation

The ages of each sequence dated within this study along with previously dated sedimentary sequences directly relevant to this thesis (Clark-Wilson, 2016; Groucutt et al., 2018; Rosenberg et al., 2013; Stimpson et al., 2016) are presented below in age order, from youngest to oldest. In some cases the ages and construction of chronologies are supported by interpretations of the sediments from Chapters 7 - 12 (e.g. KAM4 lake 1). All ages are shown in Table 6.7.

*Table 6.7 – Summary data for all luminescence data discussed in following sections. Data generated by me prior to commencement of the PhD includes Al Wusta and Site 16.3 (Clark-Wilson, 2016; Groucutt et al., 2018). Unpublished and published luminescence data that directly relate to sedimentary sequences studied in this thesis include TAG and KAM4 lakes 1 and 2. Abbreviations: US – sands underlying lake deposits. IL – inlake. WS – waterlain sands. WZ – waterlain silts. PS – playa sands. Q – quartz. F – feldspar. Db – burial dose. OD – overdispersion. Dr – total environmental dose rate. *Al Wusta Playa samples PD49 calculated using different oversaturation criteria (Section 6.3.2).*

Site	Sample	Context	Min.	Grain size (µm)	Db (Gy)	OD (%)	Dr (Gy/ka)	Age (ka)	Ref.
Alathar	PD60	US	Q (OSL)	180 – 210	111±10	34±7	0.44 ± 0.02	255 ± 27	This thesis/Stewart et al. (2020a)
	PD61	IL	Q (OSL)	180 – 210	115±9	28±5	0.95 ± 0.04	121 ± 11	This thesis/Stewart et al. (2020a)
	PD62	IL	Q (OSL)	180 – 210	121±9	39±5	1.08 ± 0.05	112 ± 10	This thesis/Stewart et al. (2020a)
WNEF16_28	PD18	US	Q (OSL)	180 – 210	73±3	21±3	0.55 ± 0.03	133 ± 10	This thesis
	PD42	WS	Q (OSL)	180 – 210	66±3	20±3	0.57 ± 0.03	117 ± 8	This thesis
KAM4 lake 1	KAM4-OSL1	US	F (pIRIR ₂₉₀)	180 - 255	673±127	55	1.63 ± 0.15	412.2 ± 86.5	Clark-Balzan pers. comm.
KAM4 lake 2	KAM4-OSL2	US	F (pIRIR ₂₉₀)	180 - 255	578±44	26	1.71 ± 0.15	337.3 ± 39.1	Clark-Balzan pers. comm.
	KAM4-OSL3	OS	F (pIRIR ₂₉₀)	180 - 255	479±58	37	1.56 ± 0.15	306.4 ± 47.2	Clark-Balzan pers. comm.
KAM4 lake 3	KAM4-OSL4	US	F (pIRIR ₂₉₀)	180 - 255	435±18	11	1.84 ± 0.15	236.6 ± 21.6	Clark-Balzan pers. comm.
	PD11b	US	Q (OSL)	180 - 210	121±6	19±3	0.78 ± 0.04	154 ± 11	This thesis
	PD12	US	Q (OSL)	180 - 210	126±5	15±2	0.84 ± 0.04	149 ± 9	This thesis
KAM4 lake 3a	PD9	US	Q (OSL)	180 - 210	118±7	25±4	0.63 ± 0.03	184 ± 14	This thesis
	PD10	IL	Q (OSL)	4 - 11	174±10	13±4	1.21 ± 0.06	143 ± 10	This thesis
KAM4 lake 3b	PD7	US	Q (OSL)	180 - 210	106±6	20±3	0.63 ± 0.03	168 ± 12	This thesis
	PD8	US	Q (OSL)	180 - 210	93±7	35±5	0.65 ± 0.03	142 ± 13	This thesis
KAM4 lake 4	KAM4-OSL5	IL	F (pIRIR ₂₉₀)	180 - 255	353±61	47	1.86 ± 0.15	189.8 ± 36.2	Clark-Balzan pers. comm.
	KAM4-OSL6	US	F (pIRIR ₂₉₀)	180 - 255	213±53	74	2.65 ± 0.16	80.4 ± 20.6	Clark-Balzan pers. comm.
	PD13	US	Q (OSL)	180 - 210	116±9	36±5	0.81 ± 0.04	141 ± 13	This thesis

	PD14	IL	Q (OSL)	60 - 90	272±14	16±3	1.39 ± 0.06	194 ± 13	This thesis
	PD14	IL	Q (OSL)	4 - 11	303±19	17±4	1.43 ± 0.06	210 ± 16	This thesis
	PD14	IL	F (pIRIR ₂₂₅)	60 - 90	318±13	6±2	1.76 ± 0.09	192 ± 20	This thesis
Al Wusta Playa*	PD47	US	Q (OSL)	180 – 210	Oversaturated				This thesis
	PD48	US	Q (OSL)	180 – 210	Oversaturated				This thesis
	PD49*	US	Q (OSL)	180 – 210	72±10	37±10	0.83 ± 0.04	86 ± 13	This thesis
	AWP1	WZ	Q (OSL)	4 - 11	39±3	23±5	2.04 ± 0.11	19 ± 2	This thesis
	PD50	WS	Q (OSL)	180 – 210	7.1±0.3	13±3	1.67 ± 0.07	4.3 ± 0.3	This thesis
	PD51	PS	Q (OSL)	180 – 210	1.97±0.2	35±9	1.51 ± 0.06	1.3 ± 0.2	This thesis
Al Wusta (single-grain)	PD15	US	Q (OSL)	180 – 210	57±3	22±4	0.62 ± 0.03	93 ± 6	Groucutt et al. (2018)
	PD16	US	Q (OSL)	180 – 210	56± 2	20±3	0.50 ± 0.02	111 ± 6	Groucutt et al. (2018)
	PD17	US	Q (OSL)	180 – 210	53±3	16±3	0.61 ± 0.03	86 ± 6	Groucutt et al. (2018)
	PD40	WS	Q (OSL)	180 – 210	50±3	26±3	0.50 ± 0.03	99 ± 7	Groucutt et al. (2018)
	PD41	US	Q (OSL)	180 – 210	50±3	20±4	0.54 ± 0.03	92 ± 7	Groucutt et al. (2018)
Site 16.3	PD1	US	Q (OSL)	180 – 210	62±7	45±8	0.60 ± 0.03	100 ± 13	Clark-Wilson (2016)
	PD2	US	Q (OSL)	180 – 210	62±5	41±6	0.71 ± 0.03	87 ± 8	Clark-Wilson (2016)
	PD3*	IL	Q (OSL)	180 – 210	58±3	21±3	0.67 ± 0.03	86 ± 6	Clark-Wilson (2016)
Ti's al Ghadah	TAG1-OSL4	Unit 7	F (pIRIR ₂₉₀)	180 – 255	629±58	24	2.16 ± 0.16	291 ± 34	Stimpson et al. (2016)
	C17.1/1	Unit 4/5	Q (OSL)	200 – 250	153±6	13	0.48 ± 0.03	328 ± 26	Rosenberg et al. (2013)
	C17.1/1	Unit 4/5	Q (TT-OSL)	200 – 250	158±5	22	0.48 ± 0.03	318 ± 25	Rosenberg et al. (2013)

6.4.1 Al Wusta Playa

Six luminescence samples were taken through the 1.49 m section at Al Wusta Playa. Sample PD48 (1.35 m below surface) is the stratigraphically lowest sample, originating from white cemented sands at the base of the sequence, while PD47 (1.36 m below surface) was sampled from unconsolidated sands that lie stratigraphically above the cemented white sands. The inversion in depths below surface between these two samples is due to the basal sample (PD48) being taken from the upper section of a wind-sculpted feature in the cemented white sands, while PD47 was taken from unconsolidated sands that lay adjacent to the wind-sculpted erosional contact between the two units. Both samples yield finite ages but the high burial doses and limited number of accepted aliquots after stringent oversaturation rejection criteria (section 6.3.2) strongly implies these sands are saturated.

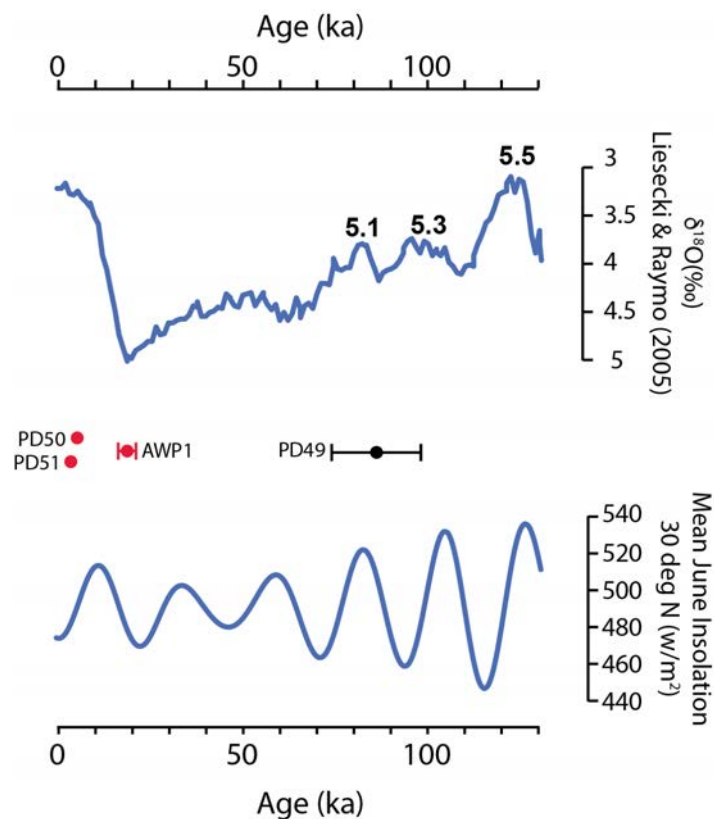


Figure 6.5 - Ages from Al Wusta Playa shown alongside the NH summer insolation at 30°N (Berger and Loutre, 1991) and the marine oxygen isotope record from the LR04 stack (Liesecki and Raymo, 2005). Red lines indicate directly dated wetland sediments. Black lines represented underlying sands. All uncertainty terms are at 1σ .

Sample PD49 (0.98 m below surface) originates from the same sedimentary unit as PD47, but from the very top of this unit. This sample yields an age of 86 ± 13 ka, which broadly corresponds to the age of the dune sands which underly the Al Wusta marl sequences (samples PD15, 17 and 41).

The OSL sample AWP1 from Unit 3 directly dates sediments (silty sands with gravel inclusions; Chapter 7) associated with humidity and yields an age of 19.1 ± 1.7 ka. This date is much earlier than either the onset of humidity at nearby Tayma, which occurs at ~ 9.2 ka (Dinies et al., 2015; Neugebauer et al., 2017), or elsewhere in southern Arabia at ~ 10 ka (Fleitmann et al., 2011, 2003). The age of AWP1 suggests either increased humidity to the Nefud prior to the onset of humidity across the rest of the Saharo-Arabian desert belt, or that the OSL date overestimates the depositional age of the playa sediments. If the age is accepted, then it is surprising in the context of the western Nefud

Desert receiving moisture in response to increased northern hemisphere insolation via tropical sources (e.g. African monsoon). This is because the Nefud would be expected to receive monsoonal moisture later relative to southern Arabia, assuming times-transgressive extension of the African monsoon in response to increased insolation. An alternative explanation, if the age for AWP1 is to be believed, is that the deposition of wetland sediments was caused by a southerly displacement of westerly storm tracks in during the last glacial maximum. However, it is more likely that the true age of the deposit is younger than the OSL date suggests. Given the lack of preheat plateau data due to limited sample and the relatively poor preheat plateau data from PD50 (Fig 6.2), it is feasible that the CAM D_b is overestimated for the sample. An overestimation of 20%, which is consistent with values yielded by some preheating regimes from the overlying sample PD50, would yield an age of ~ 19 ka when the true age is closer to ~ 15 ka and consistent with the onset of the Holocene Humid Period (deMenocal et al., 2000). The latter explanation is the most plausible, meaning that AWP1 overestimates the sediments true age. Sample PD50 which lies ~ 6 cm above AWP1, also directly dates humidity, and yields an age of 4.3 ± 0.3 ka. Sample PD51 (0.27 m below surface) originates from the final unit of loosely consolidated and horizontally laminated sands representing depositional conditions similar to that of today and yields an age of 1.3 ± 0.2 ka.

6.4.2 Site 16.3

Three luminescence samples were taken at site 16.3. The sands underlying the lake carbonates yield ages of 100 ± 13 ka (PD1) and 87 ± 8 ka (PD2) while sands within the marl itself yielded an age of 86 ± 6 ka (PD3) (Clark-Wilson, 2016). The latter age directly dates the timing of humidity at the site which places the age of the lake to late MIS 5, and closely corresponds to the ~ 84 ka NH summer insolation peak.

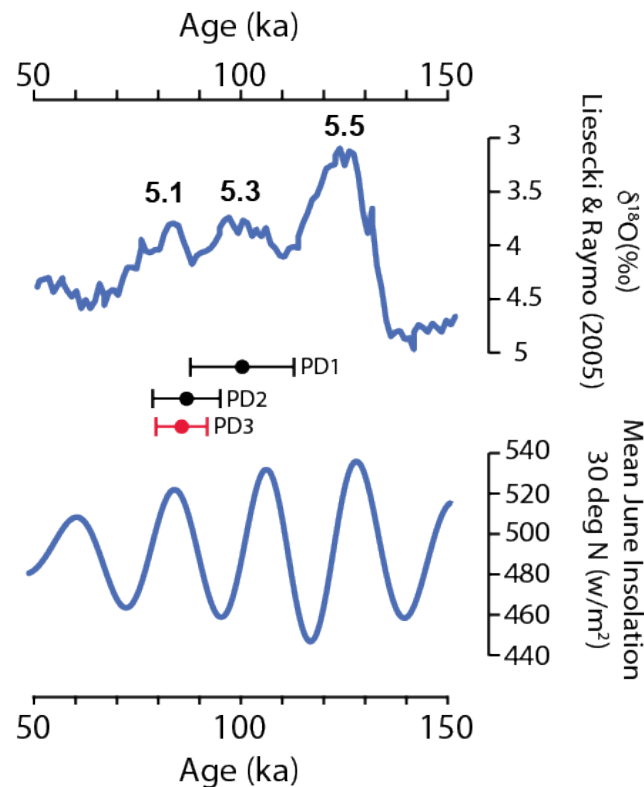


Figure 6.6 – Ages from site 16.3 (Clark-Wilson, 2016) shown alongside NH summer insolation at 30°N (Berger and Loutre, 1991) and the marine oxygen isotope record from the LR04 stack (Liesecki and Raymo, 2005). Red lines indicate directly dated wetland sediments. Black lines represented underlying sands. All uncertainty terms are at 1σ .

6.4.3 Al Wusta

A total of five luminescence samples were taken from Al Wusta. Four of these samples derive from the dune sands underlying the carbonate sediment: PD15, 16, 17 and 41. Taking the maximum and minimum ages from these samples suggests the age of sand deposition prior to carbonate deposition occurred at some point between 80 – 118 ka. The waterlain sands overlying the carbonate sediment (PD40) dates to 99 ± 7 ka and is therefore consistent with the suite of ages from the underlying sands. Groucutt et al. (2018) combine the OSL ages from PD15, 17, 40 and 41 with direct U-series and combined U-ESR dating on a human phalanx (AW-1, lab-code 3675) and a hippopotamus tooth (lab code WU1601) from the overlying waterlain sand unit, to produce a Bayesian model for the timing of deposition at Al Wusta. This model suggests that units 2 (carbonate sediments) and 3 (waterlain sands) were deposited between 92.2 ± 2.6 ka and 90.4 ± 3.9 ka ($\sim 86 - 95$ ka) (Groucutt et al., 2018), a period which correlates with late MIS 5 and NH summer insolation minimum. However, Groucutt et al. (2018) suggest that the lake at Al Wusta formed during a NH summer insolation peak at ~ 84 ka following

the orbital-monsoon hypothesis where increases in insolation lead to increased humidity.

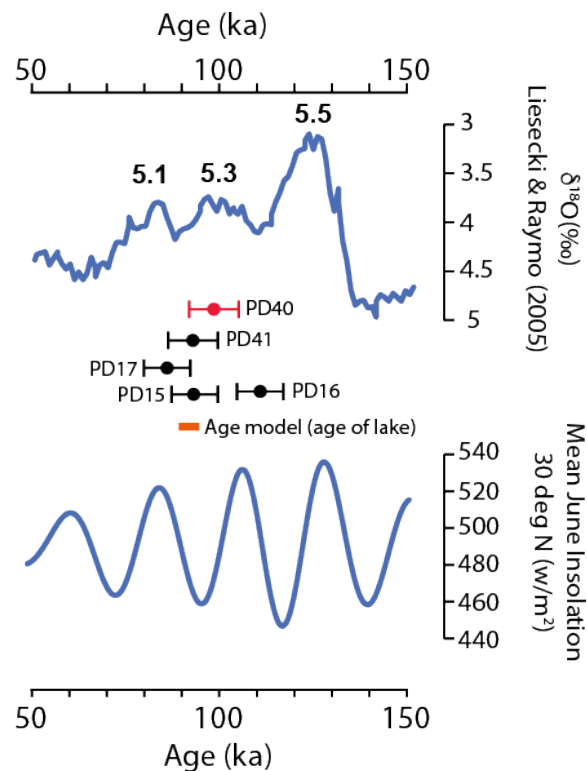


Figure 6.7 - Ages from Al Wusta (Groucutt et al., 2018) shown alongside NH summer insolation at 30°N (Berger and Loutre, 1991) and the marine oxygen isotope record from the LR04 stack (Liesecki and Raymo, 2005). Red lines indicate directly dated wetland sediments. Black lines represented underlying sands. All uncertainty terms are at 1σ .

It is important to note that this model did not include luminescence sample PD16 from the inner carbonate ridge (see Chapter 5.2.2.1 for site description) which dates to 111 ± 7 ka. If it is assumed the sands underlying the carbonate sediments represent the age of the lake, then this age suggests a second distinct phase of lake formation during an earlier insolation peak during MIS 5. However, micromorphological and isotopic affinities between the two ridges along with the site geomorphology strongly indicate that the ridges were formed within the same waterbody (see Chapter 8). This interpretation suggests that, in the case of trench PD16, the underlying sands are considerably older than the overlying lake sediments. Consequently, where palaeolakes in the western Nefud have only been dated based on the age of the dune sands which underlie palaeolake sediments, only the maximum possible age of humidity can be determined (i.e. humidity represented by overlying lake sediments could not be older

than underlying sediments). This is further supported by the suite of ages from Alathar, presented below.

6.4.4 Alathar

A total of three luminescence samples were taken at Alathar. The age of the loose sands underlying lake sediments from Alathar are 255 ± 27 ka (PD60) whilst the sands within the lake sediments are 121 ± 11 ka (PD61) and 112 ± 10 ka (PD62). As with sample PD16 at Al Wusta, the age for sample PD60 demonstrates that the underlying sands at Alathar do not provide an accurate estimate of the age of the overlying lake and associated phase of humidity. Instead they indicate active dune deflation revealing old dune sands towards the surface prior to the onset of lacustrine conditions. The dating results presented here suggest that the Alathar paleolake existed at some point between 121 ± 11 ka (PD61; Unit 2) and 112 ± 10 ka (PD62; Unit 5). These ages relate to early MIS 5, and most likely relate to increased humidity during MIS 5e in response to the NH summer insolation maximum at ~ 128 ka. The sands underlying the palaeolake sediments date to 255 ± 27 ka and likely relate to a phase of dune activity and aridity during MIS 8.

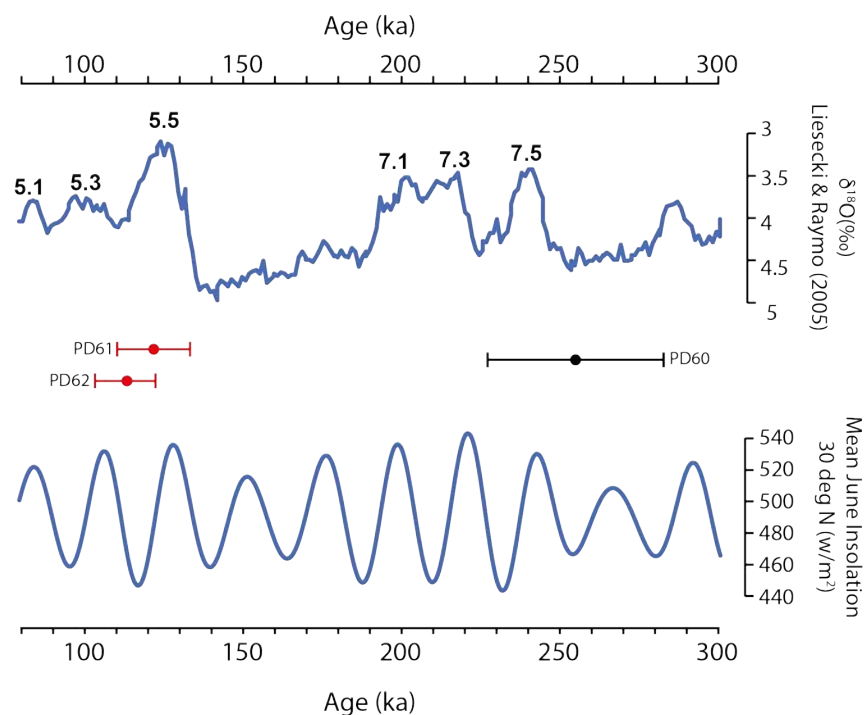


Figure 6.8 - Ages from Alathar shown alongside NH summer insolation at $30^\circ N$ (Berger and Loutre, 1991) and the marine oxygen isotope record from the LR04 stack (Liescecki and Raymo, 2005). Red lines indicate directly dated wetland sediments. Black lines represented underlying sands. All uncertainty terms are at 1σ .

6.4.5 WNEF16_28

Two luminescence samples were taken from WNEF16_28. Loose sands underlying the lake sediment yields a maximum age for humidity of 133 ± 10 ka (PD18) while waterlain sands overlying carbonate sediments yields an of 117 ± 8 ka (PD42). Assuming the waterlain sands were deposited immediately following the desiccation of the lake body then the age of these sands directly dates humidity. At 1σ uncertainties this age ranges from 109 – 125 ka and places the lake to early/mid MIS 5. We suggest, on balance, that this relates to the NH summer insolation peak at ~ 128 ka.

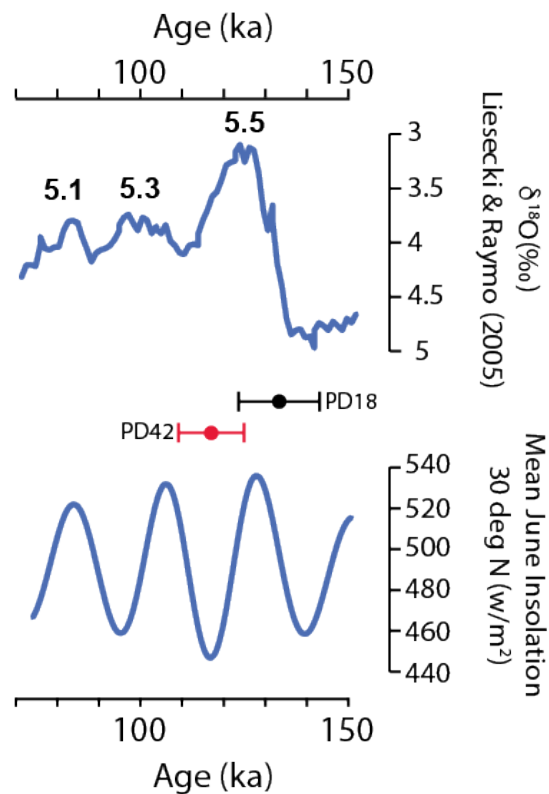


Figure 6.9 - Ages from WNEF16_28 shown alongside NH summer insolation at 30°N (Berger and Loutre, 1991) and the marine oxygen isotope record from the LR04 stack (Lieisecki and Raymo, 2005). Red lines indicate directly dated wetland sediments. Black lines represented underlying sands. All uncertainty terms are at 1σ .

6.4.6 KAM4

A total of 14 luminescence samples yielding 16 ages were taken across the six sedimentary sequences within the KAM4 interdunal basin. Samples were collected from either loose sands beneath or from sands/silts within all six sedimentary sequences. Sample codes KAM4-OSL1 to KAM4-OSL6 represent samples taken by Laine Clark-Balzan

where preliminary analysis was carried out at Oxford Luminescence Laboratory. These samples are from KAM4 Lakes 1,2,3 and 4, and no samples were taken from lakes 3A and 3B. Clark-Balzan's analysis used the pIRIR₂₉₀ signal from feldspars. Her ages are treated with caution in the following analysis since only a small number of aliquots were measured from each sample due to low feldspar abundance, and most samples yielded very high overdispersion values. These data are presented alongside more complete data analysis carried out as part of this thesis. Samples from KAM4 with codes prefixed "PD" were measured as part of this thesis, whereas samples with codes prefixed "OSL" were measured by Clark-Balzan (Fig 6.10). Nonetheless, Clark-Balzan's data are particularly important for lakes 1 and 2, where we were unable to sample due to time constraints on fieldwork.

6.4.6.1 KAM4 Lake 1

A single luminescence sample (KAM4-OSL1) was recovered from bedded sands with gravel clasts that underlie carbonate sediments at KAM4 lake 1 by Clark-Balzan (per comms). The sample yields an age of 412 ± 87 ka with the large uncertainty reflecting high overdispersion (55%) from a limited number of accepted aliquots ($n = 9$). The 1σ age range of 326 – 499 ka precludes assigning the carbonate deposit to a particular MIS stage, with the age range encompassing MIS 9, 11 and 13a (Fig 6.10). While it is not possible to assign the lake deposit to an MIS stage, it is evidently the oldest lake deposit within the KAM4 basin based not just on age (it overlaps with lake 2 on uncertainties) but also on the heavily diagenetically nature of the sediment (iron induration) (Chapter 12.2). Furthermore, this is the only sample where aliquots ($n = 4$) failed pIRIR₂₉₀ analysis due to oversaturation. For these reasons, the KAM4 L1 deposit is the oldest sedimentary sequence studied within this thesis.

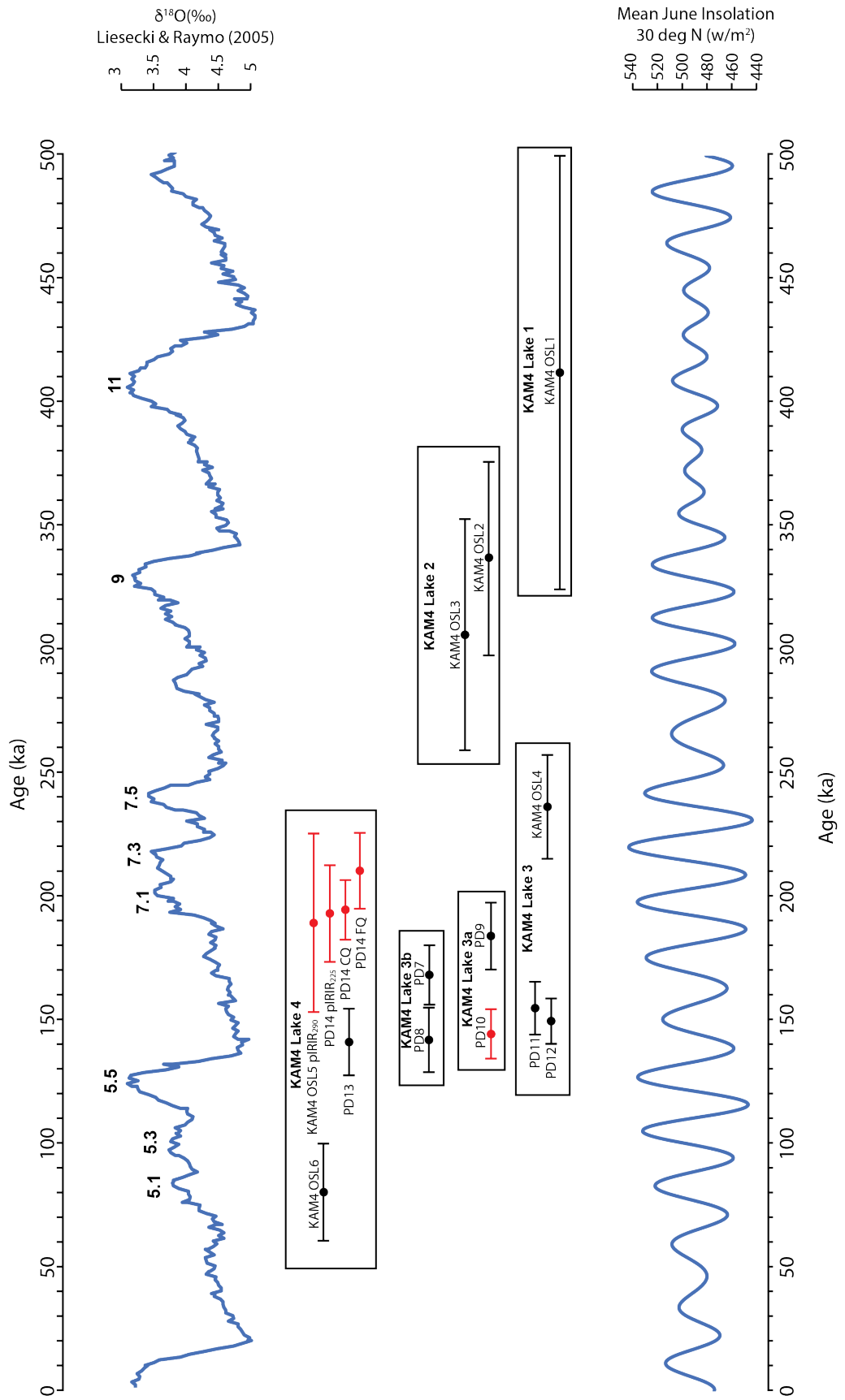


Figure 6.10 - Ages from KAM4 shown alongside NH summer insolation at 30°N (Berger and Loutre, 1991) and the marine oxygen isotope record from the LR04 stack (Liessecki and Raymo, 2005). Red lines indicate directly dated wetland sediments. Black lines represented underlying sands. All uncertainty terms are at 1 σ .

6.4.6.2 KAM4 Lake 2

Two luminescence samples were retrieved from KAM4 lake 2. KAM4-OSL2 was recovered from underlying bedded sands with an age of 337 ± 39 ka, while KAM4-OSL2 was retrieved from a wedge of calcareous sands within the marl sediments and dates to 306 ± 47 ka (Clark-Balzan, per comms). The overdispersion of these samples is 26% and 37%. These values are high but more consistent with overdispersion from quartz samples analysed within this thesis than other samples measured by Clark-Balzan. The two ages bracket the carbonate sediments. Taking the combined maximum and minimum ages based on 1σ uncertainties suggests an age range of 259 - 376 ka for lake development and humidity, and this is consistent with an MIS 9 age for the palaeolake deposit.

6.4.6.3 KAM4 Lakes 3, 3A and 3B

Three samples from the dune sands underlying the carbonate sediments were taken from lake 3; KAM4-OSL4, PD11b and PD12. These yield ages of 237 ± 22 ka, 154 ± 11 ka, and 149 ± 9 ka respectively. The inconsistency between the pIRIR₂₉₀ age produced by Clark-Balzan (KAM4-OSL4) and the quartz OSL ages from this thesis is notable. The samples analysed as part of this thesis are considered to be more reliable since they are consistent with one another and were produced using a greater number of accepted aliquots ($n = 27$ (PD11b), 24 (PD12)). Two samples were taken from the underlying sands at lake 3b, yielding ages of 168 ± 12 ka (PD7) and 142 ± 13 ka (PD8). A further sand sample underlying lake 3a (PD9) yielded an age of 184 ± 14 ka. Since these samples were taken in sands underlying lake deposits, they may be considerably older than the overlying carbonate sediments, but do provide a maximum age of lake formation.

A single sample from lake 3a (PD10) comes directly from the lake sediment at this sequence and yields an age of 143 ± 10 ka. The 1σ age range of 133 – 153 ka mainly falls within late MIS 6, though the upper boundary of the age lies at the MIS 6/5e transition. The attribution of lake 3a to MIS 6 would provide the first evidence of humidity during this period. Conversely, if the lake is of MIS 5e age then this is consistent with early MIS

5 ages from Alathar and WNEF16_28. Given the weight of evidence for humidity during early MIS 5e, and the lack of regional evidence for MIS 6 humidity in the Arabian Peninsula including records that lie further to the south and should therefore be more sensitive to increases in monsoonal rainfall such as Hoti and Mukalla (Nicholson et al., 2019), we suggest that an early MIS 5 age is more probable.

It is also not clear on geomorphic grounds whether the lake 3 and 3b sedimentary sequences formed at the same time as the lake 3a within the same water body, or whether they represent discrete humid intervals. Importantly, all samples from the underlying sands from lakes 3 and 3b, excluding sample KAM4-OSL4, are either indistinguishable from or stratigraphically consistent with the direct date of lake 3a. The consistency of this data along with the proximal location of each sequence suggests that lakes 3, 3a and 3b were produced either by the same waterbody or during the same humid period.

6.4.6.4 KAM4 Lake 4

A total of three luminescence samples were taken from KAM4 lake 4, yielding six age estimates. Four ages were generated as part of this thesis (PD13, PD14 quartz fine-grain, PD14 quartz coarse-grain and PD14 feldspar coarse-grain) and two pIRIR₂₉₀ ages were generated during preliminary analysis (KAM4-OSL5 and KAM4-OSL6; Clark-Balzan, per comms).

Beginning with preliminary analysis, KAM4-OSL5 was recovered from a silty-clay unit wedged between two marl beds and yielded an age of 189 ± 36 ka. KAM4-OSL6 was retrieved from the underlying sands and yielded an age of 80 ± 21 ka. Overdispersion on both samples is large with 47% (KAM4-OSL5) and 74% (KAM4-OSL6). The large overdispersion on KAM4-OSL6 based on only 9 aliquots makes the CAM generated age for this sample unreliable.

Moving to samples worked on as part of this thesis, a single sample (PD13) equivalent to KAM4-OSL6 was taken from the underlying sands. This yielded an age of 141 ± 13 ka,

though the overdispersion (35%) is lower than for KAM4-OSL6. As such the age for sample PD13 is regarded as more reliable than that for KAM4-OSL6. PD13 (141 ± 13 ka) is significantly older than KAM4-OSL6 (80.4 ± 20.6 ka) from the same stratigraphic unit. As noted above, the overdispersion of the KAM4-OSL6 data suggest that the age is unreliable. It is also notable that the total environmental dose rate for KAM4-OSL6 is substantially larger than that for PD13. The total environmental dose rate for KAM4-OSL6 (excluding the internal beta dose rate) is ~ 1.84 Gy/ka compared to ~ 0.81 Gy/ka for PD13. The discrepancy between these dose rates is due to different beta dose rates (1.08 ± 0.05 Gy/ka for KAM4-OSL6 and 0.33 ± 0.03 Gy/ka for PD13). Given the similar stratigraphic contexts of these samples it is difficult to explain such a large difference in dose rate. It is notable that the dose rate for PD13 is consistent with other samples from aeolian sands from the KAM4 basin and within the Nefud Desert more generally, while that for KAM4-OSL6 is not.

Sample PD14 is stratigraphically equivalent to KAM4-OSL5 and originates from a silty-clay unit sandwiched between two marl beds. Consequently, it directly dates the timing of humidity represented by the KAM4 lake 4 sequence. For PD14, fine-grained quartz ($4 - 11 \mu\text{m}$), coarse-grain quartz ($60 - 90 \mu\text{m}$) and coarse-grain feldspar ($60 - 90 \mu\text{m}$; pIRIR₂₂₅) yield ages of 210 ± 16 , 194 ± 13 and 192 ± 20 ka respectively. These ages compare well with the age from KAM4-OSL5 of 189 ± 36 ka. As a combination of 5 ages from samples with different physical (i.e. grain size and mineral) and luminescence signals (pIRIR₂₂₅, pIRIR₂₉₀ and OSL) produce consistent ages there is a strong degree of confidence in the age of KAM4 lake 4. At the most conservative estimate and excluding the preliminary data from Clark-Balzan, the potential age range of the sediment is $172 - 226$ ka and most probably relates to a humid period during MIS 7.

Despite the confidence in the age of sample PD14 directly from carbonate sediment from KAM4 lake 4, there is still a stratigraphic age inversion with the underlying sands (141 ± 13 ka). The cause of this age inversion is not clear but it could be due to the following factors: (1) The introduction of younger grains into the unconsolidated PD13 and KAM4-OSL6 due to post-depositional mixing, (2) partial bleaching of PD14 sample leading to age overestimation for this sample, or (3) problems with the dose rate

determination for either PD13 or PD14. Post-depositional mixing is considered unlikely as care was taken during sampling to avoid visible burrows/roots. Overdispersion from the three subsamples from PD14 ranges from 6 to 17% suggesting that the sample was well-bleached prior to deposition. There is nothing obviously anomalous in the dose rate determination for samples PD13 and PD14. Consequently, it is currently difficult to explain the age inversion between PD13 and PD14.

6.4.7 Ti's al Ghadah

The sedimentary sequence analysed as part of this thesis at Ti's al Ghadah has been comprehensively dated in previous studies (Rosenberg et al., 2013; Stimpson et al., 2016), and no further luminescence dates were analysed. Previous luminescence data from Ti's al Ghadah is included in Table 6.7 and briefly described here. A single luminescence sample comes directly from lacustrine sediments (unit 7) and yields an age of 291 ± 34 ka (pIRIR₂₉₀, [Stimpson et al., 2016]). A further luminescence sample was from underlying horizontally-bedded pebbly green sands that contain root traces (units 4/5; Stimpson et al., 2016). This sample yields ages of 328 ± 26 ka (OSL) and 318 ± 24 ka (TT-OSL) (Rosenberg et al., 2013). All samples are consistent within uncertainties. Assuming that the underlying waterlain sands and overlying lake sediment relate to the same humid interval, then the maximum age range for humidity based on 1σ uncertainties from all these ages range from 257 – 354 ka and is consistent with lake formation during MIS 9.

It is important to note that fossils from Unit 5 have been directly dated using both U-series and Electron Spin Resonance (ESR) dating. U-series dating yields minimum ages of c. 500 ka whilst combined ESR/U-series dating yielded ages of $473 +50-33$ ka, and $554 +79-76$ ka, respectively, for *Oryx* teeth (Stimpson et al., 2016). This is far older than the associated luminescence data. However, it is noted that only 2/5 teeth could be measured from TAG due to exceptionally high U concentration, thus giving a relatively small sample size with unusual U concentrations. Moreover, later research (Stewart et al., 2020a) has also shown U-series and U-ESR dates that are much older than the associated luminescence dates at Alathar. Stewart et al. (2020a) argue that this may be

explained via uranium leaching (making samples appear older than they really are) or if the fossil material associated with lake sediments is reworked from older deposits. Stuart et al. (2020) suggest that the latter is more likely since present-day uranium concentrations in these samples are high, so for leaching to be a viable explanation of the ages, initial uranium concentrations would need to have been unreasonably high. The same may be true of TAG where multiple fossil assemblages at the site of differing ages attest to multiple occupations of fauna in the basin over the Pleistocene (Stewart et al., 2019). Additionally, the consistency of the luminescence data, which includes both TT-OSL and OSL on quartz and pIRIR₂₉₀ on feldspars, adds confidence to this geochronological method. As such, we follow the ages implied from the luminescence data.

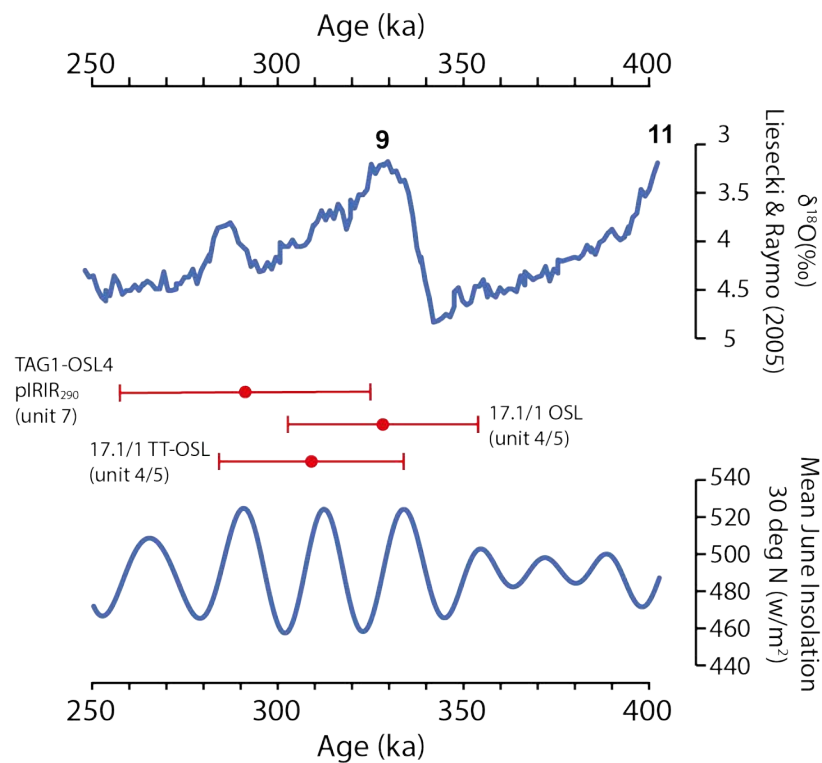


Figure 6.11 - Ages from *Ti's al Ghadah* (Rosenberg et al., 2013; Stimpson et al., 2016) shown alongside NH summer insolation at 30°N (Berger and Loutre, 1991) and the marine oxygen isotope record from the LR04 stack (Liesecki and Raymo, 2005). Red lines indicate directly dated wetland sediments. Black lines represented underlying sands. All uncertainty terms are at 1 σ .

6.5 Division of sites into a chronological framework

The twelve sedimentary sequences presented in this thesis span multiple humid phases that correlate with warm marine isotope stages (MIS 5e, 7, 9 and 11/13a) and substages (MIS 5a) over the past ~500 ka (Table 6.7, Fig 6.12). The uncertainties on these ages prevent assigning these ages to peaks in NH insolation peaks, though following the orbital-monsoon hypothesis (Rossignol-Strick, 1983) and various climate models (Herold and Lohmann, 2009; Gierz et al., 2017; Jennings et al., 2015) it is probable that humid phases occurred during periods of increased NH insolation.

The youngest evidence for humidity comes from Al Wusta Playa where two samples taken directly from a sedimentary unit demonstrate a period of increased humidity during some period within the past 20 ka, and most probably in association with the Holocene Humid Period. The sample just 8 cm below this unit (PD49) yields an age of 86 ± 13 ka, and the hiatus between the two ages implies sediment deflation within the Al Wusta interdunal basin during an intervening arid phase during MIS 4/3/2. No evidence of humidity is found during MIS 3 from the sites presented here. The next phase of humidity is represented by sediments at two sites – Site 16.3 and Al Wusta. These are dated to late MIS 5 and most probably formed in association with the ~84 ka NH insolation peak (Clark-Wilson, 2016; Groucutt et al., 2018). Two further sites – Alathar and WNEF16_28 – demonstrate humidity during late MIS 5 and most probably in response to a ~128 ka insolation peak. This suite of ages demonstrates the occurrence of at least two discrete humid intervals within the western Nefud Desert during early MIS 5. We also suggest that KAM4 lakes 3, 3a and 3b formed during early MIS 5 due to increased humidity in response to the ~128 ka insolation peak.

KAM4 lake 4 demonstrates humidity during MIS 7, Ti's al Ghadah (Rosenberg et al., 2013) and KAM4 lake 2 (Clark-Balzan, per comms) date to MIS 9, while KAM4 lake 1 (Clark-Balzan, per comms) represents the oldest sedimentary sequence presented in this thesis and probably relates to MIS 11/13.

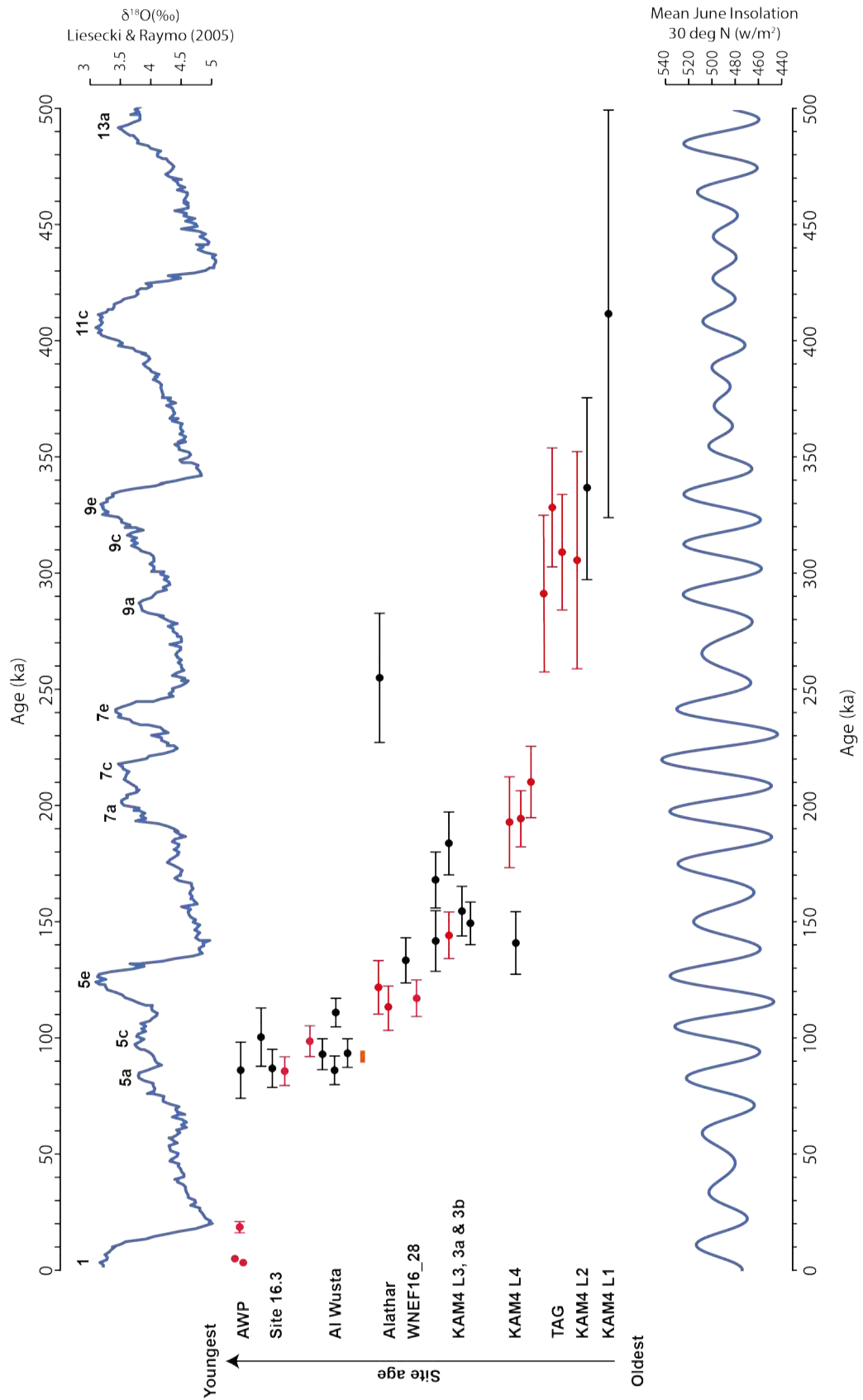


Figure 6.12 – Summary of all ages relevant to sedimentary sequences studied in this thesis shown alongside NH summer insolation at 30°N (Berger and Loutre, 1991) and the marine oxygen isotope record from the LR04 stack (Lisiecki and Raymo, 2005). Red lines indicate directly dated wetland sediments. Black lines represented underlying sands. All uncertainty terms are at 1σ .

6.6 Northern Hemisphere (NH) insolation as a key control on amount of rainfall to the Nefud

The previous discussion on ages has attributed humid phases to warm marine isotope stages (MIS 5e, 7, 9, 11/13a) or sub-stages (e.g. MIS 5a), and suggests they may relate to NH insolation peaks during these periods. This inference is made on the basis that the northward expansion of the African monsoon or the enhanced activity of other tropical rainfall sources (e.g. Active Red Sea Trough or Tropical Plumes) is directly related to increased summer insolation (Prell and Kutzbach, 1987; Rossignol-Strick, 1983). However, it is important to discuss whether this assumption is justified moving back over the past 500 ka, as uncertainties on luminescence data beyond MIS 5 make it impossible to correlate lake development in the region to specific NH insolation peaks and even MIS sub-stages.

It is first worth looking at the timing of humidity during the Holocene Humid Period as this yields the most precisely dated records of increased humidity across the Saharo-Arabian desert belt. These records can be compared to the period of maximum NH summer insolation during the Holocene, and any lags between insolation maxima and regional humidity can be observed. The main phase of Holocene lake development at Jubbah dates to 8.6 ± 0.6 ka (Parton et al., 2018). Likewise, the onset of the main period lake development and grassland expansion at Tayma occurred between ca 8.6 – 8 ka cal BP though lake onset occurred at 9.2 ka (Dinies et al., 2015; Neugebauer et al., 2017). NH maximum summer insolation at 30°N occurred at ~11 ka (513.2 w/m^2) (Berger and Loutre, 1991). This suggests that Holocene humidity in the Nefud Desert lags behind NH insolation maxima by ~2.5 ka, which is a similar time period to the lag observed between sapropel S1 and NH summer insolation maxima (Lourens et al., 1996). Unfortunately, the resolution of dating from the Al Wusta Playa does not allow this interpretation to be extended directly into the western Nefud sand sea. However, dating of hearths at Alshabah which lies in the sand sea shows humans were present in the area during the mid-Holocene (6.5 ± 0.7 ka and 7.3 ± 0.9 ka) based on luminescence dating of hearths and ^{14}C dating of charcoal (Scerri et al., 2018a). This suggests that humans were able to

utilise the western Nefud Desert into the middle Holocene, which suggests some water availability during this period which lagged NH insolation maximum.

Moving back into the Pleistocene, uncertainties on the ages of lacustrine records in the Nefud are too large to test the association between NH summer insolation and humidity. However, U/Th dating on speleothem records that formed in response to a northward expansion of monsoon rainfall during MIS 5e can provide better precision. The most appropriate record to look at regarding this is Wadi Sannar Cave, Egypt which lies at a similar latitude to the Nefud and is argued to form in response to a northward expansion of the African monsoon (El-Shenawry et al., 2018). U/Th dating places speleothem formation, and therefore increased humidity, during MIS 5e to between 130.46 – 127.53 ka encompassing the maximum and minimum ages at 2σ uncertainty on the speleothem. This predates NH summer insolation maxima during MIS 5e which occurs at ~127 ka at 30°N (535.9 w/m²), thus suggesting humidity leads NH summer insolation maxima by 1 or 2 ka, in contrast to northern Holocene records within or close to the Nefud Desert. Interestingly, humidity at Wadi Sannur Cave during MIS 5e lags the insolation value of 513.2 w/m² (Berger and Loutre, 1991), by ~1 – 4 ka. This is a comparable lag to the Holocene. Consequently, this tentatively suggests humidity in the western Nefud Desert and northeast Africa lags insolation once it has passed a critical value of somewhere in the region of 513.2 w/m². Since both Holocene and MIS 5e humid periods in precisely dated records occur in close association with NH summer insolation peaks, it is reasonable to assume that this was the case moving backwards into the Middle Pleistocene.

6.7 Summary

This chapter has discussed the methodology and results of the luminescence dating undertaken within this thesis. Key points are:

- A combination of optically stimulated luminescence dating on coarse- and fine-grain quartz, and a single pIRIR₂₂₅ measurement on feldspar was used to construct a chronology of humid phases in the western Nefud Desert.

- Sampling targeted the aeolian sands which underlie carbonate/siliceous sediments, sands within carbonate/siliceous sediment and sands deposited via waterlain processes that overlie carbonate/siliceous sediment. In most cases at least two of these three sampling strategies was undertaken, enabling direct or bracketed ages of carbonate/siliceous deposits and therefore environmental humidity.
- Luminescence characteristics of quartz show they are prone to a high number of infrared (IR) depletion fails due to feldspar inclusions, consistent with previous research. Fine-grained quartz (4 – 11 μm) had a much better acceptance rate, as did pIRIR₂₂₅ analysis on feldspars.
- The ages show that carbonate/siliceous sediments formed during interglacial periods (e.g. MIS 5e, 7, 9 and 11/13) as well as interstadial periods (MIS 5a). These results are consistent with previous geochronological work in the western Nefud Desert (Rosenberg et al., 2013), though adds the first evidence for lake development during MIS 7. We also suggest humidity most probably occurred during periods of high northern hemisphere insolation based on existing evidence from climate models, however it is not possible to definitively confirm this due to uncertainties on ages.

The following chapters (7 to 12) will focus on the palaeoenvironmental reconstruction from each sedimentary sequence, presented in age order from youngest to oldest.

Chapter 7 – Al Wusta Playa palaeoenvironmental results

7.1 Introduction

The Al Wusta Playa is a recharge playa that lies in the modern-day depression of the Al Wusta basin on the southwestern edge of the Nefud Desert (N 27.42, E 39.40, ~925 msl) (Fig 7.1). Geochronological work at the site (Chapter 6) is poorly resolved, though shows that sediments related to wetter conditions (see description in this chapter) were deposited in the last ~20 ka and most likely during the Holocene. A single trench of 1.5 m depth was dug into the floor of the recharge playa, with the bottom of the base reaching consolidated white sands. A combination of bulk sedimentology and microfacies analysis was carried out in order to reconstruct the depositional environment that these sediments were deposited in.

7.2 Sedimentology

7.2.1 Bulk-sedimentology

The sedimentary sequence of the Al Wusta playa is split into 5 units measured from the base upwards (Fig 7.2). **Unit 1 (0 – 29 cm)** is composed of cemented white sands. **Unit 2 (29 – 68 cm)** consists of unconsolidated and well-sorted reddish sands. **Unit 3 (68 – 78 cm)** consists of silty sands with gravel clasts present. X-ray diffraction on this unit shows that calcite (8.2%), gypsum (5.3%) and birnessite (2.6%) are present while quartz was the dominant component (83.8%). **Unit 4 (78 – 116 cm)** contains sandy silts with gravel clasts present. **Unit 5 (116 – 149 cm)** contains horizontally laminated and poorly consolidated sands with some gravel inclusions.

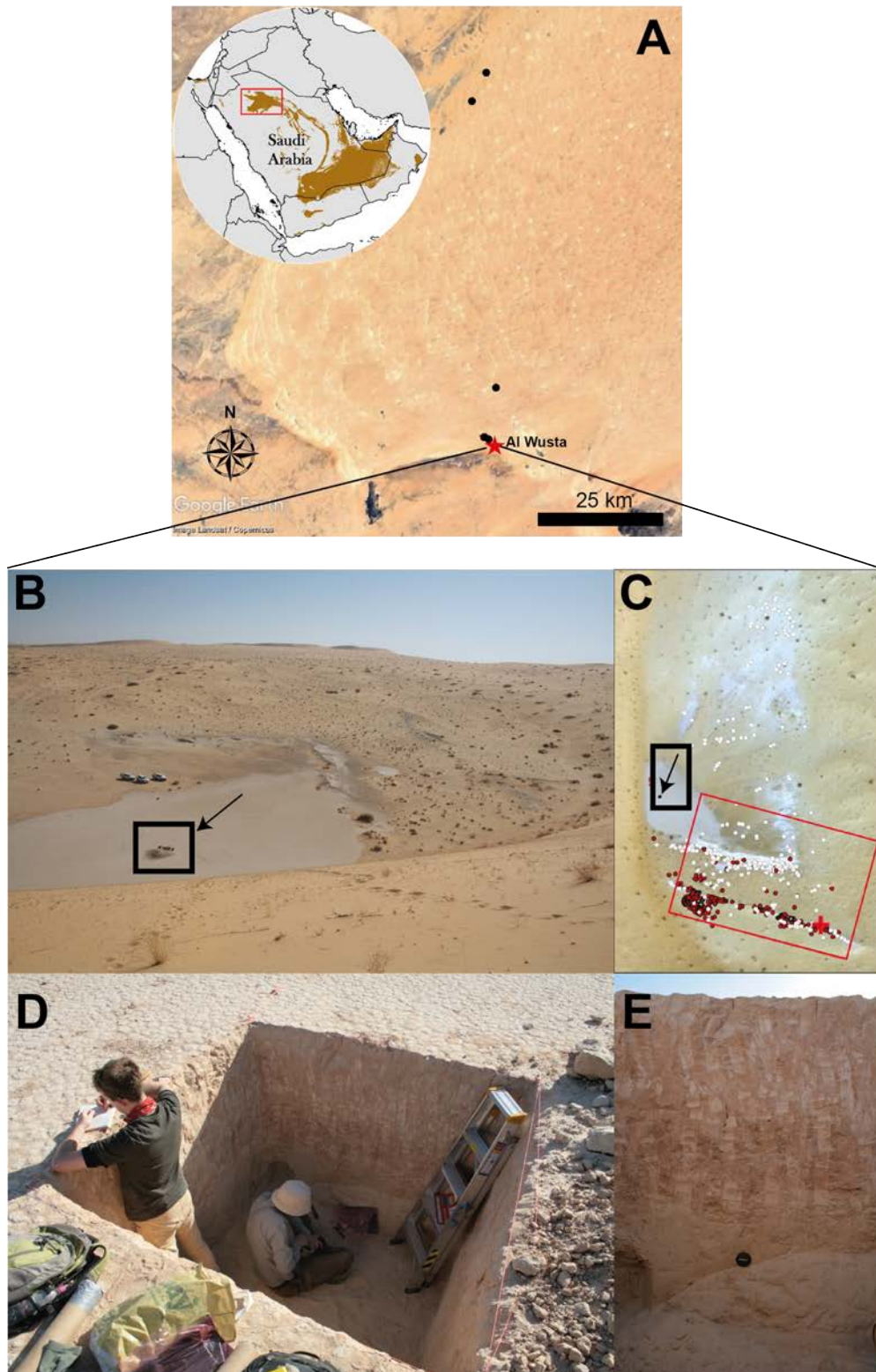


Figure 7.1 – Overview of the recharge playa within the Al Wusta interdunal basin. (A) Location of the Al Wusta basin (red star) in the western Nefud Desert. (B) Site picture taken from the top of the barchonoid dune facing eastwards towards the Al Wusta interdunal basin. Note the three cars for scale. The recharge playa occurs at the lowest point in the basin in the central and left hand portion of the picture. The trench dug into the playa is highlighted by a black square. (C) Overhead view of the Al Wusta basin, with the site of the trench dug in the recharge playa highlighted by a black rectangle and arrow. (D) Close up view of sediment and OSL sampling in the trench. (E) The 1.49 m sedimentary sequence of the Al Wusta playa. The camera cap is resting on a wind-sculpted feature into the cemented white sands (unit 1). These white sands are observed underlying a number of paleolakes across the western Nefud (Rosenberg et al., 2013).

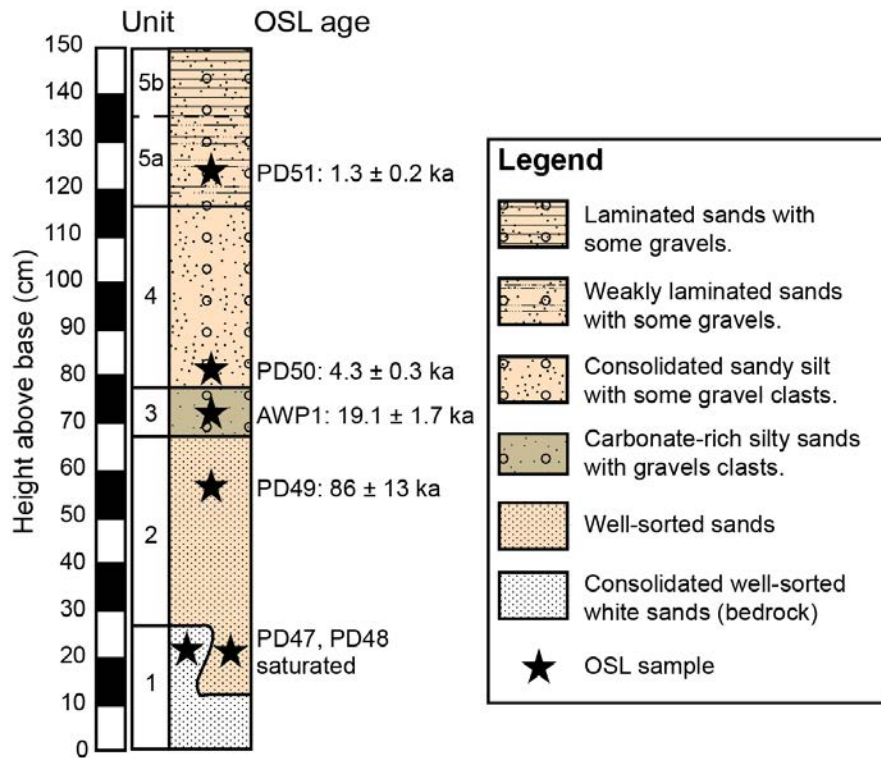


Figure 7.2 – Sedimentary sequence from the trench dug into the Al Wusta Playa. The base of the sequence (unit 1) is composed of white well-sorted sands that have been described beneath numerous palaeolake sequences across the western Nefud. There is a wind-sculpted erosional contact between units 1 and 2. OSL ages are presented, however the chronology is problematic.



Figure 7.3 – Close up image of unit 3. Bulk sedimentology shows this unit consists of silty sands with gravels and contains a small component of calcite, gypsum and birnessite. The microfacies of this unit is shown in Fig 7.4 panel B. Numerous gravel clasts are found within this unit and are highlighted by black circles. This unit represents the ‘wettest’ phase observed in the sedimentary sequence.

7.2.2 Microfacies analysis

A total of four samples for microfacies analysis were taken from the sedimentary sequence, with a single sample taken from units 2, 3, 4 and 5. The microfacies from unit 2 (60 – 62 cm above base) consists of fine to coarse sands and are finely coated by micrite, which acts as cement (see Fig 7.4, panel A). The microfacies from unit 3 (72 – 75 cm above base) contains silts to very coarse sands, while it is important to note that gravel clasts were present at the macroscale. The coverage of allogenic grains is less than all other units, though still high (~33 to ~50%). The matrix (groundmass) is composed of a fine-grained authigenic micrite (see Fig 7.4, B). The microfacies from unit 4 (83 – 86 cm) contains silts to coarse sands with gravel present at the macroscale. There is a greater grain/matrix ratio compared to the microfacies from unit 3, with more allogenic silts and sands relative to micritic matrix. Brecciated micritic intraclasts are also present (Fig 7.4, panel C). The microfacies from unit 5 (131 – 133 cm above base) consists of fine to coarse sands which are finely coated by micrite.

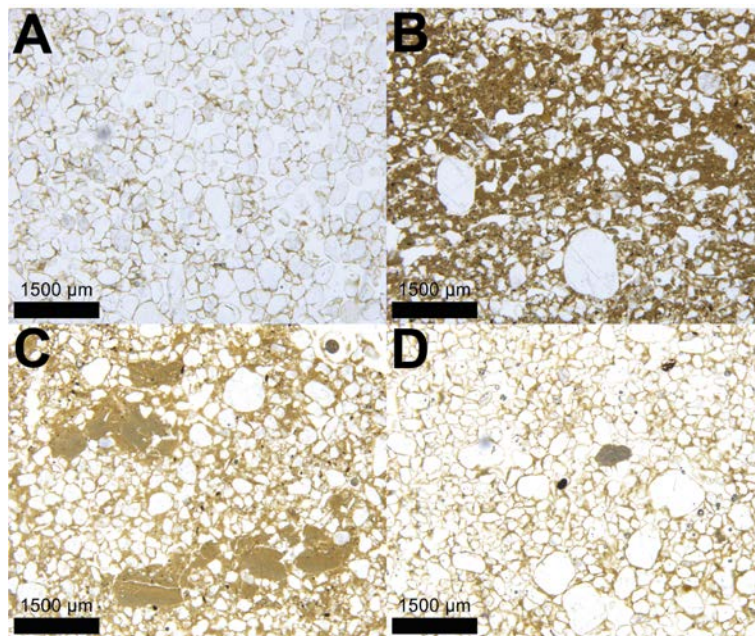


Figure 7.4 – Photomicrographs in plane-polarised light from the Al Wusta recharge playa. (A) 60 – 62 cm above base from unit 2. This microfacies shows tightly packed and well sorted fine to coarse sands coated by fine-grained micrite. (B) 72 – 75 cm above base from unit 3. The microfacies shows silts to very coarse sands embedded within a micritic matrix. (C) 83 – 86 cm above base from unit 4. This shows silts to coarse sands that are tightly-packed and lie within a micritic matrix. The grain-matrix ratio is much higher in this microfacies relative to the microfacies shown in panel B. Micritic intraclasts are present that are interpreted as rip-up marls, eroded from older carbonate beds in the basin and washed in to the playa. (D) 131 – 133 cm above base from unit 5. This microfacies shows tightly packed and well sorted fine to coarse sands coated by fine-grained micrite and is very similar to that shown in panel A.

7.3 Depositional model

The sedimentary evidence described above is used to construct a depositional model for the Al Wusta Playa sequence. Four main phases of sediment deposition are recorded. Unit 1 consists of well-cemented white sands, and these are consistent with descriptions of white sands that underlie numerous palaeolake sequences across the western Nefud (Rosenberg et al., 2013). This is interpreted as an ancient dune system (Rosenberg et al., 2013), and this is supported by the saturated luminescence signal (Chapter 6.4.1). Unit 2 consists of well-sorted fine to coarse reddish sands. These probably represent dune migration and aeolian sand deposition during an arid period.

Unit 3 consists of silty sands with gravel clasts present. Authigenic calcite is present in thin-section while XRD analysis shows that calcite (8.2%), gypsum (5.3%) and birnessite (2.6%) are present. This suite of sediments is indicative of deposition within a shallow ephemeral waterbody. Gravel clasts and sands were washed into the basin via sheet wash during flooding events, while the silt component is predominantly composed of authigenic calcite and gypsum. Authigenic calcite and gypsum were likely precipitated via the evaporitic concentration and evolution of ions within a shallow ephemeral waterbody where evaporation exceeds inflows into the basin. Alternatively, these minerals may have formed as an interstitial salt crust within the playa sediments where groundwaters, and the equilibrium deflation surface, would have been close to the surface due to higher ground water levels during a humid interval (Talbot and Allen, 1990). Ions would probably be provided into the basin via the chemical weathering of MIS 5 lake carbonates within the same basin (see Chapter 8).

Unit 4 contains silty sands with gravel clasts, and a similar depositional environment to the unit described above. This unit is differentiated from the unit below as it contains a lower proportion of silts, as is observed at the macroscale and is shown in thin-section (see Fig 7.4, panel C). It also contains brecciated micritic intraclasts, which are interpreted as rip up marls (see Fig 7.4 panel C). These were likely physically weathered from older marl deposits within the basin and transported into the playa during sheet wash events.

Unit 5 consists of weakly laminated to laminated sands with gravel present, with the upper section being friable. The laminated sands and gravel are consistent with deposition within a recharge playa, where surficial dune sands and gravel are transported into the basin via sheet flooding and ground waters lie well below the surface of the playa preventing the formation of evaporitic crusts. Such deposits typically produce flat sandy laminae capped by a mud drape as the flow dissipates (Talbot and Allen, 1990). As the sediment dries the surface is readily blown away, removing the fine-grained component (mud drape) but leaving sands and silts. This unit also reflects the present-day depositional environment within the Al Wusta basin.

7.4 Summary

The key points from this sedimentary sequence are:

- A 1.49 m trench was dug into the surface of the recharge playa that lies in the Al Wusta interdunal basin.
- This revealed a sedimentary sequence with five units that represent four main phases of deposition.
- Unit 1 represents an ancient dune system, as reflected by its well cemented nature and further supported by a saturated luminescence signal (see Chapter 6). Unit 2 reflects more recent aeolian dune activity, though luminescence dating from the base of this unit yields saturated luminescence signal demonstrating it is still of considerable antiquity. The uppermost section of unit 2 yields an age of 86 ± 13 ka when strict rejection criteria were applied for saturated aliquots (see Chapter 6.3.2.1).
- Units 3 and 4 reflect sedimentation in a shallow ephemeral water body, with unit 3 representing peak humidity. Gravel clasts reflect sheet flooding while the presence of authigenic calcite suggests that a shallow waterbody was present in which the mineral precipitated, likely via evaporitic enrichment. The presence of evaporites (gypsum) formed as the waterbody contracted or below the surface of the playa as an interstitial salt crust. Luminescence dating is poorly resolved

in this unit, and this may be a consequence of the presence of gypsum (Clark-Balzan et al., 2017).

- Unit 5 represents sedimentation within a recharge playa, and this is the present state of the deposit today.

Chapter 8 – Al Wusta palaeoenvironmental results

8.1 Introduction

The Al Wusta carbonate sedimentary sequence (site code: WNEF16_30) lies within an interdunal depression ~1.5 km from the southwestern edge of the Nefud Desert (N 27.42, E 39.40, ~925 msl). Geochronological work discussed in chapter 6 shows that the deposit relates to a humid phase during MIS 5a (Groucutt et al., 2018). The deposit itself consists of two E - W trending ridges of exposed carbonate-rich sediments that lie parallel to one another and dip gently towards the lee-side of the modern-day barchanoid dune (see Fig 8.1). It is not clear if these ridges are two independent features or if they are connected, though this is discussed briefly later in the chapter. The outer ridge extends for ~240 m, with the highest outcrop to the east at ~926 m ASL and lowest outcrop just above the current interdunal floor at ~918 m ASL (Fig 8.1). The inner ridge extends for ~120 m with the highest outcrop at ~918.5 m ASL and the lowest at ~918 m ASL (Fig 8.1). A single trench from the outer ridge (PD40) was focused on as part of this thesis. This was chosen as it had the most extensive sedimentary sequence in terms of thickness and number of units. A combination of bulk sedimentology, microfacies analysis and $\delta^{18}\text{O}$ and $\delta^{13}\text{C}$ analysis were undertaken to construct a depositional model. This analysis will then be compared to previous research undertaken as part of my Masters thesis (Clark-Wilson, 2016), along with diatom palaeoecology work was carried out by Dr. Wing Wai Sung as part of the Palaeodeserts research project.

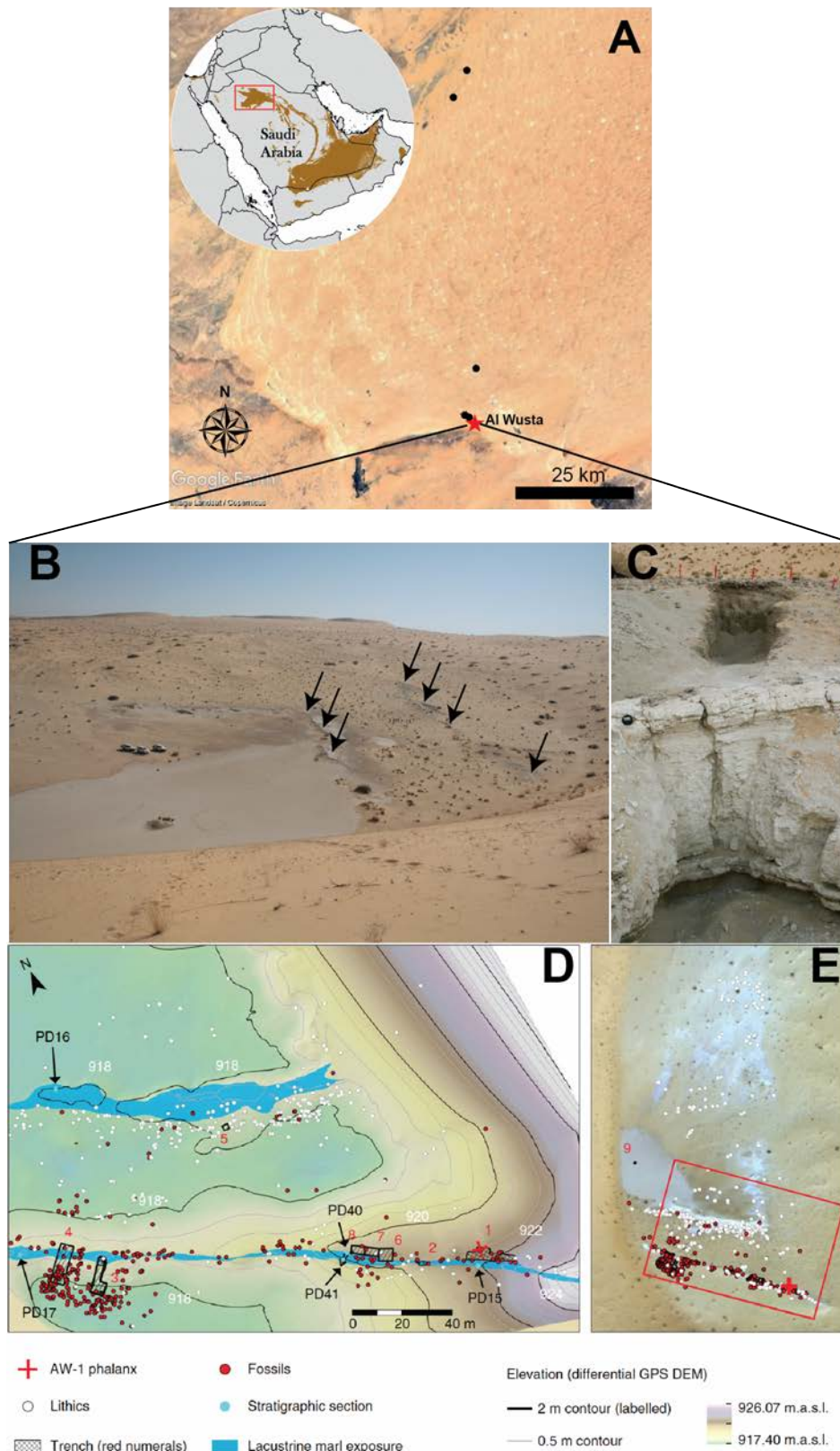


Figure 8.1 – Overview of the Al Wusta site. (A) Location of the Al Wusta basin (red star) in the western Nefud Desert. (B) Site picture taken from the top of the barchonoid dune facing eastwards towards the Al Wusta interdunal basin. Both the inner and outer marl ridges are visible in the right-hand portion of the image and are highlighted by black arrows. (C) The sedimentary sequence from trench PD40, the most extensive sequence at the site. (D) Topographic map of the interdunal basin with marl ridges highlighted in light blue, along with various labels for trench, fossil and lithic locations. (E) Overhead view of the interdunal basin with fossil and lithic locations marked. The area within the red rectangle represents the area shown in picture D. Images D and E from Groucutt et al. (2018).

8.2 Sedimentology of PD40

8.2.1 Bulk-sedimentology

The sedimentary sequence at Al Wusta is split into three units: 1) well-sorted loose sands; 2) fine-grained calcium carbonate rich marl; 3) crudely horizontally-laminated medium to coarse sands with gravel inclusions and contains calcitic rhizoliths. The sequence is measured from base of the carbonate-rich marls (Unit 2) upwards. The carbonate-rich marls of Unit 2 (0 – 100 cm) contains some variability. As such, this unit is split into four sub-units and these are characterised as follows.

Unit 2a (0 – 13 cm) contains light-grey fine-grained carbonate sediment interdigitated with darker, minerogenic bands towards the base (0 – 6 cm). This grades into homogenous fine-grained carbonate (6 – 10 cm) and is capped by a 3 cm sand-rich bed between 10 – 13 cm. Calcium carbonate content within this unit are 50% (0 cm) and 66% (10 cm) while X-ray diffraction analysis shows quartz and calcite are the only minerals present. Quartz is predominant in the lowermost sample at 0 cm (91.3% weight) while calcite is present (8.7% weight). Conversely, calcite quickly becomes dominant by 5 cm (84.7% weight) with quartz the only other mineral present. **Unit 2b (13 – 60 cm)** consists of homogenous fine-grained carbonate that is well consolidated. There is evidence for weak horizontal laminations in the carbonate between 13 – 30 cm and at ~50 cm. Calcium carbonate content through this unit ranges from 61 – 87%. **Unit 2c (60 – 88 cm)** consists of friable fine-grained carbonates with some evidence for weak laminations. **Unit 2d (88 – 100 cm)** consists of structurally consolidated, well-cemented fine-grain carbonate with small tubular voids. Calcium carbonate content in this unit drops to 46% at the very top (100 cm) of the sequence.

Following the cessation of carbonate-rich marl sedimentation, **Unit 3 (100 – 181 cm)** is composed of crudely laminated sands with rip-up carbonates, occasional gravel clasts, shells of *Melanoides tuberculata* and *Planorbis* sp and sand-rich calcitic rhizoliths.

Table 8.1 – X-ray diffraction results from trenches PD40. Only two samples were taken for analysis from Unit 2a, as this unit is novel compared to those observed in Clark-Wilson (2016). The results of the XRD analysis from PD15, PD16 and PD17 are presented in Table 8.4.

Trench	Height above base (cm)	Unit	Calcite (%)	Quartz (%)	Gypsum (%)	Halite (%)
PD40	1	2a	21	79	0	0
	5	2a	96	4	0	0

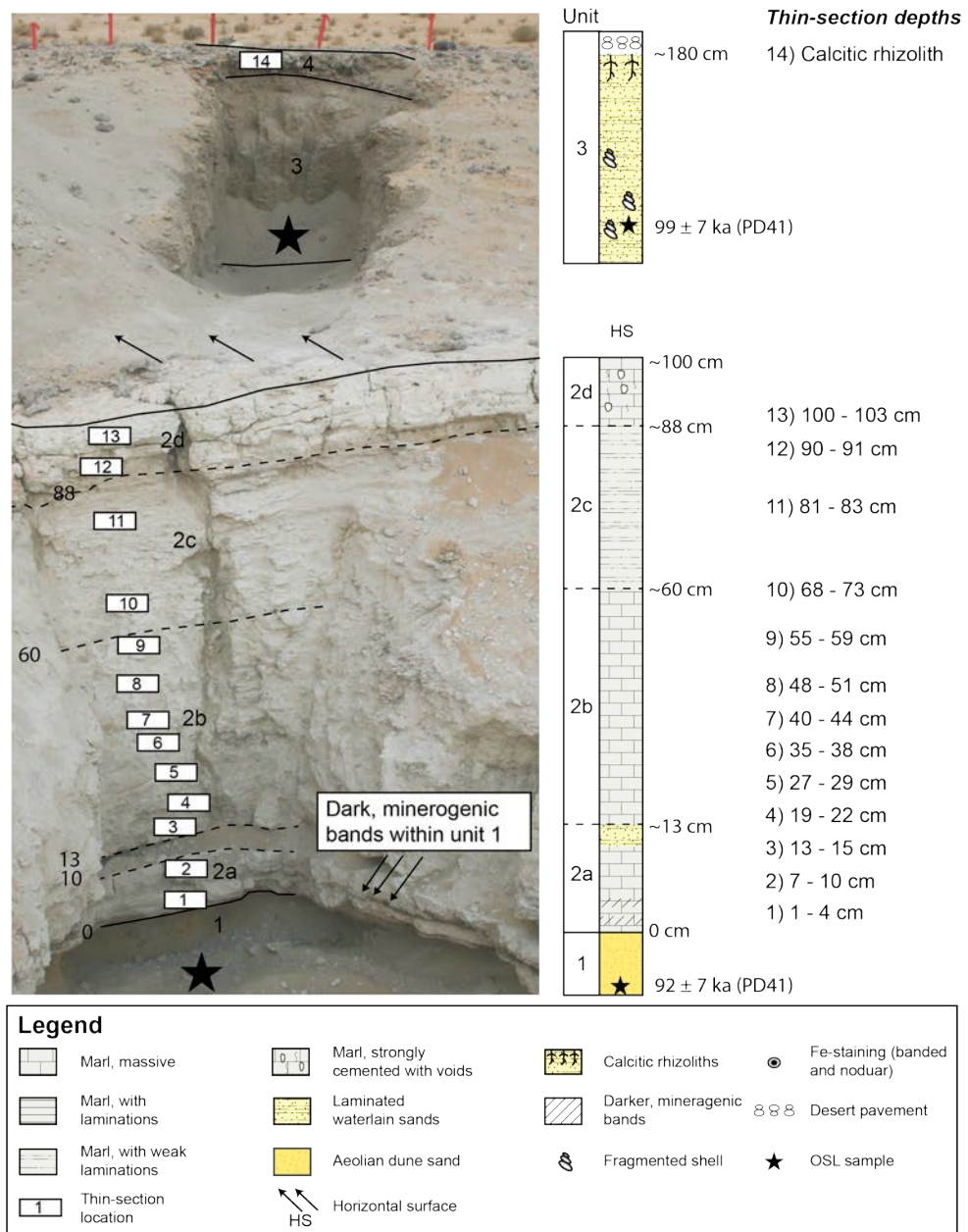


Figure 8.2 – Sedimentary sequence from trench PD40. Black stars represent the approximate position of luminescence samples, unit boundaries are outlined by a solid black line while sub-units are separated by a dashed black line. Thin-section sample locations through the sequence are also outlined, with sample depths shown on the right-hand side of the figure.

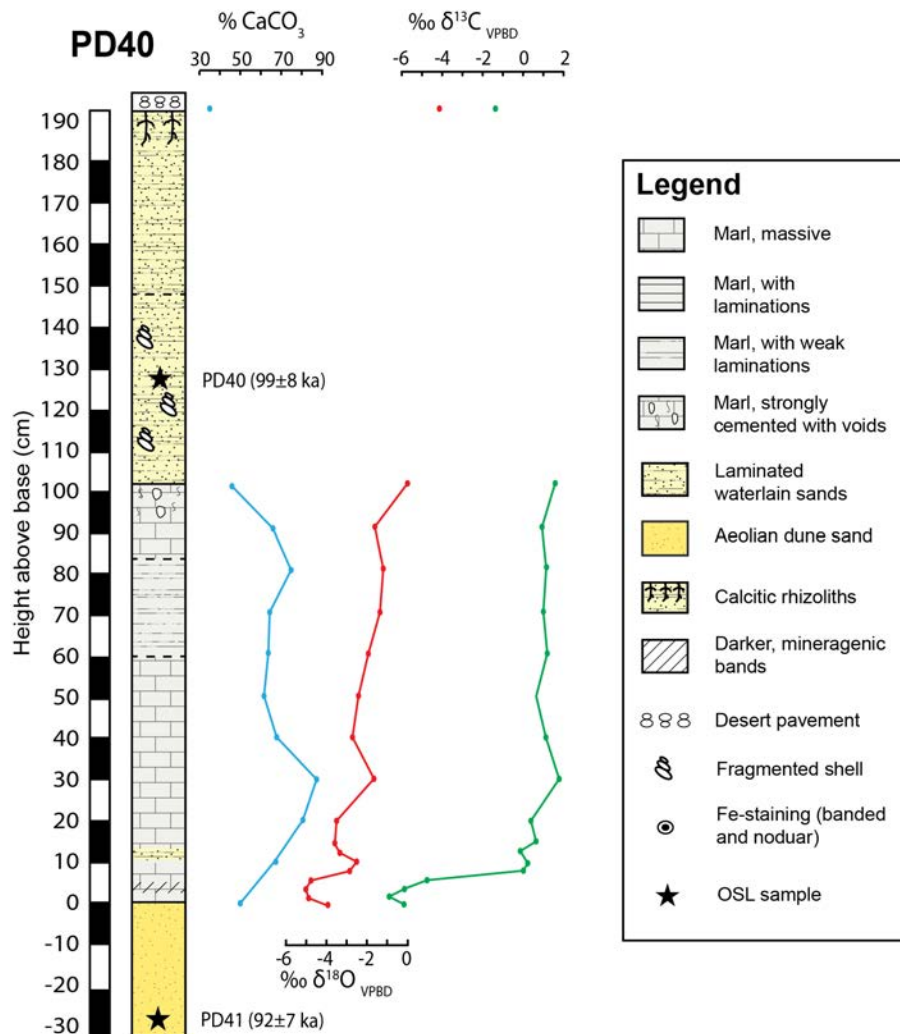


Figure 8.3 – Sedimentary log of PD40 along with CaCO_3 (blue), $\delta^{18}\text{O}$ (red) and $\delta^{13}\text{C}$ (green). Luminescence ages are also highlighted, with OSL sample locations marked by black stars. Note that the age of this deposited is constructed using a Bayesian model which includes these luminescence ages along with uranium series and uranium series plus electron spin resonance dates on fossils (see section 6.4.3).

8.2.2 Microfacies analysis

A total of 14 samples for microfacies analysis were taken from the fine-grained carbonate rich marls (Unit 2) at PD40. Microfacies analysis demonstrates that microstructure and groundmass of the sediments across all trenches are comprised of either homogenous microsparite (Fig 8.4, panel C) or weakly laminated microsparite/micrite (Fig 8.4, panel B). Allogenic sand and silt grains are rare throughout the sequence with typical coverage of between 2 – 5% (see Fig 8.4). However, allogenic grains increase noticeably at the end of the sequence (PD40 100 - 103 cm) where

coverage rises to 33%. Biogenic material is rare through the majority of the sequence. Shell fragments, unidentifiable to species level, are rare or non-existent in the first 90 cm of the sequence. There is a small rise in frequency of shell fragments in the final thin-section of the PD40 sequence at 100 cm. Root remains that display cellular preservation are typically rare but more frequent at 40 – 44 cm and 90 – 91 cm (see Fig 8.4, panel C), while amorphous organics occur at a low-level through the sequence. Sponge-spicules are highly concentrated in two bands in the lowermost thin-section in the sequence (Fig 8.4, panel A) and are present at a low concentration through the rest of the sequence. Rare to light etching of quartz grains is present through the sequence, while sparite infills along with rare planar voids are present in thin-sections between 19 – 40 cm. A yellow iron-hypocoating is present at 50 cm. Aside from this, no other iron nodules or iron staining are observed and there is no obvious trend in any feature moving upwards through the sequence, with the exception of allogenic sand/silt grains. All microfacies are shown in Appendices 2.

8.3 $\delta^{18}\text{O}$ and $\delta^{13}\text{C}$ analysis of PD40

$\delta^{18}\text{O}$ values range from -5.02‰ (4cm) to -0.09‰ (100 cm), with mean and median values of -2.81‰ and -2.74‰ respectively. The isotope stratigraphy can be split into three zones on the basis of $\delta^{18}\text{O}$ values. The first zone lies between 0 – 6 cm with $\delta^{18}\text{O}$ values between -3.98‰ and -5.02‰ with a mean value of -4.69‰. The second zone, between 8 – 20 cm, display slightly more positive $\delta^{18}\text{O}$ values between -2.46‰ and -3.63‰ with a mean of -3.19‰. The final zone, between 30 – 100 cm, displays more positive values again between -2.74‰ and -0.09‰, with a mean of -1.63‰. The final $\delta^{18}\text{O}$ value from the calcitic rhizolith that caps the sequence is 1.58‰. There is a trend of $\delta^{18}\text{O}$ enrichment throughout the sequence with the most depleted values occurring in zone 1 and the most enriched at the end of zone 3 (see Fig 8.3). $\delta^{13}\text{C}$ values of the marls range from -6.57‰ (2cm) to 1.75‰ (30 cm), with mean and median values of -0.75‰ and 0.61‰ respectively. The difference between the mean and median values suggests the mean is skewed towards negative values by outliers. These occur in zone 1 (between 0 – 6cm) where $\delta^{13}\text{C}$ values lie between -4.79‰ and -6.57‰ with a mean value of -5.75‰. These correspond with the most depleted $\delta^{18}\text{O}$ values. Zone 2 (8 – 20 cm) $\delta^{13}\text{C}$ values lie

between 0.62‰ and -0.12‰ with a mean value of 0.22‰. Zone 3 (30 – 100 cm) $\delta^{13}\text{C}$ values lie between 0.61‰ and 1.75‰ with a mean value of 1.14‰. While there is a trend in enriching values over the first 30 cm of the sequence, there is no clear trend within zone 3 between 30 – 100 cm (see Fig 8.3).

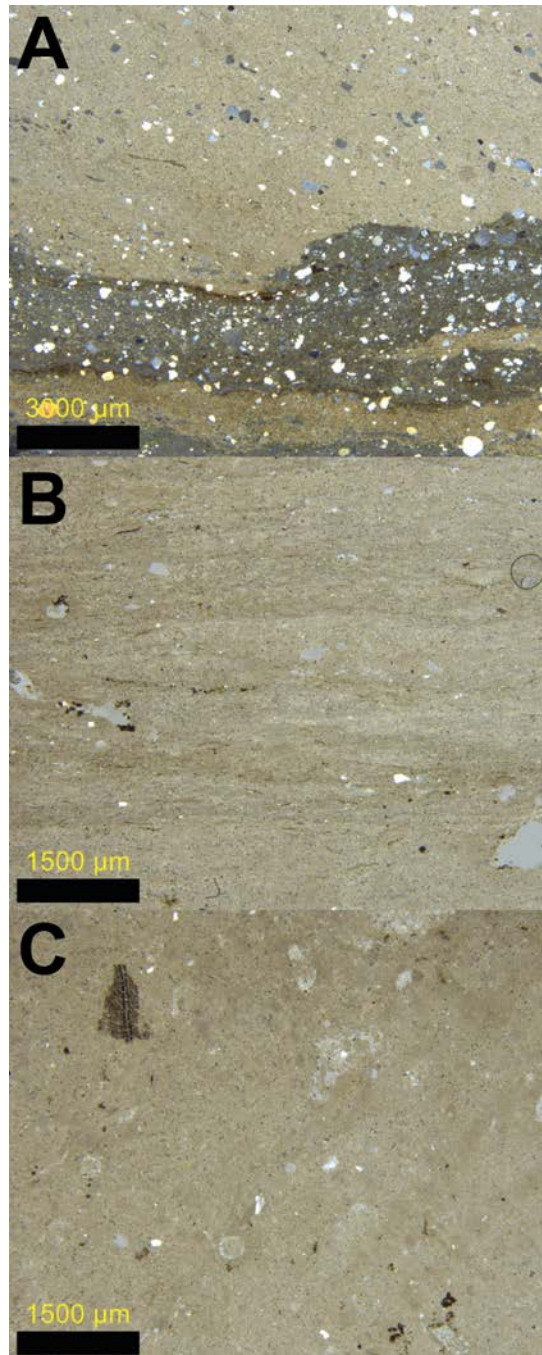


Figure 8.4 – Photomicrographs in cross-polar (XPL) light of thin-sections from trench PD40. (A) 1 – 4 cm above base from Unit 2a, at the very onset of the carbonate-rich marls. The microfacies consists of fine-grained homogenous microsparite with a dark band that consists of densely packed sponge spicules and allogenic grains. (B) 19 – 22 cm above base. This microfacies shows subtle laminations in crystal size (microsparite and micrite) that pinch in and out (lenticular). (C) 40 – 44 cm above base. This microfacies is very similar to that of 19 – 22 cm, though is just homogenous microsparite. There is evidence for organic remains with cellular preservation in the top left portion of this panel.

Comparing the bulk $\delta^{18}\text{O}$ and $\delta^{13}\text{C}$ isotopic data generated from the Al Wusta site produces an R^2 coefficient of 0.67 with a p-value = 5.3×10^{-05} (Fig 8.5, B). However, this value is skewed by zone 1 of PD40 as the $\delta^{18}\text{O}$ and $\delta^{13}\text{C}$ values are distinctly depleted when compared to the rest of the dataset. This implies they formed in a different hydrological environment with high levels of throughflow at the onset and end of humidity (Talbot, 1990). When removing these samples from the analysis along with the calcitic rhizolith sample, the R^2 coefficient for PD40 is 0.53 with a p-value of 4.65×10^{-3} (Fig 8.5, A).

Table 8.2 - Descriptive statistics for $\delta^{18}\text{O}$ values of lake carbonates at Al Wusta, including trenches PD15, PD16 and PD17 from Clark-Wilson (2016). With the exception of PD40 – Z1, the $\delta^{18}\text{O}$ values from all sequences are similar. *Excluding rhizolith sample.

Zone	Height above base (cm)	N	Mean (‰)	Median (‰)	SD (1 σ) (‰)	Min (‰)	Max (‰)	Range (‰)
PD40 - Z1	0 - 6	4	-4.69	-4.88	0.48	-5.02	-3.98	1.03
PD40 - Z2	8 - 20	5	-3.19	-3.40	0.51	-3.63	-2.46	1.17
PD40 - Z3	30 - 100	8	-1.63	-1.65	0.81	-2.74	-0.09	2.65
PD40 – all marls*	N/A	17	-2.81	-2.74	1.42	-5.02	-0.09	4.93
PD40 - rhizolith	Unit 3	1	N/A	N/A	N/A	1.58		N/A
PD15	N/A	5	-2.25	-2.33	0.42	-2.79	-1.66	1.13
PD16	N/A	8	-2.18	-2.26	0.94	-3.55	-0.68	2.86
PD17	N/A	4	-2.28	-2.24	0.11	-2.45	-2.20	0.25
All marls*	N/A	34	-2.53	-2.40	1.13	-5.02	-0.09	4.93

Table 8.3 - Descriptive statistics for $\delta^{13}\text{C}$ values of lake carbonates including trenches PD15, PD16 and PD17 from Clark-Wilson (2016). These follow the same zones at the $\delta^{18}\text{O}$ data. Note that the large range in PD16 is skewed by the uppermost sample which has a value of -5.24‰. When excluding this value the range at PD16 is 1.71‰. As with the $\delta^{18}\text{O}$ data, the $\delta^{13}\text{C}$ values are similar across all trenches.

Zone	Height above base (cm)	N	Mean (‰)	Median (‰)	SD (1 σ) (‰)	Min (‰)	Max (‰)	Range (‰)
PD40 - Z1	0 - 6	4	-5.75	-5.81	0.73	-6.57	-4.79	1.78
PD40 - Z2	8 - 20	5	0.22	0.21	0.29	-0.12	0.62	0.74

PD40 - Z3	30 - 100	8	1.14	1.1	0.35	0.61	1.75	1.13
PD40 – all marls	N/A	17	-0.75	0.61	2.91	-6.57	1.75	8.32
PD40 - rhizolith	Unit 3	1	N/A	N/A	N/A		-1.12	N/A
PD15	N/A	5	0.66	0.94	0.76	-0.69	1.13	1.82
PD16	N/A	7	0.04	0.73	2.20	-5.24	1.87	7.11
PD17	N/A	4	1.16	1.27	0.82	0.17	1.94	1.77
All marls	N/A	34	-0.13	0.79	2.4	-6.57	1.94	8.51

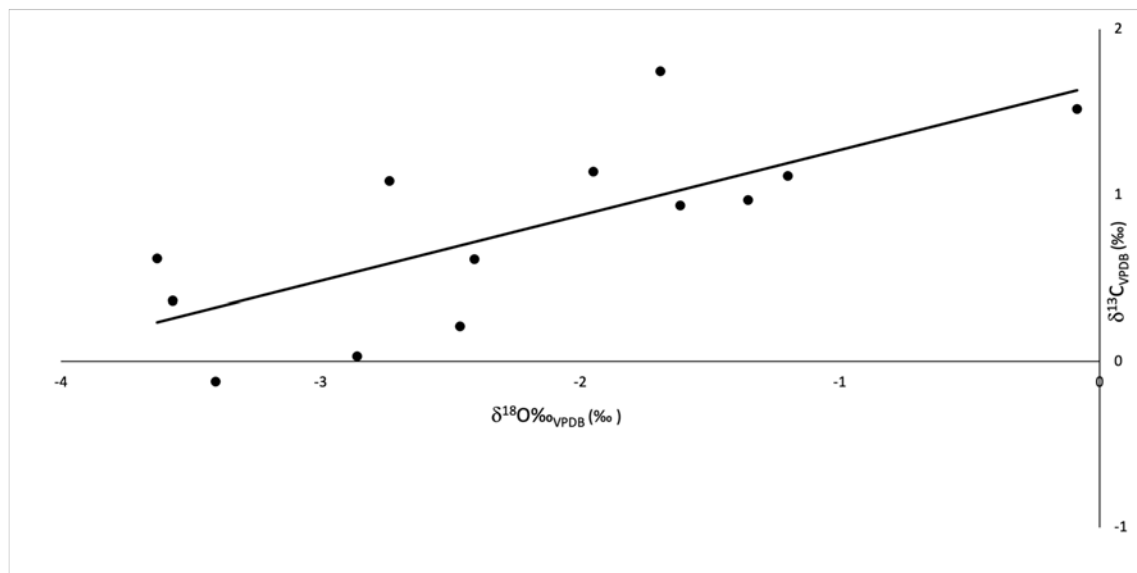


Figure 8.5 – Covariation between $\delta^{18}\text{O}$ and $\delta^{13}\text{C}$ at PD40 excluding zone 1. The R^2 value is 0.53 with a p -value of 4.27×10^{-3} .

8.4 Depositional model for PD40

The sedimentary evidence described above is used to construct a depositional model for PD40. Three main phases of sediment deposition are recorded at the site. Unit 1 consists of loose, well-sorted sands and represents dune migration and aeolian sand deposition during an arid period. Unit 2 consists of fine-grained carbonate-rich marls and represents the development of an interdunal lacustrine basin in which carbonate was precipitated. Unit 3 consists of crudely horizontally bedded medium to coarse sands with gravel inclusions, shells of *Melanoides tuberculata* and *Planorbis* sp, and calcitic

rhizoliths formed. This is indicative of in-washing sands into the basin via sheet wash, following the desiccation of the lake body. The calcitic rhizoliths within this unit are organosedimentary structures that preserve root structures (Klappa, 1980) and reflect fully terrestrial sedimentation at the very end of the sequence.

Multi-proxy palaeoenvironmental analysis of the carbonate-rich marl sediments (unit 2) identifies three subtly different depositional phases during the existence of the lake basin. Unit 2a (0 – 13 cm) represents a dynamic and shallow lake system at the inception of a humid phase. Over the initial 6 cm of the unit the sediments consist of fine-grained carbonate interdigitated with mineral-rich beds and dense accumulations of sponge spicules (0 – 6 cm). The initial thin-section from 1 – 4 cm contains a homogenous microsparite groundmass but is punctuated by two, sand-rich black bands (in XPL light) (see Fig 8.4 panel A). The black colour in XPL light is caused by a dense accumulation of isotropic sponge spicules. Furthermore, the CaCO₃ content at this level (0 cm) is only 50% while XRD shows quartz is dominant. These features probably reflect periods of landscape instability at the onset of a pluvial phase. Here heavy rainfall events combined with limited vegetative cover in the landscape lead to large input of poorly stabilised allogenic sands/silts into the lake basin. This subsequently increased the silica content of waters leading to high accumulations of sponge spicules. The $\delta^{18}\text{O}$ and $\delta^{13}\text{C}$ values from the initial 6 cm of the sequence also reflect a more dynamic lake system, as they are more negative than values from the rest of the sequence with mean values of -4.69‰ ($\delta^{18}\text{O}$) and -5.75‰ ($\delta^{13}\text{C}$). Such negative values most likely reflect rapid throughflow and limited residence time of waters, with little time for the isotopic content of water to be affected by evaporitic enrichment ($\delta^{18}\text{O}$) or equilibrium with atmospheric CO₂ ($\delta^{13}\text{C}$) (Talbot, 1990).

The lake then moves towards a shallow, perennial lake that is stable (Alonso-Zarza, 2003). This is reflected by the homogenous microsparite with sparse and random distribution of medium silt to medium sand sized allogenic material between 6 – 10 cm. The higher CaCO₃ content of 66% (10 cm) reflects the greater proportion of authigenic material, while $\delta^{18}\text{O}$ and $\delta^{13}\text{C}$ both move towards more positive values (8 cm, 10 cm).

The latter probably reflects slower throughflow and an increased residence time of waters in the lake basin leading to increased evaporitic enrichment of the $\delta^{18}\text{O}$ and the $\delta^{13}\text{C}$ moving into equilibrium with atmospheric CO_2 (Talbot, 1990). The final phase of instability in the carbonate sequence is reflected by a ~3 cm thick sand-rich bed that caps Unit 2a. This reflects a large input of allogenic material into the basin. It is not clear whether this represents a single storm event or a brief deterioration in climate where there was a lowering of the lake level and a move towards waterlain sand sedimentation. $\delta^{18}\text{O}$ and $\delta^{13}\text{C}$ values either side of this sand-bed reflect values consistent with those between 8 – 100 cm, as opposed to the initial 6 cm where negative values were observed. This suggests lake water throughflow did not increase and the sand bed may relate to a single storm event.

Unit 2b (13 – 60 cm) and Unit 2c (60 – 88 cm) differ slightly in terms of their macroscale sedimentology, with the latter being more friable. However, multi-proxy analysis demonstrates that they reflect the same depositional environment and will therefore be described together. These units reflect a stable, shallow and perennial freshwater lake system. $\delta^{18}\text{O}$ and $\delta^{13}\text{C}$ isotopic data through this unit suggests that deposition occurred in a non-evaporitic, open, freshwater lake. There is positive covariance between carbon and oxygen isotope ratios with R^2 coefficient of 0.51 (for samples from Unit 2b and 2c). However, this lies short of the 0.7 value which is indicative of closed, evaporitic systems (Talbot, 1990). This coupled with a low range in $\delta^{18}\text{O}$ (1.87‰) indicates that lake systems had inflows and outflows (i.e. hydrologically open) with limited evaporative concentration (Talbot, 1990). This interpretation is supported by XRD and diatom analysis undertaken in previous research (see section 8.5). Microfacies analysis through these units shows microfacies typical of sedimentation within a shallow but perennial water body (Fig 8.4). Microfacies are predominantly characterised by homogenous microsparite or faintly and discontinuously laminated microsparite/micrite and have no evidence for pedogenic alteration or desiccation (see Fig 8.4). Homogenous microsparite is indicative of sedimentation in a shallow oxygenated environment where sediment is mixed via surface winds and/or bioturbation in the epilimnion (Wright, 1990). There is a lack of any pedogenic or

desiccation features in the microfacies, suggested that the lakebed was not subaerially exposed and that the lake itself was perennial (Alonso-Zarza, 2003).

The final phase of carbonate deposition is represented by Unit 2d (88 – 100 cm). This suggests deposition occurred in a slightly shallower near shore setting in the littoral zone. The microfacies in this unit does not differ from the units below, but the macroscale is characterised by mechanically strong, well-cemented marls with small tubular voids, low CaCO₃ content relative to the rest of the sequence (65% at 90 cm, 46% at 100 cm), greater frequency of shell fragments in thin-section, and a high allogenic sand/silt input. The tubular voids reflect traces of rooted vegetation, as does the well-cemented nature of the carbonate as calcite precipitation is concentrated around macrophyte roots (Wright, 1990). The rise in allogenic sands and decrease in CaCO₃ content reflect the shift in balance between authigenic and allogenic sedimentation. Such a shift may have been caused by: (1) progressive sedimentation causing the waterbody to contract causing the lake edge and associated siliclastic inwash to move closer to the site of sedimentation; (2) local vegetation decreasing at the lake edges and in the local environment in response to increasing environmental aridity, removing sediment buffers and increasing sediment availability from the landscape. The final $\delta^{18}\text{O}$ value from the carbonate sequence (100 cm) is also the most positive (-0.09‰), probably highlighting increased evaporitic enrichment of the waterbody as it desiccated. Evaporites are still negligible suggesting that the waterbody remained fresh.

8.5 Comparison of PD40 with previous research at Al Wusta

The new data presented above supports previous bulk-sedimentology, microfacies and stable isotope analysis undertaken on the carbonate-rich marls in Clark-Wilson (2016) and diatom analysis undertaken in Groucutt et al. (2018). These analyses focused on shorter sedimentary sequences from PD15 and PD17 (outer ridge) and PD16 (inner ridge) (see Fig 8.1), which suggested that these sediments were deposited in a shallow, freshwater and perennial lake. Given that PD15 and PD17 originate from the same carbonate ridge as PD40, the relationship between these sedimentary sequences and PD40 is clear (see Fig 8.2). The relationship between the inner ridge where PD16 was

recorded is less clear. However, micromorphological and isotopic affinities between this sequence and those from the outer ridge strongly suggest they formed within the same water body.

Bulk sedimentology from PD15, PD16 and PD17 shows these sequences consisted of carbonate-rich marls with CaCO₃ content varying between 49 – 80%, which is consistent with PD40. XRD analysis from these trenches demonstrated that calcite is dominant (92 – 97%) with negligible levels of quartz (1.4 – 3.5%) (Table 8.4). Evaporitic minerals (gypsum and halite) formed via the evaporitic concentration and evolution of ions within lake waters during phases where evaporation exceeds inflows into the basin are also present at low levels (0.2 – 4.7%). These XRD data are consistent with sediment formation under freshwater conditions where recharge dominates over evaporation, consistent with isotopic data from PD40. No further XRD was undertaken on PD40, with the exception of two samples from the base of the sequence, due to the sufficient results presented in Clark-Wilson (2016) and the clear relationship between PD15 and PD17 with PD40.

Table 8.4 – X-ray diffraction results from all trenches across Al Wusta (Clark-Wilson, 2016). Calcite is dominant throughout the sequence with the exception of 1 cm above base at PD40 where quartz is dominant. Minerals formed via evaporitic concentration of ions within the lake body are <5% in all samples.

Trench	Height above base (cm)	Unit	Calcite (%)	Quartz (%)	Gypsum (%)	Halite (%)
PD15	10	2	93.9	3.5	1.6	1
	30	2	92.4	2	0.8	4.7
	40	2	96.7	1.7	0.7	0.9
	50	2	97.4	1.8	0.7	0.2
PD16	30	2	95.9	2.2	1.5	0.3
	40	2	96.6	1.7	1.4	0.3
	80	2	97.3	1.4	1.1	0.2
PD17	20	2	93.8	3.3	1.3	1.6
	30	2	96.7	1.8	0.9	0.6
	40	2	87.3	11	0.7	1
PD40	1	2a	21	79	0	0
	5	2a	96	4	0	0

Microfacies from trenches PD15, PD16 and PD17 are dominated by homogenous microsparite with rare allogenic sand/silt grains and rare evidence of organic remains. There is no evidence for pedogenesis or desiccation (Groucutt et al., 2018). This is consistent with microfacies from PD40, and supports the interpretation of sedimentation in a shallow, oxygenated but perennial environment where sediment is mixed via surface winds and/or bioturbation in the epilimnion (Wright, 1990).

Stable isotope analysis yields indistinguishable $\delta^{18}\text{O}$ and $\delta^{13}\text{C}$ values between trench PD40 and the other trenches (see Tables 8.2 and 8.3), though the depleted values observed in zone 1 at PD40 (0 – 6 cm) are not observed in any other sequence. This suggests that the initial onset of carbonate sedimentation was either not present at the other trenches or was not sampled due to a lower sampling resolution. Taking the $\delta^{18}\text{O}$ and $\delta^{13}\text{C}$ values from PD15, PD16 and PD17 together yields an R^2 value of 0.24 ($n = 17$). This is lower than PD40 but remains consistent with the observation that covariance is not significant. Combining the isotopic data from all sequences yields an R^2 value of 0.59 ($n = 34$) and an R^2 value of 0.19 when excluding zone 1 from PD40. Ranges in $\delta^{18}\text{O}$ are $<5\text{‰}$ across all sequences. This evidence supports the bulk sedimentology analysis that shows recharge dominated over evaporation within the lake at Al Wusta.

Diatom analysis was not undertaken on PD40 but was on from trenches PD15 (outer ridge) and PD16 (inner ridge). This analysis supports the XRD and isotope data discussed above and demonstrates that lake waters were fresh (Groucutt et al., 2018). PD15 is divided into three significant zones (Fig 8.6). Zone 1 (basal unit) contains a higher proportion of planktonic species (e.g. *Lindavia rossi*, *Cyclotella krammeri* and *Lindavia ocellata*) and this is reflected in a high planktonic: benthic ratio. Deeper water conditions are inferred from this assemblage. Zone 2 (10 – 20 cm) reflects a change in species from mainly planktonic to an increase in benthic taxa (e.g. *Cymbella affinis* and *Nitzschia angustata*) and periphytic taxa (*Staurosirella lapponica* and *Ulnaria ulna*). This assemblage probably reflects a shallowing in water levels which then remain low through zone 3. The dominant taxa in zone 3 (20 – 40 cm) are *Aulacoseira italica* (periphytic/tychoplanktonic) and *Aulacoseira granulata* (planktonic). Both taxa imply

that lake levels were shallow (Verschuren et al., 2000), a few metres in depth and turbulent (Chalié and Gasse, 2002).

PD16 is also split into three zones (Fig 8.7). The dominant taxa in the first zone are *Stephanodiscus* and *Aulacoseira*, whilst the second zone shows a large decrease in the tychoplanktonic *Aulacoseira italica*, and a subsequent rise in the proportion of benthic taxa. The planktonic: benthic ratio and habitat summary for these zones are indicative of lower water levels. Zone 3 sees a rise in planktonic and tychoplanktonic species such as *Lindavia rossi* and *Cyclotella krammeri*, indicating higher water levels. A key point is that all species found, except for *Epithemia argus*, are freshwater taxa, thus indicating that waters were fresh. Diatom preservation in PD17 was too poor for analysis.

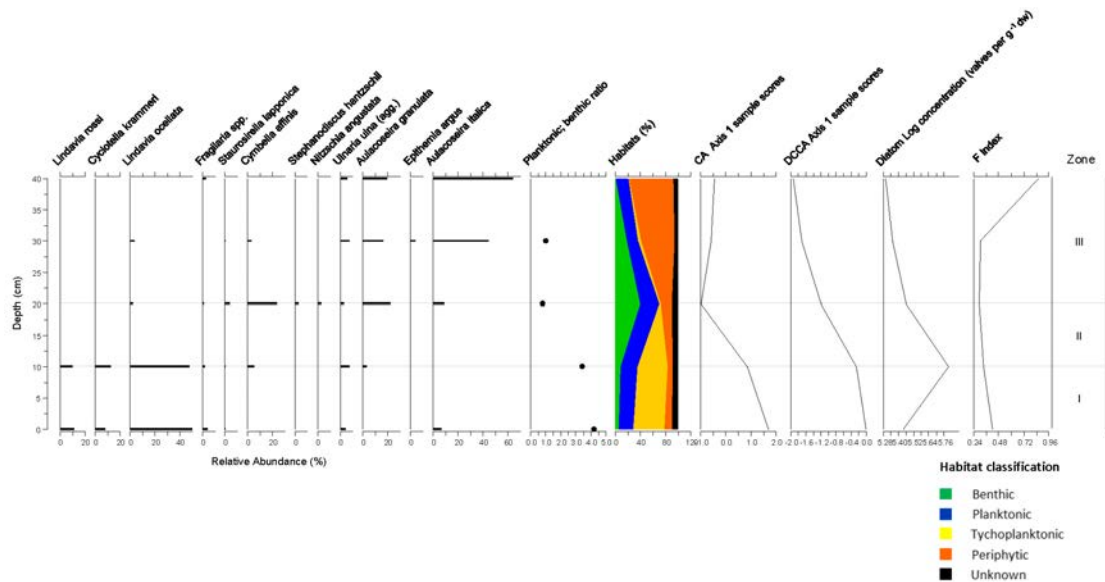


Figure 8.6 - Summary diagram of diatom assemblage from trench PD15, produced by Wing-Wai Sung. All taxa with relative abundances of $\geq 3\%$ are shown. The diatoms are ordered according to their weighted averaging distribution and divided up into assemblage zones derived from the optimal-sum-of-squares partitioning using the programme ZONE (Lotter and Juggins, 1991; unpublished). Statistically significant zones were deduced by comparison with the Broken-stick model using the program BSTICK version 1 (Bennett, 1990).

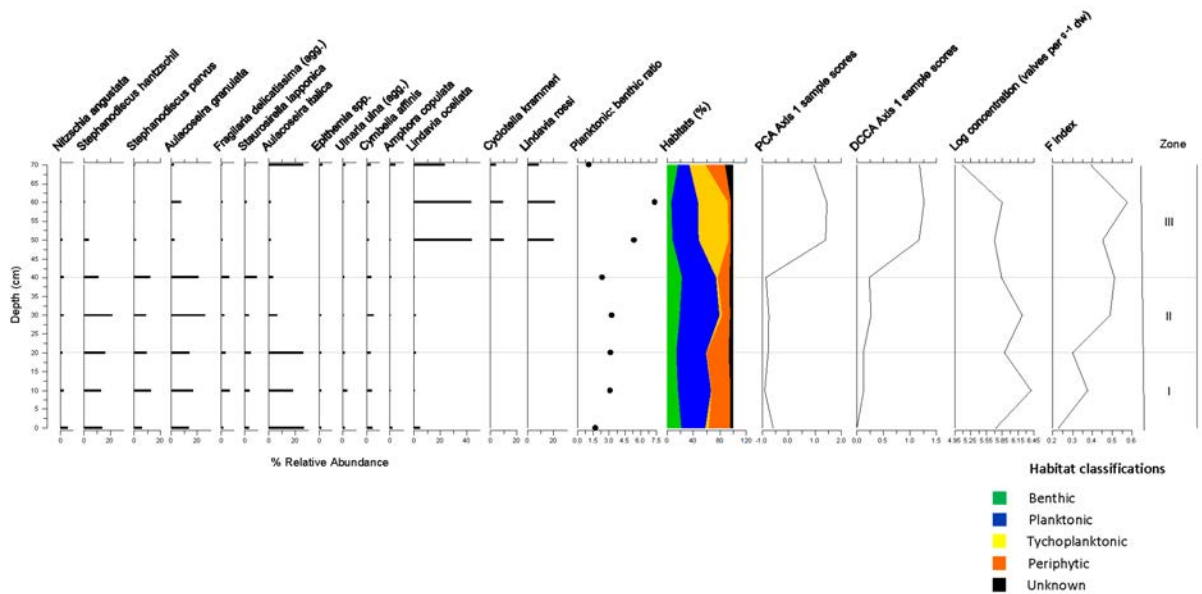


Figure 8.7 - Summary diagram of diatom assemblage from trench PD16, produced by Wing-Wai Sung. All taxa with relative abundances of $\geq 3\%$ are shown. The diatoms are ordered according to their weighted averaging distribution and divided up into assemblage zones derived from the optimal-sum-of-squares partitioning using the programme ZONE (Lotter and Juggins, 1991; unpublished). Statistically significant zones were deduced by comparison with the Broken-stick model using the program BSTICK version 1 (Bennett, 1990).

The microfacies and diatom assemblages of the carbonate-rich marls are consistent with a shallow waterbody, but it is not possible to estimate the depth of the water body from this analysis. However, the geomorphology of the marl deposits (Unit 2) can be used to support the sedimentology and palaeoecological data. The outer marl ridge dips from E-W from a height of ~ 926 m ASL to ~ 918 m ASL over ~ 250 m (Fig 8.1). This probably reflects a marl slope in the sublittoral zone of a lacustrine basin that prograded towards the centre of the lake basin. The inner marl ridge lies approximately ~ 80 m to the north of the outer ridge and also dips from E-W from a height of ~ 918.5 m ASL to ~ 918 m ASL (see Fig. 8.8). Based on the E-W dipping beds, it is possible to estimate a minimum lake depth during the maximum extent of the lake. The highest marl outcrop occurs at the eastern extent of the outer ridge and lies at ~ 926.07 m ASL, though the ridge may continue underneath modern dune sands to the east. The lowest elevation occurs at the base of the PD16 trench on the inner ridge at ~ 917.4 m ASL. Subtracting the minimum elevation from the maximum elevation suggests that at the lakes greatest volume the minimum depth was ~ 8.5 m.

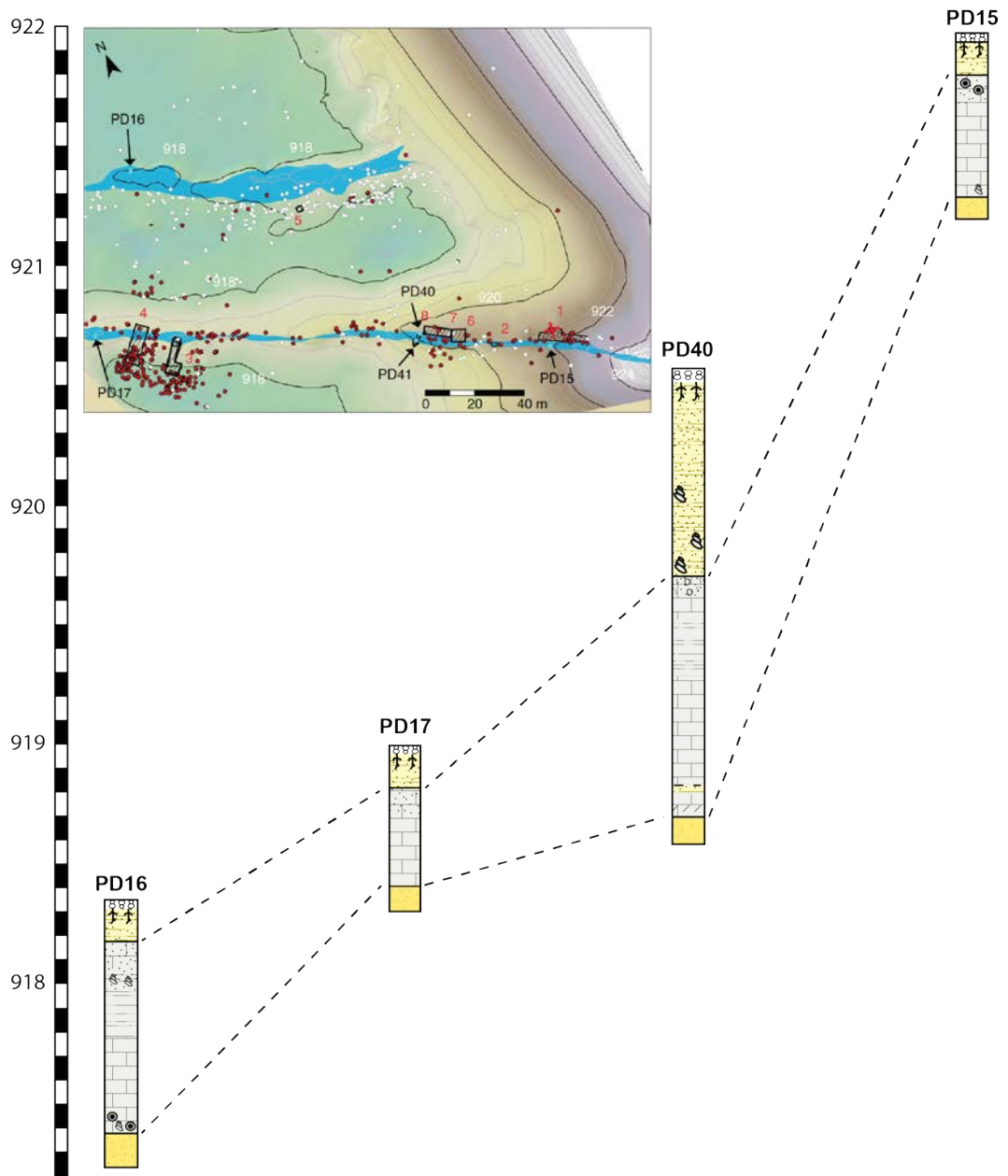


Figure 8.8 – Altitudinal relationship between each sedimentary sequence. Inset shows the same topographic map from Fig 8.1 and is included for quick reference to the location of each sequence. For map key, please refer to figure 8.1. The altitudinal relationship between the sedimentary sequences can give an indication of the depth of the water body (see section 8.6).

8.6 Summary

The key points from this chapter are as follows:

- Sequence PD40 from the Al Wusta interdunal depression was investigated as part of this thesis. The sequence contained three units: (1) aeolian sands; (2)

carbonate-rich marls (~1 m thickness); (3) crudely laminated sands with gravel inclusions and capped by calcitic rhizoliths.

- The carbonate-rich marls were further divided into four sub-units. A combination of bulk-sedimentology, micromorphology and stable isotope analysis suggests these carbonate-rich marls were deposited on the bed of a shallow, perennial and freshwater lake.
- This interpretation is consistent with previous work on trenches PD15, PD16 and PD17 which contained short (0.4 – 0.8 m) carbonate rich marl sequences. XRD and diatom analysis from these trenches further supports the interpretations drawn from the PD40 sequence.
- Using the geomorphology of the carbonate ridges, it is estimated that the MIS 5a lake at Al Wusta was at least ~8.5 m deep at its greatest extent.
- Groucutt et al. (2018) record the presence of a directly dated *Homo sapiens* fossil along with other fauna including *Hippopotamus* and *Kobus*. The latter two species requires permanent muddy, fluvial or lacustrine conditions and this strongly supports the sedimentary analysis.
- In summary, the Al Wusta interdunal depression contains a sedimentary sequence that reflects the depositional history of a humid phase in the western Nefud desert that occurred during MIS 5a. While it is impossible to know how complete a record of a humid phase this sequence represents it is noticeable that the sediments, as interpreted above, reflect the transition from arid (Aeolian dunes) through humid (lacustrine marls) back to arid (surface wash sands) again. It is therefore plausible to argue that the sequence presented here (PD40) reflects a full humid phase cycle.

Chapter 9 – Alathar palaeoenvironmental results

9.1 Introduction

The Alathar sedimentary deposit (site code: WNEF17_1) is situated within an interdunal depression ~13 km from the southwestern edge of the Nefud Desert (Fig 9.1) (N 27.52; E 39.40; altitude 955 msl). The deposit sits as an inverted relief feature rising above the modern interdunal basin floor and comprises a ~1.8 m thick deposit that overlies aeolian dune sands (Fig 9.2 and 9.3). The topography of the palaeolake deposit is well-preserved with a subtle concave shape that dips towards the centre of the remaining deposit (see Fig 9.2). Erosion is evident on the lee-side facing section of the deposit, with large sediment blocks falling to the west towards the modern topographic low of the interdunal depression (Fig 9.3). Consequently, the former extent of the palaeolake deposit is not clear. Luminescence dating of the lake sediments demonstrates that the Alathar deposit dates to early MIS 5, most likely MIS 5e. Bulk sedimentology and microfacies analysis was undertaken at the site, while no isotopic analysis was carried out due to the lack of carbonate in the sequence. Diatom palaeoecology was carried out by Dr. David Ryves as part of the Palaeodeserts project and is described here.

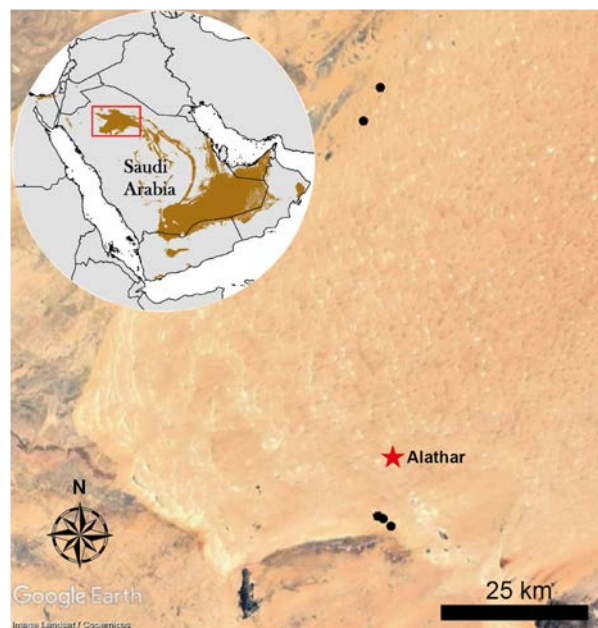


Figure 9.1 – Location of the Alathar interdunal basin within the western Nefud Desert (red star). Other black dots represent other interdunal sites studied in this thesis. Inset map shows the location of the Nefud Desert on the Arabian Peninsula.

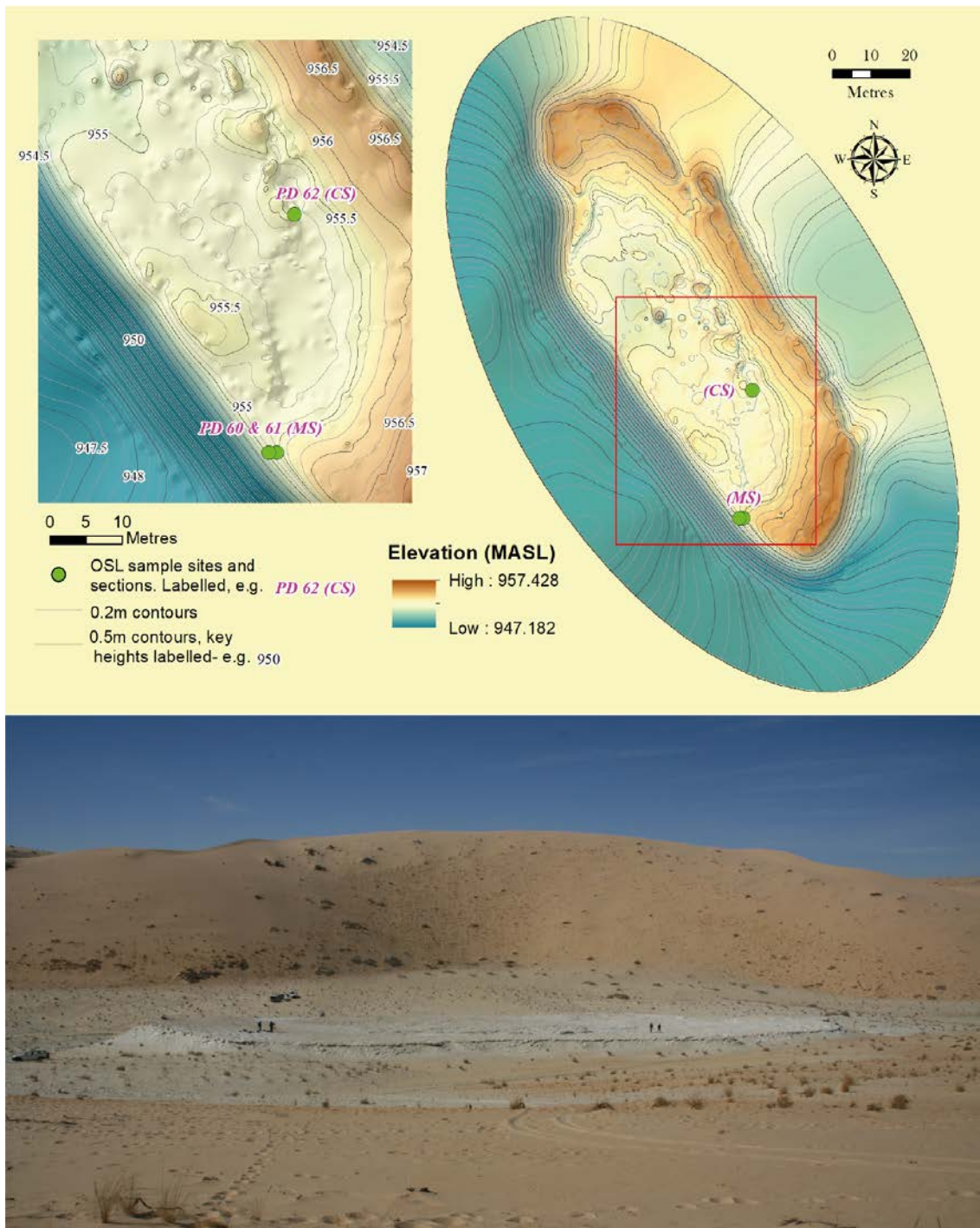


Figure 9.2 – Overview of the Alathar interdunal basin. Top: Topographic maps of the Alathar palaeolake deposit within the modern-day interdunal depression produced by Breeze (unpub). Top right: Overview of the entire Alathar interdunal basin with the inverted palaeolake deposit in the centre. The green dots representing OSL sample sites and sedimentary sections. MS – main/first section (units 1 – 4b). This contains the most extensive sedimentary sequence at the site and Hominin footprints are found on the surface. CS – second/composite section (units 5 – 7) lies more towards the centre of the deposit and overlies the first section and footprints. The stratigraphic relationship between the two sequences is visually traced in the field. Top left – Close-up view of the palaeolake deposit with OSL/sedimentary sequences labelled along with 0.2 and 0.5 m contour lines. Tracing the contour lines shows the stratigraphic relationship between the two sedimentary sections. Bottom: Image of the interdunal palaeolake looking from the northeast towards the southwest.

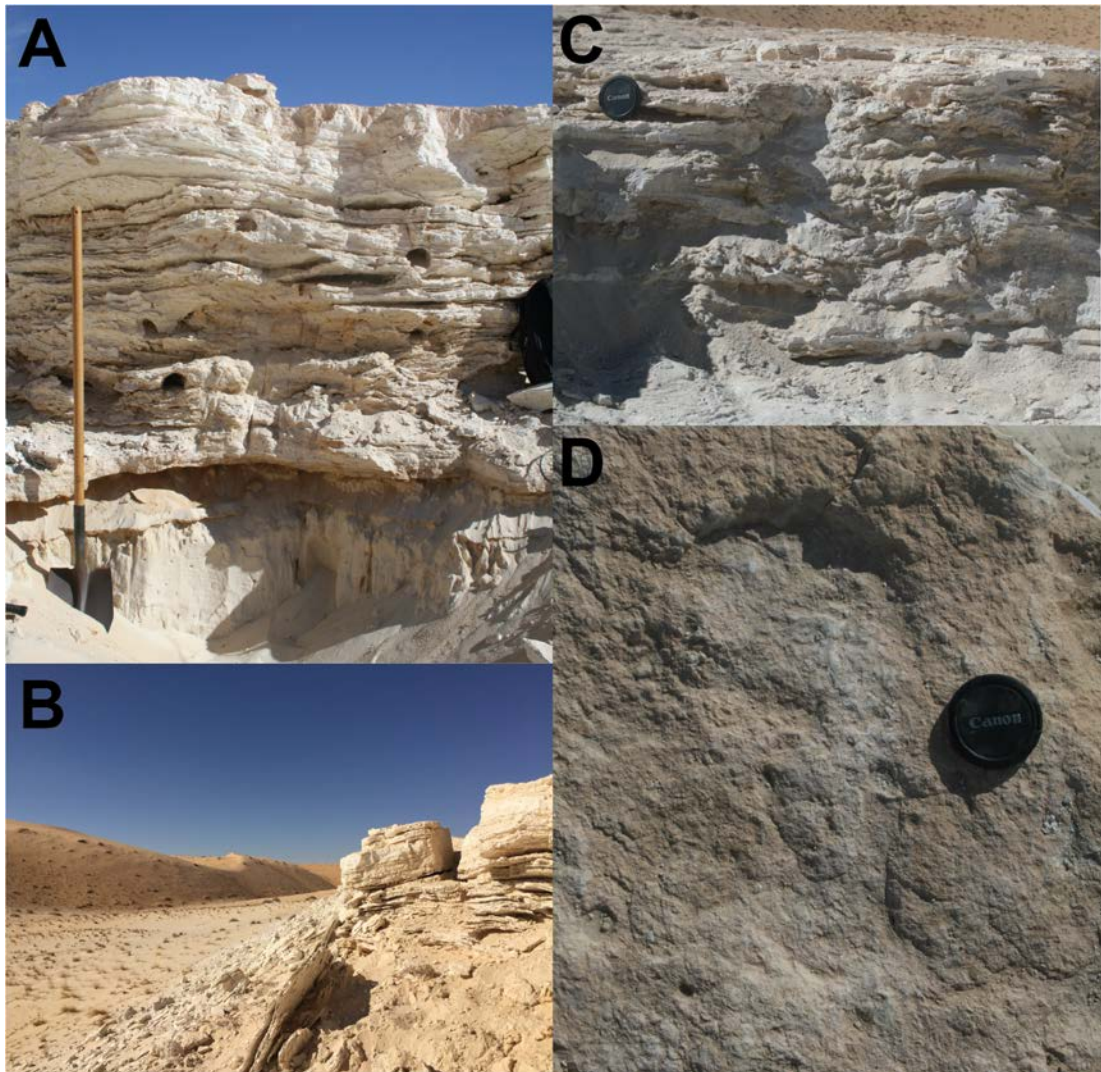


Figure 9.3 – Site pictures from Alathar. A) The first (main) sedimentary sequence where units 1 – 4 are preserved (labelled MS on Fig 9.2). B) Image taken standing directly next to palaeolake outcrop, looking to the northwest. Blocks are seen eroding out and falling towards the modern interdune basin. C) The second sedimentary sequence that stratigraphically overlies the first sedimentary sequence but lies ~30 m to the north in the centre of the palaeolake deposit (labelled CS on Fig 9.2). D) Human footprint preserved on the surface of the first sedimentary section (Unit 4).

9.2 Sedimentology

9.2.1 Bulk sedimentology

Two sedimentary sections were recorded at the site and a composite section formed from both (Fig 9.4). The two sections are located ~30 meters apart, and the relationship between them is visibly traced in the field. The exact relationship between the two sequences can be traced via the 0.2 m contour lines in the top left panel of Fig 9.2. The first section (~142 cm in height; units 1 - 4) is located on the western margin of the deposit and faces the lee side of the dune to the east (Fig 9.2 and 9.3). This forms the

thickest vertical sediment exposure and was the best available exposure. A second sediment section (~39 cm in height; Units 5 – 7) that stratigraphically lies above the first section was logged near the centre of the modern-day surface of the palaeolake deposit (Fig 9.3, panel C and Fig 9.4).

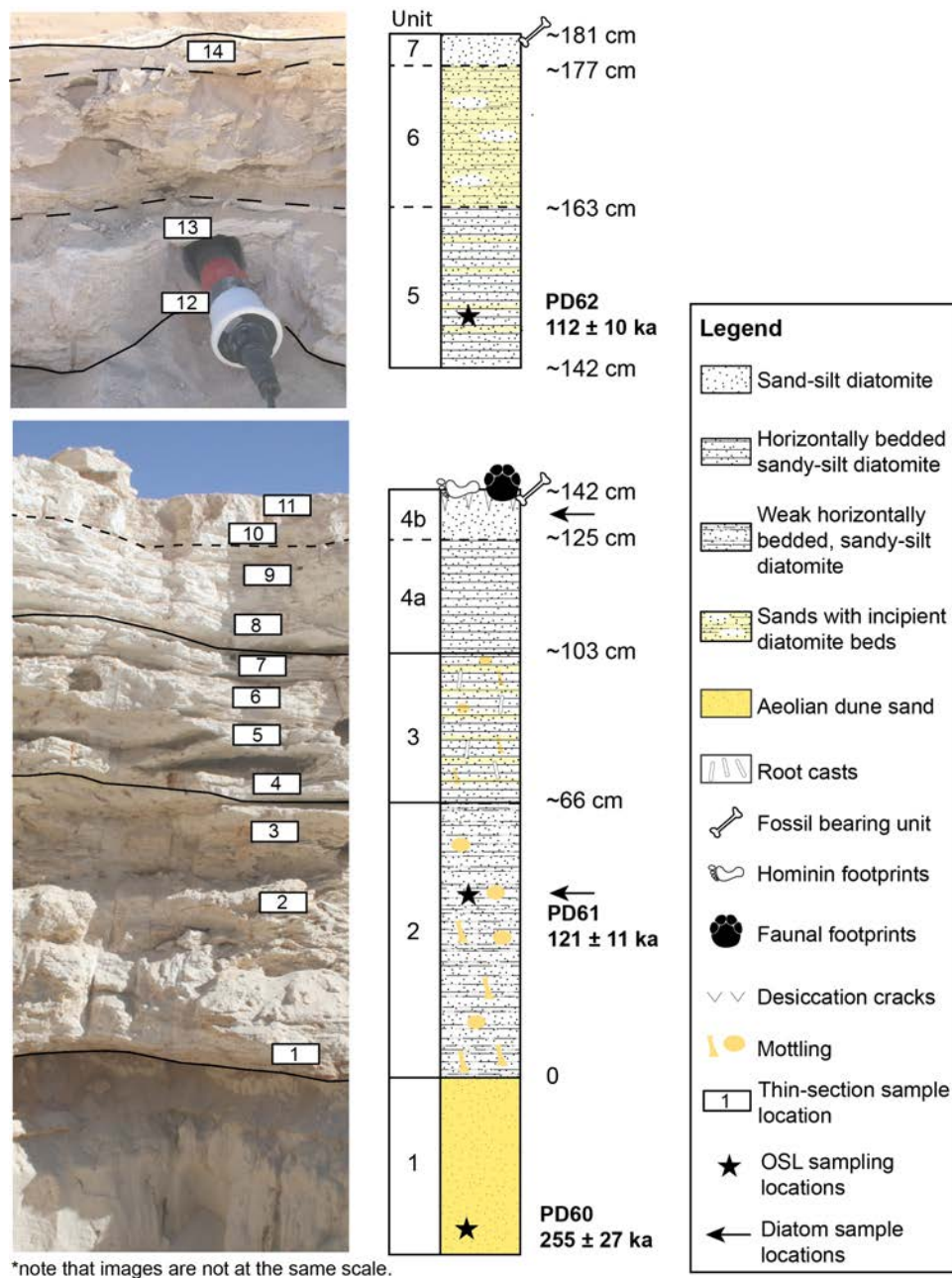


Figure 9.4 - Stratigraphic log of the first section (units 1 – 4) and the second section (units 5 – 7). Note that unit 1 consists of aeolian sands, and that sediments were consistently measured upwards from the beginning of the palaeolake sediments. As such, aeolian sands are consistently referred to as ‘underlying sands’. The relationship between the first section and the second section can be observed in Fig 9.1.

The composite sedimentary sequence is split into seven units, measured from the base of the waterlain sediments (Unit 2) upwards (Fig 9.4). Unit 1 is composed of loose bleached sands that directly underlie the first diatomite section. Units 2 – 7 are broadly similar and consist of sand-rich consolidated sediment, but are distinguished from one another by sedimentary structures (e.g. horizontal bedding and amount of mottling present) and the amount of allochthonous sands present. Calcimetry shows there is no carbonate within the sedimentary sequence, while XRD analysis samples were taken at regular intervals between 40 – 179 cm. These show the sediment mineralogy to be between 97.5 – 100% quartz and 0 – 2.5% anorthoclase. There are subtle sedimentary differences between units 2 - 7, and these are outlined below. As Units 2 – 7 contain no carbonate, are composed of >97.5% quartz and contain diatoms, these sedimentary units are referred to as diatomite.

Unit 2 (0 – 65 cm) consists of loosely consolidated sandy-silt diatomite with some evidence for horizontal bedding. There is also evidence of orange coloured, thin, elongate mottling. **Unit 3 (65 – 103 cm)** is characterised by horizontally bedded sandy-silt diatomite beds that interdigitates with sand beds. Obvious orange mottling continues, as does centimetre-scale root casts that run between the horizontal diatomite bedding planes. The unit ends with a ~3 cm discontinuous desiccation crack (103 – 106 cm). **Unit 4 (106 – 142 cm)** is split into two sub-units. **Unit 4a (~106 – 125 cm)** is formed of consolidated and horizontally bedded sandy-silt diatomite that interdigitates with laterally continuous sand beds. There is no evidence of mottling or root casts, while the sediment is almost pure white. **Unit 4b (~125–142 cm)** is a structureless, pure white sandy-silt diatomite that is consolidated, has no horizontal bedding features, and contains desiccation cracks at the surface. Faunal and hominin footprints and fossils were found on top of this unit. **Unit 5 (~142 - 163 cm)** consists of a sandy-silt diatomite that interdigitates with bedded sands. **Unit 6 (~163 - 177 cm)** is composed of sands with laterally discontinuous but consolidated sandy-silt diatomite beds with reworked rip-up diatomite clasts. **Unit 7 (~177 – 181 cm)** is composed of homogenous sandy-silt diatomite.

Table 9.1 - X-ray diffraction results for Alathar. This shows quartz was dominant, with a small proportion of anorthoclase in Units 5 – 7. No carbonate was present, in contrast to all other sites studied in this thesis.

Sample height above base (cm)	Unit	Quartz (%)	Anorthoclase (%)
80	3	100	0
110	4b	100	0
142 - 181	5 - 7	97.5	2.5

9.2.2 Microfacies analysis

A total of 14 samples for microfacies analysis were taken across both sections and show little compositional variability. All contained sub-angular to well-rounded grains that ranged from medium silts to very coarse sands (based on measuring the smallest and largest sand grains in each slide in thin-section), frequent diatoms/sponge spicules and a fine-grained, brown siliceous amorphous matrix. The main variation across the sedimentary sequences is in the grain to matrix ratio. The lower two thin-sections from Unit 2, which comprise loosely consolidated sandy-silt diatomite, have no evidence of structure and contain the most densely packed allogenic grains (~50% cover) (Fig 9.5 panel A). The thin-sections in all following units are densely packed with allogenic grains (~25–33% cover) but contain bands or patches where the density of grains is much less (~5–10% cover), while there is a notable decrease in allogenic grains in Unit 4b and all units in section 2 (Units 5 – 7) (see Fig 9.5, panel B and C). There is no evidence of iron-staining except for the lowermost thin-section from Unit 2 and Unit 5. Organic material is rare, with occasional amorphous organic materials in some thin-sections (though showing no trend throughout the sequence) and a single section with rare evidence of organics with cellular preservation.

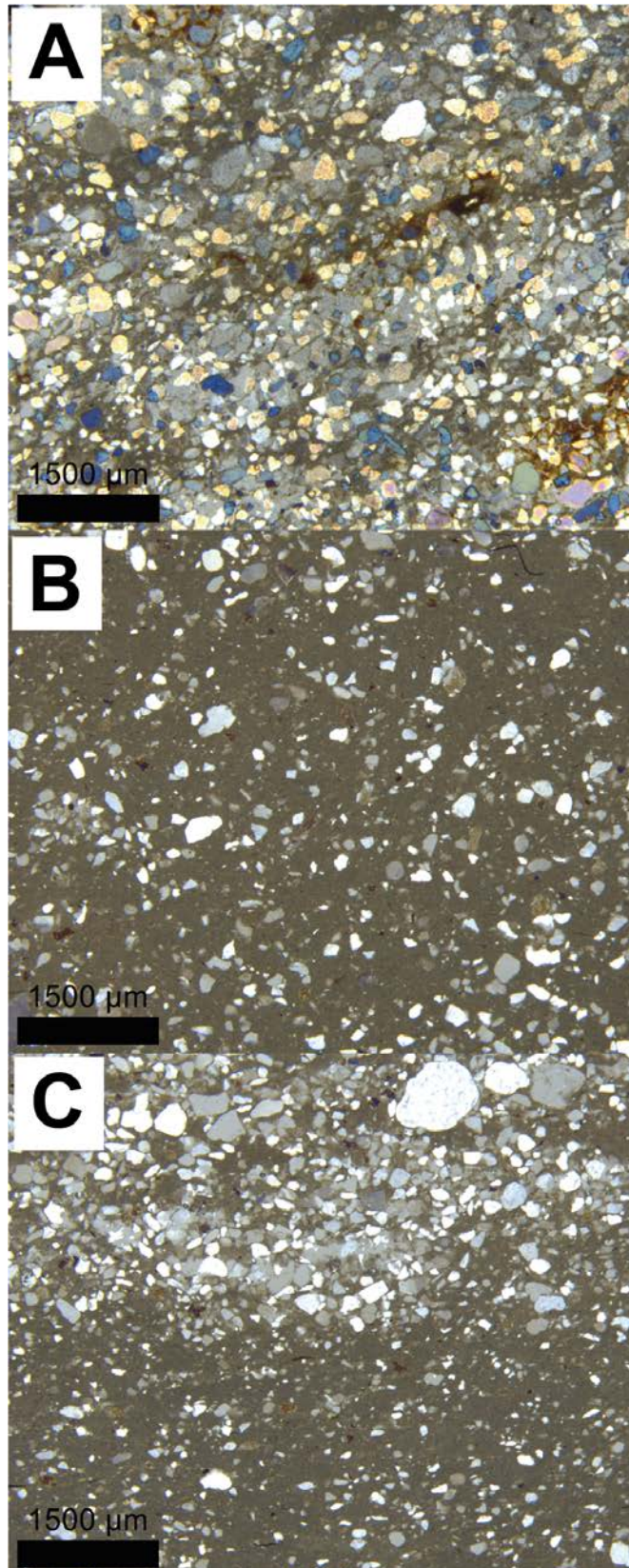


Figure 9.5 – Photomicrographs of thin-sections taken from the Alathar palaeolake bed. (A) 40 – 45 cm above base from unit 2. There are a high number of allogenic grains in thin-sections from this unit. (B) 139 – 141 cm above the base from unit 4b. The number of allogenic grains is reduced relative to Unit 2. (C) 152 – 163 cm above base from unit 5. The density of allogenic grains in the upper half of the thin-section is more dense (~50% coverage) relative to the lower half of the thin-section (5 – 10% coverage).

9.3 Diatom palaeoecology

Three diatom samples were taken at 40 cm (Unit 2), 140 cm (Unit 4b) and 175 cm (Unit 7) and analysed by Dr. David Ryves from Loughborough University. The data is presented here as it is integral to forming the depositional model for the site and has been reported fully in Stewart et al. (2020a). The basal sample (40 cm) has low abundances of brackish species such as *Amphora copulata* and *Navicula oblonga* though freshwater species such as *Cymbella* (tychoplanktonic), *Ulnaria* spp., *Cyclotella* (now *Lindavia*) *ocellata*, *Aulacoseira granulata* and *A. ambigua* are also found (Stewart et al., 2020a). The sample from 140 cm has a similar assemblage but contains a lower abundance of brackish taxa, includes aerophilous *Hantzschia amphioxys*, and valve breakage is greater while valve dissolution declines (Stewart et al., 2020a). The uppermost sample contains a similar assemblage to the previous samples, with the addition of the brackish planktonic taxon *Thalassiosira pseudonana* and the absence of *L. ocellata* (Stewart et al., 2020a).

Diatom assemblages from all three samples suggest freshwater conditions, with diatom inferred conductivity for all samples ranging between 220 $\mu\text{S cm}^{-1}$ (140 cm) and 350 $\mu\text{S cm}^{-1}$ (175 cm) (Stewart et al., 2020a). The species recovered indicate subtle differences between each sample. The suite of characteristics from 140 cm, with greater valve breakage and the aerophilous *Hantzschia amphioxys* suggests this sample may have been more prone to sediment in-wash and turbulent mixing than the other two samples (Stewart et al., 2020a). Chrysophyte cysts are present in all samples and support the presence of a freshwater lake body (Stewart et al., 2020a). The diatom palaeoecology is consistent with a fairly freshwater lake with low/medium nutrient conditions (Stewart et al., 2020a).

9.4 Depositional model

The sedimentary evidence described in this chapter is used to construct a depositional model. Two main phases of sediment deposition are recorded at the site. Unit 1 consists of loose, well-sorted sands and represents dune migration during an arid phase. Units 2 – 7 consist of loose to moderately consolidated, sand, silt and diatom-rich sediment that is dominated by quartz. As such, these units are characterised as sandy-silt diatomite

and represent deposition in a shallow water body. The sedimentary facies contains horizontal bedding planes in Units 2, 3 and 4a and homogenous sandy-silt diatomite in others (e.g. Units 4b and 7). The three diatom samples taken through the sequence contain predominantly freshwater oligo- to meso-trophic freshwater diatom species. These characteristics indicate the sediments were deposited in an oligotrophic-mesotrophic shallow freshwater lake that was subject to episodic desiccation. However, there are subtle changes in the depositional environment shown by the subtle differences between each unit. These are outlined below.

Unit 2 (0 – 66 cm) represents a shallow lake system in an unstable landscape with low vegetation cover at the onset of a humid interval. At the macro-scale the sediment is friable relative to the units above it, and microfacies analysis shows this is due to the high proportion of allogenic sands relative to fine-grained silicious matrix. The greater degree of allogenic sand grains likely represents sedimentation during the onset of humidity, with the surrounding landscape yet to respond to increased moisture. Limited vegetation cover/density in the landscape would result in unstable surficial dune sands that would readily be transported into the basin during rainfall events. Faint horizontal-bedding is present and indicative of periodic in-wash events. Furthermore, the presence of vegetation is also evidenced by thin-elongate orange mottling resulting from local chemical and biological heterogeneities where organic matter has been oxidised (Collinson, 1996). The diatom assemblage recovered from this unit has inferred conductivity consistent with freshwater conditions, though brackish species are also present.

Unit 3 (66 – 103 cm) displays very similar characteristics to Unit 2 with the key differences being that horizontal bedding planes are more obvious with consolidated sandy-silt diatomite clearly interdigitated with sand beds (Fig 9.4). The proportion of allogenic grains to matrix within the diatomite is slightly lower than the previous unit, perhaps suggesting a more stable surrounding environment moving further into the humid phase. The well-developed horizontal bedding structures of sandy-silt diatomite reflects a deeper waterbody, while sand beds reflect increased in wash to the site of sedimentation likely caused by periods of lake contraction moving the lake edge closer

to the site of deposition. Mottling is still present through this unit, implying vegetation was present.

Unit 4a (106 – 125 cm) is similar to the previous unit in that obvious horizontal bedding between sandy-silt diatomite and sand beds is present, along with a high allogenic grain input. However, mottling is no longer present while the sediment is a purer white colour. The lack of mottling suggests that vegetation was not present within this unit. Unit 4b (125 – 142 cm) is again very similar to the others, but horizontal bedding ceases and the sediment is massive, while the microfacies from this unit (130 – 132 cm, 139 – 141 cm; Fig 9.5 panel B) shows a reduction in allogenic sands and a greater proportion of brown siliceous matrix. The reduction in allogenic sands in the diatomite and the lack of horizontal-bedding suggests that Unit 4b may have been deposited during a period where the surrounding landscape was stabilised by vegetation, or that allogenic inputs into the basin moved away from the site of sedimentation. The homogenous nature of the sediment along with the presence of aerophilous diatom species *Hantzschia amphioxys*, *Aulacoseira granulata* – which is present in shallow turbid systems – and the high degree of valve breakage show that waters were shallow and turbulent (Stewart et al., 2020a). The surface of Unit 4b contains desiccation cracks along with hominin and elephant footprints (Fig 9.6) showing that the lake fully desiccated at the end of this unit.

Units 5 – 7 represent the re-establishment of shallow lacustrine conditions after the desiccation episode at the top of unit 4b. The sedimentary, microfacies and diatom assemblage from units 5 and 7 are consistent with those from the first section (units 2 – 4b) in that they contain sandy-silt diatomite, with an abundance of allogenic grains and a dominance of freshwater diatom species. Unit 6 contains sands with incipient diatomite beds and reflects an episodic shallowing event.



Figure 9.6 – The surface of unit 4b. This shows a human footprint (located to the right of the camera lens cap). A desiccation crack runs directly through the footprint, while another is located in the top left portion of the picture.

The lack of carbonate through the Alathar sedimentary sequence is uncommon when compared to other palaeolake sequences within this thesis, though diatomite has been reported before from the western Nefud Desert (Rosenberg et al., 2013; Whitney and Gettings, 1982). The lack of carbonate could be due to multiple factors: (1) there may have been limited biogenic activity at the lake that failed to biologically mediate the precipitation of carbonate via raising the lake water pH; (2) the lake may have been subject to high levels of throughflow restricting carbonate precipitation; (3) groundwaters feeding the site may not have been enriched in the ions necessary for carbonate precipitation (Ca^{2+} and CO_3^{2-}); (4) the site may have been predominantly rain-fall fed – i.e. a recharge playa – and had limited interaction with ion-rich groundwaters. The presence of root casts, mottling and abundant diatoms suggests that option 1 – a lack of biological productivity to precipitate carbonate – is unlikely. Aside from this, it is not clear which of the other factors can explain the lack of carbonate at the site.

9.5 Summary

Key points from this chapter are as follows:

- The sedimentary sequence at Alathar consist of sandy-silt diatomite, contains little variability and records the presence of an oligo- to meso- trophic, shallow freshwater lake that was subject to episodic desiccation.
- It is not clear whether desiccation events occurred frequently (i.e. the lake was primarily rainfall fed and underwent seasonal desiccation) or if desiccation events were rare. Nonetheless, during one desiccation event humans and other fauna occupied the lake surface, leaving footprints embedded within the surface of unit 4b (Stewart et al., 2020a).
- It is also interesting to note that the total amount of allogenic sand/silt grains through the sequence at Alathar is in contrast to all other sequences presented in this thesis where allogenic sands are minimal. It is not clear whether the locally unstable environment at Alathar is a consequence of local hydrological factors (Alathar is more elevated and situated further from the edge of the present-day dune field) or reflects different climatic conditions during its existence.
- In summary, Alathar provided a fresh waterbody and vital resources for hominins and fauna in the western Nefud Desert, Saudi Arabia during Marine Isotope Stage 5e. The presence of a hominin, and probably *Homo sapiens* footprint at the site confirms that humans used this resource (Stewart et al., 2020a).

Chapter 10 – WNEF16_28 palaeoenvironmental results

10.1 Introduction

The WNEF16_28 sedimentary deposit lies ~3 km from the southwestern edge of the Nefud Desert (N 27.43, E 39.38, 930 m ASL) (Fig 10.1). Luminescence dating of the aeolian sands underlying the carbonate sediments, and waterlain sands overlying them, shows that this deposit most probably formed during Marine Isotope Stage 5e. The deposit itself is exposed as a single carbonate ridge to the east of the closest interdunal depression. A combination of bulk sedimentology, microfacies analysis and $\delta^{18}\text{O}$ and $\delta^{13}\text{C}$ analysis were undertaken to reconstruct a depositional model. Qualitative diatom palaeoecology work was carried out by Dr. Dave Ryves as part of the Palaeodeserts research project to support the other proxies used here, and the results of this analysis are described here.

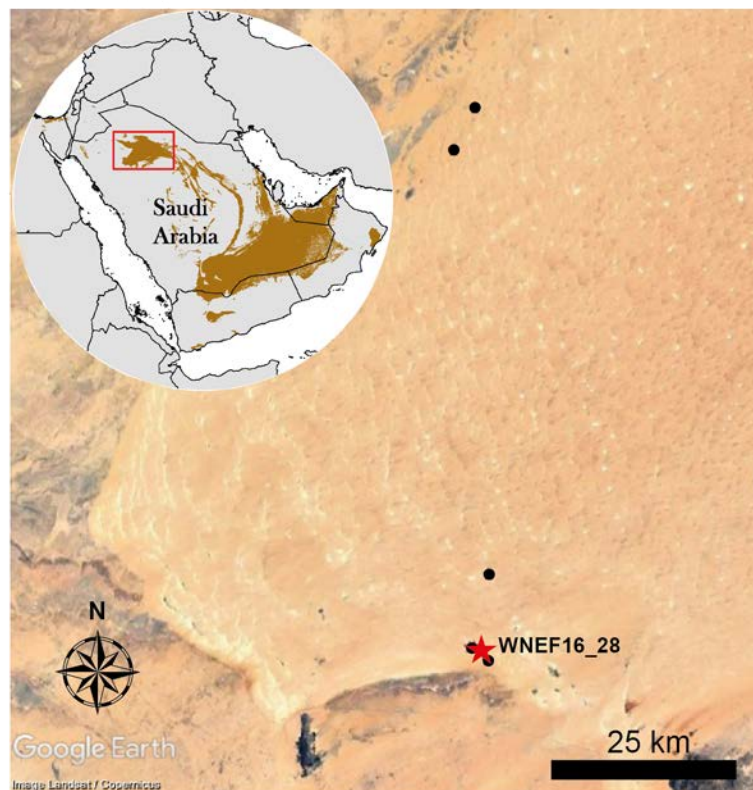


Figure 10.1 - Location of the WNEF16_28 interdunal basin within the western Nefud Desert (red star). Other black dots represent other interdunal sites studied in this thesis. Inset map shows the location of the Nefud Desert on the Arabian Peninsula.

10.2 Sedimentology

10.2.1 Bulk-sedimentology

The sedimentary sequence at WNEF16_28 consists of three units: 1) well-sorted loose sands (unit 1); 2) fine-grained calcium carbonate rich marl (unit 2); 3) crudely horizontally-bedded medium to coarse sands with rhizoliths forming within them (unit 3). The sedimentary sequence is measured from the base of the carbonate-rich marls upwards, and the well-sorted loose sands are described as underlying sands. The fine-grained carbonate-rich marls (Unit 2; 0 – 108 cm) contain some variability and is split into four sub-units and these are characterised as follows.

Unit 2a (0 – 14 cm) consists of structureless and homogenous fine-grained carbonate with clear sand lenses over the first 8 cm of the sequence. Calcium carbonate content within this unit is ~50% while XRD analysis shows between 50 – 61 % calcite and 39 – 50% quartz (Table 10.1). **Unit 2b (14 – 70 cm)** consists of discontinuously but finely laminated fine-grained carbonates with multiple iron bands (~2 – 3 cm thick) present between 15 – 35 cm. A sand-rich layer is present between 38 – 39 cm (see Fig 10.2). Calcium carbonate content ranges between 52 – 72% while XRD analysis shows calcite is predominant (81 – 93%) with a small quartz component (4 – 8%) (Table 10.1). Halite is also present at ~50 and ~70 cm with proportions of 10% and 3% respectively (Table 10.1). **Unit 2c (70 – 93 cm)** consists of a more friable carbonate than that of Unit 2b. In the field this is expressed by the fact unit 2c is set back from Unit 2b. Unit 2c carbonates are homogenous, structureless and friable with mottling present and easily break down into peds. Calcium carbonate content in this section ranges between 31 – 63% with the lower value at the end of the unit. XRD analysis from 90 cm shows quartz is dominant (68%) with calcite (32%) and a negligible gypsum component (0.6%) present. **Unit 2d (93 – 108 cm)** consists of mechanically strong, well-cemented nodular fine-grained carbonate with tubular voids.

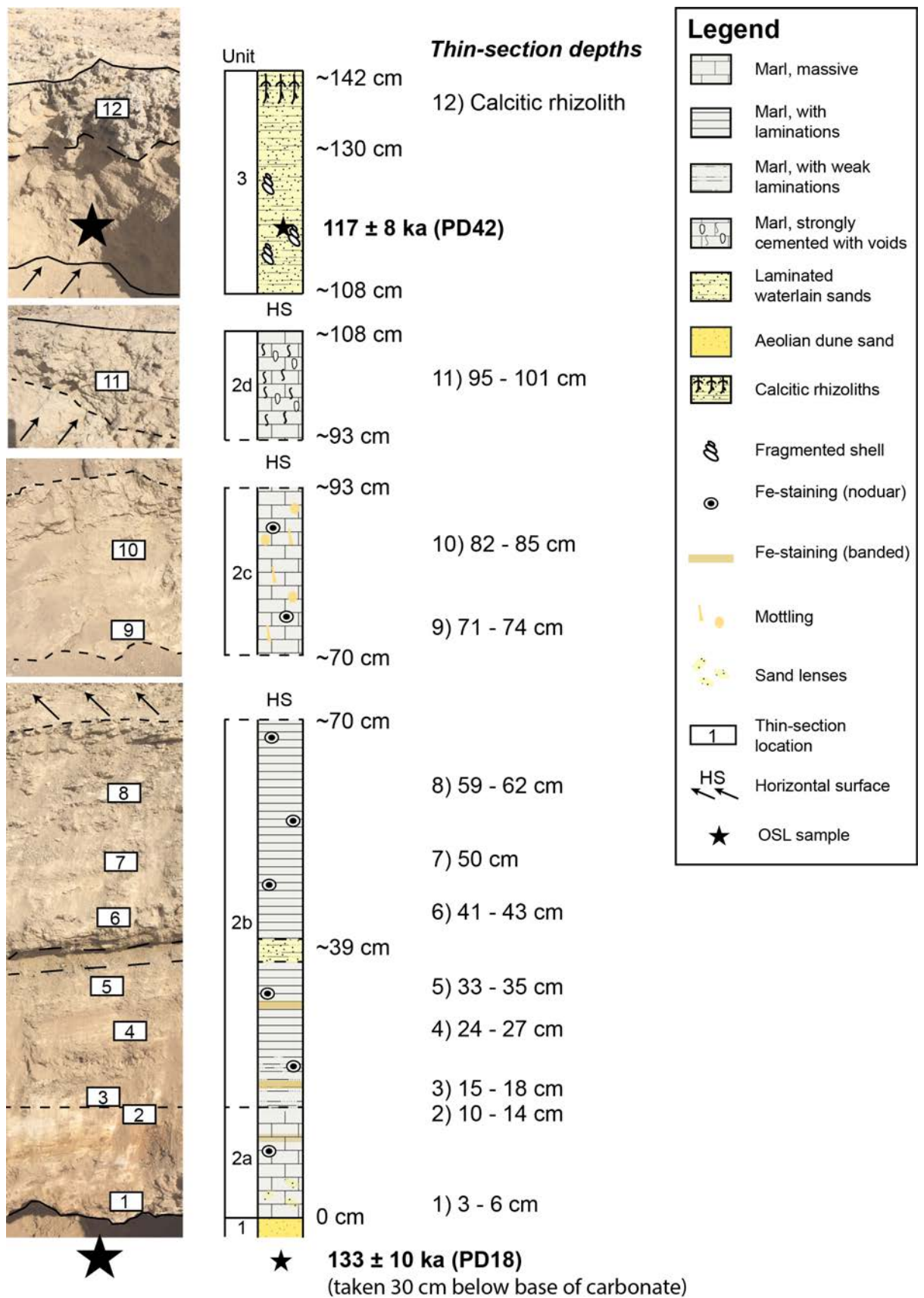


Figure 10.2 – Sedimentary sequence from WNEF16_28. Note that images are not all at the same scale. Unit boundaries are outlined by a solid black line while sub-units are separated by a dashed black line. Thin-section sample locations through the sequence are also outlined, with sample depths shown on the right-hand side of the figure.

Table 10.1 – X-ray diffraction results from WNEF16_28. Calcite is dominate with the exception of the beginning and end of the sequence, where the propotion of quartz increases. Evaporites are negligible throughout with the exception of 50 cm where Halite is present at 9.8% weight.

Height above base (cm)	Unit	Calcite (%)	Quartz (%)	Gypsum (%)	Halite (%)
0	2a	50.4	49.6	0	0
10	2a	61.1	38.9	0	0
30	2b	93.2	6.8	0	0
50	2b	81.2	8.3	0.6	9.8
70	2b	92.7	4.2	0	3.1
90	2c	31.7	67.6	0.6	0

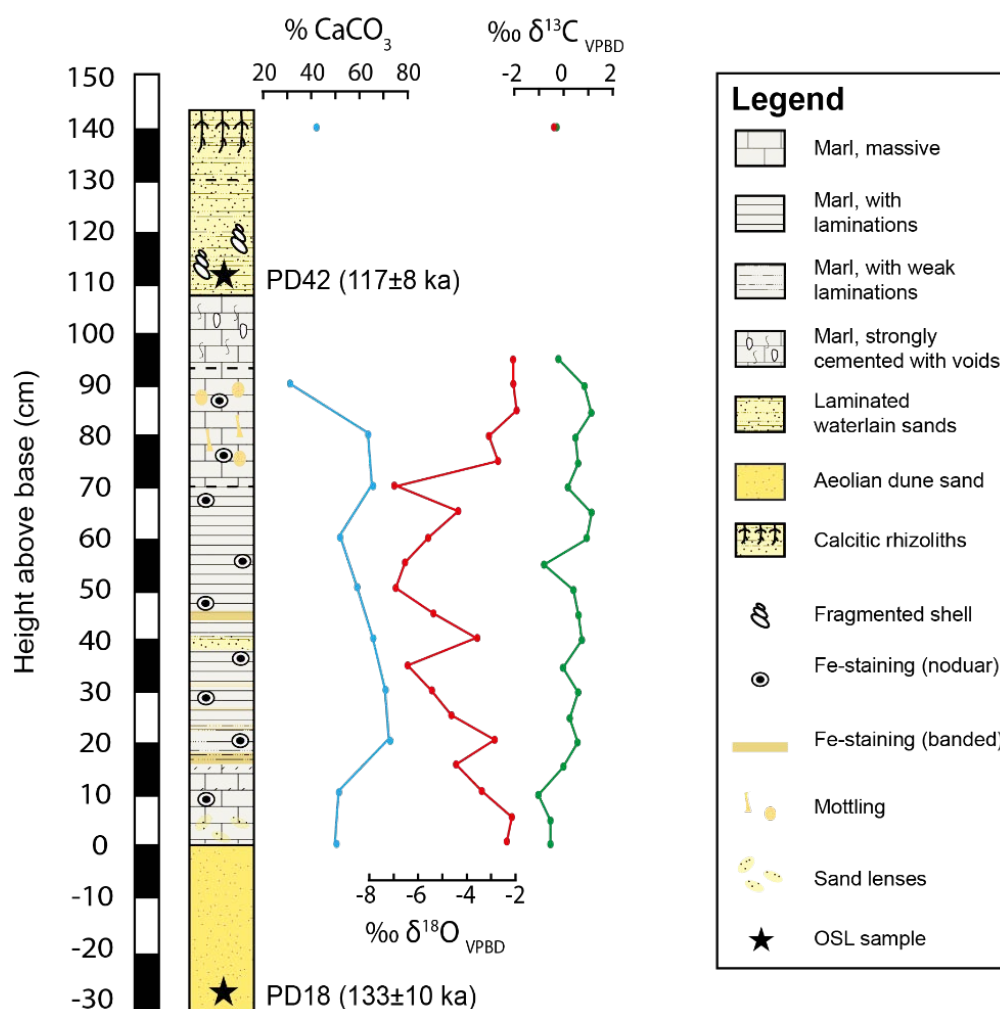


Figure 10.3 – Sedimentary logs along with CaCO₃ (blue), δ¹⁸O (red) and δ¹³C (green) stratigraphies for the sedimentary sequence at WNEF16_28. Luminescence ages are also shown, with sample locations marked by black stars.

10.2.2 Microfacies analysis

A total of 11 samples for microfacies analysis were taken from the carbonate-rich sediments (Unit 2a – 2d). This analysis shows that all sections have either a homogenous, weakly or finely laminated microstructure with a groundmass composed of microsparite or micrite with sparse allogenic sand material. Evidence for iron and/or manganese staining is present at varying degrees throughout the sequence, while organic remains are rare. Microfacies from unit 2a (0 – 14 cm) are characterised by homogenous microsparite (see Fig 10.4 panel A). Heavy iron and manganese staining is evident between 10 – 14 cm. Microfacies from unit 2b (14 – 70 cm) begin with weak discontinuous lamination couplets between microsparite and micrite with some evidence of iron staining (15 – 18 cm). These transition into fine but mainly discontinuous lamination couplets or triplets moving up through the sequence to 70 cm (Fig 10.4, panel B and C). Lamination couplets consist of repeating laminations of microsparite and micrite (see Fig 10.4 panel C). Lamination triplets are between microsparite, micrite and iron stained calcite (Fig 10.4 panel B). Quartz bands are occasionally present while laminations are sometimes interrupted by homogenous and mixed calcite that lie directly next to intact laminations.

Microfacies from units 2c and 2d (Fig 10.4 panel D), have a homogenous microstructure with a predominantly microsparite groundmass with some micrite present. There is also an increase in larger sand grains (very coarse sand) that are randomly distributed while the number of planar voids increase (though not enough for the microstructure to be described as prismatic). The final section of the carbonate sequence (95 – 101 cm), correlated with macroscale observations of a cemented ‘hardpan’ marl, shows a microfacies with a prismatic structure with planar and blocky voids, a greater proportion of micrite, a greater number of amorphous organic remains and a greater frequency of large allogenic sand grains. The capping calcitic rhizoliths consists of densely packed sand grains cemented by large sparite crystals. Rare shell fragments are present in this section.

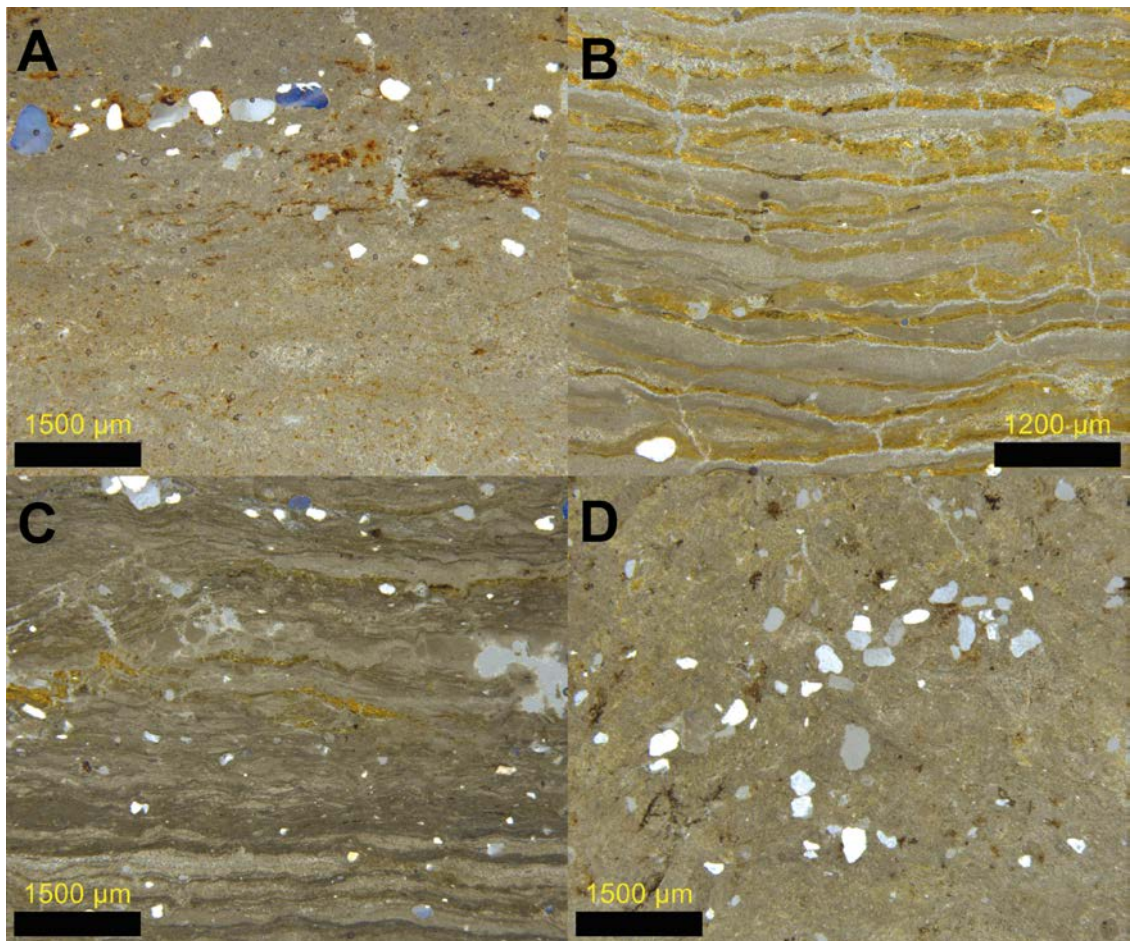


Figure 10.4 – Photomicrographs of thin-sections through the sedimentary sequence. (A) 3 – 6 cm above base from unit 2a. This microfacies contains a massive structure with a microsparitic groundmass. There is some evidence for iron staining and there are rare sand sized grains. (B) 32 – 36 cm above base from unit 2b. This microfacies contains lamination triplets with repeating laminations of microsparite, micrite and iron-stained micrite. Allogenic sand/silt grains are rare. (C) 59 – 62 cm above base from unit 2b. This microfacies contains lamination couplets between microsparite and micrite. Allogenic grains are rare. (D) 82 – 85 cm above base from unit 2c. Here the microfacies returns to massive microsparite.

10.3 $\delta^{18}\text{O}$ and $\delta^{13}\text{C}$

$\delta^{18}\text{O}$ values within the carbonate-rich sediments (Unit 2) range between -6.59‰ and -1.73‰ with mean and median values of -3.88‰ and -3.77‰ respectively. The $\delta^{18}\text{O}$ stratigraphy is split into three zones and closely follows the sedimentology. The first zone, from 0 – 20 cm contains values from -1.88‰ to -4.18‰ with a mean value of -2.79‰ and a median value of -2.67‰ . The second zone, from 25 – 70 cm, yields more depleted $\delta^{18}\text{O}$ values ranging from -3.44‰ to -6.59‰ with a mean of -5.28‰ and a median of -5.23‰ . The third zone, between 75 – 95 cm, contains more positive values between -2.85‰ and -1.73‰ with a mean of -2.15‰ and median of -1.87‰ . The largest

isotopic shift occurs at the transition of zones 2 and 3 (70 – 75 cm), where there is an isotopic enrichment of 4.08‰. This reflects the transition between sedimentary Units 2b and 2c. It is notable that this is also picked out in the microfacies analysis where laminations are replaced by a massive microstructure (compare panels C and D in Fig 10.4).

The $\delta^{13}\text{C}$ stratigraphy varies very little, with all samples lying between -1.01‰ and 1.09‰ with mean and median values (excluding the calcitic rhizolith) of 0.22‰ and 0.44‰ respectively. There is no evidence for significant covariance between $\delta^{18}\text{O}$ and $\delta^{13}\text{C}$ with an R^2 coefficient of 0.00 (excluding the calcitic rhizolith) with a p-value of 0.89 (Fig 10.5). The calcitic rhizolith from the top of the sequence yields a $\delta^{18}\text{O}$ value of 0.40‰ and a $\delta^{13}\text{C}$ value of -0.36‰.

Table 10.2 - Descriptive statistics for $\delta^{18}\text{O}$ values of lake carbonates at WNEF16_28. *Excluding rhizolith sample.

Zone	Height above base (cm)	N	Mean (‰)	Median (‰)	SD (1 σ) (‰)	Min (‰)	Max (‰)	Range (‰)
Z1	0 - 20	5	-2.79	-2.67	0.93	-4.18	-1.88	2.31
Z2	25 - 70	10	-5.28	-5.23	1.08	-6.59	-3.44	3.15
Z3	75 - 95	5	-2.15	-1.87	0.48	-2.85	-1.73	1.12
Rhizolith	Unit 3	1	N/A	N/A	N/A	0.4		N/A
All*	N/A	20	-3.88	-3.77	1.71	-6.59	-1.73	4.86

Table 10.3 - Descriptive statistics for $\delta^{13}\text{C}$ values of lake carbonates at WNEF16_28. Note that these values do not fall into distinct zones and are therefore described together.

Zone	Height above base (cm)	N	Mean (‰)	Median (‰)	SD (1 σ) (‰)	Min (‰)	Max (‰)	Range (‰)
All	0 - 95	20	0.22	0.44	0.64	-1.01	1.09	2.1
Rhizolith	Unit 3	1	N/A	N/A	N/A	-0.36		N/A

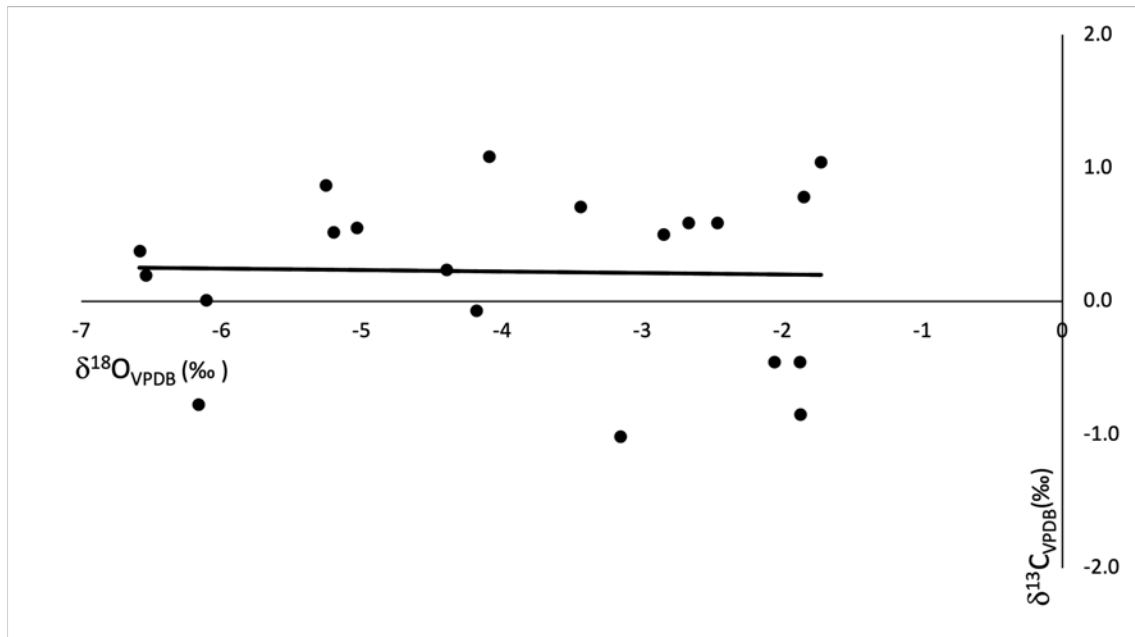


Figure 10.5 – Covariance between $\delta^{18}\text{O}$ and $\delta^{13}\text{C}$ at WNEF16_28 excluding the calcitic rhizolith. The R^2 value is 0.00 with a p -value of 0.89.

10.4 Diatom palaeoecology

Preservation of diatoms varied through the sequence, with abundant well-preserved diatoms at 50 cm and 80 cm above base, some dissolution at 30 cm and 100 cm above base but very poor preservation the base of the sequence (0 cm). Where preservation was better (at 50, 80 and 100 cm), planktonic and tychoplanktonic taxa were dominant, including several species of *Aulacoseira* (including *A. italica*), *Cyclotella/Lindavia* (including *L. ocellata* and *C. krammeri*, both indicative of deeper waters), and *Ulnaria* (*U. acus* and *U. ulna*). Freshwater benthic species such as *Encyonema muelleri*, *Fragilaria vaucheriae* and *Nitzschia amphibia* were also present, while there was an abundance of chrysophyte cysts – indicative of lower nutrient levels and freshwater – and sponge spicules at 50 cm. Some valves of the slightly saline-indicating *Halamphora veneta* were seen in the 50 cm sample, but this was a rare occurrence. Overall, this qualitative analysis shows that diatom assemblages across all levels were typical of freshwater lakes (Ryves, per comms).

10.5 Depositional model

The sedimentary evidence described in this chapter is used to construct a depositional model for the site. Three phases of sediment deposition are recorded. Unit 1 consists of loose, well-sorted sands and represents dune migration and aeolian sand deposition during an arid phase. Unit 2 consists of fine-grained carbonate rich marls and represents the development of an interdunal lake during a humid interval. Unit 3 consists of loose and horizontally-bedded medium to coarse sands with shell fragments and calcitic rhizoliths at the upper surface. This reflects waterlain sedimentation in response to sheet/surface wash events following the desiccation of the lake body, while the calcitic rhizoliths reflect terrestrial sedimentation and root networks at the land surface at the end of the humid interval.

Multi-proxy analysis of the carbonate-rich marl sediments reveals four subtly differing depositional environments during the existence of the lake body. Unit 2a (0 – 14 cm) reflects deposition in a shallow but perennial lake system in an unstable landscape. Macroscale analysis shows carbonate with sand lenses and dark bands that mirror those observed at macro-scale in the lowermost carbonate unit at PD40 at Al Wusta. The carbonate content in this section is relatively low (50%) and XRD shows high quartz contents (38.9 – 49.6%). The carbonate itself is composed of a homogenous microstructure with a microsparite groundmass, sparse distribution of allogenic sand grains, iron and manganese staining and no evidence of desiccation or pedogenic alteration. This combination of features suggests that the carbonate formed in a shallow, perennial and polymictic lake where bottom waters were oxygenated, and sediment was mixed via surface winds or bioturbation (Alonso-Zarza, 2003). The presence of sand lenses along with the relatively high quartz content compared to the rest of the sequence attests to an unstable, poorly (low-density) vegetated local landscape that enabled large amounts of allogenic material to be washed into the lake basin during the initial stage the lakes existence. $\delta^{18}\text{O}$ values through this section lie between -1.88 and -2.06‰ and are among the most positive in the sequence. This

probably reflects lower amounts of rainfall, given that the lack of covariance suggests limited evaporitic enrichment of the $\delta^{18}\text{O}$ signal. $\delta^{13}\text{C}$ values are consistent with other units (between -1.01‰ and 1.09‰) and are typical of a lacustrine body in equilibrium with the atmospheric CO_2 (Leng and Marshall, 2004).

The lake body then transitions to a deeper system, with sedimentation occurring in the profundal zone of the lake. This is reflected in the sedimentology of Unit 2b (14 – 70 cm), where the homogenous microsparite of the previous unit is replaced by mm-scale discontinuous lamination couplets between microsparite and micrite, or triplets between microsparite, micrite and iron-stained micrite. The preservation of laminations is indicative of deeper waters. Lake depth and stratification protect the lake beds from water turbulence caused by surface winds and/or bioturbation. The latter is a consequence of sedimentation under anoxic conditions in the hypolimnion (bottom waters) of thermally stratified lakes.

The nature of the laminations themselves can provide further insight into the characteristics of the lake. Lamination couplets between microsparite and micrite reflect variations in lake productivity. Smaller crystal sizes (micrite) relate to peak supersaturation brought on by peak productivity (Wright, 1990). This is perhaps in relation to an initial spring/summer bloom. Larger crystal sizes (microsparite) relate to lower levels of saturation as productivity decreases (Wright, 1990). These characteristics may reflect episodic variations in productivity, and it is not clear if there is any seasonal control on the lamination couplets. The laminations also appear to pinch in and out, with a lenticular form often present (Fig 10.4, panel B and C). It is therefore impossible to pick out chronological data from them. It is also important to note that iron-staining occurs throughout these sections, often in the form of discrete hypo-coatings around vughs but does not occur along discrete laminations as is described below. This suggests that iron staining relates to waters moving through pore spaces after sediment deposition (Davinson, 1993).

Between 32 – 36 cm the lamination couplets turn into lamination triplets where an iron-stained lamination occurs in addition to non-iron stained microsparite and micrite

laminations (Fig 10.4, panel B). Unlike the lamination couplets, these appear to be continuous and regular laminations. As per above, the variations in calcite crystal size probably relates to variations in productivity, while the addition of an iron-stained lamination may reflect cyclic changes in the redox conditions within the lake (Davison, 1993). This may be related to seasonal lake turnover events. For example, reducing (anoxic) conditions occur in thermally stratified lakes where oxygen consumption in isolated bottom waters (hypolimnion) leads to anoxia (Davison, 1993). This could relate to the summer monsoon season in the western Nefud, with increased moisture and temperatures leading to greater lake volume and temperature induced stratification. Lake turnover could then occur in the winter months, as moisture availability and temperatures dropped. This would lead to a reduction in lake volume promoting wind induced mixing of waters, while lower surface water temperatures could inhibit thermal stratification. These processes could lead to lake turnover and replenish oxygen in the hypolimnion, leading to the oxidation and precipitation of iron. Phases of oxygenated bottom waters within this unit are evidenced by microfacies that have been partially bioturbated. Alternatively, the iron-stained laminations may be post-depositional and relate to fine-grained micritic laminations capturing percolating water with subsequent iron-precipitation.

Isotopic data from Unit 2b is consistent with microfacies analysis, in that they are consistent with an increase in humidity via either increased lake volume or a greater amount of rainfall. The $\delta^{18}\text{O}$ values are typically depleted throughout this unit with a mean value of -4.83‰ , median value of -5.04‰ and minimum value of -6.59‰ . Such depleted values relative to those at the start and end of the sequence could be indicative of a lake of greater volume whereby the $\delta^{18}\text{O}$ of lake waters would be less prone to evaporitic enrichment, subsequently leading to more negative $\delta^{18}\text{O}$ values. Alternatively, the depleted $\delta^{18}\text{O}$ values may reflect greater amounts of precipitation as there is a negative trend in $\delta^{18}\text{O}$ values in response to increasing rainfall in the tropics (Rozanski, 1993). It could also be that water temperatures were high at the time of calcite precipitation, depleting the $\delta^{18}\text{O}$ of calcite (Leng and Marshall, 2004). $\delta^{13}\text{C}$ values remain stable throughout the unit, lying between -0.77‰ and 1.09‰ typical of a

lacustrine body in equilibrium with atmospheric CO₂ (Leng and Marshall, 2004). There is no significant covariance between $\delta^{18}\text{O}$ and $\delta^{13}\text{C}$ with an R² coefficient of 0.00 through the unit, indicative of a hydrologically-open lake system (Talbot, 1990).

While the microfacies and isotopic data suggests sedimentation in a relatively deep and perennial lake environment, the presence of a sand-bed at the macroscale at 38 – 39 cm suggests some environmental instability with rare periods of large allogenic sand/silt input into the lake. Interestingly, the $\delta^{18}\text{O}$ isotope value at 40 cm is considerably more positive (-3.44‰) compared to those either side of it (35 cm = -6.11, 45 cm = -5.04). It is possible that the isotopic enrichment relates to the amount effect where lower rainfall levels lead to more positive $\delta^{18}\text{O}$ in precipitation (Rosanski, 1993). This itself may have reduced lake volume and led to a slight increase in evaporitic enrichment, though this is unquantifiable. As this coincides at the macroscale with a clear sand-rich bed, it suggests that a brief climatic event may have occurred destabilising the local environment. Similar but smaller isotopic enrichments occur between 15 – 20 cm and 60 – 65 cm, that may reflect similar events where the total amount of rainfall decreased.

The evaporitic mineral halite is also observed within Unit 2b at ~50 and ~70 cm. While the amount of halite is relatively low (3.1 – 9.8%) it is not negligible. Halite forms via the evaporitic concentration and evolution of ions within lake waters during phases where evaporation exceeds inflows (Verrecchia, 2007), and may represent brief arid phases.

After deposition of Unit 2b, lake levels dropped as is demonstrated by the sediments and isotopic data from Unit 2c (70 – 93 cm). At the macroscale, the sediments became more friable and could easily be broken into peds, indicating a reduction in fine-grained material and increase in allogenic sands. This is reflected by the decreasing CaCO₃ content which falls to 31% at 90 cm, while XRD analysis from the same level shows quartz is dominant (67.6%). Mottling is also present within this unit and implies the presence of vegetation (macrophytes) in shallow water conditions. Here redox processes concentrated around macrophyte roots leads to the formation of mottles. The microfacies is characterised by massive microsparite with some micrite present (Fig 10.4, panel D). This suite of sedimentary characteristics represents a shallow, well-

oxygenated polymictic lake effected by wind-induced mixing of lake waters or bioturbation of lake floor sediments. This suggests a contraction of the water body relative to the previous unit (Unit 2b), which brought the lake edge closer to the site of sedimentation. Contraction of the lake could be due to the progressive infilling of the basin through the humid interval or relate to increased aridity and a drop in the water level. The $\delta^{18}\text{O}$ values support this latter scenario, since they are far more positive than those in the previous unit and similar to Unit 2a. This probably reflects lower rainfall levels. $\delta^{13}\text{C}$ values remain unchanged from those in other sections, and are consistent with deposition under a water body in equilibrium with the atmosphere.

The final phase of carbonate sedimentation (Unit 2d) reflects deposition in the littoral zone of the lake. At the macro-scale the sediments are mechanically strong, well-cemented fine-grained carbonate with small tubular voids that closely mirror those observed at Unit 2d at Al Wusta. At the micro-scale they consist of a prismatic microstructure composed of a micritic to microsparite groundmass with numerous planar voids. Such characteristics are indicative of a vegetated, shallow water environment, where calcite precipitation is concentrated around macrophyte roots.

10.6 Summary

The key points from this chapter are as follows:

- A sedimentary sequence from site WNEF16_28 was investigated. The sequence contained three units: (1) aeolian sands; (2) carbonate-rich marls (~1.1 m thickness); (3) crudely laminated sands with gravel inclusions and capped by calcitic rhizoliths.
- The carbonate-rich marls were further divided into four sub-units. A combination of bulk-sedimentology, micromorphology and stable isotope analysis suggests that the sediments represent a perennial and freshwater lake. Variations in the microfacies and isotopic data suggest fluctuations in lake depth and the amount

of rainfall, with a lake of greater volume (Unit 2b) sandwiched by sediments that reflect a shallower but still perennial waterbody (Units 2a, 2c and 2d).

- The $\delta^{18}\text{O}$ values from unit 2b are the lowest observed in any sequence in the western Nefud Desert.
- Diatom analysis carried out by colleagues reveals assemblages dominated by freshwater species, and this supports the interpretation drawn by the bulk sedimentary, microfacies and stable isotope analysis.
- In summary, the sedimentary sequence at WNEF16_28 reflects the depositional history of a humid phase in the western Nefud desert that occurred during MIS 5e. While it is impossible to know how complete a record of a humid phase this sequence represents it is noticeable that the sediments reflect the transition from arid (aeolian dunes) through humid (lacustrine marls) back to arid (surface wash sands) again. It is therefore plausible to argue that the sequence presented here reflects a full humid phase cycle. It is also notable how similar the broad pattern of the sedimentary sequence is to that of trench PD40 at Al Wusta.

Chapter 11 – Ti's al Ghadah palaeoenvironmental results

11.1 Introduction

Ti's al Ghadah (TAG) lies in an interdunal depression ~3 km from the southwestern edge of the Nefud Desert, Saudi Arabia (N 27.43, E 39.37) (Fig 11.1). The basin lies between two major NW-SE trending traverse barchanoid compound dunes. The dominant feature within the basin is a large 620 m NW-SE trending marl ridge ('Upper lake deposit': Fig 11.1), that rises up to 6 m from the basin floor and dips gently downwards from NW to SE. The full sedimentary sequence excavated at TAG is ~10 m in depth (see Fig 11.2) and has been discussed extensively in previous publications (Stimpson et al., 2016; Stewart et al., 2019). However, no microfacies, XRD or isotopic analysis has previously been undertaken at the site. The stratigraphic sequence was originally split into 9 units (Fig 11.2) (Stimpson et al., 2016), with an additional unit (Iron Lake; IL) added following renewed investigations at the site in 2017 (Fig 11.2) (Stewart et al., 2019). The sequence consists of dune sands (Unit 1), ancient iron-indurated fine-grained carbonate (IL), waterlain sands (Units 2 – 5) and a complex sequence of interbedded fine-grained carbonate and sand beds (Units 6 – 9). It is this latter sequence that is discussed within this thesis, named here as "Ti's al Ghadah 1". Previous geochronological work suggests that units 5 – 9 date to between 300 – 500 ka (Rosenberg et al., 2013; Stimpson et al., 2016).

The Ti's al Ghadah 1 sedimentary sequence relates to a trench pit dug into the southern section of the Ti's al Ghadah lake surface during a previous field season (Fig 11.1). The base and upper surface of this sequence correlates to Unit 5 and Unit 9 respectively of Stimpson et al. (2016) and Stewart et al. (2019) (Table 11.1). The Ti's al Ghadah 1 sequence is described in its own right and the units described here are correlated with those previously published (see Table 11.1). An additional sedimentary sequence named Ti's al Ghadah 2 is also described here for the first time. This lies towards the northern end of the 'upper lake deposit' (see Fig 11.1). As this sequence is dug into the same marl ridge that runs through the basin, it is assumed that it formed within the same

waterbody as Ti's al Ghadah 1. Consequently, the depositional model will consider both sequences together. A combination of bulk sedimentology, microfacies analysis and $\delta^{18}\text{O}$ and $\delta^{13}\text{C}$ have been undertaken to construct a depositional model. Diatom palaeoecology has also been carried out by Dr. Wing Wai Sung as part of the Palaeodeserts research project and published by Stewart et al. (2019), but the data is included here as it strongly supports the depositional model provided by the other proxy data.

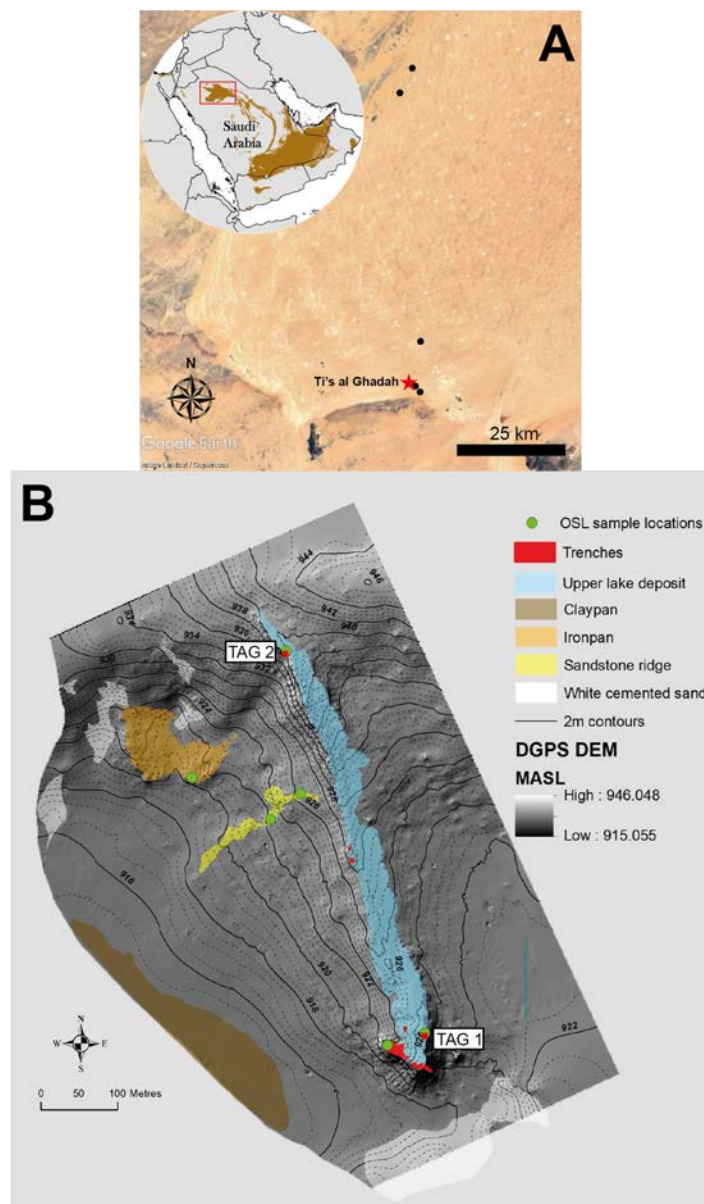


Figure 11.1 – (A) Location of the Ti's al Ghadah interdunal basin within the western Nefud Desert (red star). Other black dots represent other interdunal sites studied in this thesis. Inset map shows the location of the Nefud Desert on the Arabian Peninsula. (B) Digital elevation model of the interdunal basin at TAG with OSL sample locations, trenches and key features highlighted (Breeze, unpub). Note that no OSL work was undertaken as part of this thesis. The

sedimentary sequences analysed here are labelled, with TAG 1 lying at the southern tip of the 'Upper lake deposit' and TAG 2 lying at the northern edge of the deposit at a higher altitude.

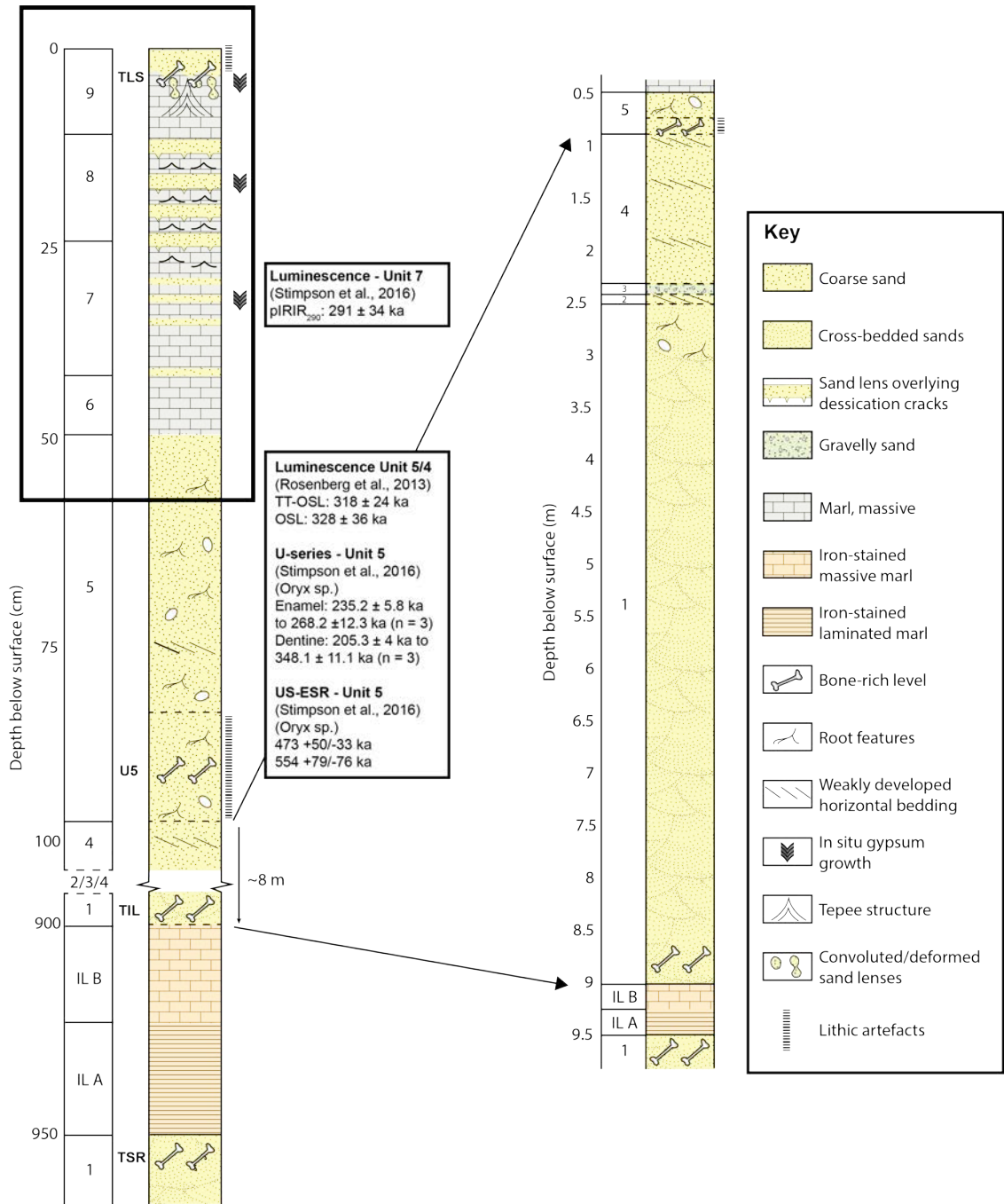


Figure 11.2 – The complete stratigraphic sequence recorded at Ti's al Ghadah as described by Stimpson et al. (2016) and later revised by Stewart et al. (2019). The rough location of the sedimentary section focused on here is outlined in a black box. Image modified from Stewart et al. (2019).

Table 11.1 – Correlation of units identified in this thesis compared with units ascribed during previous work (see Fig 11.2).

Unit correlation		
Stimpson et al. 2016 units	Ti's al Ghadah 1 (this thesis) units	Ti's al Ghadah 2 (this thesis) units
5	1	1
6/7	2a, 2b	2
8	3	Not present
9	4/5	3

11.2 Ti's al Ghadah 1

11.2.1 Sedimentology

11.2.1.1 Bulk sedimentology

The sedimentary sequence at Ti's al Ghadah 1 is split into five units from the base upwards (Fig 11.3). **Unit 1 (0 – 14 cm)** consists of loosely consolidated green sands with weak horizontal bedding and small gravel inclusions. This grades into **unit 2a (14 – 27 cm)** which consists of fine-grained carbonate-rich marls with cm-scale sand beds. This grades into **unit 2b (27 – 35 cm)** which is composed of consolidated fine-grained carbonate-rich marl. Carbonate content within units 2a and 2b range between 72 – 85%, while XRD analysis from 25 – 27 cm shows calcite is dominant (92.7%) with a small fraction of quartz (7.3%). There is a sharp transition into **unit 3 (35 – 57 cm)** which is composed of interdigitated fine-grained carbonate-rich marl and sand beds. The carbonate beds are typically ~2 – 4 cm thick, well-consolidated and homogenous. They preserve the form of ripple bedding and also contain desiccation features such as tepee structures. Carbonate content taken from two distinct marl beds within this unit is 81% while XRD analysis shows calcite is predominant (92.5 – 97.5%) with quartz the only other mineral present (2.5 – 7.5%). Sand beds within this unit are ~2 – 7 cm thick. **Unit 4 (57 – 65 cm)** consists of well-cemented homogenous marls with gravel inclusions and is capped by desiccation features. Carbonate content is much lower within this unit at 55% while XRD shows calcite is also much lower (56.6%) with a greater quartz component (37.2%) and a small proportion of gypsum (6.2%). **Unit 5 (65 – 87 cm)** is

separated from the unit below by an erosional contact. The unit itself consists of cemented, laminated coarse sands and gravel clasts.

Table 11.2 – X-ray diffraction results from Ti's al Ghadah 1. Calcite is dominant though it is important to note that sand beds separate carbonate beds in unit 3. The proportion of quartz increases in unit 4, and there is a small proportion gypsum.

Height above base (cm)	Unit	Calcite (%)	Quartz (%)	Gypsum (%)
29	2b	92.7	7.3	0
37 - 43	3	92.5	7.5	0
51 - 53	3	97.5	2.5	0
60	4	56.6	37.2	6.2

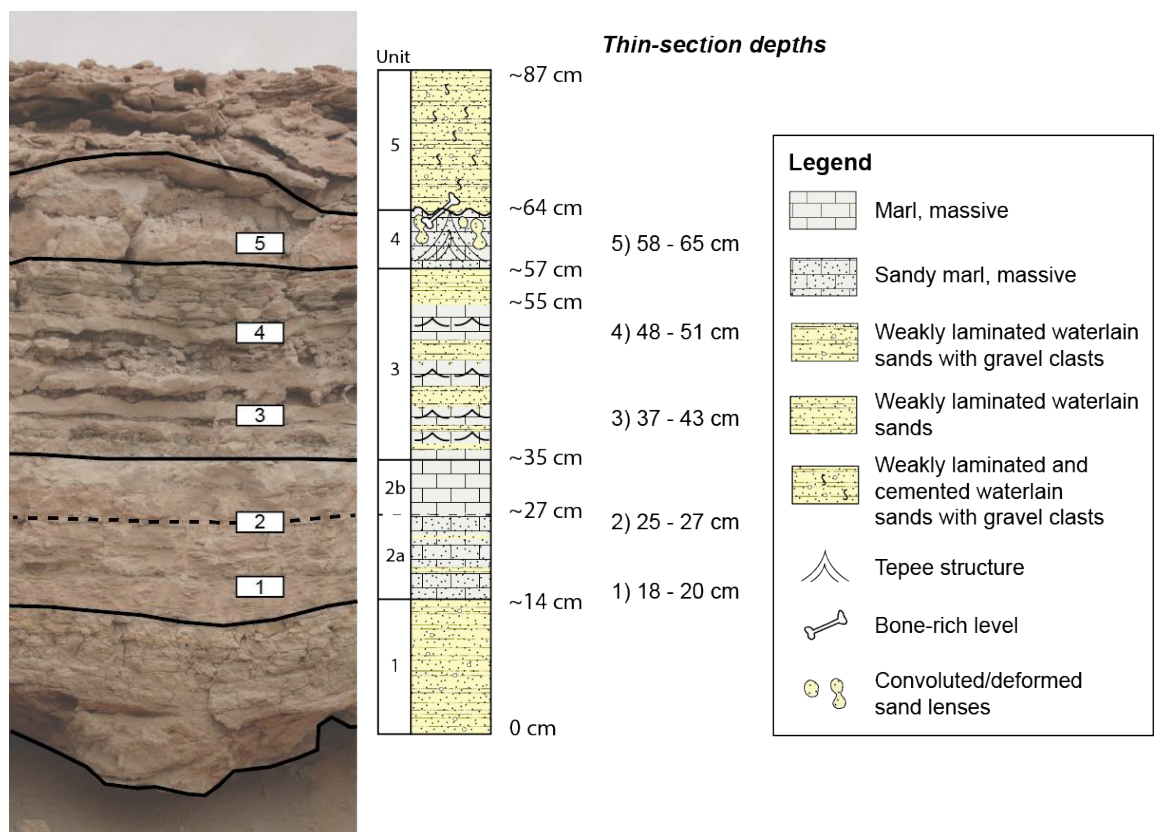


Figure 11.3 – Sedimentary sequence at Ti's al Ghadah 1, with thin-section sample locations highlighted. Solid black lines represent unit boundaries while dashed black lines represent sub-unit boundaries.

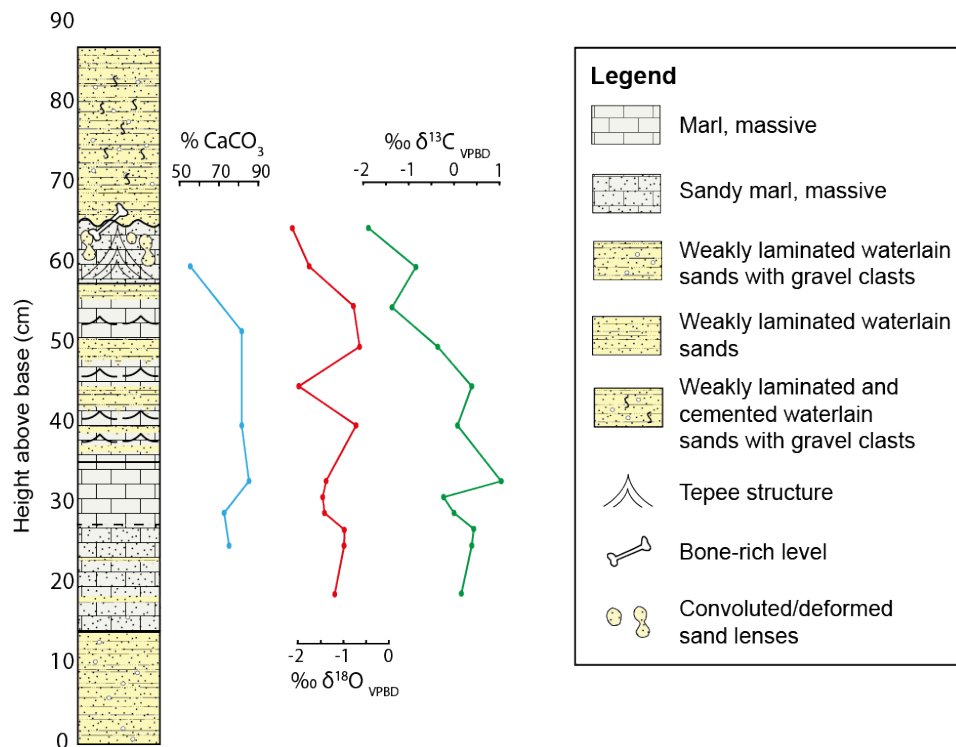


Figure 11.4 - Sedimentary log along with CaCO₃ (blue), δ¹⁸O (red) and δ¹³C (green) for Ti's al Ghadah 1.

11.2.1.2 Microfacies descriptions

A total of five samples were taken for microfacies analysis through the sequence. Unit 2a and 2b contained microfacies with a homogenous or laminated microstructure with a groundmass dominated by microsparite and micrite, with a sparse coverage of allogenic sand grains (5 – 10%) but with patches with greater coverage (33%) (Fig 11.5, panel A). Shell fragments were frequent in the thin-section from Unit 2a (18 – 20 cm), concentrated around patches of greater allogenic grain frequency, but not present in the upper thin-section that sits on the boundary of Unit 2a and 2b (see Fig 11.3). Units 3 and 4 contained microfacies with a predominantly homogenous microstructure but with some patches that are prismatic (Fig 11.5, panel B). The groundmass was predominantly composed of microsparite, but with some patches of larger sparite crystals. Allogenic grain coverage is patchy, with some sections of sparse coverage (2 – 5%) and other sections of dense coverage (33%). The final thin-section (~58 – 65 cm) shows even and dense allogenic grain coverage (10 – 25%). Shell fragments are present and frequent in unit 3, but not present in unit 4. Sparite grain coatings and void fillings are observed across all thin-sections from Units 3 and 4.

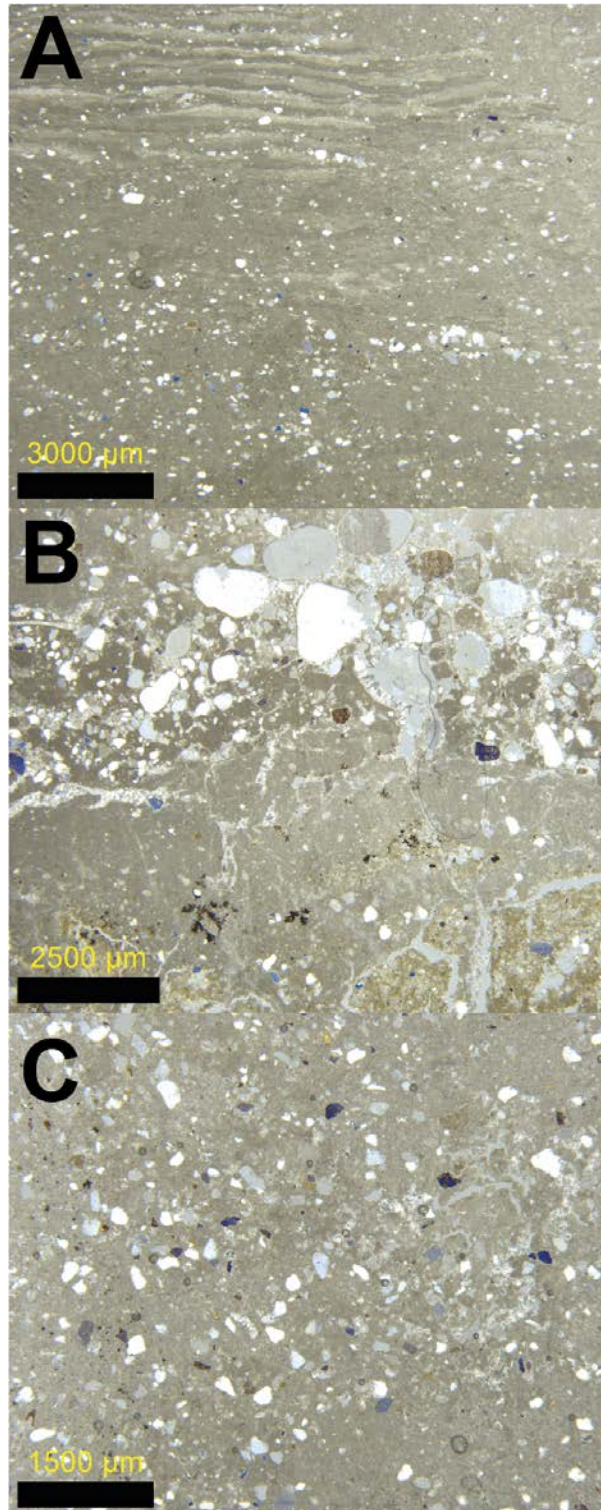


Figure 11.5 – Photomicrographs of thin-sections through the sedimentary sequence at Ti’s al Ghadah 1. (A) 25 – 27 cm above base from the Unit 2a/2b boundary. This is composed of a predominantly massive microsparite with laminations between microsparite crystal sizes observed at the top of the microfacies. Allogenic grain coverage is evenly spread across the slide. (B) 37 – 43 cm above base from a marl bed in Unit 3. This thin-section contains a more prismatic structure with a microsparite groundmass. Numerous planar voids are present and there is an inwash of coarse sand grains to silt grains that runs through the thin-section. (C) 58 – 65 cm above base from Unit 4. This is composed of a massive microstructure with a groundmass of microsparite with some patches of sparite. Rare planar voids and chambers infilled with sparite are present. Allogenic grain coverage is evenly spread across the slide.

11.2.3 $\delta^{18}\text{O}$ and $\delta^{13}\text{C}$

$\delta^{18}\text{O}$ values range between -0.61‰ and -2.12‰ and have a mean and median value of -1.26‰ . Values are stable over the first 33 cm but fluctuate between 40 – 65 cm (Units 3 and 4; Fig 11.4). Nonetheless, the range of $\delta^{18}\text{O}$ values is small throughout the sequence (1.51‰). The $\delta^{13}\text{C}$ values lie between 1.07‰ and -1.85‰ , with a mean value of -0.15‰ and a median of 0.07‰ . Though the values have a relatively small range (2.93‰), it is notable that there is a depleting trend from the top of Unit 2b to Unit 5, with the final three samples the most negative. The R^2 coefficient between $\delta^{18}\text{O}$ and $\delta^{13}\text{C}$ through the sequence is 0.06 with a p-value of 0.47 (Fig 11.6).

Table 11.3 - Descriptive statistics for $\delta^{18}\text{O}$ values of lake carbonates at Ti's al Ghadah 1.

Site	Height above base (cm)	N	Mean (‰)	Median (‰)	SD (1σ) (‰)	Min (‰)	Max (‰)	Range (‰)
TAG1	19 – 65	12	-1.26	-1.26	0.49	-2.12	-0.16	1.51

Table 11.4 - Descriptive statistics for $\delta^{13}\text{C}$ values of lake carbonates at Ti's al Ghadah (TAG) 1.

Site	Height above base (cm)	N	Mean (‰)	Median (‰)	SD (1σ) (‰)	Min (‰)	Max (‰)	Range (‰)
TAG1	19 – 65	12	-0.15	0.07	0.32	-1.85	1.07	2.93

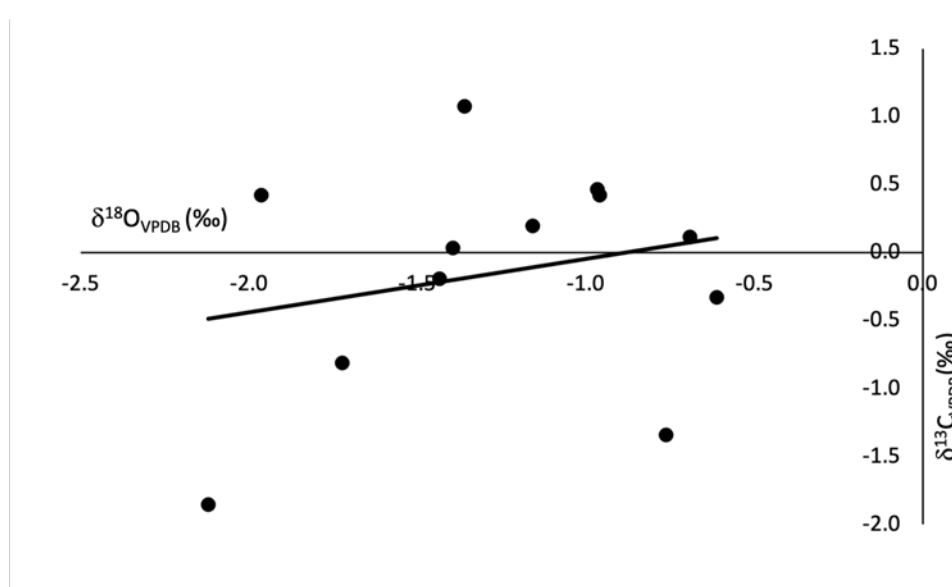


Figure 11.6 - Covariation between $\delta^{18}\text{O}$ and $\delta^{13}\text{C}$ at Ti's al Ghadah 1. The R^2 value is 0.06 with a p-value of 0.47.

11.2.4 Diatom palaeoecology

Diatom palaeoecology has been undertaken in previous research and is described in Stewart et al. (2019). Diatom samples were taken at a 5 cm interval through 'Unit 6' as described by Stimpson et al. (2016) which correlates with Unit 2. Diatom preservation was poor and only a single sample contained enough diatoms to plot percentage abundances of diatom taxa present. This sample yielded half of what is considered sufficient for a statistically valid dataset (Stewart et al., 2019). Nonetheless, diatom taxa are dominated by freshwater species such as *Staurosira construens* var. *construens*, *Staurosira pinnata* var. *pinnata* and *Staurosira pinnata* var. *intercedens* (Stewart et al., 2019). A single brackish species, *Nitzschia sigma*, is present but at a very low concentration. The diatom assemblage present contains species which differ in their preferred environment with *Aulacoseira crassipunctata* preferring more acidic lakes (pH ~5 – 6) and *S. pinnata* var. *intercedens* preferring more neutral/alkaline waters (pH ~6.9 – 8.2). Importantly, the assemblage is dominated by freshwater species demonstrating that the water body during the deposition of this unit was predominantly fresh.

11.3 Ti's al Ghadah 2

11.3.1 Sedimentology

11.3.1.1 Bulk sedimentology

The sedimentary sequence at Ti's al Ghadah 2 is split into three units (Fig 11.7). **Unit 1 (0 – 14 cm)** consists of unconsolidated white sands with gravel inclusions that grades into finer brown sands towards the top of the sequence. **Unit 2 (14 – 41 cm)** consists of homogenous and consolidated fine-grained carbonate-rich marls. Calcium carbonate content ranges between 64% and 90%, with lower values at towards the bottom of the unit rising to consistently high values in the middle and upper part of this unit (Fig 11.8). XRD shows calcite is predominant (84 - 91%) with a small proportion of quartz (9 – 16%) (Table 11.5). **Unit 3 (41 – 43 cm)** consists of cemented sands with some gravel inclusions.

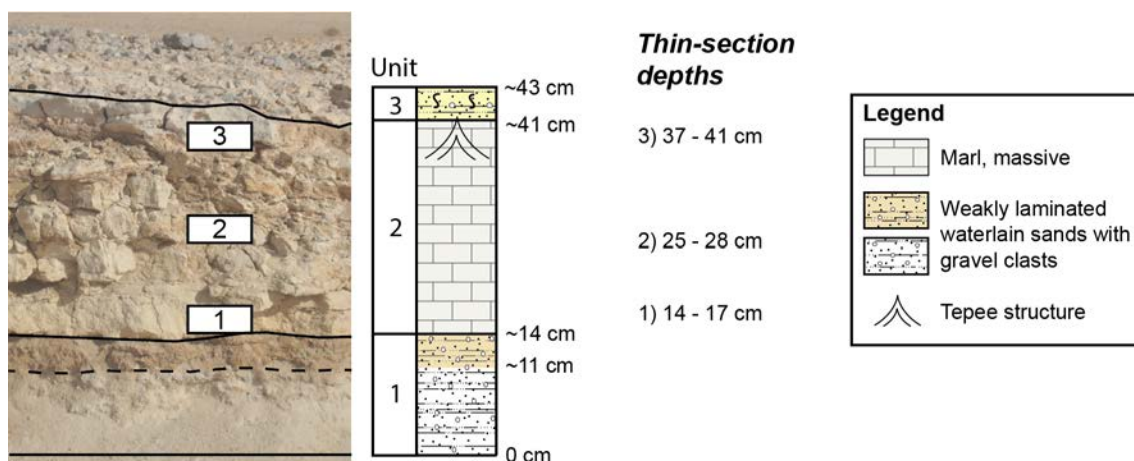


Figure 11.7 - Sedimentary sequence at Ti's al Ghadah 2, with thin-section sample locations highlighted. Solid black lines represent unit boundaries while dashed black lines represent sub-unit boundaries.

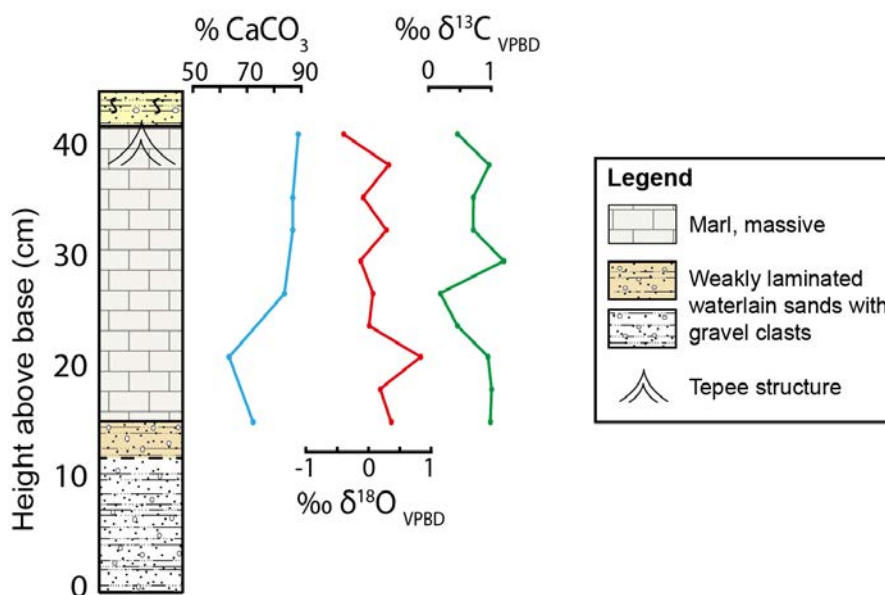


Figure 11.8 - Sedimentary log along with CaCO_3 (blue), $\delta^{18}\text{O}$ (red) and $\delta^{13}\text{C}$ (green) for Ti's al Ghadah 2.

Table 11.5 – X-ray diffraction results from Ti's al Ghadah 2. Calcite is dominant though it is important to note that sand beds separate carbonate beds in unit 3. The proportion of quartz increases in unit 4, and there is a small proportion gypsum.

Height above base (cm)	Unit	Calcite (%)	Quartz (%)
20	2	84	16
32	2	91.1	8.9
41	2	87.8	12.2

11.3.1.2 Microfacies descriptions

A total of three samples for microfacies analysis were taken across unit 2, the homogenous fine-grained carbonate rich marls. The lower two samples from 14 – 17cm and 25 – 28 cm display similar microfacies, dominated by homogenous microstructure with a microsparite groundmass, low void coverage (<5%) but with rare planar voids, low allogenic grain coverage (2 – 5%), rare shell fragments and no depletion or concentration features. The uppermost thin-section at 37 – 41 cm also contains a homogenous microstructure that predominantly consists of microsparite though contains patches of sparite. There is a low void coverage (<5%) and low allogenic grain coverage (~2%). Unlike the two sections below, shell fragments are frequent as are concentration/depletion features with sparite grain coatings and iron staining concentrated around rare planar voids.

11.3.2 $\delta^{18}\text{O}$ and $\delta^{13}\text{C}$

$\delta^{18}\text{O}$ values range between 0.87‰ and -0.40‰, have a mean and median value of 0.16‰ and 0.14‰ respectively. The $\delta^{13}\text{C}$ values lie between 1.26‰ and 0.23‰, with mean and median values of 0.82‰ and 0.89‰ respectively. The R^2 coefficient between $\delta^{18}\text{O}$ and $\delta^{13}\text{C}$ through the sequence is 0.14 with a p-value of 0.29.

Table 11.6 - Descriptive statistics for $\delta^{18}\text{O}$ values of lake carbonates at Ti's al Ghadah (TAG) 2.

Site	Height above base (cm)	N	Mean (‰)	Median (‰)	SD (‰)	Min (‰)	Max (‰)	Range (‰)	Range
TAG2	14 - 41	10	0.16	0.11	0.14	0.35	-0.4	0.87	1.27

Table 11.7 - Descriptive statistics for $\delta^{13}\text{C}$ values of lake carbonates at Ti's al Ghadah (TAG) 2.

Site	Height above base (cm)	N	Mean (‰)	Median (‰)	SD (‰)	Min (‰)	Max (‰)	Range (‰)	Range
TAG2	14 - 41	10	0.82	0.1	-0.89	0.32	0.23	1.26	1.03

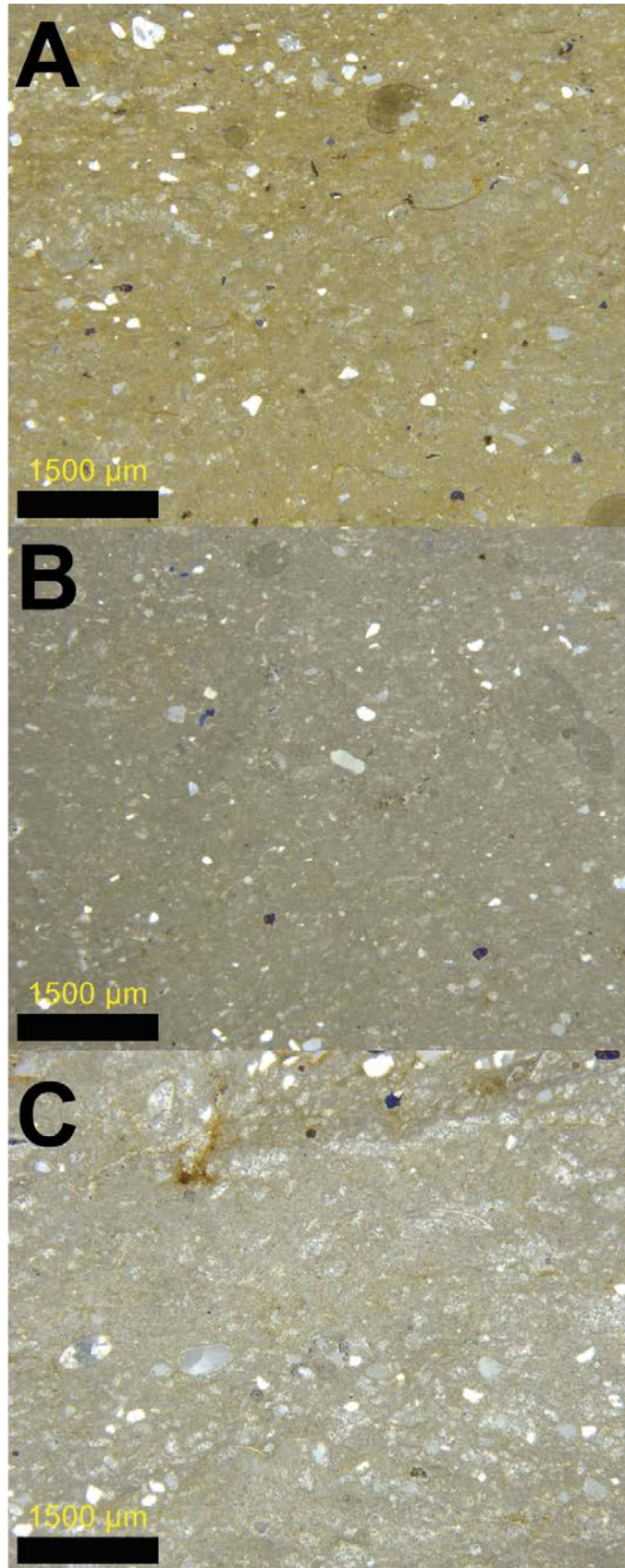


Figure 11.9 – Photomicrographs of microfacies from Ti's al Ghadah 2. (A) 14 – 17 cm above base from Unit 2. (B) 25 – 28 cm above base from Unit 2. (C) 37 – 41 cm above base from Unit 2. Note that all microfacies are similar with a homogenous microstructure and a microsparite groundmass. The upper most section (panel C) contains a greater number of sparite patches.

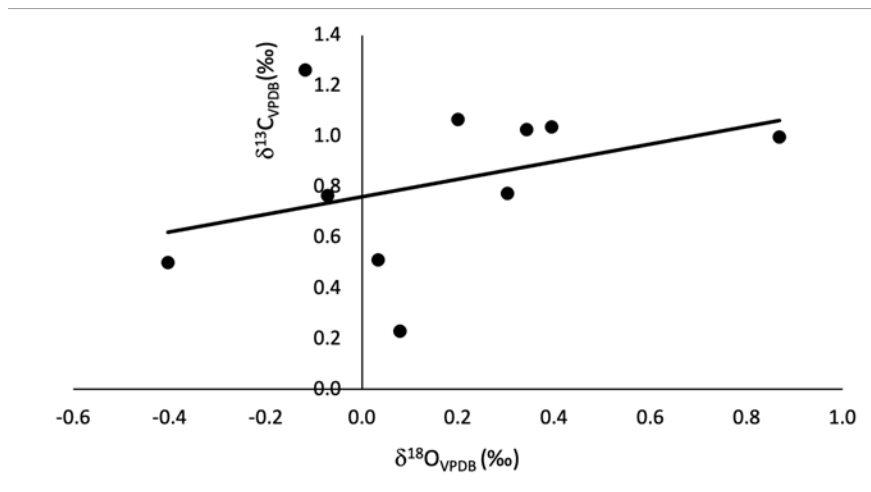


Figure 11.10 - Covariation between $\delta^{18}\text{O}$ and $\delta^{13}\text{C}$ at Ti's al Ghadah 2. The R^2 value is 0.14 with a p -value of 0.29.

11.4 Depositional model

The sedimentary evidence described in this chapter is used to construct a depositional model for the upper carbonate deposits at the site. Four main phases of sediment deposition are recorded in the sedimentary sequence. Unit 1 at both Ti's al Ghadah 1 and Ti's al Ghadah 2 consist of weakly horizontally laminated sands with occasional gravel clasts. The presence of a coarse grain component (gravels) is indicative of waterlain sedimentation at the margin of a shallow wetland. Sands were probably deposited via sheet wash processes after heavy rainfall events at the onset of a humid period. This interpretation is consistent with that of Unit 5 (Stimpson et al., 2016; Stewart et al., 2019).

The waterbody then transitioned towards a more extensive lake body as reflected Units 2a and 2b at Ti's al Ghadah 1, and Unit 2 at Ti's al Ghadah 2. Here the sediments gradually transition from horizontally bedded sands to fine-grained carbonate rich marls with occasional sand beds (Unit 2a; Ti's al Ghadah 1). The sand beds become less frequent moving upwards through the sequence until homogenous and consolidated fine-grained carbonate is present (Ti's al Ghadah 1; Unit 2, Ti's al Ghadah 2). The microfacies across these units consist of homogenous and faintly laminated microstructure with a microsparitic groundmass (Fig 11.5 and 11.9). Allogenic sand coverage is minimal

(between 2 – 10% coverage) and there is a lack of any desiccation features. XRD shows calcite is dominant (84 – 93%) with the remaining mineralogy made up of quartz (7 – 16%). $\delta^{13}\text{C}$ values range between -0.19‰ and 1.26‰ consistent with a waterbody in equilibrium with atmospheric CO_2 , while prior diatom analysis suggests the lake waters were fresh (Stewart et al., 2019). Taken together, these characteristics suggests that Units 2a and 2b at Ti's al Ghadah 1 and Unit 2 at Ti's al Ghadah 2 were deposited within a shallow but perennial freshwater lake body. The presence of a perennial water body is supported by fossil evidence recovered from the waterlain sands below the marls, where the remains of a large osteoglosiform fish was recovered (Stimpson et al., 2015, 2016).

The lake then shallows and becomes more dynamic, as represented by the change in sedimentation style at Ti's al Ghadah 1 and the cessation of sedimentation at Ti's al Ghadah 2 where the water level presumably dropped below ~ 938 m asl. Unit 3 at Ti's al Ghadah 1 is composed of interdigitated fine-grained carbonate with sand beds, with the former deposited during periods of greater lake volume and the latter during periods of lower lake volume. Carbonate beds are horizontally continuous, well consolidated, contain tepee structures and are between 2 – 6 cm thick. Microfacies analysis of these beds reveal either microsparite with numerous planar voids and a range of allogenic grain sizes (Fig 11.5, panel B) or homogenous microsparite with a range of allogenic grain sizes. The former microfacies is consistent with deposition in a palustrine environment where the sediment was sub-aerially exposed following deposition leading to the development of desiccation features such as planar voids. The latter microfacies is more consistent with a shallow well-mixed waterbody and reflects a period during which a shallow but perennial lake body formed. The presence of tepee structures within the marl beds, which form as authigenic minerals grow during periods of increased evaporation leading to brecciation, attests to periodic desiccation of the waterbody as demonstrated by the microfacies in Fig 11.5, panel B. When desiccation of the waterbody occurred, the style of sedimentation transitioned from geochemical to clastic and sand beds were deposited. Here coarse-grain sediment (sands) are more likely to be deposited as lake volume reduces and contracts, and the site of sedimentation is

therefore closer to the lake edge. Conversely, during high lake stands the coarse grain sediment is unlikely to reach the centre of the basin.

The final phase of lacustrine sedimentation is represented by Unit 4 at Ti's al Ghadah 1. This unit consists of well-cemented homogenous fine-grained carbonate with gravel inclusions at the macroscale. The microfacies consists of homogenous microsparite with some chambers infilled with sparite crystals and a relatively high coverage of allogenic sand and silt grains at the microscale. These characteristics are consistent with sedimentation in a nearshore, shallow lake environment. The gravel inclusions are indicative of high-energy sheet/surface wash events transporting siliclastic material into the basin, while the high-number of allogenic sand grains is consistent with a nearshore lacustrine environment where the lake has contracted bringing the site of sedimentation closer to the lake edge. The higher allogenic content is supported by the XRD analysis which shows a substantial increase in quartz (see Table 11.2) Additionally, the surrounding landscape may have been less vegetated as the climate shifted back towards aridity at the end of a humid phase, making surficial dune sands readily available for transportation during intense rainfall events. Both $\delta^{13}\text{C}$ and $\delta^{18}\text{O}$ values are at their most negative in this section (see Fig 11.4), which may reflect increased throughflow in a shallow lake environment. Tepee structures in the upper part of this unit represent the final desiccation of the waterbody, while the presence of gypsum (6.2%) in XRD suggests the waterbody was affected by greater evaporation than previous units.

The final phase of sediment deposition is reflected by Unit 5 at Ti's al Ghadah 1 and Unit 3 at Ti's al Ghadah 2. These consist of cemented and laminated sands with gravel inclusions (see Fig 11.3, Unit 5) and are separated from the units beneath them by an erosional contact. These were likely deposited under sheet or surface wash conditions at the edge of a shallow waterbody and represent the final phase of humidity as the climate transitioned back towards aridity.

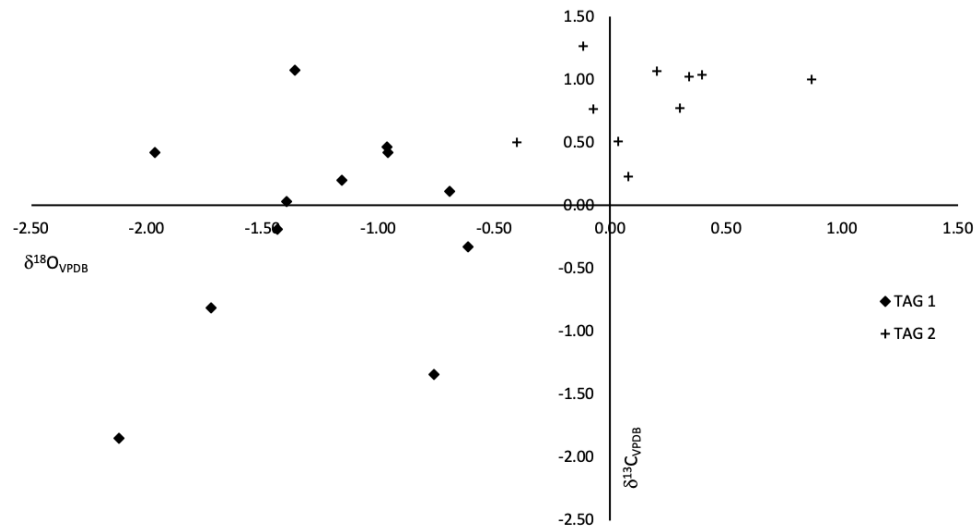


Figure 11.11 - $\delta^{18}\text{O}$ and $\delta^{13}\text{C}$ from Ti's al Ghadah 1 (diamonds) plotted against Ti's al Ghadah 2 (crosses). While the $\delta^{13}\text{C}$ values overlap with one another the $\delta^{18}\text{O}$ values do not overlap, with Ti's al Ghadah 2 values more positive.

As noted in the introduction, Ti's al Ghadah 1 and Ti's al Ghadah 2 are assumed to have formed within the same waterbody based on geomorphological observations (i.e. both sequences derive from trenches dug into the surface of the same marl ridge that runs through the interdunal basin). This is supported by both the microfacies analysis and $\delta^{13}\text{C}$ values which are broadly consistent with deposition within the same waterbody. However, the $\delta^{18}\text{O}$ values from each sequence are distinctly different with no overlap when plotted alongside one another on a scatter plot (see Fig 11.11). Moreover, while the $\delta^{13}\text{C}$ values overlap between the two sequences, those from Ti's al Ghadah 2 are generally more positive than those from Ti's al Ghadah 1.

This difference in isotopic values is hard to reconcile given that both carbonate sequences were deposited at broadly the same period within the same waterbody. One key difference between the two sequences is in their height. Ti's al Ghadah 2 lies at the northern end of the ridge at an altitude of approximately ~938 m while Ti's al Ghadah 1 lies towards the southern end of the ridge at approximately ~925 m (see Fig 11.1). Consequently, the Ti's al Ghadah 2 deposit lay in a more nearshore and marginal lake setting than Ti's al Ghadah 1 and this may have influenced the $\delta^{18}\text{O}$ values of each sequence, though it is not entirely clear how.

The difference in height along the marl bench also provides semi-qualitative information on potential lake depth at the lake bodies peak volume. Given the height at the northern end of the marl ridge is ~938 m and the height at the southern end of the marl ridge is ~924 m, this suggests a lake depth of at least 14 metres. Again, a lake of such depth is consistent with presence of large osteoglosiform fish and species of bird with aquatic affinities such as grebe and duck (Stimpson et al., 2015, 2016).

11.5 Summary

The key points from the Ti's al Ghadah sedimentary sequences are:

- The site contains multiple lacustrine sequences (see Fig 11.2) but we focus on sediments on the 'Upper lake surface' (Units 5 – 9; Stewart et al., 2019) which are dated to between 300 – 500 ka.
- Bulk sedimentology, microfacies and $\delta^{18}\text{O}$ and $\delta^{13}\text{C}$ analysis suggest that the sedimentary sequences analysed here represents the inception of a shallow waterbody accumulating siliclastic sediments, that transitions towards a stable, perennial, carbonate-precipitating freshwater lake of at least ~14 m depth during peak humidity. As humidity decreased the waterbody contracted and became dynamic with fluctuating water-levels, as represented by the cessation of sedimentation at Ti's al Ghadah 2 and the interdigitated carbonate and sand beds in unit 3/4 at Ti's al Ghadah 1. The final unit represents the in-washing of sands into a shallow waterbody following the contraction of the lake body.
- This analysis is consistent with previous diatom research presented in Stewart et al. (2019) that indicates the lake at Ti's al Ghadah was freshwater, and faunal research presented in Thomas et al. (1998), Stimpson et al. (2015, 2016) and Stewart et al. (2019) that demonstrate the presence of large osteoglosiform fish, species of bird with aquatic affinities such as grebe and duck, and large mammals that require good access to water resources such as *Elephantidae*.
- Finally, evidence from Roberts et al. (2018) shows V-shaped cut marks in ungulate rib fragments from unit 5 (correlated with unit 1 at both Ti's al Ghadah 1 and Ti's al Ghadah 2) showing the site was utilised by humans. This is discussed in more detail in Chapter 14.

Chapter 12 – Khall Amayshan 4 (KAM4) palaeoenvironmental results

12.1 Introduction

Khall Amayshan 4 (KAM4) interdunal basin is located ~4 km from the northwestern edge of the western Nefud Desert (N 28.08°, E 39.35°, ~915 m asl) (Fig 12.1). The basin contains multiple distinct carbonate beds that formed during discrete humid phases over the past ~500,000 ka (Fig 12.1). Sedimentary sequences were analysed from each of these deposits. Here we present a combination of bulk sedimentology, microfacies analysis and $\delta^{18}\text{O}$ and $\delta^{13}\text{C}$ analysis for each carbonate deposit. Diatom palaeoecology work has been carried out by Dr. Wing Wai Sung at multiple sequences across the site while invertebrate palaeoecology work has been carried out by Dr. Tom White at lake 4. These analyses were undertaken as part of the Palaeodeserts research project. Their data are included here since they provide a useful supplement to the other proxy data.

12.2 KAM4 lake 1

The KAM4 lake 1 (KAM4 L1) sedimentary sequence lies in the western-central portion of the KAM4 interdunal basin and is located immediately adjacent to the lee side of the barchanoid dune that forms the western edge of the basin (Fig 12.1). Luminescence dating of the loose sands underlying the carbonate deposit yields an age of 412 ± 87 ka (Clark-Balzan, per comms), though there is no direct age from the sediments themselves. Nevertheless, the sediments are distinct from all other deposits within the basin in that they are heavily iron indurated and cemented. This is indicative of the sediments being exposed to multiple phases of groundwater movement and attests to their antiquity relative to the other sedimentary sequences at the site.

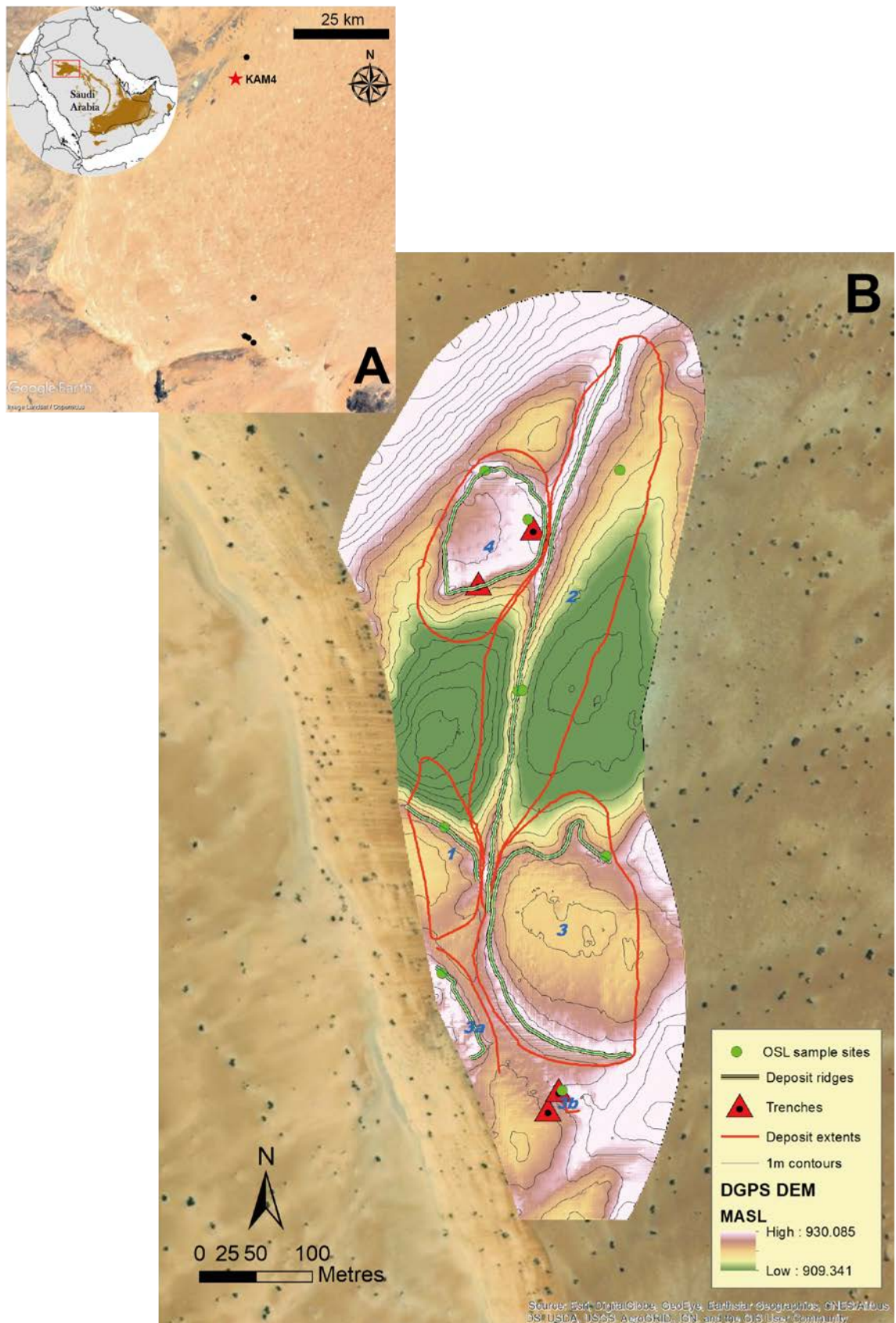


Figure 12.1 – (A) Location of the KAM4 interdunal basin within the western Nefud Desert (red star). Other black dots represent other interdunal sites studied in this thesis. Inset map shows the location of the Nefud Desert on the Arabian Peninsula. (B) Overhead view of the KAM4 basin with lakes labelled from 1 – 4. Trenches are highlighted by red triangles. OSL sample locations are indicated by green dots. Produced by Paul Breeze as part of the Palaeodeserts Project.

12.2.1 Sedimentology

12.2.1.1 Bulk sedimentology

The sedimentary sequence of KAM4 L1 is split into two units (Units 2 and 3) measured from the base of the waterlain sediments (carbonate-rich marls) upwards, with Unit 1 consisting of loose sands which underlie the carbonate sediments. All carbonate sediments are heavily iron indurated. **Unit 2 (0 – 30 cm)** predominantly consists of iron-stained fine-grained carbonate rich marls. The sediment is laminated at mm-scale between coarse- and fine-grained calcite, or between fine-grained calcite and iron-stained calcite/goethite. Calcium carbonate content within this section is >70% throughout, while XRD shows that calcite is dominant (between 89.6 – 97% weight) with a small proportion of goethite (1.6 – 3.5% weight) and quartz (1.4 – 6.1% weight). The top of this section is capped with desiccation cracks. **Unit 3 (30 – 50 cm)** is bedded at the cm-scale with sand beds alternating with horizontally continuous fine-grained carbonate rich marl beds. Calcium carbonate content in this unit is lower and lies between 48 – 54%. However, like Unit 2, Unit 3 also contains a large proportion of calcite (84.6% weight) with goethite (8.9%) and quartz (6.6%) also present.

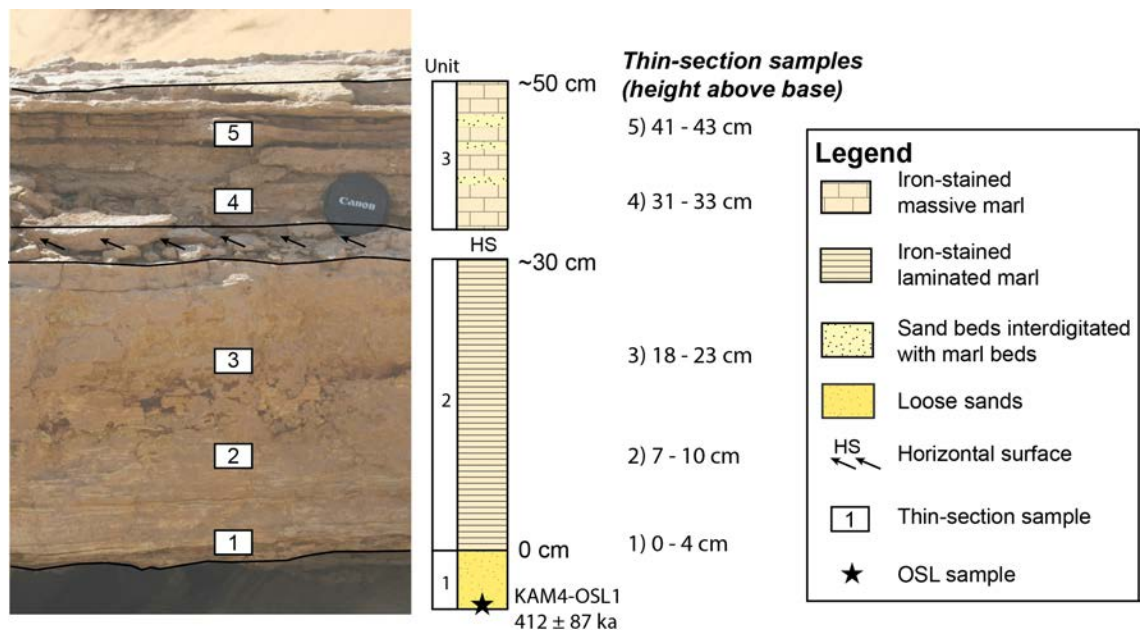


Figure 12.2 – Sedimentary sequence from KAM4 lake 1. Unit boundaries are represented by a solid black line. Thin-section sample locations through the sequence are shown, with the corresponding thin-section heights above base of the marl unit noted on the right side of the figure. OSL age is shown, produced by Clark-Balzan (per comms).

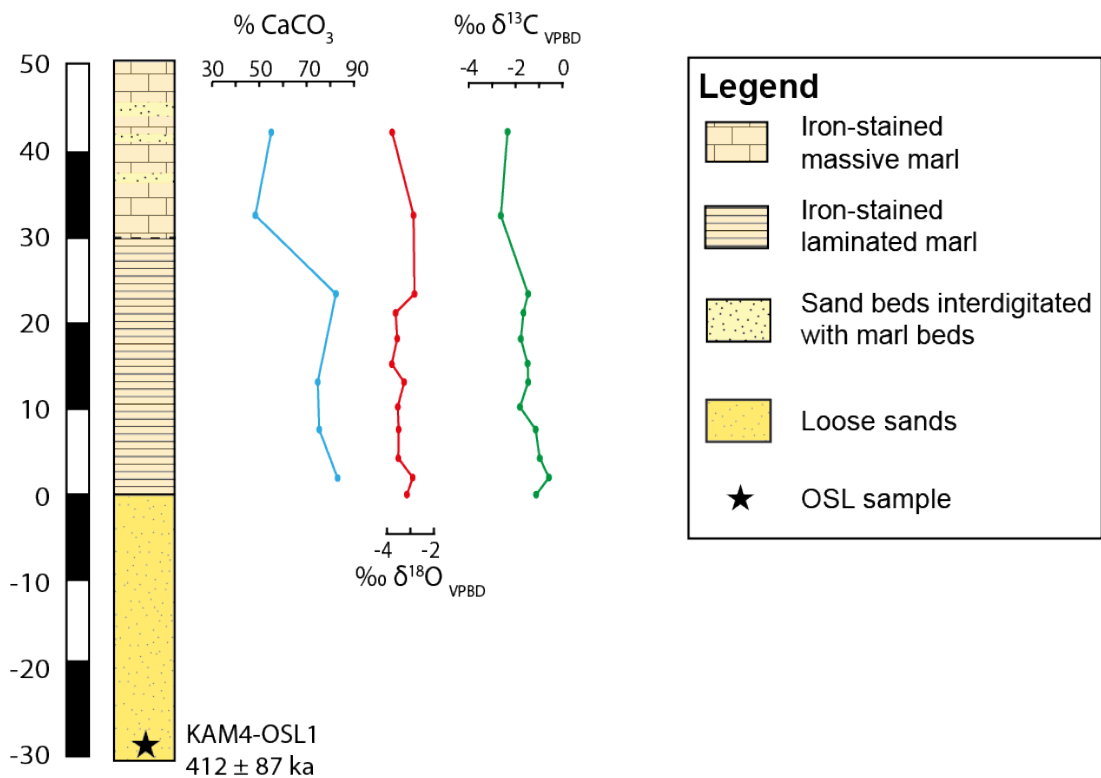


Figure 12.3 - Sedimentary log along with CaCO_3 (blue), $\delta^{18}\text{O}$ (red) and $\delta^{13}\text{C}$ (green) stratigraphy for KAM4 lake 1.

Table 12.1 – X-ray diffraction results from KAM4 lake 1. This shows calcite was dominant through the sequence, with low levels of quartz present. Goethite is also present through the sequence, but increases in proportion in unit 3.

Height above base (cm)	Unit	Calcite (%)	Quartz (%)	Goethite (%)	Muscovite (%)
7	2	89.6	6.1	3.5	0.8
23	2	97	1.4	1.6	0
41 - 43	3	84.7	6.5	8.9	0

12.2.1.2 Microfacies descriptions

A total of five samples were taken for microfacies analysis through the sequence, with three samples from unit 2 and two samples from Unit 3. Common attributes across all microfacies include low total void coverage (<5%), low percentage coverage of allogenic grains (<2%) and rare organic remains (i.e. shells, sponge spicules, amorphous organics). The microstructure of samples from Unit 2 are finely but discontinuously laminated, with laminations pinching in and out and often lenticular in form. The nature of the laminations and the groundmass they contain differs between the lowermost sample (0

– 4 cm) and the two samples above it (7 – 10 cm; 18 – 23 cm) (see the difference between panel A and B in Fig 12.4). The groundmass of the lowermost sample is composed of laminated microsparite and micrite, with limited evidence of iron-staining and/or goethite (Fig 12.4, A). In contrast, laminations in the upper two samples from unit 2 are composed of laminations between microsparite/sparite and goethite (Fig 12.4, B). It is notable that the goethite content increases moving upwards through Unit 2. Microfacies from Unit 3 exhibit a microstructure that contains laminations between microsparite/sparite and goethite, though these are frequently brecciated (Fig 12.4, C). These samples also contain a greater proportion of goethite, with large bands of homogenous goethite present. This is consistent with XRD analysis from these units, that shows goethite increases in proportion in Unit 3. Sparite and microsparite accumulations within internal cracks and planar voids are also observed within these two samples.

12.2.2 $\delta^{18}\text{O}$ and $\delta^{13}\text{C}$

$\delta^{18}\text{O}$ values lie between -3.76‰ and -2.78‰ , have a mean value of -3.32‰ and a median value of -3.46‰ . The $\delta^{18}\text{O}$ values remain stable through the sequence and there is no clear trend. $\delta^{13}\text{C}$ values lie between -0.55‰ and -2.60‰ , with a mean value of -1.51‰ and a median of -1.46‰ . There is a depleting trend (positive to negative values) moving upwards through the sequence. The R^2 coefficient between $\delta^{18}\text{O}$ and $\delta^{13}\text{C}$ through the sequence is 0.02 with a p-value of 0.64 (Fig 12.5).

Table 12.2 - Descriptive statistics for $\delta^{18}\text{O}$ values of lake carbonates at KAM4 lake 1.

Site	Height above base (cm)	N	Mean (‰)	Median (‰)	SD (1 σ) (‰)	Min (‰)	Max (‰)	Range (‰)
KAM4 L1	0 - 42	12	-3.32	-3.46	0.35	-3.76	-2.78	0.98

Table 12.3 - Descriptive statistics for $\delta^{13}\text{C}$ values of lake carbonates at KAM4 lake 1.

Site	Height above base (cm)	N	Mean (‰)	Median (‰)	SD (1 σ) (‰)	Min (‰)	Max (‰)	Range (‰)
KAM4 L1	0 - 42	12	-1.51	-1.46	0.57	-2.6	-0.55	2.05

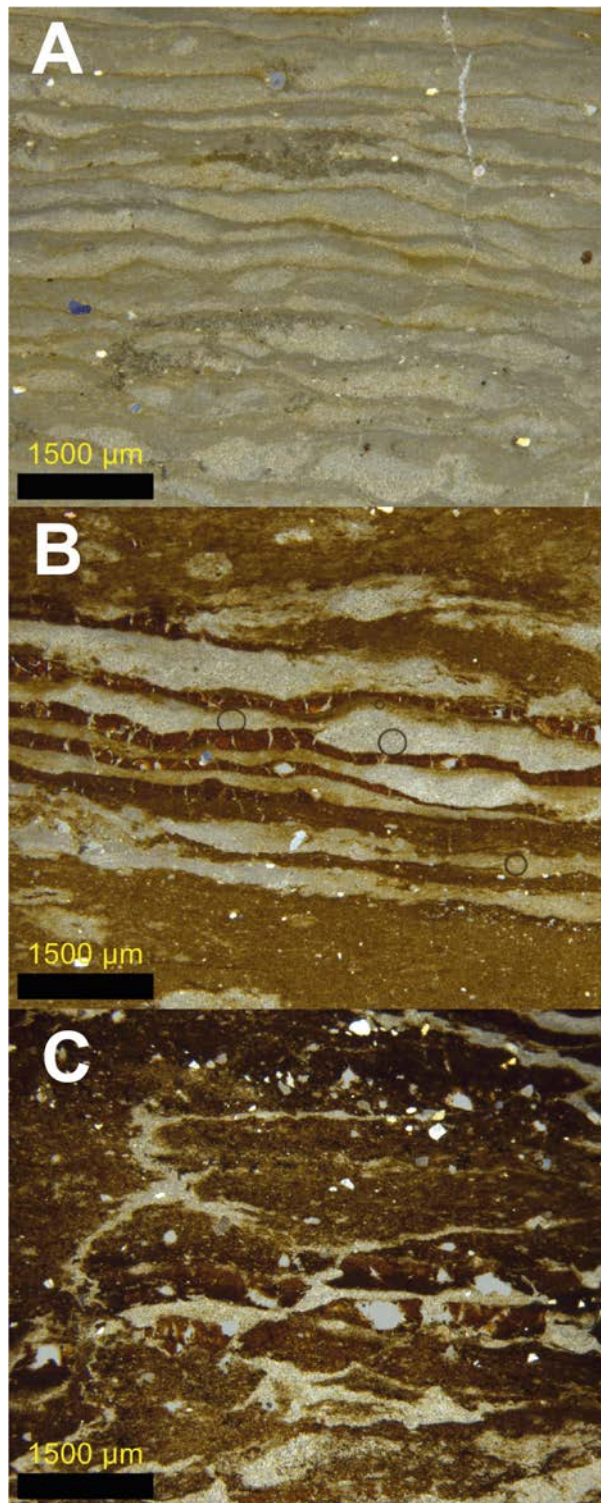


Figure 12.4 – Photomicrographs of thin-sections from KAM4 lake 1. (A) 0 – 4 cm above base from unit 2. This microfacies shows fine but discontinuously laminated microsparite/micrite where laminations pinch in and out. There is minimal iron staining in this section relative to other thin-sections. (B) 18 – 23 cm above base from unit 2. This microfacies shows fine and continuous laminations between microsparite and goethite. (C) 31 – 33 cm above base from a carbonate bed in unit 4. This microfacies shows brecciated laminations of microsparite and goethite, as well as portions of homogeneous goethite. Allogenic sand/silt grains are rare through all microfacies.

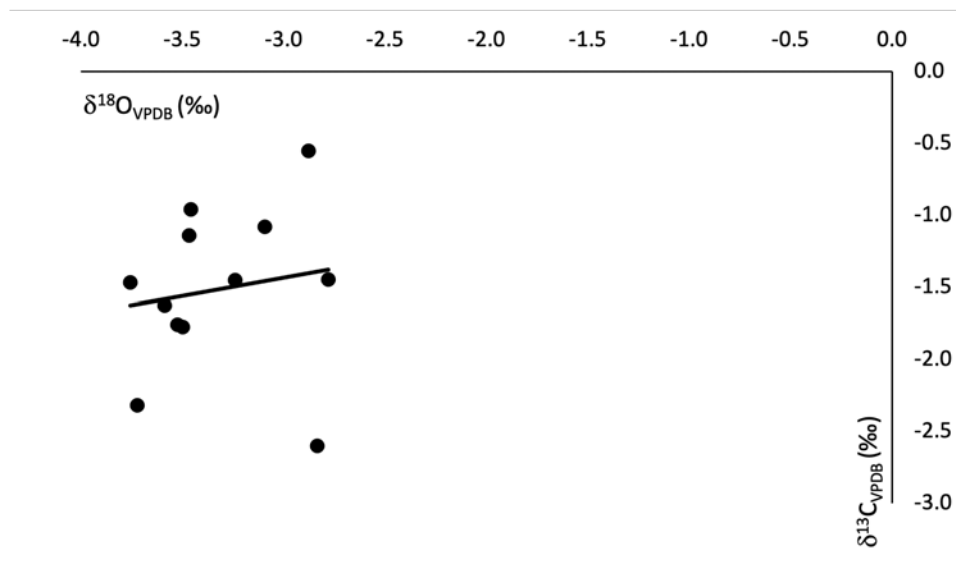


Figure 12.5 - Covariation between $\delta^{18}\text{O}$ and $\delta^{13}\text{C}$ for KAM4 lake 1. The R^2 value is 0.02 with a p-value of 0.64.

12.2.3 Diatom palaeoecology

Diatom abundances are low and only two samples could be used for taxonomic identification (contain >100 valves). As such, interpretations need to be made with caution. It is also important to note that because the diatom samples were collected during previous fieldwork, the diatom stratigraphy has been described from the surface downwards (Fig 12.6). This is in contrast with sedimentary descriptions within this thesis which describe the sediment from the base of the carbonate sediments upwards. Nevertheless, the depths of the two samples broadly correspond to ~2 cm and ~18 cm above base based on our measurement of the sedimentary sequence. Consequently, both samples lie in Unit 2.

Twenty-four diatom taxa were identified, and chrysophytes were also present. The lowermost sample was dominated by freshwater species such as *Staurosirella lapponica* (40% weight) with *Tabularia fasciculata*, *Staurosirella pinnata* and *Melosira varians* also present at abundances >5%. Species at this level are predominantly benthic (*Denticula eximia* and *Tabularia fasciculata*) or periphytic (*Staurosirella lapponica*) and suggest shallow waters (Kelly et al., 2005). The presence of *Lindavia comensis* and *Lindavia ocellata* in this level suggest oligotrophic to mesotrophic conditions. At the upper level

(~18 cm above base) brackish species such as *Denticula kuetzingii* and *Campylodiscus clypeus* replace freshwater species such as *Stausosirella lapponica*, *Stausosirella pinnata* and *Melosira varians*. This rise in saline-tolerant species coincides with an increase in the planktonic:benthic ratio which suggests deeper water conditions than the lower level.

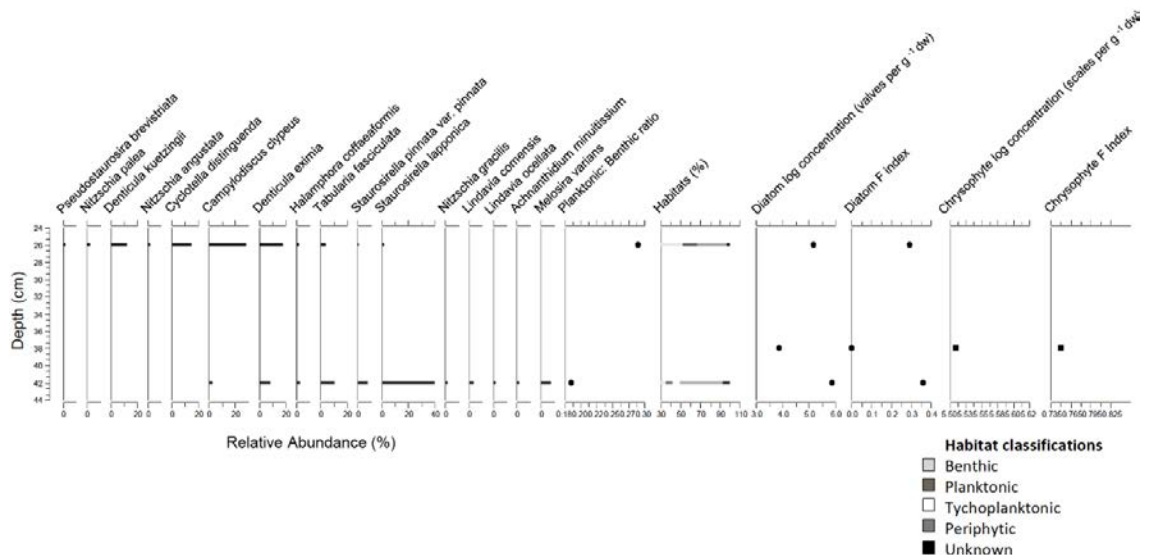


Figure 12.6 – Summary diagram of KAM4 lake 1 diatom assemblage analysed by Wing Wai Sung. Note that the y-axis measures the depth below surface as opposed to the height above base (see text for clarification). Both samples originate from unit 2, with the lowermost sample occurring 2 cm above base and the uppermost sample occurring 18 cm above base.

12.2.4 Depositional model

The sedimentary evidence described in this section is used to construct a depositional model for KAM4 lake 1. Three main phases of sediment deposition are recorded. Unit 1 consists of loose sands. These were probably deposited by aeolian processes prior to the onset of humidity. Units 2 and 3 consists of fine-grained carbonate rich marls, with the latter also containing sand beds, and these units represent the development of an interdunal lacustrine basin. Multi-proxy palaeoenvironmental analysis provides further palaeoenvironmental details relating to these units.

Unit 2 contains finely but discontinuously laminated microsparite and micrite (Fig 12.4, panel A) or laminations between microsparite/sparite and goethite (Fig 12.4, panel B).

The former lamination type (i.e. between microsparite and micrite) probably reflect variations in productivity, with smaller micritic crystals formed during peak productivity and larger microsparite crystals formed as productivity declined. Laminations between microsparite/sparite and goethite probably reflect a similar process but with diagenetic alteration leading to iron accumulation and precipitation along former micritic laminations, where the lower porosity due to the fine-grained nature of the micrite would promote storage and precipitation of iron over multiple cycles of groundwater pulses. The preservation of laminations within this unit itself indicates a relatively deep lake , where bottom sediments were protected from water turbulence caused by surface winds or also from bioturbation.

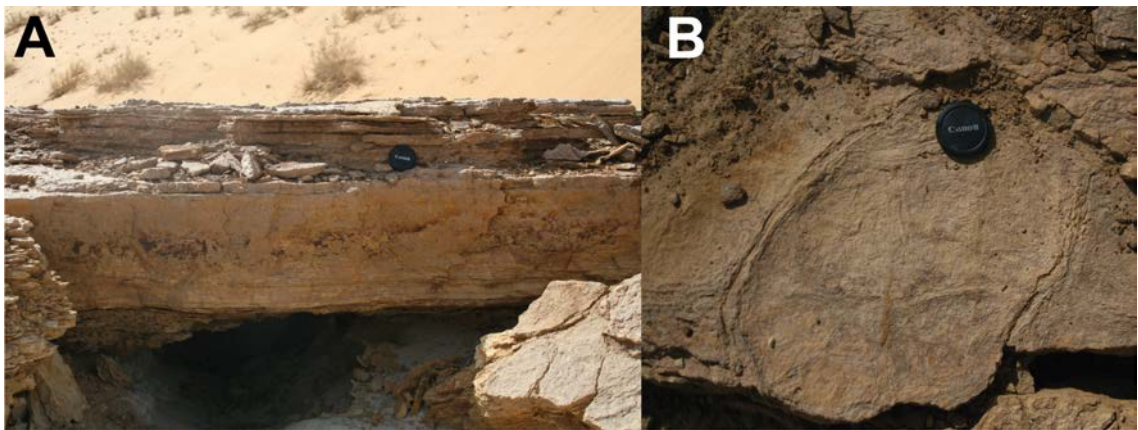


Figure 12.7 – The sedimentary section of KAM4 lake 1. (A) Overview of the section. The fine-grained carbonate rich marls are underlain by loose sands. The carbonate sediments themselves are heavily iron indurated, while there is an erosional surface between unit 2 and 3, with desiccation cracks present on the surface of unit 2. (B) Desiccation cracks on the surface of unit 2.

The transition between Unit 2 and Unit 3 is clear at the macroscale. Desiccation cracks at the surface of Unit 2 (Fig 12.7) suggest the waterbody completely desiccated prior to reflooding as represented by the sediments in Unit 3. The sedimentology itself changes from finely-laminated carbonate (Unit 2), to laterally continuous carbonate beds interdigitated with laterally continuous sand beds (Unit 3). Carbonate beds were deposited during periods of higher water levels and increased humidity. Conversely, sand beds were deposited during periods of lower water levels where the lake edge contracted, and the site of sedimentation lay closer to the lake edge or fully exposed. It is not clear whether the natural infilling of the lake over time made the site of sedimentation more susceptible to lake level fluctuations. Alternatively, the sediments

may have been deposited at a time when the hydroclimate was more unstable relative to Unit 2.

The microfacies of the carbonate in Unit 3 is consistent with deposition in a shallower lake body than that of unit 2. Laminations between microsparite/sparite and goethite are still present but not as clear, while there is a greater proportion of microsparite and goethite with a brecciated fabric. The latter is typical of sediment mixing and/or bioturbation in a shallow oxygenated lake system. It is likely the goethite has precipitated around and replaced finer, less porous micritic crystals. CaCO_3 values decline in Unit 3, reflecting the increased proportion of goethite and allogenic sand material. Nevertheless, the XRD data still support a dominance of calcite within this unit along with a lack of evaporites, suggesting any evaporitic effects were minimal.

Both $\delta^{18}\text{O}$ and $\delta^{13}\text{C}$ are stable with small ranges through the sedimentary sequence. $\delta^{18}\text{O}$ values range between -3.76‰ and -2.78‰ (range of 0.98‰), while $\delta^{13}\text{C}$ values range between -0.55‰ and -2.60‰ (range of 2.05‰). These relatively small ranges suggest the lake hydrology and wider climate were not affected by abrupt events. The small variability between $\delta^{18}\text{O}$ values of Unit 2 and 3 also suggest that hydrological changes between the two units were minimal. However, the slightly more negative $\delta^{13}\text{C}$ values in unit 3 may suggest there were slightly higher levels of throughflow. This is consistent with a shallower waterbody as displayed by the sediment and microfacies analysis.

It is important to consider the potential role of diagenetic alteration of the isotopic signature given the age of the deposit and evidence for multiple phases of groundwater flow through the sediments. The microfacies showed varying degrees of goethite, indicative of previous groundwater levels and potential post-depositional alteration of the sediment. However, while some larger sparitic crystal was present in the upper four thin-sections, microsparite was dominant and evidence of aggrading neomorphism – a process where calcite crystals grow larger in response to repeated wet phases – is minimal. The varied microfacies, but limited variability in the $\delta^{18}\text{O}$ or $\delta^{13}\text{C}$ values,

suggests that diagenetic alteration of the sediment has not affected the isotopic signature of the sediment.

Diatom palaeoecology is indicative of a fresh to brackish water body. Both diatom samples with high-enough abundance for quantitative analysis lie within Unit 2. The lower sample (~2 cm above base) is indicative of a shallow freshwater lake, based on the dominance of freshwater, benthic and periphytic species. The upper sample (~18 cm above base) contains a greater proportion of brackish species such as *Denticula kuetzingerii* and *Campylodiscus clypeus* and suggests a transition to slightly more saline waters. This may have resulted from increased evaporation, though the lack of evaporites (i.e. gypsum or halite) and small range of $\delta^{18}\text{O}$ values and limited covariance between $\delta^{18}\text{O}$ and $\delta^{13}\text{C}$ (0.02) suggest any evaporation within the waterbody did not meaningfully alter water chemistry. It is also important to note that diatom abundances were low, and preservation was poor, meaning that these interpretations need to be used with caution.

Overall, the sedimentary sequence represented by KAM4 L1 represents the transition from active dune movement, to a fresh to brackish perennial waterbody with sufficient depth to preserve laminations, to a waterbody affected by fluctuating water levels and potentially periodic desiccation. The sedimentary sequence is unique relative to other sedimentary sequences in the KAM4 basin as the carbonate sediments are heavily iron-indurated, due to multiple pulses of groundwater through the sedimentary sequence. The heavily altered sediments support the relatively ancient nature of this sedimentary sequence relative to others in the basin, as highlighted by luminescence dating.

12.3 KAM4 lake 2

The KAM4 lake 2 (KAM4 L2) sedimentary deposit is elongate and trends from north to south, running across the centre of the modern-day interdune depression and parallel to the lee side of the barchanoid dune to the west (Fig 12.1). Luminescence dating yields an age of 337 ± 39 ka for the underlying sands, and an age of 306 ± 47 ka for the overlying sands (Clark-Balzan, per comms). This places the timing of humidity represented by KAM4 lake 2 to sometime during MIS 9.

12.3.1 Sedimentology

12.3.1.1 Bulk sedimentology

The sedimentary sequence at KAM4 L2 is split into 5 units, though is measured from the base of the waterlain sediments (marl) upwards (Units 2 – 5; Fig 12.8). Unit 1 consists of loose sands that underlie the carbonate-rich marl sediments. **Unit 2 (0 – 7 cm)** is composed of weakly laminated fine-grained carbonate rich marls. Calcium carbonate values in this unit lie between 75 – 91%, while XRD data shows the mineralogy is dominated by calcite (99% weight). **Unit 3 (7 – 27 cm)** is composed of cemented and homogenous fine-grained carbonate rich marl with sand lenses. Calcium carbonate values lie between 82 – 94% while XRD shows calcite dominates (98.4%). **Unit 4 (27 – 33 cm)** is composed of laminated fine-grained carbonate rich marls at the macro-scale. Calcium carbonate content lies between 71 - 74%, while XRD analysis shows aragonite is dominant (79.9%) with a component of calcite (17.7%) and small component of quartz (2.4%). **Unit 5 (33 – 36 cm)** is composed of homogenous fine-grained carbonate rich marl with a calcium carbonate content of 91% while XRD analysis shows calcite is dominant (98.4%).

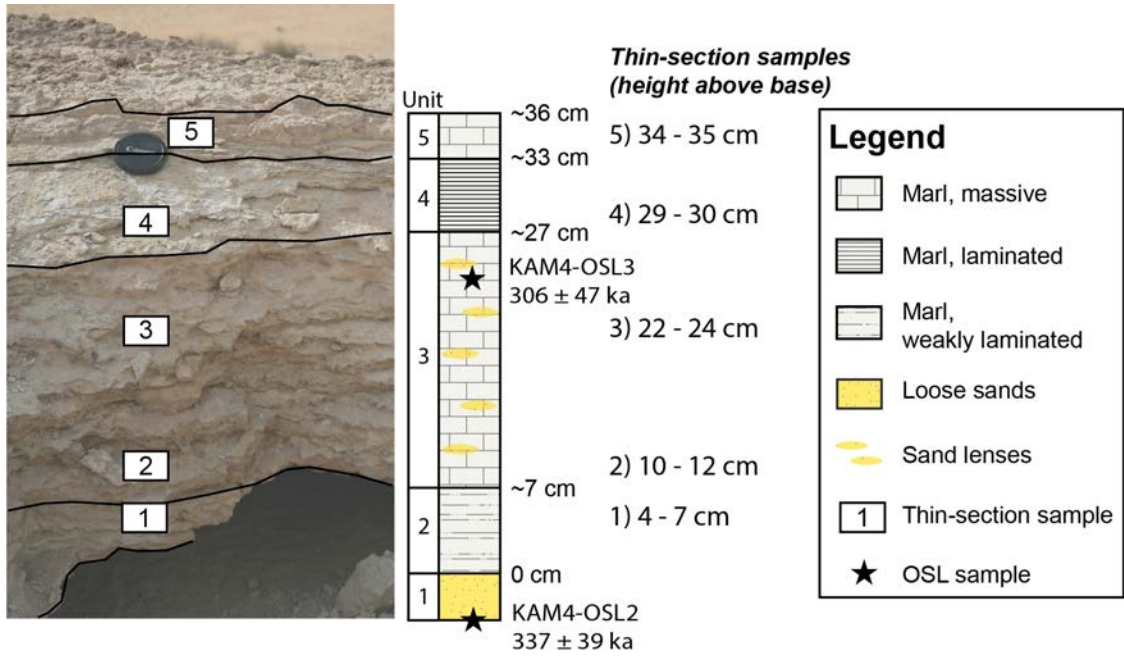


Figure 12.8 - Sedimentary sequence from KAM4 lake 2. Unit boundaries are represented by a solid black line. Thin-section sample locations through the sequence are shown, with the corresponding thin-section heights above base of the marl unit noted on the right side of the figure. OSL ages produced by Clark-Balzan (per comms) are shown. Note that positioning of the OSL samples is approximate as the samples were collected and analysed outside of this thesis.

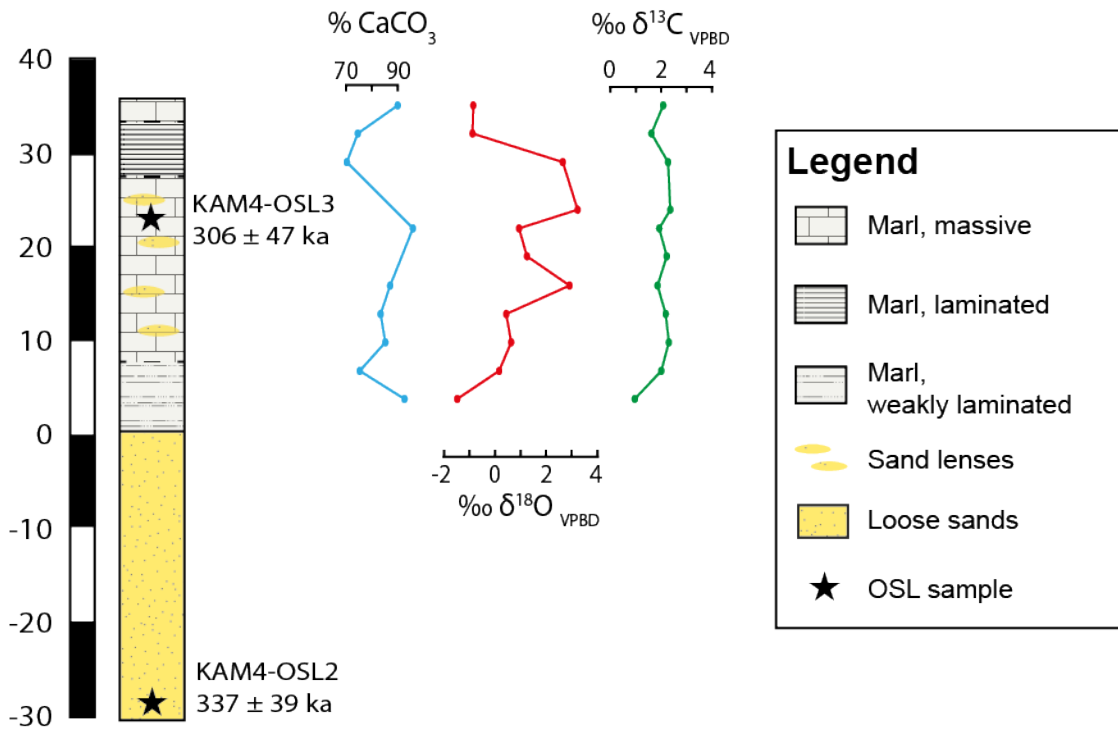


Figure 12.9 – Sedimentary log with CaCO_3 (blue), $\delta^{18}\text{O}$ (red) and $\delta^{13}\text{C}$ (green) curves for KAM4 Lake 2. Note that the position of OSL ages is approximate given that they were collected and analysed outside of this PhD by Clark-Balzan (per comms).

Table 12.4 - X-ray diffraction data from KAM4 lake 2. Calcite is dominant throughout with the exception of unit 4 where aragonite is dominant.

Height base (cm)	above	Unit	Calcite (%)	Aragonite (%)	Quartz (%)
4		2	99	0	1
22 - 23		3	98.4	0	1.6
29		4	17.7	79.9	2.4
35		5	98.4	0	1.6

12.3.1.2 Microfacies descriptions

A total of five samples were taken for microfacies analysis. Common attributes across all microfacies include low void coverage (<5%), low allogenic grain coverage (mostly <2%), a lack of depletion/concentration features and rare biogenic material present (i.e. rare shell fragments). Thin sections from Units 2 and 3 (4 – 7 cm, 10 – 12 cm and 22 – 24 cm) display a large sparite crystal groundmass with patches of micrite/microsparite (see Fig 12.10, panels A and B). The thin-section from unit 4 (29 – 30 cm) contains a similar microstructure but with a lower proportion of sparite and greater proportion of microsparite relative to the previous unit. The final thin-section (34 – 35 cm; Unit 5) is composed of homogenous microsparite/micrite with little to no evidence of sparite. This thin section also sees a distinct rise in the frequency of shell fragments present.

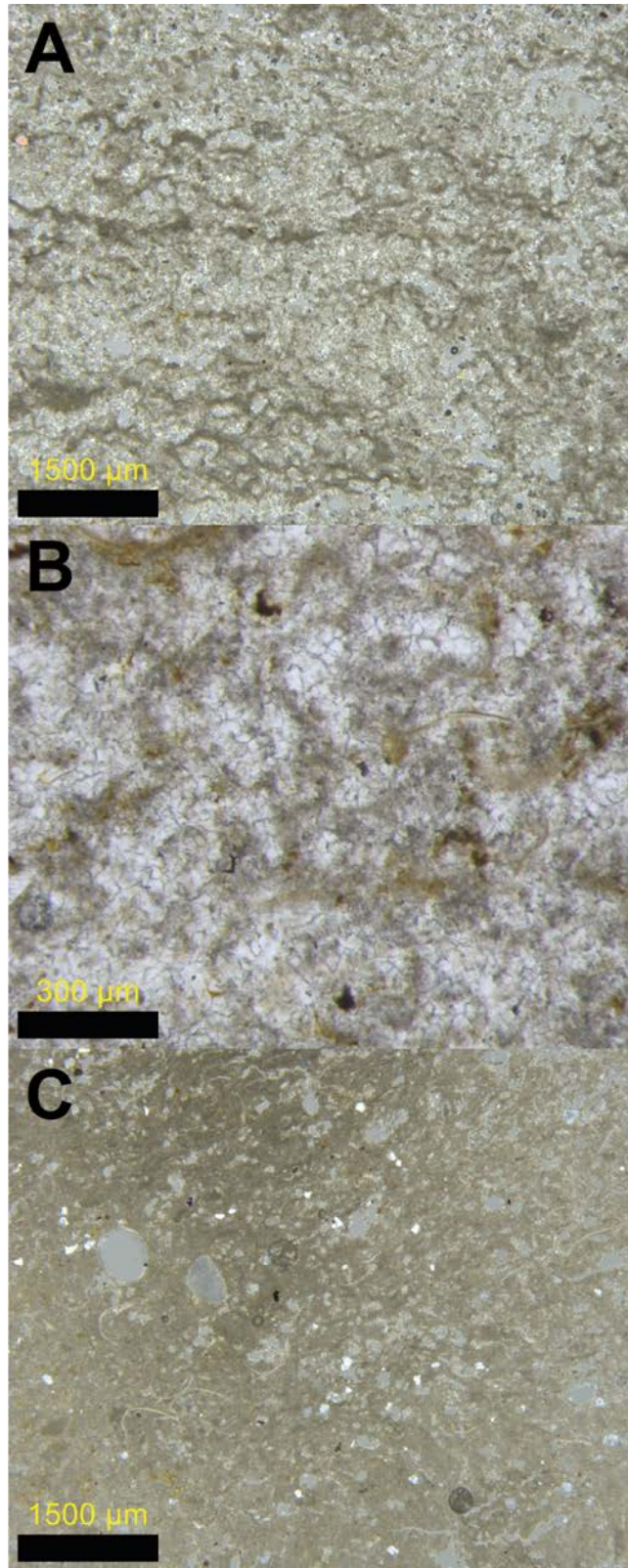


Figure 12.10 - Photomicrographs of thin-sections from KAM4 lake 2. (A) 10 – 12 cm above base from Unit 3. This microfacies is dominated by a groundmass with large sparitic crystals with patches of micrite present. (B) 22 – 24 cm above base from Unit 3. This microfacies displays the same characteristics as the above. This image is at a higher magnification and shows a sparitic 'mosaic'. (C) 34 – 35 cm above base from Unit 5. This microfacies is composed of a massive microstructure with a microsparitic groundmass. This section also sees an increase in shell fragments.

12.3.2 $\delta^{18}\text{O}$ and $\delta^{13}\text{C}$

$\delta^{18}\text{O}$ values lie between -1.47‰ and 3.67‰ , have a mean value of 0.85‰ and a median of 0.66‰ . The most negative values lie at the beginning and end of the sequence while the values between 16 – 29 cm are the most positive (Fig 12.9). The $\delta^{13}\text{C}$ values lie between 0.94‰ and 2.33‰ (range = 1.39‰), with a mean value of 1.94‰ and a median of 2.03‰ . The R^2 coefficient between $\delta^{18}\text{O}$ and $\delta^{13}\text{C}$ through the sequence is 0.37 with a p-value of 0.05.

Table 12.5 - Descriptive statistics for $\delta^{18}\text{O}$ values of lake carbonates at KAM4 lake 2.

Site	Height above base (cm)	N	Mean (‰)	Median (‰)	SD (1 σ) (‰)	Min (‰)	Max (‰)	Range (‰)
KAM4 L2	4 - 35	11	0.85	0.66	1.6	-1.47	3.27	4.74

Table 12.6 - Descriptive statistics for $\delta^{13}\text{C}$ values of lake carbonates at KAM4 lake 2.

Site	Height above base (cm)	N	Mean (‰)	Median (‰)	SD (1 σ) (‰)	Min (‰)	Max (‰)	Range (‰)
KAM4 L2	4 - 35	11	1.94	2.03	0.4	0.94	2.33	1.4

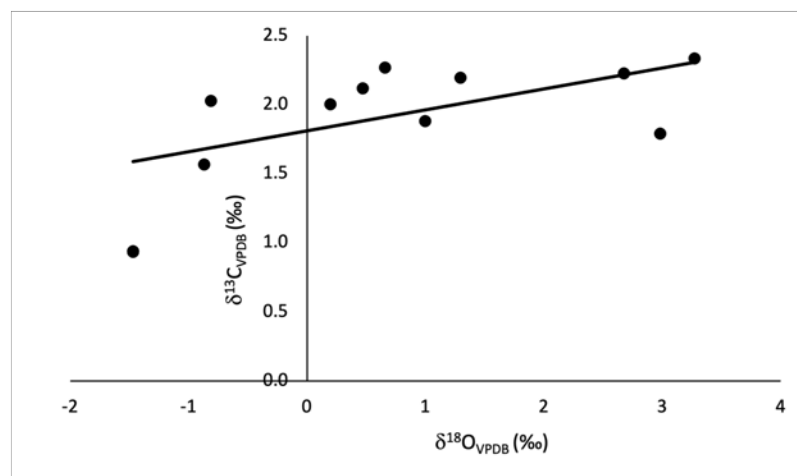


Figure 12.11 - Covariance between $\delta^{18}\text{O}$ and $\delta^{13}\text{C}$ at KAM4 Lake 2. The R^2 coefficient is 0.37 with a p-value of 0.05.

12.3.3 Diatom palaeoecology

Four diatom samples were taken from KAM4 L2 but only a single sample, 4 cm from the surface (Unit 4/5), contained sufficient preserved diatoms (>100 diatom valves) for taxonomic identification (Sung per coms). Thirty species were identified and the predominant taxa are planktonic freshwater species *Aulacoseira crassipunctata*, *Hannaea arcus* and *Aulacoseira granulata* (Fig 12.12). Brackish (*Navicula protracta*, *Campylodiscus clypeus*) and saline (*Hantzschia amphioyxs*) species are also present. Benthic and periphytic taxa were also present at low levels (see Fig 12.12). The taxa present suggest mesotrophic to eutrophic lake conditions. The other three samples from KAM4 L2 all contained chrysophytes, suggesting that these sediments were deposited under freshwaters with low nutrient availability (Sung per comms).

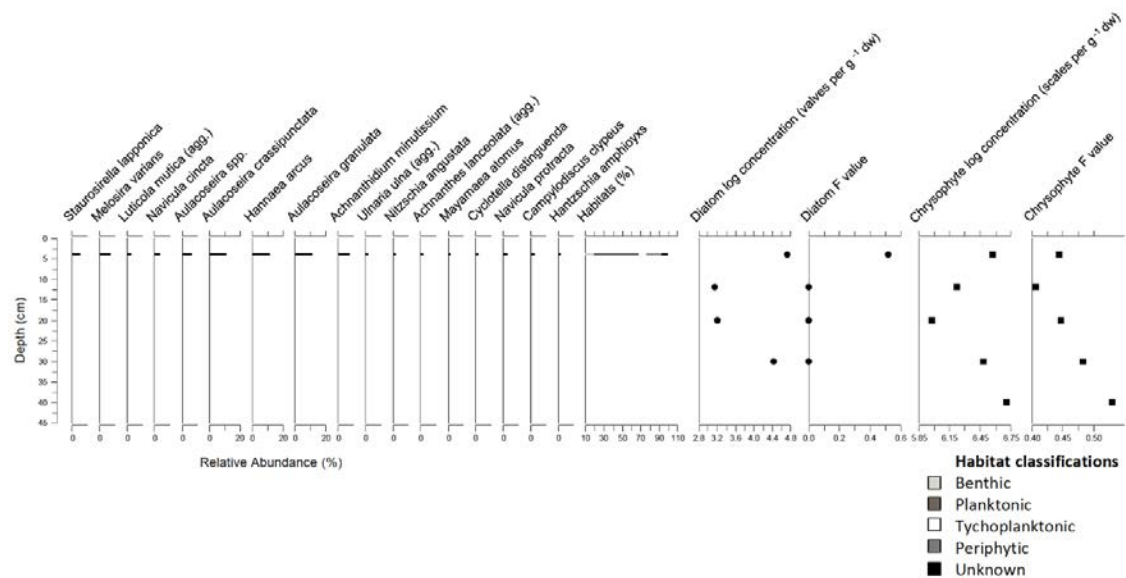


Figure 12.12 - Summary diagram of KAM4 lake 1 diatom assemblage analysed by Wing Wai Sung. Note that the y-axis measures the depth below surface as opposed to the height above base. This sample originates from 4 cm beneath the surface and relates to unit 4.

12.3.4 Depositional Model

The evidence described in this section is used to construct a depositional model for the sequence at KAM4 lake 2. Unit 1 consists of loose sands and probably relate to aeolian sand deposition prior to the onset of humidity. Units 2 – 5 consist of fine-grained carbonate rich marls and all represent deposition in a shallow, perennial and freshwater

body. All these units contain CaCO_3 levels in excess of 70%, are dominated by calcite (typically >98% weight) with Unit 4 dominated by aragonite (79.9%), contain very little allogenic material in both thin-section and as shown by % weight of quartz in XRD analysis, and lack any pedogenic alteration of the sediment. $\delta^{13}\text{C}$ values range between 0.94‰ and 2.33‰ and are typical of sedimentation in a lake body that is in equilibrium with atmospheric CO_2 (Leng and Marshall, 2004). Covariance between $\delta^{18}\text{O}$ and $\delta^{13}\text{C}$ is not significant ($R^2 = 0.37$), while the single diatom sample from Unit 4/5 is dominated by freshwater planktonic species with some brackish or saline tolerant benthic and periphytic taxa present at low-levels. This suite of characteristics provides strong evidence that the KAM4 lake 2 waterbody was freshwater, shallow and perennial, with the site of sedimentation away from any sediment inputs as per the distinct lack of allogenic sands and dominance of authigenic material.

Nonetheless, there are subtle differences between these units which represent slightly different depositional settings. Unit 2 consists of friable and weakly laminated fine-grained carbonate rich marls at the macroscale. At the microscale this unit displays a microstructure with a sparitic and micritic groundmass. The prevalence of large sparitic crystals is indicative of aggrading neomorphism – a process whereby original micritic crystals have been replaced/recrystallised into larger crystal (sparite) mosaics during subsequent wet phases (see Fig 12.10) (Armenteros, 2010). The $\delta^{18}\text{O}$ values from this unit are among the most negative through the sequence and suggests greater rainfall amount or higher rates of throughflow/less evaporitic enrichment compared to Unit 3.

Unit 3 contains a similar microfacies to Unit 2 (see Fig 12.10, panel B), suggesting the depositional environment was similar: i.e. shallow, fresh and perennial waterbody. However, there are obvious sand lenses present at the macroscale while $\delta^{18}\text{O}$ values are more positive and variable (see Fig 12.9). The increase in allogenic material in washing to the basin suggests the site of sedimentation lay closer to the lake edge, meaning the lake had contracted relative to the previous unit. Alternatively, more heavy rainfall events and/or a less stable surrounding environment (i.e. lower vegetation density leading to less stable surficial sands) may have led to the allogenic sand lenses observed.

The concurrent rise and variability in $\delta^{18}\text{O}$ values, which suggests increased evaporitic enrichment or lower rainfall amounts, is consistent with lower lake volumes and reduced humidity during the deposition of this unit.

Unit 4 consists of laminated aragonite and is the only unit across all sedimentary sections analysed within this thesis that contains, let alone is dominated by, aragonite. The presence of aragonite suggests that water chemistry changed relative to the other units described. Aragonite is typically precipitated in favour of calcite when levels of magnesium (Mg) are high, and when waters are slightly more brackish or saline (Talbot and Allen, 1990). The microfacies of Unit 4 are similar to those from the units below but contains less sparite and a greater proportion of micrite. $\delta^{18}\text{O}$ values remain high in this section, though it is important to note that aragonite $\delta^{18}\text{O}$ values are typically 0.6‰ higher than equivalent calcite $\delta^{18}\text{O}$ values (Abell and Williams, 1989; Grossman and Ku, 1986; Leng and Marshall, 2004). Despite this, $\delta^{18}\text{O}$ are still high relative to Unit 2 and are consistent with Unit 3.

It is difficult to definitively answer the question of why aragonite is present in this unit, and whether its presence is a result of different diagenetic or climatic conditions relative to other units. In terms of diagenesis, aragonite is metastable (i.e. stable provided it is not subject to disturbances such as diagenesis) in the geological record. The most common diagenetic process is calcitization, where aragonite components are replaced by calcite (Armenteros, 2010). Such a diagenetic process requires 'wet' conditions, with neomorphic transformation occurring through a film of water (Armenteros, 2010). It is therefore possible that other units were originally aragonite but have since undergone calcitization, whereas Unit 4 has preserved its original mineral state through an absence of diagenetic processes. This is considered unlikely as it is not clear why other units would undergo calcitization, including the unit above it, and not Unit 4. In terms of climatic/hydrological differences, the best way to explain the presence of aragonite would be an increase in the magnesium content of waters due to more evaporatively evolved waters. As calcite precipitates the Mg/Ca levels gradually increase as Ca^{2+} is lost from solution (Decampo, 2010). Aragonite is then precipitated where the Mg/Ca ratio

increases past ~10 (Decampo, 2010). The presence of aragonite may therefore be explained by a more evaporatively evolved water body within a more arid environment relative to the depositional environment of other units. It is also plausible that there was an increase in magnesium in the lake waters. Magnesium can derive from the weathering of volcanic rocks, which are dominant across western Arabia (Groucutt et al., 2020). There is a long history of volcanism in western Arabia over the timeframe of this study (Groucutt et al., 2020), raising the possibility that there may have been a direct input of Mg rich volcanic material into the lake basin, promoting the precipitation of Mg-rich minerals such as aragonite.

Unit 5 consists of homogenous fine-grained carbonate rich marls, with a homogenous microstructure with a microsparite/micrite groundmass. The latter is a distinct change from previous units where the groundmass is dominated by large sparite crystals. This probably reflects higher productivity (i.e. smaller crystals are produced in response to fast crystallisation and high productivity), or the unit has been less affected by aggrading neomorphism. Microfacies analysis also shows a number of shell fragments. $\delta^{18}\text{O}$ values are far more negative relative to Units 3 and 4, and are more consistent with Unit 2. These values suggest a greater amount of rainfall, or that the lake waters were less prone to evaporation. Taken together, the sedimentary analysis from this unit suggests deposition in a slightly deeper (relative to Units 3 and 4) but still shallow, perennial waterbody.

It is important to note that microfacies from Units 2 and 3 display evidence for diagenetic alteration of the primary calcite via aggrading morphism. It is possible that this process altered the original isotopic signature of the host material. As such, caution is required when interpreting the isotopic data from this sequence. Despite this there is no clear difference in the $\delta^{13}\text{C}$ values between the sparite dominated Units (2 and 3) and Units 4 and 5 which contain a more homogenous microsparite/micrite groundmass with limited evidence for neomorphism. This suggests that the impact of neomorphism on the isotopic signal may be minimal.

12.4 KAM4 lake 3

The KAM4 lake 3 sedimentary deposit lies in the southern central portion of the KAM4 interdunal basin (Fig 12.1). Luminescence dating of the underlying sands undertaken as part of this thesis yields ages of 154 ± 11 ka (PD11b) and 149 ± 9 ka (PD12) for quartz OSL. This provides a maximum age of the carbonate marls which overlie these sands, and these marls may relate to an MIS 6 or MIS 5 humid interval.

12.4.1 Sedimentology

12.4.1.1 Bulk sedimentology

The sedimentary sequence at KAM lake 3 is split into six units but is measured from the base of waterlain sediments (marl) upwards (Units 2 – 6) (Fig 12.13). Unit 1 consists of loose sands and lies beneath the base of the marl bed. **Unit 2 (0 – 5 cm)** consists of partially laminated fine-grained carbonate rich marls. Calcium carbonate content within this unit lies between 77 – 85% while XRD shows calcite is dominant (99.1%). **Unit 3 (5 – 25 cm)** consists of iron-stained and homogenous fine-grained carbonate rich marl. Calcium carbonate content within this unit lies between 80 – 88% while XRD shows calcite is dominant (98.2%). **Unit 4 (25 – 28 cm)** consists of well consolidated fine-grained carbonate rich marl with small tubular voids. Calcium carbonate levels within this unit are 89% while XRD shows calcite is dominant (98.6%). **Unit 5 (28 – 38 cm)** consists of homogenous fine-grained carbonate rich marl. Calcium carbonate levels in this unit lie between 53 – 83% while XRD shows calcite is dominant (95.9%). **Unit 6 (38 – 48)** consists of stem-rich cemented marls. Calcium carbonate value in this unit is at 90% while XRD shows calcite was dominant (99.2%). The only other mineral present in XRD analysis is quartz.

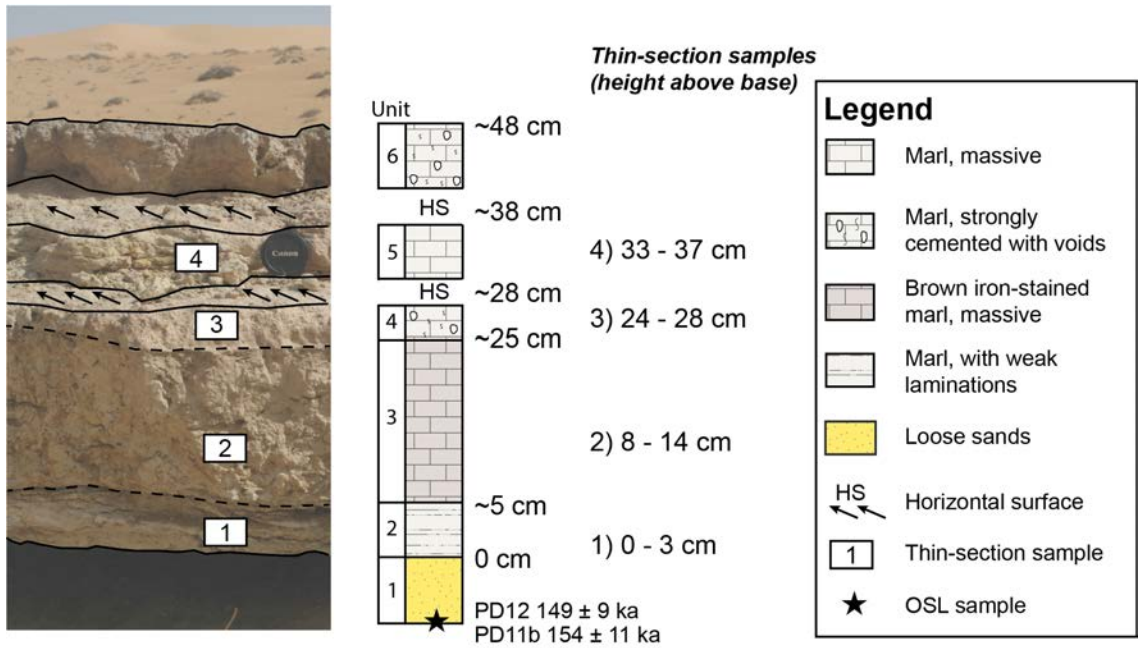


Figure 12.13 – Sedimentary sequence from KAM4 lake 3. Unit boundaries are represented by a solid black line. Thin-section sample locations through the sequence are shown, with the corresponding thin-section heights above base of the marl unit noted on the right side of the figure. OSL ages produced as part of this thesis are shown.

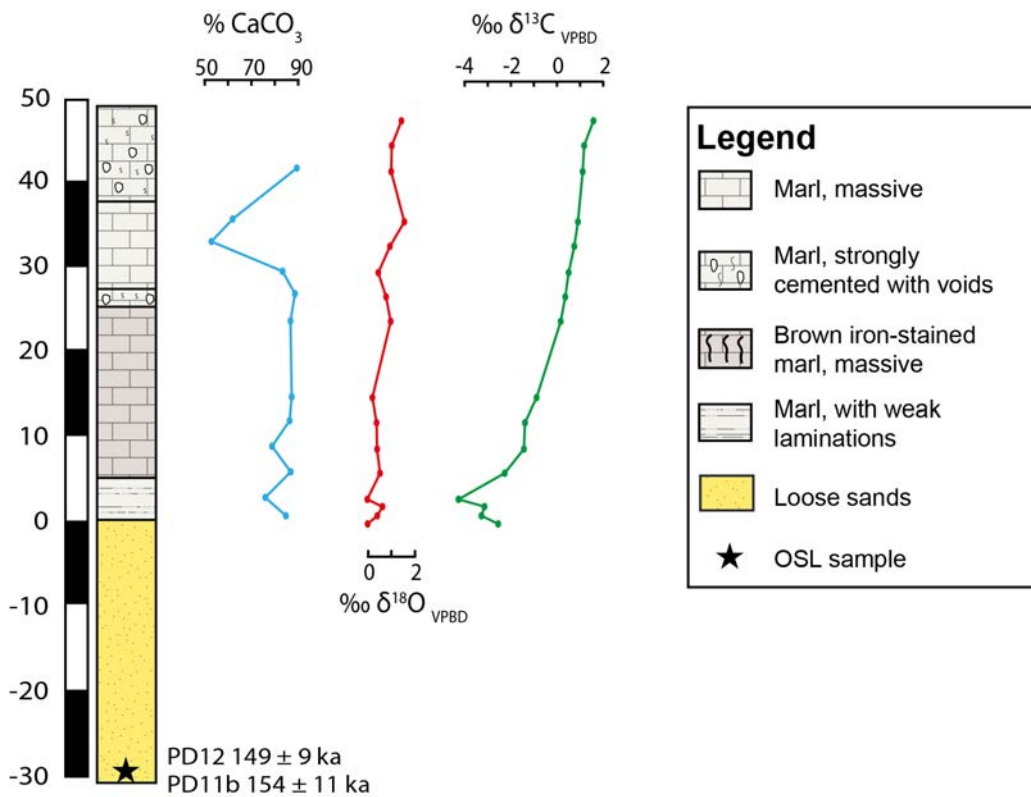


Figure 12.14 – Sedimentary log with CaCO₃ (blue), δ¹⁸O (red) and δ¹³C (green) curves for KAM4 lake 3.

Table 12.7 – X-ray diffraction data from KAM4 lake 3. Calcite is dominant throughout the sequence.

Height above base (cm)	Unit	Calcite (%)	Quartz (%)
1	2	99.1	0.9
12	3	98.2	1.8
27	4	98.6	1.4
36	5	95.9	4.1
42	6	99.2	0.8

12.4.1.2 Microfacies descriptions

A total of four samples for microfacies analysis were taken from the fine-grained carbonate rich marls, with one sample (0 – 3 cm) from Unit 2, one sample (8 – 14 cm) from Unit 3, one sample (24 – 28 cm) from Unit 4 and a final sample (33 – 37 cm) from Unit 5 (see Fig 12.15). Common attributes across all thin sections are the homogenous microstructure with a groundmass composed of microsparite/micrite, low total void coverage, rare biogenic remains with some evidence of class 4 amorphous organic remains and rare shell fragments, the presence of sponge spicules, and light grain etching. Microfacies from Units 2, 3 and 4 differ from Unit 5 as they contain a low coverage (>2%) of allogenic sand grains along with a small degree of iron staining around class 4 amorphous root remains, around small chamber and vugh voids, and within the groundmass. The sample from Unit 4 also contains iron nodules with internal cracking. Conversely, Unit 5 contains an increased coverage of allogenic grains (33%) with no evidence of any iron staining but contains carbonate nodules.

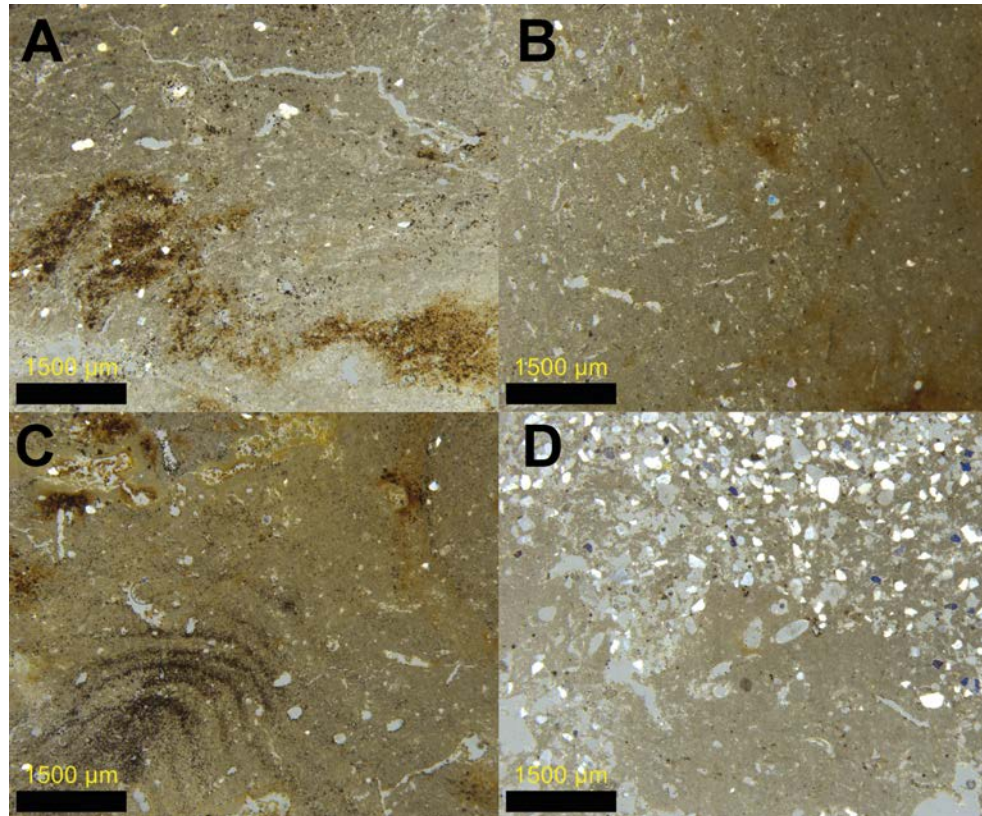


Figure 12.15 – Photomicrographs of thin-sections from KAM4 lake 3. (A) 0 – 3 cm above base from unit 2. (B) 8 – 14 cm above base from unit 3. (C) 24 – 28 cm above base from unit 4. (D) 33 – 37 cm above base from unit 5. All microfacies display a massive microstructure composed of microsparite/micrite with a low total void coverage. Unit 5 (panel D) differs from the other microfacies in that it contains a high proportion of allogenic sand/silt grains while there is no evidence of iron-staining.

12.4.2 $\delta^{18}\text{O}$ and $\delta^{13}\text{C}$

$\delta^{18}\text{O}$ values range between 0.02‰ and 1.62‰, have a mean value of 0.71‰ and a median value of 0.63‰. The $\delta^{18}\text{O}$ stratigraphy is split into two zones. The first runs from 0 – 15 cm, with values ranging from 0.02‰ to 0.46‰ and a mean value of 0.36‰. The second zone runs from 24 – 48 cm, with values ranging from 0.51‰ to 1.62‰ and a mean value of 1.07‰. There is a trend towards increasing $\delta^{18}\text{O}$ values moving upwards through the sequence (see Fig 12.14). The $\delta^{13}\text{C}$ values lie between -4.24‰ and 1.53‰, with a mean value of -0.80‰ and a median of -0.38‰. The most negative values occur over the first 6 cm, though there is a clear trend in increasing (more positive) values moving through the sequence (see Fig 12.14). The R^2 coefficient between $\delta^{18}\text{O}$ and $\delta^{13}\text{C}$ through the sequence is 0.6 with a p-value of 4.08×10^{-4} (Fig 12.16).

Table 12.8 - Descriptive statistics for $\delta^{18}\text{O}$ values of lake carbonates at KAM4 lake 3.

Site	Height above base (cm)	N	Mean (‰)	Median (‰)	SD (1 σ) (‰)	Min (‰)	Max (‰)	Range (‰)
KAM L3	0 – 48	16	0.71	0.63	0.47	0.02	1.62	1.6

Table 12.9 - Descriptive statistics for $\delta^{13}\text{C}$ values of lake carbonates at KAM4 lake 3.

Site	Height above base (cm)	N	Mean (‰)	Median (‰)	SD (1 σ) (‰)	Min (‰)	Max (‰)	Range (‰)
KAM L3	0 – 48	16	-0.8	-0.38	1.84	-4.24	1.53	5.77

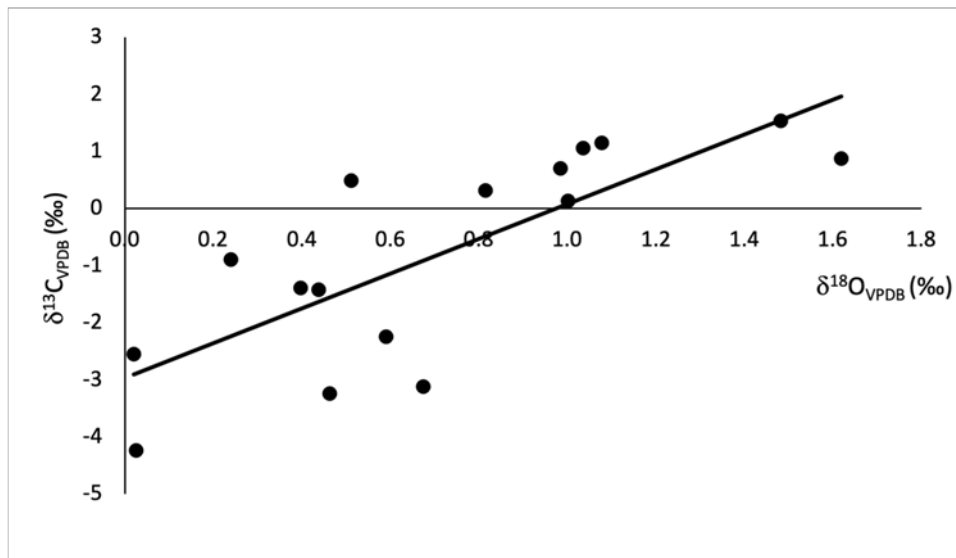


Figure 12.16 - Covariation between $\delta^{18}\text{O}$ and $\delta^{13}\text{C}$ at KAM4 Lake 3. The R^2 coefficient is 0.6 with a p -value of 4.08×10^{-4} .

12.4.3 Diatom palaeoecology

Low diatom abundances within this lake mean that no meaningful diatom analysis could be carried out, though it should be noted that chrysophytes occur at low abundances through all levels analysed (Fig 12.17) (Sung per comms). This suggests that these sediments were deposited in freshwaters with low nutrient availability.

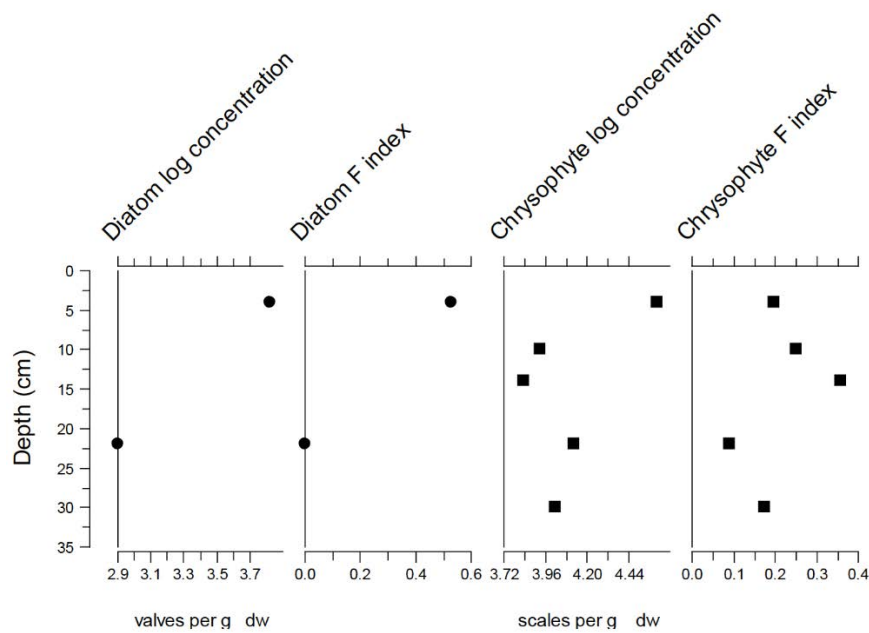


Figure 12.17 - Summary diagram of diatom assemblage from KAM4 lake 3. Note that low diatom abundances meant no diatom taxonomy work was carried out.

12.4.4 Depositional model

The sedimentary evidence described in this chapter is used to construct a depositional model for the KAM4 lake 3 sequence. Two main phases of sediment deposition are recorded at the site. Unit 1 consists of loose sands and probably represents aeolian sand accumulation resulting from dune movement prior to the onset of humidity. Units 2 – 6 all consist of subtly differing fine-grained carbonate rich marls and represents the development of an interdunal lake which precipitated carbonate. Each unit (2 – 6) is indicative of slightly different lacustrine conditions and these are outlined below.

Unit 2 (0 – 5 cm) consists of weakly laminated and friable marls at the macroscale while the microfacies is composed of homogenous microsparite with low void cover but rare planar voids. Such a microfacies is typical of sedimentation within a shallow waterbody where the lakebed is exposed to sediment mixing via surface winds or by bioturbation (Wright, 1990). The $\delta^{13}\text{C}$ values in this section are more depleted relative to the rest of the sequence and lie between -2.55‰ and -4.24‰. This probably reflects greater rates of throughflow at the onset of lake development, where lake water $\delta^{13}\text{C}$ did not have time to equilibrate with the atmosphere.

Unit 3 consists of brown, iron-stained massive marls at the macroscale while at the microscale the microfacies is similar to the previous section in that it contains a homogenous microstructure with a groundmass dominated by microsparite and micrite. This implies that the depositional environment was very similar to the previous section. However, $\delta^{13}\text{C}$ values demonstrate a subtle change as they are more positive than the previous unit as they lie between -2.24‰ and 0.13‰ and consistently enrich (become more positive) through the unit. The more positive values implies that the lake waters represented by this unit may have progressively had slower throughflow and therefore longer residence times moving upwards through the sequence meaning that the $\delta^{13}\text{C}$ signal could equilibrate with the atmosphere.

Unit 4 consists of strongly cemented fine-grained carbonate relative to the units below, though the microfacies and $\delta^{13}\text{C}$ values do not indicate a notable change in depositional environment. The stronger cementation may relate to increased vegetation at the time of deposition, promoting calcite precipitation around macrophyte roots (Wright, 1990).

Unit 5 consists of massive fine-grained carbonate and contains a microfacies that again is similar to the previous units as it is composed of homogenous microsparite. One key difference is that there is large increase in allogenic sands in one half of the microfacies (Fig 12.15, panel D). The increase in allogenic sands in the microfacies is supported by the reduction in CaCO_3 content to 53 - 62% (33, 36 cm), though the calcite levels as determined by XRD remain high (95.9%). The inconsistency between the microfacies, CaCO_3 content and XRD analysis may reflect variability in the allogenic sand content in the unit as the microfacies contains areas of both low and high allogenic grain content. Nevertheless, the increased allogenic sand content and reduction in CaCO_3 within this unit points to an increase in sand in wash into the lake, which may relate to reduced vegetation cover in the landscape, and increased landscape instability.

Unit 6 consists of well cemented marls with voids and has a high CaCO_3 content (90%) and calcite value (99%). As with unit 4, this may reflect increased vegetation encouraging calcite precipitation around macrophyte roots.

The isotopic data progressively enriches through the sequence (Fig 12.14), which probably represents slowing throughflow, increased water residence time and increased evaporation moving through the sequence. This interpretation is supported by the relatively high-level of covariance between $\delta^{18}\text{O}$ and $\delta^{13}\text{C}$ ($R^2 = 0.6$) (Talbot, 1990). However, the range in $\delta^{18}\text{O}$ values is low (1.60‰) while no evaporitic minerals are present and there is no evidence of desiccation or sub-aerial exposure. In this instance this suite of data suggests that while evaporation increased moving through the sequence, it was not enough to lead to brackish/saline waters or the desiccation of the water body.

12.5 KAM4 lake 3a

The KAM4 lake 3a sedimentary sequence lies in the southwestern corner of the KAM4 basin, with the lee side of the barchanoid dune directly to its west and the KAM4 lake 3 deposit to its east (Fig 12.1). Luminescence dating at the site undertaken as part of this thesis shows the underlying sands date to 184 ± 14 ka (PD9), while a sample taken directly from the lake sediment yielded an age of 143 ± 10 ka (PD10). The latter sample places a direct age on humidity and suggests the lake may relate to a humid phase during MIS 6 (~152 ka) or MIS 5e (~128 ka).

12.5.1 Sedimentology

12.5.1.1 Bulk sedimentology

The sedimentary sequence at KAM lake 3a is split four units, measured from the base of waterlain sediments (Unit 2) upwards. Unit 1 consists of loose sands and lies beneath the base of the sequence. Unit 2 (0 – 44 cm) is split into two sub-units. Unit 2a (0 – 25 cm) is composed of weakly consolidated and horizontally laminated sands. Unit 2b (25 – 44 cm) is composed of a mixture of weakly consolidated sands, silts and clays with evidence for mottling. Calcium carbonate content in this unit is 23%. XRD analysis shows a range of minerals present with calcite (42.4%), quartz (39.1) and illite (18.4%) present. Unit 3 (44 – 66 cm) is also split into two units. Unit 3a (44 – 60 cm) consists of friable

fine-grained carbonate rich marls and this grades into unit 3b (60 – 66 cm) that contains more consolidated but homogenous fine-grained carbonate rich marls. Calcium carbonate values in this level lie between 74 – 81%, while XRD shows calcite is the dominant mineral (81.1%) with a component of quartz (18.9%). Unit 4 (66 – 71 cm) is composed of strongly cemented calcrete that caps the sequence.

Table 12.10 - X-ray diffraction results from KAM4 lake 3a. Unit 2 shows a high proportion of clay (illite) along with calcite and quartz. Calcite becomes dominant in unit 3 with no clay present.

Height above base (cm)	Unit	Calcite (%)	Quartz (%)	Illite (%)	Montmorillonite (%)
25 – 44 cm	2b	42.4	39.1	18.4	0.2
44 – 66 cm	3	81.1	18.9	0	0

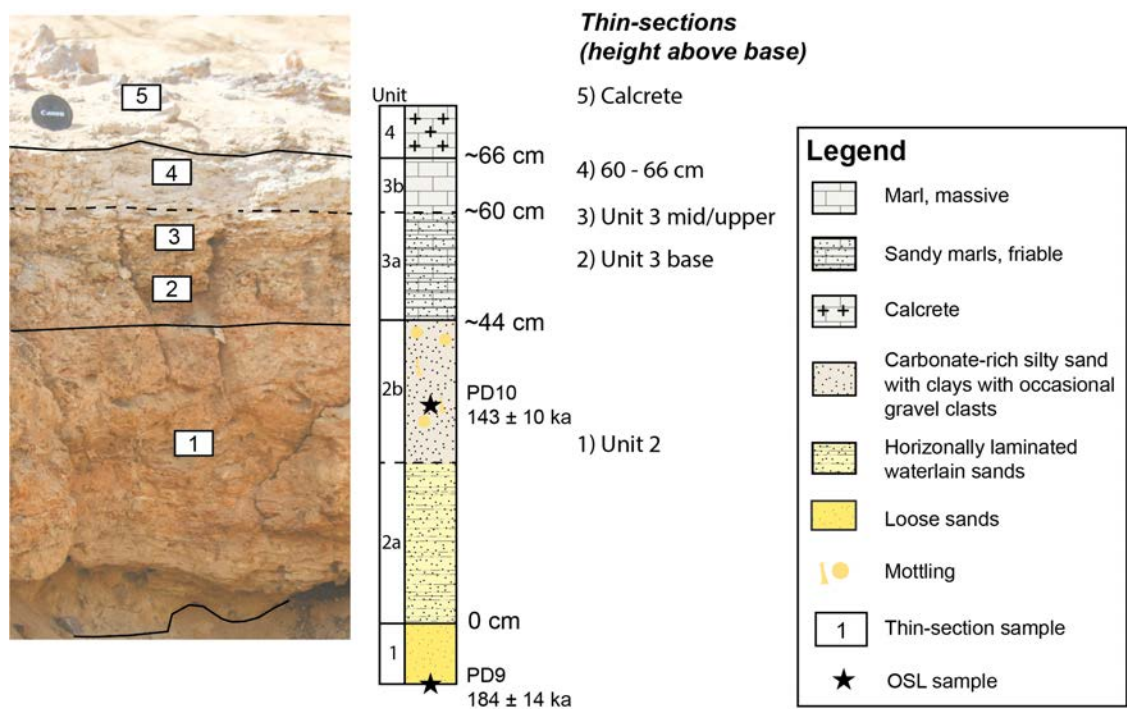


Figure 12.18 - Sedimentary sequence from KAM L3a. Unit boundaries are represented by a solid black line and sub-unit boundaries by a dashed line. Thin-section sample locations through the sequence are shown, with the corresponding thin-section heights above base of the marl unit noted on the right side of the figure. OSL ages produced as part of this thesis are shown.

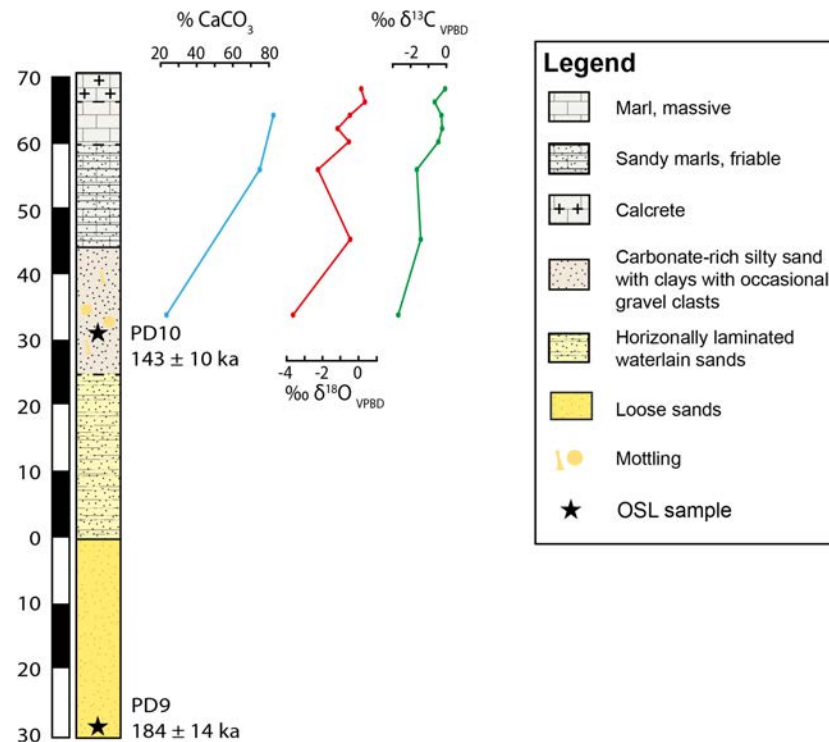


Figure 12.19 - Sedimentary log with CaCO_3 (blue), $\delta^{18}\text{O}$ (red) and $\delta^{13}\text{C}$ (green) curves for KAM4 Lake 3a. OSL ages produced as part of this thesis are shown.

12.5.1.2 Microfacies descriptions

A total of five samples were taken for microfacies analysis: one sample from Unit 2, two samples from Unit 3a (one from the base and one towards the centre), one sample from Unit 3b and one from Unit 4 (see Fig 12.18). Unit 2 contains a microfacies with a heterogenous and prismatic microstructure with clays and calcite dominant, along with a high proportion of allogenic silt and sand grains (10 – 25% coverage), planar voids, manganese staining and iron-stained clay nodules (Fig 12.20, panel A). Organic material is rare, though shell fragments are present at a very low abundance. Both microfacies from Unit 3a consisted of homogenous microsparite or micrite with a limited input of allogenic silt and sand grains (5 - 10% coverage), rare planar, vugh or vesicle voids (<5% coverage), low-abundance of shell-fragments and sponge spicules, light allogenic grain etching and rare iron staining. The microfacies from Unit 3b is similar to those in the previous unit in terms of microstructure (homogenous) and groundmass (microsparite/micrite), but contains fewer allogenic sands/silts (<2%) and more vugh and vesicle voids. The calcrete (Unit 4) closely resemble the sample from Unit 3b,

however there is a greater proportion of micrite with numerous vugh and vesicle voids infilled with sparite crystals.

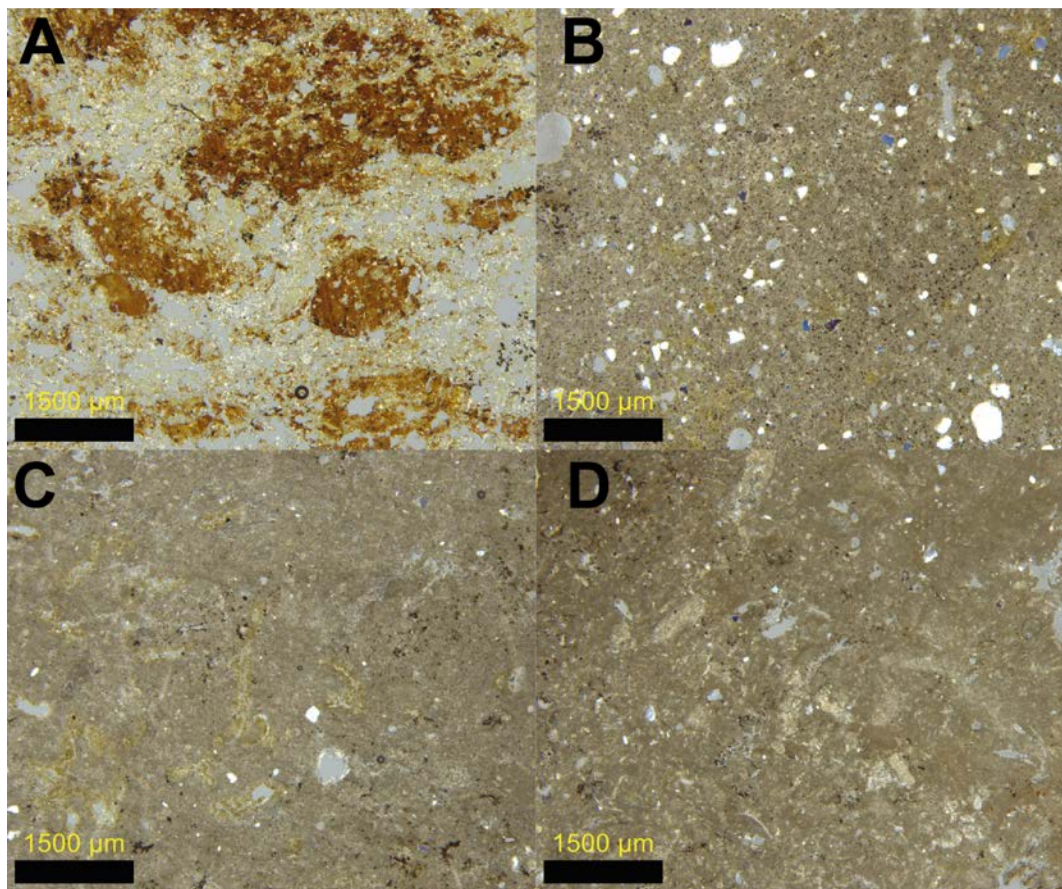


Figure 12.20 - Photomicrographs of thin-sections from KAM4 lake 3a. (A) Microfacies from unit 2. This microfacies shows a heterogenous microstructure composed of clay (illite) and calcite. (B) Microfacies from unit 3a consisting of massive microsparite and micrite. Allogenic sand and silt grains are present and evenly distributed across the thin-section. (C) Microfacies from unit 3b (60 – 66 cm). This is similar to the previous microfacies though contains fewer allogenic sand/silt grains. (D) Microfacies from the calcrete. Again this microfacies is similar to that from unit 3a and 3b, though contains a greater proportion of micrite, and has numerous vugh and vesicle voids infilled with sparite crystals.

12.5.2 $\delta^{18}\text{O}$ and $\delta^{13}\text{C}$

$\delta^{18}\text{O}$ values ranged from -3.74‰ to 0.23‰ with a mean value of -1.03‰ and a median value of -0.58‰ . The $\delta^{18}\text{O}$ values generally become more positive moving upwards through the sequence (Fig 12.19). Unit 2 contains the most negative value of -3.74‰ . Unit 3a and 3b have $\delta^{18}\text{O}$ values ranging between -2.17 and 0.23 while the calcrete has a $\delta^{18}\text{O}$ value of 0.13 . The $\delta^{13}\text{C}$ values range between -2.87‰ and -0.05‰ and follow a similar trend to the $\delta^{18}\text{O}$ values. Unit 2 is the most depleted at -2.87‰ . Unit 3a and 3b

have $\delta^{13}\text{C}$ values ranging between -1.89‰ and -0.15‰ with a mean value of -0.77‰ while the calcrete has the most positive value of -0.05‰ . The R^2 coefficient between $\delta^{18}\text{O}$ and $\delta^{13}\text{C}$ through the sequence is 0.65 with a p-value of 0.03, though this needs to be interpreted with caution given the low number of datapoints.

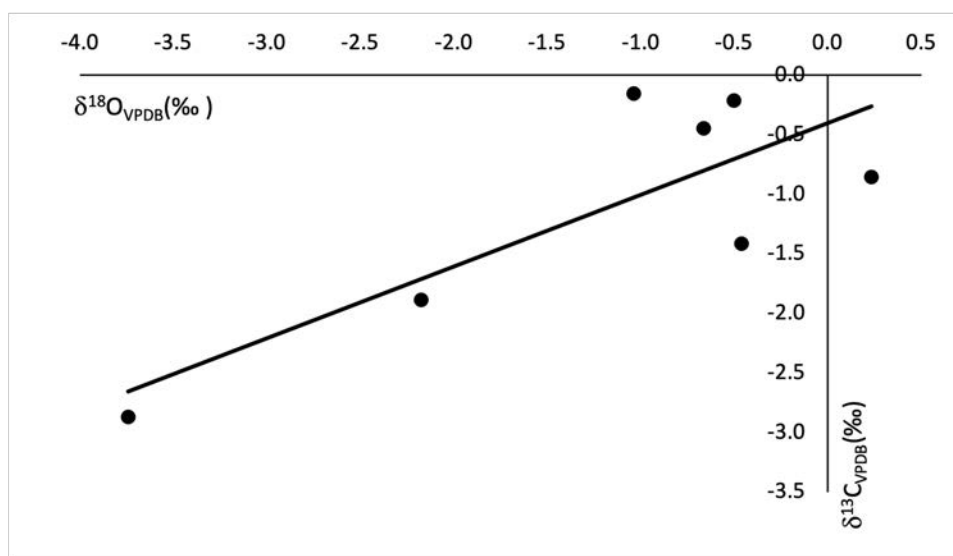


Figure 12.21 – Covariance between $\delta^{18}\text{O}$ and $\delta^{13}\text{C}$ for KAM4 lake 3a. The R^2 coefficient is 0.65 with a p-value of 0.03.

Table 12.11 - Descriptive statistics for $\delta^{18}\text{O}$ values of lake carbonates at KAM4 lake 3a.

Site	Height above base (cm)	N	Mean (‰)	Median (‰)	SD (‰)	Min (‰)	Max (‰)	Range (‰)
KAM4 L3a	25 – 66	7	-1.19	-0.66	1.34	-3.74	0.23	3.97
KAM4 L3a	Calcrete	1	N/A	N/A	N/A	0.13	N/A	N/A

Table 12.12 - Descriptive statistics for $\delta^{13}\text{C}$ values of lake carbonates at KAM4 lake 3a.

Site	Height above base (cm)	N	Mean (‰)	Median (‰)	SD (‰)	Min (‰)	Max (‰)	Range (‰)
KAM4 L3a	25 - 66	7	-1.12	-0.86	1	-2.87	-0.15	2.72
KAM4 L3a	Calcrete	1	N/A	N/A	N/A	-0.05	N/A	N/A

12.5.3 Depositional model

The sedimentary evidence described above is used to construct a depositional model for the sequence at KAM4 lake 3b. Three main phases of sediment deposition are recorded at the site. Unit 1 consists of loose sands and probably represents aeolian sand deposition and dune movement at the site prior to the humid interval represented by the overlying sediments. Units 2a and 2b reflect the onset of water accumulation at the site. Unit 2a consists of horizontally laminated sands and were probably deposited via sheet wash at the margins of a wetland. This occurred at the onset of a humid interval while the local landscape was unvegetated and surficial dune sands were unstable. Unit 2a then grades into Unit 2b, which consists of carbonate rich silty sands with abundant clay present as shown by the presence of illite (18.4%). The microfacies from this unit contains a heterogenous microstructure with relatively high number of allogenic grains. The latter is also shown by XRD analysis, which indicates relatively high proportions of quartz (39.1%). These sedimentary features are combined with the lowest $\delta^{18}\text{O}$ (-3.74‰) and $\delta^{13}\text{C}$ (-2.87‰) values from the sequence. These characteristics are typical of an ephemeral palustrine environment where calcite precipitates in shallow (<1 m) waters with relatively high levels of throughflow. The water level episodically dropped, allowing pedogenesis or desiccation to occur, as reflected by the heterogenous and prismatic structure caused by root activity or desiccation (Alonso-Zarza, 2003), and the accumulation of clays.

Unit 3a and 3b consist of fine-grained carbonate rich marls and reflect the transition from a palustrine environment as represented by Unit 2 to a perennial but shallow water body in the basin. The microstructure of the sediment is homogenous and the groundmass is composed microsparite with a low coverage of allogenic silts and sands. These features are consistent with a shallow but well-mixed lake where the sediment bed is mixed via surface winds or bioturbation (Wright, 1990). $\delta^{13}\text{C}$ values within this unit range from -1.89‰ to -0.15‰ and are typical of lake waters in equilibrium with the atmosphere. $\delta^{18}\text{O}$ values have a small range (2.4‰) indicative of stable hydrology.

The final unit (Unit 4) consists of mechanically strong, well cemented fine-grained carbonate typical of hardpan pedogenic calcrete. At the microscale, the presence of spherulites – 100 µm fibro-radial features that typically occur high up in calcrete profiles – is further evidence for calcrete formation where calcite precipitation is promoted around root networks, algal mats and other biological organisms (Alonso-Zarza and Wright, 2010). Pedogenic calcretes in arid environments typically have positive $\delta^{13}\text{C}$ values due to limited soil respiration and the dominance of C4 grasses (Alonso-Zarza and Wright, 2010). The $\delta^{13}\text{C}$ value of -0.05‰ from unit 4 is consistent with this. Unit 4 represents the final phase of humidity after the shallow waterbody had desiccated. The calcrete was probably formed on the surface of the lacustrine carbonates via laterally flowing shallow groundwaters after the complete desiccation of the lake body (Alonso-Zarza and Wright, 2010). Carbonate precipitation in such a depositional setting is promoted by plant roots (Alonso-Zarza and Wright, 2010).

12.6 KAM4 lake 3b

The KAM4 Lake 3b sequence lies approximately 50 m to the west of the lee side of the modern barchanoid dune and is the southern-most palaeolake deposit in the KAM4 basin (Fig 12.1). KAM4 lake 3b lies to the southeast of lake 3a and directly to the south of lake 3. The lake 3 deposit is separated from lake 3b by a sharp ridge. Luminescence dating of sands underlying the lake 3b sediments yielded ages of 168 ± 12 ka (PD7) and 142 ± 13 ka (PD8). These provide maximum ages for the timing of lake formation, and indicate lake formation occurred during MIS 6 or MIS 5.

12.6.1 Sedimentology

12.6.1.1 Bulk sedimentology

The sedimentary sequence at KAM lake 3b is split into three units, measured from the base of the waterlain sediments (marl) upwards (Fig 12.22). Unit 1 consists of loose sands and lies beneath the base of the carbonate bed. **Unit 2 (0 – 5 cm)** contains friable fine-grained carbonate rich marls with sand lenses. No calcium carbonate analysis was

undertaken from this unit, though XRD shows that it is primarily composed of calcite (97.8%) with a small proportion of quartz (2.1%). This grades into **Unit 3 (5 – 17 cm)** which consists of massive and consolidated marls with no obvious structure. Calcium carbonate content within unit 3 was consistently >80%, while XRD analysis shows calcite to be the dominant mineral (91 - 93%), with a small proportion of quartz (7 – 9%). The sequence is capped by pedogenic calcrete, which lie fragmented on the surface of Unit 2b.

Table 12.13 - X-ray diffraction results from KAM4 lake 3b. Calcite is dominant with a small proportion of quartz.

Height above base (cm)	Unit	Calcite (%)	Quartz (%)
2 – 5	2a	91.1	8.9
10 – 12	2b	93.1	6.9

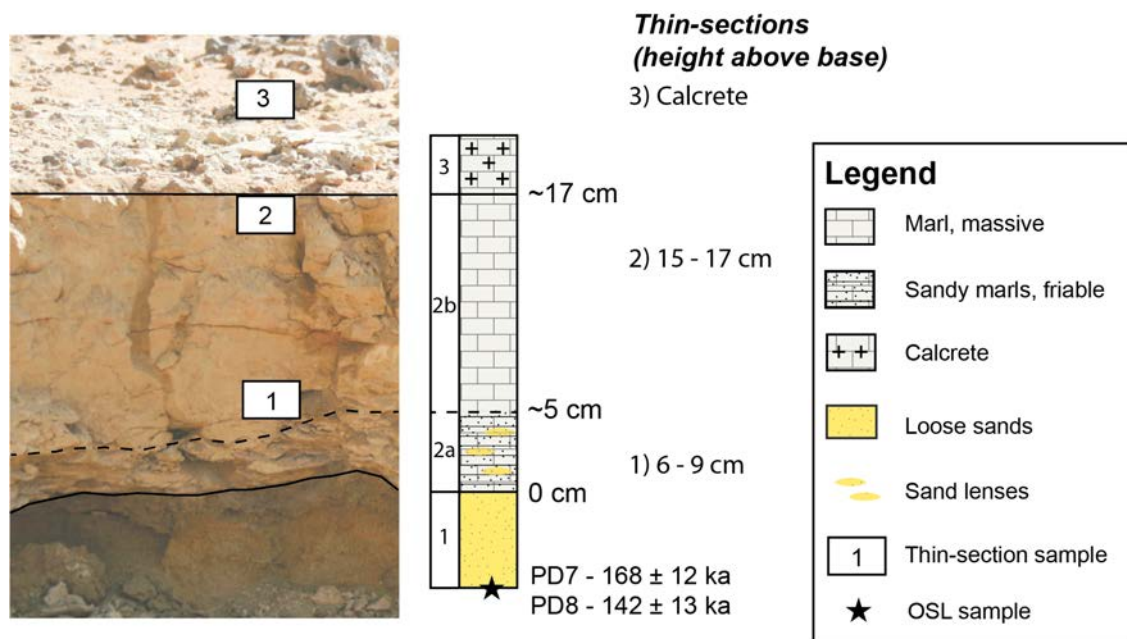


Figure 12.22 - Sedimentary sequence from KAM L3b. Unit boundaries are represented by a solid black line and sub-unit boundaries by a dashed line. Thin-section sample locations through the sequence are shown, with the corresponding thin-section heights above base of the marl unit noted on the right side of the figure. OSL ages produced as part of this thesis are shown.

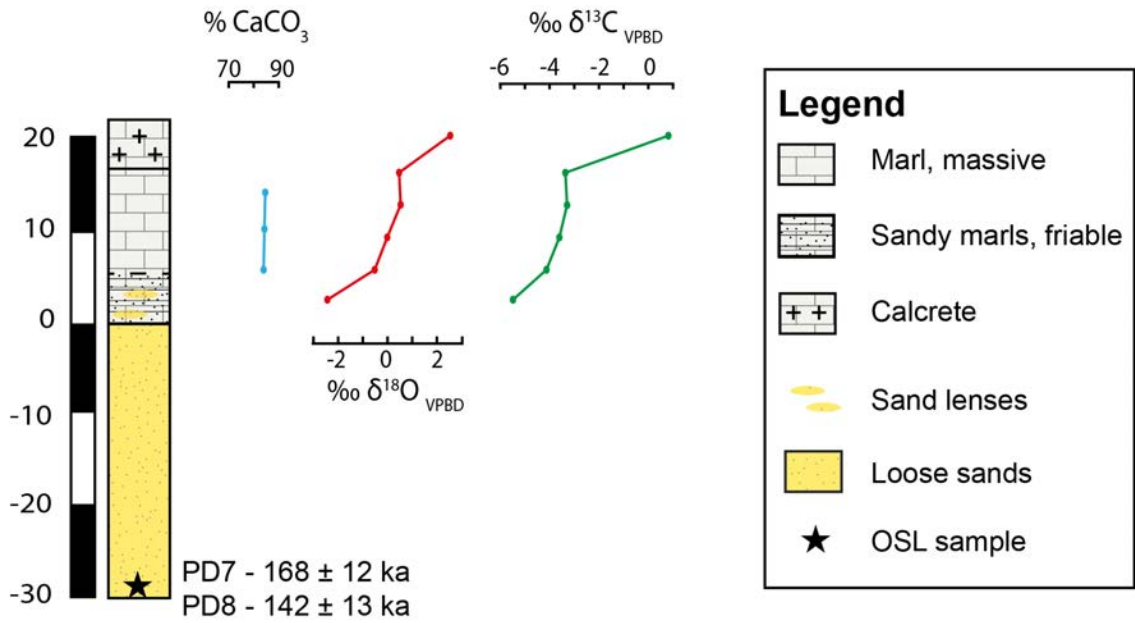


Figure 12.23 - Sedimentary log with CaCO_3 (blue), $\delta^{18}\text{O}$ (red) and $\delta^{13}\text{C}$ (green) curves for KAM4 Lake 3b. OSL ages produced as part of this thesis are shown.

12.6.1.2 Microfacies descriptions

Two samples were taken for microfacies analysis from Unit 3 and a single sample from the pedogenic calcrete for microfacies analysis. No samples were taken from Unit 2 as the material was too friable and did not survive transportation from the field to the laboratory. Both samples from Unit 3 display almost identical microfacies. They are characterised by a homogenous microstructure with a groundmass consisting of microsparite with rare allogenic silt and sand sized grains, no voids, no evidence of organic material, and no evidence of depletion or concentration features. The pedogenic calcrete is composed of a greater proportion dense micrite with a large number of vughs, vesicles and spherulites.

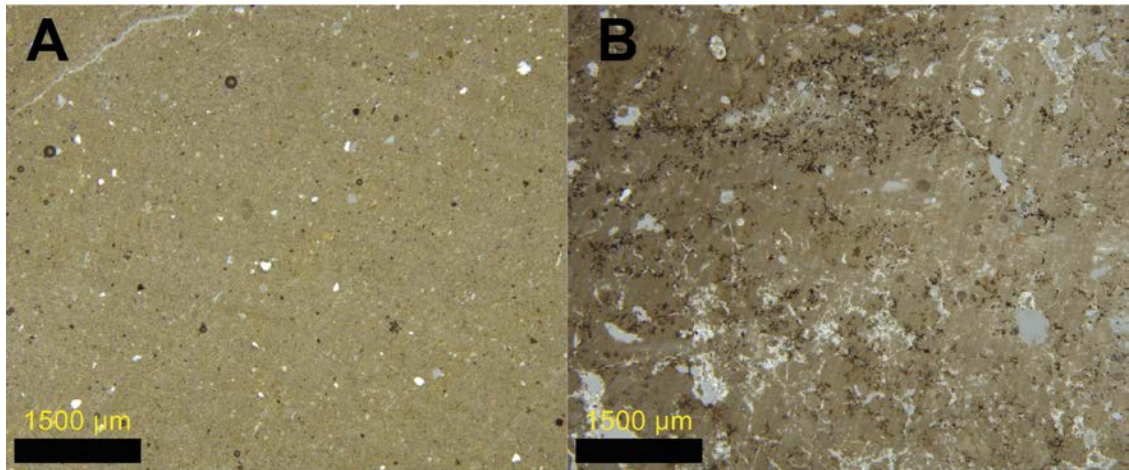


Figure 12.24 - Photomicrographs of thin-sections from KAM4 lake 3b. (A) 6 – 9 cm above base from unit 2a. This microfacies consists of a massive microstructure with a homogenous microsparitic groundmass. Allogenic grains are rare and spread evenly across the slide. (B) Calcrete that caps the sequence. This microfacies is dominated by massive microsparite and has numerous vugh and vesicle voids infilled with sparite crystals.

12.6.2 $\delta^{18}\text{O}$ and $\delta^{13}\text{C}$

$\delta^{18}\text{O}$ values range between -2.32‰ and 2.44‰ with a mean value of 0.09‰ and a median value of 0.21‰ . There is a clear trend towards more positive values moving upwards through the sequence (see Fig 12.23), with the lowest value of -2.32‰ in Unit 2 and the highest value of 2.44‰ in the calcrete (Unit 4). $\delta^{13}\text{C}$ values range between -5.56‰ and 0.94‰ with a mean value of -3.22‰ and median value of -3.63‰ . The most negative value of -5.56‰ occurs in Unit 2 while the positive value of 0.94‰ is from the calcrete. This follows a similar trend to the $\delta^{18}\text{O}$ values, with isotope values increasing moving upwards through the sequence. The R^2 coefficient between $\delta^{18}\text{O}$ and $\delta^{13}\text{C}$ through the sequence is 0.87 with a p-value of 1.18×10^{-4} , though this is based on a small number of data points ($n = 5$).

Table 12.14 - Descriptive statistics for $\delta^{18}\text{O}$ values of lake carbonates at KAM4 lake 3b.

Site	Height above base (cm)	N	Mean (‰)	Median (‰)	SD (1σ) (‰)	Min (‰)	Max (‰)	Range (‰)	Range
KAM4 L3b	2 – 17	5	-0.38	0.53	-0.04	1.18	-2.32	0.57	2.89
KAM4 L3b	Calcrete	1	N/A	N/A	N/A	N/A	2.44		N/A

Table 12.15 - Descriptive statistics for $\delta^{13}\text{C}$ values of lake carbonates at KAM4 lake 3b.

Site	Height above base (cm)	N	Mean (‰)	Median (‰)	SD (1σ) (‰)	Min (‰)	Max (‰)	Range (‰)	Range
KAM4 L3b	2 – 17	5	-4.05	0.4	-3.83	0.9	-5.56	-3.36	2.21
KAM4 L3b	Calcrete	1	N/A	N/A	N/A	N/A	0.94		N/A

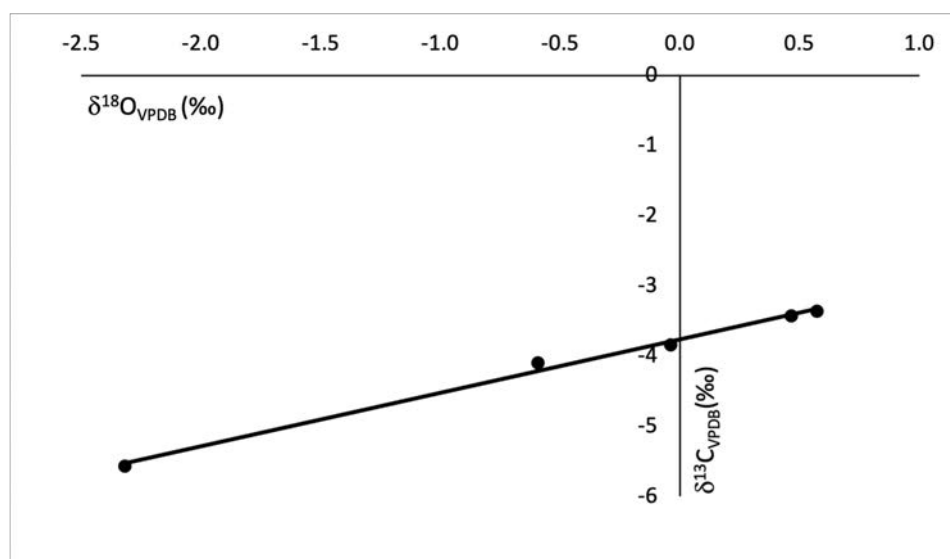


Figure 12.25 – Covariance between $\delta^{18}\text{O}$ and $\delta^{13}\text{C}$ at KAM4 lake 3b. The R^2 coefficient between $\delta^{18}\text{O}$ and $\delta^{13}\text{C}$ through the sequence is 0.87 with a p -value of 1.18×10^{-4} .

12.6.3 Depositional model

The sedimentary evidence described in this section is used to construct a depositional model for the KAM4 lake 3b sequence. Unit 1 consists of loose sands and represents dune activity prior to the onset of humidity. The fine-grained carbonate rich marls of Units 2 and 3 represents the development of an interdunal lacustrine basin in which carbonate was precipitated. Unit 2a (0 – 5 cm) contains fine-grained carbonate with sand lenses at the macroscale. The presence of sand lenses in this unit suggests an unstable, unvegetated or partially vegetated surrounding landscape that had yet to fully respond to pluvial conditions. This readily provided surficial dune sands for transportation into the lake basin during periods of rainfall. The negative $\delta^{13}\text{C}$ and $\delta^{18}\text{O}$ values from this unit is typical of high-levels of throughflow in a shallow lacustrine system (Talbot, 1990).

Unit 2b (5 – 17 cm) is composed of homogenous fine-grained carbonate rich marls. At the microscale the unit contains a homogenous microstructure with a microsparitic groundmass and rare allogenic grains. There is no evidence of desiccation or pedogenesis. Such a microfacies is typical of a shallow and perennial waterbody where the lakebed is mixed via surface winds or bioturbation. The lack of allogenic grains suggests a more stable surrounding environment and/or that the lake expanded relative to the previous unit and the site of sedimentation lay further from the lake edge and clastic inputs into the basin. The $\delta^{13}\text{C}$ values remain relatively negative compared to other sequences at KAM4 as they lie between -4.09‰ and -3.42‰ , which suggests high levels of throughflow throughout the lake's existence (Talbot, 1990).

Unit 3 consists of mechanically-strong, well-cemented fine-grained carbonate. At the microscale it is dominated by micrite with very rare allogenic grains. This suite of features is consistent with hardpan pedogenic calcrete (Alonso-Zarza and Wright, 2010), and is almost identical to the pedogenic calcrete observed at KAM4 lake 3a. As with that sequence, the pedogenic calcrete observed here was probably formed on the surface of the lacustrine carbonates via laterally flowing shallow groundwaters after the desiccation of the lake body (Alonso-Zarza and Wright, 2010). Unit 3 therefore represents the final phase of humidity. Both $\delta^{18}\text{O}$ and $\delta^{13}\text{C}$ values are more positive than the lake carbonates below and the pedogenic calcrete at KAM4 lake 3a, with values of 2.44‰ and 0.94‰ respectively. This suggests this calcrete may have formed under slightly more arid conditions compared the comparable calcrete at KAM4 lake 3a.

Both $\delta^{18}\text{O}$ and $\delta^{13}\text{C}$ progressively enrich moving upwards through the sequence and this is reflected by a R^2 coefficient of 0.87. This suggests evaporation is the dominant control on isotopic values from this sequence, and that evaporitic enrichment increases moving upwards through the sequence. However, this R^2 coefficient is based on only a small number of data points ($n - 6$). Consequently, interpretations derived from this data must be taken with caution.

12.7 KAM4 lake 4

The KAM4 lake 4 sedimentary deposit lies in the northwestern portion of the KAM4 interdunal basin. Sands underlying the lake sequence yielded a luminescence age of 141 ± 13 ka (PD13) while samples taken directly from the lake sediments (PD14) yields ages of 194 ± 13 ka (60 – 90 μm quartz), 210 ± 16 (4 – 11 μm quartz) and 192 ± 20 ka (60 – 90 μm feldspar). As discussed in Chapter 6, we regard the ages for PD14 as more reliable. On this basis the lake 4 sequence dates to MIS 7. As noted in the introduction to this Chapter, samples were taken and analysed for diatom palaeoecology and invertebrate palaeoecology during previous fieldwork seasons. It is important to state that multiple trenches have been dug into the KAM4 lake 4 sedimentary deposit over multiple field seasons, and it is not clear whether these samples originate from the same trench as the sedimentary and isotope samples collected as part of this project. Nevertheless, given that they originate from the same deposit they will be used to support the depositional model.

12.7.1 Sedimentology

12.7.1.1 Bulk sedimentology

The sedimentary sequence at KAM lake 4 is split into three units, with the depths measured from the base of marl sediments (Unit 2) upwards (Fig 12.26). Unit 1 consists of loose sands and lies beneath the base of the carbonate bed. Unit 2 is split into Sub-Units 2a and 2b. Unit 2a (0 – 10 cm) consists of interdigitated friable fine-grained carbonate rich marls and sands. Due to the friable nature of this unit, no consolidated block sediments could be taken and no calcimetry, XRD or stable isotope analysis was undertaken. Field observations suggest a high allogenic sand content. Unit 2a grades into **Unit 2b (10 – 27 cm)** which consists of well consolidated homogenous fine-grained carbonate rich marls. Calcium carbonate content in this unit ranges from 84% at 10 cm to 55% at 26 cm. XRD shows that calcite is dominant (91.6 - 100%) with small proportion of quartz (0 – 8.4%). **Unit 3 (27 – 65 cm)** consists of carbonate rich silty sands with clay present along with gravel inclusions. Mottling is present and the unit also contains rip-up marl intraclasts. Calcium carbonate content in Unit 3 ranges from 45% to 39%, while XRD shows calcite is dominant (72.8%) alongside a smaller proportion of quartz (27.2%).

While no clay minerals were detected during XRD analysis, clay-sized particles are clearly present in thin-section (see Fig X, panel X). **Unit 4a (65 – 95 cm)** is composed of homogenous fine-grained carbonate-rich marls containing in situ gastropod shells. Calcium carbonate content in this unit ranges from 57% to 69% while XRD shows calcite is dominant (49 – 72.8%) with smaller proportions of quartz (27.2 – 37.4%) and orthoclase (0 – 13.6%). **Unit 4b (95 – 118 cm)** consists of friable but still homogenous fine-grained carbonate rich marls with a greater allogenic sand component and contains rip-up marls. Calcium carbonate content in this unit ranges from 21% to 28%, while XRD shows calcite is dominant (40.5%) with smaller proportions of quartz (51.2%) and anorthoclase (8.3%).

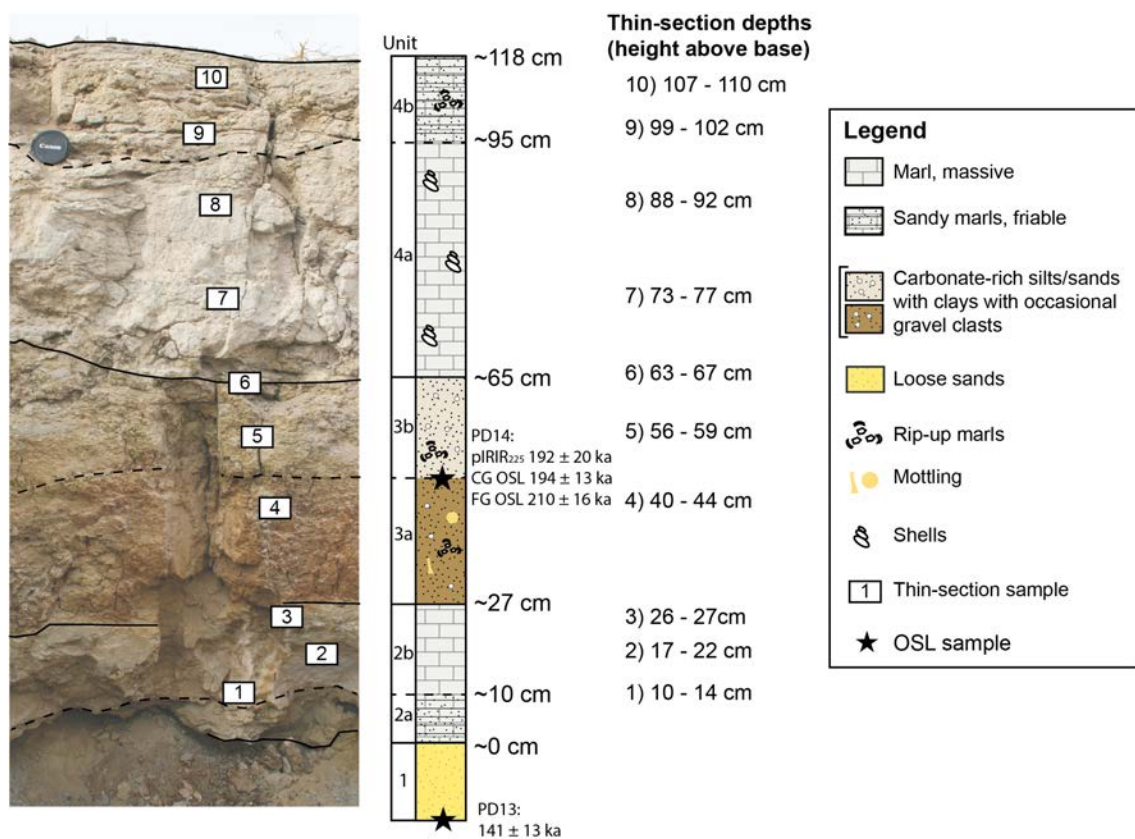


Figure 12.26 - Sedimentary sequence from KAM lake 4. Unit boundaries are represented by a solid black line and sub-unit boundaries by a dashed line. Thin-section sample locations through the sequence are shown, with the corresponding thin-section heights above base of the marl unit noted on the right side of the figure. OSL ages produced as part of this thesis are also shown.

Table 12.16 - X-ray diffraction results from KAM4 lake 4. Calcite is dominant through all samples with the exception of the final sample (111 – 114 cm). The proportion of calcite is greatest in Unit 2b and falls in Unit 3, 4a and 4b, with a greater amount of quartz and some anorthoclase/orthoclase present in these units.

Height above base (cm)	Unit	Calcite (%)	Quartz (%)	Anorthoclase (%)	Orthoclase (%)
10	2b	91.6	8.4	0	0
25	2b	100	0	0	0
40 – 42	3a	72.8	27.2	0	0
72 – 77	4a	49	37.4	0	13.6
90	4a	67.7	32.3	0	0
111 – 114	4b	40.5	51.2	8.3	0

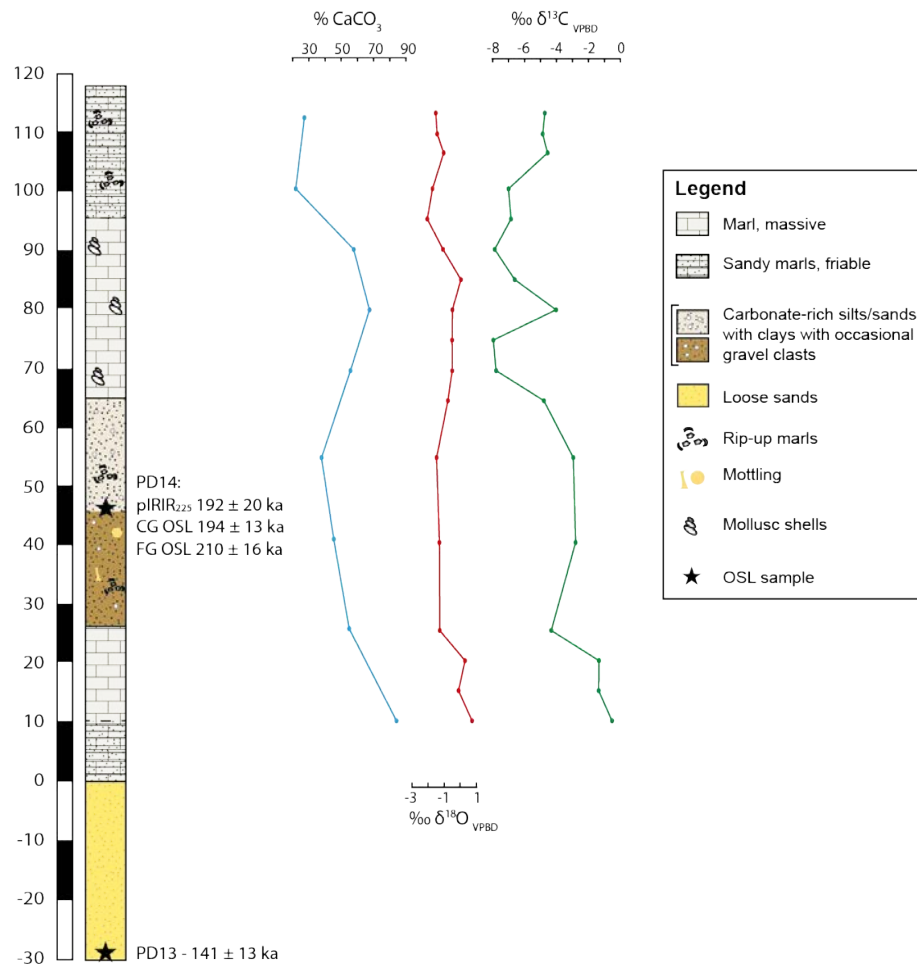


Figure 12.27 - Sedimentary log with CaCO₃ (blue), δ¹⁸O (red) and δ¹³C (green) curves for KAM4 lake 4. OSL ages produced as part of this thesis are shown.

12.7.1.2 Microfacies descriptions

A total of 10 samples were taken for microfacies analysis through the sequence. No samples were taken from Unit 2a as the material was too friable. Three samples were taken in Unit 2b. These samples display similar characteristics. All contain a predominantly homogenous microstructure, though small sections with a prismatic structure are observed at 10 – 14 cm and 26 – 27 cm, and all contain a groundmass composed of predominantly homogenous microsparite. However, there are subtle differences. The lowermost (10 – 14 cm) sample contains an obvious lamination of micrite and some planar and blocky voids where others do not. Both the lowermost sample (10 – 14 cm) and the uppermost sample (26 – 27 cm) from Unit 2 contain a higher proportion of allogenic grains (5 – 10%) coverage, relative to the middle sample (17 – 22 cm; <2% coverage). The lowermost sample contains rare shell fragments and ostracod remains, though the following two samples see an increase with a small number (2 – 4) ostracod shells present along with other non-identifiable shell fragments.

Samples from Unit 3a and 3b contain a prismatic microstructure with numerous irregular planar voids (Fig 12.28, panel B). The groundmass is composed of a mixture of microsparite, micrite and yellow to orange clays. Shell fragments are frequent and the lower thin-section at 40 – 44 cm displays iron staining, which is also obvious at the macro-scale (see Unit 3a; Fig 12.26). Allogenic sand grains are present but rare (<2% coverage).

A single thin-section from 63 – 67 cm represents the transition between Units 3 and 4a. This contains both a massive and prismatic structure in sections and has a groundmass predominantly composed of microsparite with small patches of micrite. Allogenic sand grain content is high (10 – 25%) relative to the sedimentary sequence below it.

Four samples were taken from Units 4a and 4b. These all have a homogenous microstructure with rare planar voids present. The groundmass is composed of homogenous microsparite (Fig 12.26, panel C and D). Allogenic grain content increases moving upwards through the units, from 2 – 5% coverage at 73 – 77cm to 25 – 33%

coverage at 107 – 110 cm. The 107-110 cm section also contains much coarser allogenic grains, with very coarse sand grains present. Shell fragments are frequent in the lower two thin-sections (73 – 77 cm and 88 – 92 cm) but rare in the upper two thin-sections. Occasional fragments of organic matter are present in the lower three thin-sections, sometimes with cellular preservation and sometimes amorphous (lack cellular preservation), while only amorphous organic matter is present in the final thin-section. The final section also contains multiple carbonate nodules that may be rip-up intraclasts.

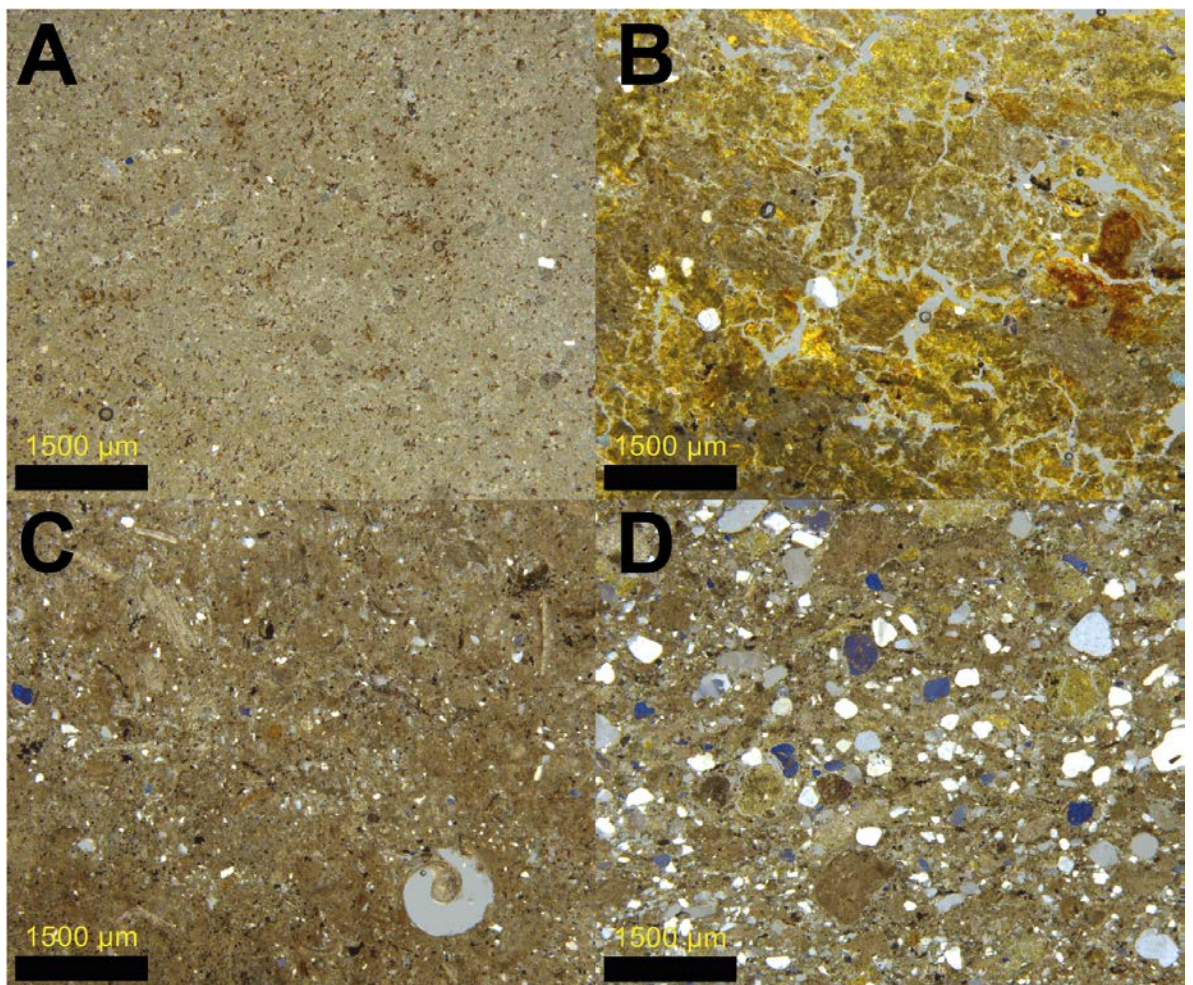


Figure 12.28 - Photomicrographs of thin-sections from KAM4 lake 4. (A) 17 – 22 cm above base from unit 2b. This microfacies consists of massive microsparite with very rare allogenic grains. (B) 56 – 59 cm from unit 3. This microfacies consists of a prismatic microstructure dominated by calcite. Clays (yellow material) are also present concentrated around planar voids. (C) 88 – 92 cm above base from 4a. This microfacies consists of a massive microstructure dominated by microsparite, though numerous shell fragments are present as are numerous allogenic silt/fine sand grains. (D) 107 – 110 cm above base from unit 4b. This consists of a massive microstructure with a groundmass composed of microsparite. The number of allogenic sand grains increases in this unit and is evident from this microfacies.

12.7.2 $\delta^{18}\text{O}$ and $\delta^{13}\text{C}$

$\delta^{18}\text{O}$ values range between -2.04‰ and 0.81‰, have a mean value of -0.84‰ and a median value of -1.05‰. Three of the four most positive values occur in the first three samples between 10 – 20 cm, but aside from this there is no clear trend through the rest of the sequence. The $\delta^{13}\text{C}$ values lie between -0.55‰ and -7.98‰, with a mean value of -4.74‰ and a median value of -4.70‰. The $\delta^{13}\text{C}$ values are more positive in the lower portion of the sequence between 10 – 20 cm. Values then decline at the top of unit 2b (25 cm) and remain relatively stable through unit 3 and the very start of unit 4a (65 cm). There is a large shift towards negative values between 65 – 70 cm, where $\delta^{13}\text{C}$ falls to -7.81‰. Values remain < -6.5‰ between 70 – 100 cm, with a single exception at 80 cm where there is a brief positive excursion to -4.8‰. The end of the sequence is characterised by more positive $\delta^{13}\text{C}$ values (though still negative relative to the first 55 cm of the sequence), that lie between -4.63‰ and -4.89‰. The R^2 coefficient between $\delta^{18}\text{O}$ and $\delta^{13}\text{C}$ through the sequence is 0.2 with a p-value of 0.07.

Table 12.17 - Descriptive statistics for $\delta^{18}\text{O}$ values of lake carbonates at KAM4 lake 4.

Site	Height above base (cm)	N	Mean (‰)	Median (‰)	SD (‰)	Min (‰)	Max (‰)	Range
KAM4 L4	10 – 114	17	-0.84	-1.05	0.76	-2.04	0.81	2.85

Table 12.18 - Descriptive statistics for $\delta^{13}\text{C}$ values of lake carbonates at KAM4 lake 4.

Site	Height above base (cm)	N	Mean (‰)	Median (‰)	SD (‰)	Min (‰)	Max (‰)	Range
KAM4 L4	10 – 114	17	-4.72	-4.7	2.39	-7.98	-0.55	7.43

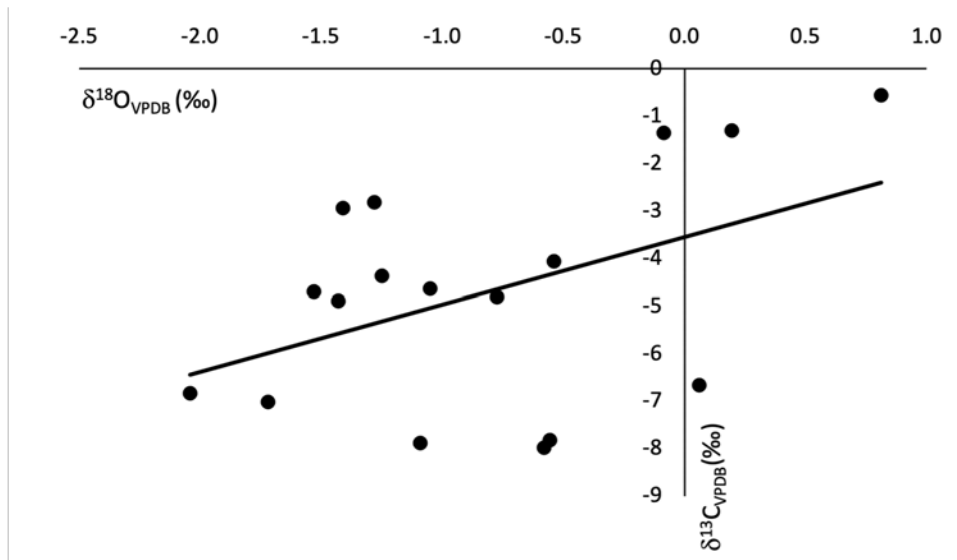


Figure 12.29 - Covariance between $\delta^{18}\text{O}$ and $\delta^{13}\text{C}$ at KAM4 lake 4. The R^2 coefficient between $\delta^{18}\text{O}$ and $\delta^{13}\text{C}$ through the sequence is 0.2 with a p -value of 0.07.

12.7.3 Diatom palaeoecology

A single sample from the top of the sedimentary sequence yielded high enough abundances for diatom taxonomy (Fig 12.30) (Sung per comms). *Brachysira brebissonii*, *Denticula eximia* and *Halamphora coffaeiformis* were the dominant taxa present. These taxa present represent a mixture of freshwater (e.g. *Brachysira brebissonii*, *Navicymbula pusilla*) and brackish (e.g. *Halamphora coffaeiformis*, *Denticula kuetzingii*) species. Benthic taxa comprise 81% of the assemblage and suggest shallow lake conditions. The dominate taxa *Brachysira brebissonii* is indicative of acidic and oligo-mesotrophic conditions, yet most other taxa suggest alkaline conditions. The assemblage also shows a range of potential trophic status from oligotrophic (*Brachysira brebissonii*), mesotrophic (*Aulacoseira granulata*) and nutrient rich waters (*Nitzschia palea*, *Nitzschia dissipata*) which is linked to phosphorous concentration (Hamilton, 2010; Bennion and Simpson, 2011).

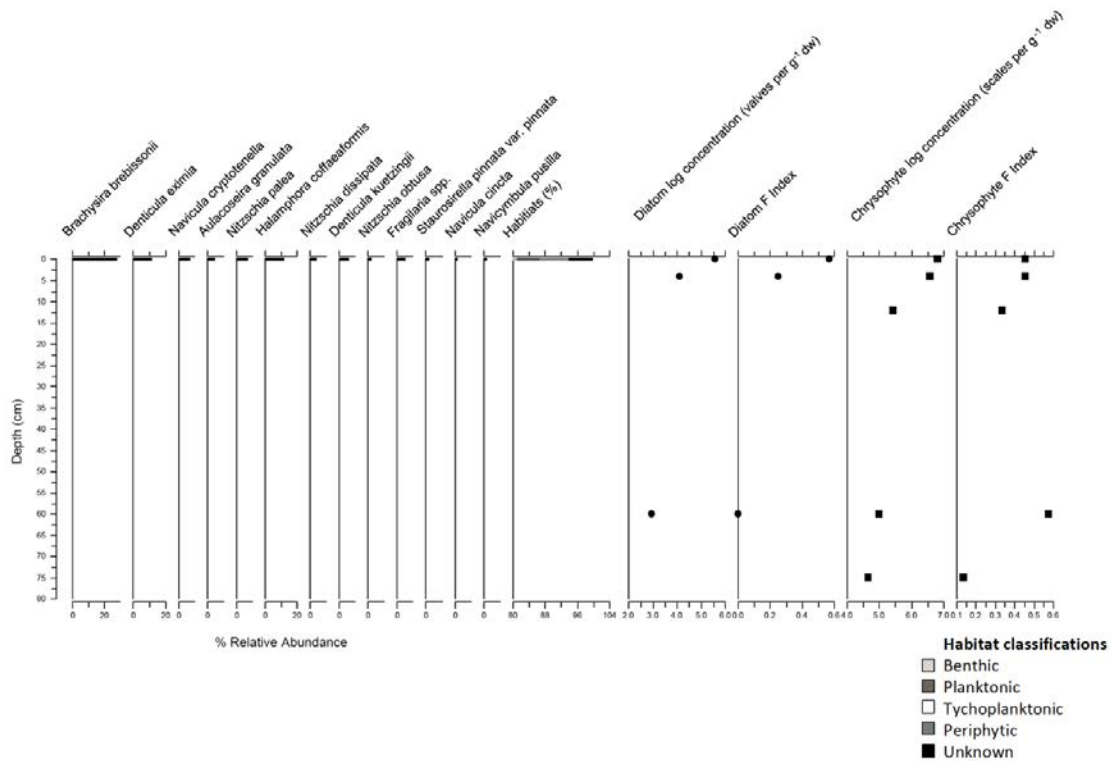


Figure 12.30 – Diatom palaeoecology of the KAM4 lake 4 sequence carried out by Wing-Wai Sung. Only a single sample from the surface of the sequence (equivalent to unit 4b) yielded high enough abundances for diatom taxonomy.

12.7.4 Invertebrate palaeoecology

Invertebrate palaeoecology was carried out by Dr. Tom White as part of the Palaeodeserts Project and is currently unpublished. The initial findings are presented here. The most common invertebrate recovered was the gastropod *Planorbis carinatus*, a calciphile freshwater species that lives in permanent (White, per comms), well-vegetated aquatic habitats ranging from ponds, lakes, slow-moving rivers and canals (Kerney, 1999). *Gyraulus crista*, a calciphile also tolerant of soft-water conditions, is common at KAM4 while other *Gyraulus* sp. are present but difficult to identify to species level (White, per comms). *Lymnaea* spp. is also present. Two non-marine ostracoda species were also identified in the sequence, *Candona candida* and *Cyprideis torosa* (White, per comms).

12.7.5 Depositional model

The sedimentary evidence described in this section is used to construct a depositional model for the KAM4 lake 4 sedimentary sequence. Unit 1 consists of loose sands and represents dune activity prior to the onset of humidity. Unit 2a consists of friable carbonate rich marls interdigitated with sands and this transitions into the well-cemented and massive fine-grained carbonate rich marls of Unit 2b. These units represent the development of a lake in the interdunal basin. The massive microsparite microfacies with no evidence of pedogenesis or desiccation is consistent with deposition in a shallow but perennial waterbody. $\delta^{13}\text{C}$ values in this unit lie between -0.55 and 1.35‰ and are consistent with this interpretation, as they are typical of a waterbody in equilibrium with atmospheric CO_2 (Leng and Marshall, 2004). The final $\delta^{13}\text{C}$ value falls to -4.37‰ and may suggest increased rates of throughflow in the final stages of deposition of this unit. The $\delta^{18}\text{O}$ values are the most enriched of the sequence and probably reflect longer residence times that allowed greater evaporitic enrichment of the $\delta^{18}\text{O}$ signal to occur.

Unit 3 represents a transition from a shallow but perennial water body to a palustrine system where the sediment bed was affected by periodic sub-aerial exposure. The sediment consists of carbonate rich silty sands with clay present. The dominant mineral is calcite (XRD – 64.2%). This may have been precipitated during lacustrine conditions as represented by the previous Unit, and subsequently altered via desiccation during subaerial exposure of the lake bed. XRD shows high levels of quartz relative to the unit below. This suggests a higher influx of allogenic sand grains into the waterbody, which may have been a consequence of the lake contracting, thereby moving the lake edge closed to the site of sedimentation. Clay is also evident in thin-section (Fig 12.28, panel B). The presence of clays along with a higher proportion of silts and sands suggest deposition in a lower-energy environment as these grain sizes may have fallen from suspension during stagnant and shallow water conditions.

Microfacies from this unit contains a prismatic microstructure with a number of large and irregular planar voids. This is indicative of sub-aerial exposure, desiccation of the lakebed and alteration of the primary lake mud (Alonso-Zarza, 2003). $\delta^{18}\text{O}$ values are consistent with units above and below, while $\delta^{13}\text{C}$ values are slightly more negative than those from Unit 2b (with the exception of 25 cm) but enriched relative to all $\delta^{13}\text{C}$ values from Units 4a and b. As isotopic values lie within or very close to the range of those in Unit 2, this suggests that the conditions under which the primary calcite was precipitated was not largely different from that unit. This supports the view that the calcite originates from similar conditions to Unit 2, and that no new calcite was generated as part of this unit. Instead, palustrine conditions led to the water-level dropping, subaerially exposing the lakebed for a period of time, and leading to the brecciation of the primary calcite.

Unit 4 consists of fine-grained carbonate rich marls and represents a shallow lacustrine environment affected by high rates of throughflow. This transition between Unit 3 and 4 is captured in thin-section between 63 – 67 cm, where proportion of primary calcite increases and evidence for clay decreases, while the abundance of planar voids also decreases. The reduction in clay and increase in unaltered primary calcite (reduction in planar voids) suggests increased energy in the depositional environment and limited to no subaerial exposure of the sediment. Instead the sedimentary evidence is more consistent with a shallow, well-mixed, perennial waterbody with high-rates of throughflow. Siliclastic input into the basin is still high based on observations in thin-section, suggesting proximity to sediment laden streams at the lake edge.

The sedimentary characteristics of the rest of Unit 4a and 4b (excluding the uppermost thin-section) contain a greater proportion of homogenous fine-grained microsparite, with the presence of planar voids becoming very rare or non-existent. These characteristics, and the lack of any pedogenic or desiccation features, are consistent with deposition in a shallow, well-mixed perennial lacustrine environment. However, the key difference in Unit 4a and 4b (70 – 100 cm) is that $\delta^{13}\text{C}$ is depleted relative to the rest of the sequence. The mean $\delta^{13}\text{C}$ value between 70 – 100 cm is -6.89‰ compared to

a mean value of -3.24‰ for the rest of the sequence (10 – 65 cm; 107 – 114 cm). The most probable explanation for the more depleted $\delta^{13}\text{C}$ values in Unit 4 is increased rates of throughflow through the system, which prevent the $\delta^{13}\text{C}$ values from moving into equilibrium with atmospheric CO_2 (Leng and Marshall, 2004). It is also possible that an increase in C3 vegetation relative to C4 vegetation in the surrounding landscape could account for such a change (Leng and Marshall, 2004). Likewise, changes in lake productivity could also explain changes in $\delta^{13}\text{C}$, such as increased decomposition of vegetation releasing lighter ^{12}C into the system leading to more negative $\delta^{13}\text{C}$ values (Leng and Marshall, 2004).

The upper section of Unit 4b (107 – 118 cm) sees an increase in coarse-grain allogenic siliclastic material as shown at the microscale (Fig 12.28, panel D) and in XRD analysis (quartz 51%; anorthoclase 8%). This is probably related to a reduction in vegetation density in the surrounding landscape in response to increased aridity at the end of the humid interval. This would lead to greater availability and transport of surficial dune sands into the lake basin. Rip-up marls, which require turbulent waters to erode and redeposit original primary lake mud, are also present. $\delta^{18}\text{O}$ values are similar to those from the underlying unit, while $\delta^{13}\text{C}$ values are slightly more enriched (-4.63 to -4.89‰) relative to those between 70 – 100 cm. This suggests rates of throughflow remained high, though presumably dropped slightly towards the end of the sequence as the rate of water supply into the basin dropped in response to increased environmental aridity.

The diatom palaeoecology is limited to a single sample from the very top of the sequence, where a mixture of freshwater and brackish species are present. There is also a prevalence of benthic species that suggests shallow water conditions. Moreover, as the diatom sample comes from the very top of the sequence it is likely that the brackish species are present due to lake contraction and an increase in solute ion concentration in the waterbody at the end of the humid phase. The invertebrate palaeoecology is consistent with fresh, hardwater conditions (White et al., per comms). However, it is not clear how the invertebrate palaeoecology data relate to the stratigraphy presented above, and the microfacies analysis shows fragmented shells and ostracods were

present throughout the sequence at some degree. While the palaeoecological data is limited due to lack of preservation, they point towards predominantly freshwater conditions, which is consistent with the sedimentary and isotopic evidence.

The sedimentary sequence at KAM4 lake 4 represents a dynamic hydrology system that fluctuated from a shallow lacustrine environment, to a palustrine environment, and back to a shallow lacustrine environment with high rates of throughflow within a single humid phase. This is unique relative to all other sedimentary sequences in the basin. Moreover, the lack of evaporitic minerals (i.e. gypsum), the lack of desiccation features in Units 2b, 4a and 4b, the lack of covariance between $\delta^{18}\text{O}$ and $\delta^{13}\text{C}$, and palaeoecological data that suggests that when the shallow waters were present they were perennial and freshwater.

12.8 Summary of KAM4 interdunal basin

The key points from the KAM4 interdunal basin are:

- A total of six sedimentary sequences, deposited during at least four different humid intervals, were analysed from the KAM4 interdunal basin.
- Palaeoenvironmental analysis of each sequence suggests that the majority (Lakes 1, 2, 3, 3a and 3b) represent a single phase of humidity in which a wetland/lake formed. There are subtle variations in microfacies, isotopic values and isotopic covariation within and between these sequences that suggests slightly differing depositional environments (e.g. higher or lower rates of throughflow or depth). However, the Lakes 1, 2, 3, 3a and 3b sequences are all similar, being characterised by the deposition of homogenous or laminated fine-grained carbonate rich marls with a high calcite content and with no evidence of evaporates.
- There is limited sedimentary complexity within these sequences, and all suggest a simple palaeohydrological evolution. This is as follows: 1) the water table rises above the basin floor in response to increased humidity; 2) a stable perennial waterbody forms for an unknown period of time, and 3) the water table falls and

the lake desiccates. It is noteworthy that the onset of lacustrine conditions appears to be relatively abrupt, because the lowermost non-aeolian units are typically composed of fine-grained carbonate rich marls. The only sequence where this is not true is lake 3a, where a palustrine system grades into a perennial lacustrine system.

- In contrast to other sequences, lake 4 contains sedimentary evidence of climatic complexity. Here the sedimentary sequence suggests that the character of the waterbody changed over time, from a perennial lake body, to a palustrine environment and back to a perennial lake body, within a single humid interval.
- It is worth noting that where palaeoecological proxies have been recovered (i.e. diatom or invertebrates samples), they suggest fresh to brackish waters. Yet samples are so poorly preserved that they only represent small snapshots of time at very specific points in the depositional history of each record. For example, only four diatom samples across all sedimentary sequences provided diatom abundances that could be used for diatom taxonomy.
- Although limited palaeoecological data is available, it does support the environmental interpretations made on the basis of sedimentological and geochemical proxies.

Chapter 13 – Comparison of the humid phases in the western Nefud Desert with the regional record over the last ~500,000 years

13.1 Introduction

Interdunal carbonate or siliceous sediments within the western Nefud Desert most probably formed during peak phases of effective precipitation between ~500 – 80 ka (Chapter 6). Multi-proxy palaeoenvironmental analysis of these sediments shows that they were deposited by freshwater perennial lakes or more rarely palustrine or ephemeral systems (Chapters 8 – 12). Furthermore, a ~1.5 m sedimentary sequence from a trench in the modern interdunal floor of the recharge playa within the Al Wusta basin shows no lacustrine carbonate-rich marls were present. In contrast, a unit containing silty sands with gravel clasts indicative of an ephemeral waterbody was present, and suggests that the humid interval during the Holocene was limited relative to Middle and Upper Pleistocene humid phases (Chapter 7).

This chapter will combine the dating and palaeoenvironmental analysis from the results chapters (Chapters 6 – 12) and discuss the record of humid phases within the western Nefud Desert over the past ~500 ka. Sites will be discussed in a series of time windows: Marine Isotope Stage (MIS) 5 (~130 – 80 ka), the Middle Pleistocene (~500 – 130 ka), and the early-mid Holocene (~11.6 – 5 ka). The depositional characteristics of each sedimentary deposit from each time interval will then be compared with one another. Following this, the palaeoenvironmental expression of humid intervals within the western Nefud Desert over the past ~500,000 years is compared with other palaeohydrological records from the Arabian Peninsula, Levant and northeast Africa.

13.2 Humid phases in the western Nefud sand sea over the last ~500 ka

13.2.1 Multiple humid phases in the western Nefud sand sea during Marine Isotope Stage 5

Marine Isotope Stage (MIS) 5 (~130 - 80 ka) is characterised by high insolation seasonality with three northern hemisphere (NH) summer insolation peaks at ~128 ka (MIS 5.5), ~106 ka (MIS 5.3) and ~84 ka (MIS 5.1) (see Figure 13.2) (Berger and Loutre, 1991). Following the orbital monsoon hypothesis (Chapter 2) (Prell and Kutzbach, 1987; Rossignol-Strick, 1983), these three NH insolation peaks could theoretically lead to three periods of increased monsoonal precipitation. It is also possible that multiple phases of enhanced tropical rain bearing systems such as the Active Red Sea Trough or Tropical Plumes contributed to multiple humid phases in the Nefud Desert (Waldmann et al., 2010; Enzel et al., 2015; Hartman et al., 2020). Here it is demonstrated that at least two discrete humid phases occurred during MIS 5, during which perennial freshwater interdunal lakes formed in the western Nefud sand sea.

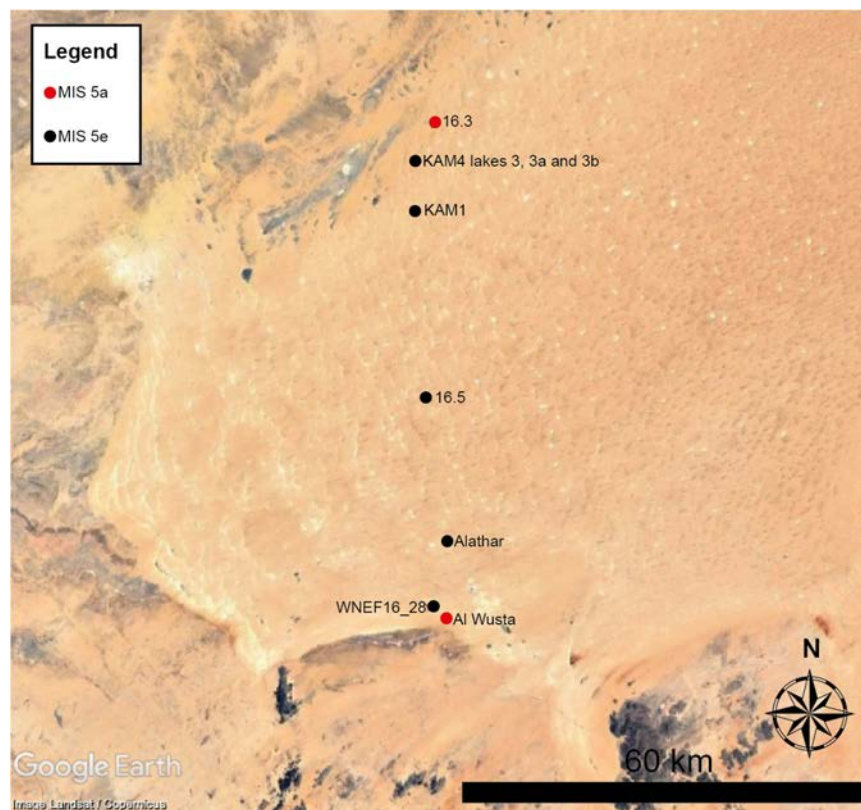


Figure 13.1 – The distribution of directly dated or bracketed MIS 5 palaeolake deposits across the western Nefud Desert. This includes palaeolakes from this thesis, Site 16.3 from Clark-Wilson (2016) and KAM1 and 16.5 from Rosenberg et al. (2013).

13.2.1.1 Chronology of MIS 5 humid phases

The chronology of MIS 5 humid phases in the western Nefud Desert is derived from the dating of seven interdunal sites containing lacustrine marls/diatomite (see Fig 13.1): Alathar, WNEF16_28, KAM4 (lakes 3, 3a and 3b), Site 16.3, Al Wusta, Khall Amayshan 1 (KAM1) and Site 16.5. Alathar, WNEF16_28 and KAM4 lakes 3, 3a and 3b were dated as part of this thesis, Site 16.3 and Al Wusta were dated as part of earlier MSc work (Clark-Wilson, 2016) and KAM1 and Site 16.5 were dated in previously published work (Rosenberg et al., 2013). The chronology of Al Wusta is also supported by additional U-series and U-ESR data along with a Bayesian model (Groucutt et al., 2018).

Site 16.3 and Al Wusta support interdunal lake development during late MIS 5, most probably in relation to a NH summer insolation peak at ~ 84 ka (Clark-Wilson, 2016; Groucutt et al., 2018). The lake sediments at Site 16.3 are directly dated to 86 ± 6 ka (PD3). The dating of lake formation at Al Wusta is more complex. The age of lake existence at Al Wusta has been determined by the bayesian modelling of OSL ages from aeolian sands that underlie, and waterlain sands which overlie, palaeolake sediments along with U-series and U-ESR ages from multiple fossils from the overlying waterlain sands. This yields an age for lake formation in late in MIS 5 between $\sim 95 - 86$ ka (Groucutt et al., 2018). It is notable that this age range falls during what would be assumed an arid phase following the orbital monsoon hypothesis, given that NH summer insolation is low. However, given the direct age of the lake sediments at Site 16.3 of 86 ± 6 ka, which is consistent with the insolation peak at ~ 84 ka, we suggest that Al Wusta most likely formed during this time interval.

Alathar, WNEF16_28 and KAM4 lakes 3, 3a and 3b support interdunal lake development during early MIS 5, most probably in relation to a NH summer insolation peak at ~ 128 ka. Lake sediments at Alathar are directly dated to 121 ± 11 ka (PD61) and 112 ± 10 ka (PD62). The lake sediments at WNEF16_28 are bracketed by underlying aeolian sands dated to 133 ± 10 ka (PD18) and overlying waterlain sands dated to 117 ± 8 ka (PD42). KAM4 lakes 3, 3a and 3b only yield a single age from palustrine sediments of 143 ± 10 ka (PD10; KAM4 lake 3a), though all other ages from aeolian sands underlying the lake

sediments are stratigraphically consistent with this age (see section 6.4.6.3). Based on these data, KAM4 lakes 3,3a and 3b could have formed during MIS 6, perhaps relating to a northern hemisphere summer insolation peak at ~150 ka. However, this most likely relates to increasing summer insolation at the MIS 6/5e boundary at ~133 ka. Palaeoclimate records from the region support this argument as they indicate enhanced humidity during this interval (e.g. Drake et al., 2013; El-Shenawry et al., 2018; Nicholson et al., 2020), whereas there is limited evidence for a wetter MIS 6. For example, there is no record of speleothem growth in Hoti or Mukalla during MIS 6 (Nicholson et al., 2020).

The evidence for early MIS 5 humidity is supported by the chronologies from the previously published sites of KAM1 and Site 16.5 (see Fig 13.1 and 13.2) (Rosenberg et al., 2013). KAM1 dates to between 117 ± 8 ka (lake sediments) and 99 ± 7 (aeolian sands underlying the lake sediments). However, since the aeolian sands at KAM1 are typically loose and prone to post-depositional mixing, luminescence dating of this material may not provide an accurate date for lake formation. Conversely, the lake sediment sample originates from grey calcareous sands with root traces and vertebrate remains and is underlain by diatomite and overlain by marl (Rosenberg et al., 2013), and therefore directly dates the timing of the humid phase. Consequently, the age of 117 ± 8 ka for the lake sediments at KAM1 is more robust, meaning that this lake most probably formed early in MIS 5. This site also contains a Middle Palaeolithic archaeological assemblage associated with the lake sediments (Scerri et al., 2015). Site 16.5 dates to between 128 ± 9 ka (sands overlying marls) and 125 ± 10 ka (sands underlying marls) indicating the presence of a lake early in MIS 5 (Rosenberg et al., 2013).

The ages presented above show that the western Nefud Desert experienced at least two discrete humid phases during MIS 5. It is inferred that these lakes formed in response to peaks in northern hemisphere summer insolation at ~84 ka (Al Wusta and Site 16.3) and ~128 ka (WNEF16_28, Alathar, KAM4 lakes 3, 3a, 3b, Khall Amayshan 1 and Site 16.5) (Fig 13.2).

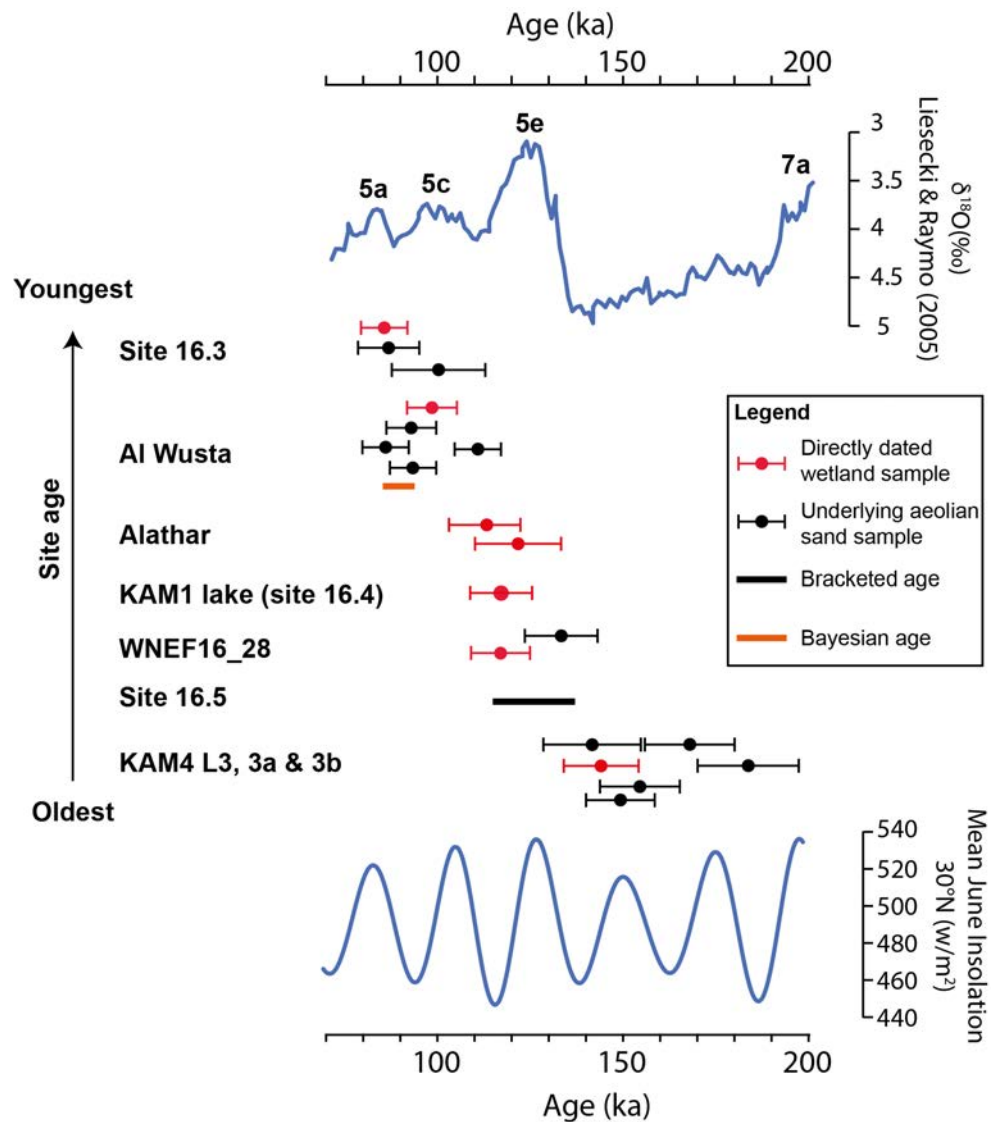


Figure 13.2 – Chronology of directly dated or bracketed MIS 5 palaeolake deposits dated to MIS 5 from the western Nefud Desert, including data from Rosenberg et al. (2013), Clark-Wilson (2016) and Groucutt et al. (2018). The single bracketed age (Site 16.5) takes the maximum and minimum ages at 1σ uncertainty from the sands which underlie and overlie the palaeolake sediments. All uncertainty terms are at 1σ .

13.2.1.2 Palaeohydrology of MIS 5 interdunal lakes

13.2.1.2.1 Carbonate palaeolake sediments (marls)

The depositional models for each MIS 5 sequence are mainly indicative of deposition on the beds of shallow perennial freshwater lakes, with little variability in their depositional environment. All lacustrine sediments are dominated by fine-grained carbonate rich marls with negligible evaporites (mostly <5%) and rare allogenic sands/silts. Allogenic material is typically more abundant at the start and end of marl sequences, which

probably relates to decreased landscape surface stability in response to limited vegetation cover at the onset/end of humid phases.

At the macroscale, the fine-grained carbonate rich marls vary subtly but predominantly display the same simple transgressive-regressive sequence (see Fig 3.2 and 3.3 in Chapter 3). Homogenous or laminated carbonate occurs abruptly at the start of the sequence (e.g. Al Wusta, Site 16.3) or gradually develop from sand-rich beds where the proportion of carbonate increases moving upwards through the sequence (e.g. KAM4 lake 3, 3a, 3b and WNEF16_28). The majority of the marl sequence then consists of homogenous or laminated carbonate with rare allogenic sands, before being capped by 'hardpan' marl with tubular voids (e.g. Unit 2d, Al Wusta; Unit 2d, WNEF16_28). The latter facies indicate deposition in shallower, near shore waters where calcite precipitation is concentrated around macrophyte roots. Marl sequences then end abruptly (e.g. Site 16.3) and are capped by crudely laminated sands with gravel inclusions and calcitic rhizoliths (e.g. Unit 3, Al Wusta; Unit 3, WNEF16_28) or by indurated calcretes (KAM4 lakes 3a and 3b).

The microfacies of the marls fall into three categories: (1) homogenous microsparite with some evidence of micrite, rare evidence of sparite and no evidence of desiccation or pedogenesis, (2) finely laminated microsparite/micrite with no evidence of desiccation or pedogenesis, and (3) prismatic microsparite/micrite with evidence of desiccation or pedogenesis. The first of these is the predominant microfacies across all MIS 5 sequences (see Fig 13.3 panels A, C and D), with finely laminated marls restricted to Unit 2b at WNEF16_28 (see Fig 13.3 panel B) and prismatic microfacies restricted to Unit 2 at KAM4 lake 3a and the very top of Site 16.3. This demonstrates that lakes were predominantly shallow and polymictic with well-oxygenated waters (Wright, 1990). The lake sediments were mixed/homogenised by surface winds and bioturbation (Alonso-Zarza, 2003; Groucutt et al., 2018; Wright, 1990). The laminated facies at WNEF16_28 suggests deeper water conditions and sedimentation in the hypolimnion (bottom waters) of thermally stratified perennial lakes (Wright, 1990). Here anoxic conditions inhibit biological activity at the lake floor and prevent bioturbation, while lake depth and stratification protect the lake beds from water turbulence caused by surface winds

(Wright, 1990). Finally, the rare prismatic microfacies are indicative of sedimentation within a waterbody that may have been subject to episodic desiccation and/or pedogenic processes (Alonso-Zarza, 2003). This is evidenced by numerous planar voids that represent desiccation features, and by clays that are related to marshy palustrine conditions that experience low-energy environments and periodic sub aerial exposure (Alonso-Zarza, 2003). An example of a palustrine facies is shown in Figure 12.20 in Chapter 12.5.1.

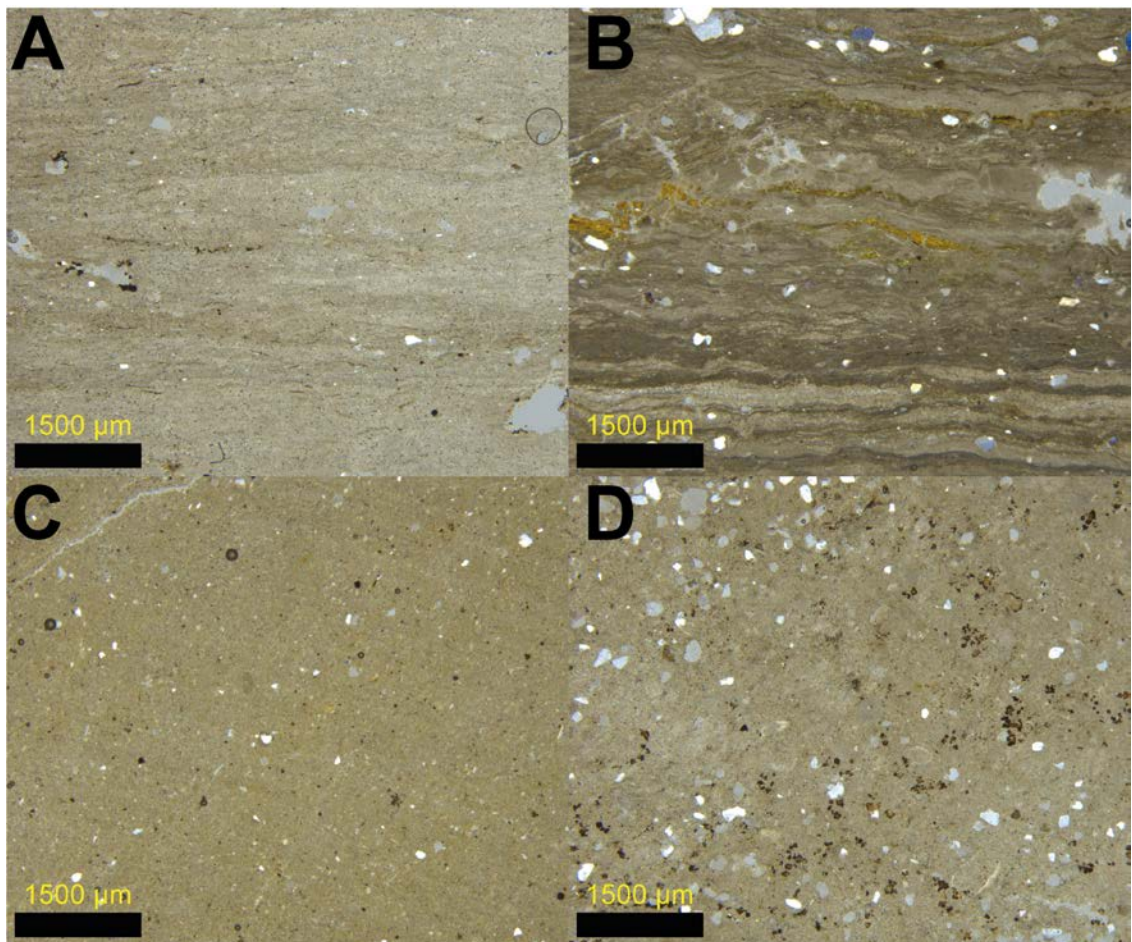


Figure 13.3 - Example photomicrographs of fine-grained carbonate rich marls across four of the MIS 5 sites presented here. Note that all microfacies contain a massive or a laminated microstructure with a groundmass dominated by microsparite or micrite. There is no evidence for pedogenic alteration or desiccation in these microfacies. Other common attributes include rare allogenic sand or silt grains and rare organic remains (i.e. shell fragments of ostracods). (A) Al Wusta 19 – 22 cm above base. (B) WNEF16_28 59 – 62 cm above base. (C) KAM4 lake 3b 6 – 9 cm above base. (D) Site 16.3 – 60 cm above base.

Carbon and oxygen isotopic evidence are consistent across the MIS 5 marl deposits (Fig 13.4). $\delta^{13}\text{C}$ values predominantly lie in a narrow range between -1 to 3‰. It is difficult to pick out the dominant driver of the $\delta^{13}\text{C}$ signal because there are multiple controls on

$\delta^{13}\text{C}_{\text{TDIC}}$. However, values in the range observed here are consistent with multiple and not mutually exclusive scenarios: (1) lake waters in equilibrium with atmospheric CO_2 , with slow throughflow and longer residence times (Leng and Marshall, 2004; Usdowski and Hoefs, 1990); (2) recharge waters derived from a low biologically productive landscape in which the $\delta^{13}\text{C}$ of groundwaters are dominated by $\delta^{13}\text{C}$ derived from marine limestones (Andrews et al., 1997); (3) recharge waters derived from a landscape dominated by C_4 or CAM vegetation (Leng and Marshall, 2004); and (4) high productivity of aquatic plants within the lake body which preferentially use ^{12}C thereby enriching the lake water in ^{13}C (Leng and Marshall, 2004). More depleted $\delta^{13}\text{C}$ values are observed at the onset of marl accumulation at Al Wusta (0 – 6 cm) and through the sequence at KAM4 lake 3b. These values are typical of spring-fed tufas with high rates of recharge, inhibiting $\delta^{13}\text{C}_{\text{TDIC}}$ of lake waters moving into equilibrium with atmospheric CO_2 (Leng and Marshall, 2004).

Table 13.1 – Summary palaeoenvironmental data of each MIS 5 sequence studied here. F = freshwater.

Site	Dominant microstructure	Groundmass/dominant mineral	Mean $\delta^{18}\text{O}$ (‰)	Range $\delta^{18}\text{O}$ (‰)	Mean $\delta^{13}\text{C}$ (‰)	R ² coefficient ($\delta^{18}\text{O}$ v. $\delta^{13}\text{C}$)	Diatom Assemblage
Al Wusta	Homogenous	Microsparite	-2.81	4.93	-0.75	0.14	F
Site 16.3	Homogenous	Microsparite	2.34	5.18	1.3	0.13	F
WNEF16_28	Homogenous/laminated	Microsparite	-3.88	4.86	0.22	0.00	F
Alathar	Homogenous	Quartz	N/A	N/A	N/A	N/A	F
KAM4 lake 3	Homogenous	Microsparite	0.71	1.60	-0.80	0.60	F
KAM4 lake 3a	Homogenous	Microsparite	-1.19	3.97	-1.12	0.65	N/A
KAM4 lake 3b	Homogenous	Microsparite	-0.38	2.89	-4.05	0.99	N/A

Covariance between $\delta^{18}\text{O}$ and $\delta^{13}\text{C}$, and the range between the minimum and maximum values of $\delta^{18}\text{O}$ through a sequence, are broad measures of hydrological closure of lacustrine systems (Chapter 3, section 3.6.4.3) (Talbot, 1990; Leng and Marshall, 2004). As described in Chapter 3, hydrologically closed lakes lose water through evaporation and seepage (Leng and Marshall, 2004). This leads to covariance between $\delta^{18}\text{O}$ and $\delta^{13}\text{C}$ due the evaporitic enrichment of the $\delta^{18}\text{O}$ and the simultaneous enrichment of $\delta^{13}\text{C}$ through a reduction in lake volume and the degassing of CO_2 (Talbot, 1990; Leng and

Marshall, 2004). The R^2 coefficient (coefficient of determination) can be used to assess the covariance, as it describes the proportion of variance in the dependent variable ($\delta^{13}\text{C}$) that can be predicted using the independent variable ($\delta^{18}\text{O}$). R^2 coefficients fall between 0 and 1, with higher values reflecting greater covariance between the variables.

R^2 coefficients in MIS 5 lacustrine sequences range from 0.00 (WNEF16_28) to 0.99 (KAM4 lake 3b) (see Table 13.1) suggesting variability in the degree of hydrological closure between interdunal palaeolakes. Within this, only the sites from KAM4 interdunal basin display strong positive covariance ($R^2 = 0.6$ to 0.99) which may indicate hydrological closure of the lake, with other sequences displaying more limited covariance ($R^2 = 0.00$ to 0.14). It is important to note that the KAM4 lake 3a ($n = 7$) and 3b ($n = 5$) sequences have small sample sizes.

Each R^2 coefficient has an associated p-value. The p-value for each term tests the null hypothesis, which is that the coefficient is equal to 0 and that there is no significant relationship between $\delta^{18}\text{O}$ and $\delta^{13}\text{C}$. The significance level was set at 0.95, meaning that a P-value equal to or less than 0.05 is required to reject the null hypothesis and accept that there is a statistically significant relationship between the variables. P-values from the MIS 5 sequences vary. Statistically significant relationships are observed at Al Wusta (p-value = 1.18×10^{-7}), KAM4 lake 3 (p-value = 4.08×10^{-4}), KAM4 lake 3a (p-value = 0.03) and KAM4 lake 3b (p-value = 1.81×10^{-4}). While there is a significant relationship at Al Wusta, it is important to note that the R^2 value is low (0.14) meaning that while there is a significant relationship the variance in $\delta^{18}\text{O}$ only explains 14% of the variance in $\delta^{13}\text{C}$ and thus there is limited covariance. In contrast the low p-values combined with the high R^2 values at KAM4 lakes 3, 3a and 3b imply significant covariance between $\delta^{18}\text{O}$ and $\delta^{13}\text{C}$. No significant relationship is observed at Site 16.3 (p-value = 0.16) and WNEF16_28 (p-value = 0.89).

The lack of a statistically significant relationship at WNEF16_28 and Site 16.3 suggests that there is no significant relationship between changes in $\delta^{18}\text{O}$ and $\delta^{13}\text{C}$ at these sites. This supports the idea that they represent open lake systems with inflows and outflows.

Regarding ranges in $\delta^{18}\text{O}$, it is suggested that large ranges are indicative of small, closed evaporitic basins which are more sensitive to environmental and seasonal changes in water balance compared to larger open systems (Leng and Marshall, 2004; Talbot, 1990). The range in $\delta^{18}\text{O}$ values through each sequence are relatively small (Fig 13.4), varying from 1.6‰ (KAM4 lake 3) to 5.18‰ (Site 16.3) (see Table 13.1 and Figure 13.4). These ranges suggest limited hydrological shifts during the deposition of the sequence. The small ranges at KAM4 lakes 3, 3a and 3b are in contrast with the high R^2 coefficients and low p-values from the same lakes, suggesting that the latter was not caused by evaporation.

It is also important to consider the whole isotopic sequence when interpreting the range in $\delta^{18}\text{O}$. For example, Al Wusta, Site 16.3 and WNEF16_28 all have similar ranges (between 4.86‰ – 5.18‰) but they have markedly different isotopic curves. The $\delta^{18}\text{O}$ sequence at WNEF16_28 follows the trend in sedimentology and inferred lake volume. More depleted $\delta^{18}\text{O}$ values occur where laminations are preserved (see Fig 13.4, D) and lake volume was presumably greater, while more positive $\delta^{18}\text{O}$ values occur in relation to homogenous microfacies and shallower waters (see Figure 10.3, Chapter 10). The Al Wusta sediments suggest gradually evolving hydrological conditions, with $\delta^{18}\text{O}$ gradually increasing upwards through the sequence, probably caused by increasing evaporitic enrichment and environmental aridity (Figure 8.3, Chapter 8). Site 16.3 shows much greater point-to-point variability, with multiple shifts in excess of 2‰, suggesting more hydrological variability through the sequence compared to the other lakes. Despite these differences, the isotopic data taken as a whole from each MIS 5 marl sequence is consistent with their deposition under waterbodies that were open and stable, with recharge balancing evaporation and outflows. Recharge (inflows) and outflows likely occurred via a combination of sub-surface storm flow during deluge rainfall events, and via groundwater flow through the permeable underlying dune sands and sandstone.

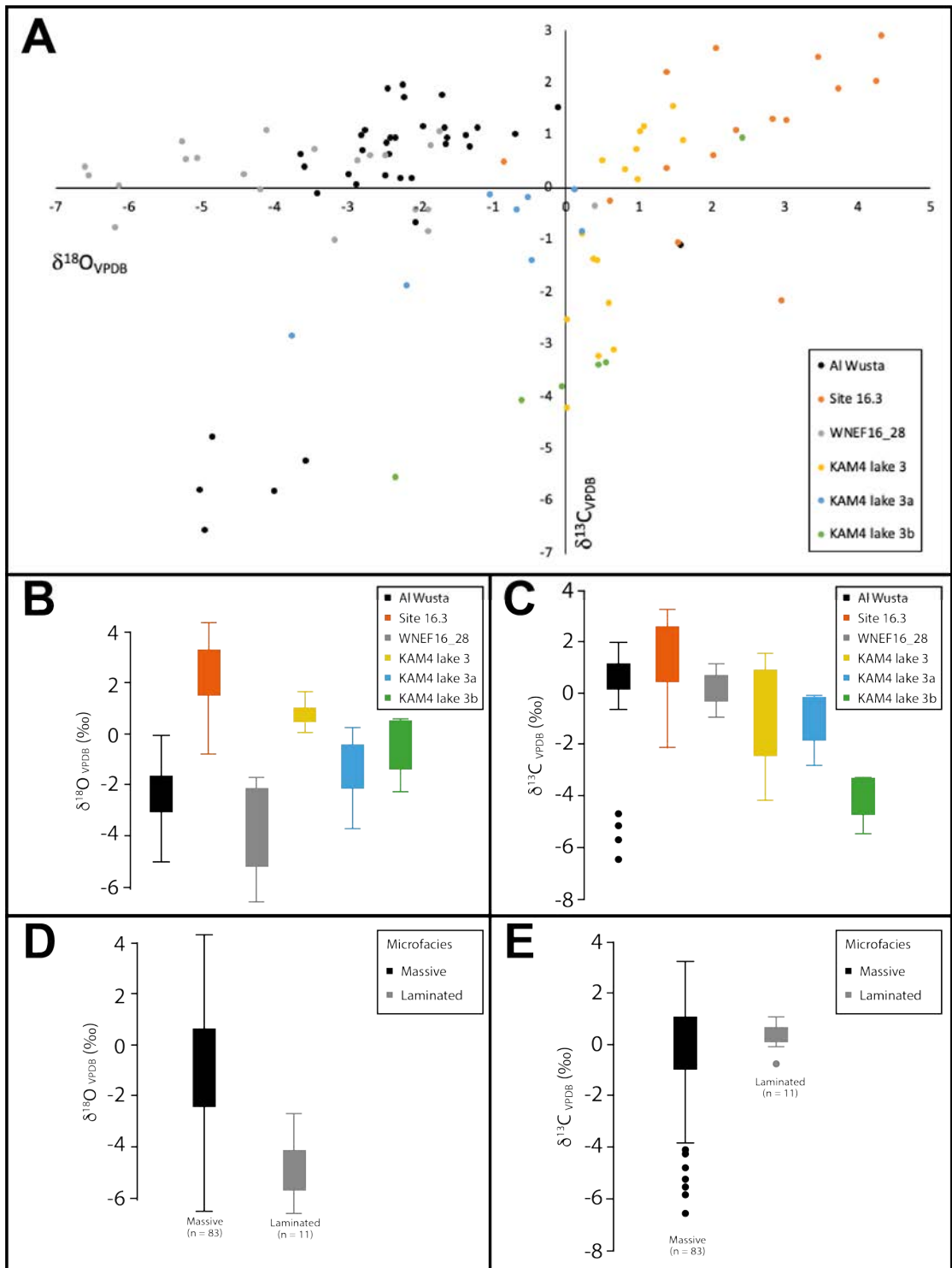


Figure 13.4 – Isotopic data for MIS 5 palaeolake sequences. (A) $\delta^{18}\text{O}$ (x-axis) vs $\delta^{13}\text{C}$ (y-axis) for all MIS 5 sites. There is a range of $\delta^{18}\text{O}$ values with the most negative occurring at WNEF16_28 (grey dots, left side) and the most positive occurring at Site 16.3 (orange dots, right side). $\delta^{13}\text{C}$ values predominantly lie between -1 to 4‰ across all sites. More negative values occur in concert with negative $\delta^{18}\text{O}$ values at the onset of the Al Wusta sequence (black dots, bottom left corner). (B) Box and whisker plot of the $\delta^{18}\text{O}$ values for each MIS 5 sequence. (C) Box and whisker plot showing the $\delta^{13}\text{C}$ values for each MIS 5 sequence. (D) Box and whisker plot showing the $\delta^{18}\text{O}$ values based on massive/homogenous vs laminated microfacies. Laminated microfacies show a more negative $\delta^{18}\text{O}$ signature. (E) Box and whisker plot showing the $\delta^{13}\text{C}$ values based on massive/homogenous vs laminated microfacies. Laminated microfacies show a much narrower range.

Diatom assemblages from each site are indicative of deposition under oligotrophic to mesotrophic freshwater conditions (Groucutt et al., 2018; Stewart et al., 2020a; Sung per comms). Dominant species include freshwater planktonic and tychoplanktonic diatoms such as *Aulacoseira italica*, *A granulata*, *Lindavia ocellata* and small *Stephanodiscus* species, and there is limited evidence for brackish or saline-tolerant species. The low sampling resolution and preservation of diatoms through these sequences makes it difficult to say more about lake hydrology using this data.

Taken together, the microfacies, isotopic and diatom evidence summarised above (see Table 13.1) demonstrates that the fine-grained carbonate rich marls observed within almost all sequences were deposited under shallow but perennial freshwater lakes that were present across the western Nefud Desert during discrete phases of MIS 5.

13.2.1.2.2 Siliceous deposits - Alathar

To this point only carbonate-rich marl sequences have been discussed. However, the interdunal deposit at Alathar is composed of sandy-silt diatomite with no carbonate present (Chapter 9). Further sedimentary analysis from Alathar shows that it represents a slightly different depositional environment from other MIS 5 marl lake deposits. At the macroscale, there are clear horizontal bedding planes between sandy silt diatomite and sand beds (Units 2, 3 and 4a; Fig 9.4). This is indicative of fluctuating water levels and episodic desiccation. Further support for this conclusion is provided by desiccation cracks on the surface of unit 4b along with hominin and elephant footprints preserved between Units 4b and 5, showing fauna traversed the lakebed during a desiccation event (Stewart et al., 2020a).

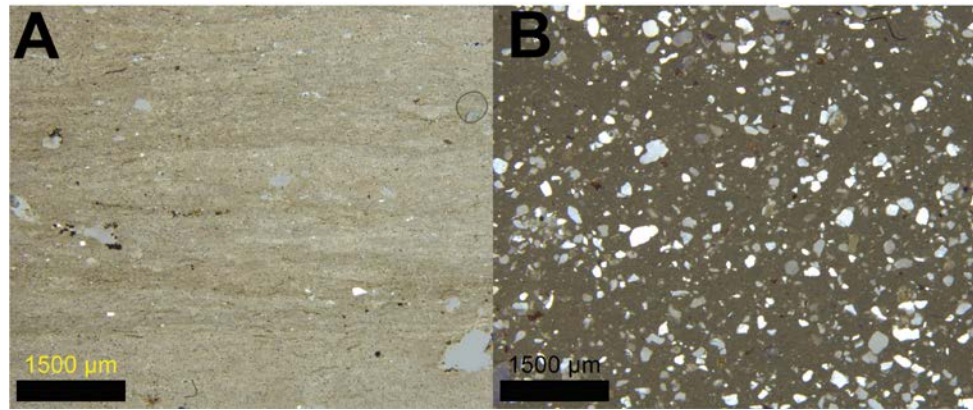


Figure 13.5 – Photomicrographs of (A) Al Wusta 19 – 22 cm above base and (B) Alathar. 139 – 141 cm above base. The microfacies on the left, Al Wusta, is composed of faintly laminated microsparite with rare allogenic grains. This microfacies is representative of the majority of microfacies observed across all sequences. In contrast, the microfacies on the right, Alathar, consists of numerous quartz grains cemented into a brown SiO matrix. No carbonate is present.

Microfacies analysis shows there is a high level of allogenic grain input into the lacustrine basin at Alathar throughout the entire sequence, implying the local landscape remained unstable throughout deposition. This is in direct contrast to the carbonate lake deposits, where allogenic sands are rare (see Fig 13.5). These differences suggest that Alathar was more sensitive to hydrological changes than the other MIS 5 sites, which may be explained by the fact that Alathar lies further into the sand sea (see Fig 13.1) and therefore further from water draining into the sand sea. Despite these differences, diatom analysis shows that the Alathar lake was fresh, while good diatom preservation suggest that desiccation events were rare (Stewart et al., 2020a).

13.2.1.3 Summary

Interdunal lake deposits formed within the western Nefud Desert during at least two discrete phases in MIS 5. The lakes were remarkably similar. All were freshwater, while all but one (Alathar) have sedimentary sequences dominated by carbonate and were perennial water bodies. The depositional models for these sequences suggest that humid intervals during both MIS 5e and 5a produced hydrologically stable lakes, where the water table rose quickly above the interdunal surface in response to increased rainfall. KAM4 lake 3a is the exception to this pattern, since it experienced a more gradual rise in water levels. Interdunal lakes were then stable as shown by the consistent homogenous and microsparitic microfacies with no evidence for desiccation or pedogenic alteration through the sequences. Lake levels fell towards the end of humid

phases either as a response to increased environmental aridity or basin infilling, and this is represented by hardpan carbonate with tubular voids (e.g. WNEF16_28 and Al Wusta). Interdunal lakes then desiccated completely as the climate transitioned back towards aridity, and this is represented by horizontally laminated sands and gravels likely washed into the basin during heavy rainfall events (e.g. Al Wusta, WNEF16_28).

13.2.2 Middle Pleistocene humid phases

The Middle Pleistocene is formally defined as beginning at the Matuyama-Brunhes boundary (MBB) ~781 ka and ending at the onset of the MIS 5 (~130 ka) (Head and Gibbard, 2015). Between ~500 ka (the extent of this study) and ~130 ka, there were multiple periods of high northern hemisphere insolation. Consequently, following the orbital-monsoon hypothesis (Rossignol-Strick, 1983), there may have been humid phases during MIS 13b/11, 9, and 7. Here we demonstrate that humid phases occurred during each of these periods, though the dating resolution precludes assigning humidity to specific insolation peaks.

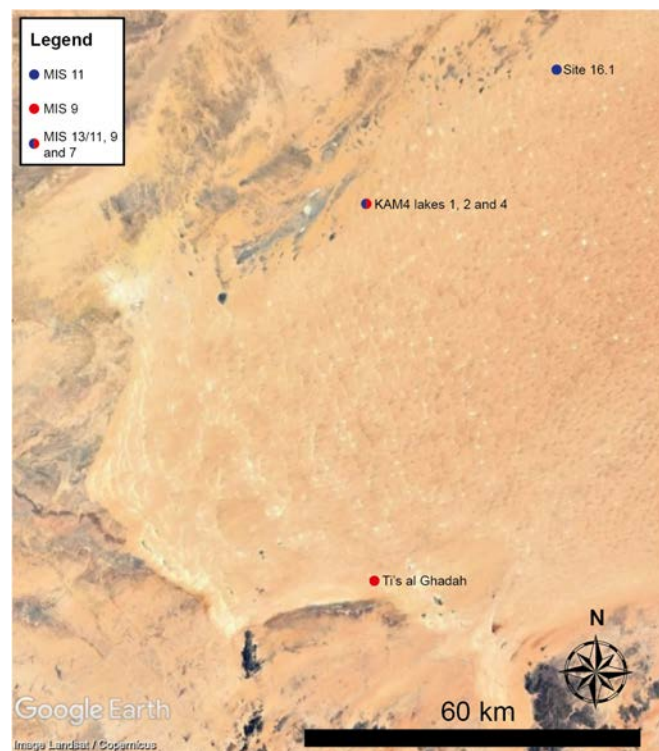


Figure 13.6 - The distribution of directly dated or bracketed Middle Pleistocene palaeolake deposits across the western Nefud Desert. This includes palaeolakes from this thesis, and site 16.1 from Rosenberg et al. (2013).

13.2.2.1 Chronology of Middle Pleistocene humid phases

The chronology of Middle Pleistocene humid phases in the western Nefud Desert is derived from the dating of six sedimentary sequences across three sites (see Fig 13.6 and 13.7). Three of these sedimentary sequences are from the KAM4 interdunal basin. Sands underlying the KAM4 lake 1 marls yield an age of 412 ± 87 ka (Clark-Balzan, per comms). While this is not a direct age, the sediments are heavily iron indurated. This level of diagenetic alteration attests to KAM4 lake 1 being the oldest marl deposit in the KAM4 basin. Sands underlying the KAM4 lake 2 marls yield an age of 337 ± 39 , while sand from a desiccation crack within the marls themselves yield an age of 306 ± 47 ka (Clark-Balzan, per comms). Sands directly from KAM4 lake 4 yield an age range of 172 – 226 ka based on quartz OSL and feldspar pIR-IRSL from this thesis. Published ages from waterlain sands underlying the marls at Ti's al Ghadah yield ages of 328 ± 26 and 318 ± 25 ka (Rosenberg et al., 2013), while sands from the lake marls at this site yield an age of 291 ± 34 ka (Stimpson et al., 2016). A published age from sand-filled desiccation cracks at Site 16.1 yields a TT-OSL age of 419 ± 39 ka (Rosenberg et al., 2013).

Rosenberg et al. (2013) reports directly dated or bracketed Middle Pleistocene palaeolake deposits from the northeastern and eastern portion of the Nefud Desert. Site 13.5 in the northeastern Nefud has a direct age of 292 ± 19 ka, while Site 10.2 in the eastern Nefud has bracketing ages of 407 ± 32 ka for sands underlying marl and 338 ± 34 ka for sands overlying marl (Rosenberg et al, 2013). Rosenberg et al. (2013) attributes a further 11 deposits to the Middle Pleistocene, though these attributions are based on ages for sands underlying lake marls, and therefore represent maximum ages for the lakes.

The ages presented above demonstrate that the western Nefud Desert experienced multiple humid phases during the Middle Pleistocene. While age uncertainties are large during this time period, and it is not possible to correlate lake deposits with one another or to NH summer insolation peaks, they can be split into three broad time periods: MIS 7, MIS 9 and MIS 11/13 (see Fig 13.6). KAM4 lake 4 is the only lake deposit that

represents humidity during MIS 7 or early MIS 6 with an age range (at 1σ uncertainty) of 172 to 226 ka. KAM4 lake 2, Ti's al Ghadah (TAG) and Site 16.1 provide evidence for humidity at some point during MIS 9, and KAM4 lake 1 and Site 16.1 provide evidence for humidity at somepoint most likely during MIS 11/13.

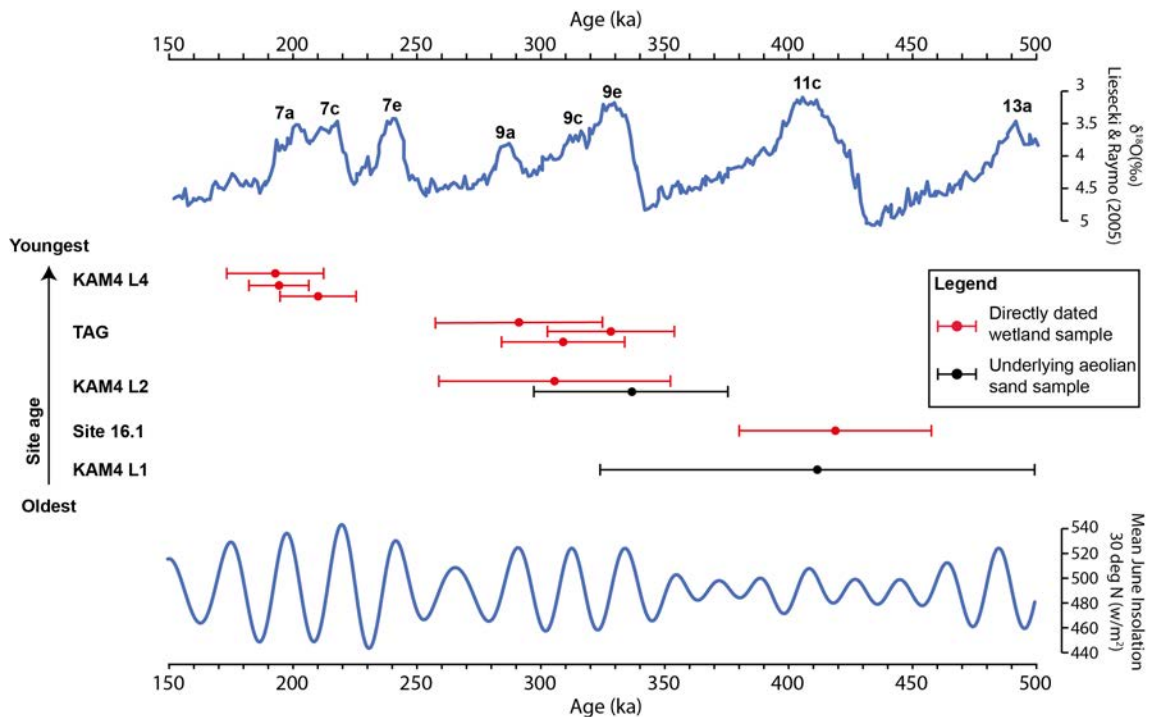


Figure 13.7 - Chronology of directly dated Middle Pleistocene palaeolake deposits dated to MIS 7, 9 and 11/13 from the western Nefud Desert. Site 16.1 are from Rosenberg et al. (2013). Note that KAM4 lake 1 is not directly dated, though the highly iron indurated nature of the sediment attests to it being the oldest marl sediments in the KAM4 basin (see Chapter 6). All uncertainty terms are at 1σ .

13.2.3.2 Palaeohydrology of Middle Pleistocene lakes

13.2.3.2.1 MIS 13, 11 and 9

As with the majority of MIS 5 sites, Middle Pleistocene carbonate-rich marl deposits were deposited on the beds of shallow, perennial and freshwater interdunal lakes. All sequences are dominated by fine-grained carbonate rich marls which contain little (mostly <5%) or no evaporitic minerals. A single unit (unit 4) from KAM4 lake 2 is dominated by aragonite as opposed to calcite. Quartz, anorthoclase, orthoclase and goethite are all present in sections, though where they occur they are predominantly

below 10% weight. As with MIS 5 sites, allogenic sands are present at an abundance towards the start or end of sequences (e.g. Ti's al Ghadah 1 and Ti's al Ghadah 2).

Table 13.2 - Summary palaeoenvironmental data of each Middle Pleistocene sequence studied here. F = freshwater. B = Brackish.

Site	Dominant microstructure	Groundmass	Mean $\delta^{18}O$ (‰)	Range $\delta^{18}O$ (‰)	Mean $\delta^{13}C$ (‰)	R ² coefficient (isotope)	Diatom Assemblage
KAM4 lake 1	Laminated/homogenous	Microsparite	-3.32	0.98	-1.51	0.20	F
KAM4 lake 2	Homogenous	Sparite	0.85	4.74	1.94	0.37	F
KAM4 lake 4	Homogenous/prismatic	Microsparite	-0.84	2.85	-4.74	0.20	F/B
TAG 1	Homogenous	Microsparite	-1.26	1.51	-0.15	0.06	F
TAG 2	Homogenous	Microsparite	0.16	1.27	0.82	0.14	N/A

At the macroscale, the marls vary subtly, but most display the same simple transgressive-regressive sequence (with the exception of KAM4 lake 4). Homogenous or laminated carbonate occurs either abruptly at the start of the sequence or gradually develop from sand-rich beds where the proportion of carbonate increases moving upwards through the sequence. Units of homogenous or laminated carbonate, or carbonate and goethite at KAM4 lake 1, represent perennial and stable freshwater lakes. Homogenous or laminated carbonates then transition to horizontally bedded carbonates interdigitated with sand-rich beds (e.g. Ti's al Ghadah 1 and KAM4 lake 1) or cease altogether (e.g. Ti's al Ghadah 2). These changes in sedimentation reflect a change in the palaeohydrology where water levels are less stable. The sequences are then capped by horizontally bedded and cemented sands (e.g. TAG 1 and 2), by hardpan carbonate (KAM4 lake 2) or end abruptly (e.g. KAM4 lake 1).

At the microscale (see Fig 13.8), the marls typically display the same three microfacies as described for MIS 5 lake sequences. As with the MIS 5 deposits, homogenous or laminated microsparite microfacies with no evidence of subaerial exposure or pedogenesis are dominant, suggesting that the majority of Middle Pleistocene deposits represent deposition on the beds of shallow, polymictic, well-oxygenated lakes. Finely laminated microfacies are present at Unit 2 in KAM4 lake 1 (see Fig 13.8, panel C),

indicating greater lake volume. Though it is important to note that goethite has replaced micrite laminations in much of this unit, indicative of diagenetic alteration. An additional microfacies, consisting of homogenous coarse sparite, is present in Units 2 and 3 at KAM4 lake 2 (see Fig 13.8, panel F). This microfacies is probably present as a result of aggrading neomorphism as opposed to a different depositional environment. It is interesting to note that the two oldest sequences at KAM4 have both been diagenetically altered, while younger sequences (KAM4 lakes 3, 3a, 3b and 4) have not been.

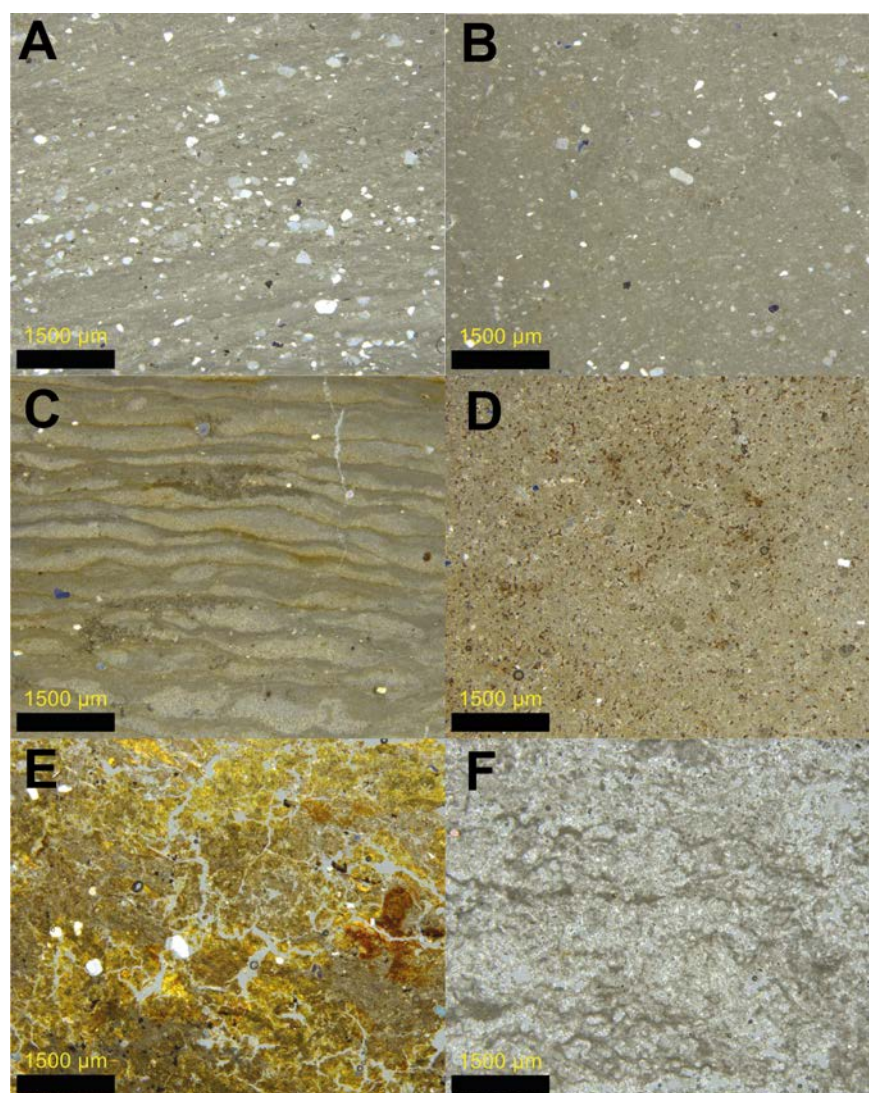


Figure 13.8 – Example photomicrographs of microfacies from Middle Pleistocene deposits. A – D show typical microfacies with a homogenous or laminated microstructure and rare allogenic grains. E – shows the microfacies from unit 3 at KAM4 lake 4. This prismatic microstructure along with the presence of clay is indicative of a palustrine environment where the primary lake mud has been subaerially exposed and modified. F – shows the sparitic microfacies from KAM4 lake 2, which is a consequence of aggrading neomorphism. (A) TAG 1 18 to 20 cm above base. (B) TAG 2 25 to 28 cm above base. (C) KAM4 lake 1 0 to 4 cm above base. (D) KAM4 lake 4 17 to 22 cm above base. (E) KAM4 lake 4 56 to 59 cm above base. (F) KAM4 lake 2 10 to 12 cm above base.

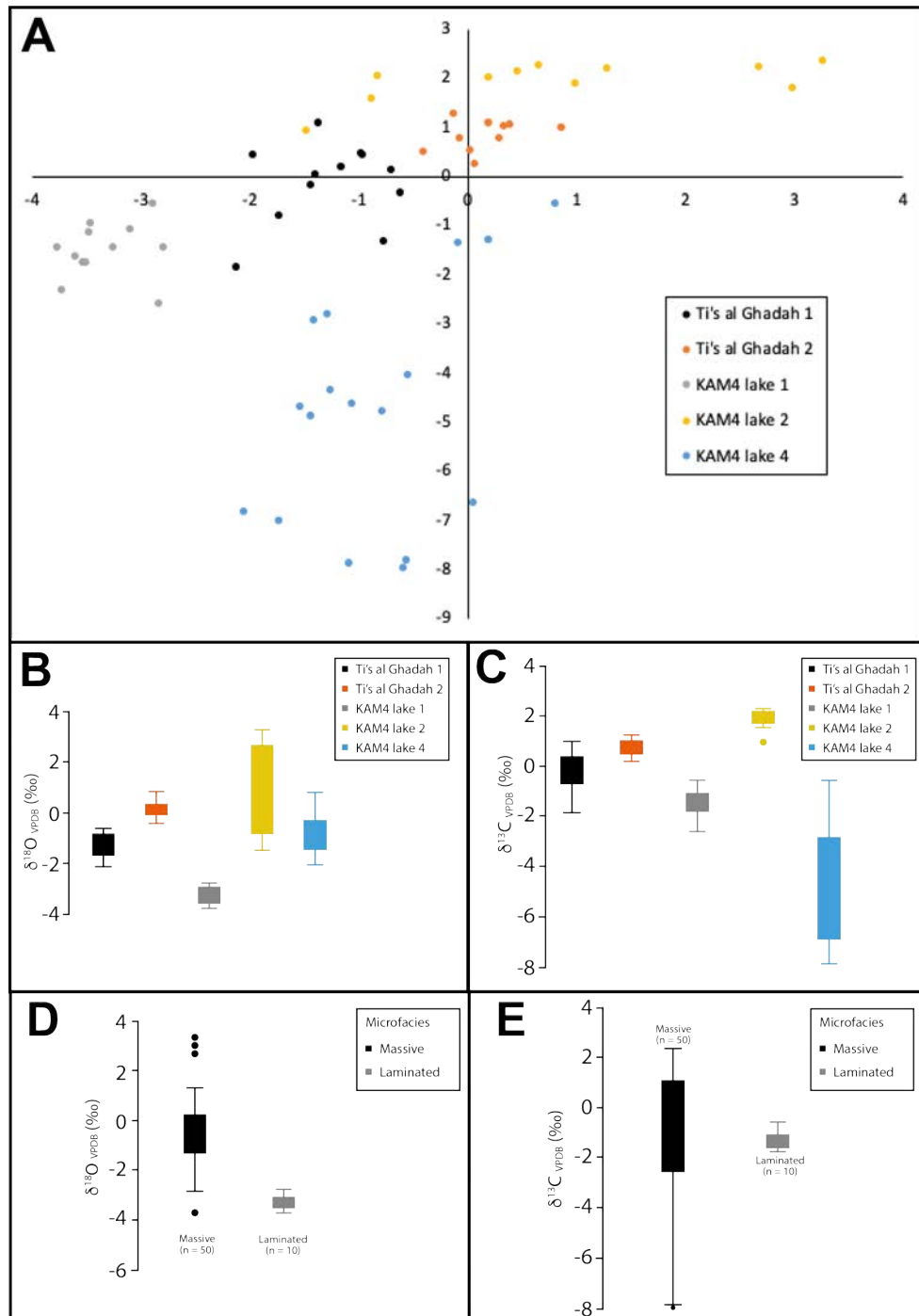


Figure 13.9 - Isotopic data for Middle Pleistocene palaeolake sequences. (A) $\delta^{18}O$ (x-axis) vs $\delta^{13}C$ (y-axis) for all Middle Pleistocene deposits. There is a range in $\delta^{18}O$ values with the most negative occurring at KAM4 lake 1 (grey dots, left side) and the most positive occurring at KAM4 lake 2 (yellow dots, right side). The majority of $\delta^{13}C$ values lie between 2‰ and -2‰, though those from unit 4 at KAM4 lake 4 (blue dots) are much more negative. (B) Box and whisker plot of the $\delta^{18}O$ values for each Middle Pleistocene sequence. This again shows that KAM4 lake 1 contained the most negative $\delta^{18}O$ values, and also demonstrates the small ranges in $\delta^{18}O$ through each sequence. (C) Box and whisker plot showing the $\delta^{13}C$ values for each Middle Pleistocene sequence. This shows that $\delta^{13}C$ values are consistently between +2 and -2‰ with the exception of KAM4 lake 4 (blue) which contains more depleted $\delta^{13}C$ values. (D) Box and whisker plot showing the $\delta^{18}O$ values based on massive/homogenous vs laminated microfacies. Laminated microfacies show more negative $\delta^{18}O$ values. (E) Box and whisker plot showing the $\delta^{13}C$ values based on massive/homogenous vs laminated microfacies. Laminated microfacies show a much narrower range.

Stable isotope data from all sequences (Fig 13.9) are predominantly consistent with sedimentation in stable, perennial waterbodies. $\delta^{13}\text{C}$ values mostly lie in a narrow range of -2 to +3‰, which is consistent with data from the majority of MIS 5 deposits (see Fig 13.4). The single exception to this is KAM4 lake 4, which is discussed in the following section. There is limited covariance between oxygen and carbon isotopes through all sequences, with R^2 coefficients between 0.06 and 0.37 (see Table 13.2). Associated p-values suggest there was a statistically significant relationship between $\delta^{18}\text{O}$ and $\delta^{13}\text{C}$ at KAM4 lake 2 (p-value = 0.05), but not at KAM4 lake 1 (p-value = 0.64), Ti's al Ghadah 1 (p-value = 0.47) and Ti's al Ghadah 2 (p-value = 0.29). The low R^2 values or lack of a significant relationship between $\delta^{18}\text{O}$ and $\delta^{13}\text{C}$ suggests that evaporation was limited, an inference supported by the small $\delta^{18}\text{O}$ ranges (<5‰) observed at all sites (see Fig 13.9, panel B). Combined, these data suggest that the marls were deposited in stable, open waterbodies unaffected by large hydrological shifts (Talbot, 1990).

Diatom palaeoecology has been carried out at all of the sequences discussed here except Ti's al Ghadah 2 (Stewart et al., 2019; Sung per comms). While preservation is often poor, sequences are dominated by freshwater diatom species such as *Brachysira brebissonii*, *Navicymbula pusilla*, *Staurosira construens* var. *contruens*, *Staurosira pinnata* var. *pinnata* and *Staurosira pinnata* var. *intercedens* (Stewart et al., 2019; Sung per comms). The occurrence of brackish or saline tolerant species such as *Nitzschia sigma.*, *Halamphora coffaeiformis* and *Denticula kuetzingii* are present but rare (Stewart et al., 2019; Sung per comms).

13.2.3.2.2 MIS 7 (KAM4 lake 4)

The MIS 7 sequence of KAM4 lake 4 is similar in many ways to other sequences as it contains units that represent a perennial freshwater body. However, it differs in that it is a stratigraphically complex sedimentary sequence indicative of notable changes in the palaeohydrology through the sequence (Fig 13.10), as opposed to a single transgressive-regressive cycle as shown by other sequences. During the humid phase there is a transition from perennial lake to shallow palustrine environment to spring fed tufa/shallow perennial lake. This is represented in the sedimentary sequence by a

transition from pure homogenous carbonate (Unit 2b) to carbonate-rich silty sands with a prismatic microstructure and some clay present (Unit 3; see Fig 13.7, panel E). A rise in the water table is then shown by a return to homogenous carbonate albeit with more depleted $\delta^{13}\text{C}$ values (Unit 4a). The latter is indicative of higher rates of throughflow typical of a spring tufa (Talbot, 1990).


Sedimentary sequence	Unit/Strat log	Sedimentary facies	Depositional environment	Water table level
	4b	Friable homogenous fine-grained carbonate-rich marls with a high sand component	Perennial waterbody with high throughflow	Falling, but remains perennial and above interdunal depression
	4a	Homogenous fine-grained carbonate-rich marls	Perennial waterbody with high throughflow	Stable and above interdunal depression
	3b	Carbonate-rich silty sands with clay and gravel present	Palustrine environment	Low-stand. Fluctuating intermittently above and below the interdune surface.
	3a			
	2b	Homogenous fine-grained carbonate-rich marls	Perennial lacustrine waterbody	High-stand, above interdune surface
	2a	Friable carbonate-rich marls and sands	Onset of lacustrine waterbody	Rising, above interdune surface
1	Well-sorted loose sands	Aeolian sands	Below interdunal surface	

Figure 13.10 – KAM4 lake 4 sedimentary sequence (118 cm from base of non-aeolian sediment (Unit 2a) to the top of Unit 4b) with sedimentary sequence, facies, depositional environment and position of water table noted. This sequence differs from all others described in that it records a rise then a prolonged fall and subsequent rise in the water table within a single humid interval.

It is important to note that the fluctuating water levels implied by this sedimentology differs from the interdigitated beds of carbonate and sand described for sequences from Ti's al Ghadah 1 and KAM 4 lake 1. In those sequences, carbonate and sand beds were only ~2 - 5 cm thick. Conversely, each unit at KAM4 lake 4 is substantially thicker (between 17 – 38 cm thick) showing that the environments represented by these units represent a greater period of time.

13.2.3.3 Summary

Interdunal carbonate deposits formed within the western Nefud Desert during at least three discrete humid phases during the Middle Pleistocene relating to MIS 7, 9 and 11/13b. As with MIS 5 deposits, the lakes were remarkably similar. All represent perennial, fresh waterbodies that sometimes transition towards more dynamic systems as shown by the interdigitated marls and siliclastic beds in KAM4 lake 1 and Ti's al Ghadah 1). This behaviour is not observed at any of the MIS 5 sites. Nevertheless, these sedimentary sequences follow simple transgressive – regressive sequences as shown in Fig 3.2 and 3.3 in Chapter 3. The only sedimentary sequence that deviates from this pattern is KAM4 lake 4, dated to MIS 7. Here there is evidence for sedimentary complexity within a single humid phase.

13.2.4 Late Glacial/Holocene

The late glacial/Holocene is represented in the western Nefud Desert by the sedimentary sequence from Al Wusta Playa (Chapter 7). This sequence is not particularly well dated, but sediments deposited in waterlain conditions from the sequence (Unit 3) appear to be late-glacial to mid Holocene in age (Chapter 6). While the uncertainty on the dating obscures the exact timing of Holocene humidity at Al Wusta Playa, the key point from the sequence is in the absence of marl sediments despite the same basin containing a ~1 m thick bed of marls dated to MIS 5a (Chapter 8). Importantly, these marls are higher in the landscape than the Al Wusta Playa sediments (see Fig 13.11), implying that the water table during MIS 5a was higher and humidity was greater relative to the Holocene.

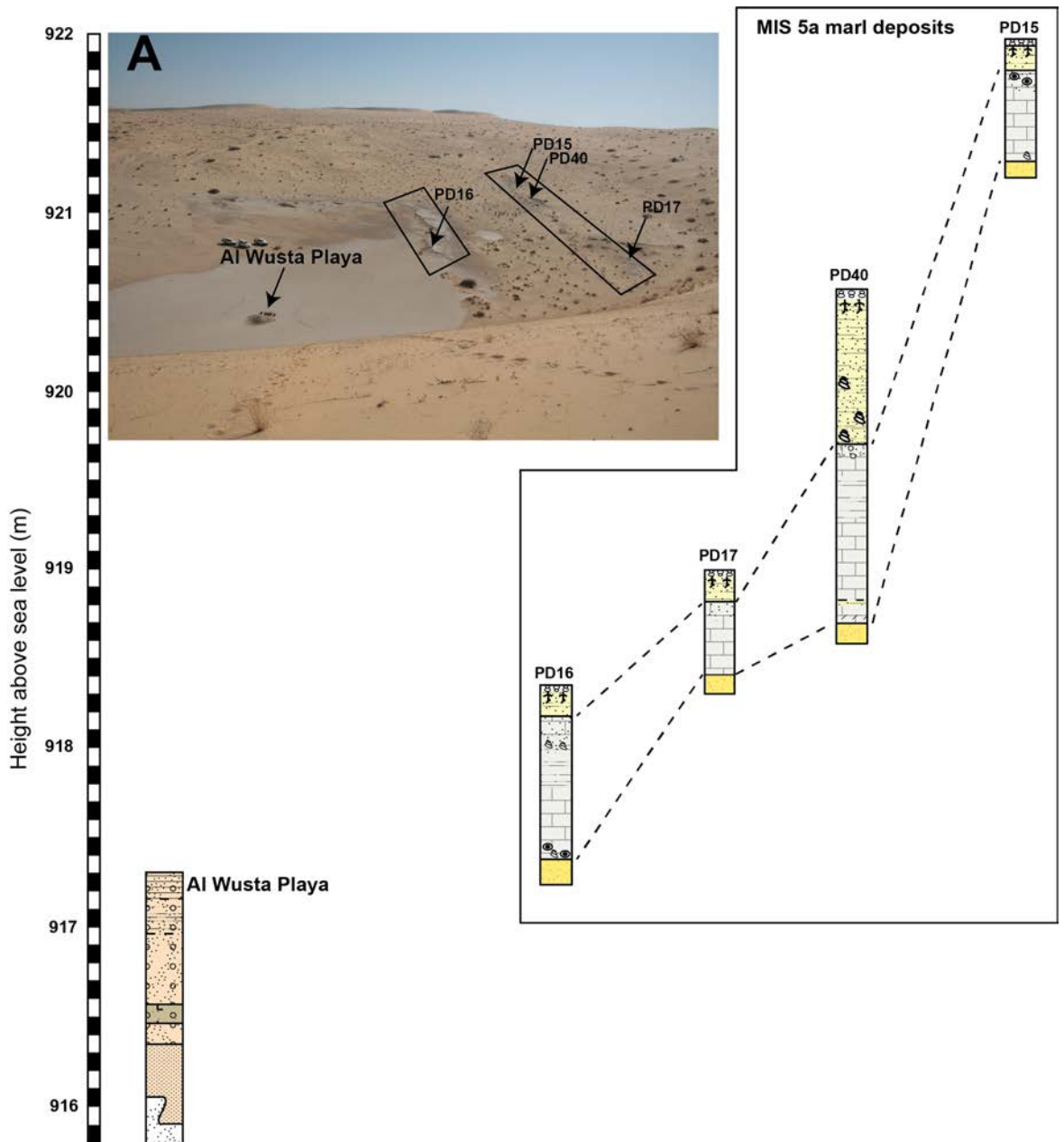


Figure 13.11 – The height above sea level (m) of Al Wusta Playa (Holocene) vs MIS 5a marl beds. No marl sediments were recorded in the Al Wusta Playa stratigraphy, while marl beds of MIS 5a age were investigated up to ~922 m above sea level and lie up to 926 m above sea level. This demonstrates the water table in the western Nefud Desert was considerably higher during MIS 5a than the Holocene. (A) Inset – a picture of the Al Wusta interdunal basin with the two marl ridges highlighted by black rectangles while each MIS 5a marl deposit is highlighted by an arrow. The Al Wusta Playa sequence is also highlighted by an arrow in the left-hand portion of the picture.

13.2.5 Comparison of humid intervals in the western Nefud Desert over the past 500,000 years.

Three key points are raised by the analysis presented in the previous section: (1) almost all of the sediment deposits, irrespective of age, follow the same simple sedimentary sequence which reflects a simple environmental pattern during humid phases; (2) a single site that dates to MIS 7 (KAM4 lake 4) contains a more complex sedimentary sequence that may reflect increased climatic complexity during this period; and (3) the Holocene appears to be less humid than the humid phases observed in any other interglacial period or period of high NH summer insolation (i.e. MIS 5a) over the past 500 ka. Each of these points will be discussed in turn.

13.2.5.1 Similarity of humid phases between ~500 – 80 ka

The nature of interdunal lakes in the western Nefud Desert show very little variation. Two exceptions to this are KAM4 lake 4, which contains a more complex sedimentary sequence and Alathar which does not contain any carbonate. The other depositional models follow a simple transgressive – regressive sedimentary sequence, where lake waters rise to form stable, perennial freshwater bodies, before falling as the climate becomes more arid (see Fig 3.2 and 3.3 in Chapter 3). The sequences typically start with a gradual or abrupt onset of marl (carbonate) sedimentation on top of aeolian sands. Where a gradual onset of marl deposition occurs, sand lenses or higher allogenic sand grain contents are observed at the base of the sequence, after which more carbonate-rich sediments are deposited (e.g. Ti's al Ghadah 1 and WNEF16_28). KAM4 lake 3A develops a palustrine environment (Unit 2b) before developing into a perennial marl precipitating lake. Sequences with abrupt onsets of carbonate sedimentation contain pure marl immediately overlying aeolian sands (e.g. KAM4 lakes 1 and 2). Whether abrupt or gradual, all sequences then consist of units with pure homogenous or laminated carbonate (calcite, or rarely aragonite) with no or negligible amounts of evaporites and rare siliclastic material. Microfacies are predominantly homogenous or laminated microsparite/micrite with no desiccation or pedogenic features, implying sedimentation on the bed of perennial waterbodies (see Figs 13.3 and 13.8). Covariance between oxygen and carbon isotopes predominantly yields R^2 values <0.4 with only

three sequences yielding R^2 values >0.6 . Even these latter sequences contain negligible quantities of evaporitic minerals and display low $\delta^{18}\text{O}$ ranges ($<5\%$) (see Figs 13.4 and 13.9), suggesting that isotopic covariance was not driven by evaporation, or that evaporitic enrichment of the isotopic signal was not enough to produce brackish or saline waters. The lack of substantial evaporation is supported by freshwater diatom and invertebrate (ostracod and mollusc) assemblages where available.

Units overlying the homogenous/laminated marls described above are suggestive of shallowing water bodies. Homogenous or laminated carbonates give way to marls interdigitated with sand-rich beds (e.g. KAM4 lake 1 and Ti's al Ghadah 1), hardpan carbonate with tubular voids (e.g. Al Wusta, WNEF16_28) or calcretes (KAM4 lakes 3a and 3b). This lake shallowing is the result of basin infilling, thereby reducing accommodation space, and/or increased environmental aridity. These units often display the highest allogenic sand content in thin-section as well as the most positive $\delta^{18}\text{O}$ values. The latter is typical of evaporitic enrichment in response to increased environmental aridity. Once carbonate sedimentation ceases, some sections are overlain by horizontally and crudely laminated sands within which small gravel clasts are present (e.g. Al Wusta, WNEF16_28, Ti's al Ghadah 1 and Ti's al Ghadah 2). These units often include shells of *Melanoides tuberculata* and are capped by calcitic rhizoliths (Al Wusta, WNEF16_28). Desiccation cracks are also observed at the top of a number of sequences (e.g. Alathar and KAM4 lake 1).

Overall, the majority of sequences represent simple transgressive-regressive cycles in response to increased tropical rainfall during peak NH summer insolation. The $\delta^{18}\text{O}$ stratigraphies from each sequence further suggest that palaeoclimatic conditions were stable, as they show relatively small ranges and few large shifts. The largest shifts in $\delta^{18}\text{O}$ occur in line with changes in sedimentology (e.g. WNEF16_28), suggesting internal hydrological lake processes drove these large shifts as opposed to climatic variability.

13.2.5.2 Is the MIS 7 humid phase different?

In contrast to other sequences, KAM4 lake 4 dated to MIS 7 shows a more complex sedimentary sequence indicative of climatic complexity during a single humid phase (Fig 13.10). This sequence shows a rise in the water table leading to a perennial but shallow marl precipitating lake (Unit 2), before a fall in water levels leading to the development of palustrine marls effected by periods of subaerial exposure and desiccation (Unit 3). This is followed by a second rise in the water table leading to a spring like tufa system that deposited homogenous microsparite with very depleted $\delta^{13}\text{C}$ values (Unit 4). This sequence is different from the other sequences within the KAM4 basin, suggesting that environmental rather than basin-specific factors are responsible. Instead, the KAM4 lake 4 sequence implies that marked changes in hydrology occurred during a single MIS 7 humid phase.

It is not possible to determine the amount of time that each unit in this lake sequence represents, though it is worth noting that each unit is at least 27 cm thick, suggesting that they represent more than a single season. However, Alonso-Zarza (2003) notes that palustrine conditions can develop over a period of just a single-season, since only the modification of primary lake mud is required to form palustrine features. Nevertheless, the palustrine unit at KAM4 lake 4 is 38 cm thick, implying a prolonged period of palustrine conditions. Here primary calcite precipitated during high water stands, in an environment consistent with the previous unit, was then altered via desiccation as the water table periodically dropped below the level of the lacustrine/palustrine floor.

It is plausible that the two marl units (Unit 2 and 4; Fig 13.10) represent deposition during two NH summer insolation maxima within MIS 7, with the palustrine sediments sandwiched between them being deposited during a more arid period, perhaps related to insolation minima such as those occurring during MIS 7b and 7d. However, the uncertainties on age estimates for the site make it impossible to test this hypothesis. Furthermore, whilst MIS 5 contains a similar insolation structure (i.e. discrete northern hemisphere insolation maxima separated by periods of northern hemisphere insolation minima) none of the sequences dating to this interval produce a similar sedimentary

sequence. Alternatively, the sedimentary sequence may represent a brief arid phase during a single substage. Evidence for brief decreases in humidity are recorded in the more recent past in southern Arabia during the Holocene Humid Phase. Aridity events at 8.2 ka and 9.2 ka are observed in the speleothem archives from Hoti and Qunf Caves (Fleitmann et al., 2007) and at Wahalah and Awafi palaeolakes where sediment influx increases between 8.3 and 7.9 cal ka BP (Parker et al., 2016). The timing of these brief aridity events closely matches cooling intervals in the North Atlantic, such as at 8.2 ka (Fleitmann et al., 2007), and this suggests a link between the tropical monsoon system and the North Atlantic. This most likely relates to mechanisms that reduce the land-sea pressure gradients or restrict atmospheric moisture content and consequently restrict monsoon circulation, leading to brief (decadal to multi-decadal) arid phases during humid intervals (Fleitmann et al., 2007; Stager et al., 2011). It is not clear what impact this would have on terrestrial freshwater systems, though Heinrich Event 1 (~15 – 18 ka) provides a useful example. Here, increased freshwater input into the North Atlantic lead to a megadrought across the Afro-Asian monsoon region between ~16 – 17 ka, with Lake Victoria completely desiccating (Stager et al., 2011). It has been proposed this megadrought event was a consequence of reduced tropical sea surface temperatures, in response to freshwater input into the North Atlantic, which reduced the evaporitic moisture content and restricted tropical rainfall (Stager et al., 2011).

13.2.5.3 Is there a Holocene humid phase in the western Nefud Desert?

While no extensive survey of Holocene basins has been carried out in the western Nefud Desert, it is noticeable that of the abundant marl beds that have been found by numerous researchers (Breeze et al., 2017; Groucutt et al., 2018; Rosenberg et al., 2013; Stimpson et al., 2015) none of them have yielded Holocene ages. If Holocene marl deposits are present, they are therefore relatively rare. This is supported by the implications of preservation potential, which mean that Holocene marl beds should be more abundant than Pleistocene examples if they did exist. The fact that the Al Wusta Playa yields evidence for only highly ephemeral water bodies while the same site records evidence for perennial lake bodies dated to MIS 5a, implies that the water table was several metres higher during MIS 5a compared to the Holocene humid period (see Fig

13.11). Even at other sites where Pleistocene marl beds have been identified but the modern Playa has not been excavated, the implication is that during the Holocene, even if marl deposits are found at depth, groundwater levels did not reach the elevation of those of earlier Pleistocene humid phases. This would again imply that the Holocene climate was drier than all known Pleistocene humid phases.

13.3 Comparison of humid intervals in the western Nefud Desert with palaeoenvironmental records from the Arabian Peninsula and Levant

13.3.1 Northern Arabia, the Negev and northeast Africa

Northern Arabia, the Negev and northeast Africa contain numerous palaeoenvironmental archives that represent past humid phases in the region (Fig 13.12). In this section the timing and nature of these records will be compared with the timing and nature of humid phases from the western Nefud Desert.

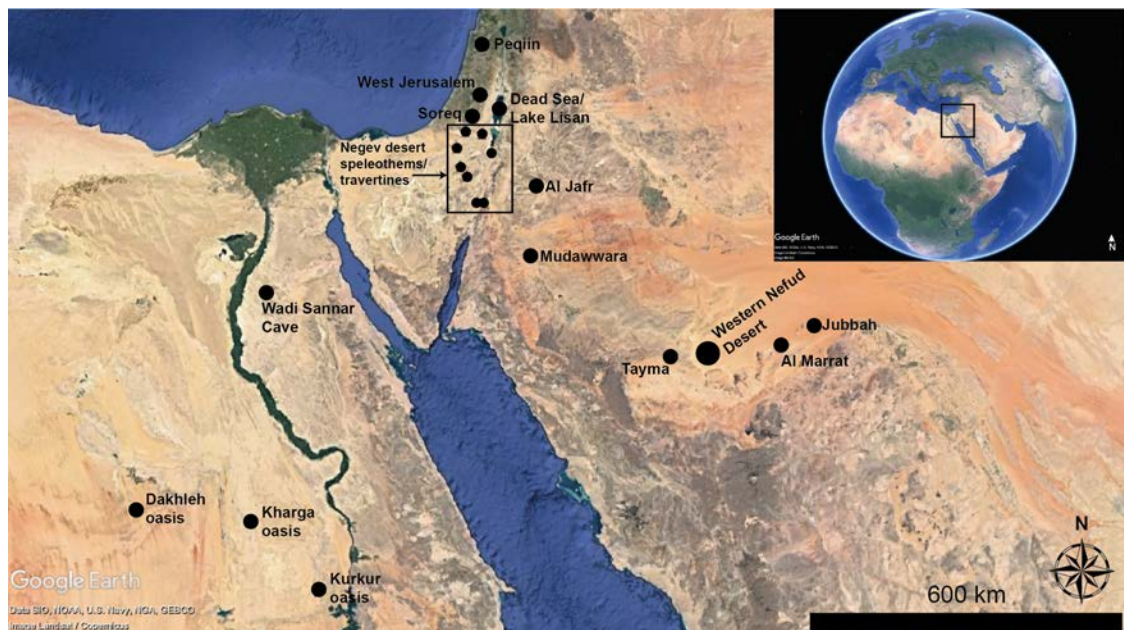


Figure 13.12 – Distribution of key terrestrial palaeoenvironmental archives that record periods of increased humidity across Northern Arabia, the Negev, the Levant and Northeast Africa that are cited in text.

13.3.1.1 The Nefud Desert: Jubbah, Jebel Quatter 1, Al Marrat Basin & Tayma.

The interdunal lakes in the western Nefud Desert presented here add a number of dated palaeolake records to those previously published (Clark-Wilson, 2016; Groucutt et al.,

2018; Rosenberg et al., 2013), and are consistent with pattern of increased humidity during periods of high northern hemisphere summer insolation. In addition, KAM4 lake 4 is the first directly dated MIS 7 palaeolake deposit in the western Nefud Desert.

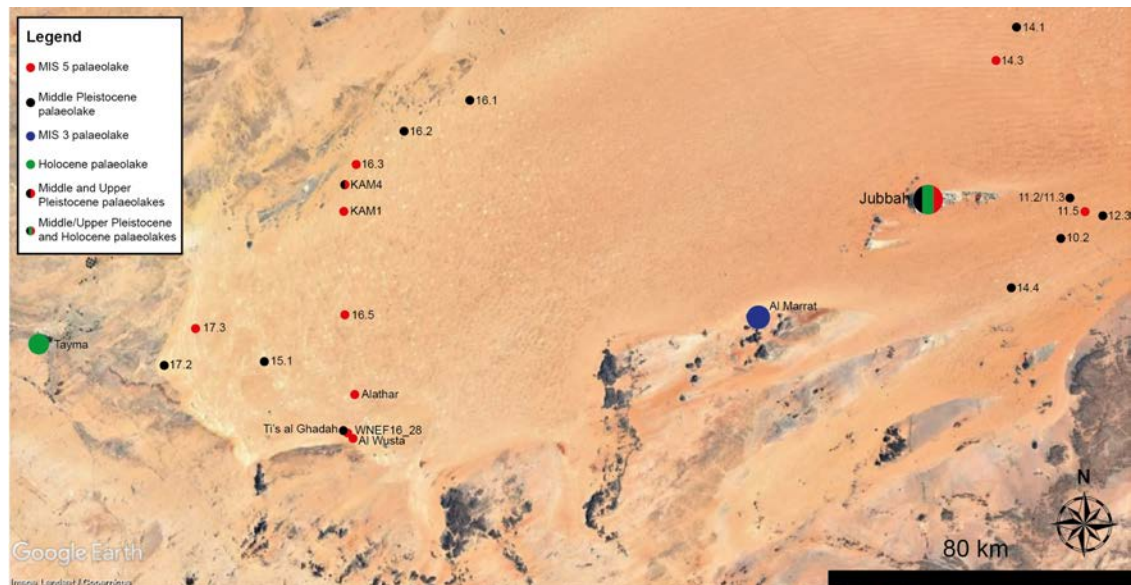


Figure 13.13 - Distribution of studied palaeolake deposits across the western Nefud Desert from this thesis, Petraglia et al. (2011, 2012), Rosenberg et al. (2013), Jennings et al. (2016), Groucutt et al. (2018) and Stewart et al. (2020a). Red circles = MIS 5 palaeolake deposits. Black circles = Middle Pleistocene palaeolake deposits. Blue circle = MIS 3 age palaeolake (Al Marrat). Green circle = Holocene age palaeolake deposit (Tayma). Black and red circles = Basins with palaeolake sediments of Middle and Upper Pleistocene age. Black, red and green circles = Basins with palaeolake sediments of Middle and Upper Pleistocene, and Holocene age. Along with directly dated or bracketed palaeolake sediments, this map also includes palaeolake sediments where only the underlying sands have been dated.

The paleoenvironmental research presented here also adds understanding to the depositional environment for interdunal lakes over the past ~500 ka. Previously, research has focused on macroscale sedimentological descriptions, with additional qualitative diatom palaeoecology and phytolith analysis undertaken at selected sites (Rosenberg et al., 2013). This approach is effective, since it allowed a large number of palaeolakes to be described within a short period of time, and diatom analysis provided information on the nature of the waterbodies (i.e. freshwater vs brackish/saline waters). However, macroscale observations miss key depositional features, making it difficult to answer questions such as whether lakes were perennial or ephemeral. Furthermore, diatom preservation is often poor. Consequently, the microfacies and isotopic work presented here builds on the work of Rosenberg et al. (2013) and has provided greater resolution to the depositional models produced, while also testing for the presence of

abrupt hydrological events through isotopic analysis. A key conclusion of this work is that there is little difference between the character of different humid phases in the timeframe 80 – 500 ka, and that interdunal lakes were probably widespread during each humid interval. This contrasts with the conclusion of Rosenberg et al. (2013) who suggested that Middle Pleistocene humid phases (MIS 11 and 9) produced deep freshwater lakes whereas MIS 5 lakes were isolated and shallow.

The palaeoenvironmental record from the central and eastern portion of the Nefud Desert record a similar pattern of humidity to that of the western Nefud Desert. At Jebel Quattar 1 in the Jubbah basin (see Fig 13.13 and 13.14), a sedimentary sequence consisting of palaeosols and calcretes separated by aeolian sands yields stratigraphically consistent ages of 211 ± 16 ka (MIS 7), 95 ± 7 ka (MIS 5c) and 75 ± 5 ka (MIS 5a) for the three palaeosol units (units J, D and B). A calcrete unit which lies between with the MIS 7 and MIS 5c palaeosol is inferred to be of MIS 5e age (Petraglia et al, 2011). Likewise, the Jubbah palaeolake sequence records humid intervals at MIS 11/9, 7, 5e, 5a, 3 and the Holocene (Parton et al., 2018), though the age uncertainties on wetland sediments beyond MIS 3 are large due to the difficulties of calculating dose rates for OSL dating in the presence of uranium-bearing gypsum (see Fig 13.14) (Clark-Balzan et al., 2017). Overall, the occurrence of increased humidity during interglacial and interstadial periods between MIS 11 – MIS 5a from palaeolake, palaeosol and calcrete sediments in the Jubbah Basin is consistent with the western Nefud record.

However, there are also some differences between the central/eastern Nefud and western Nefud records. Jubbah palaeolake (Parton et al., 2018) and an additional record from the Al Marrat basin (Jennings et al., 2016) both record increased humidity during MIS 3, which is absent in the western Nefud. Furthermore, Jubbah palaeolake (Parton et al., 2018) and Tayma palaeolake (Dinies et al., 2015; Engel et al., 2011; Neugebauer et al., 2017) record lake development during the early- to mid- Holocene humid period which is only represented by siliclastic silty sands with gravel inclusions in the western Nefud Desert (Al Wusta Playa). However, the overall pattern of lower effective precipitation during the Holocene is also observed within the sequence at Jubbah palaeolake where the Holocene sediments suggest the presence of a fluctuating and

brackish lacustrine/palustrine environment compared to a large perennial lake during MIS 5e (Parton et al., 2018).

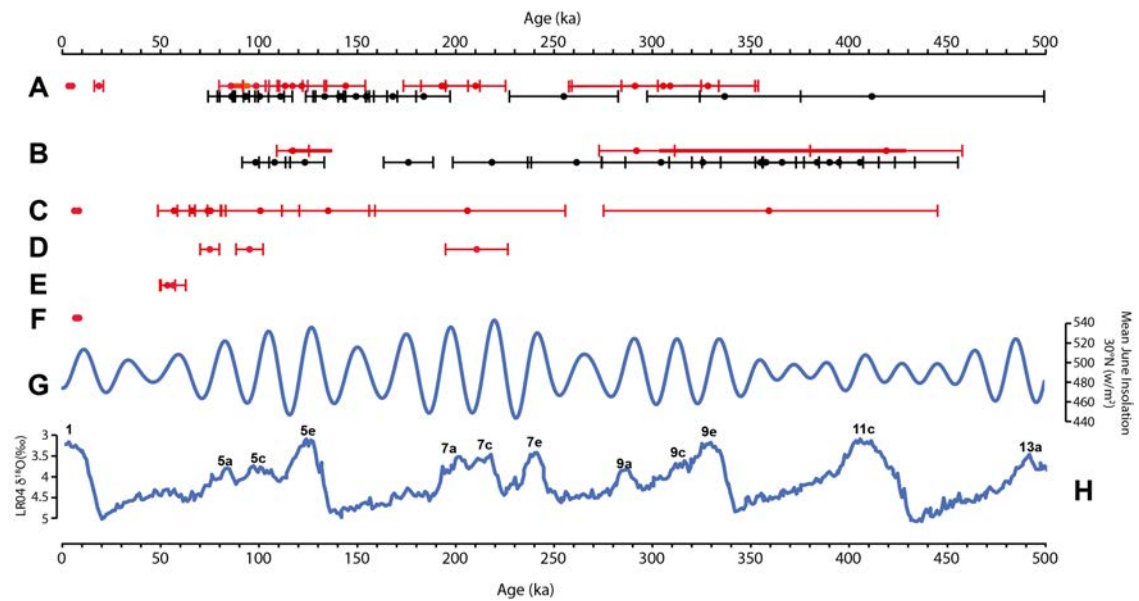


Figure 13.14 – Distribution of ages for all palaeoenvironmental records from the Nefud Desert over the past ~500 ka. All ages are displayed with uncertainties at 1σ , with the exception of the radiocarbon ages from Tayma (F) where uncertainties are at 2σ . (A) OSL and pIR-IRSL ages produced as part of this thesis and my MSc thesis (Clark-Wilson, 2016), along with dates produced by Clark-Balzan (per comms). Red dates are directly dated wetland sediments, and this includes the ephemeral Al Wusta Playa. Black dates are from aeolian sands which underlie wetland sediments. (B) OSL and TT-OSL ages from Rosenberg et al. (2013). Red dates are directly dated wetland sediments or bracketed wetland sediments. For bracketed ages a red bar is shown, where the minimum age equates to the lowest age from the underlying or overlying sands at 1σ and the maximum age equates to the oldest age at 1σ . Black dates represent ages from aeolian sands underlying marl sediments. (C) OSL and pIR-IRSL ages from the Jubbah palaeolake (Parton et al., 2018). (D) OSL ages from palaeosol and calcrete sediments from Jebel Qattar (JQ1) from the Jubbah basin (Petraglia et al., 2011). (E) OSL ages from Al Marrat (Jennings et al., 2016). (F) Radiocarbon ages from Tayma palaeolake (Dinies et al., 2015). Note that these ages place lake highstand at Tayma to between 8.7 and 8 ka (Dinies et al., 2015). (G) Northern hemisphere summer insolation at 30°N (Berger and Loutre, 1991). (H) Marine oxygen isotope record from the LR04 stack (Lisiecki and Raymo, 2005).

Taken together, the palaeolake, palaeosol and calcrete sediments show that humid phases led to lake and soil development across the Nefud Desert (Fig 13.13), and occurred during high northern hemisphere insolation (i.e. interglacial and interstadial periods) over the past ~500 ka (Fig 13.14). It also shows that effective precipitation was lower during the early-mid Holocene than in any other interglacial period over the past 500 ka. Interstadial periods such as MIS 3 were also humid enough to lead to lake development within structural basins on the fringes of the Nefud Desert though not humid enough to induce lake development in the sand sea itself.

13.3.1.2 Northern Arabia: Mudawwara and Al Jafr

The Mudawwara depression, located 100 km to the east of the Gulf of Aqaba in southern Jordan (29 N, 36 E) (Fig 13.12), is currently an arid depression consisting of large clay pans and sebkha (Petit-Maire et al., 2010). However, the depression contains extensive deposits of lacustrine coquina up to 20 m above the basin floor representing a perennial fresh-to-brackish lake with a maximum area of 2000 km² and >40 m depth (Petit-Maire et al., 2010). U/Th dating on *Cerastoderma* shells from a number of sequences in the depression suggest that a lake was present during MIS 7a/6e (samples JM7/1 and JM7/7b), MIS 5e (samples JM1, 3, 4, 7/7a), MIS 5c – a (samples JM11, JM12, JM7/9) (see Fig 13.15, H). It is noteworthy that a single sample dates to 150 +8/-7 ka which is consistent with MIS 6 (Petit-Maire et al., 2010). This is consistent with the timing of a NH summer insolation peak at ~150 ka (Petit-Maire et al., 2010). This suite of ages is broadly consistent with the timing of interdunal lake formation in the western Nefud Desert from MIS 7/6a (KAM4 lake 4), MIS 5e (WNEF16_28 and Alathar) and MIS 5c-a (Al Wusta, Site 16.3). Given the proximity of Mudawwara to the Nefud Desert, it is not surprising that the timing of lake formation in both regions is similar. This suggests that the same moisture source(s) may be responsible for the increase in effective precipitation to both regions. Petit-Maire et al. (2010) suggests that a combination of both westerly (winter) and monsoonal (summer) rainfall would be needed to maintain a lake the size of that recorded in the Mudawwara basin given the high evaporation rate at 29°N latitude. It is plausible that a similar regime occurred in the western Nefud Desert.

There is currently no direct evidence of Holocene lake activity at Mudawwara. Petit-Maire et al. (2010) suggest that undated gypsum-rich marls found in a core in the southern end of the deposit may be of Holocene age. It is also possible that Holocene age deposits have been eroded in the Jordanian portion of the Mudawwara basin, but that they might be present in the uninvestigated Saudi Arabian sector. Alternatively, it is equally possible that no Holocene deposition took place (Petit-Maire et al., 2010). If the latter hypothesis is correct, then the Mudawwara basin has a similar

palaeohydrological history to the Nefud Desert, with the Holocene humid period being less pronounced than humid periods in Middle and Upper Pleistocene.

A further Pleistocene lacustrine/wetland deposit is recorded in southeastern Jordan at Al Jafr (30.32 N, 36.17 E) (Macumber, 2008; Mischke et al., 2015). Lacustrine deposits interpreted as shallow freshwater to slightly oligohaline slow flowing ponds, rich with aquatic vegetation, have been assigned a minimum age of MIS 3 on the basis of radiocarbon dating, though the authors acknowledge potential problems with the chronology and suggest the deposits may be older (Mischke et al., 2015). Consequently, it is difficult to compare the Al Jafr record with that from the Nefud Desert.

13.3.1.3 The Negev Desert

Speleothems from the Negev Desert (30.49 N to 30.94 N; Fig 13.15) record increased effective precipitation at times consistent with the formation of lakes in the western Nefud (Fig 13.16) (Vaks et al., 2013, 2010, 2007, 2006). Based on present day growth patterns, speleothem growth in the Negev only occurs during periods where rainfall is greater than 300 mm yr⁻¹ (Vaks et al., 2013, 2010). In the central and southern Negev Desert, speleothem growth is restricted to four 'Negev Humid Phases' (NHPs). These occur between 350 – 310 ka (NHP-4), 310 – 290 ka (NHP-3), 220 – 190 ka (NHP-2) and 142 – 109 ka (NHP-1). Further speleothem growth in the Negev is recorded at ~156 – 158 ka at Makhtesh-ha-Qatan cave, at ~87/88 ka at Even-Sid Cave and there is an additional ancient sample beyond the limits of U/Th dating was recorded at Even-Sid Cave (Vaks et al., 2010).

NHP moisture appears to be sourced from both an increase in Atlantic-Mediterranean cyclones along and increased monsoonal rainfall in response to a weakening of the high-pressure cell over the North Atlantic (Vaks et al., 2007; 2010). Speleothem $\delta^{18}\text{O}$ values shed further light on the source of rainfall. During peak interglacial humid phases (NHP4, 2 and 1) and MIS 5a, speleothems yield depleted $\delta^{18}\text{O}$ values, typically ranging from -7‰ to -10‰ (Vaks et al., 2006). In contrast, NHP3, MIS 6 at Makhtesh-ha-Qatan Cave and the glacial age speleothems in the northern Negev record more positive $\delta^{18}\text{O}$ values,

from -2.8‰ to -4.6‰ (Vaks et al., 2006). It has been suggested that the more depleted values relate to increased Nile discharge into the eastern Mediterranean basin due to enhanced monsoonal rainfall (Vaks et al., 2010; Rohling et al., 2013) or to the Rayleigh distillation of monsoonal rainfall sourced from the Atlantic (El-Shenawry et al., 2018). The more positive $\delta^{18}\text{O}$ values relate to periods where there is no input of monsoonal rain, either to the source waters (eastern Mediterranean) or directly to the sites.

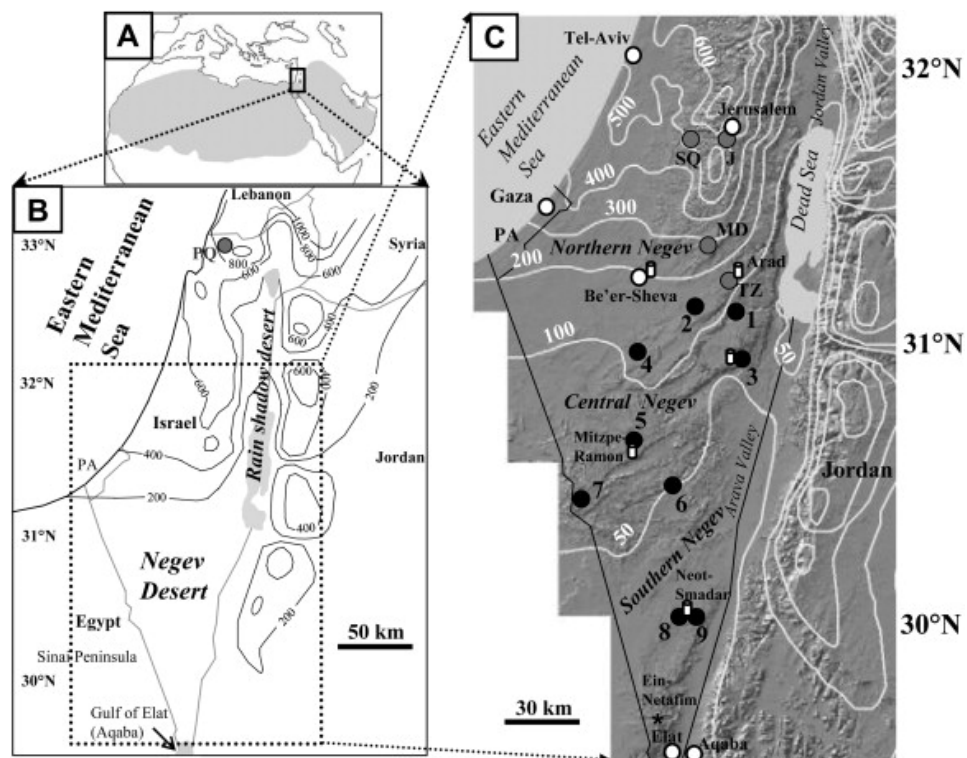


Figure 13.15 – Location of the Negev Desert (panels A and B) along with the location of speleothem records from Vaks et al. (2010). Modern day isohyets are marked by white lines in panel C and show the distinct north-south gradient of rainfall in the region. Current speleothem growth is restricted to areas in receipt of 300mm yr^{-1} of rainfall per year. Central and southern Negev speleothems are marked from 1 – 9, and these only record growth during past interglacials or periods of high northern hemisphere summer insolation (Vaks et al., 2007). No Holocene growth is recorded in these records. Northern Negev speleothems (TZ = Tzavoa Cave, MD = Ma'ale-Dragot Cave) record increased humidity during both interglacial and glacial periods.

NHPs correlate closely with lake phases in the western Nefud Desert. NHPs 4 and 3 are approximately contemporaneous with the MIS 9 age deposits at TAG and KAM4 lake 2. Given the clear monsoonal influence on NHP4, based on depleted $\delta^{18}\text{O}$ values, we suggest this period most likely correlates with MIS 9 deposits in the western Nefud. However, age uncertainties mean this cannot be asserted unequivocally. NHP 2 relates

to MIS 7 age deposit KAM4 lake 4, while NHP 1 correlates with early MIS 5 deposits WNEF16_28 and Alathar. Additionally, the speleothem growth at Even Sid dated to 87/88 ka correlates with MIS 5a age lake deposits at Al Wusta and Site 16.3. It is also notable that no Holocene speleothems have been reported from the Negev (Vaks et al., 2010), which is consistent with the lack of Holocene age interdunal lakes in the western Nefud Desert and at Mudawwara.

Travertines in the Negev Desert and Arava Valley also record increased humidity in the region at ca. 230, 174, 128, 105, and 84 ka (Fig 13.15) (Waldmann et al., 2010). These periods are broadly consistent with the timing of speleothem formation in the region, though the age uncertainties beyond MIS 5 yield a broad spread in ages from ca. 180 – 250 ka making it difficult to pick out discrete phases of increased humidity (Fig 13.16) (Waldmann et al., 2010). Periods of travertine growth are also recorded during the early Holocene at 8 ka, and at 70 and 40 ka which are in contrast with the western Nefud Desert. Palaeosol sequences in the Sinai Peninsula also attest to periods of increased humidity, though they are not sufficiently precisely dated to allow comparison with other records (Roskin et al., 2013).

13.3.1.4 Northeast Africa

Tufa records from Kharga, Dakhleh and Kurkur Oases in the Western Desert (~25°N) (Smith et al., 2004, 2007; Crombie et al., 1999) along with speleothem records from Wadi Sannar Cave (~29°N) (El-Shenawy et al., 2018; Osmond and Dabous, 2004) record increased humidity in northeast Africa (Fig 13.12). At Kharga Oasis, U/Th dating on multiple tufa deposits related to Middle Palaeolithic archaeological material consistently yields MIS 5 ages (127.9 ± 1.3 ka to 103.4 ± 14 ka) (Smith et al., 2007). Furthermore, averaging the uranium-series dates on the Wadi Midawwara tufa yields an age of ~133 ka suggesting increased spring flow at the onset of MIS 5e (Smith et al., 2007). Further tufa deposits dated to the MIS 6/5e transition and MIS 5 are recorded at Kharga, Dakhleh and Kurkur Oases in Egypt (Crombie et al., 1997; Smith et al., 2004) at Bir Sahara/Bir Tarfawi in northern Sudan (Szabo et al., 1995). These records match well with the ages of lakes at WNEF16_28 and Alathar in the western Nefud Desert. Before

the MIS 6/5e transition tufa ages from northeast Africa do not cluster around specific time intervals, primarily due to the large uncertainties on individual U/Th ages in this time range (Smith et al., 2007).

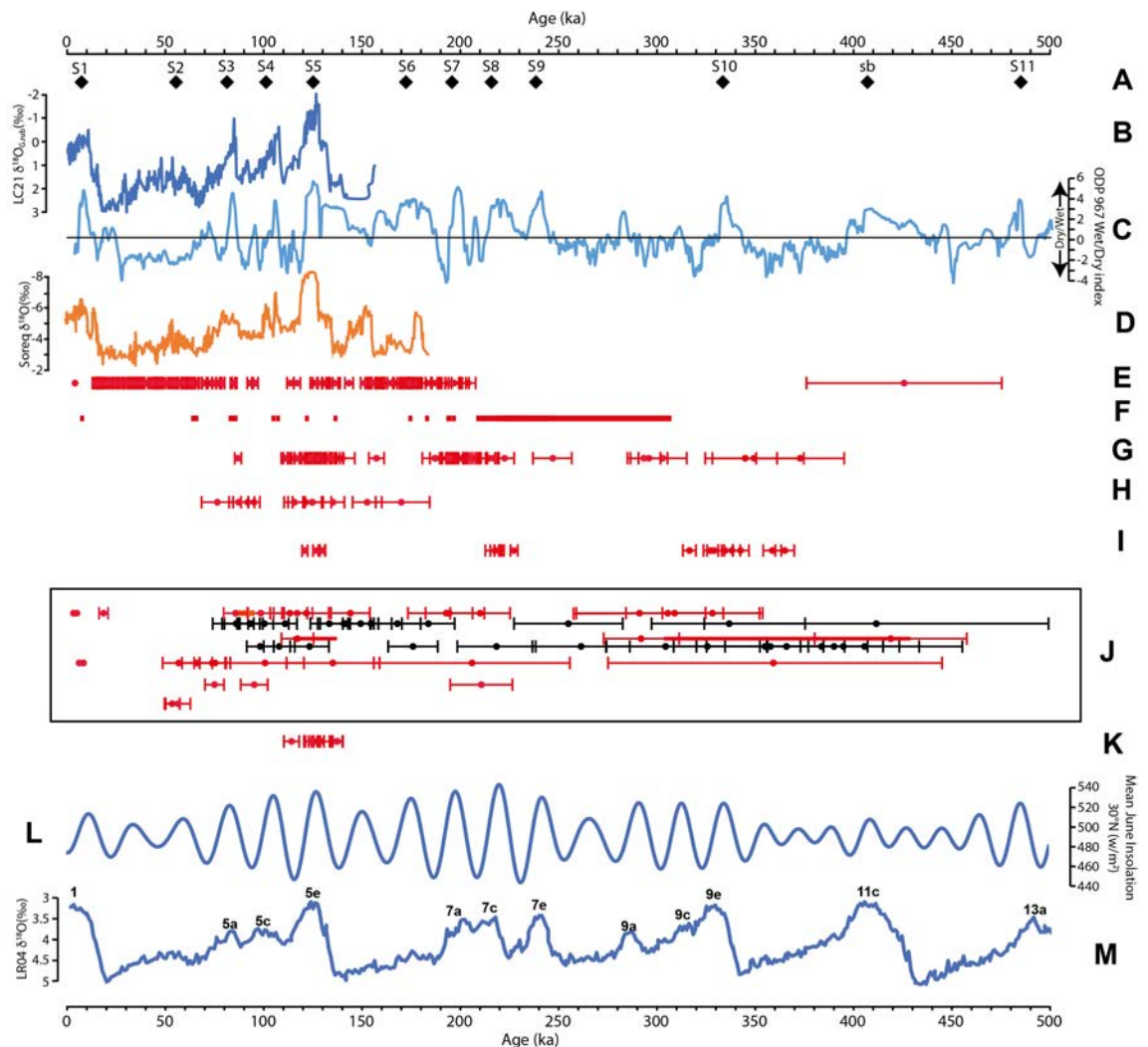


Figure 13.16 – Distribution of ages for key palaeoenvironmental records that record increased humidity across Northern Arabia, the Negev Desert, Northeast Africa and the Levant over the past ~500 ka. Ages are presented in latitudinal order, with southern sites at the bottom of the figure and northern sites at the top of the figure. All U/Th dates (E, F, G, H, I and K) display uncertainties at 2σ . Luminescence dates display uncertainties at 1σ . (A) Sapropel events in the eastern Mediterranean (Grant et al., 2017; Ziegler et al., 2010). (B) LC21 $\delta^{18}O_{G,rub}$ record from the Aegean Sea (Grant et al., 2012). Note the reversed axis. More negative $\delta^{18}O$ values reflect freshening of the eastern Mediterranean due to increased freshwater discharge, associated with increased tropical rainfall. (C) Wet/Dry North African index from ODP 967 (Grant et al., 2017). More positive values reflect greater humidity and more negative values reflect greater aridity. (D) $\delta^{18}O$ record from Soreq Cave, Israel (Bar-Matthews et al., 2003). Note reversed axis. More negative $\delta^{18}O$ values reflect freshening of the eastern Mediterranean source water in response to increased freshwater input. (E) U/Th dates from northern Negev Caves of Tzavoa and Ma’ae-Dragnet (see Fig 13.15). These record humidity during both glacial and interglacial periods. (F) U/Th ages of Arava Valley travertines (Schwarz et al., 1979; Livnat and Kronfeld, 1985; Enmar, 1999; Waldmann et al., 2010). Note that data was taken from Waldmann et al. (2010) and no uncertainty terms were provided, though age ranges for some samples were given. (G) U/Th ages on speleothems for central and southern Negev (Vaks et al., 2007). (H) U/Th dates from Mudawwara palaeolake, Jordan (Petit-Maire et al., 2010). (I) U/Th ages from the Wadi Sannar speleothem record, Egypt. (J) All OSL ages from the Nefud Desert including data from this thesis alongside that of Petraglia et al. (2011), Rosenberg et al. (2013), Stimpson et al. (2015), Jennings et al. (2016) Clark-Wilson (2016), Groucutt et al. (2018) and Stewart et al. (2020a). For a more detailed breakdown of these dates please refer to Figure 13.14. (K) U/Th dates on tufas from Kharga Oasis, Egypt (Smith et al., 2007). (L) Northern hemisphere summer insolation at $30^{\circ}N$ (Berger and Loutre, 1991). (M) Marine oxygen isotope record from the LR04 stack (Lisiecki and Raymo, 2005).

Hamdan and Brook (2015) carried out work on tufa deposits from the Eastern Desert (east of the Nile) and the Sinai Peninsula, where they collected a total of fifty-six samples for analysis. Radiocarbon ages for these samples suggest that they formed during two discrete periods: the more recent period occurs between 12,058 and 6678 cal yr BP, while the earlier period dates to 31,200 – 22,500 cal yr BP with greater growth during this period (Hamdan and Brook, 2015). While the age of 12,058 and 6678 cal yr BP is consistent with increased regional humidity during the Holocene Humid Period, enhanced tufa growth between 31,200 – 22,500 cal yr BP is inconsistent with other regional records of humidity.

It is plausible that the tufa growth periods recorded in the Eastern Desert by Hamdan and Brook (2015) reflects erroneous radiocarbon dates. Early research from the western Nefud Desert that utilised radiocarbon dating suggested a similar phasing of humid phases (Schulz and Whitney, 1986), though was later shown to be erroneous by subsequent geochronological work using luminescence dating and U/Th dating (e.g. Rosenberg et al., 2013; Groucutt et al., 2018). Rosenberg et al. (2013) suggests that the issue with radiocarbon dating was the contamination by younger carbon, leading to underestimated ages. Hamdan et al. (2015) date insoluble organic material and the carbonate matrix as pairs to attempt to overcome potential issues with contamination by younger carbon. 'Holocene' tufas yielded well matched pairs, giving confidence for these ages (Hamdan et al., 2015). However, the tufas that date to the ~23 - 31 ka period rarely yielded consistent paired ages, with the carbonate fraction being consistently older than the organic fraction (Hamdan et al., 2015). Hamdan et al. (2015) suggests that this is caused by younger plant roots penetrating porous tufa, leading to young carbon contamination thus explaining the younger ages for organic residues. However, it is noteworthy that difference in radiocarbon ages between pairs of organic residues and carbonate matrix is up to 34,790 ^{14}C yr BP (Hamdan et al., 2015). From the above discussion it is clear that these tufas may be considerably older than 31,200 – 22,500 cal yr BP. Interestingly, there is a distinct difference between the $\delta^{18}\text{O}$ values of the tufas formed between ~23 – 31 ka and the 'Holocene' tufas, with the former more depleted than the latter. This suggests that the ~23 – 31 ka tufas were deposited during periods

with a greater amount of rainfall relative to the Holocene. However, without a reliable chronology it is difficult to utilise this potentially useful palaeoclimatic information.

The most precisely dated record of increased humidity in northeast Africa comes from the Wadi Sannar Cave (28°37'N) speleothem. The cave lies at a similar latitude to the western Nefud Desert (Fig 13.12) (Osmond and Dabous, 2004; El-Shenawy et al., 2018). Speleothem growth only occurs during periods of increased humidity, with the most recent dating work suggesting speleothem growth occurred during MIS 5e (130.46 – 127.53 ka), MIS 7c (219.4 ± 7.3 ka) and early MIS 9 (335 ± 12 ka). No growth has been reported from MIS 5a or the Holocene, though this may be an artefact of sampling. El-Shenawy et al. (2018) argue that the source of moisture to Wadi Sannar Cave is the summer monsoon, based on the depleted $\delta^{18}\text{O}$ values. The $\delta^{18}\text{O}$ becomes depleted through Rayleigh distillation, as moisture is transported via zonal flow from the Atlantic and across the North African continent to NE Africa and the Levant (El-Shenawy et al., 2018). It is notable that the negative $\delta^{18}\text{O}$ values obtained from the Wadi Sannar Cave speleothem are consistent with those from Negev speleothems formed during peak interglacial periods (Vaks et al., 2006).

The timings of speleothem growth at Wadi Sannar are also broadly consistent with interdunal lake development in the western Nefud over the past ~350 ka (see Fig 13.16). However, no speleothem growth is recorded during MIS 5a at Wadi Sannar. If the lack of speleothem growth during MIS 5a is due to lower humidity at Wadi Sannar during this time period, then this represents a key difference between this record and our reconstruction of humidity in the western Nefud. However, the pattern of lower absolute humidity is reflected in the western Nefud Desert where the MIS 5e deposit WNEF16_28 has more depleted $\delta^{18}\text{O}$ values and a microfacies indicative of sedimentation in a deeper waterbody than nearby MIS 5a sites of Al Wusta and site 16.3.

13.3.2 Levant and the Eastern Mediterranean Basin

Levantine speleothems demonstrate the influence of increased summer monsoon rainfall and show that this influence occurs in line with interdunal lake development in

the western Nefud sand sea. A $\delta^{18}\text{O}$ depletion event that occurred during MIS 5e is evident in a number of Levantine speleothems (e.g. Fig 13.16, D) (Bar-Matthews et al., 2003; Frumkin et al., 1999; Nehme et al., 2015), while more subdued depletion events also occur during MIS 5c and 5a at Soreq, Pequin and West Jerusalem Caves (Bar-Matthews et al., 2003; Frumkin et al., 1999). Such depletion events occur for two reasons: 1) due to the freshening of eastern Mediterranean source waters in response to increased Nile discharge resulting from increased monsoonal rainfall (Bar-Matthews et al., 2019) and 2) increased rainfall over the Mediterranean basin from North Atlantic storms (Rodriguez-Sanz et al., 2017). Surface water freshening is also implied in the eastern Mediterranean sea where the *G. ruber* $\delta^{18}\text{O}$ record from the LC21 ocean core is depleted by 5‰ during interglacial phases (Fig 13.16, B) (Grant et al., 2012). Such freshwater impulses into the eastern Mediterranean are also recorded by sapropel layers, with S5, S4 and S3 from ODP 967 relating to insolation peaks related to MIS 5e, 5c and 5a (Fig 13.16, A) (Lourens, 2004; Ziegler et al., 2010). The direct input of monsoonal rains to the Levant has been recorded at Soreq Cave by Orland et al. (2019). Using high-resolution isotope analysis across annual bands dated to MIS 5e, 5d and 5c, Orland et al. (2019) show that both summer monsoon rainfall and winter westerly rainfall fell over the Levant during periods of high summer insolation (i.e. MIS 5e and MIS 5c) but not during periods of low summer insolation (i.e. MIS 5d). This empirical evidence is supported by an isotope-enabled climate model from the same study. However, it is not clear exactly how much monsoonal rainfall fell in the Levant and northern Arabia, and whether this would have been enough to lead to interdunal lake development (Hartman et al., 2020).

Further records of increased humidity in the Levant during MIS 5 include the $\delta^{13}\text{C}$ records from Soreq and Peqi'in (Bar-Matthews et al., 2003). Here, $\delta^{13}\text{C}$ values are more positive during MIS 5e than during glacial periods. This is argued to relate to 'deluge events', where the dominant carbonate source switched from C3 vegetation to the carbonate from the weathering of the host dolomitic rock (Bar-Matthews et al., 2000, 2003, 2019). Pollen assemblages from the central Levant also point towards warm and wet conditions during MIS 5e (e.g. Langgut et al., 2011).

In contrast to the wetter conditions during the last interglacial, Lake Lisan (Dead Sea) experienced lower water levels during MIS 5 and peak water levels during the last glacial between 23 – 27 ka BP (Torfstein et al., 2015). Despite this, there is evidence for more humid conditions between ~128 – 122 ka during MIS 5e, when halite deposition during the early period of MIS 5e is succeeded by sequences of flood deposits (Torfstein et al., 2015). It is also suggested that the level of Lake Lisan during the glacial period is not a good indicator of rainfall, but instead records total water balance (Bar-Matthews et al., 2019). Bar-Matthews et al. (2019) note that temperatures were colder during the last glacial, resulting in lower evaporation rates, while short lived warm events may also have induced snow melt and drained large amounts of freshwater into Lake Lisan. These mechanisms may explain the discrepancy between the hydroclimate recorded by Lake Lisan and that inferred from analysis of speleothems, eastern Mediterranean ocean cores and pollen sequences.

From the analysis above it is evident that the Levant and eastern Mediterranean experienced periods of increased humidity that are consistent with those observed in the western Nefud Desert during MIS 5e (Alathar and WNEF16_28), and possibly during MIS 5c and 5a.

13.3.3 Southern and Central Arabia

A number of archives in southern and central Arabia record periods of increased humidity over the past ~500 ka (Fig 13.17 and 13.21). These include speleothem records from Hoti and Mukalla (Burns et al., 2001; Fleitmann et al., 2011, 2007, 2003; Nicholson et al., 2020), interdunal palaeolakes from the Empty Quarter (Crassard et al., 2013; Groucutt et al., 2015d; Matter et al., 2015b; McClure, 1984, 1976; Rosenberg et al., 2011) and the Ramlat as-Sab'atayn (Lézine et al., 2010, 1998), alluvial/fluvial records from central Arabia (McLaren et al., 2009; Matter et al., 2016), and marine sediments (deMenocal, 1995; Tierney et al., 2017a).

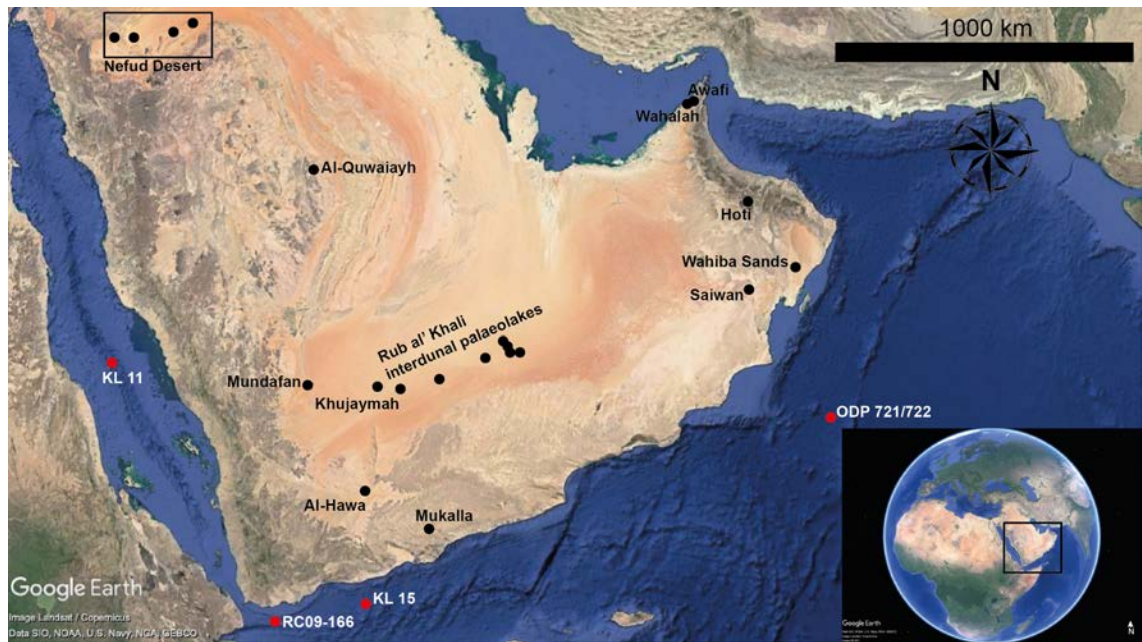


Figure 13.17 - Distribution of key terrestrial (black dots) and marine (red dots) palaeoenvironmental archives cited in text that record periods of increased humidity across the central and southern portion of the Arabian Peninsula. Note Nefud Desert in the top left corner of the map.

13.3.3.1 South Arabian Humid Periods (SAHPs): Hoti and Mukalla speleothem records

The occurrence of South Arabian Humid Periods (SAHPs) have been proposed on the basis of periods of speleothem growth from Hoti (Oman; southeastern Arabia) and Mukalla (Yemen; southern Arabia) caves (Burns et al., 2001; Fleitmann et al., 2011, 2007, 2003; Nicholson et al., 2020). There are no actively growing speleothems in these caves, and they only record growth during periods that are more humid than the present day. Speleothem growth on the Arabian Peninsula is argued to occur when rainfall exceeds 300 mm yr^{-1} , based on growth patterns in the Negev and Levant (Nicholson et al., 2020; Vaks et al., 2010). Consequently, speleothem growth at Hoti and Mukalla Caves implies precipitation above 300 mm yr^{-1} , though the height and diameter of some speleothems (Y99 and H13) suggests rainfall far exceeded this value (Nicholson et al., 2020).

U/Th dating on speleothems from both caves reveals eight SAHPs over the past 350 ka (Fig 13.18). These occur during MIS 1, 5a, 5c, 5e, 7a, 7e, 9c and 9e (Burns et al., 2001; Fleitmann et al., 2011, 2003; Fleitmann and Matter, 2009; Nicholson et al., 2020). Twelve further growth intervals from stalagmite Y99 from Mukalla Cave are observed based on macroscopic evidence for discontinuities and abrupt shifts in $\delta^{18}\text{O}$ immediately

prior to the end of stalagmite growth phases (Fig 13.18) (Nicholson et al., 2020). These growth intervals are beyond the limit of U/Th dating but are assigned absolute ages via U/Pb dating in combination with orbital tuning to the LR04 stack (Lisiecki and Raymo, 2005). Combining the orbitally-tuned and U/Pb ages with the U/Th dated growth phases results in 21 SAHPs over the past 1.1 Ma, and 10 SAHPs over the past 500 ka (Fig 13.18). The independently dated record over the past 350 ka are consistent with peak interglacial periods, and as such are consistent with the timing interdunal lake development in the western Nefud Desert. This consistency demonstrates that both southern and northern Arabia were humid at the same time, implying that the hydroclimate of both regions is driven by the same orbital-forcing mechanism.

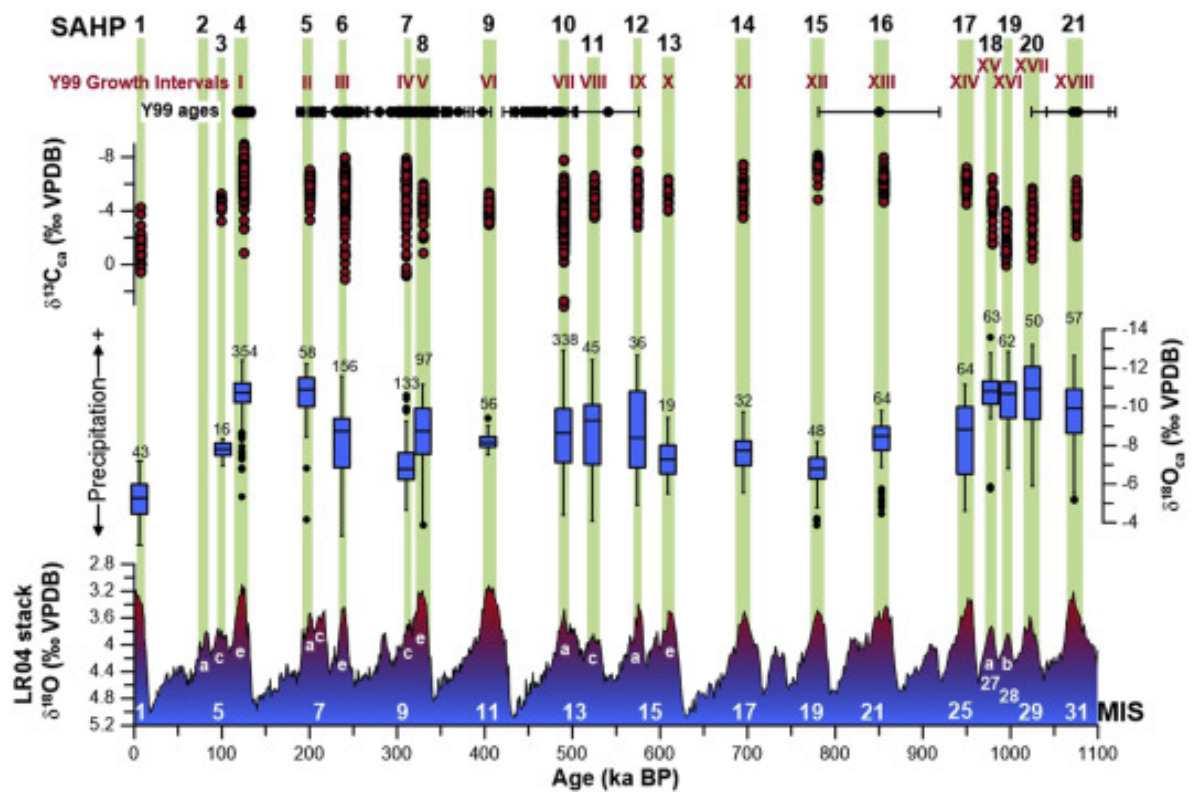


Figure 13.18 – The timing and palaeoenvironmental record of the Y99 speleothem, Mukalla Cave, Oman from Nicholson et al. (2020). Southern Arabian Humid Periods (SAHPs) are shaded in green and numbered at the top. Y99 growth intervals are numbered in red, while the distribution of U/Th ages is shown in black. Uncertainties are at 2σ . Boxplots show the range in $\delta^{18}\text{O}$ for each growth interval. Note the reversed scale. More positive $\delta^{18}\text{O}$ values reflect greater environmental aridity while more negative $\delta^{18}\text{O}$ values reflect greater environment humidity, as per the amount effect (see discussion in text).

Fluid inclusion $\delta^{18}\text{O}$ values are used to trace the source of the rainfall to the Hoti and Mukalla cave during humid intervals (Nicholson et al., 2020). The depleted $\delta^{18}\text{O}$ values of fluid inclusions from SAHPs 1 (Holocene) and 4 (MIS 5e) shows that the source of increased rainfall over southern Arabia was the Indian Ocean Summer Monsoon (ISM) as opposed to westerly derived rainfall (Nicholson et al., 2020). Additionally, ultra-high resolution $\delta^{18}\text{O}$ analysis across distinct annual layers, composed of a dark summer band and a white winter band, demonstrate that southern Arabia experienced highly seasonal rainfall with a wet summer monsoon season and a drier winter (Nicholson et al., 2020). An east-west precipitation gradient is observed in the $\delta^{18}\text{O}$ data from Hoti and Mukalla, with the latter site being further west and yielding more negative isotopic values (Nicholson et al., 2020). The source and seasonality of moisture, and the pattern of stable isotope variation between Mukalla and Hoti Caves are consistent with the output of isotope-enabled climate model of Herold and Lohmann (2009). This provides confidence that the output of this model is accurate with respect to the rainfall pattern, even if the rainfall amount is questionable. It is worth noting that the same isotope enabled climate model indicates increased rainfall over the western Nefud Desert during MIS 5e, with the moisture being sourced from the African monsoon (Fig 13.19, A). The same broad rainfall pattern is produced in other climate models focused on the last interglacial (Fig 13.19, B and C) (Jennings et al., 2015; Kutzbach et al., 2020), though it is worth noting that others do not show this pattern (Fig 13.19, D) (Orland et al., 2019). Additionally, the northerly extent of increased rainfall during the last interglacial varies between reaching the Levant (Fig 13.19, D) (Orland et al., 2019) and lying at or just beneath the Nefud Desert (Fig 13.19, B) (Kutzbach et al., 2020).

The $\delta^{18}\text{O}$ records from the Y99 speleothem from Mukalla also allows a comparison between the amount of rainfall between humid intervals over the past 1.1 Ma (Fig 13.18). More negative $\delta^{18}\text{O}$ values equate to periods of greater rainfall amount because of the 'amount effect' on isotopic fractionation (Rozanski, 1993; Chapter 3.6.4). MIS 5e and 7a have the most negative $\delta^{18}\text{O}$ values and are therefore the wettest humid phases in the last ~500 ka, while the Holocene has the most positive $\delta^{18}\text{O}$ and is the driest (Fig 13.18) (Nicholson et al., 2020).

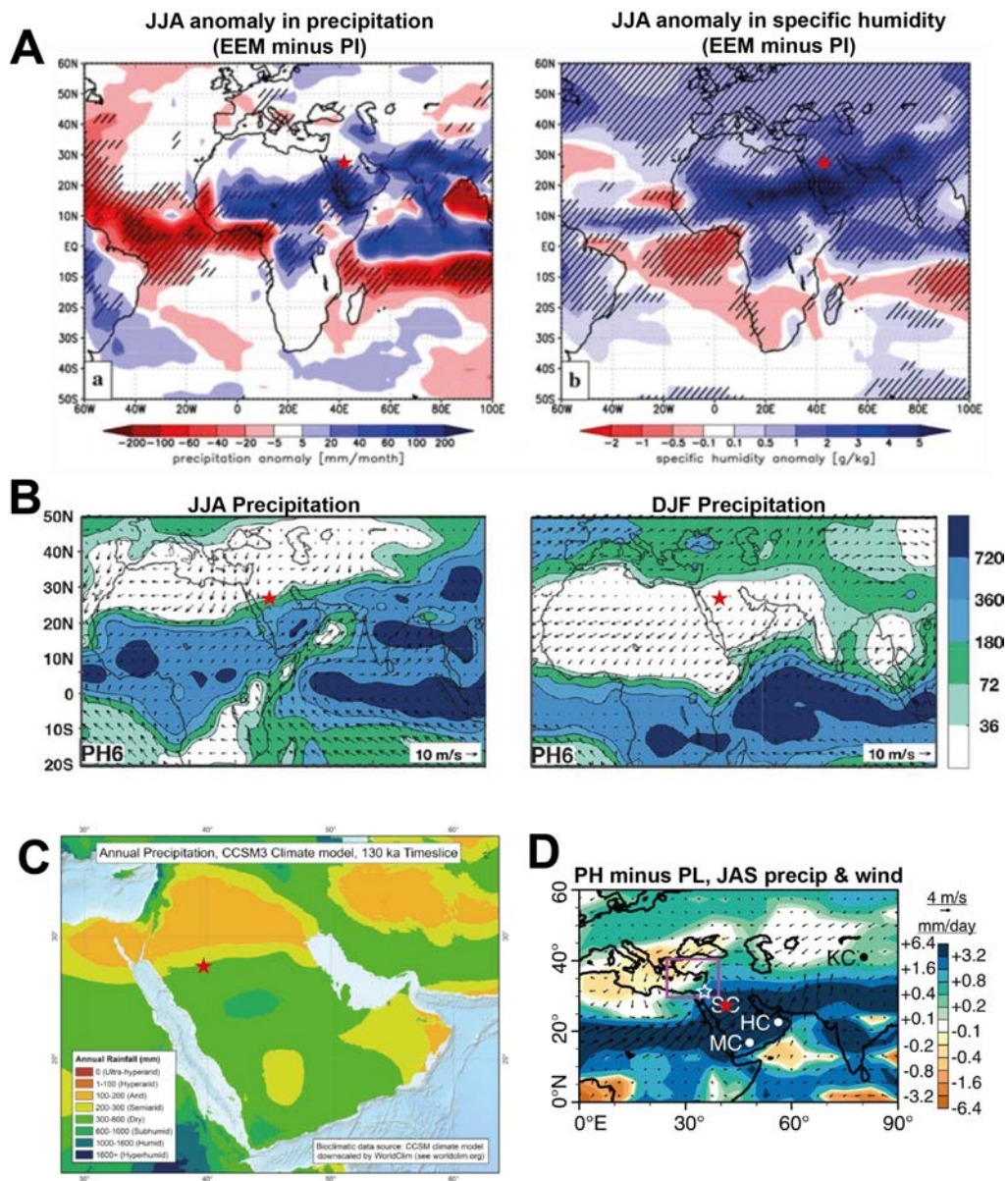


Figure 13.19 – Compilation of climate models that precipitation pattern and amount over the Arabian Peninsula during the last interglacial. A red star shows the approximate position of the western Nefud Desert. EEM = Eemian. PI = preindustrial. JJA = June July August. DJF = December January February. PH = precession high. PL = precession low. (A) Boreal summer anomalies (EEM minus PI) for precipitation in mm/month on the left and for specific humidity (g/kg) from Herold and Lohmann (2009). (B) Boreal summer (left) and winter (right) precipitation (mm/per season) at PH (~126 ka) from Kutzbach et al. (2020). (C) CCSM3 climate model which shows annual precipitation over the Arabian Peninsula at ~130 ka from Jennings et al. (2015). (D) July, August, September precipitation (mm/day) at 125 ka (PH) relative to 115 ka (PL) from Orland et al. (2019).

It is not possible to obtain similar information from the Nefud palaeolakes, though some inferences and comparisons can be made. For example, the MIS 5e sequence at WNEF16_28 has the most negative $\delta^{18}\text{O}$ values and also contains finely laminated microfacies. The former is suggestive of more rainfall in this time period as per the

amount effect or reduced impact of evaporitic enrichment due to greater lake volume, while the latter suggests that the MIS 5e lake was deeper than those formed during other humid periods as the preservation of laminations requires greater lake depth. This correlates well with the Mukalla record, which suggests MIS 5e is one of the most humid periods. The lack of Holocene lake development in the western Nefud Desert also corroborates the isotopic evidence from Mukalla, which suggests that this was the driest interglacial over the past 1.1 Ma. These data suggest that the pattern (strength and timing) of humidity in northern and southern Arabia is similar over the past 500 ka, and that it was probably driven by the strength of the enhanced monsoon systems.

13.3.3.2 Rub' al Khali Desert and Ramlat as-Sab'atayn: Mundafan, Khujaymah and al-Hawa

Humid periods dating to MIS 5 and the Holocene are also evident in south and south-central Arabia, from the lacustrine/palustrine records in the Rub' al Khali and Ramlat as-Sab'atayn deserts (Fig 13.17) (Crassard et al., 2013; Groucutt et al., 2015d; Lézine et al., 1998; McClure, 1984, 1976; Rosenberg et al., 2011) along with palaeolake Saiwan in Oman (Rosenberg et al., 2013). Initial work at Mundafan and the southwestern/central portion of the Rub' al Khali identified a number of lakebed facies. These predominantly consisted of autochthonous off-white to light grey lake 'marls' that contain fine micritic calcite, diatoms, ostracods and gastropods (mainly *Melanoides* or *Planorbis*) in varying proportions (McClure, 1984). Dolomitic and occasional evaporite (gypsum) facies are also described from the lake beds (McClure, 1984). Rosenberg et al. (2011) used OSL and radiocarbon dating to show that lake development at Mundafan and Khujaymah occurred during the Holocene and at multiple stages during MIS 5 (~80, ~100 and ~125 ka). Lake development during the later phase of MIS 5 (~97 to 77 ka) is supported by OSL dating at the MDF-61 site (Groucutt et al., 2015).

Further paleoenvironmental analysis was undertaken at Mundafan by Rosenberg et al. (2011) and Groucutt et al. (2015), and within the southwestern/central portion of the Rub' al Khali by Matter et al. (2015). Rosenberg et al. (2011) show that both the Holocene and MIS 5 lake marls at Mundafan were deposited by perennial freshwater

lakes, based on the ostracod assemblage which included species such as *Cypretta* sp., and *Darwinula stevensoni*. Groucutt et al. (2015) also presented a depositional environment for MIS 5a at Mundafan based on the sedimentary sequence at MDF-61. They argue that the late MIS 5 deposit was formed under three depositional environments. An initial substantial waterbody was succeeded by a palustrine environment with salinities greater than 5%, after which deposition occurred in a fully terrestrial setting. Rosenberg et al. (2011) estimate the surface area and depth of the Mundafan lake based on the spatial extent of lacustrine sediments. The Holocene lake was estimated to have had a surface area of ~50 km² with a maximum depth of ~10 m (Rosenberg et al., 2011). In contrast, the MIS 5 lake is estimated to have had a surface area of ~300 km² with an average depth of 12 m and a maximum depth of 25 – 30 m (Rosenberg et al., 2011). This pattern of greater humidity during MIS 5 compared with the Holocene is consistent with that in the western Nefud sand sea.

Matter et al. (2015) reports the presence of remnant interdunal palaeolake deposits, dated to the Holocene and MIS 5, across the Rub' al Khali. Three sedimentary facies are observed: a limestone facies, a marl facies and a sandy facies (Matter et al., 2015). The limestone facies are the most abundant and consist of fossiliferous beige micrites/microsparite that measure between 60 and 270 cm (Matter et al., 2015). At the microscale broken ostracod shells along with charophyte gyrogonites and stems are also abundant within a homogenous micrite/microsparite matrix with rare allogenic material (see Fig 13.20) (Matter et al., 2015). Fossiliferous material are mostly freshwater molluscs with *M. tuberculatus* being the most common at all sites (Matter et al., 2015). However, the most notable mollusc present is the mussel from the genus *Unio*, which is strictly depend on the presence of freshwater fish species which host their larvae (Bauer, 2001; Matter et al., 2015). The indirect evidence of fish suggests that interdunal lakes supported diverse fauna and flora (Matter et al., 2015), while it is also consistent with the presence of fossil fish at Ti's al Ghadah in the western Nefud Desert (Thomas et al., 1998; Stimpson et al., 2015, 2016; Stewart et al., 2019).

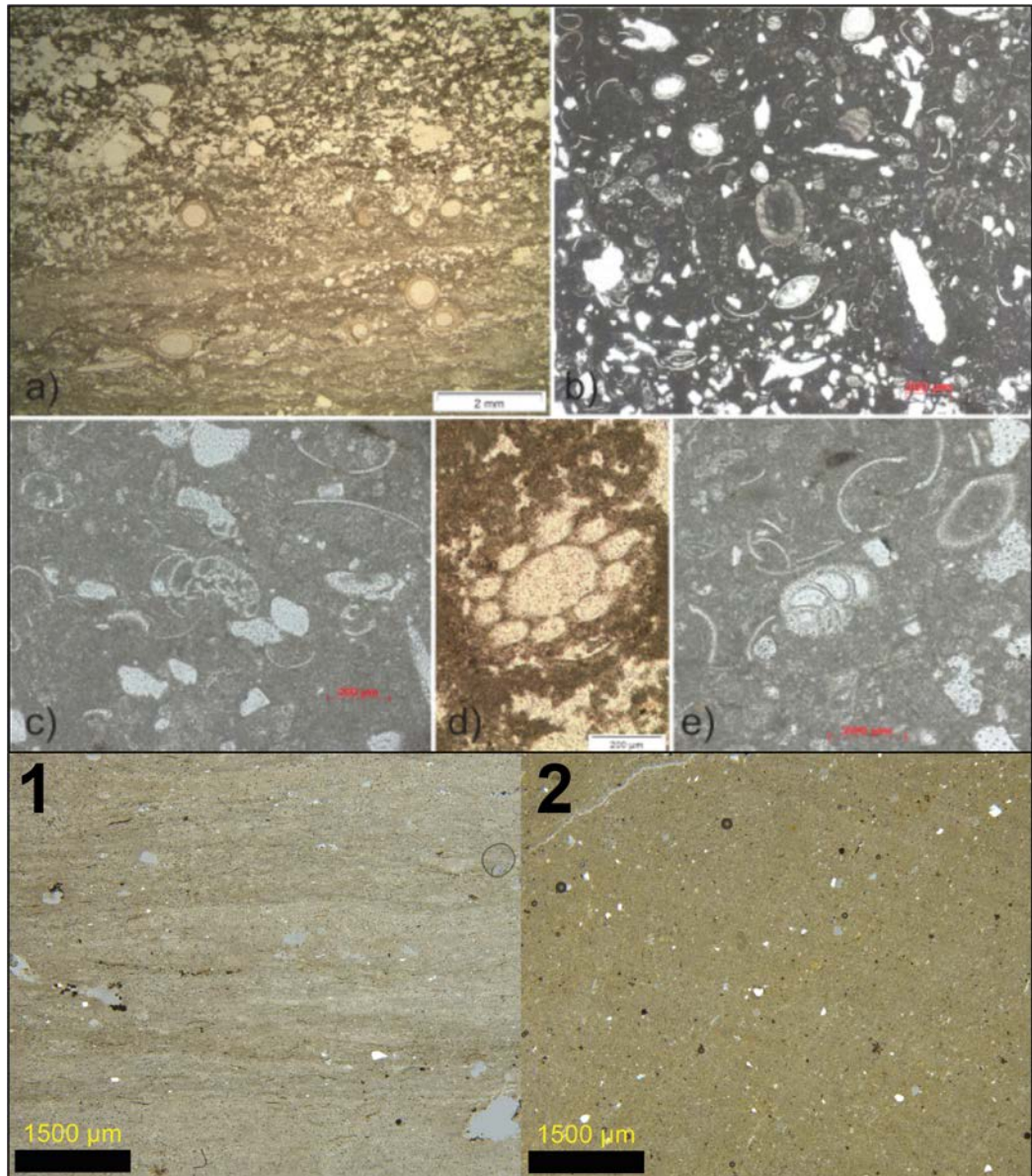


Figure 13.20 – Comparison of the microfacies of the ‘limestone facies’ of MIS 5 Rub’ al Khali interdunal lakes (a – e) from Matter et al. (2015) with microfacies from MIS 5 interdunal lakes from the western Nefud Desert (1 and 2). Note the key similarities in that both are composed of homogenous micrite/microsparite with rare allogenic grains, but also the differences in that the Rub’ al Khali microfacies contains abundant broken ostracod shells (b, c and e) along with charophyte gyrogonites and stems (a, d).

The sedimentology and fauna of the MIS 5 ‘limestone’ facies show these sediments were deposited on the beds of perennial and open lakes in the Rub’ al Khali (Matter et al., 2015). This is similar to the depositional environment reconstructed for the majority of lakes in the western Nefud Desert during both MIS 5 and Middle Pleistocene, as described in this thesis. Despite the similarities in the sedimentology between the limestone facies and interdunal palaeolake sediments in the western Nefud (i.e. both are dominated by homogenous micritic/microsparite with rare allogenic grains; Fig

13.20), some important differences are evident. Firstly, there are numerous broken ostracod shells in the limestone facies of the Rub' al Khali lakes while shell fragments are mostly rare in the western Nefud Desert sediments (Fig 13.20). Secondly, charophyte gyrogonites and stems are also abundant in the limestone facies in the Rub al Khali, suggesting the presence of submerged flora and a water depth of less than 6 m. These are never observed in the western Nefud Desert. Both these points indicate that the sedimentary facies of the Rub al Khali represent depositional environment closer the littoral zone of the lake, whereas the western Nefud Desert facies are more typical of the sub-littoral/profundal zone (see Fig 3.5). Nevertheless, the interpretation that the Rub al Khali palaeolakes were deposited in an open perennial freshwater and open lake, fed through groundwater discharge during periods where the groundwater was much higher (Matter et al., 2015) is strikingly similar to the depositional model for palaeolakes in the western Nefud Desert.

It is also important to note that 'marl' facies as described by Matter et al. (2015) consist of thin-beds (25 cm thick) of weakly consolidated gypsiferous sandy marl. This differs from the fine-grained carbonate rich sediments presented here which have sometimes been referred to as marls. It is also noteworthy that no gypsiferous deposits such as those described in the Rub al Khali were found within the western Nefud Desert.

Southern and southeastern Arabia contains further lacustrine/palustrine records of early to mid-Holocene age. These occur in the al-Hawa depression in the Ramlat as-Sabtayn desert, northern Yemen (Lézine et al., 1998), the Wahiba Sands, Oman (Lézine et al., 2010; Radies et al., 2004), Wahalah and Awafi, United Arab Emirates (Parker et al., 2016, 2006a). These were all interpreted as freshwater lakes, and their presence is in direct contrast to the absence of Holocene perennial waterbodies in the western Nefud sand sea, though is consistent with lake development in northern Arabia at Tayma and Jubbah. This may represent drainage catchment size, where larger catchments (i.e. Tayma, Jubbah) more readily produced lakes due to a greater amount of water funnelling into a single basin, whereas the drainage catchment for each individual interdunal lake in the western Nefud was likely small.

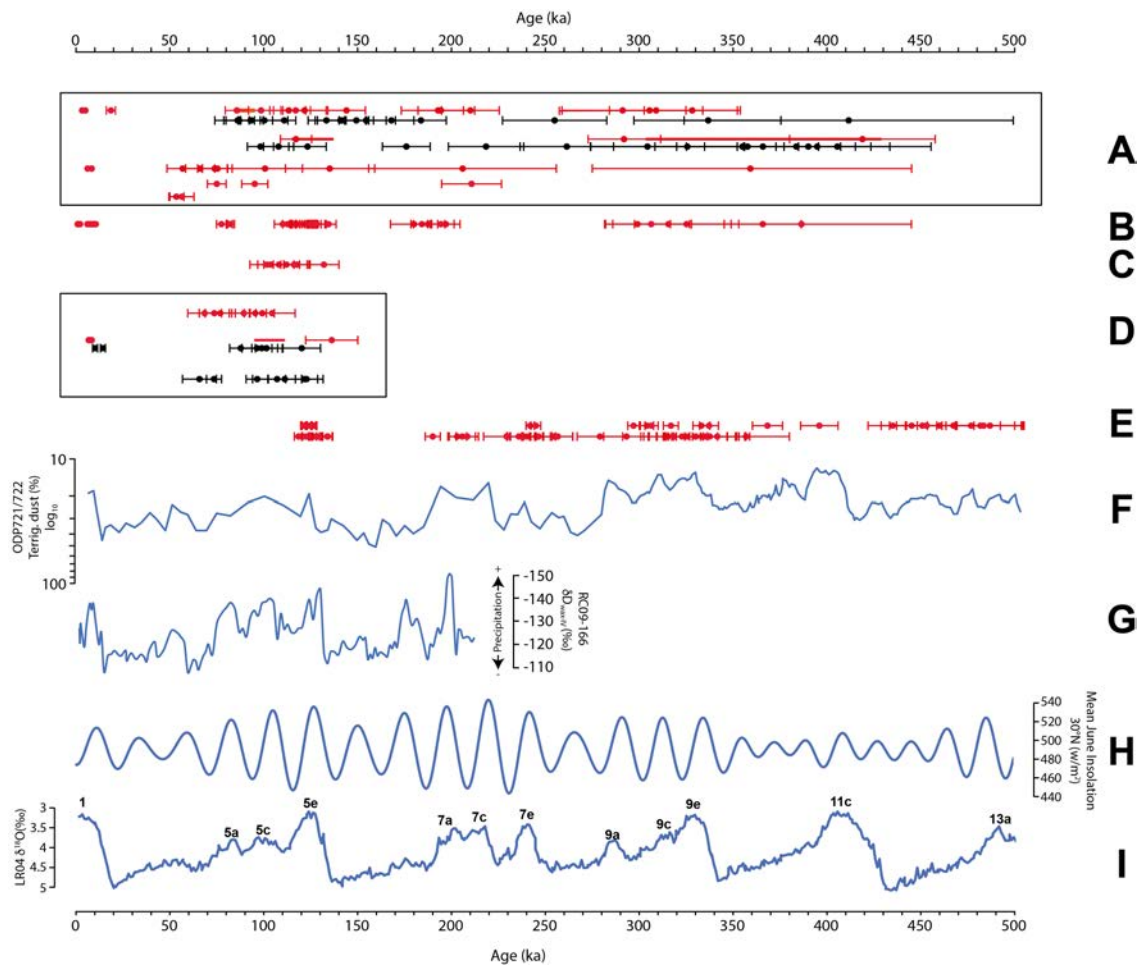


Figure 13.21 – Distribution of ages for key palaeoenvironmental records that record increased humidity across southern Arabia over the past ~500 ka, compared with the record from the Nefud Desert (A). Ages are presented in latitudinal order, with southern sites at the bottom of the figure and northern sites at the top of the figure. All U/Th dates (B, E) display uncertainties at 2σ . Luminescence dates display uncertainties at 1σ (A, C, D). Note that records that only record Holocene humidity are not included in this diagram (e.g. Wahalah, Awafi, Al-Hawa). (A) All OSL ages from the Nefud Desert including data from this thesis alongside that of Petraglia et al. (2011), Rosenberg et al. (2013), Stimpson et al. (2015), Jennings et al. (2016) Clark-Wilson (2016), Groucutt et al. (2018) and Stewart et al. (2020a). For a more detailed breakdown of these dates please refer to Figure 13.14. (B) U/Th dates recording speleothem growth intervals at Hoti Cave, Oman (Fleitmann et al., 2003). (C) OSL ages of lake formation at Saiwan palaeolake, Oman (Rosenberg et al., 2012). (D) OSL ages from Mundafan, Khujaymah and interdunal palaeolakes from the Rub' al Khali (Rosenberg et al., 2011; Groucutt et al., 2015; Matter et al., 2015). Red ages represent directly dated or bracketed sediments and black dates represent ages from the aeolian sands underlying palaeolake sediments. (E) U/Th ages for speleothem growth at Mukalla. Note the top line are ages from Nicholson et al. (2020) while the lower line shows ages from Fleitmann et al. (2011). (F) Terrigenous dust (%) from ODP721/722 from the Arabian Sea (deMenocal, 1995). (G) δD_{waxIV} record from RC09-166 in the Gulf of Aden (Tierney et al., 2017). (H) Northern hemisphere summer insolation at $30^\circ N$ (Berger and Loutre, 1991). (I) Marine oxygen isotope record from the LR04 stack (Lisiecki and Raymo, 2005).

13.3.4 Central Arabia

Palaeoenvironmental records from central Arabia are scarce. Episodic flooding events dated to ~ 54 ka, ~ 39 ka and ~ 0.8 ka have been recorded at Al-Quwaiyah (McLaren et al., 2009). The timing of these flooding events does not closely match evidence for increased humidity in the western Nefud sand sea. However, the flooding events at 54

ka are contemporary with MIS 3 humidity at the Al Marrat and Jubbah basins on the southern fringes of the Nefud Desert (Jennings et al., 2016; Parton et al., 2018). It is worth noting that such fluvial sediments could have been deposited by strong precipitation events under similar climatic conditions as today (Hoffmann et al., 2015). Matter et al. (2016) demonstrate that the Wadi ad Dawasir fluvial system, that runs from the Asir Mountains to the Arabian Gulf, was active during the Holocene humid phase between ~9 – 7 ka.

13.3.5 Marine sediments

Marine sediments from locations surrounding the Arabian Peninsula and North Africa (see Fig 13.17) record hydroclimatic change across the Saharo-Arabian desert belt over the Quaternary (see Chapter 2.3.1).

Sapropel layers in marine sediments in the eastern Mediterranean Basin (ODP 967) record periods of high Nile discharge due to increased monsoonal precipitation (Rohling et al., 2015; Rossignol-Strick, 1983). Sapropel layers are dated via orbital-tuning (see Chapter 2.3.1.1) and a number of sapropel layers are recorded over the past ~500 ka (see Fig 13.16, A) (Ziegler et al., 2010; Grant et al., 2017). Multiple sapropel layers are recorded during MIS 5 (S3, S4 and S5; Fig 13.16), consistent with the occurrence of discrete periods of humidity in the western Nefud Desert during MIS 5a (Al Wusta, Site 16.3) and MIS 5e (WNEF16_28, Alathar, KAM4 lakes 3, 3a and 3b). Multiple sapropel layers are also recorded during MIS 7 (S7, S8 and S9; Fig 13.16), which is consistent with the presence of MIS 7 humidity in the western Nefud Desert as recorded by KAM4 lake 4. The dating resolution at this scale prevents the correlation of KAM4 lake 4 with a distinct sapropel event. A sapropel event is also recorded during MIS 9 (S10) which is consistent with the age of palaeolake sediments from Ti's al Ghadah and KAM4 lake 2. Sapropels also occur during MIS 11 (sb) and MIS 13 (S11). The age of Site 16.1 (Rosenberg et al., 2013) is consistent with the 'sb' sapropel, while the age range of KAM4 lake 1 encompasses both MIS 11 and MIS 13 sapropels. Notably, sapropel events are also recorded during glacial periods with S2 occurring during MIS 3 at ~55 ka and S6 occurring during MIS 6 at ~175 ka (Ziegler et al., 2010; Grant et al., 2017). Neither of

these time periods yield evidence for interdunal lakes in the western Nefud Desert, though humidity is recorded during MIS 3 at Al Marrat basin and Jubbah on the southern fringe of the Nefud Desert (Jennings et al., 2016; Parton et al., 2018).

Grant et al. (2017) combines sapropel layers from ODP967 with the terrigenous dust record of Larrasoana et al. (2003) to create a North African humidity/aridity index for the past 3 million years (see Fig 2.7 and 13.16, C; Chapter 2.3.1.2). Given that this index records the sapropel layers from the same marine core as discussed above, the broad picture is the same; that humid phases typically match those observed in the western Nefud Desert. However, the Grant et al. (2017) North African humidity/aridity index does not record increased humidity during MIS 3 which is more consistent with the hydrological record from the western Nefud. However, the index does record greater humidity during MIS 6 with index values greater than or comparable to those observed during MIS 9, 11 and 13 (see Fig 13.16, C; Grant et al., 2017). That the index records humidity during MIS 6 is inconsistent with the palaeolake record from the western Nefud Desert, while 'lower' indexes for MIS 9, 11 and 13 is also inconsistent as interdunal lake development occurred during these periods in the western Nefud.

Multiple marine sediments record multiple periods of increased humidity over the past 500 ka in the Arabian Sea, Gulf of Aden and Red Sea. The terrigenous dust record from ODP 721/722 in the Arabian Sea shows reduced dust supply during the Holocene, MIS 5, 7, 9 and 11 though the record is of a low resolution and no discrete peaks are observed within interglacial periods (see Fig 13.21, F) (deMenocal, 1995). Terrigenous dust records are also present in the Red Sea (KL 15; Fleitmann, 1997, referenced in Nicholson et al., 2020) and the Gulf of Aden (KL 11; Fleitmann, 1997, referenced in Nicholson et al., 2020). Both these records show a reduction in median grain size during the Holocene, MIS 5, 7 and 9, consistent with the timing of increased humidity in the western Nefud Desert. Tierney et al. (2017) use δD_{wax} from the RC09-166 core in the Gulf of Aden to record rainfall amount (Chapter 2.3.1.3) from the Horn of Africa and Afar regions (Fig 13.21, G). Multiple isotopic depletions are observed during MIS 5 while the largest negative excursion occurs during MIS 7 (see Fig 13.21, G) (Tierney et al., 2017). This is consistent with the timing of interdunal lake development in the western Nefud

Desert. A Holocene peak is also observed in this record but is smaller than all MIS 5 peaks (5a, 5c, 5e) and the MIS 7 peak, consistent with the idea that the Holocene humid phase was limited relative to Pleistocene humid intervals. Finally, a peak is also observed at ~175 ka during MIS 6 which is consistent with the North African humidity/aridity index (Grant et al., 2017) and sapropel S6, though is not consistent with humidity in the western Nefud Desert.

13.4 Summary

This chapter has compared the record of humid phases over the past 500 ka within the western Nefud Desert (section 13.2), before comparing the record from the western Nefud Desert with palaeoenvironmental records from across the Arabian Peninsula, the Levant and Northeast Africa (section 13.3). Key findings are as follows:

- Perennial freshwater lakes existed in the western Nefud Desert during MIS 5a, 5e, 7, 9 and 11/13a.
- The evolution of most of these lakes is similar, with a simple transgressive-regressive hydrological cycle where lake levels rise, stabilise, then fall in response to changes effective precipitation. The only outlier to this pattern is KAM4 lake 4, dated to MIS 7, which changes from a lacustrine to a palustrine system and then back to a lacustrine/tufa system before finally desiccating.
- There is no evidence of perennial lakes forming in the western Nefud Desert during the Holocene humid phase, with evidence only for ephemeral and short-lived interdunal waterbodies during this time period. This suggests that the water table during the Holocene humid phase was lower than during any other Pleistocene humid phase.
- Records from the Arabian Peninsula, Negev, and northeast Africa also all suggest that the Holocene is less humid than other Pleistocene humid phases. For example, no Holocene-aged lake deposits are recorded at Mudawwara, Jordan despite the presence of a large lake that existed during MIS 5 and 7 (Petit-Maire et al., 2010). Similarly, no speleothem growth recorded at Wadi Sannur Cave (El-Shenawry et al., 2018) or in the Negev Desert (Vaks et al., 2006), while the total rainfall amount as recorded by $\delta^{18}\text{O}$ in the Mukalla record suggest the Holocene

was the 'driest' humid phase over the past 1.1 Ma (Nicholson et al., 2020). These data pose an important question: Why was the Holocene less humid than previous interglacials?

- Palaeoclimate archives from across Arabia (north and south), the Negev Desert, Sinai Peninsula, northeastern Africa, the Levant, the eastern Mediterranean sea, Red Sea, Gulf of Aden and the Arabian Sea record phases of increased humidity during periods of high northern hemisphere insolation over the past ~500 ka, comparable to the timing of humid phases in the western Nefud Desert. However, records beyond MIS 5 are rather scarce.
- That palaeoenvironmental archives from spatially widespread areas in the Arabian Peninsula, Levant and northeast Africa record humidity at similar time intervals during the Pleistocene suggests that increased humidity probably occurred in response to each northern hemisphere insolation peaks, and therefore synchronously, across the region in response to a combination of increased monsoonal rainfall and rainfall from other tropical sources. However, this hypothesis is difficult to test due to the age uncertainties. Moreover, there are some inconsistencies between records with evidence for humidity during MIS 3 and 6 in some records but not others.
- If synchronous humid periods did occur across northeast Africa, the Levant and Arabia, these could have allowed dispersals of fauna from Africa into Arabia and *vice versa*. This type of connectivity, where there are small distances that humans could traverse between freshwater resources, between northeast Africa and the western Nefud during MIS 5 has been proposed by Breeze et al. (2016).
- It is also likely northern and southern Arabia were connected by a more humid landscape in receipt of monsoonal rainfall (Nicholson et al., 2020), though further work is required in central Arabia to confirm this.
- Interconnected humid landscapes which were probably capable of supporting human habitation have clear implications for hominin dispersals over the past ~500 ka, and this topic is discussed in the next chapter.

Chapter 14 – Human demography and dispersals in the western Nefud Desert and Arabian Peninsula over the past ~500 ka

14.1 Introduction

The western Nefud Desert contained freshwater and perennial lakes during multiple humid phases over the past c. 500 ka, most probably related to precession peaks and, therefore, highs in NH summer insolation. Humidity was not confined to the western Nefud Desert, and well-dated palaeohydrological proxies across the Arabian Peninsula, Levant and NE Africa show humidity was widespread and possibly synchronous (see previous chapter). These orbitally-driven humid phases in present-day arid regions have played a key role in facilitating ancient human dispersals, range expansions and have been used to explain population structure across Africa and Arabia over the Pleistocene (Groucutt et al., 2015a; Scerri et al., 2019). This chapter will discuss the chronology and palaeohydrology of interdunal lakes in the western Nefud Desert in relation to human demographic processes over the past c. 500 ka in Northern Arabia. It will then go on to place the western Nefud Desert in the context of wider dispersal ‘pathways’ or ‘landscapes’ between Africa and Asia, through which hominins dispersed during periods of increased humidity.

14.2 Human history in the western Nefud Desert

The western Nefud Desert lies in northern Arabia and was probably accessible to hominin populations from the Sinai, the Levant and the Gulf during multiple humid phases over the past c. 500 ka. As such, it is likely to have had a complex demographic history, with multiple turnovers in hominin populations in response to wet and dry phases. Such population turnover is attested to by the presence of Lower Palaeolithic, Middle Palaeolithic and Holocene/Neolithic archaeology in direct association with palaeolake or playa deposits (Fig 14.1) (Breeze et al., 2017; Groucutt et al., 2018; Scerri et al., 2018a). Notably there is no evidence of Upper or Epi-Palaeolithic assemblages in the western Nefud Desert, though the latter has been reported at nearby Jubbah

(Hilbert et al., 2014). In addition to archaeological records, *H. sapiens* fossil material from the Nefud Desert has been dated to ~85 ka (Groucutt et al., 2018), hominin (likely *H. sapiens*) footprints have been recorded in sediments dating to ~120 ka (Stewart et al., 2020a), and evidence for butchery in the form of V-shaped cut marks in ungulate rib fragments has been dated to between ~300 – 500 ka (Roberts et al., 2018). While it is evident that the western Nefud Desert has been a locus for hominin activity, the timing of this activity and the way in which humans interacted with the landscape are poorly understood. To gain a better understanding of this it is critical to investigate the nature, scale and dynamics of Pleistocene palaeohydrological change in the region (Breeze et al., 2017). At the most basic level, it is important to consider whether interdunal lakes provided ‘drinkable’ freshwater resources or whether they contained saline waters. It is also important to consider whether waters were available year-round (perennial) or if they were seasonal (ephemeral). Furthermore, have interdunal lakes consistently provided the same resources in each humid phase, or have they varied? These questions have been answered in the preceding chapters, but are placed in the context of human demography and dispersals in northwestern Arabia here.

14.2.1 Drinkable, perennial water resources during the Middle and Upper Pleistocene

The ‘Water Optimisation Hypothesis’ argues that *Homo sapiens* (and hominin) demography and dispersal was heavily dependent on the availability and distribution of freshwater resources. Modern humans require ~3 litres of water a day in order to survive, and this requirement increases in hot semi-arid regions such as the Nefud Desert (Finlayson, 2013; Sawka et al., 2005). Evidence from the Arabian interior supports the Water Optimisation Hypothesis, since in this region the median distance of Middle Palaeolithic sites from palaeohydrologically modelled fluvial or lacustrine resources during humid phases is only 13.6 km (Breeze et al., 2015). The palaeoenvironmental analysis clearly demonstrates that during peak humid phases from MIS 5a to MIS 13/11, interdunal lakes within the western Nefud Desert repeatedly yielded fresh ‘drinkable’ water for humans and the prey that they may have been tracking.

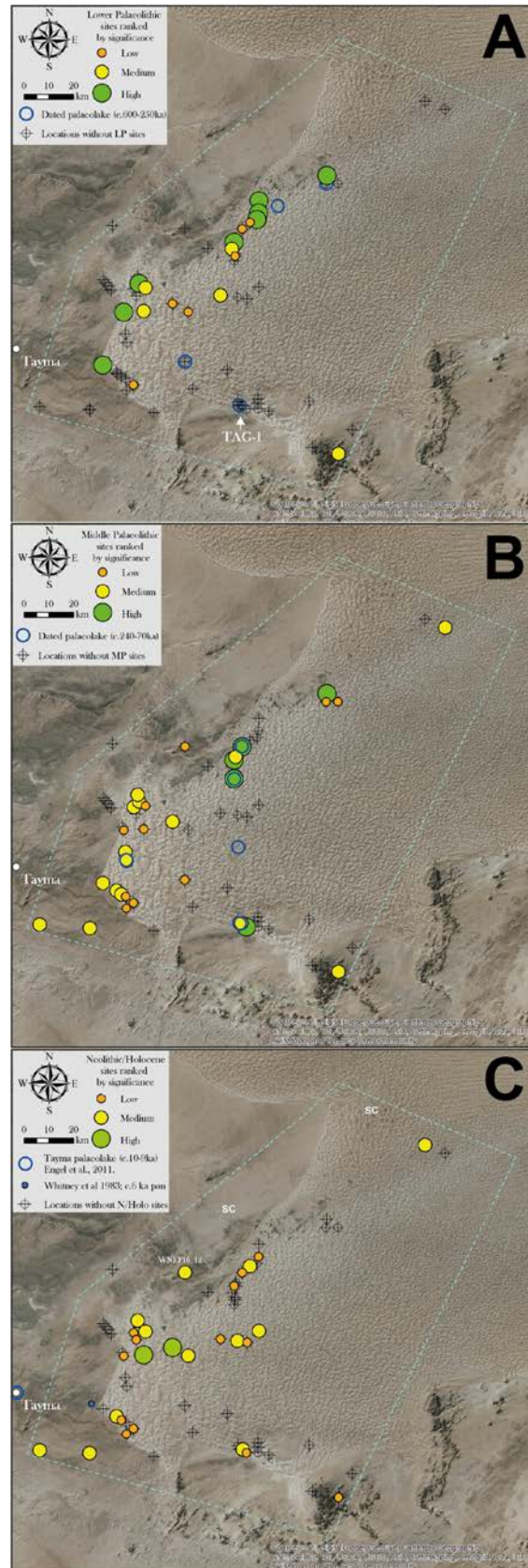


Figure 14.1 – Distribution of archaeological sites across the western Nefud Desert modified from Breeze et al. (2017). Green circles = high significance. Yellow circles = medium significance. Orange circles = low significance. Refer to Table 5.1 in Chapter 5 for discussion on significance. (A) Lower Palaeolithic sites. (B) Middle Palaeolithic sites. (C) Neolithic/Holocene sites. Note the higher frequency of sites in the interior of the the western Nefud Desert, despite limited humidity relative to Middle and Upper Pleistocene humid phases.

These freshwater resources were predominantly perennial, as shown by the dominance of homogenous or laminated microfacies with no evidence of pedogenesis or sub-aerial exposure (see Chapters 7 - 12). Such microfacies are present in units within all palaeolake deposits presented in this thesis. The existence of perennial waterbodies is further supported by the fossil assemblages at certain sites. For example, *Hippopotamus*, which requires permanent muddy, fluvial or lacustrine conditions (Estes, 1991) is present at Al Wusta, Site 16.3 and KAM4 lake 4 (Groucutt et al., 2018; Stewart et al., 2020b). Moreover, the presence of large-bodied fish (*Pisces oteoglossiformes*) (Thomas et al., 1998), Aves with aquatic affinities (grebe and duck) and large mammals such as Elephantidae (who live in large family groups and require up to 360 l of water a day) further indicate the presence of at least a large seasonal standing water body at Ti's al Ghadah (Stimpson et al., 2016; Stewart et al., 2019). The presence of perennial waterbodies demonstrates that the western Nefud would have been able to support year-round human occupation during humid phases from MIS 5a to MIS 13/11, by providing a reliable source of freshwater.

It is important to note that many sequences also show evidence for ephemeral lake conditions that precedes or follows the perennial stage of the lake body. For example, interdigitation of marl or diatomite (~2 – 6 cm thick) with siliclastic beds at the base of the lake sequences at the base of TAG 1, Unit 3 at KAM4 lake 1 and Alathar. Palustrine conditions are also present preceding the lacustrine marls at KAM4 lake 3a, and sandwiched between lacustrine marls at KAM4 lake 4. This evidence for ephemeral lake and palustrine environments suggest that water may have only been episodically available during intervals of lower effective precipitation. Nevertheless, the footprints at Alathar demonstrate that humans and other fauna (e.g. elephants) foraged on the exposed lakebed surface during periods of subaerial exposure (Stewart et al., 2020a). This indicates that humans utilised these environments during more arid phases, and not only during peak humid phases. It is also probable that mobile hunter-gatherers could utilise nearby 'hubs' with more reliable standing water resources such as Tayma (Dinies et al., 2015; Engel et al., 2011) and Jubbah (Parton et al., 2018; Petraglia et al., 2012, 2011) during climatic downturns (i.e. brief arid periods), as is argued to be the

case during the Holocene (Petraglia et al., 2020). It is also possible that the western volcanic highlands (e.g. Harrat Khaybar; Fig 14.2) provided a resource rich landscape during climatic downturns (Fig 14.2) (Groucutt, 2020). Holocene stone structures have been reported from these sites, and it is plausible that Middle and Upper Pleistocene humans may have inhabited these areas (Groucutt et al., 2020).

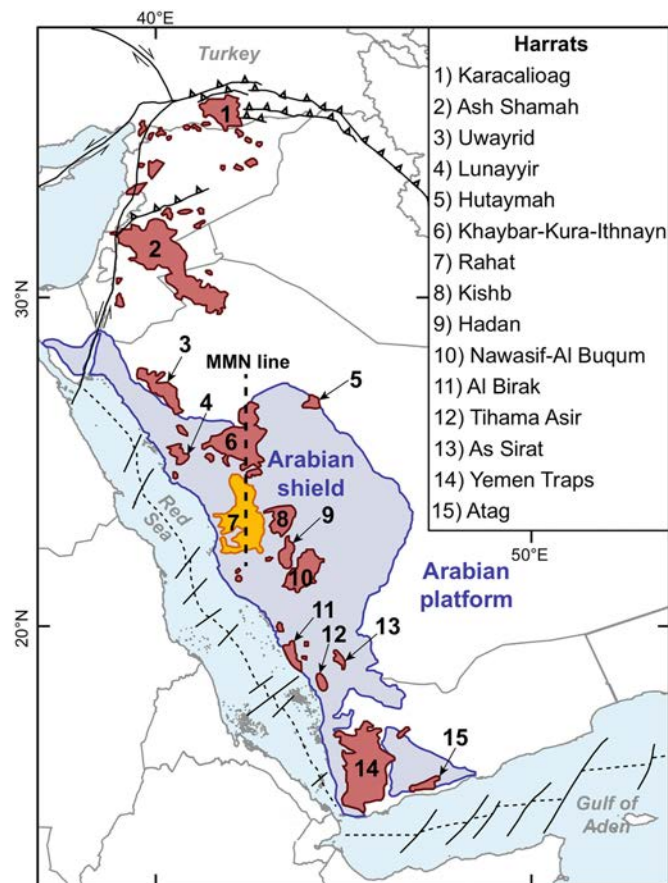


Figure 14.2 – Map of harrats of Arabia, taken from Groucutt et al. (2020). Note that Harrat Khaybar (6) lies immediately to the south of the western Nefud Desert, and may have provided a refugium during climatic downturns in the western Nefud Desert.

Here we also demonstrate that palaeolake sites in the western Nefud Desert are widespread, with evidence for freshwater availability in association with archaeology, cut-marked bone, human footprints or fossils in the southern (Al Wusta, TAG, WNEF16_28), south-central (Alathar) and northern (Site 16.3, KAM4) sections of the western Nefud sand sea. In addition to this, Rosenberg et al. (2013) show further freshwater sites dated to both MIS 5 and the Middle Pleistocene within the central portion (Site 16.5, Bi’r Hayzan), and the western edge (Sites 17.2 and 17.3) of the

western Nefud Desert, though they do not report archaeological material in association with these sites. Nevertheless, the ages of the sites reported by Rosenberg et al. (2013) broadly match with the ages for sites reported here that are in association with archaeology, though the uncertainties make it impossible to confidently correlate sites. Taken together, the sites reported in this thesis and Rosenberg et al. (2013) demonstrate that freshwater was available across the entire western Nefud Desert on several occasions during the last 500 ka. Freshwater was not restricted to isolated basins towards the edge of the sand sea.

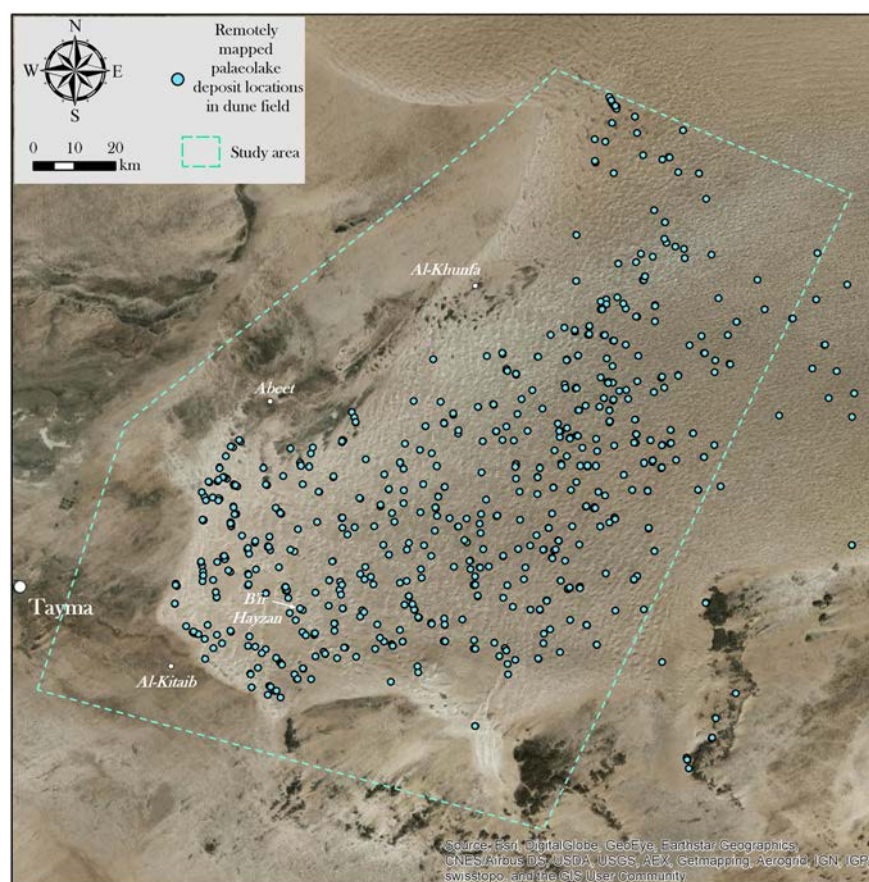


Figure 14.3 – The distribution of palaeolake deposits across the western Nefud Desert from Breeze et al. (2017) as mapped by multi-spectral classifications and GIS analysis (Breeze et al., 2015). It is probable that numerous interdunal lakes existed during each humid phase, based on the distribution of freshwater lakes presented in this thesis and by Rosenberg et al. (2013). Consequently, the entire western Nefud Desert was likely habitable during humid phases.

It is probable that each humid phase produced numerous freshwater interdunal lakes across the entire western Nefud Desert. The region is underlain by permeable sandstones (Rosenberg et al., 2013; Breeze et al., 2017) meaning that interdunal lake bodies do not form in association with freshwater springs/oases that could remain

active long into arid phases, but instead requires a regional rise in the water table in response to increased regional humidity. This implies that during each humid phase, an extensive system of groundwater connected but discrete surficial interdunal waterbodies may have existed in the western Nefud sand sea. This implication is supported by the spatial distribution of dated freshwater deposits outlined above, and also by spectral analysis using GIS software, which shows that interdunal palaeolake deposits are present throughout the entire western Nefud Desert (Fig 14.3) ($n = 730$, Breeze et al., 2015). It is also notable that Rosenberg et al. (2013) report numerous Middle and Upper Pleistocene age palaeolake deposits from the eastern Nefud, suggesting that the entire Nefud Desert may have been habitable during some humid periods. Further multi-proxy palaeoenvironmental work and archaeological exploration should be undertaken in the eastern Nefud Desert to test this hypothesis.

It is also important to consider whether there is a difference in the way hominins utilised the Nefud between the Middle Pleistocene, Upper Pleistocene and Holocene humid phases, and if there is a difference whether or not this was driven by hydrological differences or other factors. Breeze et al. (2017) show that sites with Lower Palaeolithic archaeological assemblages are restricted to the edge of the present-day dune field, with only a single site 20 km into the dune field (Fig 14.1, A). Conversely, Middle Palaeolithic assemblages are more widespread (Figure 14.1, B). This pattern suggests that hominins using Middle Palaeolithic technologies were more mobile than those using Lower Palaeolithic toolkits. Until now it has not been clear whether Middle Palaeolithic populations were more mobile than their predecessors due to some technological or cultural adaptation, or whether they benefitted from greater resource availability during humid phases. The results here show that there is little difference in the palaeohydrology between sites associated with Lower Palaeolithic assemblages (e.g. KAM4 basin sites) and Middle Palaeolithic assemblages (e.g. Site 16.3, Al Wusta, WNEF16_28), with all containing freshwater perennial deposits. The resources were also likely to have been widespread across the western Nefud Desert during each humid phase, as discussed above. Consequently, the difference between the spatial distribution of Lower and Middle Palaeolithic assemblages probably relates to some aspect of behaviour or technology that enabled greater mobility. Breeze et al. (2017)

suggests that raw material availability was a constraining factor for Lower Palaeolithic hominins, since almost all sites are close to raw material sources. The single Lower Palaeolithic site further into the dune field also contains outcropping bedrock (Breeze et al., 2017). In contrast, Middle Palaeolithic assemblages do not appear to be constrained by raw material availability suggesting that Middle Palaeolithic humans were more mobile, perhaps as a result of technological innovation or greater social networks (Breeze et al., 2017).

14.2.2 Human activity during the Holocene humid phase

The Holocene differs from previous humid phases in that it does not appear to be wet enough to lead to interdunal lake development in the western Nefud Desert. This suggests that during the Holocene, the area experienced a distinctly different environment from previous humid phases. Nevertheless, it is probable that the regional water table was close to the dune surface since a region wide increased humidity and rainfall increase of 300% is recorded during the Holocene (Engel et al., 2011). Under these conditions, heavy rainfall events could readily lead to ephemeral (perhaps seasonal) standing waterbodies (recharge playas) within interdunal depressions, such as that at Al Wusta Playa (Chapter 7). Consequently, the western Nefud sand sea did provide ephemeral freshwater resources for humans during the Holocene humid phase.

Archaeological evidence demonstrates that highly mobile hunter gathers and pastoralists utilised resources within the western Nefud sand sea between ~9 – 5.3 ka (Fig 14.4; Alshabah). The site of Alshabah, deep within the western Nefud sand sea, shows humans practising mobile pastoralism between 6.5 ± 0.7 ka and 7.3 ± 0.9 ka based on luminescence dating of hearths and ^{14}C dating of charcoal (Scerri et al., 2018a). Undated sites in the same area contain hearths, ostrich eggshell fragments, grindstone fragments, arrowheads and pottery (Breeze et al., 2017). The presence of hearths and lack of architectural structures within the sand sea are indicative of mobile populations that may have had an extensive knowledge of the landscape and were consequently able to take advantage of localised rainfall events and surface water availability (Petraglia et al., 2020). Evidence for contemporary highly mobile populations to the east

of the western Nefud sand sea comes from Jebel Oraf 2 and Jebel Oraf rockshelter, where numerous hearths and archaeological material dated to between ~ 7.2 ka to 6.3 ka, indicating repeated occupation of the area (Guagnin et al., 2020, 2017).

Taking this evidence together, it is clear that highly mobile hunter-gatherers and pastoralists exploited seasonal standing waterbodies in the western Nefud sand sea and other nearby areas during the Holocene humid phase between $\sim 9 - 5.3$ ka. During arid seasons or years where surface freshwater was not available, populations would have been able to access freshwater 'hubs' at Jubbah and Tayma Oases where shallow aquifers in combination with developing water management techniques provided reliable resources during periods of aridity (Petraglia et al., 2020). Such a strategy, where sand seas were only accessed seasonally, is distinct from that of earlier humid phases where the sand seas contained perennial freshwater sources.

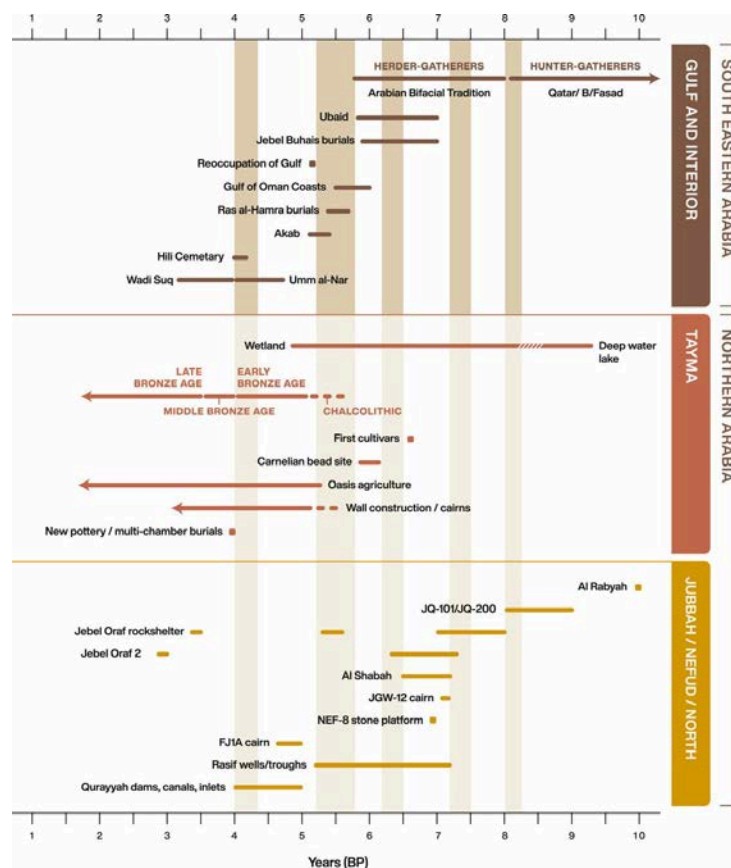


Figure 14.4 – Key dated Holocene archaeological sites and cultural transformations across the Arabian Peninsula from Petraglia et al. (2020) and references therein. The site of Al Shabah lies in the western Nefud Desert and shows humans practising mobile pastoralism between 6.5 ± 0.7 ka and 7.3 ± 0.9 ka, where they likely took advantage of ephemeral standing water bodies on playa surfaces, such as that represented by Al Wusta Playa (Chapter 7).

As the climate became more arid in the later Holocene, freshwater was no longer available in the western Nefud sand sea, and expeditions into the region presumably became rare or ceased altogether. The playa sediments at Al Wusta Playa (4.3 ± 0.3 ka) suggests that standing water may occasionally have been available at this time. However, it is not clear whether contemporaneous populations would have had the desire or ability to use these resources in the light of a societal shift towards investment in singular places (Petraglia et al., 2020).

14.2.3 Summary

The evidence presented above demonstrates that the western Nefud sand sea has repeatedly been a habitable environment, littered with perennial freshwater sources during several humid phases which occurred between c. 80 – 500 ka. Conversely, only ephemeral water bodies existed during the Holocene. The archaeological (Scerri et al., 2015; Groucutt et al., 2018), ichnological (Stewart et al., 2020a) and fossil (Stimpson et al., 2015, 2016; Groucutt et al., 2018; Stewart et al., 2017, 2019, 2020b) evidence directly associated with Middle and Upper Pleistocene deposits demonstrate that humans and other fauna repeatedly took advantage of perennial freshwater sources. This raises two important questions regarding the region's role in wider hominin demography and dispersals. Did the Nefud Desert form part of a continental dispersal landscape, enabling hominins to disperse across the Arabian interior? Was such a landscape available on multiple occasions, supporting several *Homo sapiens* expansions beyond Africa during the Middle/Upper Pleistocene? These questions will be addressed in the following section.

14.3 The western Nefud Desert as part of a wider dispersal route out of Africa

The timing and routes of human dispersals and movements between Africa, Arabia and Asia are a key but debated topic within human evolutionary studies. The western Nefud Desert lies in a critical region for such dispersals as it is situated ~550 km southwest of the Sinai Peninsula, the only terrestrial connection between Africa and Arabia since the

Miocene (Fernandes et al., 2006). This section will address the way in which the western Nefud has played a key role in wider patterns of human movement over the past 500 ka. Three aspects of human movement will be discussed: 1) a continental dispersal route using palaeohydrological corridors; 2) Middle Pleistocene hominin population dynamics (MIS 13 - 7), and 3) Multiple *Homo sapiens* dispersals (MIS 9 – MIS 5a).

14.3.1 A continental dispersal route using palaeohydrological corridors – the western Nefud Desert as part of a wider habitable landscape.

Two major hypotheses have been proposed regarding dispersal pathways used by *Homo sapiens* between Africa and Eurasia, though these hypotheses are also relevant to earlier hominin movements during the Middle Pleistocene. The first hypothesis invokes a coastal route where nearshore freshwater resources were utilised, possibly combined with marine resources, during periods of lower global sea level (Stringer, 2000). Coastal dispersals may have either a) tracked along the southern Arabian coastline after crossing the southern Red Sea before following the Indian Ocean rim to Sahul (Lambeck et al., 2011; Macaulay et al., 2005; Rasmussen et al., 2011; Stringer, 2000) or b) followed the western Arabian coastline after a northern exit from Africa via the Sinai Peninsula (Bailey et al., 2015).

Alternatively, the second hypothesis proposes a continental route where humans tracked interior freshwater highways (palaeorivers and palaeolakes) activated during periods of orbitally-driven humidity in the Saharo-Arabian desert belt (Breeze et al., 2016; Scerri et al., 2014a). Potential routes include the 'Tabuk corridor', a palaeohydrological corridor connecting northeast Africa to the western Nefud Desert following a northern exit from Africa (see Fig 14.5) (Breeze et al., 2016) or routes that track eastwards or northwards across the Arabian Peninsula after crossing the southern Red Sea (Armitage et al., 2011). The latter routes are more poorly defined relative to the northern route. However Lower and Middle Palaeolithic archeological assemblages are present along the southern route (Groucutt et al., 2015d; Groucutt and Petraglia, 2012), freshwater resources were available in the Rub al Khali (Groucutt et al., 2015d; Rosenberg et al., 2011) and climate models show southern and central Arabia were in

receipt of increased monsoonal rainfall (Jennings et al., 2015) during relevant time periods. Implicit in all dispersal models is the assumption that access to freshwater facilitated dispersal, either via coastal springs during periods of lowered sea-levels (coastal routes) or surface freshwater in wetter climates (continental routes).

Here we have demonstrated that over the past 500 ka, the western Nefud Desert repeatedly contained perennial freshwater bodies. Archaeological and fossil records demonstrate that the area was also a locus of human activity. As such, the western Nefud consistently formed a habitable region that was an important part of a wider dispersal landscape across the interior of the Arabian Peninsula. This may have been part of the southern dispersal route, where humans tracked monsoonal rains northwards after crossing the southern Red Sea. However, current archaeological and fossil evidence suggests it is most probable that *Homo sapiens* reached the western Nefud from Africa via a northern route, crossing the Sinai Peninsula and traversing the Tabuk Corridor (Breeze et al., 2016).

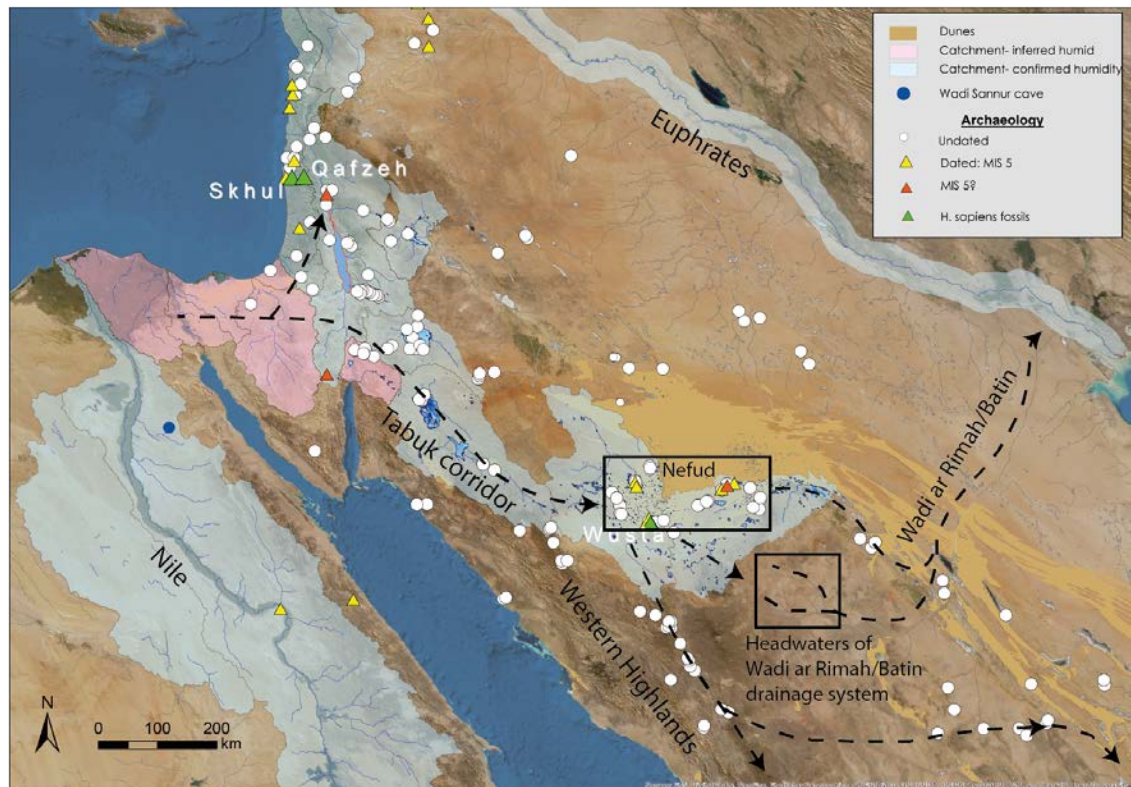


Figure 14.5 - The archaeological and palaeohydrological context of the Nefud Desert focused on MIS 5, though such a route is plausible for other humid phases. Dashed lines represent potential continental dispersal routes. Note that the "Tabuk corridor" leads from the Levant/Sinai to the Nefud Desert. The dashed lines extending beyond the south-eastern end of the Tabuk corridor show a plausible but unconfirmed dispersal routes across the Arabian Peninsula,

with one utilising the Wadi ar Rimah/Batin drainage system. Homo sapiens fossil sites (green triangles), archaeological sites dated to MIS 5 (yellow triangles), archaeological sites assumed to be MIS 5 in age (red triangles) and undated Middle Palaeolithic sites (white circles) after Breeze et al. (2016). The western Nefud Desert is highlighted by a black rectangle. The headwaters of the Wadi ar Rimah/Batin drainage system are highlighted by a black square that lies to the south-east of the Nefud Desert. The Nile and Euphrates catchments are also shown, as is the location of Wadi Sannur Cave which is discussed in text. Catchments with inferred humidity (pink shading) are regions where humidity has not been directly observed but where humidity has been observed immediately west or east of the catchment (Breeze et al., 2016). Catchments with confirmed humidity (blue shading) are regions where dated palaeoenvironmental evidence demonstrates increased humidity in the catchment (Breeze et al., 2016).

Assuming the humans entered the Nefud from a northern route, it is likely that they would be able to move further southwards into a landscape receiving increased monsoonal rainfall. While moving southwards, they may have met a series of major transcontinental west-east flowing drainage systems, activated during phases of maximum monsoonal rainfall (Fig 14.5). Such systems would have formed a freshwater highway that cut through the interior of the Arabian Peninsula to the Gulf, and provided a route to southern and eastern Asia (Breeze et al., 2015; Matter et al., 2016). While several drainage systems may have provided routes across the Arabian Peninsula, a particularly plausible candidate is the Wadi ar Rimah/Batin, since it is associated with undated Middle Palaeolithic archaeology (Groucutt and Petraglia, 2012). Consequently, dating the Wadi ar Rimah/Batin drainage system and associated archaeology should be considered as a priority for future research.

While it is evident that the western Nefud Desert experienced multiple humid phases over the past 500 ka, the number of dated palaeoenvironmental archives predating MIS 5 is small, making it difficult to demonstrate that habitable dispersal landscapes existed during earlier humid intervals. Nonetheless, the record of increased humidity during the Middle Pleistocene from the western Nefud Desert (this thesis and references cited herein), southern Arabia (Nicholson et al., 2020) and northeast Africa (El-Shenawy et al., 2018) suggests that such landscapes were present. These landscapes enabled episodic population connectivity between African and non-African populations, as well as providing a dispersal route between Africa and Eurasia. The importance of humid phases for Middle and Upper Pleistocene population dynamics, and the role of the western Nefud Desert, is discussed below.

14.3.2 Middle Pleistocene hominin population dynamics

The Middle Pleistocene (~781 – ~130 ka) contains a number of important events in hominin prehistory where the Arabian Peninsula and the Nefud Desert may have played a role. It is during the Middle Pleistocene that it is argued *Homo sapiens* and *Homo neanderthalensis* split from their last common ancestor (LCA) sometime between 400 – 765 ka (Arsuaga et al., 2014; Endicott et al., 2010; Martínón-Torres et al., 2012; Stringer, 2016, 2012). The LCA is debated (Grün et al., 2020) though is often considered to be *Homo heidelbergensis* or *Homo rhodesiensis* (Stringer, 2016). Profico et al. (2016) suggest an African origin of *Homo heidelbergensis*, based on the Melka Kinture fossils from Gombore II, Ethiopia, dated to ~850 ka by $^{40}\text{Ar}/^{39}\text{Ar}$ on fine-grained volcanic ash. If *Homo heidelbergensis* did originate in Africa, then the timing of the species' dispersal into Eurasia becomes an important question and one that may be relevant to the timing of humid periods in the Saharo-Arabian desert belt.

Models for the timing for hominin dispersals during the Middle Pleistocene have predominantly focused on climatic conditions of east Africa (deMenocal, 1995; Maslin et al., 2014) or Eurasia (Muttoni et al., 2010; Kahlke et al., 2011), with little consideration for Saharo-Arabian climatic conditions (Nicholson et al., 2020). However, the role of Saharo-Arabian climatic conditions has been brought into focus by recent research revealing repeated humid intervals in southern Arabia over the past 1.1 Ma (Nicholson et al., 2019). Nicholson et al. (2020) argue that 'frequent windows of opportunity' arose for hominin migrations across the Saharo-Arabian belt due to increased monsoonal rainfall as recorded via speleothem growth in southern Arabia. The record from the western Nefud Desert presented here corroborates the speleothem evidence over the past 500 ka. Ancient but undated iron indurated deposits at Ti's al Ghadah (Stewart et al., 2019) suggest humidity before 500 ka and likely correlate to one or more Southern Arabian Humid Phases (SAHPs) observed in the Y99 speleothem record from Mukalla Cave. Crucially, the palaeolake records from the western Nefud Desert record the landscape at the scale at which humans interact. They demonstrate that the increased effective precipitation during humid phases, as recorded in speleothems, yielded a landscape that provided perennial freshwater resources and would have supported

year-round occupation in the Arabian Peninsula for species such as *Homo heidelbergensis* during the Middle Pleistocene.

Evidence that Middle Pleistocene hominins expanded into the Arabian Peninsula and utilised freshwater resources is provided by the presence of Acheulean stone tool assemblages (Lower Palaeolithic) at multiple sites in the western Nefud Desert (e.g. Scerri et al., 2015). This includes KAM4, where perennial freshwater bodies have been dated to MIS 13a/11 (KAM4 lake 1), MIS 9 (KAM4 lake 2) and MIS 7 (KAM4 lake 4). However, at KAM4 and elsewhere in the Arabian Peninsula, the archaeology is found on the surface, making it difficult to directly correlate it with the lake deposit upon which it was found. This is a constant issue in arid/semi-arid environments, where deflation means archaeology is found on land surface rather than in section and therefore lacks stratigraphic or chronological control (Scerri et al., 2018). Further evidence for Lower Palaeolithic hominin occupation within the western Nefud Desert comes from TAG, where V-shaped cut marks on ungulate rib fragments were found within Unit 5 (Roberts et al., 2018), which dates to between 300 – 500 ka (Rosenberg et al., 2013; Stimpson et al., 2016).

Achuelean assemblages are also present elsewhere in the Arabian Peninsula at Dawadmi in central Arabia (Scerri et al., 2018b; Shipton et al., 2018), Wadi Fatimah in western Arabia (Groucutt and Petraglia, 2012) and various other locations (see Fig 4 in Groucutt and Petraglia, 2012), though as at KAM4 precise chronological control is difficult to establish for these sites. The best dated Achuelean artefacts are from Saffaqah in central Arabia, where they were found in section and have been dated to MIS 7, providing a terminal Achuelean age of ~190 ka (Scerri et al., 2018). If it is assumed that the Achuelean artefacts from KAM4 are the same age as the lake deposits upon which they were found, then combined with Saffaqah, they suggest that there were multiple excursions into the western Nefud Desert and wider Arabian Peninsula associated with multiple humid phases.

Acheulean assemblages across the Arabian Peninsula show varying technological traits. For example, the Acheulean complex at Saffaqah does not resemble that found in the

southwestern Nefud, but does resemble late Acheulean sites in eastern Africa. Conversely, the southwestern Nefud Acheulean is more similar to the late Acheulean in the Levant (Scerri et al., 2018). This latter point may attest to a ‘freshwater highway’ connecting the two regions during humid phases, as is demonstrated during MIS 5 by the ‘Tabuk’ corridor (Breeze et al., 2016). The spatial variability in Acheulean techno-complex across the Arabian Peninsula supports the idea of multiple hominin expansions into the Arabian Peninsula associated with humid intervals. Whether these populations became locally extinct or retreated to refugia as aridity returned is unclear. The episodic hydrological connectivity between Africa, Arabia and Asia may have facilitated gene flow and interaction between hominin populations from each of these regions through the Middle Pleistocene. If this is the case, then it is consistent with descriptions of a ‘pan-African’ origin for *Homo sapiens*, whereby anatomically modern humans derived from shifting structured populations that were episodically connected/disconnected following environmental shifts (Scerri et al., 2014, 2018, 2019).

14.3.3 Multiple *Homo sapiens* dispersals (MIS 9 – 5a dispersals)

While the lineage of *Homo sapiens* originated between ~400 – 700 ka (Stringer, 2016), the first early *Homo sapiens* (i.e. species with a mixture of modern human and primitive features) appear across Africa approximately ~300 ka ago at Jebel Irhoud, Morocco (Hublin et al., 2017) and ~260 ka at Florisbad, South Africa (Grün et al., 1996) (Fig 14.6, C). This suggests a pan-African origin of *Homo sapiens*, where discrete *Homo sapiens* populations existed across the African continent and occasionally experienced connectivity and gene flow (Scerri et al., 2014, 2018, 2019). The first appearances of early *Homo sapiens* beyond Africa occur at ~210 ka (MIS 7) at Apidema Cave, Greece (Harvati et al., 2019) and between 177 – 194 ka (MIS 7 – 6e) at Mislaya Cave in the Levant (Hershkovitz et al., 2018) (Fig 14.6, D and E), though the dating of the latter is debated (Sharp and Paces, 2018). Further *Homo sapiens* fossils have been dated to between ~90 – 120 ka MIS 5 from Skhul and Qafzeh Caves in the Levant (Fig 14.6, E) (Groucutt et al., 2019; Mercier et al., 1993; Mercier and Valladas, 2003; Schwarcz et al., 1988; Stringer et al., 1989; Valladas et al., 1988). This evidence suggests that there were multiple *Homo*

sapiens expansions into western Asia and southeastern Europe between ~210 – 80 ka ago, possibly associated with humid phases during MIS 7 and MIS 5.

The record from the western Nefud Desert presented in this thesis and associated publications (Groucutt et al., 2018; Stewart et al., 2020a) shows that *Homo sapiens* expanded into the Arabian Peninsula multiple times between ~130 – 80 ka. At Al Wusta, a *Homo sapiens* fossil is dated to between ~85 – 95 ka (Groucutt et al., 2018), while footprints of potentially *Homo sapiens* origin are dated to between 102 – 132 ka at Alathar (Stewart et al., 2020a) (Fig 14.6, F). Further sites with Middle Palaeolithic assemblages date to discrete periods of MIS 5, with Site 16.3 dating to 86 ± 6 ka and WNEF16_28 to between 133 ± 10 ka and 117 ± 8 ka. It is important to note that Middle Palaeolithic assemblages display very similar characteristics, focussing on centripetally prepared Levallois technology (Scerri et al., 2015). As this technology has now been found directly associated with a *Homo sapiens* fossil at Al Wusta (Groucutt et al., 2018), it is reasonable to suggest that *Homo sapiens* were the makers of other MIS 5 Middle Palaeolithic assemblages across the western Nefud.

There is also a single lacustrine record, KAM4 lake 4, that dates to between 172 – 226 ka (MIS 7/6e) in the western Nefud Desert. If *Homo sapiens* did utilise the western Nefud Desert during MIS 7, then it is notable that this would overlap with the Acheulean complex in central Arabia at Saffaqah (Scerri et al., 2018b). This may suggest multiple hominin species were present on the Arabian Peninsula at the same period. This is consistent with observations in Africa where *Homo heidelbergensis*, *Homo naledi* and *Homo sapiens* coexisted and Eurasia where *Homo neanderthalensis*, *Homo denisova*, *Homo floresiensis* and *Homo erectus* coexisted (Stringer, 2016).

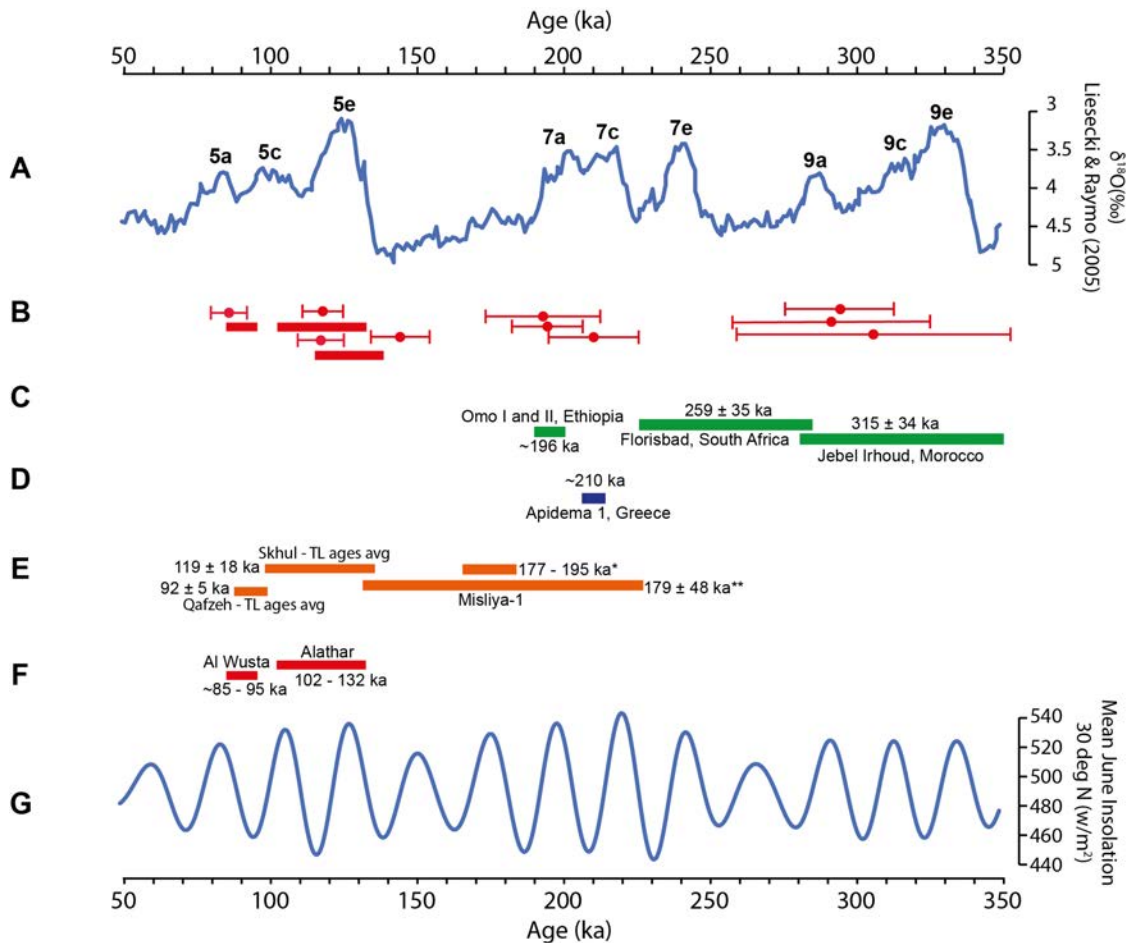


Figure 14.6 – Key points in *Homo sapiens* origin and out-of-Africa dispersals relative to directly dated wetland sediments from the western Nefud Desert. (A) LR04 marine $\delta^{18}\text{O}$ stack (Lisiecki and Raymo, 2005). (B) Directly dated wetland sediments from the western Nefud Desert produced as part of this thesis, Clark-Balzan (per comms), Groucutt et al. (2018), Stewart et al. (2020a) and Rosenberg et al. (2013). (C) Dates of earliest fossils attributed to the *Homo sapiens* clade from Africa. Jebel Irhoud age is a weighted average of thermoluminescence (TL) ages directly associated with the *Homo sapiens* fossil (Richter et al., 2017). Florisbad age is calculated from the weighted mean of ESR measurements on a hominin tooth recorded in stratigraphic position (Grun et al., 1996). Omo I and II ages estimated based on $^{40}\text{Ar}/^{39}\text{Ar}$ ages from the dates from the Nakaa'kire Tuff in Member 1 in the Kibish Formation (Aubert et al., 2012; McDougall et al., 2005). (D) Apidema 1 *Homo sapiens* fossil crania from Greece, the earliest evidence for *Homo sapiens* outside of Africa. The age of ~210 ka is a minimum age based on U-series dating of the Apidema-1 fossil (Harvati et al., 2019). (E) Ages of *Homo sapiens* fossils from the Levant. Misliya-1 is a fossil maxilla (jaw bone) and the age range of 177 – 195 ka* is based on the U/Th date providing a minimum age and the U-ESR date providing a maximum age. However, this age is debated (Sharp and Paces, 2018). More robust is the average age of the TL dates on burnt flints in association with the fossil, which yields an age of 179 ± 48 ka**. The Skhul and Qafzeh ages represent the timing of *Homo sapiens* occupation of the Levant during MIS 5 based on average thermoluminescence (TL) ages. (Mercier et al., 1993; Valladas et al., 1988). These are deemed the most reliable age estimates for each site (Groucutt et al., 2019). (F) Evidence for *Homo sapiens* occupation of the western Nefud Desert. The *Homo sapiens* fossil from Al Wusta is dated to between ~85 – 95 ka based on a Bayesian age model (Groucutt et al., 2018). *Homo sapiens* footprints at Alathar were dated to between 102 – 132 ka based on the minimum and maximum ages at 1σ of the two direct OSL ages from the Alathar lake (Stewart et al., 2020a). (G) Summer insolation at 30°N (bottom, blue line) (Berger and Loutre, 1991).

14.4 Summary

This chapter has discussed the palaeoclimatic record from the western Nefud Desert and the Arabian Peninsula in the context of hominin demographic history over the past ~500 ka. Key points are:

- The hominin demographic history of the western Nefud Desert is complex, driven by episodic humid phases over the past ~500 ka.
- A combination of palaeoenvironmental, archaeological, ichnographical and fossil analysis demonstrates that multiple and discrete hominin populations, from *Homo sapiens* to earlier species (potentially *H. heidelbergensis*) have repeatedly utilised freshwater and perennial resources, before being driven out of the area due to environmental aridity.
- Combining this record with wider palaeoenvironmental and archaeological analysis across the Arabian Peninsula, northeast Africa and the Levant shows the western Nefud Desert played a key role in facilitating hominin dispersals across the interior of the Arabian Peninsula during the Middle and Upper Pleistocene.
- The periodic hydrological connectivity between Africa, Arabia and the Levant may have also facilitated admixture between distinct hominin populations, making northern Arabia a critical location for understanding hominin evolutionary history.

Chapter 15 - Conclusion

15.1 Conclusions and key findings

This work has focused on reconstructing the timing and past environments of humid phases in the western Nefud Desert, Saudi Arabia, over the past ~500 ka. To do this, this thesis has applied geochronological and multi-proxy paleoenvironmental analysis to carbonate and siliceous sediments, interpreted as palaeolakes, preserved in interdunal basins across the western Nefud Desert. The main findings of this work are:

- The luminescence chronology shows interdunal lakes most likely formed during multiple humid phases over the past ~500 ka that occurred during warm marine isotope stages (e.g. MIS 5e, 7, 9 and 11/13a) and sub-stages (e.g. MIS 5a) when northern hemisphere summer insolation was high.
- There were at least two discrete periods of interdunal lake formation in the western Nefud Desert during MIS 5.
- Sedimentological analysis shows that the majority of sedimentary sequences were composed of fine-grained carbonate-rich marls. The only exception to this is Alathar, which is composed of sandy-silt diatomite with no carbonate present. Additionally, evaporites such as gypsum or halite are rarely present, and where they do occur they are usually less than 5% by weight.
- Microfacies analysis shows that the fine-grained carbonate rich marls are predominantly composed of homogenous or laminated microsparite/micrite with no evidence of pedogenic alteration or desiccation. This implies that the sediments were deposited on the beds of perennial lacustrine waterbodies, rather than in palustrine systems where the sediment bed would be sub-aerially exposed, and the primary sediment modified.
- Stable oxygen and carbon isotope analysis of the carbonate sequences shows that there is no significant covariance between oxygen and carbon. The $\delta^{18}\text{O}$ data from individual sites have small ranges (>5‰) through the sequence, and there are rarely significant shifts in the $\delta^{18}\text{O}$ through sequences. This suggests lake bodies were hydrologically stable and non-evaporitic, with inflows balancing outflows. $\delta^{13}\text{C}$ values predominantly lie between +3‰ and -1‰, typical of

lacustrine systems in equilibrium with atmospheric CO₂ (Leng and Marsahll, 2004).

- Diatom palaeoecology carried out by colleagues supports the presence of non-evaporitic and perennial waterbodies, as assemblages predominantly consist of freshwater species.
- Overall, interdunal lakes dated to MIS 11, 9, 5e and 5a show very little variability, with all palaeoenvironmental analysis suggesting they represent simple transgressive-regressive sequences where water levels rise, remain stable for a period of time and then fall. At peak humidity these sequences represent perennial waterbodies, while they were freshwater throughout their existence as demonstrated by the lack of evaporates, lack of isotopic covariance and dominance of freshwater diatom species.
- A single interdunal lake dated to MIS 7 shows greater sedimentary complexity, with a sequence that transitions from a lacustrine to a palustrine to a spring-fed tufa system. This represents an initial rise, then fall, then rise in the water table within a single humid phase. This is not observed in any other sequence, and it is not clear why this sequence is different from the others in the western Nefud.
- There is no evidence of lake marls dating to the Holocene, though the sedimentology at the Al Wusta Playa shows evidence for Holocene aged silty-sands with gravel inclusions that represent an ephemeral waterbody. Importantly, the presence of a 1 m thick bed of MIS 5a aged marls at the same site (Al Wusta) but higher in the landscape directly demonstrates that the water table was higher during this period than the Holocene. Consequently, the Holocene climate was less wet than climates during other humid phases over the past 500 ka. This is consistent with palaeoenvironmental data from across the Arabian Peninsula which also suggest humidity was lower during the Holocene (e.g. Nicholson et al., 2020).
- Perennial and freshwater lakes during the Middle and Upper Pleistocene contained drinkable water, which repeatedly provided resources for dispersing humans and their prey over the past ~500 ka. The occurrence of repeated human occupations of the western Nefud is evidenced by a *Homo sapiens* fossil at Al

Wusta dated to MIS 5a (Groucutt et al., 2018), hominin footprints on the surface of Alathar palaeolake dated to MIS 5e (Stewart et al., 2020a), butchery at Ti's al Ghadah dated to MIS 9 (Roberts et al., 2018) and Lower and Middle Palaeolithic and Holocene/Neolithic archaeology (Scerri et al., 2015) across the region.

- The existence of perennial lakes in the western Nefud Desert provided year-round resources for hominins and their prey during peak humidity during a number of humid phases.
- The presence of human footprints on the surface of Alathar palaeolake deposit suggest that humans were also present in the region during dry periods towards the end of humid phases where waterbodies had contracted (Stewart et al., 2020a). It is likely that humans and fauna were attracted to such watering holes as aridity increased and freshwater resources in the western Nefud Desert dwindled (Stewart et al., 2020a).
- Repeated resource availability in the western Nefud Desert demonstrates that continental dispersal routes, which have historically been overlooked in favour of coastal routes owing to the assumption that the Saharo-Arabian desert would be inhospitable, have provided a habitable landscape multiple times over the past 500 ka. This is consistent with the existence of repeated early *Homo sapiens* expansions beyond Africa between MIS 7 – 5a.
- Perennial freshwater lakes in the western Nefud Desert also demonstrates that “humidity”, as identified from marine and speleothem records across the Saharo-Arabian region, does actually translate into a habitable landscape in the presently hyper-arid Nefud Desert.
- The Nefud lies close to the headwaters of a major west-east drainage system leading to the Gulf. Assuming that this system was activated during humid phases, it is probable that human populations present in the Nefud were able to disperse further into Eurasia.

15.2 Future work

The palaeohydrological record of the western Nefud Desert demonstrates that the continental interior of the Arabian Peninsula provided a landscape through which

humans could disperse. Palaeohydrological modelling demonstrate major west-east drainage systems likely ran across the Arabian interior to the Gulf during humid periods providing 'freshwater highways' (Breeze et al., 2015). Undated Middle Palaeolithic archaeology has been found along the course of these systems (Groucutt and Petraglia, 2012), and empirical paleoenvironmental evidence also suggests that they were active during the Holocene (Matter et al., 2016). Future work should therefore focus on identifying and dating fluvial sections in association with Middle Palaeolithic archaeology. This offers the opportunity to identify specific continental routes along which humans may have dispersed from Africa to central and eastern Asia.

Questions also remain as to the source of moisture to northern Arabia during humid phases. The palaeolakes presented here are predominantly composed of authigenic carbonate, and were formed by non-evaporitic lacustrine waterbodies. Consequently, $\delta^{18}\text{O}$ analysis has the potential to answer broader palaeoclimatic questions about the source of moisture to the region. However, in order to conduct this analysis, it is necessary to assume that the $\delta^{18}\text{O}$ of carbonate accurately represents the isotopic signature of the lake water. This assumption is problematic in the geological record, where no modern analogue exists, because the temperature at which calcite is precipitated is unknown but exerts a major influence on the $\delta^{18}\text{O}$ composition of calcite. Clumped isotope analysis provides the opportunity to overcome this by providing estimates of lake water temperature (Bernasconi et al., 2018; Eiler, 2011). Consequently, it may be possible to back calculate the $\delta^{18}\text{O}$ of lake water, and therefore the isotopic signature of precipitation, assuming limited evaporitic enrichment. The $\delta^{18}\text{O}$ of precipitation can then be used as a proxy for moisture source, with more depleted values probably indicating an African monsoon source, and more positive values related to systems such as the Mediterranean westerly rainfall (Nicholson et al., 2020). Combining this data with $\delta^{18}\text{O}$ of fluid inclusions from southern Arabia (Nicholson et al., 2020) and focusing on a specific humid period (e.g. MIS 5e), would make it possible to estimate the amount of rainfall across the Arabian Peninsula during a particular time interval. This approach assumes that $\delta^{18}\text{O}$ values of precipitation are controlled by the amount effect. The output of such analysis could be compared to isotope-enabled

climate models, which are typically poor at reconstructing tropical rainfall. The potential of clumped isotope analysis on western Nefud Desert carbonates is promising, based on preliminary analysis from WNEF16_28.

Bibliography

- Abell, P.I., Williams, M.A.J., 1989. Oxygen and carbon isotope ratios in gastropod shells as indicators of paleoenvironments in the afar region of ethiopia. *Palaeogeogr. Palaeoclimatol. Palaeoecol.* 74, 265–278. [https://doi.org/10.1016/0031-0182\(89\)90065-5](https://doi.org/10.1016/0031-0182(89)90065-5)
- Adamiec, G., Aitken, M., 1998. Dose-rate conversion factors: update. *Anc. TLL* 16, 37–50.
- Aitken, M.J., 1998. An introduction to optical dating: The dating of Quaternary sediments by the use of photon-stimulated luminescence. Oxford Sci. Publ.
- Aitken, M.J., 1985. Alpha particle effectiveness: numerical relationship between systems. *Anc. TL* 3, 22–25.
- Aitken, M.J., Bowman, S.G.E., 1975. Thermoluminescent Dating: Assessment of Alpha Particle Contribution. *Archaeometry* 17, 132–138. <https://doi.org/10.1111/j.1475-4754.1975.tb00127.x>
- Aitken, M.J., Xie, J., 1990. Moisture correction for annual gamma dose. *Anc. TL* 8, 6–9.
- Alonso-Zarza, A.M., 2003. Palaeoenvironmental significance of palustrine carbonates and calcretes in the geological record. *Earth-Science Rev.* 60, 261–298. [https://doi.org/10.1016/S0012-8252\(02\)00106-X](https://doi.org/10.1016/S0012-8252(02)00106-X)
- Alsharhan, A.S., Rizk, Z.A., Nairn, A.E.M., Bakhit, D.W., Alhajari, S.A., 2001. *Hydrogeology of an Arid Region: The Arabian Gulf and Adjoining Areas*. Elsevier. <https://doi.org/10.1016/b978-0-444-50225-4.x5000-3>
- Andrews, J.E., Riding, R., Dennis, P.F., 1997. The stable isotope record of environmental and climatic signals in modern terrestrial microbial carbonates from Europe. *Palaeogeogr. Palaeoclimatol. Palaeoecol.* 129, 171–189.
- Armenteros, I., 2010. Diagenesis of Carbonates in Continental Settings, in: Alonso-Zarza, A.M., Tanner, L.H. (Eds.), *Carbonates in Continental Settings: Geochemistry, Diagenesis and Applications*. Elsevier, pp. 61–152.
- Armitage, S.J., Bailey, R.M., 2005. The measured dependence of laboratory beta dose rates on sample grain size. *Radiat. Meas.* 39, 123–127. <https://doi.org/10.1016/j.radmeas.2004.06.008>
- Armitage, S.J., Bristow, C.S., Drake, N.A., 2015. West African monsoon dynamics inferred from abrupt fluctuations of Lake Mega-Chad. *Proc. Natl. Acad. Sci.* 112, 8543–8548. <https://doi.org/10.1073/pnas.1417655112>
- Armitage, S.J., Drake, N.A., Stokes, S., El-Hawat, A., Salem, M.J., White, K., Turner, P., McLaren, S.J., 2007. Multiple phases of North African humidity recorded in lacustrine sediments from the Fazzan Basin, Libyan Sahara. *Quat. Geochronol.* 2, 181–186. <https://doi.org/10.1016/j.quageo.2006.05.019>
- Armitage, S.J., Jasim, S.A., Marks, A.E., Parker, A.G., Usik, V.I., Uerpmann, H.-P., 2011. The Southern Route “Out of Africa”: Evidence for an Early Expansion of Modern Humans into Arabia. *Science* (80-.). 453, 453–456. <https://doi.org/10.1126/science.1199113>
- Armitage, S.J., Krishna, A., Parker, L.E., King, G.E., 2019. Optically stimulated luminescence dating of heat retainer hearths from the Sahara: Insights into signal accumulation and measurement. *Quat. Geochronol.* 49, 249–253. <https://doi.org/10.1016/j.quageo.2018.03.004>
- Armon, M., Dente, E., Smith, J.A., Enzel, Y., Morin, E., 2018. Synoptic-scale control over

- modern rainfall and flood patterns in the Levant drylands with implications for past climates. *J. Hydrometeorol.* 19, 1077–1096. <https://doi.org/10.1175/JHM-D-18-0013.1>
- Armon, M., Morin, E., Enzel, Y., 2019. Overview of modern atmospheric patterns controlling rainfall and floods into the Dead Sea: Implications for the lake's sedimentology and paleohydrology. *Quat. Sci. Rev.* 216, 58–73. <https://doi.org/10.1016/j.quascirev.2019.06.005>
- Arsuaga, J.L., Martínez, I., Arnold, L.J., Aranburu, A., Gracia-Téllez, A., Sharp, W.D., Quam, R.M., Falguères, C., Pantoja-Pérez, A., Bischoff, J., Poza-Rey, E., Parés, J.M., Carretero, J.M., Demuro, M., Lorenzo, C., Sala, N., Martínón-Torres, M., García, N., Alcázar De Velasco, A., Cuenca-Bescós, G., Gómez-Olivencia, A., Moreno, D., Pablos, A., Shen, C.C., Rodríguez, L., Ortega, A.I., García, R., Bonmatí, A., Bermúdez De Castro, J.M., Carbonell, E., 2014. Neandertal roots: Cranial and chronological evidence from Sima de los Huesos. *Science* (80-). 344, 1358–1363. <https://doi.org/10.1126/science.1253958>
- Aubert, M., Pike, A.W.G., Stringer, C., Bartsiakos, A., Kinsley, L., Eggins, S., Day, M., Grün, R., 2012. Confirmation of a late middle Pleistocene age for the Omo Kibish 1 cranium by direct uranium-series dating. *J. Hum. Evol.* 63, 704–710. <https://doi.org/10.1016/j.jhevol.2012.07.006>
- Bailey, G.N., Devès, M.H., Inglis, R.H., Meredith-Williams, M.G., Momber, G., Sakellariou, D., Sinclair, A.G.M., Rousakis, G., Al Ghamdi, S., Alsharekh, A.M., 2015. Blue Arabia: Palaeolithic and underwater survey in SW Saudi Arabia and the role of coasts in Pleistocene dispersals. *Quat. Int.* 382, 42–57. <https://doi.org/10.1016/j.quaint.2015.01.002>
- Bailey, R.M., 2001. Towards a general kinetic model for optically and thermally stimulated luminescence of quartz. *Radiat. Meas.* 33, 17–45. [https://doi.org/10.1016/S1350-4487\(00\)00100-1](https://doi.org/10.1016/S1350-4487(00)00100-1)
- Bailey, R.M., 1997. Optical detrapping of charge from the 110°C quartz TL region. *Anc. TL* 15, 7–10.
- Bailey, R.M., Singarayer, J.S., Ward, S., Stokes, S., 2003. Identification of partial resetting using De as a function of illumination time. *Radiat. Meas.* 37, 511–518. [https://doi.org/10.1016/S1350-4487\(03\)00063-5](https://doi.org/10.1016/S1350-4487(03)00063-5)
- Bailey, R.M., Smith, B.W., Rhodes, E.J., 1997. Partial bleaching and the decay form characteristics of quartz OSL. *Radiat. Meas.* 27, 123–136. [https://doi.org/10.1016/S1350-4487\(96\)00157-6](https://doi.org/10.1016/S1350-4487(96)00157-6)
- Balescu, S., Lamothe, M., 1994. Comparison of TL and IRSL age estimates of feldspar coarse grains from waterlain sediments. *Quat. Sci. Rev.* 13, 437–444. [https://doi.org/10.1016/0277-3791\(94\)90056-6](https://doi.org/10.1016/0277-3791(94)90056-6)
- Banerjee, D., Bøtter-Jensen, L., Murray, A.S., 2000. Retrospective dosimetry: estimation of the dose to quartz using the single-aliquot regenerative-dose protocol. *Appl. Radiat. Isot.* 52, 831–844.
- Bar-Matthews, M., Ayalon, A., Gilmour, M., Matthews, A., Hawkesworth, C.J., 2003. Sea–land oxygen isotopic relationships from planktonic foraminifera and speleothems in the Eastern Mediterranean region and their implication for paleorainfall during interglacial intervals. ... *Cosmochim. Acta* 67, 3181–3199.
- Bar-Matthews, M., Ayalon, A., Kaufman, A., 2000. Timing and hydrological conditions of Sapropel events in the Eastern Mediterranean, as evident from speleothems,

- Soreq cave, Israel. *Chem. Geol.* 169, 145–156. [https://doi.org/10.1016/S0009-2541\(99\)00232-6](https://doi.org/10.1016/S0009-2541(99)00232-6)
- Bar-Matthews, M., Keinan, J., Ayalon, A., 2019. Hydro-climate research of the late quaternary of the Eastern Mediterranean-Levant region based on speleothems research – A review. *Quat. Sci. Rev.* 221, 105872. <https://doi.org/10.1016/j.quascirev.2019.105872>
- Barbouti, A.I., Rastin, B.C., 1983. A study of the absolute intensity of muons at sea level and under various thicknesses of absorber. *J. Phys. G Nucl. Phys.* 9, 1577–1595. <https://doi.org/10.1088/0305-4616/9/12/018>
- Battarbee, R.W., Juggins, S., Gasse, F., Anderson, N.H., Bennion, H., Cameron, D., Ryves, D.B., Pailles, C., Chalief, F., Telford, R., 2001. The European Diatom Database (EDDI): An information system for palaeoenvironmental reconstruction. Environmental Change Research Centre (ECRC) Research Report No. 81.
- Battarbee, R.W., Kneen, M.J., 1982. The use of electronically counted microspheres in absolute diatom analysis. *Limnol. Oceanogr.* 27, 184–188. <https://doi.org/10.4319/lo.1982.27.1.0184>
- Bell, W.T., 1980. Alpha attenuation in Quartz grains for Thermoluminescence Dating. *Anc. TL* 12, 4–8.
- Bell, W.T., 1979. Attenuation factors for the absorbed radiation dose in quartz inclusions for thermoluminescence dating. *Anc. TL* 8, 1–12.
- Bennett, K.D., 1996. Determination of the number of zones in a biostratigraphical sequence. *New Phytol.* 132, 155–170. <https://doi.org/10.1111/j.1469-8137.1996.tb04521.x>
- Berger, A., Loutre, M.F., 1991. Insolation values for the climate of the last 10 million years. *Quat. Sci. Rev.* 10, 297–317.
- Bernasconi, S.M., Müller, I.A., Bergmann, K.D., Breitenbach, S.F.M., Fernandez, A., Hodell, D.A., Jaggi, M., Meckler, A.N., Millan, I., Ziegler, M., 2018. Reducing Uncertainties in Carbonate Clumped Isotope Analysis Through Consistent Carbonate-Based Standardization. *Geochemistry, Geophys. Geosystems* 19, 2895–2914. <https://doi.org/10.1029/2017GC007385>
- Blome, M.W., Cohen, A.S., Tryon, C.A., Brooks, A.S., Russell, J., 2012. The environmental context for the origins of modern human diversity: A synthesis of regional variability in African climate 150,000–30,000 years ago. *J. Hum. Evol.* 62, 563–592. <https://doi.org/10.1016/j.jhevol.2012.01.011>
- Bøtter-Jensen, L., Andersen, C.E., Duller, G.A.T., Murray, A.S., 2003. Developments in radiation, stimulation and observation facilities in luminescence measurements. *Radiat. Meas.* 37, 535–541. [https://doi.org/10.1016/S1350-4487\(03\)00020-9](https://doi.org/10.1016/S1350-4487(03)00020-9)
- Bøtter-Jensen, L., Mejdahl, V., 1988. Assessment of beta dose-rate using a GM multicounter system. *Int. J. Radiat. Appl. Instrumentation. Part 14*, 187–191. [https://doi.org/10.1016/1359-0189\(88\)90062-3](https://doi.org/10.1016/1359-0189(88)90062-3)
- Breeze, P.S., Drake, N.A., Groucutt, H.S., Parton, A., Jennings, R.P., White, T.S., Clark-Balzan, L., Shipton, C., Scerri, E.M.L., Stimpson, C.M., Crassard, R., Hilbert, Y., Alsharekh, A., Al-Omari, A., Petraglia, M.D., 2015. Remote sensing and GIS techniques for reconstructing Arabian palaeohydrology and identifying archaeological sites. *Quat. Int.* 382, 98–119. <https://doi.org/10.1016/j.quaint.2015.01.022>
- Breeze, P.S., Groucutt, H.S., Drake, N.A., Louys, J., Scerri, E.M.L., Armitage, S.J.,

- Zalmout, I.S.A., Memesh, A.M., Haptari, M.A., Soubhi, S.A., Matari, A.H., Zahir, M., Al-Omari, A., Alsharekh, A.M., Petraglia, M.D., 2017. Prehistory and palaeoenvironments of the western Nefud Desert, Saudi Arabia. *Archaeol. Res. Asia* 10, 1–16. <https://doi.org/10.1016/j.ara.2017.02.002>
- Breeze, P.S., Groucutt, H.S., Drake, N.A., White, T.S., Jennings, R.P., Petraglia, M.D., 2016. Palaeohydrological corridors for hominin dispersals in the Middle East ~250-70,000 years ago. *Quat. Sci. Rev.* 144, 155–185. <https://doi.org/10.1016/j.quascirev.2016.05.012>
- Brennan, B.J., 2003. Beta doses to spherical grains. *Radiat. Meas.* 37, 299–303. [https://doi.org/10.1016/S1350-4487\(03\)00011-8](https://doi.org/10.1016/S1350-4487(03)00011-8)
- Burns, S.J., Fleitmann, D., Matter, A., Neff, U., Mangini, A., 2001. Speleothem evidence from Oman for continental pluvial events during interglacial periods. *Geology* 29, 623–626. [https://doi.org/10.1130/0091-7613\(2001\)029<0623:SEFOFC>2.0.CO;2](https://doi.org/10.1130/0091-7613(2001)029<0623:SEFOFC>2.0.CO;2)
- Burow, C., 2017. `calc_CentralDose()`: Apply the central age model (CAM) after Galbraith et al. (1999) to a given De distribution. Function version 1.3.2., in: Kreutzer, S., Dietze, M., Burow, C., Fuchs, M.C., Schmidt, C., Fischer, M., Friedrich, J. (2017). *Luminescence: Comprehensive Luminescence Dating Data Analysis*. R Package Version 0.7.5. <https://CRAN.R-Project.Org/Package=Luminescence>.
- Buylaert, J.P., Jain, M., Murray, A.S., Thomsen, K.J., Thiel, C., Sohbaty, R., 2012. A robust feldspar luminescence dating method for Middle and Late Pleistocene sediments. *Boreas* 41, 435–451. <https://doi.org/10.1111/j.1502-3885.2012.00248.x>
- Causse, C., Ghaleb, B., Chkir, N., Zouari, K., Oueddou, H. Ben, Mamou, A., 2003. Humidity changes in southern Tunisia during the Late Pleistocene inferred from U-Th dating of mollusc shells. *Appl. Geochemistry* 18, 1691–1703. [https://doi.org/10.1016/S0883-2927\(03\)00043-X](https://doi.org/10.1016/S0883-2927(03)00043-X)
- Chalié, F., Gasse, F., 2002. Late Glacial-Holocene diatom record of water chemistry and lake level change from the tropical East African Rift Lake Abiyata (Ethiopia). *Palaeogeogr. Palaeoclimatol. Palaeoecol.* 187, 259–283. [https://doi.org/10.1016/S0031-0182\(02\)00480-7](https://doi.org/10.1016/S0031-0182(02)00480-7)
- Chauhan, N., Singhvi, A.K., 2011. Distribution in sar palaeodoses due to spatial heterogeneity of natural beta dose. *Geochronometria* 38, 190–198. <https://doi.org/10.2478/s13386-011-0024-7>
- Choi, J.H., Murray, A.S., Jain, M., Cheong, C.S., Chang, H.W., 2003. Luminescence dating of well-sorted marine terrace sediments on the southeastern coast of Korea. *Quat. Sci. Rev.* 22, 407–421. [https://doi.org/10.1016/S0277-3791\(02\)00136-1](https://doi.org/10.1016/S0277-3791(02)00136-1)
- Clark-Balzan, L., Parton, A., Breeze, P.S., Groucutt, H.S., Petraglia, M.D., 2017. Resolving problematic luminescence chronologies for carbonate- and evaporite-rich sediments spanning multiple humid periods in the Jubbah basin, Saudi Arabia. *Quat. Geochronol.* 45, 50–73. <https://doi.org/10.1016/j.quageo.2017.06.002>
- Clark-Wilson, R., 2016. *Palaeoenvironments of Lacustrine Sediments in the Western Nefud Desert, Saudi Arabia*. Royal Holloway, University of London.
- Clark, I.D., Fritz, P., 1997. *Environmental isotopes in hydrogeology*. Lewis Publishers, New York.
- Collinson, J.D., 1996. Alluvial sediments, in: *Sedimentary Environments: Processes, Facies and Stratigraphy*. Blackwell, pp. 37–81.

- Cordova, C.E., Nowell, A., Bisson, M., Ames, C.J.H., Pokines, J., Chang, M., al-Nahar, M., 2013. Interglacial and glacial desert refugia and the Middle Paleolithic of the Azraq Oasis, Jordan. *Quat. Int.* 300, 94–110.
<https://doi.org/10.1016/j.quaint.2012.09.019>
- Craig, H., 1965. The measurement of oxygen isotope palaeotemperatures, in: Tongiorgi, E. (Ed.), *Stable Isotopes in Oceanographic Studies and Palaeotemperatures*. Consiglio Nazionale delle Ricerche Laboratorio di Geologia Nucleare, Pisa, pp. 161–182.
- Craig, H., 1961. Isotopic variations in meteoric waters. *Science* (80-). 133, 1833–1834.
- Crassard, R., Petraglia, M.D., Drake, N.A., Breeze, P., Gratuze, B., Alsharekh, A., Arbach, M., Groucutt, H.S., Khalidi, L., Michelsen, N., Robin, C.J., Schiettecatte, J., 2013. Middle Palaeolithic and Neolithic Occupations around Mundafan Palaeolake, Saudi Arabia: Implications for Climate Change and Human Dispersals. *PLoS One*.
<https://doi.org/10.1371/journal.pone.0069665>
- Crawford, R.M., Likhoshway, Y. V., Jahn, R., 2003. Morphology and identity of *Aulacoseira italic* and typification of *Aulacoseira* (Bacillariophyta). *Diatom Res.* 18, 1–19.
- Crombie, M.K., Arvidson, R.E., Sturchio, N.C., El Alfy, Z., Abu Zeid, K., 1997. Age and isotopic constraints on pleistocene pluvial episodes in the Western Desert, Egypt. *Palaeogeogr. Palaeoclimatol. Palaeoecol.* 130, 337–355.
[https://doi.org/10.1016/S0031-0182\(96\)00134-4](https://doi.org/10.1016/S0031-0182(96)00134-4)
- Darling, W.G., 2004. Hydrological factors in the interpretation of stable isotopic proxy data present and past: A European perspective. *Quat. Sci. Rev.* 23, 743–770.
<https://doi.org/10.1016/j.quascirev.2003.06.016>
- Davison, W., 1993. Iron and manganese in lakes. *Earth Sci. Rev.* 34, 119–163.
[https://doi.org/10.1016/0012-8252\(93\)90029-7](https://doi.org/10.1016/0012-8252(93)90029-7)
- De Corte, F., Vandenberghe, D., Hossain, S.M., De Wispelaere, A., Buylaert, J.P., Van Den Haute, P., 2007. Preparation and characterization of loess sediment for use as a reference material in the annual radiation dose determination for luminescence dating. *J. Radioanal. Nucl. Chem.* 272, 311–319.
<https://doi.org/10.1007/s10967-007-0522-5>
- De Vries, A.J., Tyrlis, E., Edry, D., Krichak, S.O., Steil, B., Lelieveld, J., 2013. Extreme precipitation events in the Middle East: Dynamics of the Active Red Sea Trough. *J. Geophys. Res. Atmos.* 118, 7087–7108. <https://doi.org/10.1002/jgrd.50569>
- Decampo, D.M., 2010. The Geochemistry of Continental Carbonates, in: Alonso-Zarza, A.M., Tanner, L.H. (Eds.), *Carbonates in Continental Settings: Geochemistry, Diagenesis and Applications*. Elsevier, pp. 1–45.
- Delagnes, A., Tribolo, C., Bertran, P., Brenet, M., Crassard, R., Jaubert, J., Khalidi, L., Mercier, N., Nomade, S., Peigne, S., Sitzia, L., Tournepiche, J.F., Al-Halibi, M., Al-Mosabi, A., MacChiarelli, R., 2012. Inland human settlement in southern Arabia 55,000 years ago. New evidence from the Wadi Surdud Middle Paleolithic site complex, western Yemen. *J. Hum. Evol.* 63, 452–474.
<https://doi.org/10.1016/j.jhevol.2012.03.008>
- deMenocal, P.B., 1995. Plio-Pleistocene African climate. *Science* (80-). 270, 53–59.
- deMenocal, P.B., Ortiz, J., Guilderson, T., Adkins, J., Sarnthein, M., Baker, L., Yarusinsky, M., 2000. Abrupt onset and termination of the African Humid Period: rapid climate responses to gradual insolation forcing. *Quat. Sci. Rev.* 19, 347–361.

- Dinies, M., Plessen, B., Neef, R., Kürschner, H., 2015. When the desert was green: Grassland expansion during the early Holocene in northwestern Arabia. *Quat. Int.* 382, 293–302. <https://doi.org/10.1016/j.quaint.2015.03.007>
- Drake, N.A., Blench, R.M., Armitage, S.J., Bristow, C.S., White, K.H., 2011. Ancient watercourses and biogeography of the Sahara explain the peopling of the desert. *Proc. Natl. Acad. Sci. U. S. A.* 108, 458–462. <https://doi.org/10.1073/pnas.1012231108>
- Duller, G.A.T., 2003. Distinguishing quartz and feldspar in single grain luminescence measurements. *Radiat. Meas.* 37, 161–165. [https://doi.org/10.1016/S1350-4487\(02\)00170-1](https://doi.org/10.1016/S1350-4487(02)00170-1)
- Duller, G.A.T., 1996. The age of the Koputaroa dunes, southwest North Island, New Zealand. *Palaeogeogr. Palaeoclimatol. Palaeoecol.* 121, 105–114. [https://doi.org/10.1016/0031-0182\(96\)00053-3](https://doi.org/10.1016/0031-0182(96)00053-3)
- Durand, N., Monger, H.C., Canti, M.G., 2010. Calcium carbonate features, in: *Interpretation of Micromorphological Features of Soils and Regoliths*. Elsevier, Amsterdam, pp. 149–194.
- Durcan, J.A., King, G.E., Duller, G.A.T., 2015. DRAC: Dose Rate and Age Calculator for trapped charge dating. *Quat. Geochronol.* 28, 54–61. <https://doi.org/10.1016/j.quageo.2015.03.012>
- Edgell, H.S., 2006a. Evolution of Arabian deserts and their chronology, in: *Arabian Deserts: Nature, Origin, and Evolution*. Springer, Dordrecht, pp. 493–511.
- Edgell, H.S., 2006b. Arabian deserts: Nature, origin, and evolution, *Arabian Deserts: Nature, Origin, and Evolution*. Springer, Dordrecht. <https://doi.org/10.1007/1-4020-3970-0>
- Eiler, J.M., 2011. Paleoclimate reconstruction using carbonate clumped isotope thermometry. *Quat. Sci. Rev.* 30, 3575–3588. <https://doi.org/10.1016/j.quascirev.2011.09.001>
- El-Shenawy, M.I., Kim, S.-T., Schwarcz, H.P., Asmerom, Y., Polyak, V.J., 2018. Speleothem evidence for the greening of the Sahara and its implications for the early human dispersal out of sub-Saharan Africa. *Quat. Sci. Rev.* 188, 67–76. <https://doi.org/10.1016/j.quascirev.2018.03.016>
- Emeis, K.C., Sakamoto, T., Wehausen, R., Brumsack, H.J., 2000. The sapropel record of the eastern Mediterranean Sea - Results of Ocean Drilling Program Leg 160. *Palaeogeogr. Palaeoclimatol. Palaeoecol.* 158, 371–395. [https://doi.org/10.1016/S0031-0182\(00\)00059-6](https://doi.org/10.1016/S0031-0182(00)00059-6)
- Endicott, P., Ho, S.Y.W., Stringer, C., 2010. Using genetic evidence to evaluate four palaeoanthropological hypotheses for the timing of Neanderthal and modern human origins. *J. Hum. Evol.* 59, 87–95. <https://doi.org/10.1016/j.jhevol.2010.04.005>
- Engel, M., Brückner, H., Pint, A., Wellbrock, K., Ginau, A., Voss, P., Grottker, M., Klasen, N., Frenzel, P., 2011. The early Holocene humid period in NW Saudi Arabia - Sediments, microfossils and palaeo-hydrological modelling. *Quat. Int.* 266, 131–141. <https://doi.org/10.1016/j.quaint.2011.04.028>
- Engel, M., Matter, A., Parker, A.G., Parton, A., Petraglia, M.D., Preston, G.W., Preusser, F., 2016. Response to Enzel et al. (in press): Lakes or wetlands? A comment on “The middle Holocene climatic records from Arabia: Reassessing lacustrine environments, shift of ITCZ in Arabian Sea, and impacts of the southwest Indian

- and African monsoons” by Enzel e. *Glob. Planet. Change* 148, 258–267.
<https://doi.org/10.1016/j.gloplacha.2016.11.003>
- Enzel, Y., Kushnir, Y., Quade, J., 2015. The middle Holocene climatic records from Arabia: Reassessing lacustrine environments, shift of ITCZ in Arabian Sea, and impacts of the southwest Indian and African monsoons. *Glob. Planet. Change* 129, 69–91. <https://doi.org/10.1016/j.gloplacha.2015.03.004>
- Estes, R., 1991. *The behavior guide to African mammals*. University of California Press, Berkeley.
- Faershtein, G., Porat, N., Avni, Y., Matmon, A., 2016. Aggradation-incision transition in arid environments at the end of the Pleistocene: An example from the Negev Highlands, southern Israel. *Geomorphology* 253, 289–304.
<https://doi.org/10.1016/j.geomorph.2015.10.017>
- Fernandes, C.A., Rohling, E.J., Siddall, M., 2006. Absence of post-Miocene Red Sea land bridges : biogeographic implications. *J. Biogeogr.* 33, 961–966.
<https://doi.org/10.1111/j.1365-2699.2006.01478.x>
- Finlayson, C., 2013. The water optimisation hypothesis and the human occupation of the mid-latitude belt in the pleistocene. *Quat. Int.* 300, 22–31.
<https://doi.org/10.1016/j.quaint.2013.03.040>
- Fleitmann, D., Burns, S.J., Mangini, A., Mudelsee, M., Kramers, J., Villa, I., Neff, U., Al-Subbary, A.A., Buettner, A., Hippler, D., Matter, A., 2007. Holocene ITCZ and Indian monsoon dynamics recorded in stalagmites from Oman and Yemen (Socotra). *Quat. Sci. Rev.* 26, 170–188.
<https://doi.org/10.1016/j.quascirev.2006.04.012>
- Fleitmann, D., Burns, S.J., Neff, U., Mangini, A., Matter, A., 2003. Changing moisture sources over the last 330,000 years in Northern Oman from fluid-inclusion evidence in speleothems. *Quat. Res.* 60, 223–232. [https://doi.org/10.1016/S0033-5894\(03\)00086-3](https://doi.org/10.1016/S0033-5894(03)00086-3)
- Fleitmann, D., Burns, S.J., Pekala, M., Mangini, A., Al-Subbary, A., Al-Aowah, M., Kramers, J., Matter, A., 2011. Holocene and Pleistocene pluvial periods in Yemen, southern Arabia. *Quat. Sci. Rev.* 30, 783–787.
<https://doi.org/10.1016/j.quascirev.2011.01.004>
- Fleitmann, D., Matter, A., 2009. The speleothem record of climate variability in Southern Arabia. *Comptes Rendus - Geosci.* 341, 633–642.
<https://doi.org/10.1016/j.crte.2009.01.006>
- Fleming, S.J., 1970. Thermoluminescent Dating: Refinement of the Quartz Inclusion Method. *Archaeometry* 12, 133–144. <https://doi.org/10.1111/j.1475-4754.1970.tb00016.x>
- Folk, R.L., 1951. A Comparison Chart for Visual Percentage Estimation. *J. Sediment. Petrol.* 1, 32–33. <https://doi.org/10.1306/d4269413-2b26-11d7-8648000102c1865d>
- Freytet, P., Verrecchia, E.P., 2002. Lacustrine and palustrine carbonate petrography: An overview. *J. Paleolimnol.* 27, 221–237.
<https://doi.org/10.1023/A:1014263722766>
- Fronval, T., Jensen, N.B., Buchardt, B., 1995. Oxygen isotope disequilibrium of calcite in lake Arreso, Denmark. *Geology* 23, 463–466.
- Frumkin, A., Ford, D.C., Schwarcz, H.P., 1999. Continental Oxygen Isotopic Record of the Last 170,000 Years in Jerusalem. *Quat. Res.* 51, 317–327.

<https://doi.org/10.1006/qres.1998.2031>

- Galbraith, R.F., Roberts, R.G., Olley, J.M., Yoshida, H., Laslett, G.M., 1999. Optical Dating of Single and Multiple Grains of Quartz From Jinmium Rock Shelter, Northern Australia: Part I, Experimental Design and Statistical Models. *Archaeometry* 41, 339–364. <https://doi.org/10.1111/j.1475-4754.1999.tb00988.x>
- Gale, S.J., Hoare, P.G., 1991. *Quaternary Sediments: Petrographic Methods for the Study of Unlithified Rocks*. Belhaven and Halsted Press.
- Garrard, A.N., Harvey, C.P.D., Switsur, V.R., 1981. Environment and settlement during the Upper Pleistocene and Holocene at Jubba in the Great Nefud, Northern Arabia. *Atlatl* 5, 137–148.
- Gasse, F., Juggins, S., Khelifa, L. Ben, 1995. Diatom-based transfer functions for inferring past hydrochemical characteristics of African lakes. *Palaeogeogr. Palaeoclimatol. Palaeoecol.* 177, 31–54. [https://doi.org/10.1016/0031-0182\(94\)00122-0](https://doi.org/10.1016/0031-0182(94)00122-0)
- Gierlowski-Kordesch, E., 2010. Lacustrine carbonates. *Dev. Sedimentol.* 61, 1–102.
- Gierz, P., Werner, M., Lohmann, G., 2017. Simulating climate and stable water isotopes during the Last Interglacial using a coupled climate-isotope model. *J. Adv. Model. Earth Syst.* 9, 2027–2045. <https://doi.org/10.1002/2017MS001056>
- Grant, K.M., Rohling, E.J., Bar-Matthews, M., Ayalon, A., Medina-Elizalde, M., Ramsey, C.B., Satow, C., Roberts, A.P., 2012. Rapid coupling between ice volume and polar temperature over the past 50,000 years. *Nature* 491, 744–747. <https://doi.org/10.1038/nature11593>
- Grant, K.M., Rohling, E.J., Westerhold, T., Zabel, M., Heslop, D., Konijnendijk, T., Lourens, L., 2017. A 3 million year index for North African humidity/aridity and the implication of potential pan-African Humid periods. *Quat. Sci. Rev.* 171, 100–118. <https://doi.org/10.1016/j.quascirev.2017.07.005>
- Grossman, E.L., Ku, T.L., 1986. Oxygen and carbon isotope fractionation in biogenic aragonite: Temperature effects. *Chem. Geol.* 59, 59–74. [https://doi.org/10.1016/0168-9622\(86\)90057-6](https://doi.org/10.1016/0168-9622(86)90057-6)
- Groucutt, H.S., 2020. Volcanism and human prehistory in Arabia. *J. Volcanol. Geotherm. Res.* 402, 107003. <https://doi.org/10.1016/j.jvolgeores.2020.107003>
- Groucutt, H.S., Blinkhorn, J., 2013. The Middle Palaeolithic in the desert and its implications for understanding hominin adaptation and dispersal. *Quat. Int.* 300, 1–12. <https://doi.org/10.1016/j.quaint.2013.03.043>
- Groucutt, H.S., Breeze, P., Drake, N.A., Jennings, R., Parton, A., White, T., Shipton, C., Clark-Balzan, L., Al-Omari, A., Cuthbertson, P., Wedage, O.M.C., Bernal, M.A., Alsharekh, A., Petraglia, M.D., 2016. The Middle Palaeolithic of the Nejd, Saudi Arabia. *J. F. Archaeol.* 4690, 1–17. <https://doi.org/10.1080/00934690.2016.1156928>
- Groucutt, H.S., Grün, R., Zalmout, I.A.S., Drake, N.A., Armitage, S.J., Candy, I., Clark-Wilson, R., Louys, J., Breeze, P.S., Duval, M., Buck, L.T., Kivell, T.L., Pomeroy, E., Stephens, N.B., Stock, J.T., Stewart, M., Price, G.J., Kinsley, L., Sung, W.W., Alsharekh, A., Al-Omari, A., Zahir, M., Memesh, A.M., Abdulshakoor, A.J., Al-Masari, A.M., Bahameem, A.A., Al Murayyi, K.M.S., Zahrani, B., Scerri, E.L.M., Petraglia, M.D., 2018. Homo sapiens in Arabia by 85,000 years ago. *Nat. Ecol. Evol.* 2, 800–809. <https://doi.org/10.1038/s41559-018-0518-2>
- Groucutt, H.S., Petraglia, M.D., 2012. The Prehistory of the Arabian Peninsula: Deserts,

- Dispersals, and Demography. *Evol. Anthropol.* 21, 113–125.
<https://doi.org/10.1002/evan.21308>
- Groucutt, H.S., Petraglia, M.D., Bailey, G., Scerri, E.M.L., Parton, A., Clark-Balzan, L., Jennings, R.P., Lewis, L., Blinkhorn, J., Drake, N.A., Breeze, P.S., Inglis, R.H., Devès, M.H., Meredith-Williams, M., Boivin, N., Thomas, M.G., Scally, A., 2015a. Rethinking the dispersal of *Homo sapiens* out of Africa. *Evol. Anthropol.* 24, 149–164. <https://doi.org/10.1002/evan.21455>
- Groucutt, H.S., Scerri, E.M.L., Lewis, L., Clark-Balzan, L., Blinkhorn, J., Jennings, R.P., Parton, A., Petraglia, M.D., 2015b. Stone tool assemblages and models for the dispersal of *Homo sapiens* out of Africa. *Quat. Int.* 382, 8–30.
<https://doi.org/10.1016/j.quaint.2015.01.039>
- Groucutt, H.S., Scerri, E.M.L., Stringer, C., Petraglia, M.D., 2019. Skhul lithic technology and the dispersal of *Homo sapiens* into Southwest Asia. *Quat. Int.* 515, 30–52.
<https://doi.org/10.1016/j.quaint.2017.12.027>
- Groucutt, H.S., Shipton, C., Alsharekh, A., Jennings, R., Scerri, E.M.L., Petraglia, M.D., 2015c. Late Pleistocene lakeshore settlement in northern Arabia: Middle Palaeolithic technology from Jebel Katefeh, Jubbah. *Quat. Int.* 382, 215–236.
<https://doi.org/10.1016/j.quaint.2014.12.001>
- Groucutt, H.S., White, T.S., Clark-Balzan, L., Parton, A., Crassard, R., Shipton, C., Jennings, R.P., Parker, A.G., Breeze, P.S., Scerri, E.M.L., Alsharekh, A., Petraglia, M.D., 2015d. Human occupation of the Arabian Empty Quarter during MIS 5: Evidence from Mundafan Al-Buhayrah, Saudi Arabia. *Quat. Sci. Rev.* 119, 116–135.
<https://doi.org/10.1016/j.quascirev.2015.04.020>
- Grun, R., Brink, J.S., Spooner, N.A., Taylor, L., Stringer, C.B., Franciscus, R.G., Murray, A.S., 1996. Direct dating of Florisbad hominid. *Nature* 382, 500–501.
<https://doi.org/10.1038/382500a0>
- Grün, R., Pike, A., McDermott, F., Eggins, S., Mortimer, G., Aubert, M., Kinsley, L., Joannes-Boyau, R., Rumsey, M., Denys, C., Brink, J., Clark, T., Stringer, C., 2020. Dating the skull from Broken Hill, Zambia, and its position in human evolution. *Nature* 580, 372–375. <https://doi.org/10.1038/s41586-020-2165-4>
- Guagnin, M., Breeze, P., Shipton, C., Ott, F., Stewart, M., Bateman, M., Martin, L., Graham, L., El-Dossary, S., Kingwell-Banham, E., Zahrani, B., Al-Omari, A., Alsharekh, A.M., Petraglia, M., 2020. The Holocene humid period in the Nefud Desert: Hunters and herders in the Jebel Oraf palaeolake basin, Saudi Arabia. *J. Arid Environ.* 178. <https://doi.org/10.1016/j.jaridenv.2020.104146>
- Guagnin, M., Shipton, C., Martin, L., Petraglia, M., 2017. The Neolithic site of Jebel Oraf 2, northern Saudi Arabia: First report of a directly dated site with faunal remains. *Archaeol. Res. Asia* 9, 63–67. <https://doi.org/10.1016/j.ara.2017.02.001>
- Guérin, G., Jain, M., J. Thomsen, K., S. Murray, A., Mercier, N., 2015. Modelling dose rate to single grains of quartz in well-sorted sand samples: The dispersion arising from the presence of potassium feldspars and implications for single grain OSL dating. *Quat. Geochronol.* 27, 52–65.
<https://doi.org/10.1016/j.quageo.2014.12.006>
- Guérin, G., Murray, A.S., Jain, M., Thomsen, K.J., Mercier, N., 2013. How confident are we in the chronology of the transition between Howieson’s Poort and Still Bay? *J. Hum. Evol.* 64, 314–317. <https://doi.org/10.1016/j.jhevol.2013.01.006>
- Hamdan, M.A., Brook, G.A., 2015. Timing and characteristics of Late Pleistocene and

- Holocene wetter periods in the Eastern Desert and Sinai of Egypt, based on ^{14}C dating and stable isotope analysis of spring tufa deposits. *Quat. Sci. Rev.* 130, 168–188. <https://doi.org/10.1016/j.quascirev.2015.09.011>
- Hartman, A., Torfstein, A., Almogi-Labin, A., 2020. Climate swings in the northern Red Sea over the last 150,000 years from ϵNd and Mg/Ca of marine sediments. *Quat. Sci. Rev.* 231. <https://doi.org/10.1016/j.quascirev.2020.106205>
- Harvati, K., Röding, C., Bosman, A.M., Karakostis, F.A., Grün, R., Stringer, C., Karkanas, P., Thompson, N.C., Koutoulidis, V., Mouloupoulos, L.A., Gorgoulis, V.G., Kouloukoussa, M., 2019. Apidima Cave fossils provide earliest evidence of *Homo sapiens* in Eurasia. *Nature* 571, 500–504. <https://doi.org/10.1038/s41586-019-1376-z>
- Hays, J.D., Imbrie, J., Shackleton, N.J., 1976. Variations in the earth's orbit: Pacemaker of the ice ages. *Science* (80-.). 194, 1121–1132. <https://doi.org/10.1126/science.194.4270.1121>
- Head, M.J., Gibbard, P.L., 2015. Formal subdivision of the Quaternary System/Period: Past, present, and future. *Quat. Int.* <https://doi.org/10.1016/j.quaint.2015.06.039>
- Herold, M., Lohmann, G., 2009. Eemian tropical and subtropical African moisture transport: An isotope modelling study. *Clim. Dyn.* 33, 1075–1088. <https://doi.org/10.1007/s00382-008-0515-2>
- Hershkovitz, I., Weber, G.W., Quam, R., Duval, M., Grün, R., Kinsley, L., Ayalon, A., Bar-Matthews, M., Valladas, H., Mercier, N., Arsuaga, J.L., Martín-Torres, M., Bermúdez de Castro, J.M., Fornai, C., Martín-Francés, L., Sarig, R., May, H., Krenn, V.A., Slon, V., Rodríguez, L., García, R., Lorenzo, C., Carretero, J.M., Frumkin, A., Shahack-Gross, R., Bar-Yosef Mayer, D.E., Cui, Y., Wu, X., Peled, N., Groman-Yaroslavski, I., Weissbrod, L., Yeshurun, R., Tsatskin, A., Zaidner, Y., Weinstein-Evron, M., 2018. The earliest modern humans outside Africa. *Science* (80-.). 359, 456–459. <https://doi.org/10.1126/science.aap8369>
- Hilbert, Y.H., White, T.S., Parton, A., Clark-Balzan, L., Crassard, R., Groucutt, H.S., Jennings, R.P., Breeze, P., Parker, A., Shipton, C., Al-Omari, A., Alsharekh, A.M., Petraglia, M.D., 2014. Epipalaeolithic occupation and palaeoenvironments of the southern Nefud Desert, Saudi Arabia, during the terminal Pleistocene and early Holocene. *J. Archaeol. Sci.* 50, 460–474. <https://doi.org/10.1016/j.jas.2014.07.023>
- Hill, M.O., Gauch, H.G., 1980. Detrended correspondence analysis: An improved ordination technique. *Vegetatio* 42, 47–58. <https://doi.org/10.1007/BF00048870>
- Hoffmann, G., Rupprechter, M., Rahn, M., Preusser, F., 2015. Fluvio-lacustrine deposits reveal precipitation pattern in SE Arabia during early MIS 3. *Quat. Int.* 382, 145–153. <https://doi.org/10.1016/j.quaint.2014.10.053>
- Horton, T.W., Defliese, W.F., Tripathi, A.K., Oze, C., 2016. Evaporation induced ^{18}O and ^{13}C enrichment in lake systems: A global perspective on hydrologic balance effects. *Quat. Sci. Rev.* 131, 365–379. <https://doi.org/10.1016/j.quascirev.2015.06.030>
- Huntley, D., Godfrey-Smith, D.I., Thewalt, M.L.W., 1985. Optical dating of sediments. *Nature* 313, 105–107. <https://doi.org/10.1038/315279a0>
- Huntley, D.J., Baril, M.R., 1997. The K content of the K-feldspars being measured in optical dating or in thermoluminescence dating. *Anc. TL* 15, 11–13.
- Huntley, D.J., Hancock, R.G. V., 2001. The Rb contents of the K-feldspar grains being measured in optical dating. *Anc. TL* 2, 43–46.

- Huntley, D.J., Lamothe, M., 2001. Ubiquity of anomalous fading in K-feldspars and the measurement and correction for it in optical dating. *Can. J. Earth Sci.* 38, 1093–1106. <https://doi.org/10.1139/e01-013>
- Hütt, G., Jaek, I., Tchonka, J., 1988. Optical dating: K-feldspars optical response stimulation spectra. *Quat. Sci. Rev.* 7, 381–385. [https://doi.org/10.1016/0277-3791\(88\)90033-9](https://doi.org/10.1016/0277-3791(88)90033-9)
- Jacobs, Z., Duller, G.A.T., Wintle, A.G., 2006. Interpretation of single grain Dedistributions and calculation of De. *Radiat. Meas.* 41, 264–277. <https://doi.org/10.1016/j.radmeas.2005.07.027>
- Jacobs, Z., Roberts, R.G., Galbraith, R.F., Deacon, H.J., Grün, R., Mackay, A., Mitchell, P., Vogelsang, R., Wadley, L., Jacobs, Z., Roberts, R.G., Galbraith, R.F., Deacon, H.J., Gr, R., Mackay, A., Mitchell, P., Vogelsang, R., Wadley, L., 2008. Ages for the Middle Stone Age of southern Africa: implications for human behavior and dispersal. *Science* 322, 733–735. <https://doi.org/10.1126/science.1162219>
- Jain, M., Choi, J.H., Thomas, P.J., 2008. The ultrafast OSL component in quartz: Origins and implications. *Radiat. Meas.* 43, 709–714. <https://doi.org/10.1016/j.radmeas.2008.01.005>
- Jain, M., Murray, A.S., Bøtter-Jensen, L., 2003. Characterisation of blue-light stimulated luminescence components in different quartz samples: Implications for dose measurement. *Radiat. Meas.* 37, 441–449. [https://doi.org/10.1016/S1350-4487\(03\)00052-0](https://doi.org/10.1016/S1350-4487(03)00052-0)
- Jennings, R.P., Parton, A., Clark-balzan, L., White, T.S., Groucutt, H.S., Breeze, P.S., Parker, A.G., Drake, N.A., Petraglia, M.D., 2016. Human occupation of the northern Arabian interior during early Marine Isotope Stage 3. *J. Quat. Sci.* 31, 953–966. <https://doi.org/10.1002/jqs.2920>
- Jennings, R.P., Singarayer, J., Stone, E.J., Krebs-Kanzow, U., Khon, V., Nisancioglu, K.H., Pfeiffer, M., Zhang, X., Parker, A., Parton, A., Groucutt, H.S., White, T.S., Drake, N.A., Petraglia, M.D., 2015. The greening of Arabia: Multiple opportunities for human occupation of the Arabian Peninsula during the Late Pleistocene inferred from an ensemble of climate model simulations. *Quat. Int.* 382, 181–199. <https://doi.org/10.1016/j.quaint.2015.01.006>
- Juggins, S., 1985. ZONE software.
- Jungclaus, J.H., Keenlyside, N., Botzet, M., Haak, H., Luo, J.J., Latif, M., Marotzke, J., Mikolajewicz, U., Roeckner, E., 2006. Ocean circulation and tropical variability in the coupled model ECHAM5/MPI-OM. *J. Clim.* 19, 3952–3972. <https://doi.org/10.1175/JCLI3827.1>
- Kerney, M.P., 1999. Atlas of the Land and Freshwater Molluscs of Britain and Ireland. Harley Books.
- Krammer, K., Lange-Bertalot, H., 1991a. Bacillariophyceae 3. Teil Centrales, Fragicariaceaa, Eunotiacea. Gustav-Fischer Verlag.
- Krammer, K., Lange-Bertalot, H., 1991b. Bacillariophyceae 4. Teil Achnanthaceae, Kritishe Ergänzungen zu Navicula (Lineolate) und Gomphonema. Gustav-Fischer Verlag.
- Krammer, K., Lange-Bertalot, H., 1988. Bacillariophyceae 2. Teil Epithemiaceae, Suiellaceae. Gustav-Fischer Verlag.
- Krbetschek, M.R., Rieser, U., Zöller, L., Heinicke, J., 1994. Radioactive disequilibria in palaeodosimetric dating of sediments. *Radiat. Meas.* 23, 485–489.

- [https://doi.org/10.1016/1350-4487\(94\)90083-3](https://doi.org/10.1016/1350-4487(94)90083-3)
- Kutzbach, J.E., Chen, G., Cheng, H., Edwards, R.L., Liu, Z., 2014. Potential role of winter rainfall in explaining increased moisture in the Mediterranean and Middle East during periods of maximum orbitally-forced insolation seasonality. *Clim. Dyn.* 42, 1079–1095. <https://doi.org/10.1007/s00382-013-1692-1>
- Kutzbach, J.E., Guan, J., He, F., Cohen, A.S., Orland, I.J., Chen, G., 2020. African climate response to orbital and glacial forcing in 140,000-y simulation with implications for early modern human environments. *Proc. Natl. Acad. Sci.* 117, 2255–2264. <https://doi.org/10.1073/pnas.1917673117>
- Kwarteng, A.Y., Dorvlo, A.S., Vijaya Kumar, G.T., 2009. Analysis of a 27-year rainfall data (1977-2003) in the Sultanate of Oman. *Int. J. Climatol.* 29, 605–617.
- Lambeck, K., Purcell, A., Flemming, N.C., Vita-Finzi, C., Alsharekh, A.M., Bailey, G.N., 2011. Sea level and shoreline reconstructions for the Red Sea: Isostatic and tectonic considerations and implications for hominin migration out of Africa. *Quat. Sci. Rev.* 30, 3542–3574. <https://doi.org/10.1016/j.quascirev.2011.08.008>
- Lamothe, M., Auclair, M., 1999. A solution to anomalous fading and age shortfalls in optical dating of feldspar minerals. *Earth Planet. Sci. Lett.* 171, 319–323. [https://doi.org/10.1016/S0012-821X\(99\)00180-6](https://doi.org/10.1016/S0012-821X(99)00180-6)
- Lamothe, M., Auclair, M., Hamzaoui, C., Huot, S., 2003. Towards a prediction of long-term anomalous fading of feldspar IRSL. *Radiat. Meas.* 37, 493–498. [https://doi.org/10.1016/S1350-4487\(03\)00016-7](https://doi.org/10.1016/S1350-4487(03)00016-7)
- Larrasoaña, J.C., Roberts, A.P., Rohling, E.J., 2013. Dynamics of Green Sahara Periods and Their Role in Hominin Evolution. *PLoS One* 8. <https://doi.org/10.1371/journal.pone.0076514>
- Larrasoaña, J.C., Roberts, A.P., Rohling, E.J., Winklhofer, M., Wehausen, R., 2003. Three million years of monsoon variability over the northern Sahara. *Clim. Dyn.* 21, 689–698. <https://doi.org/10.1007/s00382-003-0355-z>
- Legendre, P., Gallagher, E.D., 2001. Ecologically meaningful transformations for ordination of species data. *Oecologia* 129, 271–280. <https://doi.org/10.1007/s004420100716>
- Leng, M.J., Marshall, J.D., 2004. Palaeoclimate interpretation of stable isotope data from lake sediment archives. *Quat. Sci. Rev.* 23, 811–831. <https://doi.org/10.1016/j.quascirev.2003.06.012>
- Lezine, A.M., Casanova, J., 1991. Correlated oceanic and continental records demonstrate past climate and hydrology of North Africa (0-140 ka). *Geology* 19, 307–310. [https://doi.org/10.1130/0091-7613\(1991\)019<0307:COACRD>2.3.CO;2](https://doi.org/10.1130/0091-7613(1991)019<0307:COACRD>2.3.CO;2)
- Lézine, A.M., Robert, C., Cleuziou, S., Inizan, M.L., Braemer, F., Saliège, J.F., Sylvestre, F., Tiercelin, J.J., Crassard, R., Méry, S., Charpentier, V., Steimer-Herbet, T., 2010. Climate change and human occupation in the Southern Arabian lowlands during the last deglaciation and the Holocene. *Glob. Planet. Change* 72, 412–428. <https://doi.org/10.1016/j.gloplacha.2010.01.016>
- Lézine, A.M., Saliège, J.F., Robert, C., Wertz, F., Inizan, M.L., 1998. Holocene lakes from Ramlat as-Sab'atayn (Yemen) illustrate the impact of Monsoon activity in Southern Arabia. *Quat. Res.* 50, 290–299. <https://doi.org/10.1006/qres.1998.1996>
- Li, B., Jacobs, Z., Roberts, R.G., Li, S.H., 2014. Review and assessment of the potential of post-irsl dating methods to circumvent the problem of anomalous fading in

- feldspar luminescence. *Geochronometria* 41, 178–201.
<https://doi.org/10.2478/s13386-013-0160-3>
- Li, B., Li, S.H., 2011. Thermal stability of infrared stimulated luminescence of sedimentary K-feldspar. *Radiat. Meas.* 46, 29–36.
<https://doi.org/10.1016/j.radmeas.2010.10.002>
- Li, B., Li, S.H., Wintle, A.G., Zhao, H., 2008. Isochron dating of sediments using luminescence of K-feldspar grains. *J. Geophys. Res. Earth Surf.* 113.
<https://doi.org/10.1029/2007JF000900>
- Li, S.H., Li, B., 2006. Dose measurement using the fast component of LM-OSL signals from quartz. *Radiat. Meas.* 41, 534–541.
<https://doi.org/10.1016/j.radmeas.2005.04.029>
- Liritzis, I., Stamoulis, K., Papachristodoulou, C., Ioannides, K., 2013. A re-evaluation of radiation dose-rate conversion factors. *Mediterr. Archaeol. Archaeom.* 13, 1–15.
- Lisiecki, L.E., Raymo, M.E., 2005. A Pliocene-Pleistocene stack of 57 globally distributed benthic $\delta^{18}\text{O}$ records. *Paleoceanogr. Paleoclimatology* 20.
<https://doi.org/10.1029/2004PA001071>
- Lloyd, J.W., Pim, R.H., 1990. The hydrogeology and groundwater resources development of the Cambro-Ordovician sandstone aquifer in Saudi Arabia and Jordan. *J. Hydrol.* 121, 1–20. [https://doi.org/10.1016/0022-1694\(90\)90221-I](https://doi.org/10.1016/0022-1694(90)90221-I)
- Lourens, L.J., 2004. Revised tuning of Ocean Drilling Program Site 964 and KC01B (Mediterranean) and implications for the $\delta^{18}\text{O}$, tephra, calcareous nannofossil, and geomagnetic reversal chronologies of the past 1.1 Myr. *Paleoceanogr. Paleoclimatology* 19. <https://doi.org/10.1029/2003PA000997>
- Lourens, L.J., Antonarakou, A., Hilgen, F.J., Van Hoof, A.A.M., Vergnaud-Grazzini, C., Zachariasse, W.J., 1996. Evaluation of the Plio-Pleistocene astronomical timescale. *Paleoceanography* 11, 391–413. <https://doi.org/10.1029/96PA01125>
- Macaulay, V., Hill, C., Achilli, A., Rengo, C., Clarke, D., Meehan, W., Blackburn, J., Semino, O., Scozzari, R., Cruciani, F., Taha, A., Shaari, N.K., Raja, J.M., Ismail, P., Zainuddin, Z., Goodwin, W., Bulbeck, D., Bandelt, H.J., Oppenheimer, S., Torroni, A., Richards, M., 2005. Single, rapid coastal settlement of Asia revealed by analysis of complete mitochondrial genomes. *Science* (80-). 308, 1034–1036.
<https://doi.org/10.1126/science.1109792>
- Macumber, P., 2008. Evolving landscape and environment in Jordan, in: *Jordan: An Archaeological Reader*. Equinox books, London, pp. 7–34.
- Marshall, J.D., Jones, R.T., Crowley, S.F., Oldfield, F., Nash, S., Bedford, A., 2002. A high resolution Late-Glacial isotopic record from Hawes Water, Northwest England. Climatic oscillations: Calibration and comparison of palaeotemperature proxies. *Palaeogeogr. Palaeoclimatol. Palaeoecol.* 185, 25–40.
[https://doi.org/10.1016/S0031-0182\(02\)00422-4](https://doi.org/10.1016/S0031-0182(02)00422-4)
- Martinón-Torres, M., Bermúdez De Castro, J.M., Gómez-Robles, A., Prado-Simón, L., Arsuaga, J.L., 2012. Morphological description and comparison of the dental remains from Atapuerca-Sima de los Huesos site (Spain). *J. Hum. Evol.* 62, 7–58.
<https://doi.org/10.1016/j.jhevol.2011.08.007>
- Matter, A., Mahjoub, A., Neubert, E., Preusser, F., Schwalb, A., Szidat, S., Wulf, G., 2016. Reactivation of the Pleistocene trans-Arabian Wadi ad Dawasir fluvial system (Saudi Arabia) during the Holocene humid phase. *Geomorphology* 270, 88–101. <https://doi.org/10.1016/j.geomorph.2016.07.013>

- Matter, A., Neubert, E., Preusser, F., Rosenberg, T., Al-Wagdani, K., 2015a. Palaeo-environmental implications derived from lake and sabkha deposits of the southern Rub' al-Khali, Saudi Arabia and Oman. *Quat. Int.* 382, 120–131. <https://doi.org/10.1016/j.quaint.2014.12.029>
- Matter, A., Neubert, E., Preusser, F., Rosenberg, T., Al-Wagdani, K., 2015b. Palaeo-environmental implications derived from lake and sabkha deposits of the southern Rub' al-Khali, Saudi Arabia and Oman. *Quat. Int.* 382, 120–131. <https://doi.org/10.1016/j.quaint.2014.12.029>
- Mayya, Y.S., Morthekai, P., Murari, M.K., Singhvi, A.K., 2006. Towards quantifying beta microdosimetric effects in single-grain quartz dose distribution. *Radiat. Meas.* 41, 1032–1039. <https://doi.org/10.1016/j.radmeas.2006.08.004>
- McClure, H.A., 1984. Late Quaternary palaeoenvironments of the Rub' al Khali. University College London.
- McClure, H.A., 1976. Radiocarbon chronology of late Quaternary lakes in the Arabian Desert. *Nature* 263, 755–756. <https://doi.org/10.1038/263755a0>
- McDougall, I., Brown, F.H., Fleagle, J.G., 2005. Stratigraphic placement and age of modern humans from Kibish, Ethiopia. *Nature* 433, 733–736. <https://doi.org/10.1038/nature03258>
- McLaren, S.J., Al-Juaidi, F., Bateman, M.D., Millington, A.C., 2009. First evidence for episodic flooding events in the arid interior of central Saudi Arabia over the last 60 ka. *J. Quat. Sci.* 24, 198–207. <https://doi.org/10.1002/jqs.1199>
- Mehterian, S., Pourmand, A., Sharifi, A., Lahijani, H.A.K., Naderi, M., Swart, P.K., 2017. Speleothem records of glacial/interglacial climate from Iran forewarn of future Water Availability in the interior of the Middle East. *Quat. Sci. Rev.* 164, 187–198. <https://doi.org/10.1016/j.quascirev.2017.03.028>
- Mejdahl, V., 1979. Thermoluminescence dating: beta-dose attenuation in quartz grains. *Archaeometry* 21, 61–72.
- Mercier, N., Falguères, C., 2007. Field gamma dose-rate measurement with a NaI (TI) detector: re-evaluation of the “threshold” technique. *Anc. TL* 25, 1–4.
- Mercier, N., Valladas, H., 2003. Reassessment of TL age estimates of burnt flints from the Paleolithic site of Tabun Cave, Israel. *J. Hum. Evol.* 45, 401–409. <https://doi.org/10.1016/j.jhevol.2003.09.004>
- Mercier, N., Valladas, H., Bar-Yosef, O., Vandermeersch, B., Stringer, C., Joron, J.L., 1993. Thermoluminescence date for the mousterian burial site of Es-Skhul, Mt. Carmel. *J. Archaeol. Sci.* 30, 169–174. <https://doi.org/10.1006/jasc.1993.1012>
- Merlis, T., 2010. The Tropical Precipitation Response to Orbital Precession. *J. Clim.* 26. <https://doi.org/10.1175/JCLI-D-12-00186.1>
- Mischke, S., Opitz, S., Kalbe, J., Ginat, H., Al-Saqarat, B., 2015. Palaeoenvironmental inferences from late Quaternary sediments of the Al Jafr Basin, Jordan. *Quat. Int.* 382, 154–167. <https://doi.org/10.1016/j.quaint.2014.12.041>
- Mohtadi, M., Prange, M., Steinke, S., 2016. Palaeoclimatic insights into forcing and response of monsoon rainfall. *Nature* 533, 191–199. <https://doi.org/10.1038/nature17450>
- Mook, W.G., 2000. Environmental isotopes in the hydrological cycle: principles and applications. *Tech. Doc. Hydrol.* 1.
- Moumani, K., Alexander, J., Bateman, M.D., 2003. Sedimentology of the Late Quaternary Wadi Hasa Marl Formation of central Jordan: A record of climate

- variability. *Palaeogeogr. Palaeoclimatol. Palaeoecol.* 191, 221–242.
[https://doi.org/10.1016/S0031-0182\(02\)00715-0](https://doi.org/10.1016/S0031-0182(02)00715-0)
- Murray, A.S., Wintle, A.G., 2003. The single aliquot regenerative dose protocol: Potential for improvements in reliability. *Radiat. Meas.* 37, 377–381.
[https://doi.org/10.1016/S1350-4487\(03\)00053-2](https://doi.org/10.1016/S1350-4487(03)00053-2)
- Murray, A.S., Wintle, A.G., 2000. Luminescence dating of quartz using an improved single- aliquot regenerative-dose protocol. *Radiat. Meas.* 32, 57–73.
[https://doi.org/10.1016/S1350-4487\(99\)00253-X](https://doi.org/10.1016/S1350-4487(99)00253-X)
- Nathan, R.P., Mauz, B., 2008. On the dose-rate estimate of carbonate-rich sediments for trapped charge dating. *Radiat. Meas.* 43, 14–25.
<https://doi.org/10.1016/j.radmeas.2007.12.012>
- Navok, T., Guillory, W.X., Julius, M.L., Theriort, E.C., Alverson, A.J., 2015. Towards a phylogenetic classification of species belonging to the diatom genus *Cyclotella* (Bacillariophyceae): Transfer of species formerly placed in *Puncticulata*, *Handmannia*, *Pliocaenicus* and *Cyclotella* to the genus *Lindavia*. *Phytotaxa* 217, 249–264.
- Nehme, C., Verheyden, S., Breitenbach, S.F.M., Gillikin, D.P., Verheyden, A., Cheng, H., Lawrence Edwards, R., Hellstrom, J., Noble, S.R., Farrant, A.R., Sahy, D., Goovaerts, T., Salem, G., Claeys, P., 2018. Climate dynamics during the penultimate glacial period recorded in a speleothem from Kanaan Cave, Lebanon (central Levant). *Quat. Res. (United States)* 90, 10–25.
<https://doi.org/10.1017/qua.2018.18>
- Nehme, C., Verheyden, S., Noble, S.R., Farrant, A.R., Sahy, D., Hellstrom, J., Delannoy, J.J., Claeys, P., 2015. Reconstruction of MIS 5 climate in the central Levant using a stalagmite from Kanaan Cave, Lebanon. *Clim. Past* 11, 1785–1799.
<https://doi.org/10.5194/cp-11-1785-2015>
- Neugebauer, I., Wulf, S., Schwab, M.J., Serb, J., Plessen, B., Appelt, O., Brauer, A., 2017. Implications of S1 tephra findings in Dead Sea and Tayma palaeolake sediments for marine reservoir age estimation and palaeoclimate synchronisation. *Quat. Sci. Rev.* 170, 269–275. <https://doi.org/10.1016/j.quascirev.2017.06.020>
- Nicholson, S.L., Pike, A.W.G., Hosfield, R., Roberts, N., Sahy, D., Woodhead, J., Cheng, H., Edwards, R.L., Affolter, S., Leuenberger, M., Burns, S.J., Matter, A., Fleitmann, D., 2020. Pluvial periods in Southern Arabia over the last 1.1 million-years. *Quat. Sci. Rev.* 229, 106112. <https://doi.org/10.1016/j.quascirev.2019.106112>
- Olley, J., Caitcheon, G., Murray, A., 1998. The distribution of apparent dose as determined by optically stimulated luminescence in small aliquots of fluvial quartz: Implications for dating young sediments. *Quat. Sci. Rev.* 17, 1033–1040.
[https://doi.org/10.1016/S0277-3791\(97\)00090-5](https://doi.org/10.1016/S0277-3791(97)00090-5)
- Olley, J.M., Murray, A., Roberts, R.G., 1996. The effects of disequilibria in the uranium and thorium decay chains on burial dose rates in fluvial sediments. *Quat. Sci. Rev.* 15, 751–760. [https://doi.org/10.1016/0277-3791\(96\)00026-1](https://doi.org/10.1016/0277-3791(96)00026-1)
- Olley, J.M., Pietsch, T., Roberts, R.G., 2004. Optical dating of Holocene sediments from a variety of geomorphic settings using single grains of quartz. *Geomorphology* 60, 337–358. <https://doi.org/10.1016/j.geomorph.2003.09.020>
- Orland, I.J., He, F., Bar-matthews, M., Chen, G., Ayalon, A., Kutzbach, J.E., 2019. Resolving seasonal rainfall changes in the Middle East during the last interglacial period. *Proc. Natl. Acad. Sci.* 116, 24985–24990.

- <https://doi.org/10.1073/pnas.1903139116>
- Osmond, J.K., Dabous, A.A., 2004. Timing and intensity of groundwater movement during Egyptian Sahara pluvial periods by U-series analysis of secondary U in ores and carbonates. *Quat. Res.* 61, 85–94.
<https://doi.org/10.1016/j.yqres.2003.09.004>
- Palmer, A.P., Lee, J.A., Kemp, R.A., Carr, S.J., 2008. Revised Laboratory Procedures for the Preparation of Thin Sections from Unconsolidated Sediments. Centre for Micromorphology Publication.
- Parker, A.G., 2009. Pleistocene climate change in Arabia: developing a framework for hominin dispersal over the last 350 ka, in: *The Evolution of Human Populations in Arabia*. Springer Netherlands, pp. 39–49. <https://doi.org/10.1007/978-90-481-2719-1>
- Parker, A.G., Goudie, A.S., Stokes, S., White, K., Hodson, M.J., Manning, M., Kennet, D., 2006a. A record of Holocene climate change from lake geochemical analyses in southeastern Arabia. *Quat. Res.* 66, 465–476.
<https://doi.org/10.1016/j.yqres.2006.07.001>
- Parker, A.G., Preston, G., Walkington, H., Hodson, M.J., 2006b. Developing a framework of Holocene climatic change and landscape archaeology for the lower Gulf region, southeastern Arabia. *Arab. Archaeol. Epigr.* 17, 125–130.
<https://doi.org/10.1111/j.1600-0471.2006.00261.x>
- Parker, A.G., Preston, G.W., Parton, A., Walkington, H., Jardine, P.E., Leng, M.J., Hodson, M.J., 2016. Low-latitude Holocene hydroclimate derived from lake sediment flux and geochemistry. *J. Quat. Sci.* 31, 286–299.
<https://doi.org/10.1002/jqs.2859>
- Parton, A., Clark-Balzan, L., Parker, A.G., Preston, G.W., Sung, W.W., Breeze, P.S., Leng, M.J., Groucutt, H.S., White, T.S., Alsharekh, A., Petraglia, M.D., 2018. Middle-late quaternary palaeoclimate variability from lake and wetland deposits in the Nefud Desert, Northern Arabia. *Quat. Sci. Rev.* 202, 78–97.
<https://doi.org/10.1016/j.quascirev.2018.10.010>
- Parton, A., Farrant, A.R., Leng, M.J., Schwenninger, J.L., Rose, J.I., Uerpmann, H.P., Parker, A.G., 2013. An early MIS 3 pluvial phase in Southeast Arabia: Climatic and archaeological implications. *Quat. Int.* 300, 62–74.
<https://doi.org/10.1016/j.quaint.2013.02.016>
- Parton, A., White, T.S., Parker, A.G., Breeze, P.S., Jennings, R., Groucutt, H.S., Petraglia, M.D., 2015. Orbital-scale climate variability in Arabia as a potential motor for human dispersals. *Quat. Int.* 382, 82–97.
<https://doi.org/10.1016/j.quaint.2015.01.005>
- Pausata, F.S.R., Messori, G., Zhang, Q., 2016. Impacts of dust reduction on the northward expansion of the African monsoon during the Green Sahara period. *Earth Planet. Sci. Lett.* 434, 298–307. <https://doi.org/10.1016/j.epsl.2015.11.049>
- Pearson, F.J.J., Coplen, T.B., 1978. Stable isotope studies of lakes, in: Lerman, A. (Ed.), *Lakes: Chemistry, Geology, Physics*. Springer Verlag, New York, pp. 325–336.
- Petit-Maire, N., Carbonel, P., Reyss, J.L., Sanlaville, P., Abed, A., Bourrouilh, R., Fontugne, M., Yasin, S., 2010. A vast Eemian palaeolake in Southern Jordan (29°N). *Glob. Planet. Change* 72, 368–373.
<https://doi.org/10.1016/j.gloplacha.2010.01.012>
- Petraglia, M.D., 2011. Trailblazers across Arabia. *Nature* 470, 50–51.

- <https://doi.org/10.1029/2006GL026152>
- Petraglia, M.D., Alsharekh, A., 2003. The Middle Palaeolithic of Arabia: Implications for modern human origins, behaviour and dispersals. *Antiquity* 77, 671–684.
<https://doi.org/10.1017/S0003598X00061639>
- Petraglia, M.D., Alsharekh, A., Breeze, P., Clarkson, C., Crassard, R., Drake, N.A., Groucutt, H.S., Jennings, R., Parker, A.G., Parton, A., Roberts, R.G., Shipton, C., Matheson, C., al-Omari, A., Veall, M.A., 2012. Hominin Dispersal into the Nefud Desert and Middle Palaeolithic Settlement along the Jubbah Palaeolake, Northern Arabia. *PLoS One* 7. <https://doi.org/10.1371/journal.pone.0049840>
- Petraglia, M.D., Alsharekh, A.M., Crassard, R., Drake, N.A., Groucutt, H., Parker, A.G., Roberts, R.G., 2011. Middle Paleolithic occupation on a Marine Isotope Stage 5 lakeshore in the Nefud Desert, Saudi Arabia. *Quat. Sci. Rev.* 30, 1555–1559.
<https://doi.org/10.1016/j.quascirev.2011.04.006>
- Petraglia, M.D., Breeze, P.S., Groucutt, H.S., 2018. *Blue Arabia, Green Arabia: Examining Human Colonisation and Dispersal Models, Geological Setting, Palaeoenvironment and Archaeology of the Red Sea*. Springer International Publishing. <https://doi.org/10.1007/978-3-319-99408-6>
- Petraglia, M.D., Groucutt, H.S., Guagnin, M., Breeze, P.S., Boivin, N., 2020. Human responses to climate and ecosystem change in ancient Arabia. *Proc. Natl. Acad. Sci.* 117, 8263–8270. <https://doi.org/10.1073/pnas.1920211117>
- Pettigrew, R.P., Rogers, S.L., Clarke, S.M., 2019. A microfacies analysis of arid continental carbonates from the Cedar Mesa Sandstone Formation, Utah, USA. *Depos. Rec.* 1–21. <https://doi.org/10.1002/dep2.99>
- Poage, M.A., Chamberlain, C.P., 2001. Empirical relationships between elevation and the stable isotope composition of precipitation and surface waters: Considerations for studies of paleoelevation change. *Am. J. Sci.* 301, 1–15.
<https://doi.org/10.2475/ajs.301.1.1>
- Prell, W.L., Kutzbach, J.E., 1987. Monsoon variability over the past 150,000 years. *J. Geophys. Res.* 92, 8411. <https://doi.org/10.1029/JD092iD07p08411>
- Prescott, J.R., Hutton, J.T., 1995. Environmental dose rates and radioactive disequilibrium from some Australian luminescence dating sites. *Quat. Sci. Rev.* 14, 439–448. [https://doi.org/10.1016/0277-3791\(95\)00037-2](https://doi.org/10.1016/0277-3791(95)00037-2)
- Prescott, J.R., Hutton, J.T., 1994. Cosmic ray contributions to dose rates for luminescence and ESR dating: Large depths and long-term time variations. *Radiat. Meas.* 23, 497–500. [https://doi.org/10.1016/1350-4487\(94\)90086-8](https://doi.org/10.1016/1350-4487(94)90086-8)
- Prescott, J.R., Hutton, J.T., 1988. Cosmic ray and gamma ray dosimetry for TL and ESR. *Int. J. Radiat. Appl. Instrumentation. Part D. Nucl. Tracks Radiat. Meas.* 14, 223–227. [https://doi.org/10.1016/1359-0189\(88\)90069-6](https://doi.org/10.1016/1359-0189(88)90069-6)
- Preusser, F., Chithambo, M.L., Götte, T., Martini, M., Ramseyer, K., Sendezera, E.J., Susino, G.J., Wintle, A.G., 2009. Quartz as a natural luminescence dosimeter. *Earth-Science Rev.* 97, 184–214. <https://doi.org/10.1016/j.earscirev.2009.09.006>
- Preusser, F., Degering, D., Fuchs, M., Hilger, A., Kadereit, A., Klasen, N., Krbetschek M., Richter D., S.J., 2008. Luminescence dating: basics, methods and applications. *Eiszeitalter und Gegenwart Quat. Sci. J.* 57, 95–149.
<https://doi.org/http://dx.doi.org/10.3285/eg.57.1-2.5>
- Profico, A., di Vincenzo, F., Gagliardi, L., Piperno, M., Manzi, G., 2016. Filling the gap. Human cranial remains from Gombore II (Melka kulture, Ethiopia; ca. 850 ka) and

- the origin of *Homo heidelbergensis*. *J. Anthropol. Sci.* 94, 41–63.
<https://doi.org/10.4436/jass.94019>
- Radies, D., Preusser, F., Matter, A., Mange, M., 2004. Eustatic and climatic controls on the development of the Wahiba Sand Sea, Sultanate of Oman. *Sedimentology* 51, 1359–1385. <https://doi.org/10.1111/j.1365-3091.2004.00678.x>
- Rasmussen, M., Guo, X., Wang, Y., Lohmueller, K.E., 2011. An Aboriginal Australian Genome Reveals Separate Human Dispersals into Asia. *Science* (80-.). 334, 94–98. <https://doi.org/10.1126/science.1211177>
- Rees-Jones, J., 1995. Optical dating of young sediments using fine-grain quartz. *Anc. TL* 13, 9–14.
- Renberg, I., 1990. A procedure for preparing large sets of diatom slides from sediment cores. *J. Paleolimnol.* 4, 87–90. <https://doi.org/10.1007/BF00208301>
- Rhodes, E., Schwenninger, J., 2007. Dose rates and radioisotope concentrations in the concrete calibration blocks at Oxford. *Anc. TL* 25, 5–8.
- Richter, D., Grün, R., Joannes-Boyau, R., Steele, T.E., Amani, F., Rué, M., Fernandes, P., Raynal, J.-P., Geraads, D., Ben-Ncer, A., Hublin, J.-J., McPherron, S.P., 2017. The age of the hominin fossils from Jebel Irhoud, Morocco, and the origins of the Middle Stone Age. *Nature* 546, 293–296. <https://doi.org/10.1038/nature22335>
- Roberts, N., Jones, M.D., Benkaddour, A., Eastwood, W.J., Filippi, M.L., Frogley, M.R., Lamb, H.F., Leng, M.J., Reed, J.M., Stein, M., Stevens, L., Valero-Garcés, B., Zanchetta, G., 2008. Stable isotope records of Late Quaternary climate and hydrology from Mediterranean lakes: the ISOMED synthesis. *Quat. Sci. Rev.* 27, 2426–2441. <https://doi.org/10.1016/j.quascirev.2008.09.005>
- Roberts, P., Stewart, M., Alagaili, A.N., Breeze, P., Candy, I., Drake, N., Groucutt, H.S., Scerri, E.M.L., Lee-Thorp, J., Louys, J., Zalmout, I.S., Al-Mufarreh, Y.S.A., Zech, J., Alsharekh, A.M., al Omari, A., Boivin, N., Petraglia, M., 2018. Fossil herbivore stable isotopes reveal middle Pleistocene hominin palaeoenvironment in ‘Green Arabia.’ *Nat. Ecol. Evol.* 2, 1871–1878. <https://doi.org/10.1038/s41559-018-0698-9>
- Roberts, R.G., Galbraith, R.F., Olley, J.M., Yoshida, H., Laslett, G.M., 1999. Optical dating of single and multiple grains of quartz from Jinmium rock shelter, northern Australia: part II, results and implications. *Archaeometry* 41, 365–395.
- Roberts, R.G., Jacobs, Z., Li, B., Jankowski, N.R., Cunningham, A.C., Rosenfeld, A.B., 2015. Optical dating in archaeology: Thirty years in retrospect and grand challenges for the future. *J. Archaeol. Sci.* 56, 41–60. <https://doi.org/10.1016/j.jas.2015.02.028>
- Rohling, E.J., Marino, G., Grant, K.M., 2015. Mediterranean climate and oceanography, and the periodic development of anoxic events (sapropels). *Earth-Science Rev.* 143, 62–97. <https://doi.org/10.1016/j.earscirev.2015.01.008>
- Romanek, C.S., Grossman, E.L., Morse, J.W., 1992. Carbon isotopic fractionation in synthetic aragonite and calcite: Effects of temperature and precipitation rate. *Geochim. Cosmochim. Acta* 56, 419–430.
- Rose, J.I., Usik, V.I., Marks, A.E., Hilbert, Y.H., Galletti, C.S., Morley, M.W., Roberts, R.G., Geiling, J.M., Viktor, C., 2011. The Nubian Complex of Dhofar , Oman : An African Middle Stone Age Industry in Southern Arabia. *PLoS One* 6. <https://doi.org/10.1371/journal.pone.0028239>
- Rosenberg, T.M., Preusser, F., Blechschmidt, I., Fleitmann, D., Jagher, R., Matter, A.,

2012. Late Pleistocene palaeolake in the interior of Oman: A potential key area for the dispersal of anatomically modern humans out-of-Africa? *J. Quat. Sci.* 27, 13–16. <https://doi.org/10.1002/jqs.1560>
- Rosenberg, T.M., Preusser, F., Fleitmann, D., Schwalb, A., Penkman, K., Schmid, T.W., Al-Shanti, M.A., Kadi, K., Matter, A., 2011. Humid periods in southern Arabia: Windows of opportunity for modern human dispersal. *Geology* 39, 1115–1118. <https://doi.org/10.1130/G32281.1>
- Rosenberg, T.M., Preusser, F., Risberg, J., Pliikk, A., Kadi, K.A., Matter, A., Fleitmann, D., 2013. Middle and Late Pleistocene humid periods recorded in palaeolake deposits of the Nafud desert, Saudi Arabia. *Quat. Sci. Rev.* 70, 109–123. <https://doi.org/10.1016/j.quascirev.2013.03.017>
- Roskin, J., Katra, I., Porat, N., Zilberman, E., 2013. Evolution of Middle to Late Pleistocene sandy calcareous paleosols underlying the northwestern Negev Desert Dunefield (Israel). *Palaeogeogr. Palaeoclimatol. Palaeoecol.* 387, 134–152. <https://doi.org/10.1016/j.palaeo.2013.07.018>
- Roskin, J., Porat, N., Tsoar, H., Blumberg, D.G., Zander, A.M., 2011. Age, origin and climatic controls on vegetated linear dunes in the northwestern Negev Desert (Israel). *Quat. Sci. Rev.* 30, 1649–1674. <https://doi.org/10.1016/j.quascirev.2011.03.010>
- Rosignol-Strick, M., 1983. African monsoons, an immediate climate response to orbital insolation. *Nature* 304, 46–49. <https://doi.org/10.1038/304046a0>
- Rozanski, K., Araguás-Araguás, L., Gonfiantini, R., 1993. Isotopic Patterns in Modern Global Precipitation, in: *Climate Change in Continental Isotopic Records. Geophysical Monograph 78.* American Geophysical Union, pp. 1–36. <https://doi.org/10.1029/GM078p0001>
- Ryves, D.B., Battarbee, R.W., Juggins, S., Fritz, S.C., Anderson, N.J., 2006. Physical and chemical predictors of diatom dissolution in freshwater and saline lake sediments in North America and West Greenland. *Limnol. Oceanogr.* 51, 1355–1368. <https://doi.org/10.4319/lo.2006.51.3.1355>
- Ryves, D.B., Juggins, S., Fritz, S.C., Battarbee, R.W., 2001. Experimental diatom dissolution and the quantification of microfossil preservation in sediments. *Palaeogeogr. Palaeoclimatol. Palaeoecol.* 172, 99–113. [https://doi.org/10.1016/S0031-0182\(01\)00273-5](https://doi.org/10.1016/S0031-0182(01)00273-5)
- Sanderson, D.C.W., Clark, R.J., 1994. Pulsed photostimulated luminescence of alkali feldspars. *Radiat. Meas.* 23, 633–639. [https://doi.org/10.1016/1350-4487\(94\)90112-0](https://doi.org/10.1016/1350-4487(94)90112-0)
- Sawka, M.N., Chevront, S.N., Carter III, R., 2005. Human Water Needs. *Nutr. Rev.* 63, 30–39. <https://doi.org/10.1301/nr.2005.jun.S30>
- Scerri, E.M.L., Breeze, P.S., Parton, A., Groucutt, H.S., White, T.S., Stimpson, C., Clark-Balzan, L., Jennings, R., Alsharekh, A., Petraglia, M.D., 2015. Middle to Late Pleistocene human habitation in the western Nefud Desert, Saudi Arabia. *Quat. Int.* 382, 200–214. <https://doi.org/10.1016/j.quaint.2014.09.036>
- Scerri, E.M.L., Chikhi, L., Thomas, M.G., 2019. Beyond multiregional and simple out-of-Africa models of human evolution. *Nat. Ecol. Evol.* 3, 1370–1372. <https://doi.org/10.1038/s41559-019-0992-1>
- Scerri, E.M.L., Drake, N.A., Jennings, R., Groucutt, H.S., 2014a. Earliest evidence for the structure of *Homo sapiens* populations in Africa. *Quat. Sci. Rev.* 101, 207–216.

- <https://doi.org/10.1016/j.quascirev.2014.07.019>
- Scerri, E.M.L., Groucutt, H.S., Jennings, R.P., Petraglia, M.D., 2014b. Unexpected technological heterogeneity in northern Arabia indicates complex Late Pleistocene demography at the gateway to Asia. *J. Hum. Evol.* 75, 125–142. <https://doi.org/10.1016/j.jhevol.2014.07.002>
- Scerri, E.M.L., Guagnin, M., Groucutt, H.S., Armitage, S.J., Parker, L.E., Drake, N., Louys, J., Breeze, P.S., Zahir, M., Alsharekh, A., Petraglia, M.D., 2018a. Neolithic pastoralism in marginal environments during the Holocene Humid Period, northern Saudi Arabia. *Antiquity* 92, 1180–1194. <https://doi.org/10.15184/aqy.2018.108>
- Scerri, E.M.L., Shipton, C., Clark-Balzan, L., Frouin, M., Schwenninger, J.L., Groucutt, H.S., Breeze, P.S., Parton, A., Blinkhorn, J., Drake, N.A., Jennings, R., Cuthbertson, P., Omari, A. Al, Alsharekh, A.M., Petraglia, M.D., 2018b. The expansion of later Acheulean hominins into the Arabian Peninsula. *Sci. Rep.* 8, 1–9. <https://doi.org/10.1038/s41598-018-35242-5>
- Schulz, E., Whitney, J.W., 1986. Upper Pleistocene and Holocene palaeoenvironments in the An Nafud, Saudi Arabia. *Hydrobiologia* 143, 175–190.
- Schulz, E., Whitney, J.W., 1985. Vegetation on the northern Arabian Shield and adjacent sand seas.
- Schwarcz, H.P., Grün, R., Vandermeersch, B., Bar-Yosef, O., Valladas, H., Tchernov, E., 1988. ESR dates for the hominid burial site of Qafzeh in Israel. *J. Hum. Evol.* [https://doi.org/10.1016/0047-2484\(88\)90063-2](https://doi.org/10.1016/0047-2484(88)90063-2)
- Sharp, W.D., Paces, J.B., 2018. Comment on “The Earliest Modern Humans outside Africa.” *Science* (80-). 362.
- Shipton, C., Blinkhorn, J., Breeze, P.S., Cuthbertson, P., Drake, N., Groucutt, H.S., Jennings, R.P., Parton, A., Scerri, E.M.L., Alsharekh, A., Petraglia, M.D., 2018. Acheulean technology and landscape use at Dawadmi, central Arabia. *PLoS One* 13. <https://doi.org/10.1371/journal.pone.0200497>
- Singarayer, J.S., Bailey, R.M., 2004. Component-resolved bleaching spectra of quartz optically stimulated luminescence: Preliminary results and implications for dating. *Radiat. Meas.* 38, 111–118. [https://doi.org/10.1016/S1350-4487\(03\)00250-6](https://doi.org/10.1016/S1350-4487(03)00250-6)
- Singarayer, J.S., Bailey, R.M., 2003. Further investigations of the quartz optically stimulated luminescence components using linear modulation. *Radiat. Meas.* 37, 451–458. [https://doi.org/10.1016/S1350-4487\(03\)00062-3](https://doi.org/10.1016/S1350-4487(03)00062-3)
- Smedley, R.K., 2018. Telling the Time with Dust, Sand and Rocks. *Elements* 14, 9–14. <https://doi.org/10.2138/gselements.14.1.9>
- Smedley, R.K., Duller, G.A.T., Pearce, N.J.G., Roberts, H.M., 2012. Determining the K-content of single-grains of feldspar for luminescence dating. *Radiat. Meas.* 47, 790–796. <https://doi.org/10.1016/j.radmeas.2012.01.014>
- Smith, B.W., Aitken, M.J., Rhodes, E.J., Robinson, P.D., Geldard, D.M., 1986. Optical Dating: Methodological Aspects. *Radiat. Prot. Dosimetry* 17, 229–233.
- Smith, B.W., Rhodes, E.J., 1994. Charge movements in quartz and their relevance to optical dating. *Radiat. Meas.* 23, 323–333. [https://doi.org/10.1016/1350-4487\(94\)90060-4](https://doi.org/10.1016/1350-4487(94)90060-4)
- Smith, J.R., Giegengack, R., Schwarcz, H.P., 2004. Constraints on Pleistocene pluvial climates through stable-isotope analysis of fossil-spring tufas and associated gastropods, Kharga Oasis, Egypt. *Palaeogeogr. Palaeoclimatol. Palaeoecol.* 206,

- 157–175. <https://doi.org/10.1016/j.palaeo.2004.01.021>
- Smith, J.R., Hawkins, A.L., Asmerom, Y., Polyak, V., Giegengack, R., 2007. New age constraints on the Middle Stone Age occupations of Kharga Oasis, Western Desert, Egypt. *J. Hum. Evol.* 52, 690–701. <https://doi.org/10.1016/j.jhevol.2007.01.004>
- Smol, J.P., Wolfe, A.P., Birks, H.J.B., Douglas, M.S.V., Jones, V.J., Korhola, A., Pienitz, R., Rühland, K., Sorvari, S., Antoniades, D., Brooks, S.J., Fallu, M.A., Hughes, M., Keatley, B.E., Laing, T.E., Michelutti, N., Nazarova, L., Nyman, M., Paterson, A.M., Perren, B., Quinlan, R., Rautio, M., Saulnier-Talbot, E., Siitonen, S., Solovieva, N., Weckström, J., 2005. Climate-driven regime shifts in the biological communities of arctic lakes. *Proc. Natl. Acad. Sci.* 102, 4397–4402. <https://doi.org/10.1073/pnas.0500245102>
- Stager, J.C., Ryves, D.B., Chase, B.M., Pausata, F.S.R., 2011. Catastrophic drought in the Afro-Asian monsoon region during Heinrich event 1. *Science* (80-.). 331, 1299–1302. <https://doi.org/10.1126/science.1198322>
- Steffen, D., Preusser, F., Schlunegger, F., 2009. OSL quartz age underestimation due to unstable signal components. *Quat. Geochronol.* 4, 353–362. <https://doi.org/10.1016/j.quageo.2009.05.015>
- Stewart, M., Clark-Wilson, R., Breeze, P.S., Janulis, K., Candy, I., Armitage, S.J., Ryves, D.B., Louys, J., Duval, M., Price, G.J., Cuthbertson, P., Bernal, M.A., Drake, N.A., Alsharekh, A.M., Zahrani, B., Al-Omari, A., Roberts, P., Groucutt, H.S., Petraglia, M.D., 2020a. Human footprints provide snapshot of last interglacial ecology in the Arabian interior. *Sci. Adv.* 6, eaba8940.
- Stewart, M., Louys, J., Breeze, P.S., Clark-Wilson, R., Drake, N.A., Scerri, E.M.L., Zalmout, I.S., Al-Mufarreah, Y.S.A., Soubhi, S.A., Haptari, M.A., Alsharekh, A.M., Groucutt, H.S., Petraglia, M.D., 2020b. A taxonomic and taphonomic study of Pleistocene fossil deposits from the western Nefud Desert, Saudi Arabia. *Quat. Res.* 1–22. <https://doi.org/10.1017/qua.2020.6>
- Stewart, M., Louys, J., Groucutt, H.S., Candy, I., Clark-Wilson, R., Breeze, P.S., Drake, N.A., Price, G.J., Al-mufarreah, Y.S.A., Soubhi, S.A., Zalmout, I.S., Alsharekh, A.M., Petraglia, M.D., 2019. Taphonomic and zooarchaeological investigations at the middle Pleistocene site of Ti ' s al Ghadah, western Nefud Desert, Saudi Arabia. *Quat. Sci. Rev.* 218, 228–253. <https://doi.org/10.1016/j.quascirev.2019.05.024>
- Stewart, M., Louys, J., Price, G.J., Drake, N.A., Groucutt, H.S., Petraglia, M.D., 2017. Middle and Late Pleistocene mammal fossils of Arabia and surrounding regions: Implications for biogeography and hominin dispersals. *Quat. Int.* <https://doi.org/10.1016/j.quaint.2017.11.052>
- Stimpson, C.M., Breeze, P.S., Clark-Balzan, L., Groucutt, H.S., Jennings, R., Parton, A., Scerri, E., White, T.S., Petraglia, M.D., 2015. Stratified Pleistocene vertebrates with a new record of a jaguar-sized pantherine (*Panthera cf. gombaszogensis*) from northern Saudi Arabia. *Quat. Int.* 382, 168–180. <https://doi.org/10.1016/j.quaint.2014.09.049>
- Stimpson, C.M., Lister, A., Parton, A., Clark-Balzan, L., Breeze, P.S., Drake, N.A., Groucutt, H.S., Jennings, R., Scerri, E.M.L., White, T.S., Zahir, M., Duval, M., Gr??n, R., Al-Omari, A., Al Murayyi, K.S.M., Zalmout, I.S., Mufarreah, Y.A., Memesh, A.M., Petraglia, M.D., 2016. Middle Pleistocene vertebrate fossils from the Nefud Desert, Saudi Arabia: Implications for biogeography and palaeoecology. *Quat. Sci.*

- Rev. 143, 13–36. <https://doi.org/10.1016/j.quascirev.2016.05.016>
- Stringer, C., 2016. The origin and evolution of *Homo sapiens*. *Philos. Trans. R. Soc. B Biol. Sci.* 371, 20150237. <https://doi.org/10.1098/rstb.2015.0237>
- Stringer, C., 2012. The status of *Homo heidelbergensis* (Schoetensack 1908). *Evol. Anthropol.* 21, 101–107. <https://doi.org/10.1002/evan.21311>
- Stringer, C., 2000. Coasting out of Africa. *Nature* 405, 25–27. <https://doi.org/10.1038/35011166>
- Stringer, C.B., Grün, R., Schwarcz, H.P., Goldberg, P., 1989. ESR dates for the hominid burial site of Es Skhul in Israel. *Nature* 338, 756–758. <https://doi.org/10.1038/338756a0>
- Szabo, B.J., Haynes, C. V., Maxwell, T.A., 1995. Ages of Quaternary pluvial episodes determined by uranium-series and radiocarbon dating of lacustrine deposits of Eastern Sahara. *Palaeogeogr. Palaeoclimatol. Palaeoecol.* 113, 227–242. [https://doi.org/10.1016/0031-0182\(95\)00052-N](https://doi.org/10.1016/0031-0182(95)00052-N)
- Talbot, M.R., 1990. A review of the palaeohydrological interpretation of carbon and oxygen isotopic ratios in primary lacustrine carbonates. *Chem. Geol. Isot. Geosci. Sect.* 80, 261–279. [https://doi.org/10.1016/0168-9622\(90\)90009-2](https://doi.org/10.1016/0168-9622(90)90009-2)
- Talbot, M.R., Allen, P.A., 1996. Lakes, in: *Sedimentary Environments: Processes, Facies and Stratigraphy*. Blackwell, pp. 83–123.
- Tanner, L.H., 2010. Continental Carbonates as Indicators of Palaeoclimate, in: Alonso-Zarza, A.M., Tanner, L.H. (Eds.), *Carbonates in Continental Settings: Geochemistry, Diagenesis and Applications*. Elsevier, pp. 179–206.
- ter Braak, C.J.F., Prentice, I.C., 1988. A Theory of Gradient Analysis. *Adv. Ecol. Res.* 18, 271–317. [https://doi.org/10.1016/S0065-2504\(08\)60183-X](https://doi.org/10.1016/S0065-2504(08)60183-X)
- ter Braak, C.J.F., Smilauer, P., 2002. *CANOCO reference manual and CanoDraw for Windows user's guide: software for canonical community ordination*.
- Thomas, H., Geraads, D., Janjou, D., Vaslet, D., Memesh, A., Billiou, D., Bocherens, H., Dobigny, G., Eisenmann, V., Gayet, M., Lapparent de Broin, F., Petter, G., Halawani, M., 1998. First Pleistocene faunas from the Arabian peninsula: an Nafud desert, Saudi Arabia. *Earth Planet. Sci.* 326, 145–152. [https://doi.org/10.1016/S1251-8050\(97\)87459-9](https://doi.org/10.1016/S1251-8050(97)87459-9)
- Thomsen, K.J., Murray, A.S., Jain, M., Bøtter-Jensen, L., 2008. Laboratory fading rates of various luminescence signals from feldspar-rich sediment extracts. *Radiat. Meas.* 43, 1474–1486. <https://doi.org/10.1016/j.radmeas.2008.06.002>
- Tierney, J.E., deMenocal, P.B., 2013. Abrupt Shifts in Horn of Africa Hydroclimate Since the Last Glacial Maximum. *Science (80-.)*. 342, 843–846. <https://doi.org/10.1126/science.1244809>
- Tierney, J.E., deMenocal, P.B., Zander, P.D., 2017a. A climatic context for the out-of-Africa migration. *Geology* 1–4. <https://doi.org/10.1130/G39457.1>
- Tierney, J.E., Lewis, S.C., Cook, B.I., LeGrande, A.N., Schmidt, G.A., 2011. Model, proxy and isotopic perspectives on the East African Humid Period. *Earth Planet. Sci. Lett.* 307, 103–112. <https://doi.org/10.1016/j.epsl.2011.04.038>
- Tierney, J.E., Pausata, F.S.R., deMenocal, P.B., 2017b. Rainfall regimes of the Green Sahara. *Sci. Adv.* 3, 1–10.
- Timmermann, A., Friedrich, T., 2016. Late Pleistocene climate drivers of early human migration. *Nature* 538, 92–95. <https://doi.org/10.1038/nature19365>
- Ting, I.P., 1985. Crassulacean acid metabolism. *Annu. Rev. Plant Physiol.* 36, 595–622.

- Toggweiler, J.R., Russell, J., 2008. Ocean circulation in a warming climate. *Nature* 451, 286–288. <https://doi.org/10.1038/nature06590>
- Torfstein, A., Goldstein, S.L., Kushnir, Y., Enzel, Y., Haug, G., Stein, M., 2015. Dead Sea drawdown and monsoonal impacts in the Levant during the last interglacial. *Earth Planet. Sci. Lett.* 412, 235–244. <https://doi.org/10.1016/j.epsl.2014.12.013>
- Tsukamoto, S., Denby, P.M., Murray, A.S., Bøtter-Jensen, L., 2006. Time-resolved luminescence from feldspars: New insight into fading. *Radiat. Meas.* 41, 790–795. <https://doi.org/10.1016/j.radmeas.2006.05.013>
- Tubi, A., Dayan, U., 2014. Tropical Plumes over the Middle East: Climatology and synoptic conditions. *Atmos. Res.* 145–146, 168–181. <https://doi.org/10.1016/j.atmosres.2014.03.028>
- Usdowski, E., Hoefs, J., 1990. Kinetic $^{13}\text{C}/^{12}\text{C}$ and $^{18}\text{O}/^{16}\text{O}$ effects upon dissolution and outgassing of CO_2 in the system $\text{CO}_2/\text{H}_2\text{O}$. *Chem. Geol. Isot. Geosci. Sect.* 80, 109–118. [https://doi.org/10.1016/0168-9622\(90\)90019-9](https://doi.org/10.1016/0168-9622(90)90019-9)
- Vaks, A., Bar-Matthews, M., Ayalon, A., Matthews, A., Frumkin, A., Dayan, U., Halicz, L., Almogi-Labin, A., Schilman, B., 2006. Paleoclimate and location of the border between Mediterranean climate region and the Saharo-Arabian Desert as revealed by speleothems from the northern Negev Desert, Israel. *Earth Planet. Sci. Lett.* 249, 384–399. <https://doi.org/10.1016/j.epsl.2006.07.009>
- Vaks, A., Bar-Matthews, M., Ayalon, A., Matthews, A., Halicz, L., Frumkin, A., 2007. Desert speleothems reveal climatic window for African exodus of early modern humans. *Geology* 35, 831–834. <https://doi.org/10.1130/G23794A.1>
- Vaks, A., Bar-Matthews, M., Matthews, A., Ayalon, A., Frumkin, A., 2010. Middle-Late Quaternary paleoclimate of northern margins of the Saharan-Arabian Desert: Reconstruction from speleothems of Negev Desert, Israel. *Quat. Sci. Rev.* 29, 2647–2662. <https://doi.org/10.1016/j.quascirev.2010.06.014>
- Vaks, A., Woodhead, J., Bar-Matthews, M., Ayalon, A., Cliff, R.A., Zilberman, T., Matthews, A., Frumkin, A., 2013. Pliocene-Pleistocene climate of the northern margin of Saharan-Arabian Desert recorded in speleothems from the Negev Desert, Israel. *Earth Planet. Sci. Lett.* 368, 88–100. <https://doi.org/10.1016/j.epsl.2013.02.027>
- Valladas, H., Reyss, J.L., Joron, J.L., Valladas, G., Bar-Yosef, O., Vandermeersch, B., 1988. Thermoluminescence dating of Mousterian Troto-Cro-Magnon' remains from Israel and the origin of modern man. *Nature* 331, 614–615. <https://doi.org/10.1038/331614a0>
- Verrecchia, E.P., 2007. Lacustrine and palustrine geochemical sediments, in: *Geochemical Sediments and Landscapes*. Blackwell Publishing Ltd, Malden, pp. 298–330.
- Verschuren, D., Lal, R., Cumming, B.F., 2000. Rainfall and drought in equatorial east Africa during the past 1,100 years. *Nature* 403, 410–414. <https://doi.org/10.1038/35000179>
- Wagner, W., 2011. *Groundwater in the Arab Middle East*. Springer Science & Business Media.
- Waldmann, N., Torfstein, A., Stein, M., 2010. Northward intrusions of low- and mid-latitude storms across the Saharo-Arabian belt during past interglacials. *Geology* 38, 567–570. <https://doi.org/10.1130/G30654.1>
- Washington, R., Bouet, C., Cautenet, G., Mackenzie, E., Ashpole, I., Engelstaedter, S.,

- Lizcano, G., Henderson, G.M., Schepanski, K., Tegen, I., 2009. Dust as a tipping element: The Bodélé Depression, Chad. *Proc. Natl. Acad. Sci.* 106, 20564–20571. <https://doi.org/10.1073/pnas.0711850106>
- Watts, N.L., 1980. Quaternary pedogenic calcretes from the Kalahari (southern Africa): mineralogy, genesis and diagenesis. *Sedimentology* 27, 661–686. <https://doi.org/10.1111/j.1365-3091.1980.tb01654.x>
- Werner, M., Langebroek, P.M., Carlsen, T., Herold, M., Lohmann, G., 2011. Stable water isotopes in the ECHAM5 general circulation model: Toward high-resolution isotope modeling on a global scale. *J. Geophys. Res. Atmos.* 116. <https://doi.org/10.1029/2011JD015681>
- Wetzel, R.G., 1975. *Limnology*. WB Sanders, Philadelphia.
- Whitney, J.W., Faulkender, D.J., Rubin, M., 1983. The environmental history and present condition of Saudi Arabia's northern sand seas.
- Whitney, J.W., Gettings, M.E., 1982. Preliminary geological investigation of the Bi'r Hayzan diatomite deposit, Kingdom of Saudi Arabia.
- Williams, M.A.J., Duller, G.A.T., Williams, F.M., Woodward, J.C., Macklin, M.G., El Tom, O.A.M., Munro, R.N., El Hajaz, Y., Barrows, T.T., 2015. Causal links between Nile floods and eastern Mediterranean sapropel formation during the past 125 kyr confirmed by OSL and radiocarbon dating of Blue and White Nile sediments. *Quat. Sci. Rev.* 130, 89–108. <https://doi.org/10.1016/j.quascirev.2015.05.024>
- Wintle, A.G., 1973. Anomalous Fading of Thermo-luminescence in Mineral Samples. *Nature* 245, 144–145. <https://doi.org/10.1038/245143a0>
- Wintle, A.G., Adamiec, G., 2017. Optically stimulated luminescence signals from quartz: A review. *Radiat. Meas.* <https://doi.org/10.1016/j.radmeas.2017.02.003>
- Wintle, A.G., Murray, A.S., 2006. A review of quartz optically stimulated luminescence characteristics and their relevance in single-aliquot regeneration dating protocols. *Radiat. Meas.* 41, 369–391. <https://doi.org/10.1016/j.radmeas.2005.11.001>
- Wright, P., 1990. Lacustrine carbonates, in: *Carbonate Sedimentology*. Blackwell, pp. 164–190.
- Ziegler, M., Tuenter, E., Lourens, L.J., 2010. The precession phase of the boreal summer monsoon as viewed from the eastern Mediterranean (ODP Site 968). *Quat. Sci. Rev.* 29, 1481–1490. <https://doi.org/10.1016/j.quascirev.2010.03.011>
- Zimmerman, D.W., 1971. Thermoluminescent Dating Using Fine Grains from Pottery. *Archaeometry* 13, 29–52. <https://doi.org/10.1111/j.1475-4754.1971.tb00028.x>
- Ziv, B., 2001. A subtropical rainstorm associated with a tropical plume over Africa and the Middle-East. *Theor. Appl. Climatol.* 69, 91–102. <https://doi.org/10.1007/s007040170037>

Appendices

Appendices 1: Stable oxygen and carbon isotope data

Table A1 - Stable oxygen and carbon isotope from Al Wusta. PD15, 16 and 17 data were generated during MSc work while trench PD40 was carried out as part of this PhD. Note that for analysis of PD40 in the thesis, samples over the first 20 cm derive from work undertaken at UCL while 30 – 100 cm derive from work from the RHUL laboratory.

Site	Trench	Name	Sample (height above base cm)	d ¹³ C corr (‰)	error (1s)	d ¹⁸ O corr (‰)	error (1s)	Est % carb	Work carried out at
Al Wusta	PD15	I16-0018	10	0.94	0.04	-2.33	0.09	58.91	RHUL
Al Wusta	PD15	I16-0019	20	0.94	0.02	-2.40	0.10	66.90	RHUL
Al Wusta	PD15	I16-0020	30	0.98	0.03	-2.79	0.09	63.25	RHUL
Al Wusta	PD15	I16-0021	40	1.13	0.04	-1.66	0.07	89.40	RHUL
Al Wusta	PD15	I16-0022	50	-0.69	0.04	-2.05	0.01	77.37	RHUL
Al Wusta	PD16	I16-0023	10	1.01	0.01	-0.68	0.02	68.31	RHUL
Al Wusta	PD16	I16-0024	20	0.17	0.04	-2.09	0.02	50.68	RHUL
Al Wusta	PD16	I16-0025	30	0.76	0.03	-1.30	0.00	67.39	RHUL
Al Wusta	PD16	I16-0026	40	0.81	0.01	-1.63	0.03	65.40	RHUL
Al Wusta	PD16	I16-0027	50	0.70	0.03	-2.78	0.04	71.15	RHUL
Al Wusta	PD16	I16-0028	60	0.22	0.02	-2.97	0.05	48.83	RHUL
Al Wusta	PD16	I16-0029	70	1.87	0.03	-2.43	0.01	70.03	RHUL
Al Wusta	PD16	I16-0030	80	-5.24	0.05	-3.55	0.01	72.18	RHUL
Al Wusta	PD17	I16-0031	10	0.84	0.01	-2.45	0.06	48.83	RHUL
Al Wusta	PD17	I16-0032	20	1.94	0.02	-2.23	0.08	85.94	RHUL
Al Wusta	PD17	I16-0033	30	1.70	0.05	-2.20	0.06	86.80	RHUL
Al Wusta	PD17	I16-0034	40	0.17	0.01	-2.26	0.00	69.16	RHUL
Al Wusta	PD40	WNEF 16-30 BASE	0	-5.81	0.03	-3.56	0.03	49.75	RHUL
Al Wusta	PD40	I16-0081	0	-5.82	0.06	-3.98	0.05		UCL
Al Wusta	PD40	I16-0082	2	-6.57	0.06	-4.94	0.05		UCL
Al Wusta	PD40	I16-0083	4	-5.80	0.06	-5.02	0.05		UCL

Al	PD40	I16-0084	6	-4.79	0.03	-4.83	0.05		UCL
Wusta									
Al	PD40	I16-0085	8	0.03	0.06	-2.86	0.05		UCL
Wusta									
Al	PD40	WNEF 16-30 10	10	0.20	0.01	-1.98	0.02	66.07	RHUL
Wusta									
Al	PD40	I16-0086	10	0.21	0.06	-2.46	0.05		UCL
Wusta									
Al	PD40	I16-0087	13	-0.12	0.06	-3.40	0.05		UCL
Wusta									
Al	PD40	I16-0088	15	0.62	0.06	-3.63	0.05		UCL
Wusta									
Al	PD40	WNEF 16-30 20	20	0.61	0.07	-2.39	0.04	80.15	RHUL
Wusta									
Al	PD40	I16-0089	20	0.36	0.06	-3.57	0.05		UCL
Wusta									
Al	PD40	WNEF 16-30 30	30	1.75	0.00	-1.69	0.04	86.95	RHUL
Wusta									
Al	PD40	WNEF 16-30 40	40	1.08	0.05	-2.74	0.00	68.05	RHUL
Wusta									
Al	PD40	WNEF 16-30 50	50	0.61	0.01	-2.41	0.06	61.44	RHUL
Wusta									
Al	PD40	WNEF 16-30 60	60	1.14	0.05	-1.95	0.03	63.44	RHUL
Wusta									
Al	PD40	WNEF 16-30 70	70	0.97	0.01	-1.35	0.03	63.91	RHUL
Wusta									
Al	PD40	WNEF 16-30 80	80	1.12	0.01	-1.20	0.10	74.46	RHUL
Wusta									
Al	PD40	WNEF 16-30 90	90	0.94	0.03	-1.61	0.04	65.26	RHUL
Wusta									
Al	PD40	WNEF 16-30 100	100	1.52	0.00	-0.09	0.10	45.68	RHUL
Wusta									
Al	PD40	Rhizolith		-1.12	0.01	1.58	0.08	36.70	RHUL
Wusta									

Table A2 - Stable oxygen and carbon isotope from Site 16.3. Data generated during MSc thesis (Clark-Wilson, 2016)

Site	Name	Sample (height above base cm)	d ¹³ C corr (‰)	error (1s)	d ¹⁸ O corr (‰)	error (1s)	Work carried out at
16.3	I16-0001	0	-1.08	0.00	1.55	0.05	RHUL
16.3	I16-0002	20	-2.18	0.03	2.97	0.06	RHUL
16.3	I16-0003	40	-0.27	0.02	0.61	0.02	RHUL
16.3	I16-0004	60	1.88	0.01	3.75	0.08	RHUL
16.3	I16-0005	80	2.02	0.00	4.27	0.08	RHUL
16.3	I16-0006	100	2.64	0.01	2.06	0.06	RHUL
16.3	I16-0007	120	3.18	0.02	2.09	0.05	RHUL
16.3	I16-0008	140	2.90	0.06	4.33	0.09	RHUL
16.3	I16-0009	160	2.19	0.01	1.40	0.05	RHUL
16.3	I16-0010	180	2.47	0.03	3.47	0.06	RHUL
16.3	I16-0011	200	3.24	0.00	2.49	0.04	RHUL
16.3	I16-0012	220	1.07	0.06	2.34	0.10	RHUL
16.3	I16-0013	240	1.29	0.05	2.85	0.04	RHUL
16.3	I16-0014	260	1.26	0.02	3.04	0.08	RHUL
16.3	I16-0015	280	0.60	0.02	2.03	0.02	RHUL
16.3	I16-0016	300	0.35	0.01	1.39	0.06	RHUL
16.3	I16-0017	320	0.48	0.03	-0.85	0.08	RHUL

Table A3 - Stable oxygen and carbon isotope from WNEF16_28.

Site	Name	Sample (height above base cm)	d ¹³ C corr (‰)	error (1s)	d ¹⁸ O corr (‰)	error (1s)	Work carried out at
WNEF16_28	I16-0052	0	-0.45	0.06	-2.06	0.05	UCL
WNEF16_28	I17-0064	5	-0.45	0.06	-1.88	0.05	UCL
WNEF16_28	I16-0053	10	-1.01	0.06	-3.16	0.05	UCL
WNEF16_28	I17-0065	15	-0.07	0.06	-4.18	0.05	UCL
WNEF16_28	I16-0054	20	0.59	0.06	-2.67	0.05	UCL
WNEF16_28	I17-0066	25	0.24	0.06	-4.40	0.05	UCL
WNEF16_28	I16-0055	30	0.52	0.06	-5.20	0.05	UCL
WNEF16_28	I17-0067	35	0.01	0.06	-6.11	0.05	UCL
WNEF16_28	I16-0056	40	0.71	0.06	-3.44	0.05	UCL
WNEF16_28	I17-0068	45	0.55	0.06	-5.04	0.05	UCL
WNEF16_28	I16-0057	50	0.38	0.06	-6.59	0.05	UCL
WNEF16_28	I17-0069	55	-0.77	0.06	-6.17	0.05	UCL
WNEF16_28	I16-0058	60	0.87	0.06	-5.26	0.05	UCL
WNEF16_28	I17-0070	65	1.09	0.06	-4.09	0.05	UCL
WNEF16_28	I16-0059	70	0.20	0.06	-6.54	0.05	UCL
WNEF16_28	I17-0071	75	0.59	0.06	-2.46	0.05	UCL
WNEF16_28	I16-0060	80	0.50	0.03	-2.85	0.05	UCL
WNEF16_28	I17-0072	85	1.05	0.06	-1.73	0.05	UCL
WNEF16_28	I16-0061	90	0.78	0.06	-1.85	0.05	UCL
WNEF16_28	I17-0073	95	-0.85	0.02	-1.87	0.06	UCL
WNEF16_28	I16-0062	Rhizolith	-0.36	0.02	0.40	0.06	UCL

Table A4 - Stable oxygen and carbon isotope from KAM4 lake 1.

Site	Name	Sample (height above base cm)	d ¹³ C corr (‰)	error (1s)	d ¹⁸ O corr (‰)	error (1s)	Work carried out at
KAM4 L1	I17-0101	0	-1.08	0.03	-3.09	0.08	UCL
KAM4 L1	I17-0102	2	-0.55	0.03	-2.88	0.08	UCL
KAM4 L1	I17-0103	4	-0.96	0.03	-3.46	0.08	UCL
KAM4 L1	I17-0104	7	-1.14	0.03	-3.47	0.08	UCL
KAM4 L1	I17-0105	10	-1.77	0.03	-3.50	0.08	UCL
KAM4 L1	I17-0106	13	-1.45	0.03	-3.24	0.08	UCL
KAM4 L1	I17-0107	15	-1.47	0.03	-3.76	0.08	UCL
KAM4 L1	I17-0108	18	-1.76	0.03	-3.52	0.08	UCL
KAM4 L1	I17-0109	21	-1.63	0.03	-3.59	0.08	UCL
KAM4 L1	I17-0110	23	-1.45	0.03	-2.78	0.08	UCL
KAM4 L1	I17-0111	32	-2.60	0.03	-2.83	0.08	UCL
KAM4 L1	I17-0112	42	-2.32	0.03	-3.72	0.08	UCL

Table A5 - Stable oxygen and carbon isotope from KAM4 lake 2.

Site	Name	Sample (height above base cm)	d ¹³ C corr (‰)	error (1s)	d ¹⁸ O corr (‰)	error (1s)	Work carried out at
KAM4 L2	I17-0090	4	0.94	0.03	-1.47	0.08	UCL
KAM4 L2	I17-0091	7	2.00	0.03	0.20	0.08	UCL
KAM4 L2	I17-0092	10	2.27	0.03	0.66	0.08	UCL
KAM4 L2	I17-0093	13	2.12	0.03	0.47	0.08	UCL
KAM4 L2	I17-0094	16	1.79	0.03	2.98	0.08	UCL
KAM4 L2	I17-0095	19	2.20	0.03	1.29	0.08	UCL
KAM4 L2	I17-0096	22	1.88	0.03	1.00	0.08	UCL
KAM4 L2	I17-0097	24	2.33	0.03	3.27	0.08	UCL
KAM4 L2	I17-0098	29	2.23	0.03	2.68	0.08	UCL
KAM4 L2	I17-0099	32	1.57	0.03	-0.87	0.08	UCL
KAM4 L2	I17-0100	35	2.03	0.03	-0.81	0.08	UCL

Table A6 - Stable oxygen and carbon isotope from KAM4 lake 3.

Site	Name	Sample (height above base cm)	d ¹³ C corr (‰)	error (1s)	d ¹⁸ O corr (‰)	error (1s)	Work carried out at
KAM4 L3	I17-0074	0	-2.55	0.03	0.02	0.08	UCL
KAM4 L3	I17-0075	1	-3.24	0.03	0.46	0.08	UCL
KAM4 L3	I17-0076	2	-3.11	0.03	0.67	0.08	UCL
KAM4 L3	I17-0077	3	-4.24	0.03	0.03	0.08	UCL
KAM4 L3	I17-0078	6	-2.24	0.03	0.59	0.08	UCL
KAM4 L3	I17-0079	9	-1.42	0.03	0.44	0.08	UCL
KAM4 L3	I17-0080	12	-1.39	0.03	0.40	0.08	UCL
KAM4 L3	I17-0081	15	-0.89	0.03	0.24	0.08	UCL
KAM4 L3	I17-0082	24	0.13	0.03	1.00	0.08	UCL
KAM4 L3	I17-0083	27	0.32	0.03	0.81	0.08	UCL
KAM4 L3	I17-0084	30	0.49	0.03	0.51	0.08	UCL
KAM4 L3	I17-0085	33	0.71	0.03	0.98	0.08	UCL
KAM4 L3	I17-0086	36	0.87	0.03	1.62	0.08	UCL
KAM4 L3	I17-0087	42	1.06	0.03	1.04	0.08	UCL
KAM4 L3	I17-0088	45	1.15	0.03	1.08	0.08	UCL
KAM4 L3	I17-0089	48	1.53	0.03	1.48	0.08	UCL

Table A7 - Stable oxygen and carbon isotope from KAM4 lake 3a.

Site	Name	Sample (height above base cm)	d ¹³ C corr (‰)	error (1s)	d ¹⁸ O corr (‰)	error (1s)	Work carried out at
KAM4 L3A	I16-0090	unit 2	-2.87	0.02	-3.74	0.06	UCL
KAM4 L3A	I16-0091	unit 3a (base)	-1.42	0.08	-0.46	0.05	UCL
KAM4 L3A	I16-0092	unit 3a (above base)	-1.89	0.08	-2.17	0.05	UCL
KAM4 L3A	I16-0093	60 (unit 3b)	-0.45	0.08	-0.66	0.05	UCL
KAM4 L3A	I16-0094	62 (unit 3b)	-0.15	0.08	-1.04	0.05	UCL
KAM4 L3A	I16-0095	64 (unit 3b)	-0.21	0.08	-0.50	0.05	UCL
KAM4 L3A	I16-0096	66 (unit 3b)	-0.86	0.08	0.23	0.05	UCL
KAM4 L3A	I16-0097	Calcrete	-0.05	0.08	0.13	0.05	UCL

Table A8 - Stable oxygen and carbon isotope from KAM4 lake 3b.

Site	Name	Sample (height above base cm)	d ¹³ C corr (‰)	error (1s)	d ¹⁸ O corr (‰)	error (1s)	Work carried out at
KAM4 L3B	I16-0075	~2 - 5cm	-5.56	0.02	-2.32	0.06	UCL
KAM4 L3B	I16-0076	5cm	-4.09	0.02	-0.59	0.06	UCL
KAM4 L3B	I16-0077	9cm	-3.83	0.02	-0.04	0.06	UCL
KAM4 L3B	I16-0078	13cm	-3.36	0.02	0.57	0.06	UCL
KAM4 L3B	I16-0079	17cm	-3.42	0.02	0.46	0.06	UCL
KAM4 L3B	I16-0080	Calcrete	0.94	0.02	2.44	0.06	UCL

Table A9 - Stable oxygen and carbon isotope from KAM4 lake 4.

Site	Name	Sample (height above base cm)	d ¹³ C corr (‰)	error (1s)	d ¹⁸ O corr (‰)	error (1s)	Work carried out at
KAM4 L4	I16-0063	10	-0.55	0.08	0.81	0.05	UCL
KAM4 L4	I16-0064	15	-1.35	0.08	-0.08	0.05	UCL
KAM4 L4	I16-0065	20	-1.30	0.08	0.20	0.05	UCL
KAM4 L4	I16-0066	25	-4.37	0.08	-1.25	0.05	UCL
KAM4 L4	I17-0211	40	-2.82	0.08	-1.28	0.05	UCL
KAM4 L4	I16-0068	55	-2.94	0.08	-1.41	0.05	UCL
KAM4 L4	I16-0069	65	-4.80	0.08	-0.77	0.05	UCL
KAM4 L4	I16-0070	70	-7.81	0.08	-0.56	0.05	UCL
KAM4 L4	I17-0185	75	-7.98	0.08	-0.58	0.05	UCL
KAM4 L4	I16-0071	80	-4.06	0.08	-0.54	0.05	UCL
KAM4 L4	I17-0186	85	-6.66	0.03	0.06	0.08	UCL
KAM4 L4	I16-0072	90	-7.88	0.08	-1.09	0.05	UCL
KAM4 L4	I17-0187	95	-6.83	0.03	-2.04	0.08	UCL
KAM4 L4	I16-0073	100	-7.01	0.08	-1.72	0.05	UCL
KAM4 L4	I17-0188	107	-4.63	0.03	-1.05	0.08	UCL
KAM4 L4	I16-0074	110	-4.89	0.08	-1.43	0.05	UCL
KAM4 L4	I17-0189	114	-4.70	0.08	-1.53	0.08	UCL

Table A10 - Stable oxygen and carbon isotope from Ti's al Ghadah (TAG) 1

Site	Name	Sample (height above base cm)	d ¹³ C corr (‰)	error (1s)	d ¹⁸ O corr (‰)	error (1s)	Work carried out at
TAG 1	I17-0163	19	0.20	0.03	-1.16	0.05	UCL
TAG 1	I17-0164	25	0.42	0.03	-0.96	0.05	UCL
TAG 1	I17-0165	27	0.46	0.03	-0.97	0.05	UCL
TAG 1	I17-0166	29	0.03	0.03	-1.40	0.05	UCL
TAG 1	I17-0167	31	-0.19	0.03	-1.44	0.05	UCL
TAG 1	I17-0168	33	1.07	0.03	-1.36	0.05	UCL
TAG 1	I17-0169	37 - 43	0.11	0.03	-0.69	0.05	UCL
TAG 1	I17-0170	45	0.42	0.03	-1.96	0.05	UCL
TAG 1	I17-0171	50	-0.33	0.03	-0.61	0.05	UCL
TAG 1	I17-0172	55	-1.34	0.03	-0.76	0.05	UCL
TAG 1	I17-0173	60	-0.81	0.03	-1.72	0.05	UCL
TAG 1	I17-0174	65	-1.85	0.03	-2.12	0.05	UCL

Table A11 - Stable oxygen and carbon isotope from Ti's al Ghadah (TAG) 2.

Site	Name	Sample (height above base cm)	d ¹³ C corr (‰)	error (1s)	d ¹⁸ O corr (‰)	error (1s)	Work carried out at
TAG 2	I17-0175	14	1.04	0.03	0.39	0.05	UCL
TAG 2	I17-0176	17	1.07	0.03	0.20	0.05	UCL
TAG 2	I17-0177	20	1.00	0.03	0.87	0.05	UCL
TAG 2	I17-0178	23	0.51	0.03	0.03	0.05	UCL
TAG 2	I17-0179	26	0.23	0.03	0.08	0.05	UCL
TAG 2	I17-0180	29	1.26	0.03	-0.12	0.05	UCL
TAG 2	I17-0181	32	0.77	0.03	0.30	0.05	UCL
TAG 2	I17-0182	35	0.77	0.03	-0.07	0.05	UCL
TAG 2	I17-0183	38	1.03	0.03	0.34	0.05	UCL
TAG 2	I17-0184	41	0.50	0.03	-0.40	0.05	UCL

Table A12 – Bulk vs sieved isotopic data from Al Wusta, Site 16.3, WNEF16_28, KAM4 lakes 3, 3a and 4. It is standard practice to analyse the <63 µm size fraction to ensure the analysed fraction is pure authigenic carbonate as opposed to a mixture of biogenic and authigenic carbonate. However, this was not always possible due to incipient cementation. To demonstrate that bulk samples did not affect the derived isotopic data, samples that were friable enough to be sieved were disaggregated using sodium hexametaphosphate. A sub-sample of disaggregated material was homogenised and is referred to as the bulk sample hereafter. The <63 µm size fraction of the disaggregated material was isolated via sieving, and is referred to as the sieved sample hereafter. There was negligible difference between the isotopic values of the sieved vs bulk samples (see Table A12; Appendices 1), demonstrating that isotopic results generated using bulk samples from cemented material primarily reflect environmental changes rather than changes in the proportion of biogenic and authigenic carbonate. See section 5.3.3.

Site name	Sample Name	Depth (height above base cm)	Bulk or Sieved	d ¹³ C corr (‰)	error (1s)	d ¹⁸ O corr (‰)	error (1s)	Analyses carried out at
Al Wusta	I16-0021	40	Bulk	1.13	0.04	-1.66	0.07	RHUL
Al Wusta	I16-0042	40	Sieved	1.40	0.02	-1.95	0.02	RHUL
Al Wusta	I16-0032	20	Bulk	1.94	0.02	-2.23	0.08	RHUL
Al Wusta	I16-0043	20	Sieved	1.94	0.02	-2.49	0.06	RHUL
Al Wusta	I16-0033	30	Bulk	1.70	0.05	-2.20	0.06	RHUL
Al Wusta	I16-0044	30	Sieved	1.67	0.01	-2.20	0.06	RHUL
Al Wusta	I16-0034	40	Bulk	0.17	0.01	-2.26	0.00	RHUL
Al Wusta	I16-0045	40	Sieved	0.23	0.00	-2.99	0.01	RHUL
16.3	I16-0002	20	Bulk	-2.18	0.03	2.97	0.06	RHUL
16.3	I16-0035	20	Sieved	-2.64	0.01	4.28	0.02	RHUL
16.3	I16-0004	60	Bulk	1.88	0.01	3.75	0.08	RHUL
16.3	I16-0036	60	Sieved	1.84	0.04	3.74	0.04	RHUL
16.3	I16-0005	80	Bulk	2.02	0.00	4.27	0.08	RHUL
16.3	I16-0037	80	Sieved	1.63	0.02	3.31	0.06	RHUL
16.3	I16-0010	180	Bulk	2.47	0.03	3.47	0.06	RHUL
16.3	I16-0038	180	Sieved	2.40	0.01	2.08	0.03	RHUL
16.3	I16-0011	200	Bulk	3.24	0.00	2.49	0.04	RHUL
16.3	I16-0039	200	Sieved	3.31	0.02	2.41	0.05	RHUL
16.3	I16-0014	260	Bulk	1.26	0.02	3.04	0.08	RHUL
16.3	I16-0040	260	Sieved	1.23	0.03	2.09	0.07	RHUL
WNEF16_28	I16-0057	50 (1)	Bulk	0.38	0.06	-6.59	0.05	UCL
WNEF16_28	I17-0202	50 cm (2)	Bulk	0.79	0.03	-4.99	0.08	UCL
WNEF16_28	I17-0190	50 cm (3)	Sieved	0.90	0.03	-5.08	0.08	UCL
WNEF16_28	I16-0058	60 (1)	Bulk	0.87	0.06	-5.26	0.05	UCL
WNEF16_28	I17-0203	60 cm (2)	Bulk	1.61	0.03	-4.43	0.08	UCL
WNEF16_28	I17-0191	60 cm (3)	Sieved	1.72	0.03	-4.63	0.08	UCL
WNEF16_28	I16-0059	70 (1)	Bulk	0.20	0.06	-6.54	0.05	UCL
WNEF16_28	I17-0204	70 cm (2)	Bulk	0.79	0.03	-5.34	0.08	UCL
WNEF16_28	I17-0192	70 cm (3)	Sieved	0.86	0.03	-5.42	0.08	UCL
WNEF16_28	I16-0061	90 (1)	Bulk	0.78	0.06	-1.85	0.05	UCL
WNEF16_28	I17-0205	90 cm (2)	Bulk	0.94	0.03	-1.96	0.08	UCL

WNEF16_28	I17-0193	90 cm (3)	Sieved	1.19	0.03	-1.15	0.08	UCL
KAM 4 lake 3b	I16-0076	5cm (1)	Bulk	-4.09	0.02	-0.59	0.06	UCL
KAM 4 lake 3b	I17-0206	5 cm (2)	Bulk	-4.18	0.03	-0.68	0.08	UCL
KAM 4 lake 3b	I17-0194	5 cm (3)	Sieved	-4.17	0.03	-0.75	0.08	UCL
KAM 4 lake 3b	I16-0077	9cm (1)	Bulk	-3.83	0.02	-0.04	0.06	UCL
KAM 4 lake 3b	I17-0207	9 cm (2)	Bulk	-3.77	0.03	0.03	0.08	UCL
KAM 4 lake 3b	I17-0195	9 cm (3)	Sieved	-3.78	0.03	-0.10	0.08	UCL
KAM 4 lake 3b	I16-0078	13 cm (1)	Bulk	-3.36	0.02	0.57	0.06	UCL
KAM 4 lake 3b	I17-0208	13 cm (2)	Bulk	-3.57	0.03	0.38	0.08	UCL
KAM 4 lake 3b	I17-0196	13 cm (3)	Sieved	-3.46	0.03	0.44	0.08	UCL
KAM 4 lake 4	I16-0063	10 (1)	Bulk	-0.55	0.08	0.81	0.05	UCL
KAM 4 lake 4	I17-0209	10 (2)	Bulk	-0.14	0.03	1.67	0.08	UCL
KAM 4 lake 4	I17-0197	10 (3)	Sieved	-0.77	0.03	1.41	0.08	UCL
KAM 4 lake 4	I16-0066	25 (1)	Bulk	-4.37	0.08	-1.25	0.05	UCL
KAM 4 lake 4	I17-0210	25 (2)	Bulk	-4.72	0.03	-1.90	0.08	UCL
KAM 4 lake 4	I17-0198	25 (3)	Sieved	-4.71	0.03	-1.97	0.08	UCL
KAM 4 lake 4	I17-0211	40 (2)	Bulk	-2.82	0.03	-1.28	0.08	UCL
KAM 4 lake 4	I17-0199	40 (3)	Sieved	-2.73	0.03	-1.21	0.08	UCL
KAM 4 lake 4	I16-0070	70 (1)	Bulk	-7.81	0.08	-0.56	0.05	UCL
KAM 4 lake 4	I17-0212	70 (2)	Bulk	-2.63	0.03	2.58	0.08	UCL
KAM 4 lake 4	I17-0200	70 (3)	Sieved	-7.17	0.03	-0.50	0.08	UCL
KAM 4 lake 4	I16-0073	100 (1)	Bulk	-7.01	0.08	-1.72	0.05	UCL
KAM 4 lake 4	I17-0213	100 (2)	Bulk	-6.68	0.03	-1.79	0.08	UCL
KAM 4 lake 4	I17-0201	100 (3)	Sieved	-6.16	0.03	-1.84	0.08	UCL

Appendices 2: Micromorphology images

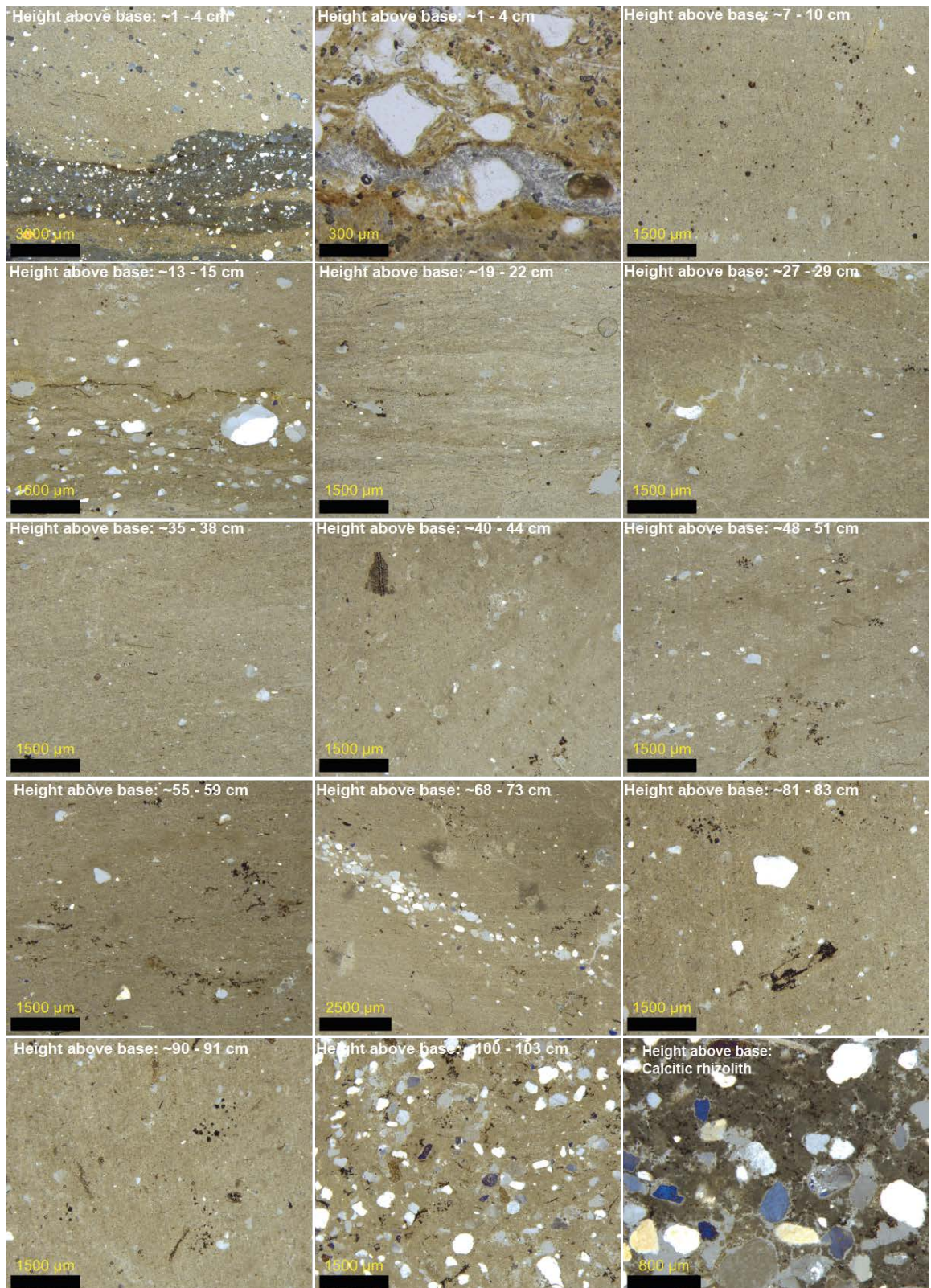


Figure A1 – Microfacies from the PD40 sequence at Al Wusta.

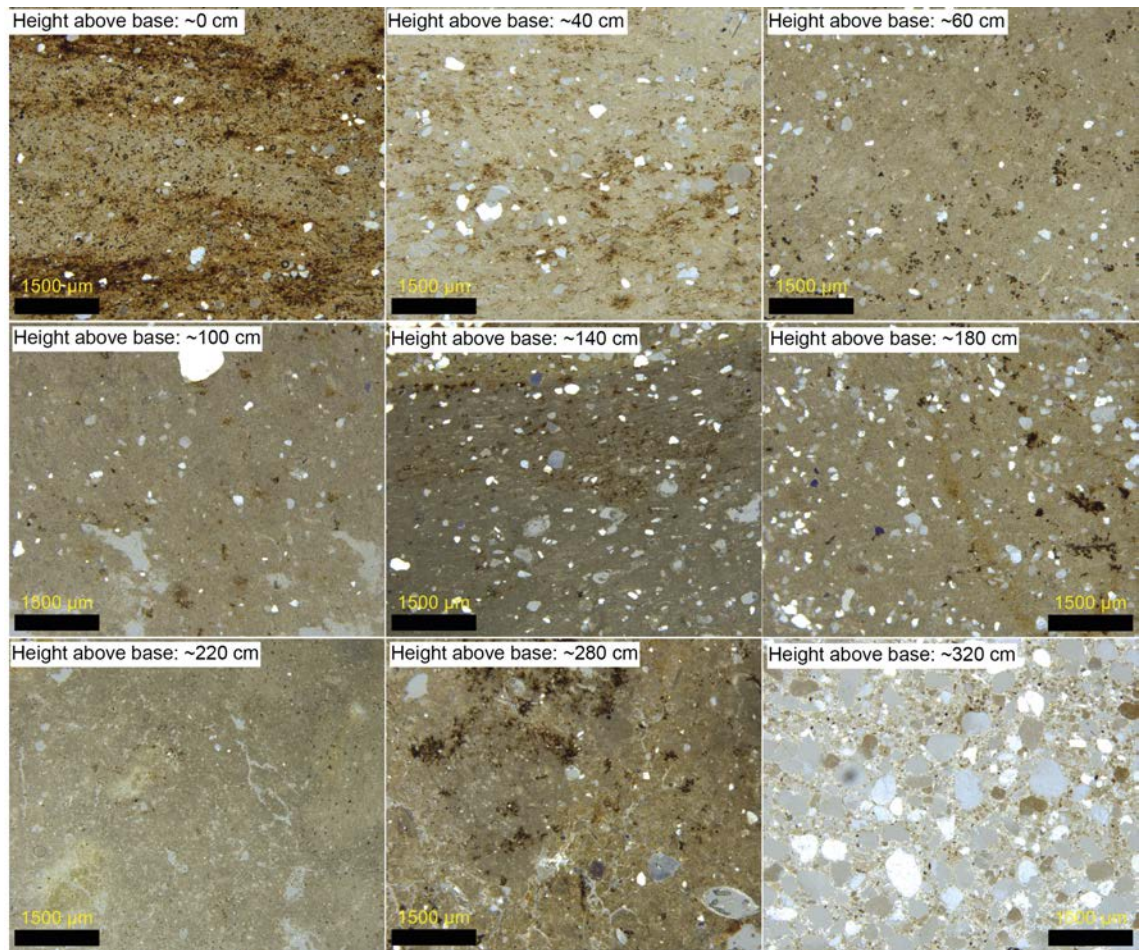


Figure A2 – Microfacies from Site 16.3. This data was generated was part of MSc research (Clark-Wilson, 2016).

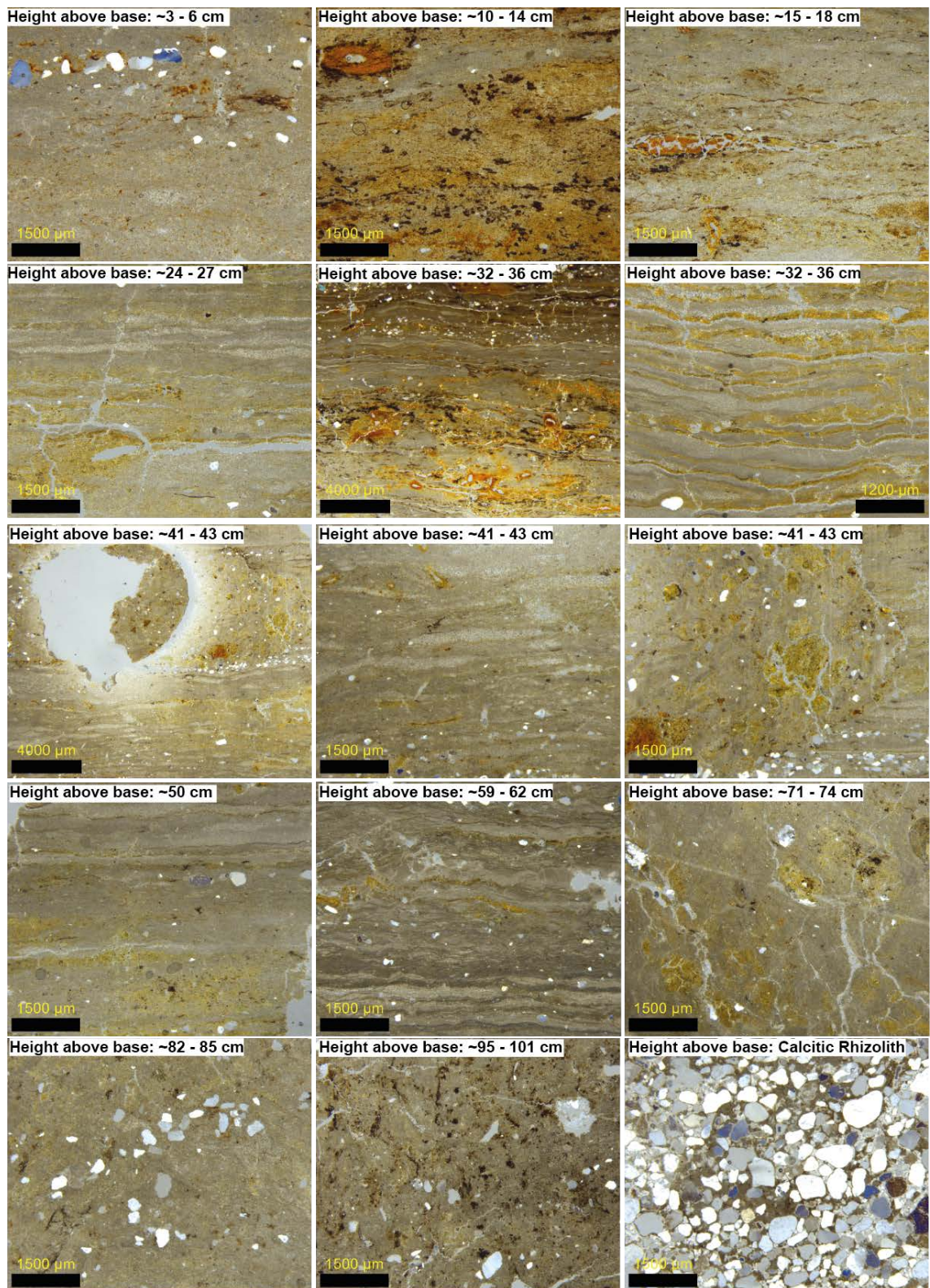


Figure A3 – Microfacies from WNEF16_28.

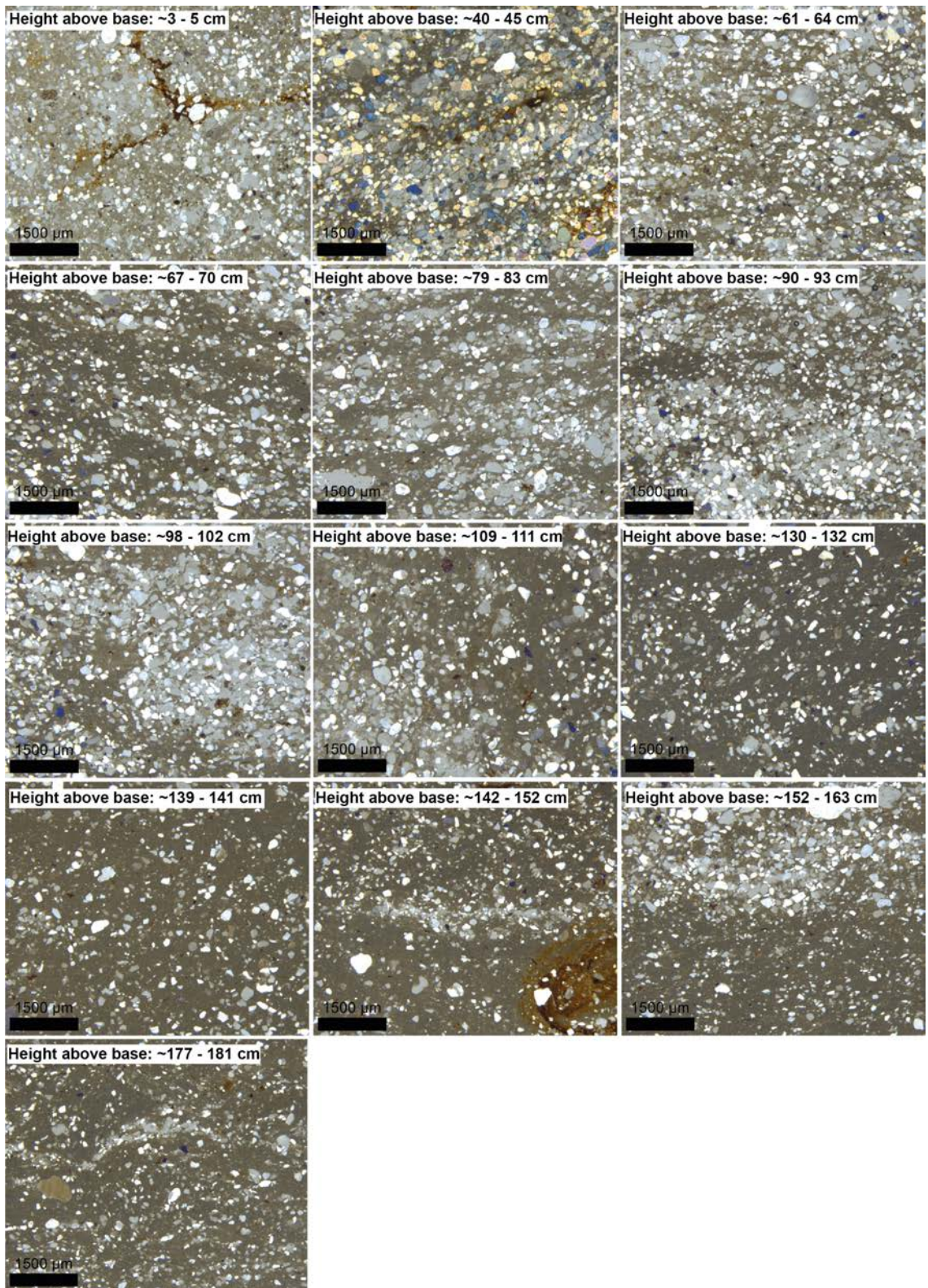


Figure A4 – Microfacies from Alathar.

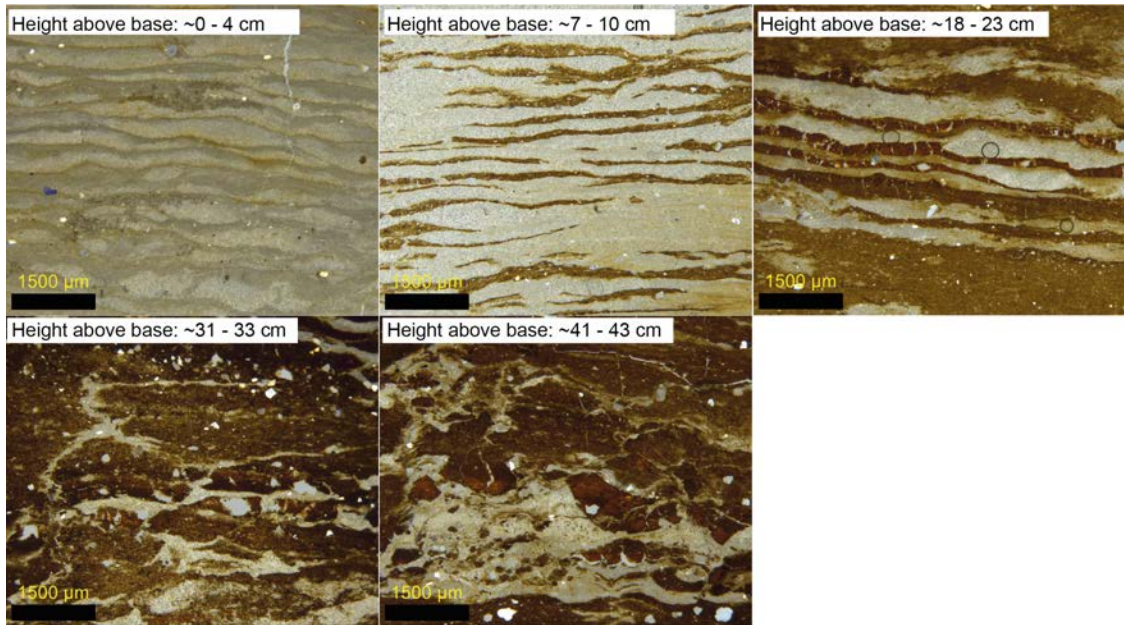


Figure A5 – Microfacies from KAM4 lake 1.

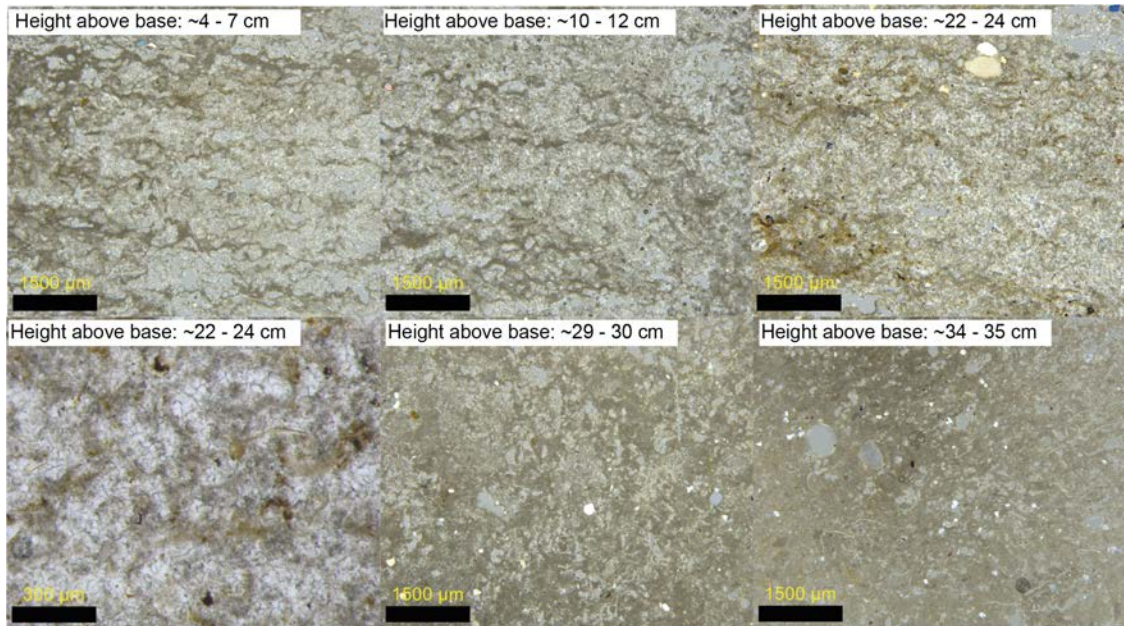


Figure A6 – Microfacies from KAM4 lake 2.

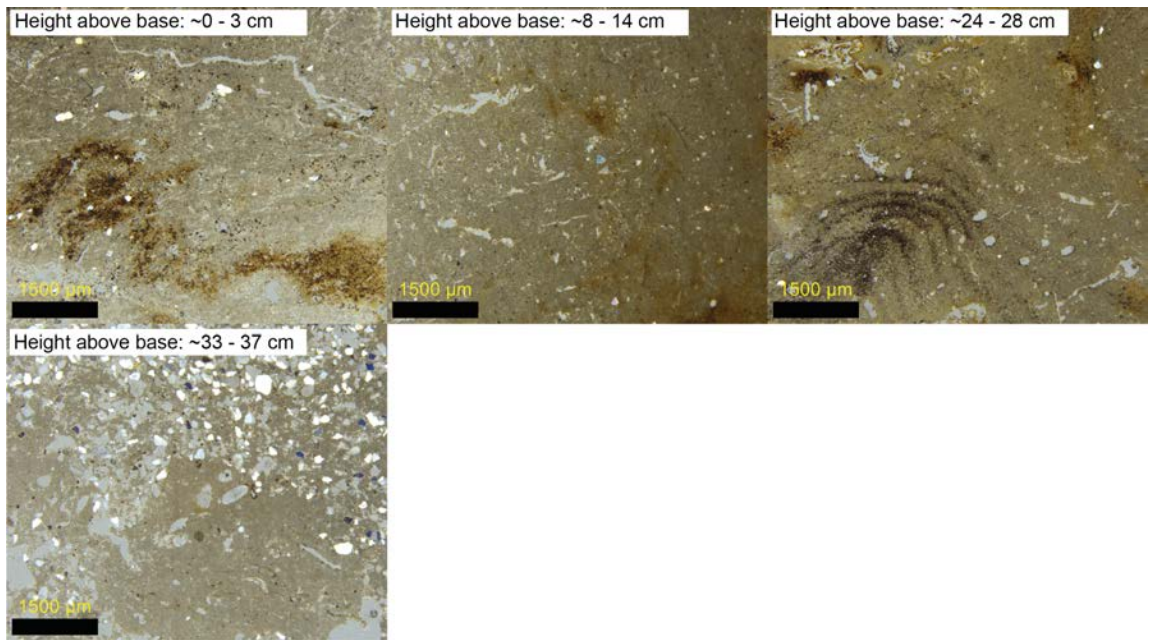


Figure A7 – Microfacies from KAM4 lake 3.

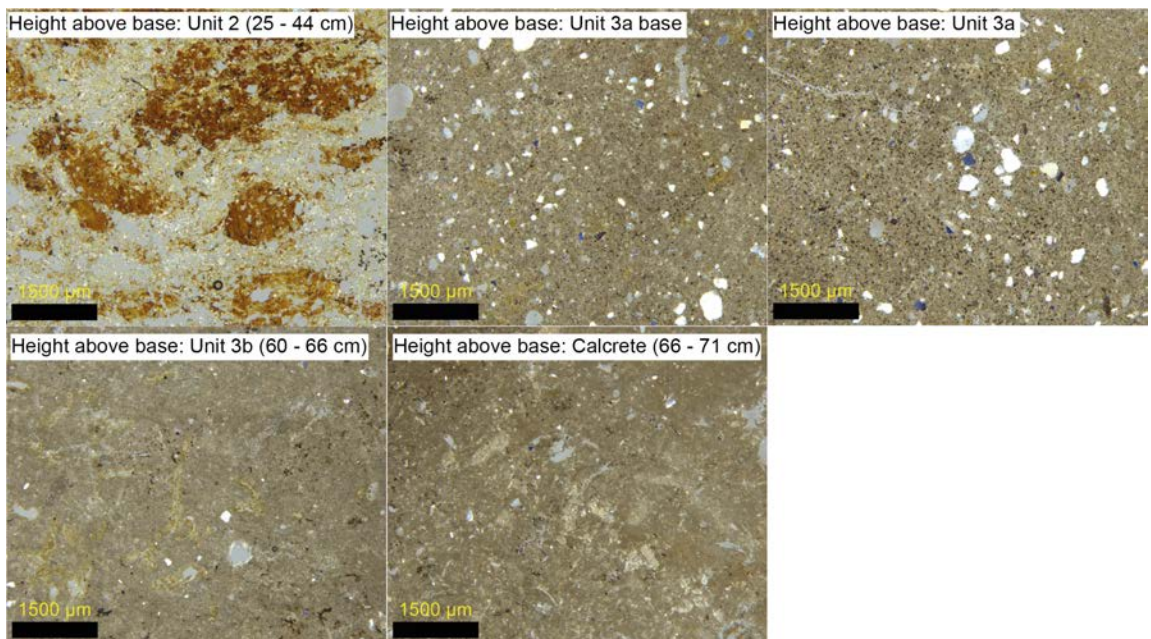


Figure A8 – Microfacies from KAM4 lake 3a.

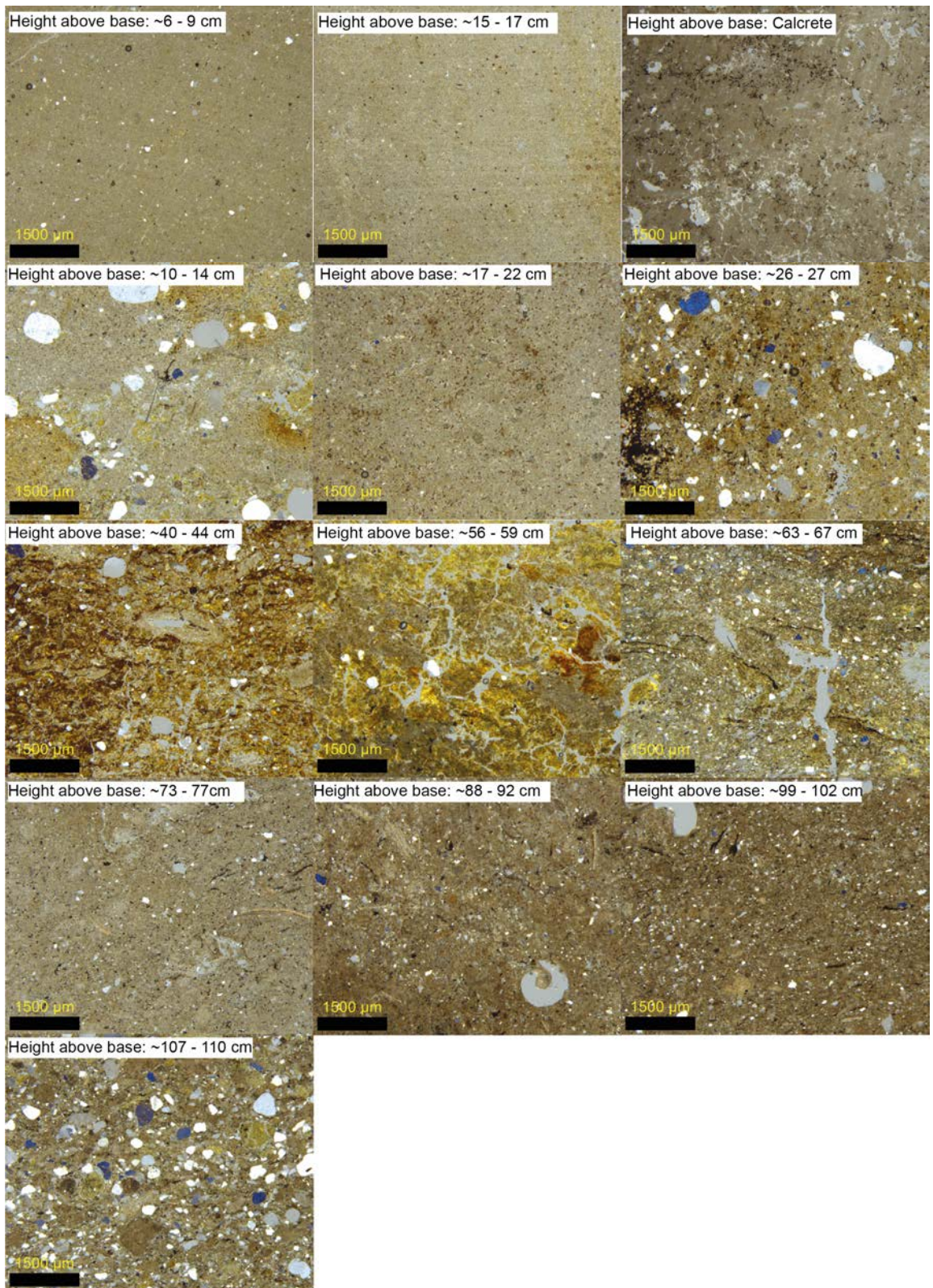


Figure A9 – Microfacies from KAM4 lake 4.

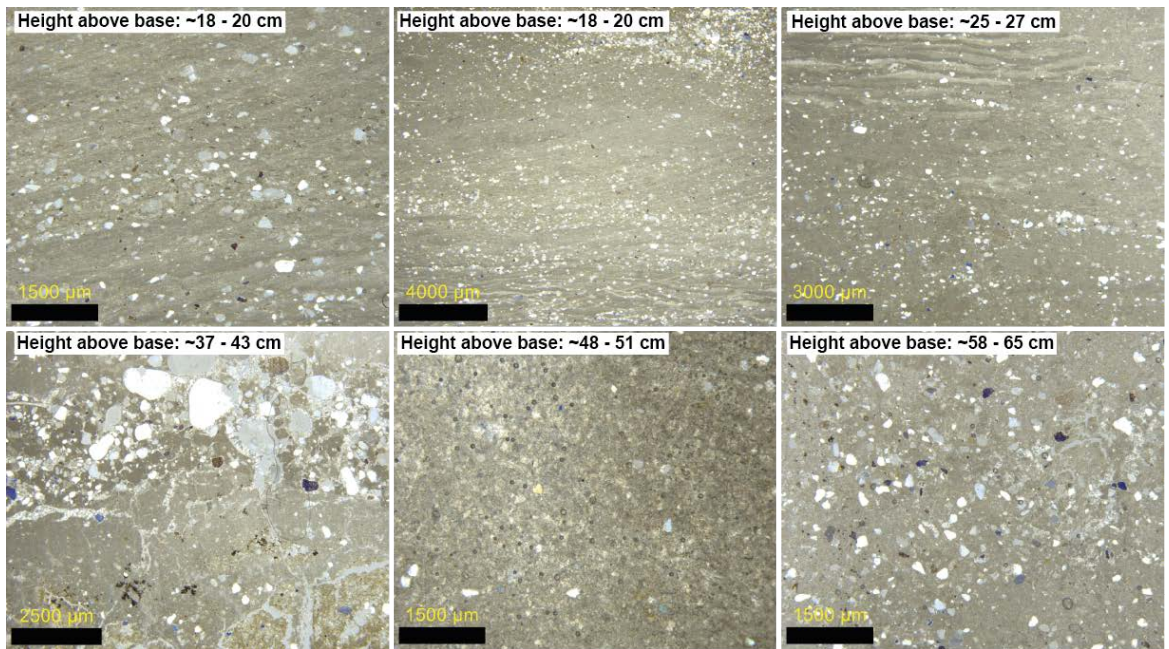


Figure A10 – Microfacies from Ti's al Ghadah 1.

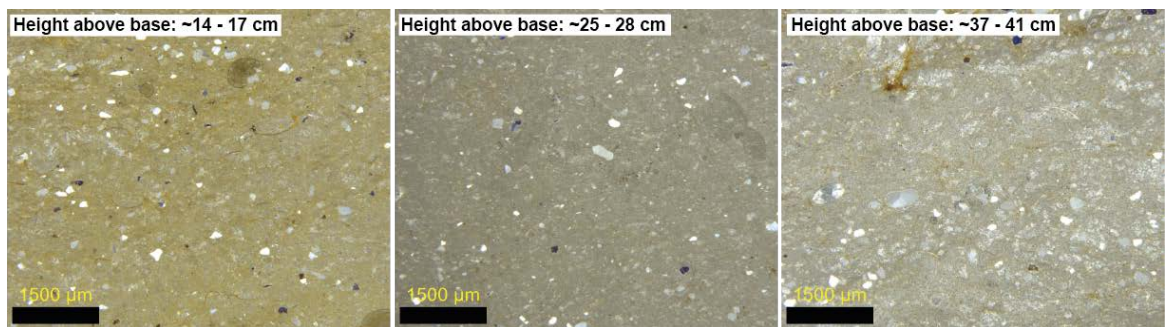


Figure A11 – Microfacies from Ti's al Ghadah 2.